FINITE ELEMENT ANALYSIS AND DESIGN OF SUSPENDED STEEL-FIBRE REINFORCED CONCRETE SLABS

OLUGBENGA BABAJIDE SOYEMI

A thesis submitted in partial fulfilment of the requirements of the University of East London for the degree of Doctor of Philosophy

August 2018

Abstract

Over the last 20 years, there has been a rapid expansion in the construction of pile-supported and elevated steel-fibre-reinforced [SFRC] concrete slabs. The use of fibres to replace some or all of the conventional steel reinforcement leads to a significant reduction in construction time. However, current guidance is limited and is dominated by approximate elastic and plastic classical solutions. The design guidelines and construction of the majority of constructed SFRC slabs is almost entirely proprietary (provided by fibre manufacturers and suppliers) and different guidelines from nations (embedded with safety concerns). As a result, designers are unwilling to underwrite current designs in the absence of adequate independent guidance.

In this research work, the behaviour of suspended SFRC slabs was studied under concentrated loadings. Available experimental data were used to study the effect of steel fibres on the post-cracking response of concrete. Subsequently, the SFRC constitutive model proposed by Lok and Xiao (1999) was adopted alongside the concrete damaged plasticity model of ABAQUS based on the validation work done. The reliability of the FE numerical model predictions was ensured by calibrating it against existing experimental data. Consequently, additional analyses were carried out examining three main case studies of SFRC slabs namely, single simply supported slabs, 4-panel pile-supported slab (i.e. statically-indeterminate) and 9-panel elevated slab. Parametric studies were carried out covering the full practical range of steel fibre dosages. The results testify that numerically steel fibres can replace rebar in slabs as obtained in the experiment and additional fibres increase the load-carrying capacity, strength and stiffness (thus enhancing response at both the serviceability and ultimate limit states). Ductility was improved by the additional Fibres, and the mode of failure was altered from brittle to ductile.

Thus three main parameters were considered in the parametric study, namely increasing the amount of fibres and characteristic strength and at the same time increasing the slab depth. The total removal of conventional reinforcement was achieved mainly by replacing them with steel-fibres. An FE numerical analysis is used to investigate the slab's structural behaviour under different loading conditions leading to transparent and well-defined design guidelines which are urgently needed by industry. Simple design equations were derived using regression analysis to estimate the yield load and the maximum load carrying capacity of the slabs with their corresponding central displacements. These equations were compared with existing design guidelines, and the equations perform better in their estimation.

List of Symbols

The following symbols were used in this thesis. Their definition is given where they were first used. Where a symbol has more than one meaning assigned to it, the correct definition will be provided where it appeared.

l	Length of Fibre
d	Equivalent diameter of a fibre
σ_C	Compressive stress in the concrete
f_{cm}	Mean value of concrete cylinder compressive strength
f_c	Peak stress
f_y	Characteristic strength in steel
σ_w	Traction applied to the crack surface
E_{cm}	Modulus of elasticity in compression
E_c	Modulus of elasticity of concrete
E_s	Modulus of elasticity of steel
f_{ck}	Characteristic compressive cylinder strength of concrete at 28 days
ε_c	Compressive strain in concrete
ε_{c1}	Compressive strain in concrete at the peak stress
ε_{cu}	Ultimate Compressive strain in concrete
σ_w	Stress at crack area
P	Applied load [maximum load obtained]
A_n	Cross-sectional area at the notch
δ	Displacement
w	Crack width
δ_p	Average displacement at peak stress
D_{BZ}^b	Energy absorption capacity [plain concrete]
$D_{BZ,2}^f$	Energy absorption capacity [influences of steel fibres]
$D_{BZ,3}^f$	Energy absorption capacity [influences of steel fibres]
M_L	Moment at mid-span
f_L	Load at the limit of proportionality
Py	Yield Load
Pmax	Peak Load
L	Span of the beam specimen
b	Width of the failed cross-section
h	Height of the failed section
T_b	Flexural toughness
δ_{tb}	Deflection of 1/150 of span
l_{cs}	Structural characteristic length
γ_c	Partial safety factor for SFRC in compression
γ_{ct}	Partial safety factor for SFRC in tension
l_x	Shorter side of a slab
l_y	Longer side of a slab
α	Moment coefficient [determined by the code]
q	Applied [action] load

M_p	Positive [sagging] moment
M_n	Negative [hogging] moment
q_u	UDL
L_e	Effective span
Q_t	Line load
q_{sw}	Self-weight of the pile supported slab
L_1	Pile to pile centres in x-direction
L_2	Pile to pile centres in y-direction
A	Cross-sectional area of the pile
l_h	Effective dimension l_h of the column head
l_{h0}	Actual dimension of the column head
l_c	Column dimension measured in the same direction as l_h
d_h	Drop height
V_{eff}	Design effective shear force
V_t	Design shear transferred to the column
v	Shear stress on a failure zone
v_{max}	Maximum shear stress at the face of the column
u_0	Perimeter of the column
τ_d	Bond stress
f_{tu}	Flexural Strength
ε_{t1}	Corresponding strain to the flexural strength
M_{cr}	Crack Moment
M_{ult}	Ultimate Moment
f_{ult}	Ultimate Load
σ_c	Compressive Strength
G_f	Fracture energy
E_0	Uniaxial initial tangent modulus
v	Poisson's ratio
α	Mean coefficient of thermal expansion
σ_t	Uniaxial cut-off tensile stress
σ_{tp}	Post-cracking uniaxial cut-off tensile stress
σ_c	Uniaxial maximum compressive stress
e_c	Uniaxial compressive strain at σ_c
σ_u	Uniaxial ultimate compressive stress u
e_u	Uniaxial strain at σ_u
ξ	Constant for tensile strain failure

Abbreviations

ACI	America Concrete Institute
ADINA	Automatic Dynamic Incremental Nonlinear Analysis
BSI	British Standard Institute
CBC	Concrete Brittle Cracking
CDP	Concrete Damaged Plasticity
CSC	Concrete Smeared Cracking
CMOD	Crack Mouth Opening Displacement
CTOD	Crack Tip Opening Displacement
ESFRC	Elevated Steel Fibre Reinforced Concrete
FEA	Finite Element Analysis
FEM	Finite Element Method
LFEA	Linear Finite Element Analysis
LVDT	Linear Vertical Displacement Transducers
MFRC	Metal-Fibre Reinforced Concrete
MFRC	Metal-Fibre Reinforced Concrete
NLFEA	Non-Linear Finite Element Analysis
SCC	Self Compacting Concrete
SFRC	Steel-Fibre Reinforced Concrete
SFRSCC	Steel-Fibre Reinforced Self Compacting Concrete
SLS	Serviceability Limit State
UDL	Uniform Distributed Load
ULS	Ultimate Limit State

List of Figures

Figure 1.1:	Plain concrete in bending	2
Figure 1.2:	(a) Crack Patter in Concrete with No Reinforcement when Load is applied	3
	(b) Crack Patter in Concrete with Steel Reinforcement when Load is applied	3
Figure 1.3:	Typical Slab Reinforcement laid on [a] Pile Foundation and [b] columns	4
Figure 1.4:	A Typical Pile-Supported Slab Layout	5
Figure 1.5:	Pile-Supported Floor Slab for Warehouse Partly finished	6
Figure 1.6:	Applications of FRC	11
Figure 1.7:	Research Outlay	13
Figure 2.1:	Sources of Fibres	19
Figure 2.2:	Types of Steel-Fibre (The Concrete Society TR63, 2007)	21
Figure 2.3:	Dramix™ RC-65/35-BN and [b] TABIX-Twincone (Bekaert, 2012, ArcelorMittal, 2011)	21
Figure 2.4:	Stress-Strain Relation of concrete in compression (BSI 2004)	23
Figure 2.5:	Stress-strain graph adapted from (Kooiman, 2000)	24
Figure 2.6:	Setup of [a] Flexural test on notched beam [b] Fracture energy evaluation	25
Figure 2.7:	Typical stress distributions in a concrete section subjected to four-point bending (Tlemat et al., 2006a)	26
Figure 2.8:	Schematic description of stress-crack opening for [a] plain concrete and [b] SFRC. Adapted from (Löfgren, 2005)	27
Figure 2.9:	High performance SFRC. Adapted from (Kooiman, 2000)	28
Figure 2.10:	Typical set-up for uni-axial tension testing (RILEM, 2001)	29
Figure 2.11:	Crack width Opening w calculation (RILEM, 2001)	30
Figure 2.12:	3-Point bending test set-up (Fall, 2014)	30
Figure 2.13:	[a-c] Load – deflection graphs [d] Load-CMOD graph	31
Figure 2.14:	4-point bending test adapted from (Kooiman, 2000)	33
Figure 2.15:	Load – deflection Curve (JCI Test)	33
Figure 2.16:	Schematic diagram of statically determinate round panel (Bernard, 2000)	34
Figure 2.17:	Load-deflection responses of [a] beams and [b] plates (Sukontasukkul, 2003)	35
Figure 2.18:	Compressive Stress-Strain of SFRC adapted from BS 8110	38
Figure 2.19:	Tensile Stress-Strain Relationship adapted from (Lok and Xiao, 1998)	39
Figure 2.20:	Compression stress-strain diagram (Barros and Figueiras, 1999)	42
Figure 2.21:	Proposed tensile stress-strain diagram adapted from (Barros and Figueiras, 1999)	43
Figure 2.22:	Schematic representation of fracture energy evaluation adapted from (Barros and Figueiras, 1999)	43
Figure 2.23:	Stress-Strain Diagram adapted from (RILEM, 2002b)	44
Figure 2.24:	3-Point Bending Test with 25mm Notch adapted from (RILEM, 2002b)	45

Figure 2.25: Load-Displacement Diagram adapted from (RILEM, 2000) 45
Figure 2.26: Tensile behaviour of SFRC adapted from (Lok and Xiao, 1998) 46
Figure 2.27: Stress-Strain constitutive model adapted from (Lok and Xiao, 1999) 47
Figure 2.28: One and Two-way slabs 51
Figure 2.29: Yield Line Development in 2-way slab 53
Figure 2.30: Folded plate yield line mechanism (The Concrete Society TR34, 2014) 54
Figure 2.31: Folded plate yield line mechanism (The Concrete Society TR34, 2014) 55
Figure 2.32: Fan yield line mechanism at pile (The Concrete Society TR34, 2014) 56
Figure 2.33: Diagrammatic Representation of Modelling Pile-Supported SFRC slabs in [a] 3D-Brick and [b] spring 57
Figure 2.34: Flat slab arrangement for a floor with [a] square columns and [b] drop panels (British Standard Institute, 1997) 60
Figure 2.35: Punching Shear Failure Mechanism Misconception 64
Figure 2.36: Punching Shear Failure Mechanism 64
Figure 2.37: Punching Shear at the support or loading area 67
Figure 2.38: Simplified stress block adapted from (TR 63, 2007) 72
Figure 2.39: Simplified stress block at ULS adapted from (NEN 6720) 73
Figure 2.40: Simplified stress block at SLS adapted from (NEN 6720) 74
Figure 2.41: Simplified stress block adapted fib Model Code 2010 (MC2010) 77

Figure 3.1: Truss Elements available in ADINA (adapter from ADINA 2012) 91
Figure 3.2: 2-D Solid Elements (adapter from ADINA 2012) 92
Figure 3.3: 3-D Solid elements adapted from (ADINA, 2012) 93
Figure 3.4: Linear and Bilinear Stress-Strain Models for Steel 94
Figure 3.5: Uniaxial stress-strain relation adapted from (ADINA, 2012) 95
Figure 3.6: Three-dimensional tensile failure envelope of concrete model (ADINA 2012) 98
Figure 3.7: Biaxial concrete compressive failure envelope (adapter from ADINA 2012) 99
Figure 3.8: Triaxial compressive failure envelope (adapter from ADINA 2012) 99
Figure 3.9: Material Moduli for Stress Calculation after Tensile Failure (adapter from ADINA 2012) 101
Figure 3.10: Stress-strain behaviour of DF-concrete adapted from (ADINA, 2012) 102
Figure 3.11: Failure Surface of the Data Fitted Concrete Material Model (adapter from ADINA 2012) 103
Figure 3.12: First crack formation of the data fitted concrete material model (a) before, and (b) after 104
Figure 3.13: Second crack formation of the data fitted concrete material model (a) before, and (b) after 104
Figure 3.14: Third crack formation of the data fitted concrete material model (a) before, and (b) after 104
Figure 3.15: Stress-strain behaviour of the data fitted concrete material model 106

Figure 3.16:	Element models in ABAQUS adapted from ABAQUS (2009)	108
Figure 3.17:	ABAQUS 2-D Solid Elements (adapter from ABAQUS 2012)	109
Figure 3.18:	ABAQUS 3-D Solid Elements (adapter from ABAQUS 2012)	110
Figure 3.19:	Uniaxial concrete behaviour adapted from (ABAQUS, 2009)	112
Figure 3.20:	Tension Stiffening Model (adapter from ABAQUS 2012)	113
Figure 3.21:	Stress-Strain Relation of concrete in compression adapted from (BS EN 1992-1-1)	116
Figure 3.22:	Compressive inelastic (or crushing) strain defining compression hardening data adapted from ABAQUS (2012)	117
Figure 3.23:	Response of Concrete to Uniaxial Loading in Compression adapted from ABAQUS (2012)	118
Figure 3.24:	Compressive Stress-Strain Curve	119
Figure 3.25:	Response of Concrete to Uniaxial Loading in tension adapted from ABAQUS (2012)	119
Figure 3.26:	Tensile Stress-Strain Curve based on Lok and Xiao (1999)	120
Figure 3.27:	Post-Failure Stress-Strain Curve adapted from ABAQUS (2012)	120
Figure 3.28:	Power Law Form of the Shear Retention Model adapted from ABAQUS (2012)	121
Figure 3.29:	Stress-strain graph Adapted from (RILEM, 2000)	123
Figure 3.30:	Schematic diagrams of crack opening without and with fibres adapted from (RILEM, 2002a)	124
Figure 3.31:	The principle of [a] single cracking and [b] multiple cracking adapted from (RILEM, 2002a)	124
Figure 3.32:	Round-Plate simply supported over (a) Isolated, (b) Continuous Supports and (c) Square-Panel with Edge supports	126
Figure 3.33:	4-Panel SFRC Slab (a) without rebar and (b) with rebar	127
Figure 3.34:	9-Panel SFRC Slab	128
Figure 4.1:	Cross-section of the Bresler-Scordelis (1963) beam	132
Figure 4.2:	Test setup for Bresler-Scordelis (1963) beam	133
Figure 4.3:	FE Model of Bresler-Scordelis (1963) beam	133
Figure 4.4:	Load-Deflection Graph for Sensitivity Analysis Bresler-Scordelis (1963) beam [ADINA]	133
Figure 4.5:	Load-Deflection Graph for Sensitivity Analysis Bresler-Scordelis (1963) beam [ABAQUS]	134
Figure 4.6:	FE Model of Bresler-Scordelis (1963) Beam [a] ADINA and [b] ABAQUS	135
Figure 4.7:	Crack pattern in Bresler-Scordelis (1963) beam [Experiment]	135
Figure 4.8:	Crack pattern for Bresler-Scordelis (1963) beam [ADINA]	136
Figure 4.9:	Crack pattern for Bresler-Scordelis (1963) beam [ABAQUS]	137
Figure 4.10:	Load-Deflection curve for Bresler-Scordelis (1963) beam	138
Figure 4.11:	Load-Deflection curve for Bresler-Scordelis (1963) beam	139
Figure 4.12:	Load-Deflection curve [Best Fits] for Bresler-Scordelis (1963) beam	139
Figure 4.13:	Set-up for Experiment for Hughes and Speirs (1982) Beam	140
Figure 4.14:	Crack pattern in Hughes and Speirs (1982) Beam [Experiment]	142
Figure 4.15:	Crack pattern in Hughes and Speirs (1982) Beam [ADINA]	143

Figure 4.16: Crack pattern in Hughes and Speirs (1982) Beam [ABAQUS] 143
Figure 4.17: Load-Deflection curve of Hughes and Speirs (1982) Beam [ADINA] 143
Figure 4.18: Load-Deflection curve of Hughes and Speirs (1982) Beam [ABAQUS] 143
Figure 4.19: Load-Deflection curve [Best Fits for ADINA and ABAQUS] 144
Figure 4.20: Experiment Setup for Barros et al SFRC Beam 2005 145
Figure 4.21: Tensile Stress-Strain Curve for Constitutive Models Barros et al SFRC Beam 2005 147
Figure 4.22: Crack-Pattern in [a] ADINA-Conc, [b] ABAQUS and [c] ADINA-DF for Barros et al SFRC Beam 2005 148
Figure 4.23: Barros et al SFRC Beam (2005) Load-Displacement Curve [ABAQUS] 148
Figure 4.24: Barros et al SFRC Beam (2005) Load-Displacement Curve [ADINA] 149
Figure 4.25: SFRC tensile Modelling in [a] ADINA-Conc and [b] ADINA-DF 149
Figure 4.26: Experiment Setup for de Montaignac et al (2011) SFRC Beam 150
Figure 4.27: Tensile Stress-Strain Curve for de Montaignac et al SFRC Beam (2011) 151
Figure 4.28: Crack Pattern for de Montaignac et al SFRC Beam (2011) 152
Figure 4.29: Load-Displacement Curve for de Montaignac et al SFRC Beam (2011) 153
Figure 4.30: Experimental Set-up for Tlemat et al (2006) SFRC Beam 154
Figure 4.31: Tensile Stress-Strain Curve for Tlemat et al SFRC Beam (2006) with V_f = 1.5% 154
Figure 4.32: Crack patterns for Tlemat et al (2006) [ABAQUS] 156
Figure 4.33: Load-Displacement Curve for Tlemat et al SFRC Beam (2006) 156
Figure 4.34: Experiment Setup for Olivito and Zuccarello's SFRC Beam (2010) 157
Figure 4.35: Tensile Stress-Strain Curve for Olivito and Zuccarello's SFRC Beam (2010) 158
Figure 4.36: Crack patterns for Olivito and Zuccarello's SFRC Beam (2010) 159
Figure 4.37: Load-Displacement Curve for Olivito and Zuccarello's SFRC Beam (2010) 159
Figure 4.38: Panel Testing in the Lab Hadi (2008) Square Plate 160
Figure 4.39: Tensile Stress-Strain Curve for Hadi's SFRC Square Panel (2008) 161
Figure 4.40: Crack patterns in Hadi's SFRC Slab (2008) [a] ABAQUS and [b] ADINA 162
Figure 4.41: Load-Displacement Curve for Hadi's SFRC Slab (2008) [a] ABAQUS and [b] ADINA 163
Figure 4.42: Tensile Stress-Strain Curve for Blanco et al's SFRC Panel (2015) 164
Figure 4.43: Crack Pattern Results [a] Experiment and [b] ABAQUS CDP 166
Figure 4.44: Load-Displacement Curve for Blanco et al's SFRC Panel (2015) 166
Figure 4.45: Experiment Set-up Montaignac et al RP (2011) 167
Figure 4.46: Crack patterns Top and Bottom [ABAQUS] Montaignac et al RP (2011) 168
Figure 4.47: Load-Displacement Curve for Montaignac et al RP (2011) 168
Figure 4.48: Experimental Setup of Soranakom et al Round Plate (2007) 169
Figure 4.49: Crack Patterns of Soranakom et al Round Plate (2007) 169
Figure 4.50: Tensile Stress-Strain Curve for Soranakom et al. Round Plate

(2007) 170
Figure 4.51: NLFEA Results of Soranakom et al Round Plate (2007) [a] Crack Pattern [b] Displacement and [c] Reaction at the support 172
Figure 4.52: Load-Displacement Curve for Soranakom et al Round Plate (2007) 172
Figure 4.53: Experimental set-up for Bernard (2000) Round Plate 173
Figure 4.54: Tensile Stress-Strain Curve for Bernard (2000) Round Plate 174
Figure 4.55: Crack Patterns in Bernard (2000) Round Plate [a] pictorial diagram of collapse mechanism [b] x-z section of the damaged panel through the centre [c] FEA crack pattern at full damage [d] FEA crack propagation at early stage 175
Figure 4.56: Load-Displacement Curve for Bernard (2000) Round Plate 175
Figure 4.57: FE representation of the Test set-up for Destree and Mandl (2008) 176
Figure 4.58: FEA Results showing Cracking Pattern at (a) bottom and (b) internal 177
Figure 4.59: Experimental Set-up of Thooft (1999) 4-Panels Slab 178
Figure 4.60: Tensile Stress-Strain Curve for Thooft (1999) Pile-Supported Slab 179
Figure 4.61: Top and Bottom face after cracking in Experimental work (Thooft, 1999) 180
Figure 4.62: FEA Results showing Cracking Pattern at (a) Top and (b) Bottom 180
Figure 4.63: Load-Displacement Curve for Thooft (1999) Pile-Supported Slab 181
Figure 4.64: Geometry of the built prototype (Barros et al 2012) 181
Figure 4.65: Prototype model of Barros et al (2012) 182
Figure 4.66: FEA Modelling of Barros et al (2012) slab 183
Figure 4.67: FEA Crack pattern of Barros et al slab [a] top and [b] bottom 183

Figure 5.1: Dimensions of Round-Plate adapted from (de Montaignac et al., 2011) 188
Figure 5.2: Tensile Stress-strain Parameters for SFRC (de Montaignac et al., 2011) 189
Figure 5.3: Tensile Stress-strain Parameters for SFRC at fcu with Different fibre volume ratios 190
Figure 5.4: Frequency-Time input Data for Loading 191
Figure 5.5: Load-Displacement Curve for range of V_f 192
Figure 5.6: Load-Displacement Curve for range of V_f = 1.00% - 2.50% 193
Figure 5.7: Load-Displacement Curve for range of V_f at f_{ck}= 30MPa – 60MPa 195
Figure 5.8: Yield load and Fibre Volume Ratio Graphs for V_f 200
Figure 5.9: Peak load and Fibre Volume Ratio Graphs for f_{cu} 200
Figure 5.10: Displacement at Yield load and Fibre Volume Ratio Graphs for f_{cu} 202
Figure 5.11: Displacement at Peak load and Fibre Volume Ratio Graphs for f_{cu} 202
Figure 5.12: Tensile Strain-Displacement Curve for range of V_f 203
Figure 5.13: Load-Displacement Curve for range of V_f up to 35mm displacement 203
Figure 5.14: Tensile Strain-Displacement Curve for range of V_f [a=1.00, b=1.25, c=1.50, d=1.75, e=2.00 and f=2.5%] 204
Figure 5.15: Principal strain contour for Case Study 1A with V_f [a= 1.00, b=1.25, c=1.50, d=1.75, e=2.00 and f=2.50%] 208
Figure 5.16: Principal strain vector for Case Study 1A with V_f = [a] 1.00%

[b] 1.25% [c] 1.50% [d] 1.75% [e] 2.00% and [f] 2.50% 209
Figure 5.17: Principal strain vector [section y-y] for Case Study 1A with V_f = [a] 1.00% [b] 1.25% [c] 1.50% [d] 1.75% [e] 2.00% and [f] 2.50% 210
Figure 5.18: Compressive Damaged patterns at the bottom of the round-plate with V_f = [a] 1.00% [b] 1.25% [c] 1.50% [d] 1.75% [e] 2.00% and [f] 2.50% 211
Figure 5.19: Compressive Damaged patterns at the top of the round-plate with V_f = [a] 1.00% [b] 1.25% [c] 1.50% [d] 1.75% [e] 2.00% and [f] 2.50% 211
Figure 5.20: Tensile Damaged patterns at the bottom of the round-plate with V_f = [a] 1.00% [b] 1.25% [c] 1.50% [d] 1.75% [e] 2.00% and [f] 2.50% 212
Figure 5.21: Tensile Damaged patterns at the bottom of the round-plate with V_f = [a] 1.00% [b] 1.25% [c] 1.50% [d] 1.75% [e] 2.00% and [f] 2.50% 212
Figure 5.22: Deflected Shapes [y-y] for the round-plate with V_f = [a] 1.00% [b] 1.25% [c] 1.50% [d] 1.75% [e] 2.00% and [f] 2.50% 213
Figure 5.23: Graph of V_f against P_{max}/P_{maxc} for f_{cu} for Case Study 1A 214
Figure 5.24: Graph of V_f against P_y/P_{yc} for f_{cu} for Case Study 1A 214
Figure 5.25: Graph of V_f against $\mu/\mu c$ for f_{cu} for Case Study 1A 215
Figure 5.26: Schematic representation of experimental set-up for Case Study 1B 215
Figure 5.27: Tensile Stress-strain Parameters for SFRC round-Panel in Case Study 1B 216
Figure 5.28: Load-Displacement Curve for range of V_f for Case Study 1B 217
Figure 5.29: Deflected Shapes [y-y] for the Case Study 1B round-plate with V_f = [a] 1.00% [b] 1.25% [c] 1.50% [d] 1.75% [e] 2.00% and [f] 2.50% 219
Figure 5.30: Principal strain contour for Case Study 1B with V_f [a= 1.00, b=1.25, c=1.50, d=1.75, e=2.00 and f=2.50%] 220
Figure 5.31: Principal strain vector for Case Study 1B with V_f = [a] 1.00% [b] 1.25% [c] 1.50% [d] 1.75% [e] 2.00% and [f] 2.50% 221
Figure 5.32: Principal strain vector for Case Study 1B [section y-y] with V_f = [a] 1.00% [b] 1.25% [c] 1.50% [d] 1.75% [e] 2.00% and [f] 2.50% 222
Figure 5.33: Tensile Damaged patterns at the top of the round-plate with V_f = [a] 1.00% [b] 1.25% [c] 1.50% [d] 1.75% [e] 2.00% and [f] 2.50% 223
Figure 5.34: Tensile Damaged patterns at the bottom of the round-plate with V_f = [a] 1.00% [b] 1.25% [c] 1.50% [d] 1.75% [e] 2.00% and [f] 2.50% 224
Figure 5.35: Compressive Damaged patterns at the top of the round-plate with V_f = [a] 1.00% [b] 1.25% [c] 1.50% [d] 1.75% [e] 2.00% and [f] 2.50% 225
Figure 5.36: Compressive Damaged patterns at the bottom of the round-plate with V_f = [a] 1.00% [b] 1.25% [c] 1.50% [d] 1.75% [e] 2.00% and [f] 2.50% 226

Figure 5.37:	Graph of V_f against P_{max}/P_{maxc} for Case Study 1B	227
Figure 5.38:	Graph of V_f against μ_y/μ_c for Case Study 1B	227
Figure 5.39:	Schematic representation of the experimental set-up for Case Study 1C	228
Figure 5.40:	Tensile stress-strain diagram	229
Figure 5.41:	Load-Displacement Curves of Experiment and FEA	229
Figure 5.42:	Tensile Stress-Strain Curve for Input Parameters for V_f	230
Figure 5.43:	Load-Displacement Curve for V_f	231
Figure 5.44:	Principal Strain Contours [section y-y] for Case Study 1C with V_f = [a] 1.00% [b] 1.25% [c] 1.50% [d] 1.75% [e] 2.00% and [f] 2.50%	232
Figure 5.45:	Principal Strain Contours for Case Study 1C with V_f = [a] 1.00% [b] 1.25% [c] 1.50% [d] 1.75% [e] 2.00% and [f] 2.50%	233
Figure 5.46:	Principal Strain Vectors for Case Study 1C with V_f = [a] 1.00% [b] 1.25% [c] 1.50% [d] 1.75% [e] 2.00% and [f] 2.50%	234
Figure 5.47:	Tensile Damaged patterns at the bottom of the square-panel with V_f = [a] 1.00% [b] 1.25% [c] 1.50% [d] 1.75% [e] 2.00% and [f] 2.50%	235
Figure 5.48:	Compressive Damaged patterns at the bottom of the square-panel with V_f = [a] 1.00% [b] 1.25% [c] 1.50% [d] 1.75% [e] 2.00% and [f] 2.50%	236
Figure 5.49:	Deflected Shapes [x-y plane] for the Case Study 1C square-panel with V_f = [a] 1.00% [b] 1.25% [c] 1.50% [d] 1.75% [e] 2.00% and [f] 2.50%	237
Figure 5.50:	Graph of V_f against P_{max}/P_{maxc} for Case Study 1C	238
Figure 5.51:	Graph of V_f against μ/μ_c for Case Study 1C	238
Figure 6.1:	Experimental Set-up (Thooft 1999)	243
Figure 6.2:	Tensile Stress-Strain Curve	245
Figure 6.3:	Load-Displacement Curve for Sensitivity Analysis	245
Figure 6.4:	Tensile Stress-Strain Curves for different fibre volume ratios [V_f]	246
Figure 6.5:	Loading Pattern of Slab without Rebar [Full and Quarter-Size]	247
Figure 6.6:	Load-Displacement Curves for Experiment and FEA	249
Figure 6.7:	Comparison between Experimental and FEA Crack Pattern [Top]	250
Figure 6.8:	Comparison between Experimental and FEA Crack Pattern [Soffit]	250
Figure 6.9:	Principal Strain Vector and Deflected Shape of FEA Model	251
Figure 6.10:	Load-Displacement Curves for various V_f under Dual Loading	253
Figure 6.11:	Principal Strain Contours for Pile-Supported SFRC Slab without Rebar with V_f [a]= 1.00%, [b]= 1.25%, [c]= 1.50%, [d]= 1.75%, [e]= 2.00% and [f]= 2.5%	254
Figure 6.12:	Principal Strain Vectors for Pile-Supported SFRC Slab without Rebar with V_f [a]= 1.00%, [b]= 1.25%, [c]= 1.50%, [d]= 1.75%, [e]= 2.00% and [f]= 2.5%	256
Figure 6.13:	Deflected Shapes for Pile-Supported SFRC Slab without Rebar with V_f [a]= 1.00%, [b]= 1.25%, [c]= 1.50%, [d]= 1.75%, [e]= 2.00% and [f]= 2.5%	257

Figure 6.14: Tensile Damaged Shapes for Pile-Supported SFRC Slab without Rebar with V_f [a]= 1.00%, [b]= 1.25%, [c]= 1.50%, [d]= 1.75%, [e]= 2.00% and [f]= 2.5% 258
Figure 6.15: Graph of V_f against $P_{max}/P_{max,c}$ 260
Figure 6.16: Graph of V_f against $P_y/P_{y,c}$ 260
Figure 6.17: Graph of V_f against μ/μ_c 261
Figure 6.18: Load-Displacement Curves for various V_f with f_{cu}=30MPa [Slab without Rebar] 263
Figure 6.19: Load-Displacement Curves for various V_f with f_{cu}=40MPa [Slab without Rebar] 263
Figure 6.20: Load-Displacement Curves for various V_f with f_{cu}=50MPa [Slab without Rebar] 263
Figure 6.21: Graph of V_f against $P_y/P_{y,c}$ with varying f_{cu} [Slab without Rebar] 264
Figure 6.22: Graph of V_f against $P_{max}/P_{max,c}$ with varying f_{cu} [Slab without Rebar] 264
Figure 6.23: Loading Pattern of Slab with Rebar [Full and Quarter-Size] 266
Figure 6.24: Load-Displacement Curves for Experiment and FEA [Slab with Rebar] 268
Figure 6.25: Comparison between Experimental and FEA Crack Pattern [a] Top and [b] soffit [Slab with Rebar] 269
Figure 6.26: Damaged Plasticity and Principal Strain Vector Shape of FEA Model [Slab with Rebar] 269
Figure 6.27: Load-Displacement Curves for various V_f [Slab with Rebar] 271
Figure 6.28: Principal Strain Contours for Pile-Supported SFRC Slab with Rebar with V_f [a]= 1.00%, [b]= 1.25%, [c]= 1.50%, [d]= 1.75%, [e]= 2.00% and [f]= 2.5% 272
Figure 6.29: Principal Strain Vectors for Pile-Supported SFRC Slab with Rebar with V_f [a]= 1.00%, [b]= 1.25%, [c]= 1.50%, [d]= 1.75%, [e]= 2.00% and [f]= 2.5% 273
Figure 6.30: Deflected Shapes for Pile-Supported SFRC Slab with Rebar with V_f [a]= 1.00%, [b]= 1.25%, [c]= 1.50%, [d]= 1.75%, [e]= 2.00% and [f]= 2.5% 274
Figure 6.31: Tensile Damaged Shapes for Pile-Supported SFRC Slab with Rebar with V_f [a]= 1.00%, [b]= 1.25%, [c]= 1.50%, [d]= 1.75%, [e]= 2.00% and [f]= 2.5% 275
Figure 6.32: Graph of V_f against $P_{max}/P_{max,c}$ [Slab with Rebar] 276
Figure 6.33: Graph of V_f against $P_y/P_{y,c}$ [Slab with Rebar] 277
Figure 6.34: Graph of V_f against μ/μ_c [Slab with Rebar] 277
Figure 6.35: Load-Displacement Curves for various V_f with f_{cu}=30MPa [Slab with Rebar] 279
Figure 6.36: Load-Displacement Curves for various V_f with f_{cu}=40MPa [Slab with Rebar] 279
Figure 6.37: Load-Displacement Curves for various V_f with f_{cu}=50MPa [Slab with Rebar] 279
Figure 6.38: Graph of V_f against $P_y/P_{y,c}$ with varying f_{cu} [Slab with Rebar] 280

Figure 6.39: Graph of V_f against $P_{max}/P_{max,c}$ with varying f_{cu} [Slab with Rebar] 280
Figure 6.40: Graph of V_f against μ/μ_c with varying f_{cu} [Slab with Rebar] 281
Figure 6.41: Load-Displacement Curve for SFRC with and without Rebar 283

Figure 7.1: Picture of the full-scale testing of the 9-Panel slab (Destrée, 2001) 288
Figure 7.2: Tensile Stress-Strain Curve 289
Figure 7.3: Load-Displacement Curve for Sensitivity Analysis 289
Figure 7.4: Tensile Stress-Strain Curves for different fibre volume ratios [V_f] 290
Figure 7.5: Loading Patterns at ULS [Full-Size] 291
Figure 7.6: Loading Pattern at ULS [Quarter-Size] for Middle Panel 292
Figure 7.7: Load-Displacement Curves for Experiment and FEA for Middle Panel 293
Figure 7.8: Load-Displacement Curves for various fibre volume ratio V_f for Middle Panel 295
Figure 7.9: Principal Strain Contours for Middle Panel with V_f [a]= 1.00%, [b]= 1.25%, [c]= 1.50%, [d]= 1.75%, [e]= 2.00% and [f]= 2.5% 296
Figure 7.10: Principal Strain Vectors for Middle Panel with V_f [a]= 1.00%, [b]= 1.25%, [c]= 1.50%, [d]= 1.75%, [e]= 2.00% and [f]= 2.5% 298
Figure 7.11: Deflected Shapes for Middle Panel with V_f [a]= 1.00%, [b]= 1.25%, [c]= 1.50%, [d]= 1.75%, [e]= 2.00% and [f]= 2.5% 299
Figure 7.12: Tensile Damaged Shapes for Middle Panel with V_f [a]= 1.00%, [b]= 1.25%, [c]= 1.50%, [d]= 1.75%, [e]= 2.00% and [f]= 2.5% 300
Figure 7.13: Graph of V_f against $P_y/P_{y,c}$ for Middle Panel 302
Figure 7.14: Graph of V_f against $P_{max}/P_{max,c}$ for Middle Panel 302
Figure 7.15: Load-Displacement Curves for various f_{cu} with fibre volume ratio V_f =1.00% for Middle Panel 304
Figure 7.16: Load-Displacement Curves for various f_{cu} with fibre volume ratio V_f =1.25% for Middle Panel 304
Figure 7.17: Load-Displacement Curves for various f_{cu} with fibre volume ratio V_f =1.50% for Middle Panel 304
Figure 7.18: Load-Displacement Curves for various f_{cu} with fibre volume ratio V_f =1.75% for Middle Panel 305
Figure 7.19: Load-Displacement Curves for various f_{cu} with fibre volume ratio V_f =2.00% for Middle Panel 305
Figure 7.20: Load-Displacement Curves for various f_{cu} with fibre volume ratio V_f =2.50% for Middle Panel 305
Figure 7.21: Graph of V_f against $P_y/P_{y,c}$ with varying f_{cu} for Middle Panel 306
Figure 7.22: Graph of V_f against $P_{max}/P_{max,c}$ with varying f_{cu} for Middle Panel 307
Figure 7.23: Loading Pattern at ULS [Quarter-Size] for Edge Panel 310
Figure 7.24: Load-Displacement Curves for Experiment and FEA for Edge Panel 311
Figure 7.25: Load-Displacement Curves for various fibre volume ratio V_f for Edge Panel 313
Figure 7.26: Comparison between Crack Patterns in Experiment and FEA for Edge Panel 313

Figure 7.27: Principal Strain Contours for Edge Panel with V_f [a]= 1.00%, [b]= 1.25%, [c]= 1.50%, [d]= 1.75%, [e]= 2.00% and [f]= 2.5% 314
Figure 7.28: Principal Strain Vectors for Edge Panel with V_f [a]= 1.00%, [b]= 1.25%, [c]= 1.50%, [d]= 1.75%, [e]= 2.00% and [f]= 2.5% 315
Figure 7.29: Deflected Shapes for Edge Panel with V_f [a]= 1.00%, [b]= 1.25%, [c]= 1.50%, [d]= 1.75%, [e]= 2.00% and [f]= 2.5% 316
Figure 7.30: Tensile Damaged Shapes [Top and Soffit] for Edge Panel with V_f [a]= 1.00%, [b]= 1.25%, [c]= 1.50%, [d]= 1.75%, [e]= 2.00% and [f]= 2.5% 317
Figure 7.31: Graph of V_f against $P_y/P_{y,c}$ for Edge Panel 318
Figure 7.32: Graph of V_f against $P_{max}/P_{max,c}$ for Edge Panel 219
Figure 7.33: Load-Displacement Curves for various V_f with f_{cu}=30MPa for Edge Panel 321
Figure 7.34: Load-Displacement Curves for various V_f with f_{cu}=40MPa for Edge Panel 321
Figure 7.35: Load-Displacement Curves for various V_f with f_{cu}=50MPa for Edge Panel 321
Figure 7.36: Graph of V_f against $P_y/P_{y,c}$ with varying f_{cu} for Edge Panel 322
Figure 7.37: Graph of V_f against $P_{max}/P_{max,c}$ with varying f_{cu} for Edge Panel 323
Figure 7.38: Loading Pattern at ULS [Quarter-Size] for Corner Panel 325
Figure 7.39: Load-Displacement Curve for Validation work for Corner Panel 326
Figure 7.40: Comparison between Crack Patterns in Experiment and FEA for Corner Panel 327
Figure 7.41: Load-Displacement Curves for various fibre volume ratio V_f for Corner Panel 328
Figure 7.42: Principal Strain Contours for Corner Panel with V_f [a]= 1.00%, [b]= 1.25%, [c]= 1.50%, [d]= 1.75%, [e]= 2.00% and [f]= 2.5% 330
Figure 7.43: Principal Strain Vectors for Corner Panel with V_f [a]= 1.00%, [b]= 1.25%, [c]= 1.50%, [d]= 1.75%, [e]= 2.00% and [f]= 2.5% 331
Figure 7.44: Deflected Shapes for Corner Panel with V_f [a]= 1.00%, [b]= 1.25%, [c]= 1.50%, [d]= 1.75%, [e]= 2.00% and [f]= 2.5% 332
Figure 7.45: Tensile Damaged Shapes [Top and Soffit] for Corner Panel with V_f [a]= 1.00%, [b]= 1.25%, [c]= 1.50%, [d]= 1.75%, [e]= 2.00% and [f]= 2.5% 333
Figure 7.46: Graph of V_f against $P_{max}/P_{max,c}$ for Corner Panel 334
Figure 7.47: Graph of V_f against $P_y/P_{y,c}$ for Corner Panel 335
Figure 7.48: Load-Displacement Curves for various V_f with f_{cu}=30MPa for Corner Panel 337
Figure 7.49: Load-Displacement Curves for various V_f with f_{cu}=40MPa for Corner Panel 337
Figure 7.50: Load-Displacement Curves for various V_f with f_{cu}=50MPa for Corner Panel 337
Figure 7.51: Graph of V_f against $P_y/P_{y,c}$ with varying f_{cu} for Corner Panel 338
Figure 7.52: Graph of V_f against $P_{max}/P_{max,c}$ with varying f_{cu} for Corner Panel 338

List of Tables

Table 2-1:	Main Test methods	36
Table 2-2:	Constitutive models in European guidelines and codes (Blanco et al., 2013)	50
Table 2-3:	Distribution of Moments in flat slabs	61
Table 2-4:	Differences between Pile-Supported and flat slabs	63
Table 2.5:	Summary of Design Methods	82
Table 3.1:	Failure Ratios for Concrete Smeared Cracking Model	113
Table 3.2:	Plasticity Parameters for Concrete Damaged Plasticity Model	115
Table 4.1:	Geometrical details and material properties of the beam	133
Table 4.2:	Compression and Tensile Parameters	136
Table 4.3:	Stress-Strain Value for Reinforcement	137
Table 4.4:	Result from FEA for Bresler-Scordelis (1963)	138
Table 4.5:	Geometrical details and material properties of the beam	140
Table 4.6:	Compression and Tensile Parameters	142
Table 4.7:	Stress-Strain Value for Reinforcement	142
Table 4.8:	Results from FEA for Hughes and Speirs (1982)	144
Table 4.9:	Tensile Stress-Strain Relationship for Constitutive Models Barros et al. SFRC Beam 2005	146
Table 4.10:	Compression and Tensile Parameters for Barros et al. SFRC Beam 2005	147
Table 4.11:	Tensile Stress-Strain Relationship for Constitutive Models de Montaignac et al SFRC Beam (2011)	151
Table 4.12:	Compression and Tensile Parameters for de Montaignac et al SFRC Beam 2011	152
Table 4.13:	Tensile Stress-Strain Relationship for Constitutive Models Tlemat et al SFRC Beam (2006)	154
Table 4.14:	Compression and Tensile Parameters for Tlemat et al SFRC Beam 2005	155
Table 4.15:	Tensile Stress-Strain for R.S. Olivito and F.A. Zuccarello (2010) SFRC Beam	157
Table 4.16:	Compression and Tensile Parameters for Olivito and Zuccarello (2010) SFRC Beam	158
Table 4.17:	Tensile Stress-Strain Relationship for Hadi's SFRC Square Panel (2008)	161
Table 4.18:	Compression and Tensile Parameters for Hadi's SFRC Square Panel (2008)	162
Table 4.19:	Tensile Stress-Strain Relationship for Blanco et al SFRC Square Panel (2015)	164
Table 4.20:	Compression and Tensile Parameters for Tlemat et al SFRC Beam 2005	165
Table 4.21:	Tensile Stress-Strain for Soranakom et al. Round Plate (2007)	170
Table 4.22:	Compression and Tensile Parameters for Soranakom et al. Round Plate (2007)	171
Table 4.23:	Tensile Stress-Strain for Bernard (2000) Round Plate	173

Table 4.24:	Compression and Tensile Parameters for Bernard (2000) Round Plate	174
Table 4.25:	Comparison of Test results with FEA for Destree and Mandl (2008)	177
Table 4.26:	Tensile Stress-Strain for Thooft (1999) Pile-Supported Slab	179
Table 4.27:	Compression and Tensile Parameters for Thooft (1999) Pile-Supported Slab	179
Table 4.28:	Composition of SFRSCC per m^3 of concrete	182
Table 4.29:	Comparison of FEM and Experimental Results	184
Table 5.1:	Tensile Stress-strain Values for Parametric Study of SFRC Round Plate	188
Table 5.2:	Tensile Stress-strain Parameters for SFRC at f_{cu} with Different fibre volume ratios	190
Table 5.3:	Results for SFRC Round Plate	197
Table 5.4:	Results for SFRC Round Plate at f_{cu}	198
Table 5.5:	Comparison of Yield Load and Peak Load against Fibre Volume Ratio	199
Table 5.6:	Comparison of Displacement at Yield Load and Peak Load against Fibre Volume Ratio	201
Table 5.7:	Tensile Stress-strain Parameters for SFRC for Case Study 1B	216
Table 5.8:	Results for SFRC Round Plate	218
Table 5.9:	Tensile Stress-strain Parameters for SFRC for Case Study 1C	230
Table 5.10:	Results for SFRC Round Plate	231
Table 5.11:	Comparison between Experiment, FEA-Based Predictions and Design Guidelines	239
Table 6.1:	Material Constituents of SFRC Per m^3	244
Table 6.2:	Tensile Stress-Strain Input	244
Table 6.3:	Mesh-Sizes and Time of Execution	246
Table 6.4:	Tensile Stress-Strain Parameters for different fibre volume ratios [V_f]	247
Table 6.5:	Comparison of Experimental and FEA Validation Results	249
Table 6.6:	Strength Parameters for f_{cu}=45MPa	252
Table 6.7:	Strength and Ductility Ratios	259
Table 6.8:	Strength and Ductility Ratios for various V_f [Slab without Rebar]	262
Table 6.9:	Strength and Ductility Ratios for various V_f [Slab without Rebar]	265
Table 6.10:	Stress-Strain Value for Reinforcement	267
Table 6.11:	Comparison of Experimental and FEA Validation Results [Slab with Rebar]	268
Table 6.12:	Strength Parameters for f_{cu}=45MPa [Slab with Rebar]	270
Table 6.13:	Strength and Ductility Ratios of Slab with Rebar	276
Table 6.14:	Strength and Ductility Ratios for various V_f [Slab with Rebar]	278
Table 6.15:	Strength and Ductility Ratios for various V_f	282
Table 6.16:	Comparison with Existing Guidelines	284
Table 7.1:	Material Constituents of SFRC Per m^3	287
Table 7.2:	Tensile Stress-Strain Input	288

Table 7.3:	Mesh-Sizes and Time of Execution	290
Table 7.4:	Tensile Stress-Strain Parameters for different fibre volume ratios [V_f]	291
Table 7.5:	Comparison of Experimental and FEA Validation Results for Middle Panel	293
Table 7.6:	Strength Parameters of Middle Panel for fcu=43.7MPa for Middle Panel	294
Table 7.7:	Strength and Ductility Ratios for Middle Panel	301
Table 7.8:	Strength Ratios for various V_f for Middle Panel	303
Table 7.9:	Strength Ratios for various V_f for Middle Panel for 180mm depth	308
Table 7.10:	Strength Ratios for various V_f for Middle Panel for 220mm depth	308
Table 7.11:	Validation Results for Edge Panel	311
Table 7.12:	Strength Parameters for Edge Panel	312
Table 7.13:	Strength Ratios for Edge Panel	318
Table 7.14:	Strength Ratios for various V_f for Edge Panel	320
Table 7.15:	Strength and Ductility Ratios for various V_f for Edge Panel	324
Table 7.16:	Comparison of Experimental and FEA Validation Results for Corner Panel	326
Table 7.17:	Strength Ratios for Corner Panel	328
Table 7.18:	Strength Ratios for Corner Panel	334
Table 7.19:	Strength Ratios for various V_f for Corner Panel	336
Table 7.20:	Strength Ratios for various V_f for Corner Panel	339
Table 7.21:	Comparison with Existing Guidelines for Maximum Loading Capacity	341

Acknowledgement

My utmost gratitude goes to the Almighty GOD for in HIS infinite wisdom and knowledge was I able to complete this PhD research work. To HIM be all the glory, honour and adoration.

This thesis is a product of the research undertaken at the University of East London, School of Architecture, Computing and Engineering [ACE] under the supervisory guidance of Dr Ali Abbas and Dr Ravi Jayaratne, to whom I am grateful. I also want to thank all the faculty in ACE, Prof Hassan S. Abdalla, Prof. Brimincombe, Dr John Walsh, Dr Jawed, and Dr Anca.

I will like to appreciate the Federal Government of Nigeria through the Tertiary Education Trust Fund [TETFund] for providing over 75% of the funds for the program.

Special thanks go to the Management of the Federal Polytechnic, Ilaro from Dr R.A. Oloyo [who approved the program], to Arc. Segun Aluko PhD [who released me for the program] and everyone who has contributed in one way or the other [Engr H.A. Sanni, Engr (Prof) Olagoke, Tpl F. Babalola, Engr F.A. Akinboboye, Engr B.S. & Engr (Mrs) M.O. Balogun, Engr (Mrs) I.K. Ogunfayo, Engr O.A. Aikulola, Mr O.O & Elder (Mrs) Oduwobi, Engr O.O & Dcns O.A. Osore, Chief [Mrs] Yemisi Oloyo, Tpl & Mrs Sunday Oyesile, Dr & Mrs Wale Ajayi,

To all my colleagues at the Federal Polytechnic Ilaro, Mr O.P. Okafor, Engr. DWS Alausa, Engr & Mrs Wale Ogunyinka, Mr Oyedeji, Engr (Dr) Olarewaju, Dr Akinbola, Lolade 'Guv' Adegbesan, Tayo Ojuawo, Sulaimon Oderinde, Funke Aiyegbusi, Engr Adeala, Kehinde Aladelusi, Ojo Adaramola, Mr Fabi, Mr Aro, Mr Adeyinka, Pst Oyenuga, Femi Feyisitan

To all Pastors in Winners' Chapel International Dartford and Ilaro [David & Kemi Oyedepo Jnr, Mike & Victoria Sekudo, Abiodun & Aarinola Idowu-Titus, Kayode & Toyin Oremakinde, Abiodun Ope, Kolade & Yemisi Abel, Rotimi Ajibola, John Awojobi, Obinna Nwokire, Matthew Adeyeye, Yuki Igbinosa, Nicholas Udoh, Pius Awulor, Richard Nana-Akyin, Nathaniel Odin, David Shiyanbade, Gbenga Babatunde, Peter Macaulay, Sylver Omeaka, Jacob Adedeji, Tolu Oralusi], I say a big thank you for your spiritual and moral supports.

All PhD students at UEL and most especially Ifueko Imason, Ahmed Albarran [Iraq], Oluwaseun Alele, Comfort Olutola, Umar Mukhtar, Raghu [India], Alice Mukaka, Rabiu Mukhtar, Ify Dan-Ogosi, Kathy-Ann [Barbados], Solomon, Ezekiel Jidong, Roxanne Gooden [Jamaica], Halima Kure, Mustapha, Aslam, Sanny [Zambia], Tarela Ike, Linah [Jordan], Abba, and those who have graduated Mohammed Garba, Bibi, Richard Otuka, Austin Nwajana, Amodu Dinken, Umaima Haider [Pakistan], Ronke Akerele, Ifiok Etim, Christiana Emmanuel-Stephen, to you all I say thank you

To these special people who made my stay in the UK very pleasurable, Dcns Catherine Adedoyin, Dcn & Dcns Muyiwa Aderoju, Kehinde Oliyide, Josephine Rufaro, Sis Constance Ogbunike, Bro Israel Adelakun (Assistant Brethren), Mummy Rita Soetan,

My entire family, Rev. & Evang. Bisi Olutade, Jumoke, Mrs Funmi Otitoju Soyemi-Tella, Lekan & Betty 'Sama' Osinnaike, Bisoye, Pst & Mrs Segun Soyemi, Tunde, Mr & Mrs Femi Ibrahim, Engr Bola Falusi, Dr Niyi & Sade Isinkaiye, Bayo & Foluso Adedeji, Jide & Yinka Olulana, Kayode & Lola Agoke, Seyi & Funmi Balogun, Hajia Idayat Hammed, Gbenga & Funmi Soyemi, Idris & Jumoke Bello, Sola & Jumoke Aguda, Fatai Osinnaike, all Gaskiya Global Forum,

To my children, Oluwaseyifunmi, Oluwademilade and IreOluwa and their cousin, Justina Olutade, thank you for holding forth for this last 3years plus.

I deeply appreciate my Love, Dr [Mrs] Jumoke. Thank you for holding forth. GOD bless you.

Dedication

This research work is dedicated to my beloved wife, Dr [Mrs] Olajumoke Abimbola Naomi SOYEMI

Table of Content

Contents

ABSTRACT I

LIST OF SYMBOLS II

ABBREVIATIONS IV

LIST OF FIGURES V

LIST OF TABLES XV

ACKNOWLEDGEMENT XVIII

DEDICATION XX

TABLE OF CONTENT XXI

CHAPTER 1: INTRODUCTION 1

1.1 Background 2

1.2 Statement of Problem 7

1.3 Aim and Objectives 9

1.4 Scope of Research 9

1.5 Application of SFRC 10

1.6 Novelty of Research 11

1.7 Research Methodology 12

CHAPTER 2: LITERATURE REVIEW 14

2.1 Introduction 15

2.1.1 Historical Development of Fibres 18

2.1.2 Classification of Fibres 19

2.1.3 Sources of fibres 19

2.1.4 Physical/Chemical properties 19

2.1.5 Mechanical properties 19

2.1.6 Shape and size 20

2.2 Steel Fibres 20
2.2.1 Shape of the Fibre 20
2.2.2 Classification of Steel-Fibre 21
2.2.3 Characterisation of steel-fibre 22
2.2.4 Basic Definition of Physical Properties 22

2.3 Properties of Steel Fibre Reinforced Concrete 22
2.3.1 Compressive Strength of SFRC 22
2.3.2 Tensile Strength of SFRC 24

2.4 Crack propagation and formulation 26

2.5 Test Methods 28
2.5.1 Uni-axial tension test 28
2.5.2 3-Point bending test 30
2.5.3 4-Point bending test 33
2.5.4 Slab (Plate) test 34
2.5.5 Review of Testing Methods of SFRC 36

2.6 Material Constitutive Models 38
2.6.1 Lok & Pei (1998) 38
2.6.2 Barros and Figueiras (1999) 41
2.6.3 Rossi (1999) 44
2.6.4 RILEM TC 162-TDF (2002) 44
2.6.5 Lok and Xiao (1999) 46
2.6.6 Review of Constitutive Models 48
2.6.7 Highlights on some constitutive models in EU guidelines and codes (Álvarez, 2013) 49

2.7 Slabs Overview 51
2.7.1 Supports for slabs 51
2.7.2 Methods of analysing and designing Elevated and Pile-supported slabs 51
2.7.3 Flat Slabs 59
2.7.4 Difference between pile-supported and flat slabs 61

2.8 Punching shear 63
2.8.1 Mechanism of Failure 64
2.8.2 Contribution of Steel Fibre 65

2.9 Design Guidelines for SFRC Slabs 65
2.9.1 RILEM TC 162-TDF (2002) 66
2.9.2 ArcelorMittal Design Guideline (2010) 69
2.9.3 Dramix by Bekaert Design Guideline (2012) 71
2.9.4 Twintec (2012) 71

2.9.5 The Concrete Society (2007) – TR 63 71
2.9.6 The Dutch Code [NEN 6720] (1995) 73
2.9.7 Eurocode 2 BS EN 1992 (2004) 74
2.9.8 The Swedish Proposal (2008) 75
2.9.9 $\boldsymbol{fib}$ Model Code 2010 (MC2010) 76
2.9.10 The Concrete Society (2014) – TR 34 78
2.9.11 Deficiencies in Existing Design Methods for Elevated or Pile-supported Slabs 79
2.9.12 Summary of Design Methods 82

2.10 Summary 84

CHAPTER 3: FINITE ELEMENT METHOD 87

3.1 Introduction 88

3.2 Finite Element Analysis 88

3.3 Non-Linear Finite Element Analysis 90

3.4 Finite Element Analysis using ADINA and ABAQUS 90

3.5 ADINA 91
3.5.1 Elements in ADINA 91
3.5.2 Meshing 93
3.5.3 Material Model for Steel 94
3.5.4 Material Models for Concrete 94

3.6 ABAQUS 107
3.6.1 Elements in ABAQUS 107
3.6.2 Concrete Material Models 111
3.6.3 Brittle cracking model 120

3.7 Material Model for Rebar 121

3.8 Philosophies of Constitutive Models 122
3.8.1 Stress-Strain Constitutive model 122
3.8.2 Stress-crack width [σ-w] constitutive model 123
3.8.3 Review of Philosophies of Constitutive Models 124

3.9 Scope of Parametric/Case Studies 125
3.9.1 Case Study 1: Round Plate SFRC Slab under Point Load 126
3.9.2 Case study 2: Four Panel Pile Supported SFRC Slab 127
3.9.3 Case study 3: Nine-Panel SFRC Elevated Slab 128

3.10 Analysis Process 129

3.6 Summary 129

CHAPTER 4: VALIDATION OF NUMERICAL MODELS USING AVAILABLE EXPERIMENTAL RESULTS 130

4.1 Introduction **131**

4.2 Reinforced Concrete Beams Cases [No Fibres] **132**
4.2.1 Bresler and Scordelis (1963) Beam – Brittle Failure 132
4.2.2 Hughes and Speirs (1982) Beam 140

4.3 Steel-Fibre Reinforced Concrete Experimental Works **144**
4.3.1 3-Point Bending Beam Tests 145
4.3.2 4-Point Bending Tests 153
4.3.3 SFRC Slabs [Plates] 160

4.4 Full-Scale Testing **176**
4.4.1 Destree X and Mandl J. (2008) Square Slab 176
4.4.3 Thooft (1999) Pile supported slabs 177
4.4.4 Barros J.A.O., Salehian H., Pires N.M.M.A and Goncalves D.M.F (2012) 181

4.5 Summary of Validation works **183**

4.6 Summary **185**

CHAPTER 5: CASE STUDY 1: SIMPLY SUPPORTED SINGLE SLABS UNDER POINT LOAD 186

5.1 Introduction **187**

5.2 Case Study 1A: R. de Montaignac, B. Massicotte, JP Charron & A. Nour Round Plate (2011) **187**
5.2.1 The Load-Displacement Curves 192
5.2.2 Strength 197
5.2.3 Ductility 206
5.2.4 Cracking Pattern 206
5.2.4.4 Deflected Shapes 212
5.2.5 Comparative Study with Experimental Results Using Non-Dimensional Ratios 213

5.3 Case Study 1B: Soranakom, C., Mobasher, B. and Destrée, X. (2007) Round Plate **215**
5.3.1 The load-Displacement Curves 217
5.3.2 Strength 218
5.3.3 Ductility 219
5.3.4 Cracking Patterns 219

5.3.5 Comparative Study with Experimental Results Using Non-Dimensional Ratios 226

5.4 Case Study 1C: Blanco, A., Cavalaro, S., De La Fuente, A., Grünewald, S., Blom, CBM & Walraven, JC Square Plate (2014) 228

5.4.1 Load-Displacement Curves 230
5.4.2 Strength 231
5.4.3 Ductility 232
5.5.4 Crack Patterns 232
5.5.5 Using Non-Dimensional Ratios for Comparative Study with Control Specimen 237
5.5.6 Comparison between FE-Based Predictions and Design Guidelines 239

5.6 Summary 240

CHAPTER 6: CASE STUDY 2 - 4-PANEL PILE-SUPPORTED SLABS WITH AND WITHOUT REBAR OVER SUPPORTS 242

6.1 Introduction 243

6.2 Sensitivity Analysis 244

6.3 Parametric Study 246

6.4 Slab without Rebar 247

6.4.1 Load-Displacement Curves [Slab without Rebar] 248
6.4.2 The Strength [Slab without Rebar] 251
6.4.3 Ductility 253
6.4.4 Crack Shapes [Slab without Rebar] 253
6.4.5 Comparative Study with Experimental Specimen using Non-Dimensional Ratios [Slab without Rebar] 258
6.4.6 Additional Analysis with Different $\boldsymbol{fcu}$ [Slab without Rebar] 261
6.4.7 Proposed Equation for Peak and Maximum Load [Slab without Rebar] 266

6.5 Case Study 2[b]: 4-Panel Slab with Rebar 266

6.5.1 Load-Displacement Curves of Slab with Rebar 267
6.5.2 The Strength of Slab with Rebar 270
6.5.3 Ductility of Slab with Rebar 271
6.5.4 Crack Shapes of Slab with Rebar 271
6.5.5 Comparative Study with Experimental Specimen using Non-Dimensional Ratios [Slab with Rebar] 276
6.5.6 Additional Analysis with Different fcu 277
6.5.7 Proposed Equation for Peak and Maximum Load 282

6.6 Comparison between SFRC Slab with and without Rebar 283

6.7 Comparison with Existing Guidelines 283

6.8 Summary 284

CHAPTER 7: CASE STUDY 3 - 9-PANEL ELEVATED SLAB UNDER POINT LOAD 286

7.1 Introduction 287

7.2 Sensitivity Analysis 288

7.3 Parametric Study 290

7.4 Loadings under Ultimate Limit State [ULS] 291

7.5 Part I: Middle Panel 292
7.5.1 Load-Displacement Curves 292
7.5.2 The Strength 294
7.5.3 Ductility 295
7.5.4 Crack Shapes 295
7.5.5 Comparative Study with Experimental Specimen using Non-Dimensional Ratios 301
7.5.6 Further Analysis with Different $\boldsymbol{fcu}$ 302
7.5.6 Proposed Equation for Maximum Load Carrying Capacity 309

7.6 Part II: Edge Panel 310
7.6.1 Load-Displacement Curves 310
7.6.2 The Strength 312
7.6.3 Comparative Study with Experimental Specimen using Non-Dimensional Ratios 318
7.6.4 Further Analysis with Different fcu for Edge Panel 319
7.6.5 Proposed Equation for Maximum Load Carrying Capacity for Edge Panel 324

7.7 Part III: Corner Panel 325
7.7.1 Load-Displacement Curves 325
7.7.2 The Strength 327
7.7.3 Comparative Study with Experimental Specimen using Non-Dimensional Ratios 334
7.7.4 Further Analysis with Different fcu for Corner Panel 335
7.7.5 Proposed Equation for Yield Load and Maximum Load Carrying Capacity for Corner Panel 340

7.8 Comparison with Existing Guidelines and Codes using Middle Panel 340

7.9 Conclusions 342

CHAPTER 8: CONCLUSIONS AND RECOMMENDATIONS 344

8.1 Summary of Research Work 345

8.2 Summary of Conclusions **346**

8.3 Recommendations and Future Work **349**

REFERENCES 350

APPENDIX 359

Chapter 1: Introduction

1.1 Background

Concrete in its natural state consists of limestone (cement), fine and coarse aggregate, and water. It has emerged the most used human-made construction material of all time (Beddar, 2004). Every year, the Association of Concrete Industrial Flooring Contractors [ACIFC] pours around 10 million m^2 of concrete for industrial flooring in the United Kingdom (Concrete Centre, 2006). In 2011 the estimated construction of industrial floors was at the level of 2.5 million m^2, an increase of 25 % compared with 2004 that seemed to be a low notation (Hedebratt, 2012a). Also, the damages reported have been on the increase in the last 30 years (Johansson, 2003).

There has been a significant improvement both in the art and usage of concrete over the years compared to when it was first used for masonry work by the Romans in which pozzolanic mortar was used as a binder. Generally, concrete is strong in compression (British Standard Institute, 1997, Lok and Xiao, 1999, Barros and Cruz, 2001, America Concrete Institute, 2002, British Standard Institute, 2004, Crowther, 2009, Abbas et al., 2014b) and possesses about one-eighth of this strength in tension. At the application of loads, the concrete member bends and cracks at the tension face as shown in Figure 1.1.

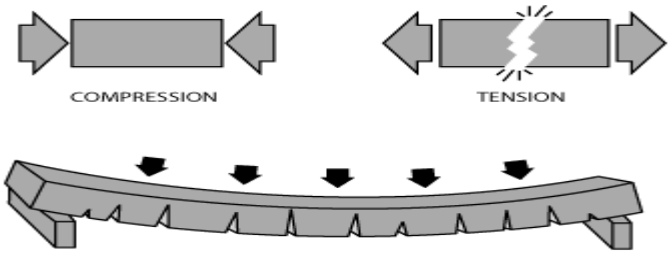

Figure 1.1: Plain concrete in bending [Adapted from https://www.quora.com/Why-do-we-put-steel-in-concrete-for-construction on November 12, 2016]

A solution was developed in the late nineteen century with the insertion of steel bars inside the concrete to withstand the stresses at the tension zone as shown in Figure 1.2. This improved solution has led to the momentous development in the construction industry leading to its adoption in a wide range of structures

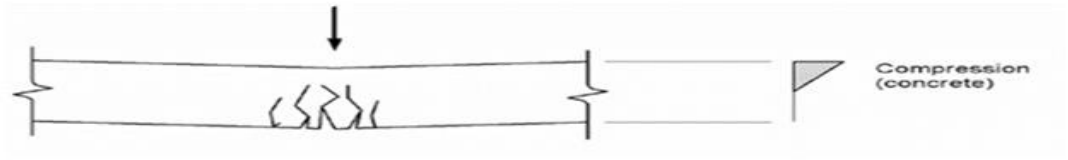

(a)

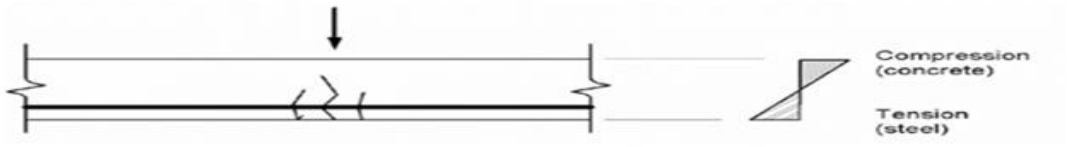

(b)

Figure 1.2: (a) Crack Pattern in Concrete with No Reinforcement when Load is Applied (b) Crack Pattern in Concrete with Steel Reinforcement when Load is applied [Adapted from www.google.com on November 12, 2016]

The overall performance of any structure, particularly the industrial and warehouses has been attributed to the concrete floor slabs (CFS) where a lot of activities take place and as businesses grow and expand its operations, the need for large industrial warehouses with consistent flooring standards emerged as a priority in the company's overall logistics plan. Concrete ground floor slabs act as the intermediary between the applied load and the soil layer. All activities in and around the structure need a sound platform to operate on; manufacturing, storage and distribution, retail, or pavement and so forth. The concrete floors form the base on which all these activities are carried out. Basically, these slabs were designed as ground-supported (Abbas et al., 2004, Barros and Figueiras, 2001, Goltermann, 2013, Simpson, 2003), but where the ground conditions are poor [in terms of strength], a most efficient solution often adopted is to construct the slab as elevated floor on piles [so the ground acts merely as a construction formwork] (Beckett, 2004, The Concrete Society, 2009, Goodchild, 2004, Regan, 1989). The structural elements of a typical piled slab are depicted in Figure 1.3.

[a] [b]

Figure 1.3: Typical Slab Reinforcement laid on [a] Pile Foundation adapted from http://nationwidediamondgroup.co.uk 25/05/2017] and [b] columns for elevated slab adapted from http://xoomtube.com/video/RKk8TEEKLBI on 25/05/2017]

Also, offices, residential buildings and other structures in which flat slab floors are constructed on the ground or supported on piles are subjected to the failure and cracking behaviour which often has been a worrying concern for clients, contractors and designers. The quality and durability of industrial floors have been a vital consideration in the construction of industrial premises, including warehouses, factories, large workshops, shopping centres and buildings for other range of applications.

Conventionally, these slabs are constructed using concrete reinforced with longitudinal steel rebar or welded mesh fabric [Figure 1.3]. A growing trend which forms an alternative to this method of construction, both in the UK and overseas, is the replacement of some or all of the reinforcement with fibres (Swamy, 1974, CHANH, 1990, Zollo, 1997, America Concrete Institute, 1999, Destrée, 2001, RILEM, 2002b, McCraven, 2002, Cameron, 2002, Cerioni et al., 2004, Beddar, 2004, Hedebratt and Silfwerbrand, 2008, Crowther, 2009, ArcelorMittal, 2011, Mohsin, 2012b, Barros et al., 2012, Rana, 2013, Abbas et al., 2014a, Ahmed, 2014, Blanco et al., 2014b, Singh, 2015). This method has proven to save construction time, reduce labour cost, reduces chances of injury on site thereby improving safety and in overall, produces cheaper slabs when compared to the traditional reinforced concrete slabs. There are various types of fibres [steel, glass, polyethene etc.], but the current research work will be carried out on the steel-fibres.

Pile-supported steel-fibre reinforced concrete [henceforth SFRC] slabs are usually constructed in square pile grids of about 3 x 3m, 5 x 5m, 6 x 6m and most recently 8 x 8m (Destree, 2004, Destrée, 2007a, Vollum, 2007, Destrée and Jürgen, 2008, The Concrete Society TR34, 2014). Their thicknesses are typically 200 - 300 mm but can be as high as 500 mm for heavily-loaded slabs and as low as 180 for residential buildings. The thickness of the slab is picked based on a minimum span-depth ratio of 15 (The Concrete Society TR63, 2007, Destrée and Jürgen, 2008). Slip membrane is commonly provided at the interface between the top of the pile and bottom of the slab [the piles are not constructed monolithically with the slab] to minimise the risk of cracking caused by restrained early-age thermal contraction and drying shrinkage. A Typical Pile-Supported Slab Layout is shown in Figure 1.4.

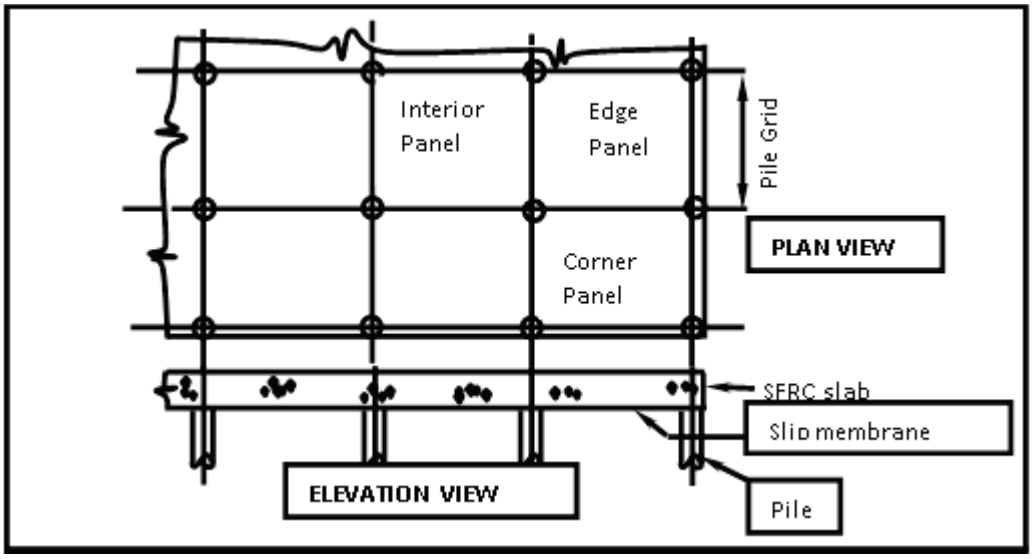

Figure 1.4: A Typical Pile-Supported Slab Layout

In plain concrete subjected to loading, cracks are propagated on the tension surface. This damage first starts as a single crack when the tensile strength of the material has been exceeded and are thus mitigated by the introduction of fibres in the concrete matrix (CHANH, 1990, Campione, 2002, Beddar, 2004, Labib and Eden, 2004, British Standard Institute, 2006, Jansson, 2011, Rai and Joshi, 2014, Ghaffar et al., 2014)

With the improvement in the knowledge and understanding of steel-fibre usage in concrete in recent time, there has been a swift expansion in the construction of steel-

fibre-reinforced concrete pile-supported slabs (Barros and Figueiras, 1999, Destrée, 2001, Cameron, 2003, Destrée, 2006, Vollum, 2007, Destrée, 2007a, Hedebratt and Silfwerbrand, 2008, Mobasher and Destrée, 2010a, ArcelorMittal, 2011, Destrée et al., 2011, Barros, 2011, Destrée and Silfwerbrand, 2012, Barros et al., 2012, Oikonomou-Mpegetis, 2013, Blanco et al., 2014a, Singh, 2015). Figure 1.5 shows the Pile-Supported Floor Slab for Warehouse Partly finished with soil acting as falsework

Figure 1.5: Pile-Supported Floor Slab for Warehouse Partly finished with soil acting as falsework [Adapted from Twintec Thailand- http://www.twintec.co.th/sfrc-jointless-internal-floor-slabs.html, downloaded on May 25, 2016]

The application of pile-supported SFRC has been in use for over three decades (Zollo, 1997, Destrée, 2001), its design has mainly been on proprietary guidelines. This is due to the non-availability of a unified, authoritative code or guidance (The Concrete Society TR63, 2007) but several nations and bodies have provided recommendations for the design and construction of SFRC slabs. Early guidelines were from RILEM TC162-TDF and followed by ACI and BSI with other countries following (America Concrete Institute, 1999, IstructE, 1999, RILEM, 2000, America Concrete Institute, 2002, British Standard

Institute, 2006, NZS, 2006, NRC, 2007, The Concrete Society TR63, 2007, Silfwerbrand, 2008, The Concrete Society TR34, 2014).

1.2 Statement of Problem

A plain unreinforced concrete matrix fails in a brittle manner at the appearance of cracking stresses due to its brittleness and lack of post-cracking resistance. Fibres have been found to enhance the ductility of concrete, by carrying stresses beyond matrix cracking and thus improve the structure's integrity and ability to accommodate deformations. Taking advantage of the statically indeterminate characteristic of slabs supported on piles or columns, and the benefits from the high post-cracking residual strength of concrete reinforced with the relatively high content of steel fibres (1.00% to 2.50% in volume) the use of SFRC has recently been explored for the construction of different types of structural system. This type of slab is generally designated by pile-supported or Elevated SFRC (Destree, 2004)

Given the information examined above with respect to properties of steel-fibres and their capability to enhance the structural response of the RC structures, it is urgent and gainful to research further and understand the behaviour of SFRC structures, particularly in suspended slabs. Earlier studies carried out by (Thooft, 1999, Destrée, 2001, Cameron, 2003, Beckett, 2004, Barros et al., 2005) are restricted to certain types of structural arrangement and only consider a low range of volume fibres fraction due to time and economic limitations. These studies are mainly experimental, which does not have the advantage of implementing full parametric examinations such as the one carried out in this present research work.

Also, some studies have been carried out to examine pile-supported and elevated SFRC slabs (Thooft, 1999, Destrée, 2001, Goodchild, 2004, Destree, 2004, Hedebratt and Silfwerbrand, 2008, Barros, 2011, Destrée and Silfwerbrand, 2012, Barros et al., 2012, Salehian and Barros, 2017) on partial or total replacement of rebar with steel-fibres. Two systems evolved from their experimental works; fibre only concrete and SFRC with rebar over the pile or columns to guide against or arrest progressive collapse and punching shear. Consequently, it is of interest to enlarge previous work to investigate the possibility of utilising various volumes of steel fibres as the only reinforcement,

understanding the behaviour of SFRC considering a wide range of fibre dosages using FEA. This will result in conclusions and recommendations to help in simplifying the design of SFRC suspended slabs.

Likewise, there are no guidelines that are accepted or adopted worldwide. Every nation in which the construction and research of SFRC have taken place provided some form of guidelines for design. Also, proprietary guidelines vary between manufacturers, and some are based on 'design assisted by testing' method (Japanese Concrete Institute, 1984, British Standard Institute, 1994, IstructE, 1999, America Concrete Institute, 2002, British Standard Institute, 2006, NZS, 2006, NRC, 2007, The Concrete Society TR63, 2007, Institute, 2007, ArcelorMittal, 2011, The Concrete Society TR34, 2014). This research work looked into these various guidelines and evaluated their responses in the design of slab supported by piles and columns and compared same with results from FEA.

The present research work purposes to produce a simplified approach for the design of SFRC suspended slab using FEA. Parametric and case studies were undertaken to propose the simplified design guidelines where possible. The focus of the present study is on SFRC suspended slabs (i.e. single panel, 4-panel and 9-panel slabs), taking into consideration the overall structural responses as well as the local response at the critical sections examined. Conclusions are then made on whether or not FEA can demonstrate the capability of SFRC to achieve sufficient strength, stiffness and ductility.

The research work investigates the following key structural issues:

- Strength: shear force, load-carrying capacity, and bending moment capacities at critical sections on the slab
- Stiffness: maximum displacement and slope
- Ductility: the ratio of maximum displacement/displacement at yield.
- Cracking: patterns, locations and controls (potential of cracking at support and point of application of load).

1.3 Aim and Objectives

Aim

To this effect, this research work is aimed at investigating the structural behaviours of steel-fibre reinforced concrete [SFRC] pile-supported and elevated slabs using the commercially available structural engineering software ADINA and ABAQUS [linear and non-linear finite element analysis (FEA)].

The objectives of the research work are to:

1. Critically examine current design guidelines by studying the corresponding elastic and yield-line analyses.
2. Collate available numerical models and evaluate them
3. Calibrate and validate the constitutive models into the FE models using ADINA and ABAQUS to Produce complete load-deflection histories from the start of loading to collapse.
    - Provide predictions of load-carrying capacities at the ultimate limit-state.
    - Determine the structural loads at first crack and the location of these initial cracks.
4. Carry out parametric studies on experimental works chosen as case studies
5. Compare the results of the numerical investigations and existing experimental data with current design guidance in order to assess the safety, serviceability and economy of the latter.
    - Use the ensuing data to establish a transparent, unified, and improved design method in the form of simplified closed-form formulae and/or design charts for eventual use by practising engineers

1.4 Scope of Research

The aim of this research work is to investigate the mechanical and structural behaviour of suspended steel-fibre reinforced concrete slabs using finite element analysis. The scope of this research work is as follows:

- Available experimental works with hooked-end and cramped steel-fibres were used for case studies.
- Three cases were studied, and these covers single [round and square] panels, 4-panel slabs, and 9-panel slabs. The single panels were used to study the behaviour of the slabs at the material level while the 4-panel and 9-panel slabs were used for the structural responses.
- parametric studies carried out on the vital parameter, particularly the volume fibre fraction V_f and characteristic strength of SFRC f_{cu} to extend it beyond the scope of the experiment.
- The V_f and f_{cu} are the main parameters that were considered in all the parametric studies and in addition, the span-depth $^{l}/_{d}$ ratio for the cases considered at the structural level. The V_f adopted were guided by the values used in the experiments considered for case studies and are 0.5%, 1.00%, 1.25%, 1.50%, 2.00% and 2.50% and f_{cu} were 30MPa, 40MPa and 50MPa.
- Also, for the Finite Element Analysis, two commercially available software, ADINA and ABAQUS, were used in the analysis. They were chosen based on their acceptability in the industry and their availability at the University of East London.

1.5 Application of SFRC

The ability to arrest crack openings effectively by the reinforcement mechanisms of steel fibres bridging the crack surfaces of Cementous materials leads to substantial increase in load carrying capacity and energy dissipation capability of the concrete structures (Barros, 2011). SFRC has been found to effectively arrest cracks and also used where irregular or complex shapes are desired. The following areas have witnessed the tremendous use of SFRC and some are shown in Figure 1.6:

- Airport Runways
- Industrial Ground floors
- Pile-Supported slabs
- Tunnel-linings
- Suspended floors

- Residential and Commercial Floor slabs
- Box culvert

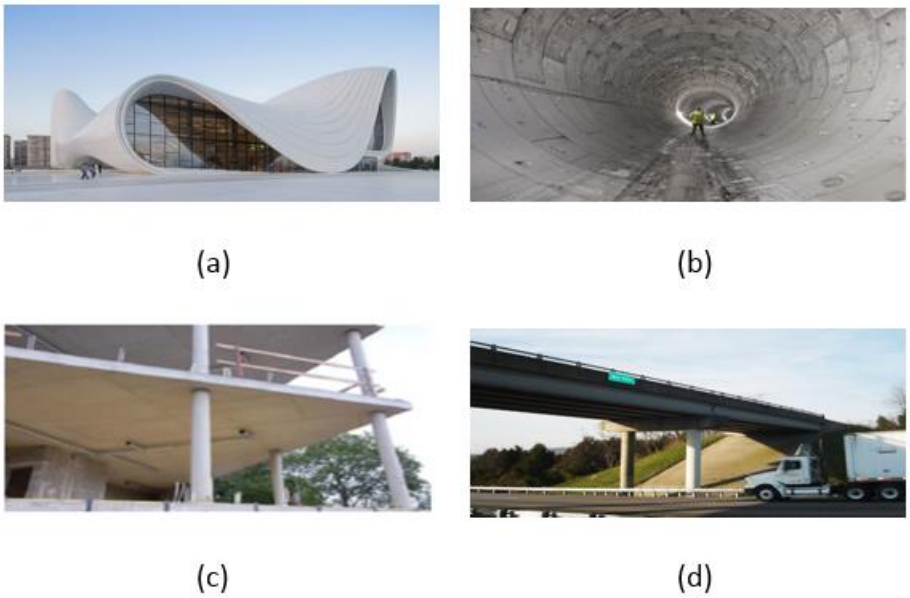

Figure 1.6: Applications of FRC
(a) Heydar Aliyev Center by Zaha Hadid, Baku, Azerbaijan. Glass-fibre reinforced concrete [adopted from www.pinterest.com on 10/05/2016]
(b) Tunnel lining [adopted from www.tunneltalk.com on 10/05/2016]
(c) Triangle Office Building Tallinn/Estonia (Destrée, 2006)
(d) Fortress Stabilization Systems [adopted from www.fortressstabilization.com on 10/05/2016]

1.6 Novelty of Research

Presently there are the procedures for the analysis and design of steel fibre reinforced concrete. Existing guidelines were made by individual nations, professional bodies and manufacturers of steel-fibre for guidance and construction. These guidelines were based on either Yield-Line Analysis [YLA] or Elastic Method [EM] (Japanese Concrete Institute, 1984, IstructE, 1999, RILEM, 2002b, America Concrete Institute, 2002, Beckett, 2004, British Standard Institute, 2006, NRC, 2007, The Concrete Society TR63, 2007, ArcelorMittal, 2011, The Concrete Society TR34, 2014). These two methods have been found to be limited as YLM is an upper bound method and EM is within the elastic limit. This research aims to produce a simplified design approach based on finite element analysis for the suspended slab.

1.7 Research Methodology

The method deployed for this research work is divided into four parts:

First, a critical review of the available literature (on reinforced concrete, fibre reinforced concrete, type of fibres, testing procedures, numerical and constitutive models, real-life applications etc.) was carried out all through the research period

Secondly, identification of existing models and design guides; gathering of available experimental data on SFRC slab with reference to samples with and without rebar, and a combination of rebar and fibres. The constitutive models were inputted into FEA software and used to determine their accuracy in predicting the responses of the experimental works correctly.

Furthermore, comparisons are made between the existing elastic design and proposed serviceability design rules at Serviceability Limit State (SLS). A complete load-deflection history at the Ultimate Limit State (ULS). An extensive parametric study using varying parameters [L/d, V_f and f_{ck}] were carried out.

Finally, based on all the above, proposed simplified design equations were developed using regression analysis and, further comparison were made with the current design guidelines and the results tabulated and published. Figure 1.7 shows the schematic diagram of this research work.

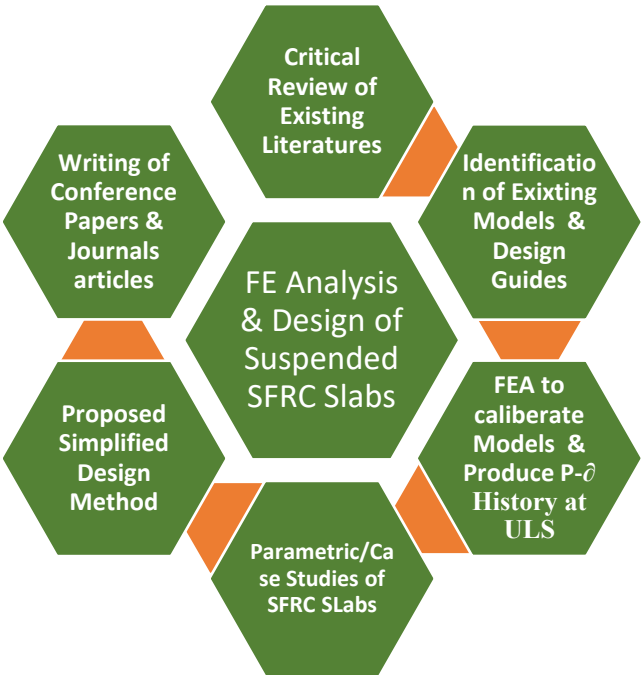

Figure 1.7: Research Outlay

Chapter 2: Literature Review

2.1 Introduction

In 1874, an American, A. Berard patented an idea in which grains of steel left-overs (waste) are mixed to the concrete to create a material that is more ductile (Berard, 1874a). In the present world, there are many types of fibres being used in the construction industry for structural and non-structural works. Examples are steel, carbon, polyethene, natural fibres and so on, but the most researched on is the steel fibre. The steel fibres come in various shapes, sizes and strength (Zollo, 1997, Destrée, 2007a). As found in earlier researches, the advantages of inclusion of steel-fibres in concrete in structural members are numerous. These include [i] enhancing the post-cracking behaviour of the concrete regarding more ductility which leads to an increase in flexural strain capacity, [ii] the significant reduction in construction time [since they are conveniently cast in large pours compared to time to lay the traditional reinforcement]; [iii] improve tensile strength and energy absorption and, [iv] reduction in crack-width giving rise to enhanced damage tolerance (RILEM, 2002a, Lok and Pei, 1998, Oslejs, 2008). However, in some other early works on SFRC provisions were made for additional reinforcement to resist peak moments over piles or supports, notably in the corner panel, and to control cracks due to early-age thermal stresses and then it was concluded that it is impossible to have steel-fibres only reinforced concrete (CHANH, 1990, IstructE, 1999). However recent experimental works on real-life full-size specimen have shown that there can be fibres-only reinforced concrete (Destree, 2004, Destrée, 2007b, Vollum, 2007, Destrée and Jürgen, 2008, Barros et al., 2012, Hedebratt and Silfwerbrand, 2014, Ragi, 2015, Khan et al., 2016, Lee et al., 2017, Najim et al., 2018)

There is the absence of a generally accepted code or standard method for the design and analysis of pile-supported or elevated SFRC slabs. The existing methods are either based on analytical material properties of SFRC established from tests on small beam specimens or empirically based on full-scale testing. General design guidance for suspended [piled supported and elevated] SFRC slabs is provided in the Concrete Society's Technical Report (TR) 63 (The Concrete Society TR63, 2007, Vollum, 2007, Eddy, 2008) and some national guides (America Concrete Institute, 2002, NZS, 2006, British Standard Institute, 2006, INRC, 2007, Institute, 2011), which are based on both elastic and yield-line analyses to calculate peak moments. To calculate flexural strength,

a stress block is proposed for SFRC sections based on a residual tensile strength derived using both the Japanese beam test (R_{e3})(Roesler and Gaedicke, 2004) and BS EN 14651 (British Standard Institute, 2005). A formula is also given for the estimation of the shear strength of SFRC sections based on RILEM recommendations (RILEM, 2003) updated to Eurocode 2 (British Standard Institute, 2004). Guidance was also provided for the reinforcement required for crack control. For elastic analysis, the slab is divided into the column and middle strips as in the design of flat slabs in BS8110 (British Standard Institute, 1997).

However, it is acknowledged that (The Concrete Society TR63, 2007) the moment coefficients recommended in BS8110 are limited for structures with the maximum imposed load is 5kN/m^2 compared to 15 kN/m^2 typical loads for industrial floors. It is thus advised that the moment coefficients recommended by the Dutch Code NEN 6720 (TGB NEN 6720, 1995) should be used instead. As for yield-line analysis, the process involves identifying critical collapse mechanisms and calculating corresponding moments of resistance. Certain assumptions are made concerning the location of yield lines (e.g. radius of potential fan mechanism) (Kennedy and Goodchild, 2004, Jansson, 2008, Barros et al., 2012, Concrete-Society, 2007). For economy reasons, the plastic analysis is favoured over elastic analysis. However, it is recognised that a separate serviceability check is required using the latter.

Proprietary design guidance is provided by Bekaert and ArcelorMittal, which are the principal suppliers of steel fibres (Dramix® and TAB-Structural system) in the UK. The Bekaert design method (Viney, 2007) relies on the elastic moment coefficient of the Dutch Code NEN 6720 and is thus similar to TR 63 guidelines (Concrete-Society, 2007). Some laboratory tests support the guidelines. Only uniformly-distributed loads are considered, and conventional steel rebar is provided within the slab at the point of contact with the piles to resist hogging moments, but no rebar is provided in the interior of the slab (Viney, 2007). The ArcelorMittal proprietary method, on the other hand, uses steel fibres to completely replace all traditional reinforcement (Destrée and Jürgen, 2008). The method is based on the examination of the experimental results of three full-scale tests and some small circular panels using yield-line theory (Destrée, 2007b). Their

main argument for using small circular panels instead of beams is that responses of beams cannot predict the behaviour of the slab.

Current design guidelines for piled SFRC slabs are dominated by yield-line theory YLT (RILEM, 2003), which only provides an upper bound estimate of the load-carrying capacity and can be unsafe if the critical mechanism is overlooked. There have been tremendous works on numerical investigations on ground-supported slabs (Abbas et al., 2004, Cerioni et al., 2004, Maya et al., 2012, Barros and Figueiras, 2001) and minimal numerical investigation works on piled floors. The YLT analysis is also incapable of providing any information regarding deformations (deflections and slopes) or cracking, which are critical for suspended floors to ensure the safe operation of mechanical handling equipment (e.g. the lift truck is susceptible to slight tilts of the floor). Current design provisions are unsatisfactory as they adopt simple span/effective depth limits which were developed for flat slabs in buildings where the aim is to minimised cracking in finishes and partitions. Therefore, there is a need for appropriate limits to be derived to suit stringent surface regularity requirements in industrial floors. Current design guidance accounts only for uniformly-distributed loads and concentrated load (whether single or multiple), often encountered in practice, are not considered. Although most floors are constructed using proprietary designs, the latter are excluded from the published guidance and require critical examination. The treatment of crack control due to restrained early-age and drying shrinkage is not precise, especially in the ArcelorMittal method which eliminates conventional reinforcement. Crack control measures are critical to piled floors since the slab is often cast in large pours with no internal joints (Beckett, 2004, Goodchild, 2004). There is an acknowledged scatter in the thicknesses recommended by current design guidelines as they utilise a range of material and loading parameters, effective spans between piles and safety factors resulting in thicknesses that could differ by 25% or even more, with proprietary designs providing the smaller slabs sections as there will be no provision for cover. (Hulett and Sketchley, 2009, Hedebratt, 2012b). The performance of existing slabs is also a source of concern. There is seemingly a need for a unified and well-defined design method.

2.1.1 Historical Development of Fibres

The inclusion of fibre materials to provide tensile strength to a cementitious material that is strong in compression is a concept credited to the Egyptians. They used straw fibre in reinforcing clay mixture in Exodus 5:7 of the Holy Bible over 4000 years ago (Thomas, 1985) to enhance its flexural resistance, consequently giving better behavioural properties once the bricks had been sun-dried. 'Other historical cases of fibre reinforcement exist: plaster reinforced with horsehair, or again with straw in the poorest building conditions, so as to avoid the unsightly occurrence of cracks due to shrinkage, counter-ceilings made of plaster reinforced through reed canes, cement conglomerates fibre-reinforced through asbestos, etc.' (Sarzalejo et al., 2008)

The development of modern fibre reinforced concrete started in 1874 when Berard patented an improvement to the artificial stone (concrete) by adding any granular waste iron (which has been rendered valueless at that time) to the concrete matrix to produce an enhanced concrete recommended for road and walkway paving (Berard, 1874b). From the early 1920s, Prestressed concrete was introduced into the industry bringing about an increase in the structural capacity and usage of concrete (Beddar, 2004). The history of fibre in modern concrete design began about 45 years ago with works by Romualdi, Batson and Mandel as reported by (Zollo, 1997).

In time past, in order to control cracking and improve on the tensile strength of ground supported slabs, fibre were been added (Edgington, 1973b, Swamy and Lankard, 1974, CHANH, 1990, Zollo, 1997, Barros and Figueiras, 2001, America Concrete Institute, 2002, Beddar, 2004, Chen, 2005, British Standard Institute, 2006, Eddy, 2008, Crowther, 2009, Jansson, 2011, Ghaffar et al., 2014, Narayan, 2014). With the improvement in the knowledge and understanding of steel-fibre usage in concrete in recent time, there has been a rapid development in the construction of steel-fibre-reinforced concrete (henceforth SFRC) pile-supported slabs (Lok and Pei, 1998, Thooft, 2000, Destrée, 2001, Cameron, 2002, RILEM, 2002b, Beton, 2004, The Concrete Society TR63, 2007, Destrée, 2007a, Vollum, 2007, Hedebratt and Silfwerbrand, 2008, Destrée and Jürgen, 2008, Jensen, 2013, Hedebratt and Silfwerbrand, 2014).

Steel fibres are provided to replace some or all of conventional steel reinforcement. It is estimated that about 2 million square metres of piled SFRC slabs (without any traditional steel reinforcement), which account for 20% of floors constructed, have been done in the UK (Concrete-Society, 2007, Eddy, 2003, The Concrete Society TR63, 2007)and 5.5 million square metres worldwide (Destrée, 2007a, Eddy, 2008).

2.1.2 Classification of Fibres

In reference to the work of (Naaman and Reinhardt, 2003), they classified fibres used in concrete composites as follows:

2.1.3 Sources of fibres

Fibres can be classified according to their source [Figure 1.6]. Moreover, these are broadly divided into three: Natural organic (cellulose, sisal, cassava, bamboo, jute etc.), natural inorganic (asbestos, wollastonite, rock wool etc.) and man-made (steel, glass, synthetic etc.)

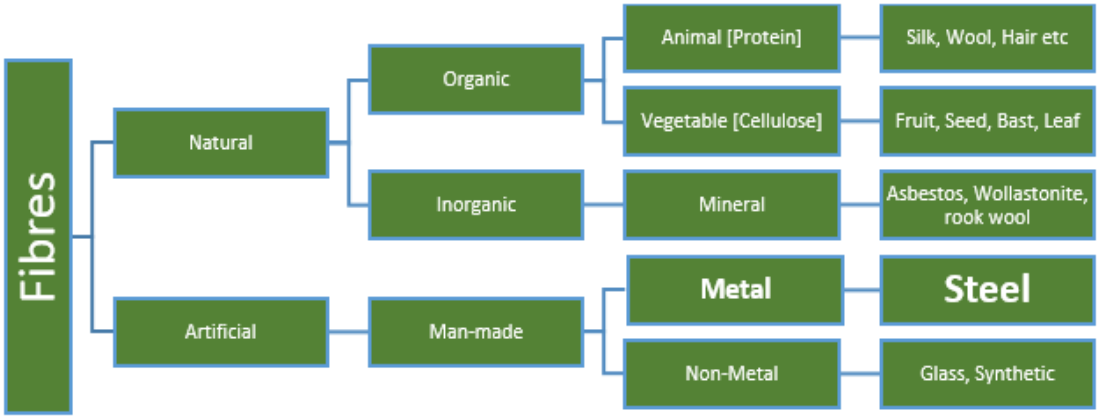

Figure 2.1: Sources of Fibres

2.1.4 Physical/Chemical properties

The classification can also be based on their physical/chemical properties such as density, flammability, surface roughness, reactivity or non-reactivity with cementitious matrix etc.

2.1.5 Mechanical properties

Fibres are also classified by their mechanical properties, e.g. compressive strength, elastic modulus, specific gravity, tensile strength, ductility, elongation to failure, stiffness, surface adhesion etc.

2.1.6 Shape and size

Geometric properties of fibres are another mode of Classification, properties such as length, diameter, cross-sectional shape, surface deformation etc. cross-sectional shape of fibres can be rectangular, circular, square, diamond, triangular, flat, and polygonal shape.

2.2 Steel Fibres

These are straight or deformed pieces of cold-drawn steel wire, straight or deformed cut sheet fibres, melt extracted fibres, shaved cold drawn wire fibres and fibres milled from steel blocks which are suitable to be homogeneously mixed into concrete or mortar. Steel fibres mixed into the concrete can be a substitute to the provision of conventional steel bars or welded fabric in some structural members. The idea has been in existence for many years (Berard, 1874b) and it has been used in a limited range of applications: among the first significant uses was the patching of bomb craters in runways during World War II. The commercial use of this material gathers momentum in the 1970s predominantly in Europe, Japan and the USA. (The Concrete Society TR63, 2007)

2.2.1 Shape of the Fibre

The steel-fibres come in various shapes and size. They can either be straight or deformed. All manufacturers are expected to declare the shape of the fibre. The Figure 2.2 below shows some readily available steel-fibres in the market.

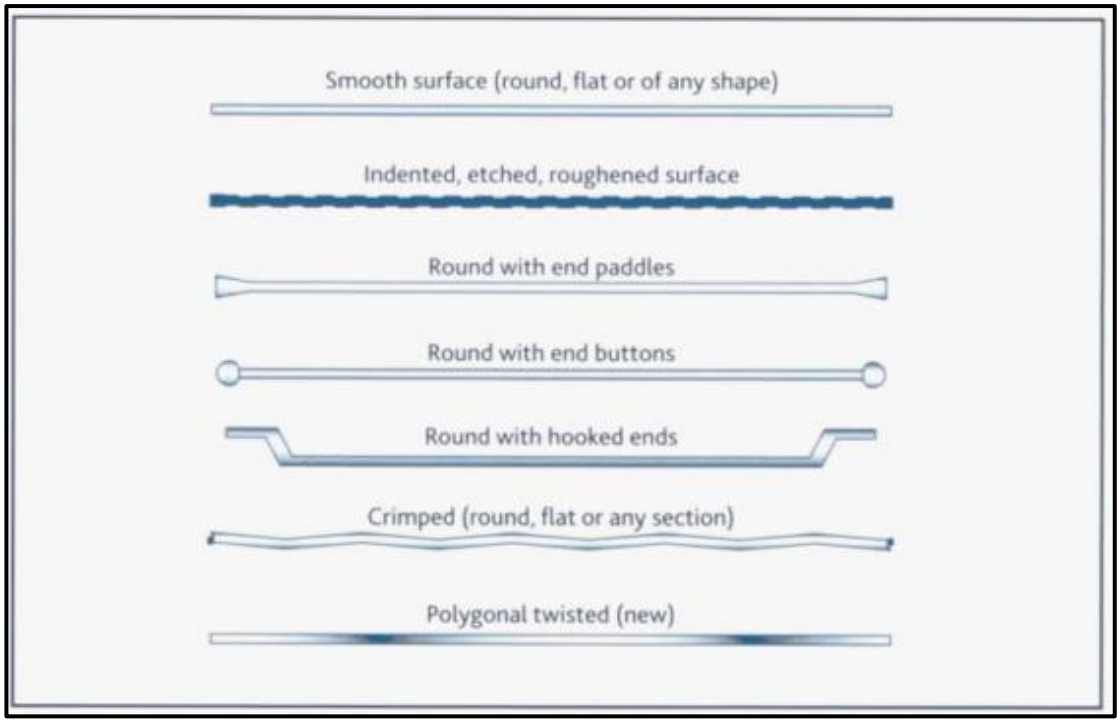

Figure 2.2: Types of Steel-Fibre adapted from (Concrete-Society, 2007)

For this research work, experimental works with different types of steel-fibre shall be considered. Two typical steel-fibres, hooked-end and crimped [Dramix^{TM} RC-65/35-BN and TABIX-Twincone] are shown below in Figure 2.3:

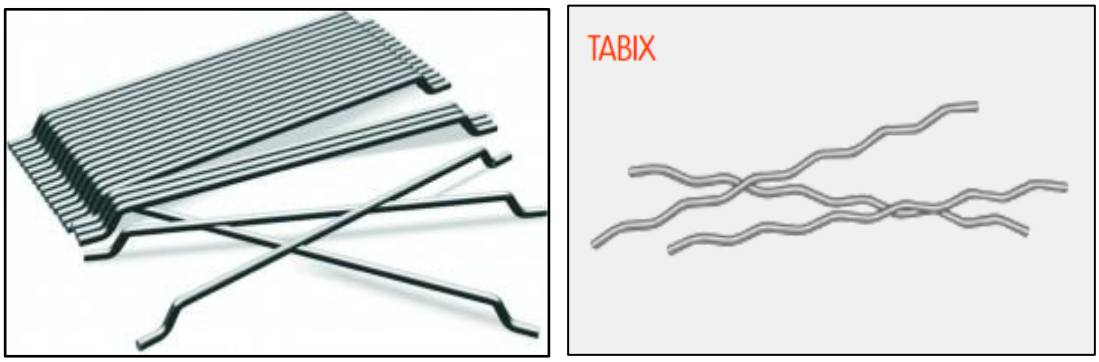

[a] [b]

Figure 2.3: [a] DramixTM RC-65/35-BN (hooked end) and [b] TABIX-Twincone (ArcelorMittal, 2011, Bekaert, 2012) (crimped)

2.2.2 Classification of Steel-Fibre

The steel-fibres are classified into five groups based on the mode of production (British Standard Institute, 2006):

Group I	-Cold-drawn wire
Group II	-Cut sheet
Group III	-Melt extracted

Group IV	-Shaved cold drawn wire
Group V	-Milled from blocks

2.2.3 Characterisation of steel-fibre

Steel-fibres can also be characterised by their physical properties:

Cross-section	-Round, flat, crescent etc.
Deformations	-Straight, wavy hook-end etc.
Length	-19 – 60 mm
Aspect Ratio	-30 – 100
Tensile strength	-345 – 1700 N/mm^2
Young's Modulus	-205 kN/mm^2

2.2.4 Basic Definition of Physical Properties

The under-listed are basic terms and their meaning that defines the steel fibres (British Standard Institute, 2006, The Concrete Society TR63, 2007)

Length (*l*):	This is the distance between the outer ends of the fibre
Equivalent diameter:	This is the diameter of a circle which has an area equal to the cross-sectional area of the fibre
Aspect ratio:	This is the ratio of the length to the equivalent diameter of the fibre (l/d)
Balling:	This describes the creation of large bunches of entangled fibres that may arise during the concrete mixing process
Fibre count:	This is the fibre concentration measured by the number

2.3 Properties of Steel Fibre Reinforced Concrete

Experimental works in SFRC has been on-going for over four decades at all levels (academics, industry, construction societies, governmental bodies, and so forth). Their findings can be summarised into the following:

2.3.1 Compressive Strength of SFRC

From various experimental and numerical results, the compressive strength steel-fibre reinforced concrete [with volume fraction of fibre ≤ 1%] and that of plain concrete are about the same, but a higher percentage of fibre fraction tends to produce a slight increase in compressive strength but they are generally assumed to be the same (Edgington, 1973a, Swamy, 1974, Naaman and Gopalaratnam, 1983, CHANH, 1990,

Wang et al., 1996, N., 2009, Zollo, 1997, Lok and Pei, 1998, Barros and Cruz, 1999, America Concrete Institute, 1999, Rossi, 1999, Neal, 2000, Carr, 2000, Kooiman, 2000, Barros and Cruz, 2001, RILEM, 2002b, America Concrete Institute, 2002, Van Chanh, 2004, Chen, 2005, British Standard Institute, 2006, Ghosh et al., 2007, Hadi, 2008, Garcia and Borrell, 2010, Jansson, 2011, Barros et al., 2012, Mohsin, 2012a, Barros et al., 2013b, Ghaffar et al., 2014, Fall, 2014, Fathima and Varghese, 2014, Xie et al., 2015).

This was idealised in the Euro Code 2, as per the Figure 2.3 and since formed the basis for assessing and analysing compression strength of plain concrete.

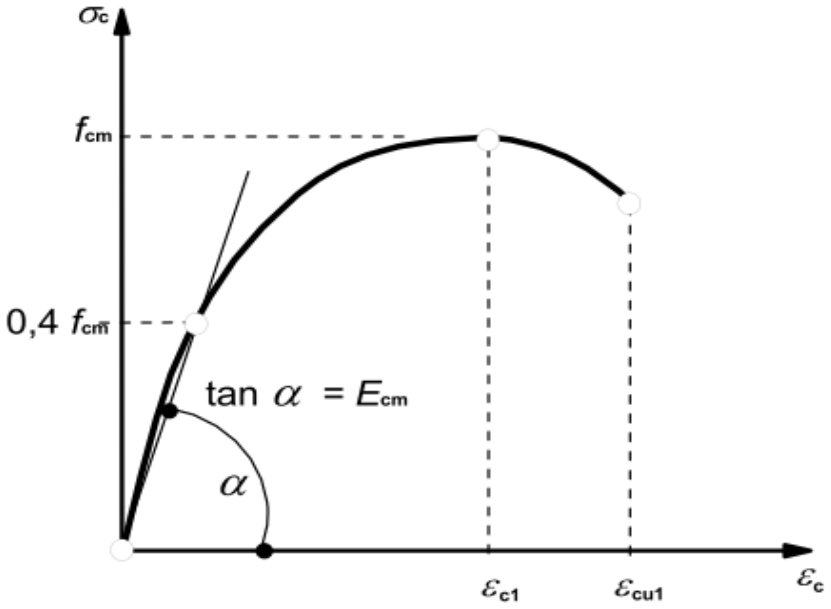

Figure 2.4: Stress-Strain Relation of concrete in compression adapted from (BSI 2004)

Where:

σ_C – Compressive stress in the concrete

f_{cm} – Mean value of concrete cylinder compressive strength

E_{cm} – Modulus of elasticity in compression

f_{ck} – Characteristic compressive cylinder strength of concrete at 28 days

ε_c – Compressive strain in concrete

ε_{c1} – Compressive strain in concrete at the peak stress f_c

ε_{cu} – Ultimate Compressive strain in concrete

Other benefits as reported by (Kooiman, 2000) shown in Figure 2-4, that there is an improved ductility in the response of the compression zone when steel-fibres are added to plain concrete.

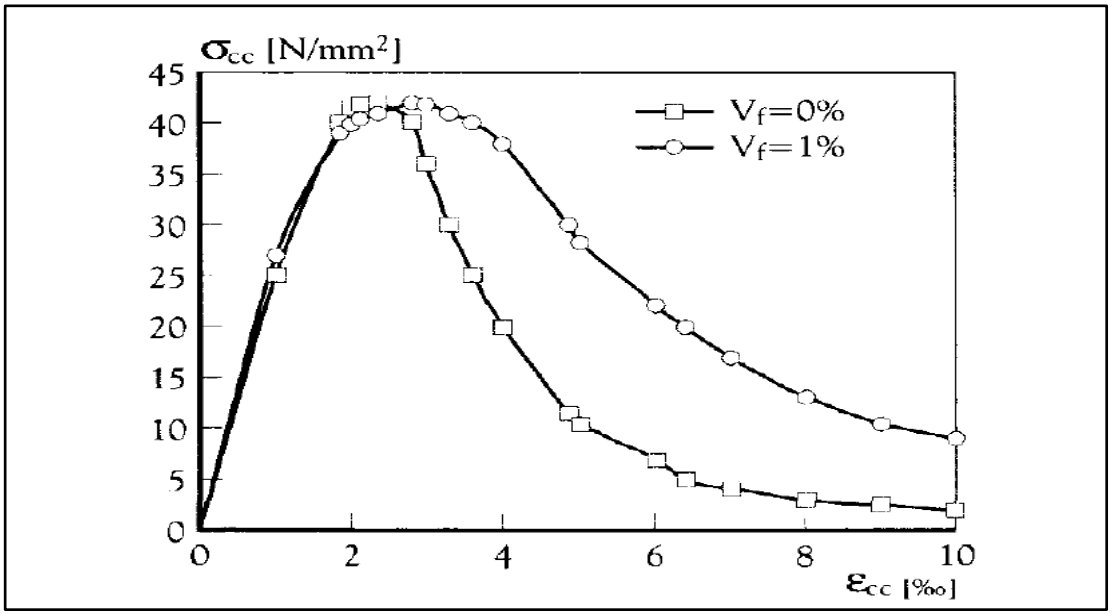

Figure 2.5: Stress-strain graph adapted from (Kooiman, 2000)

2.3.2 Tensile Strength of SFRC

The addition of steel fibres to plain concrete has a significant impact in its flexural response, more so than in the case of tension or compression (Swamy and Lankard, 1974, CHANH, 1990, Lok and Pei, 1998, Kooiman, 2000, Barros and Antunes, 2003, Oliveira, 2010). The 3- and 4-point bending tests [Figures 2.11 and 2.13] are generally used to get the fracture toughness behaviour of different fibrous materials. The tests form a reliable datum for comparing different types of fibres with one other. Assessment of the toughness behaviour of steel fibres is by calculating the area under the load-deflection response, as demonstrated in Figure 2.12 [a-c]. The measure of fracture toughness is indicated by the post-cracking behaviour of the concrete and is strongly influenced by the fibre dosage added. When stresses are higher than the ultimate tensile strength, the brittle concrete matrix would not be able to carry it. The excess stresses will lead to micro-cracks being formed in the beam, leading to a transfer in stresses from

the brittle concrete matrix to the ductile steel fibres. The process is illustrated by (Barros and Cruz, 1999) in Figure 2.5

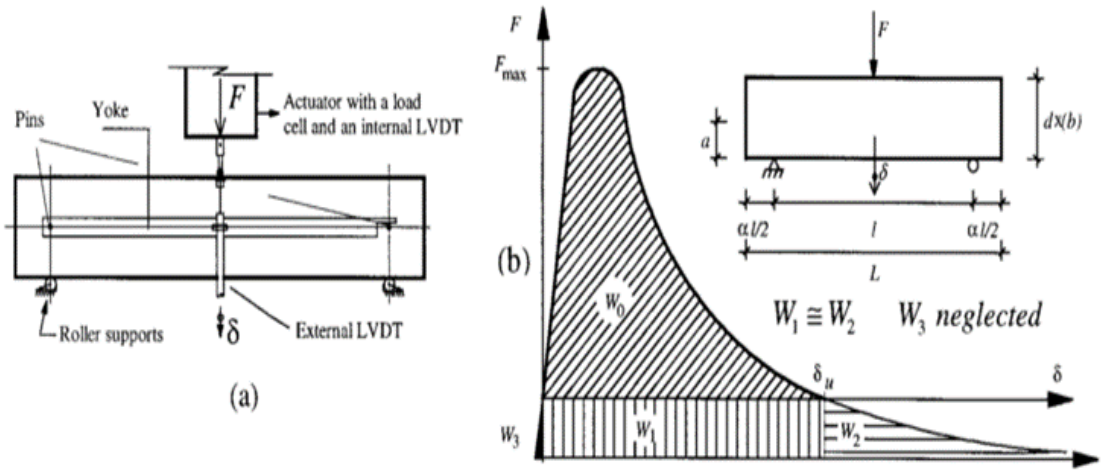

Figure 2.6: Setup of [a] Flexural test on notched beam [b] Fracture energy evaluation (Barros and Cruz, 1999)

As soon as the first micro-crack propagates [Figure 2.6], the neutral axis of the beam shifts upwards, as shown in Phase 2. At this stage, the micro-crack is bridged by a combination of aggregate interlock and steel fibres. In Phase 3, the crack propagates upwards through the section. The steel fibres now bridge the crack, and significant stresses build up at the concrete matrix-fibre interface. Finally, Phase 4 is affected by the pull-out and/or fracture of the steel fibres which governs the failure of the specimen (Tlemat et al., 2006b).

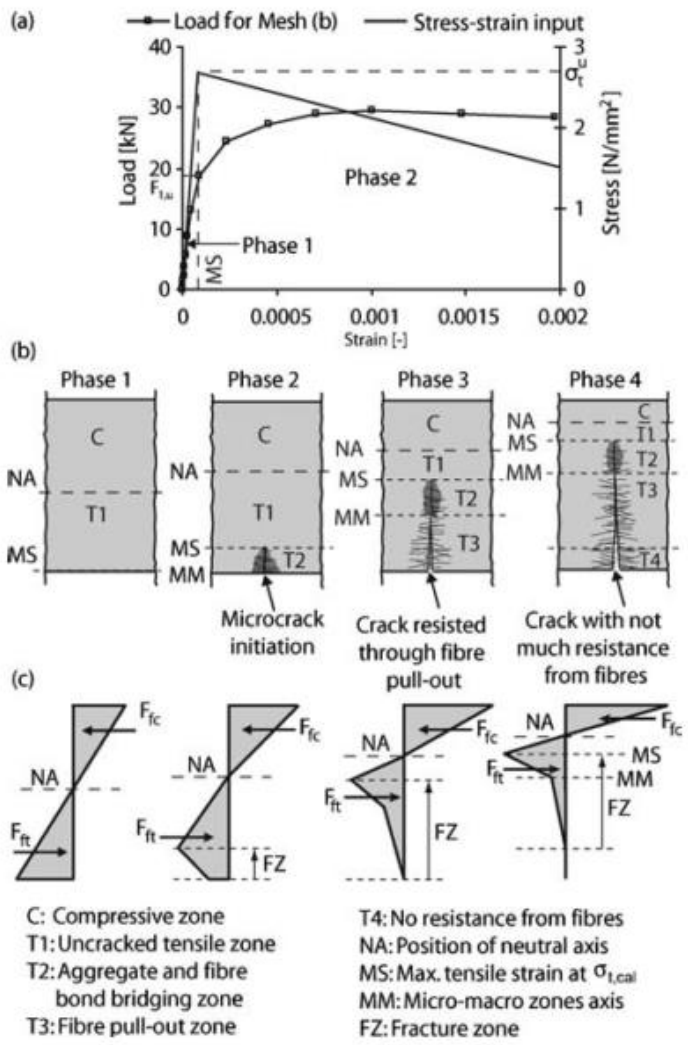

Figure 2.7: Typical stress distributions in a concrete section subjected to four-point bending (Tlemat et al., 2006a)

2.4 Crack propagation and formulation

The main advantage of fibres in the concrete matrix is their ability to transfer stresses across a crack, and thus enhancing the toughness and ductility of the concrete as well as the energy absorption capacity (Barros and Cruz, 1999, America Concrete Institute, 2002, The Concrete Society TR63, 2007, Destrée, 2007b, Institute, 2007, Hadi, 2008, Abbas et al., 2014b, Fathima and Varghese, 2014). Concrete is a composite material with pores and micro-cracks caused by shrinkage, expansion and thermal strains, which have been restrained by coarse aggregates and boundary conditions. During loading, the concrete matrix transfers part of the load to the fibres before any macro-crack is formed. Therefore, it is hypothetically possible to increase the strength of the material by adding fibres (Døssland, 2008). Likewise, when a small volume of fibre [<0.5%] is added to

conventional concrete, the fibre reinforcement does not cause noticeable improvement of strength. The small fibre dosage is related to the low tensile strain capacity of the cementitious matrix and also to the increased porosity that the fibre addition may induce. (Löfgren, 2005)

With continuous loading, the micro-cracks will then start to expand and ultimately lead to a macro-crack which covers numerous micro-cracks (Kooiman et al., 2000, Barros, 2004, Tlemat et al., 2006b, Richardson, 2008, Bernardi et al., 2013). Post-crack tensile strength is provided to the concrete by the bridging of fibres across cracks as illustrated in Figure 2-8[b]. Other mechanics of the fibre like plastic deformation and matrix spalling might be present in addition to debonding and fibre pull-out. Figure 2.8 shows (Löfgren, 2005) an overview of the mechanics of crack formation.

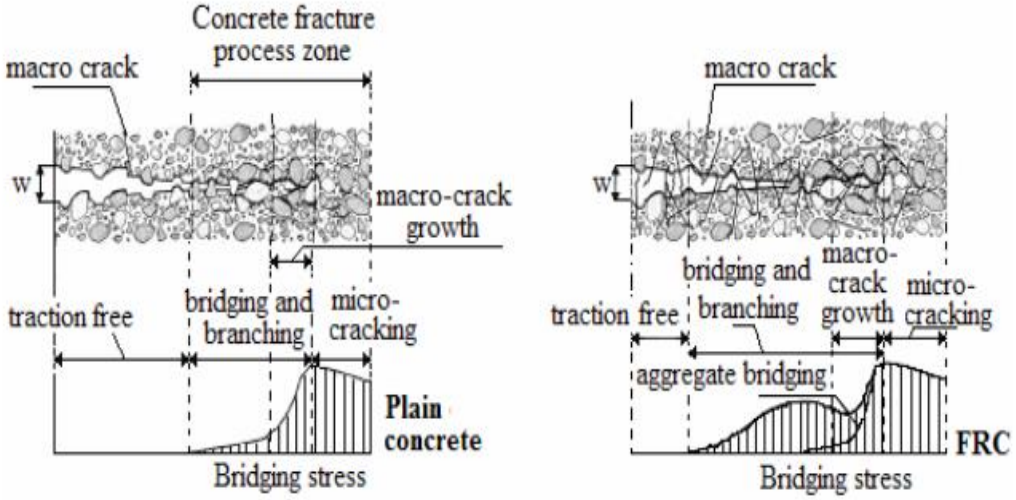

[a] [b]

Figure 2.8: Schematic description of stress-crack opening for [a] plain concrete and [b] SFRC. Adapted from (Löfgren, 2005)

The post-crack stress can be larger than the cracking load subject to the number of fibres crossing the crack and on the concrete-fibre-bonding matrix, resulting in strain hardening behaviour where multiple cracking occurs [Figure 2-8]. Nevertheless, for usual fibre dosages [<1%] the material exhibit strain softening behaviour, i.e. the damage localises immediately after initiation of the first crack.

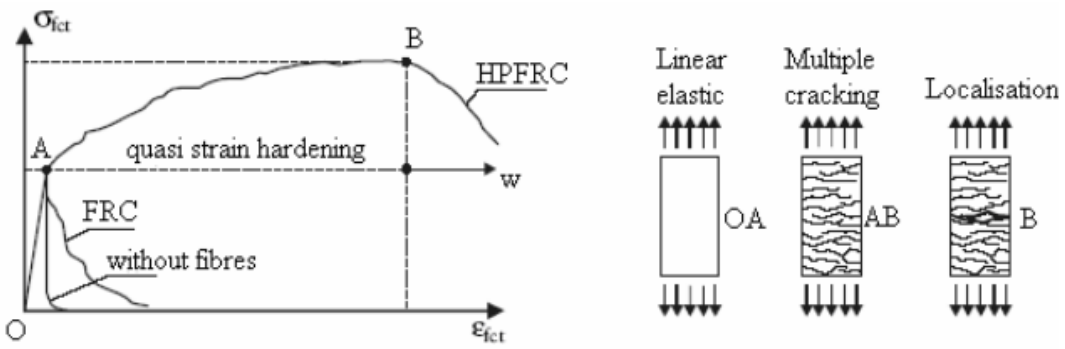

Figure 2.9: High-performance SFRC. Adapted from (Kooiman, 2000)

2.5 Test Methods

Over the years, various researchers and research institutes (Lok and Pei, 1998, IstructE, 1999, America Concrete Institute, 1999, Kooiman et al., 2000, RILEM, 2002b, America Concrete Institute, 2002, Concrete-Society, 2007, Ferrara et al., 2012) have provided different test methods for determining the mechanical properties and flexural response of SFRC. The most common among them are enumerated and explained below:

2.5.1 Uni-axial tension test

The test is used to determine the stress-crack opening relationship, σ_w-w, for SFRC (RILEM, 2001, Institute, 2007). The test method was primarily designed for SFRC which exhibit strain softening behaviour and can be used for any other fibre reinforced concrete including plain concrete which display strain softening behaviour. Tensile strength cannot be determined by the test. Technically, the test is expensive and difficult to perform, particularly at the point of fastening the specimen to the machine to prevent rotation (Dupont, 2003). The test set-up is shown in Figure 2.10.

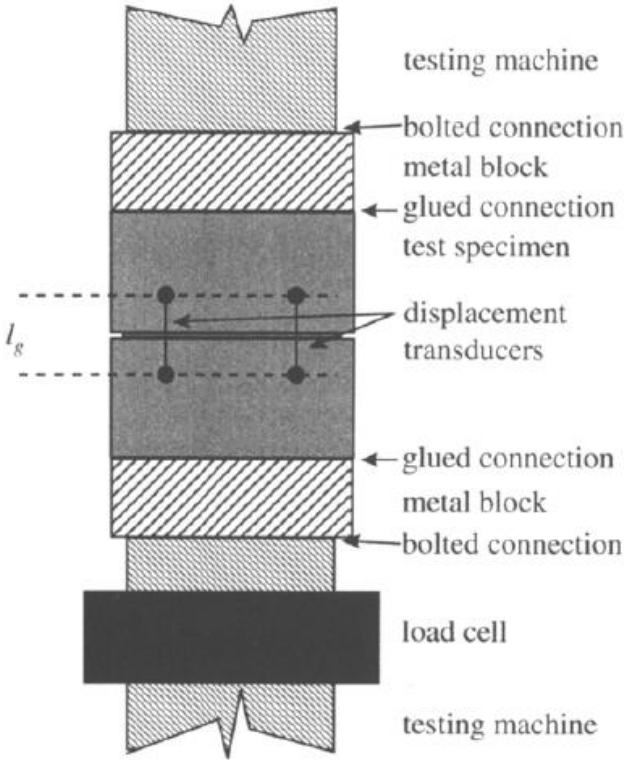

Figure 2.10: Typical set-up for uni-axial tension testing adapted from (RILEM, 2001)

The test specimen is a cylinder with a diameter of 150 mm and a height of 150 mm sawn out of a cylinder with a height of 300 mm, by cutting off from the top and bottom 75 mm each. At mid-height, a circumferential notch is cut with a depth of 15 mm. Over this notch, three [3] LVDT's [Linear Voltage Displacement Transducer] are placed at 120°. The gauge length of the LVDT's is set at 30 mm.

The stresses are calculated directly by just dividing the load P by the cross-sectional area at the notch A_n

$$\sigma_w = \frac{P}{A_n} \qquad \text{Eqn. 2.1}$$

The crack opening w is otained from the average signal of the displacement transducers by subtracting the average displacement at peak stress, neglecting the elastic unloading. Thus, denoting the displacement readings of the individual n transducers δj, j = 1, 2 . . . . . n, the average signal δ is calculated from

$$\delta = \frac{1}{n}\sum_{j=1}^{n} \delta j \qquad \text{Eqn. 2.2}$$

Taking the average displacement at peak stress as δp, the crack opening w is calculated from

$$w = \delta - \delta p \qquad \text{Eqn. 2.3}$$

Figure 2.11 shows he stress-deformation curve in which crack width opening w is estimated.

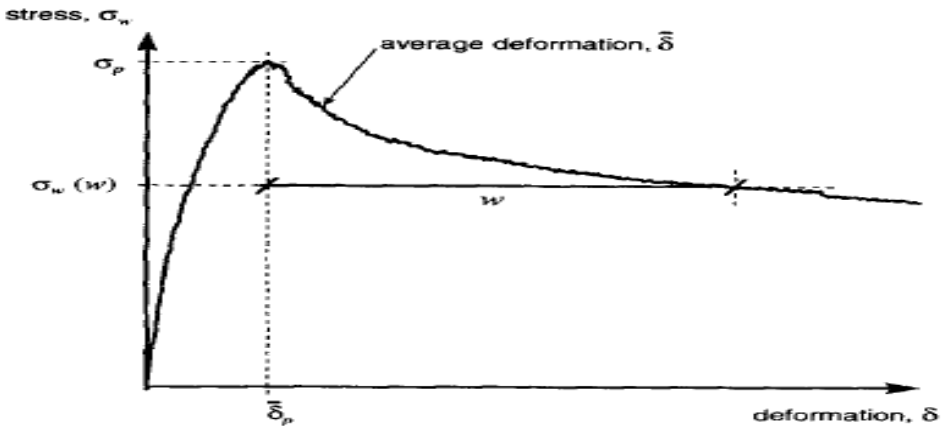

Figure 2.11: Crack width Opening w calculation adapted from (RILEM, 2001)

2.5.2 3-Point bending test

In 2002, RILEM Technical Committee proposed a 3-point bending test for the evaluation of the flexural behaviour SFRC (RILEM, 2002b, Institute, 2007). The test includes a notch at the centre for predicting the failure pattern of the beam specimen. The set-up of the test is shown below in Figure 2.12:

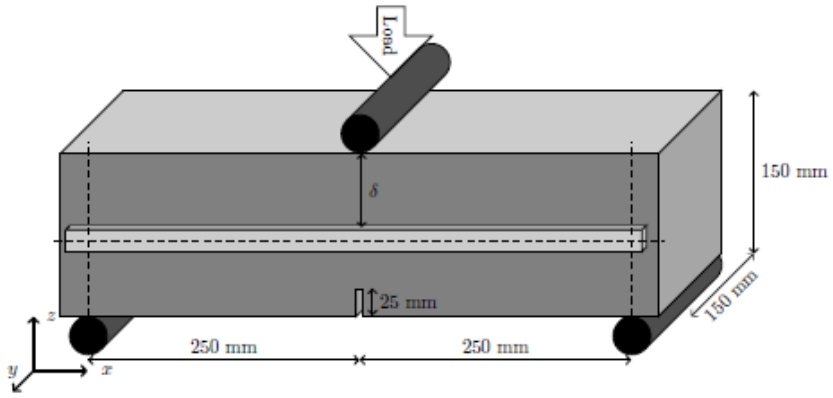

Figure 2.12: 3-Point bending test set-up adapted from (Fall, 2014)

The test specimen is a rectangle with a minimum length of 550mm and a square cross-section of 150mm over a span of 500mm and a notch of 25mm. Two linear variable differential transformers [LVDT] are fixed to the beam to measure the deflection on the

top surface and a clip gauge for measuring the crack mouth opening displacement [CMOD] in the notch.

The 3-point test method can be used to determine [1] the limit of proportionality (LOP), i.e. the point at which the stress and strain are proportional on the load-deflection or load-crack mouth opening displacement curve; [2] the two equivalent flexural tensile strengths which identify the material behaviour up to the selected deflection, and [3] the four residual flexural tensile strengths which identify the material behaviour at a selected deflection or CMOD. If the equivalent flexural tensile strength is required, it is necessary to measure the deflection. However, if only residual flexural tensile strengths are calculated, one can choose between the measurement of deflection and/or CMOD (RILEM, 2002b)

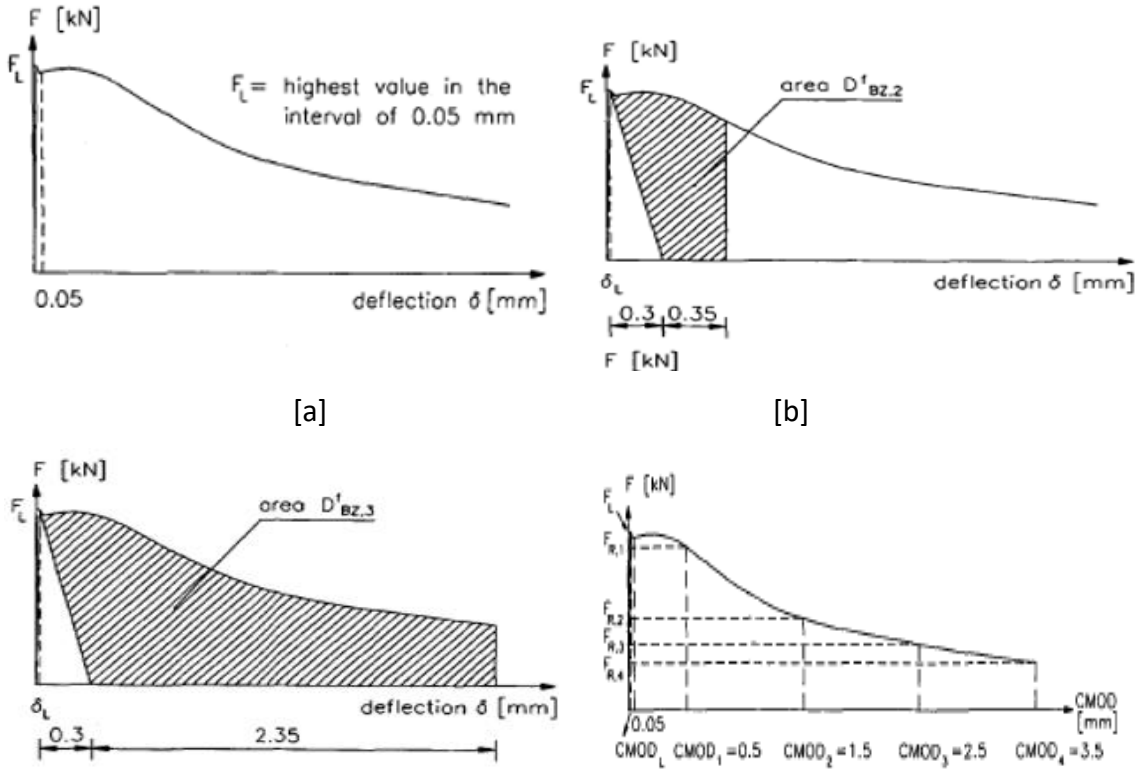

Figure 2.13: [a-c]: Load – deflection graphs [d] Load-CMOD graph

The area under the load-deflection curve, Figure 2.13 [b, c], up to the deflection δ_2 [δ_3] is the energy absorption capacity $D_{BZ,2}$ [$D_{BZ,3}$]. These consist of two parts:

D_{BZ}^{b} [Nmm] – Plain concrete

$D_{BZ,2}^{f}$ and $D_{BZ,3}^{f}$ [Nmm] – the influence of steel fibres

The moment at mid-span of the test beam is:

$$M_L = \frac{F_L}{2} . \frac{L}{2} \quad \text{Eqn. 2.4}$$

Where

M_L – Moment at mid-span

F_L – Load at the limit of proportionality

L – Span of the beam specimen

Also, the relationship between the CMOD and δ is expressed as:

$$CMOD = 1.18\delta + \beta \text{ while } \beta = -0.0416mm \quad \text{Eqn. 2.5}$$

The equation is only applicable to the post-peak region of the load-CMOD [load-δ] curve. The response of the beam at CMOD 0.5 mm, 1.5 mm, 2.5 mm and 3.5 mm is of special interest. They are expressed as follows:

$\delta_{R,1}$ = 0.46mm – $CMOD_1$ = 0.5mm

$\delta_{R,2}$ = 1.31mm – $CMOD_2$ = 1.5mm

$\delta_{R,3}$ = 2.15mm – $CMOD_3$ = 2.5mm

$\delta_{R,4}$ = 0.46mm – $CMOD_4$ = 3.5mm

The equivalent flexural tensile strength $f_{eq,2}$ and $f_{eq,3}$ are expressed as follows:

$$f_{eq,2} = \frac{3}{2}\left(\frac{D_{BZ,2}^{f}}{0.50}\right)\frac{L}{bh_{sp}^{2}} \text{ [N/mm}^2\text{]} \quad \text{Eqn. 2.6}$$

$$f_{eq,3} = \frac{3}{2}\left(\frac{D_{BZ,3}^{f}}{2.50}\right)\frac{L}{bh_{sp}^{2}} \text{ [N/mm}^2\text{]} \quad \text{Eqn. 2.7}$$

2.5.3 4-Point bending test

The 4-point bending test is similar to that of the 3-point bending test with a different set-up configuration having the beam divided into three equal parts and two-point loads on the beam. The setup is shown Figure 2.14

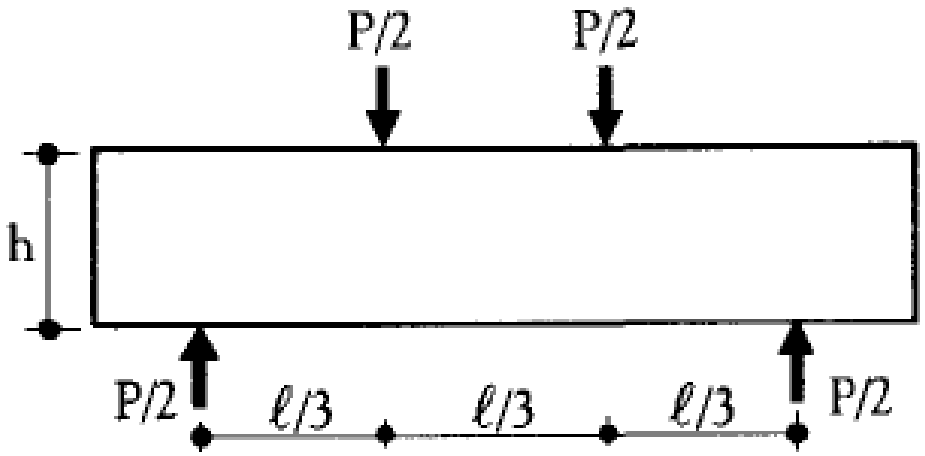

Figure 2.14: 4-point bending test adapted from (Kooiman, 2000)

The Japanese method of test for flexural strength of SFRC uses the 4-point bending test (Japanese Concrete Institute, 1984). The test is used to determine the flexural strength (σ_b) and flexural toughness factor (σ'_b) of a SFRC. The load-deflection curve is shown in Figure 2.15.

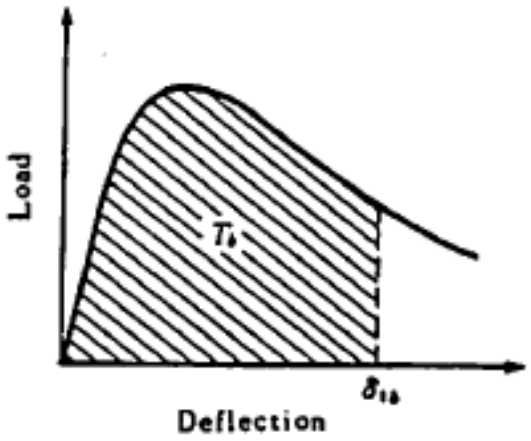

Figure 2.15: Load-deflection curve adapted from (JCI Test)

Flexural strength (σ_b) = $\frac{Pl}{bh^2}$ [N/mm^2] Eqn. 2.8

Where,

P –maximum load obtained [N]

l –span [mm]

b –width of the failed cross-section [mm]

h –height of the failed section [mm]

Flexural toughness factor (σ'_b) = $\frac{Tb}{\delta_{tb}}.\frac{l}{bh^2}$ [N/mm2] Eqn. 2.9

Where,

T_b –Flexural toughness [J]

δ_{tb} –deflection of 1/150 of span [mm]

[2mm when the span is 300mm and 3mm when the span is 450mm]

2.5.4 Slab (Plate) test

There are different tests method advocated by different bodies (Japanese Concrete Institute, 1984, IstructE, 1999, RILEM, 2002b, America Concrete Institute, 2002, British Standard Institute, 2005, British Standard Institute, 2006, NZS, 2006, NRC, 2007, The Concrete Society TR63, 2007). Some researchers (Bernard, 2000, Destrée, 2001, Sukontasukkul, 2003, Beton, 2004, Barros et al., 2007, Destrée and Jürgen, 2008, Hedebratt and Silfwerbrand, 2008, Nakov, 2012, Hedebratt, 2012a) argued that the beam bending tests cannot represent the flexural behaviour of SFRC slab accurately, so the need for the plate tests for slabs.

The panel can be square [600 x 600 x 100mm] or circular [diameter ≥ 600mm] with clear span ≥ 500mm. Supports are provided at the corners or the edges. The test can be statically determinate or indeterminate. The area under the load-deflection curve up to 25mm of the central deflection is the fracture toughness.

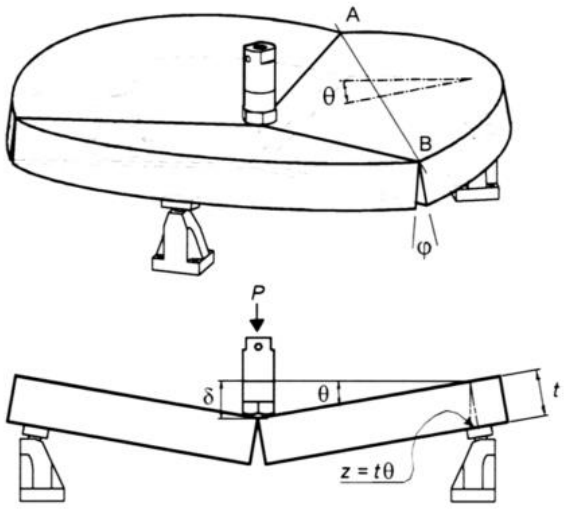

Figure 2.16: Schematic diagram of a statically determinate round panel adapted from (Bernard, 2000)

Plate tests have some distinct merits, as well as demerits, in comparison with beam bending tests. The response of the plates is perhaps more representative of the in situ flexural response of a pile-supported or elevated slab with the development of multiple cracks (The Concrete Society TR63, 2007, Destrée and Jürgen, 2008). The crack pattern is a right resemblance of the failure and a distinct benefit in the understanding of the SFRC slabs (Destrée, 2007a, Hedebratt and Silfwerbrand, 2008, Jansson, 2011)

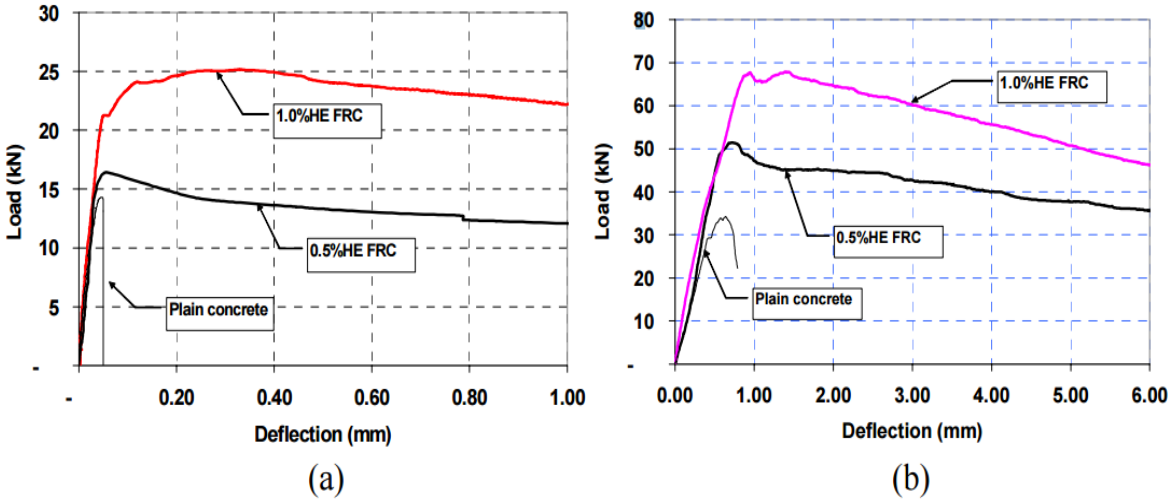

Figure 2.17: Load-deflection responses of [a] beams and [b] plates (Sukontasukkul, 2003)

As plate tests produce more cracks than beams, therefore they can absorb more fracture energy (Sukontasukkul, 2003). This enables the fibres to demonstrate their ability in bridging a crack [Figure 2.17].

The summary of the test methods for SFRC provided for in various guidelines and codes is presented in Table 2.1 and as adapted from (Blanco et al., 2013).

Table 2.1: Main Test methods adapted from (Blanco et al., 2013)

Test	Standard / Reference	Setup	Dimensions[1] [mm]
3-point bending test	EN 14651:2005	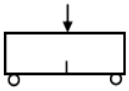	600 x 150 x 150
4-point bending test	NBN B 15-238	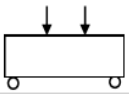	600 x 150 x 150
Uniaxial tensile test	RILEM TC 162-TDF recommendations	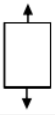	Φ150 x 150
Wedge-splitting test	Tschegg and Linsbauer (1986)		150 x 150 x 150
Barcelona test	UNE 83515:2010		Φ150 x 150
Double-edge wedge splitting test	di Prisco *et al.* (2010)		150 x 150 x 150
EFNARC panel test	EFNARC European Specification for Sprayed Concrete	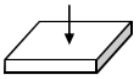	600 x 600 x 10
Round panel test	ASTM C1550 - 10a	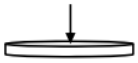	Φ800 x 75

The dimension preceded by the symbol Φ indicates a diameter

2.5.5 Review of Testing Methods of SFRC

Sections 2.5 and 2.6 presented the brief about the test methods and their origins as presently used in the industry. A review of these methods as it affects the analysis and design of elevated and pile-supported SFRC slabs is at this moment presented.

2.5.5.1 Beam Tests

The beam tests have a crucial advantage in that they provide the material properties. However, the results can reveal significant scatter. Also, many researchers and manufacturers still believe that the beam test does not correctly model the response in pile-supported SFRC slabs and that load re-distribution that will occur in pile-supported SFRC slabs during cracking will not occur in a simply supported beam (Destree, 2004, Concrete-Society, 2007).

There is a drop in the flexural load which is a characteristic of tension softening after the start of crack formation. The statically indeterminate nature of pile-supported SFRC slabs does not allow this drop. Therefore, after the initial crack, there is a re-distribution of stresses in the slab which tends to initial hardening process. It can be said that material properties are derivable from beam tests and structural responses from plate tests (Destrée, 2007a, Barros et al., 2012).

Within the beam tests, the RILEM beam test has a better way of measuring the CMOD than the JCI-SF4. In JCI-SF4 test, information concerning CMOD is not available, this is a significant setback in its usage in estimating crack width while the notch in the RILEM beam test predetermined the location of the crack where the CMOD can be measured (Kooiman, 2000, RILEM, 2002b, Barros, 2004). The main disadvantage of the notch system is that CMOD is taking at the notch area [central displacement] rather than the weakest point on the beam

2.5.5.2 Plate Tests of SFRC

The plate tests fall under statically determinate and indeterminate plates, each with their merits and demerit. Under the determinate plate test is the Round Panel Tests [RPT] (Bernard, 2000). The RPT's response, i.e. the formation of multiple cracks is more descriptive of the actual structural response of a pile-supported slab (The Concrete Society TR64, 2007). The difficulty in recording the crack width is a principal constraint of this method.

On the other hand, the statically indeterminate plates are mainly used to understand the structural behaviour of SFRC concerning some applications (Bernard, 2000, British Standard Institute, 2006, ArcelorMittal, 2011) and not to get their material properties. This is mainly because stress distribution is unknown due to the indeterminate boundary condition. With all these facts, it can be said that indeterminate slab and plate tests should be used to understand and monitor the structural response of SFRC slabs and not to be used to determine the properties of the material.

2.6 Material Constitutive Models

The benefits obtained by the introduction of steel-fibres in reinforced concrete has led to a sharp increase in its usage in a variety of practical applications (Swamy, 1974, CHANH, 1990, Zollo, 1997, Loks and Xiao, 1999, Destrée, 2001, Cameron, 2002, Beddar, 2004, Døssland, 2008, Eddy, 2008, Hedebratt and Silfwerbrand, 2008, ArcelorMittal, 2011, Ghaffar et al., 2014). This posed a research challenge to introduce and produce a constitutive model to emulate the structural behaviour of SFRC. Over the years, various researchers have conducted research into understanding the compressive and flexural behaviour of SFRC and coming out with constitutive models to describe SFRC. Some of them are examined and reported below:

2.6.1 Lok & Pei (1998)

The proposed constitutive model was based on the stress-strain relationship. The model consists of the compressive behaviour which was based on the compressive behaviour for plain concrete in BS 8110 (1985) since the effect of steel-fibre on compressive strength of SFRC is minimal or negligible. Its tensile behaviour incorporates a bilinear strain softening. The model is defined by the properties of the composite material and that of steel-fibres. These properties include the characteristic strength of concrete in compression and tensile strength [f_{cu}, f_t], fibre aspect ratio [$^{L}/_{d}$], fibre volume [V_f] and bond stress of fibre-concrete matrix [τ_d]. These properties determines the response of the matrix to either exhibit strain softening or hardening.

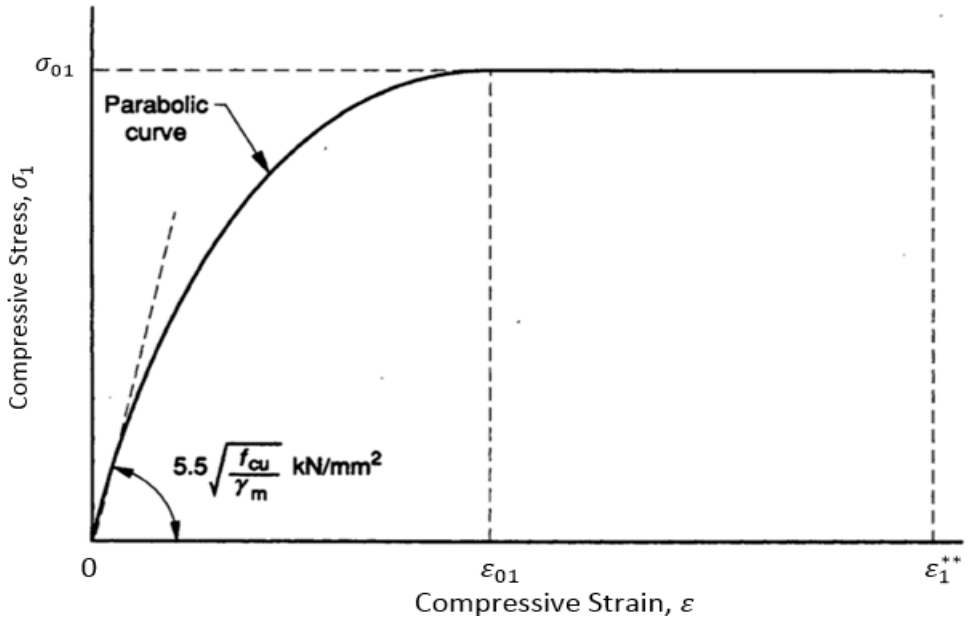

Figure 2.18: Compressive Stress-Strain of SFRC adapted from BS 8110

The ultimate compressive stress, σ_{01} is taken as

$$\sigma_{01} = 0.67 \frac{f_{cu}}{\gamma_m} \quad \text{Eqn. 2.10}$$

Where f_{cu} - Characteristic cube strength

γ_m - Partial safety factor for the material

The corresponding strain to the ultimate compressive stress, ε_{01} is taken as

$$\varepsilon_{01} = 2.4\ x\ 10^{-4} \sqrt{\frac{f_{cu}}{\gamma_m}} \quad \text{Eqn. 2.11}$$

The parabolic section of the compressive behaviour is defined regarding stress

$$\sigma_1 = \sigma_{01} - \left(\frac{\sigma_{01}}{(\varepsilon_{01})^2}\right)(\varepsilon_1 - \varepsilon_{01})^2 \quad \text{Eqn. 2.12}$$

Moreover, the failure strain at compression ε_1^{**} is taken as 0.0035 (adapted from BS 8110: 1985). The initial tangent modulus of elasticity of concrete in compression is given by E_{0c} and this is computed as:

$$E_{0c} = 5.5 \sqrt{\frac{f_{cu}}{\gamma_m}}\ kN/m^2 \quad \text{Eqn. 2.13}$$

The proposed tensile stress-strain behaviour for SFRC is shown in Figure 2.18. It comprises of two phases, the pre-cracking phase [no crack in the matrix] and the post-cracking phase [when the crack is in the matrix].

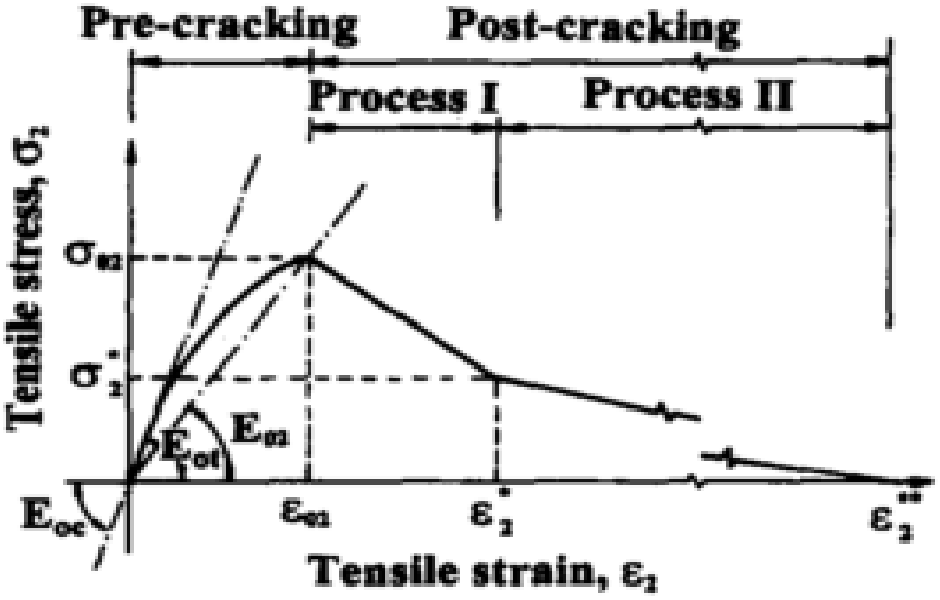

Figure 2.19: Tensile Stress-Strain Relationship adapted from (Lok and Xiao, 1998)

In the first phase, a parabolic curve was proposed to the point [σ_{02}, ε_{02}]. The first crack occurs at the point [σ_{02}, ε_{02}]. Up to this point, the fibre has little or no effect on the

matrix. This point represents the ultimate tensile stress, σ_{02} and the corresponding tensile strain, ε_{02}. These are defined as

$\sigma_{02} = f_t$ Eqn. 2.14

$\varepsilon_{02} = \frac{\varepsilon_{01}}{\sigma_{01}} \sigma_{02}$ Eqn. 2.15

Where:

f_t – Direct tensile strength

Likewise, the tensile modulus of elasticity is taken as equal to that of compression

$E_{0c} = E_{0t}$

$E_{0t} = 2E_{02}$

Where E_{0t} = Tangent Modulus of concrete in tension

E_{02} = Tensile modulus of SFRC in tension

The parabolic relationship of tensile stress and strain is given as:

$\sigma_2 = \sigma_{02} - \frac{\sigma_{02}}{(\varepsilon_{02})^2} (\varepsilon_2 - \varepsilon_{02})^2$ Eqn. 2.16

It was assumed that the steel-fibres bond flawlessly with the concrete matrix and there was no slippage happening at the fibre-concrete interface. Phase two [2] adopted a bilinear descending process to simplify the post-cracking phase of the proposed tensile model. Phase 2 has two processes. The process one [I] is a linear relation which is from $[\sigma_{02}, \varepsilon_{02}]$ to $[\sigma_2^*, \varepsilon_2^*]$. In this process, the concrete matrix contributed to the bonding while the bond stress, τ_d developed gradually with the steel-fibres being strained. σ_2^* is the flexural residual stress and ε_2^* is the corresponding tensile strain and these are estimated as

$\sigma_2^* = F^*N$ Eqn. 2.17

$F^* = \tau_d \pi d \frac{L}{4}$ Eqn. 2.18

$N = \frac{1}{2} \frac{V_f}{\pi r^2}$ Eqn. 2.19

$\sigma_2^* = \frac{1}{2} V_f \tau_d \frac{L}{d}$ Eqn. 2.20

$\varepsilon_2^* = \tau_d \frac{L}{d} \frac{1}{E_{fp}}$ Eqn. 2.21

Where E_{fp} = the modulus of elasticity of steel-fibres

L = Length of fibre

d = Equivalent diameter of fibre

F – Force in fibre

N – Equivalent number of fibres

The process [II] represents the pullout of the fibre from the concrete matrix and at this the dynamic bond stress, τ_d is fully developed and remain constant throughout. The process [II] starts from $[\sigma_2^*, \varepsilon_2^*]$ and ends at [0, ε_2^{**}]. The maximum tensile strain after failure ε_2^{**} can be taken as 2 x 10^4 micro-strain (Craig et al., 1987 cited in Lok and Pei, 1998), 1.45 x 10^4 micro-strain (Chuang and Mai, 1987 cited in Lok and Pei, 1998), or 10 x 10^4 micro-strain (Sakai and Nakamura, 1986 cited in Lok and Pei, 1998). The dynamic bond stress, τ_d can be taken from other research if not provided.

2.6.2 Barros and Figueiras (1999)

In their work (Barros and Figueiras, 1999) on "Flexural Behaviour of SFRC: Testing and Modelling, the outcomes of tests performed on specimens, using the 3-point bending test for steel fibre reinforced concrete (SFRC) were presented. The Fibre volume content used in the concrete ranges from 0 to 60 kg/m^3 [0- 0.75%]. Two types of fibres were used, the Dramix ZP 30/.50 [L=30mm, d =0.50mm] and Dramix ZX 60/.80 [L=60mm, d =0.80mm]. A stress-strain relationship for fibre concrete in compression was derived from the results of the uniaxial compression tests performed under displacement control condition.

$$\sigma_c = f_{cm} \frac{\frac{\varepsilon_c}{\varepsilon_1}}{(1-p-q)+q\left(\frac{\varepsilon_c}{\varepsilon_1}\right)+p\left(\frac{\varepsilon_c}{\varepsilon_1}\right)^{(1-q)/p}} \qquad \text{Eqn. 2.22}$$

Where

$$q = 1 - p - \left(\frac{E_{cl}}{E_{ci}}\right); \quad p + q \in]0,1[; \qquad \frac{1-q}{p} > 0$$

Also,

$$E_{cl} = \frac{f_{cm}}{\varepsilon_{cl}} \qquad \text{Eqn. 2.23}$$

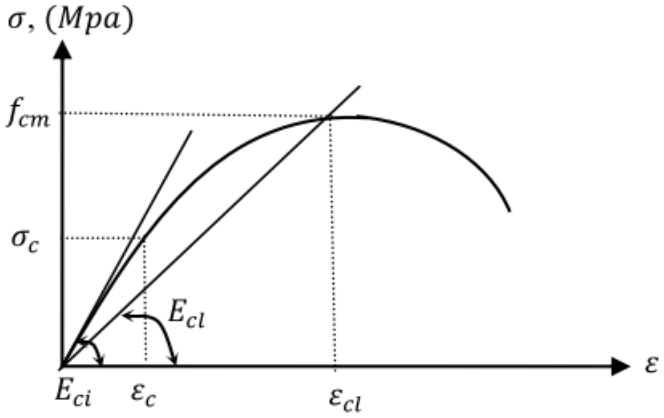

Figure 2.20: Compression stress-strain diagram (Barros and Figueiras, 1999)

Where f_{cm} = average compressive strength

E_{cl} = Secant modulus of elasticity

ε_{cl} = Ultimate strain

The relationship between the parameters based on computed average compression strength values for each fibre are expressed below:

For ZP30/.50 fibres

$$\varepsilon_{c1} = \varepsilon_{c10} + 0.0002W_f \quad \text{Eqn. 2.24}$$

$$p = 1.0 - 0.919\exp(-0.394W_f) \quad \text{Eqn. 2.25}$$

And for ZX60/.80 fibres

$$\varepsilon_{c1} = \varepsilon_{c10} + 0.00026W_f \quad \text{Eqn. 2.26}$$

$$p = 1.0 - 0.722\exp(-144W_f) \quad \text{Eqn. 2.27}$$

Where ε_{c10} = strain at peak for plain concrete [2.2 x 10^{-3} (CEB-FIP 1993 cited in (Barros and Figueiras, 1999))]

W_f = Percentage of fibre weight in the mixture

There was little difference when fibres were added between the peak strength, f_{cm} and the tangent modulus of elasticity, E_{ci} of plain concrete and that of SFRC.

The fracture energy model was used to evaluate the post-peak tensile behaviour, and a numerical model was developed. A bilinear tensile stress-strain relationship was used to depicts the strain softening behaviour of the beam [Figure 2.21]

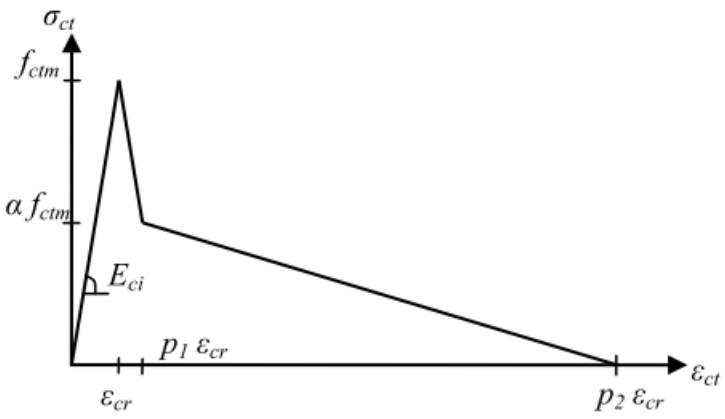

Figure 2.21: Proposed tensile stress-strain diagram adapted from (Barros and Figueiras, 1999)

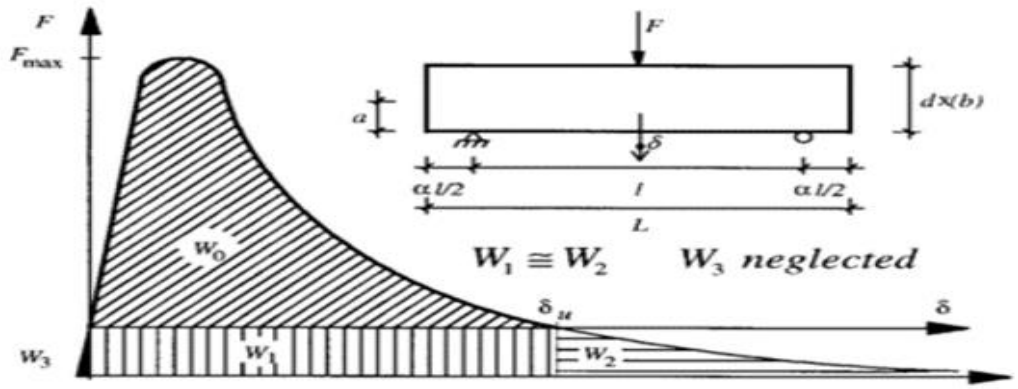

Figure 2.22: Schematic representation of fracture energy evaluation adapted from (Barros and Figueiras, 1999)

The main substantial improvement imparted by the addition of fibres to a concrete matrix is the significant increase in the energy absorption capacity. The fracture energy was evaluated through a simulation of the post-cracking behaviour using the three-point bending tests on notched beams as seen in Figure 2.22. A layered model for the analysis and design of SFRC cross sections was developed based on the constitutive relationships derived from the experiments.

The expression derived for compressive behaviour are:

Compressive Strength

$$\boldsymbol{\sigma}_c = f_{cm} \frac{\frac{\varepsilon_c}{\varepsilon_{c1}}}{(1-p-q)+q\left(\frac{\varepsilon_c}{\varepsilon_{c1}}\right)+p\,(\frac{\varepsilon_c}{\varepsilon_{c1}})^{(1-q)/p}} \qquad \text{Eqn. 2.28}$$

Fracture energy G_f

$$\mathbf{G_f} = \frac{W0+W1+W2}{b(d-a)} = \frac{W0}{b(d-a)} + \frac{m(1-\propto^2)g\delta u}{b(d-a)} = G_f^F + G_f^{pp} \qquad \text{Eqn. 2.29}$$

There were a good agreement results from the simulations [moment-curvature curves] with the model applied when compared to the slabs experimental results. The fibre volume ranges from 0.38 – 0.75%.

2.6.3 Rossi (1999)

Rossi proposed a probabilistic discrete cracking model for non-steel fibre reinforced concrete (Rossi probabilistic discrete cracking model) and a fundamental examination of its extension to steel fibre reinforced concrete. The Rossi probabilistic discrete cracking model applied to steel fibre reinforced concrete is proposed. In this model, 'cracking is modelled through contact elements which will have a perfect elastic-plastic behaviour with brittle fracture'. The plastic step, as well as the post-cracking energy, are uncorrelated random variables. The numerical work entails a perfect elastic-plastic behaviour with a brittle fracture and the adaptation of the existing contact elements.

2.6.4 RILEM TC 162-TDF (2002)

In a 3-point bending test on several beams, the RILEM TC 162-TDF Recommendation (2002) proposed a stress-strain relation for SFRC with compressive strengths up to C50/60. The design of SFRC according to the $\sigma - \varepsilon$ method [Figure 2.23] for compression adopted was on the same fundamentals as the design of normal reinforced concrete.

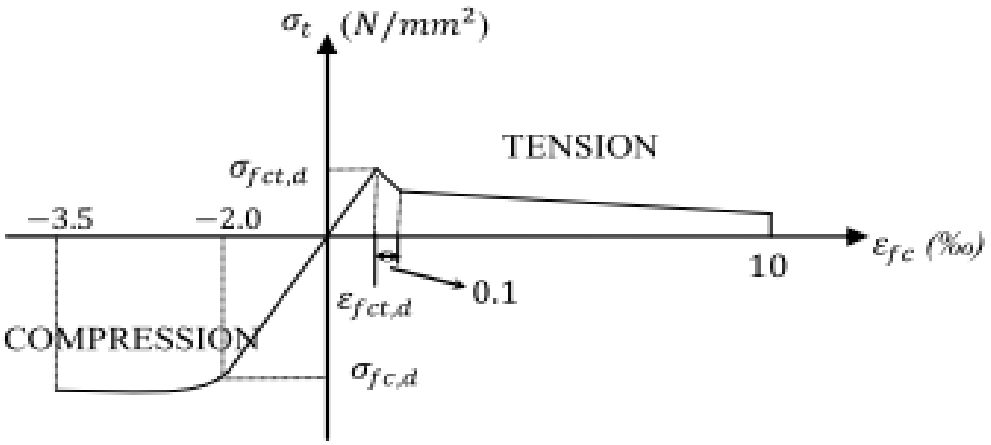

Figure 2.23: Stress-Strain Diagram adapted from (RILEM, 2002b)

The compressive strength is determined using standard tests of either concrete cylinders (Φ=150mm) or cubes (length=150mm). A series of specimens were investigated under compressive and flexural tests to understand the post-cracking behaviour for SFRC.

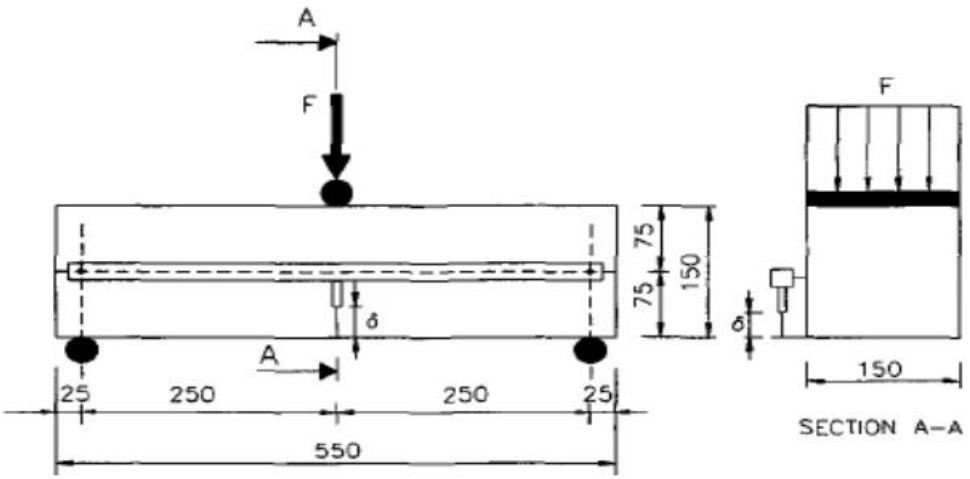

Figure 2.24: 3-Point Bending Test with 25mm Notch adapted from (RILEM, 2002b)

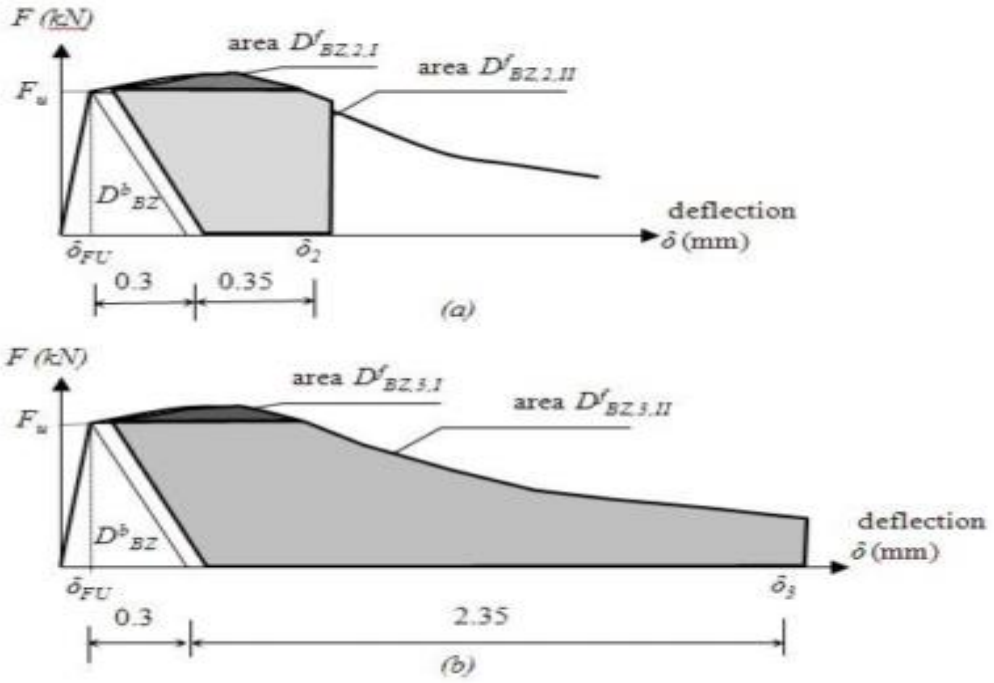

Figure 2.25: Load-Displacement Diagram adapted from (RILEM, 2000)

The load-deflection resulting from the bending test (see Figure 2.25) was required to determine the values of equivalent flexural strengths, $f_{eq,2}$ and $f_{eq,3}$. The method and associated equations are stated below:

$$f_{eq,2} = \frac{3}{2}\left[\frac{D^f_{BZ,2,I}}{0.65} + \frac{D^f_{BZ,2,II}}{0.50}\right]\frac{L}{bh^2_{sp}}\ (\text{N/mm}^2) \qquad \text{Eqn. 2.30}$$

$$f_{eq,3} = \frac{3}{2}\left[\frac{D^f_{BZ,3,I}}{0.65} + \frac{D^f_{BZ,3,II}}{0.50}\right]\frac{L}{bh^2_{sp}}\ (\text{N/mm}^2) \qquad \text{Eqn. 2.31}$$

Where

b = width of the specimen (mm)

h_{sp} = distance between the tip of the notch and the top of the cross-section (mm)

L = span of the specimen (mm)

$D^f_{BZ,2,I}$, $D^f_{BZ,2,II}$, $D^f_{BZ,3,I}$, $D^f_{BZ,3,II}$ = contribution of steel-fibres

The $f_{eq,2}$ and $f_{eq,3}$ were taken at a total deformation of 0.65mm and 2.65mm respectively.

2.6.5 Lok and Xiao (1999)

Based on their previous works which resulted in the accurate prediction of the steel-fibre reinforced concrete (SFRC) flexural response from a constitutive model, unambiguous expressions for the first crack and the ultimate flexural strength are derived in the work. This present analytical model uses parameters such as the direct tensile strength, residual strength, the product of bond strength τ_d and fibre aspect ratio (L/d) in the investigation in which the ‘‘bond-aspect ratio’’ index τ_d(L/d) and fibre volume fraction play vital roles in influencing the flexural behaviour of SFRC.

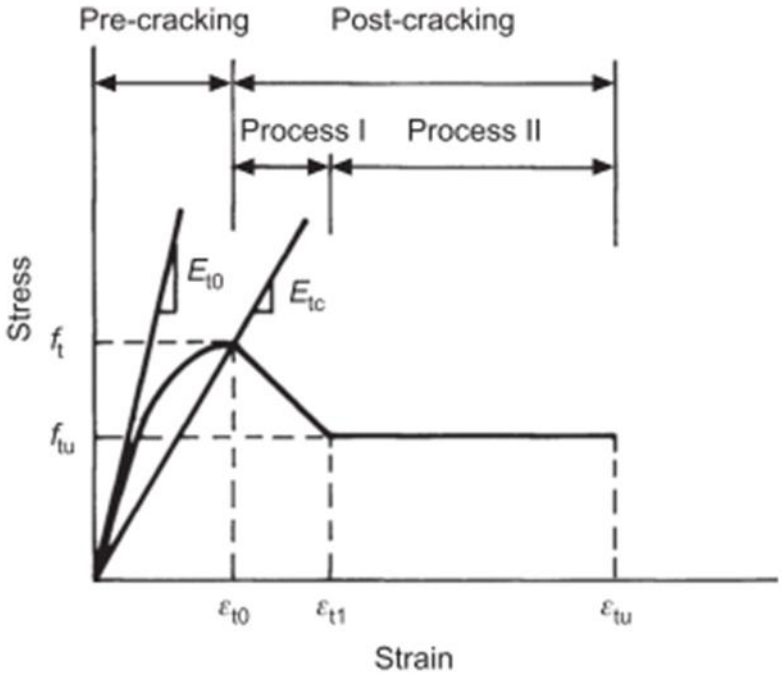

Figure 2.26: Tensile behaviour of SFRC adapted from (Lok and Xiao, 1998)

There was an agreement between calculated strengths and experimental data used for validation works in Chapter 4. Further investigation on the behaviour of basic parameters [f_{ult}, f_t, and $\tau_d(L/d)$] were conducted on a range of practical fibre volume concentration V_f [1.0-3.0%] thus simplifying the ultimate strength prediction and from which expression is derived.

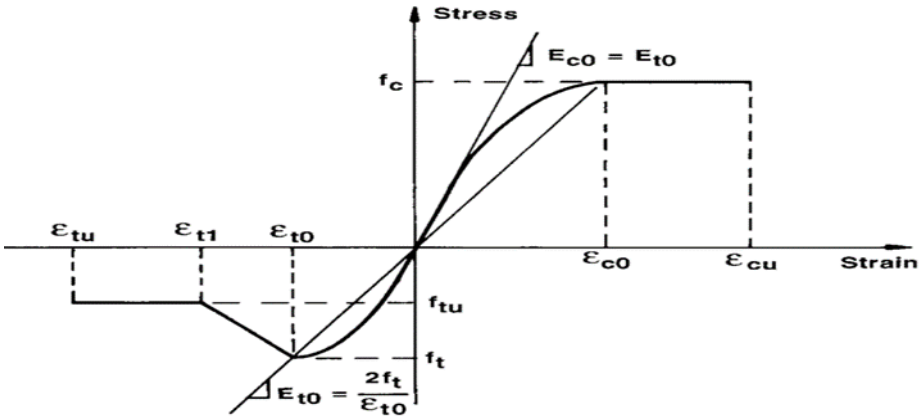

Figure 2.27: Stress-Strain constitutive model adapted from (Lok and Xiao, 1999)

The tensile stress-strain relationship that governs the tensile behaviour in Figure 2.26 is given for each phase of the strain:

$$\sigma = f_t[2\left(\frac{\varepsilon}{\varepsilon_{t0}}\right) - \left(\frac{\varepsilon}{\varepsilon_{t0}}\right)^2] \quad \text{for } (0 \leq \varepsilon \leq \varepsilon_{t0}) \quad \text{Eqn. 2.32}$$

$$\sigma = f_t[1 - \left(1 - \frac{f_{tu}}{f_t}\right)\left(\frac{\varepsilon - \varepsilon_{t0}}{\varepsilon_{t1} - \varepsilon_{t0}}\right)] \quad \text{for } (\varepsilon_{t0} \leq \varepsilon \leq \varepsilon_{t1}) \quad \text{Eqn. 2.33}$$

$$\sigma = f_{tu} \quad \text{for } (\varepsilon_{t1} \leq \varepsilon \leq \varepsilon_{tu}) \quad \text{Eqn. 2.34}$$

Where

f_t = Ultimate tensile strength

ε_{t0} = corresponding ultimate strain

f_{tu} = Residual strength

ε_{t1} = corresponding strain to residual strength

The simplified expression arrived at are stated below:

Bond stress

$$\tau_d = \frac{f_m}{0.405\, Vf(L/d)} \quad \text{Eqn. 2.35}$$

Flexural Strength

$f_{tu} = \eta\ V_f \tau_d (L/d)$ Eqn. 2.36

Corresponding strain to the flexural strength

$$\varepsilon_{t1} = \tau_d \frac{L}{d} . \frac{1}{E_s}$$ Eqn. 2.37

From the above, the following can also be defined:

V_f = fibre volume ratio

η = fibre orientation factor

E_s = Modulus elasticity of steel

Later, the following section analysis parameters shall be used in the analysis and design of beam and slab sections.

Crack Moment M_{cr}

$$M_{cr} = \frac{\int_0^{\varepsilon c} \sigma_c \varepsilon\, d\varepsilon + \int_0^{\varepsilon t0} \sigma_t \varepsilon\, d\varepsilon}{\emptyset_{cr}^2} = 0.236 f_t H^2$$ Eqn. 2.38

Ultimate Moment Mult

$$M_{ult} = \frac{\int_0^{\varepsilon c} \sigma_c \varepsilon\, d\varepsilon + \int_0^{\varepsilon t0} \sigma_t \varepsilon\, d\varepsilon}{\emptyset_{ult}^2} - \frac{\frac{2}{3}\sigma^{\frac{3}{2}} + \alpha + \beta - \frac{1}{4}}{(\lambda + \sqrt{\alpha})} f_t H^2$$ Eqn. 2.39

Ultimate Load f_{ult}

$$f_{ult} = 6 \frac{\frac{2}{3}\sigma^{\frac{3}{2}} + \alpha + \beta - \frac{1}{4}}{(\lambda + \sqrt{\alpha})}$$ Eqn. 2.40

There was good agreement when the Predictions obtained by using the simplified ultimate strength expression are compared with results obtained from both the above analytical procedure and experimental data. The approaches serve as an effective tool for flexural strength assessment of SFRC.

The results were adequately accurate to justify the linear assumptions made. The outlined approaches provide a simplified and useful tool to evaluate the flexural strength of SFRC. One main benefit of this model is that it allows for the high volume of fibre [up to 3%]

2.6.6 Review of Constitutive Models

The Lok & Xiao constitutive model is chosen for all the works done based on its agreement with experimental results and also due to its incorporation of high volume

fibre fraction (0-3%) while Barros and Figueiras (1999) model have a maximum volume fibre fraction of 1%. The results are shown in chapter 3.

2.6.7 Highlights on some constitutive models in EU guidelines and codes (Álvarez, 2013)

In the works of (Blanco et al., 2014a, Álvarez, 2013, Blanco et al., 2013), the European codes and guidelines for the design of FRC structural sections were understudied and reported, according to the sequential order of publication, the DBV (DBV 2001), the RILEM recommendations (Vandewalle et al. 2003), the CNR-DT 204/2006 (CNR 2006), the EHE-08 (CPH 2008) and the Model Code 2010 (fib 2010). From now on, they shall be designated as DBV, RILEM, CNR-DT 204, EHE-08 and MC2010, respectively. The results were published in Table 2-2. The constitutive models proposed in the documents grouped according to the type of diagram (namely rectangular, bilinear and trilinear or multilinear), indicating the parameters that define each one of the models. Also too, Table 2.1 also includes the tests required to obtain the values of these parameters. In Table 2.2, the main criteria considered in each of the constitutive models are presented

Table 2.2: Constitutive models in European guidelines and codes adapted from (Blanco et al., 2013)

Diagram	Parameters	Characterization test	
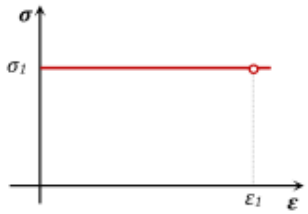	$\sigma_1 = f_{eq,ctd,II} = f_{eq,ctk,II} \cdot \alpha_c^f \cdot \alpha_{sys} / \gamma_{cf}^f \leq f_{eq,ctd,I}$ (α_{sys}: coefficient for size effect; α_c^f: coefficient for long-term strength behaviour) $\varepsilon_1 = \varepsilon_u = 10‰$	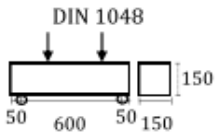	DBV
	$\sigma_1 = f_{Ftu} = f_{eq2}/3$ $\varepsilon_1 = \varepsilon_u$= [20‰ softening ; 10‰ hardening]	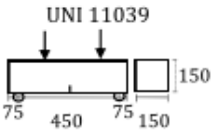	CNR-DT 204
	$\sigma_1 = f_{ctRd} = 0.33 f_{R,3,d}$ $\varepsilon_1 = \varepsilon_u$=[20‰ bending; 10‰ tensile]	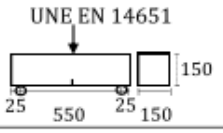	EHE-08
	$\sigma_1 = f_{Ftu} = f_{R3}/3$ $\varepsilon_1 = \varepsilon_u$= [20‰ softening ; 10‰ hardening]	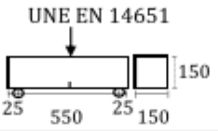	MC2010
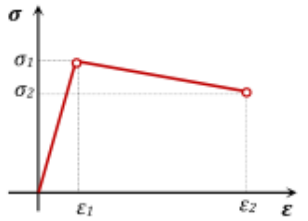	$\sigma_1 = f_{eq,ctd,I} = f_{eq,ctk,I} \cdot \alpha_c^f \cdot \alpha_{sys} / \gamma_{cf}^f$ $\sigma_2 = f_{eq,ctd,II} = f_{eq,ctk,II} \cdot \alpha_c^f \cdot \alpha_{sys} / \gamma_{cf}^f \leq f_{eq,ctd,I}$ $\varepsilon_2 = \varepsilon_u = 10‰$	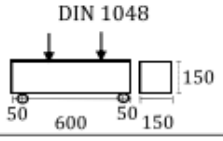	DBV
	$\sigma_1 = f_{Fts} = 0.45 f_{eq1}$ $\sigma_2 = f_{Ftu} = k[f_{Fts} - (w_u/w_{12})(f_{Fts} - 0.5 f_{eq2} + 0.2 f_{eq1})]$ k=[0.7pure tension, 1 other cases] $\varepsilon_2 = \varepsilon_u$= [20‰ softening; 10‰ hardening]	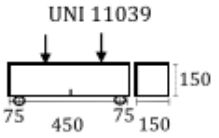	CNR-DT 204
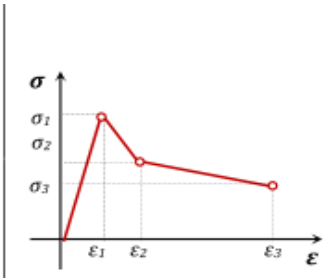	$\sigma_1 = f_{cfd} = \alpha_c^f \cdot f_{ctk,fl} / \gamma_{ct}^f$ $\sigma_2 = f_{eq,ctd,I} = f_{eq,ctk,I} \cdot \alpha_c^f \cdot \alpha_{sys} / \gamma_{cf}^f$ $\sigma_3 = f_{eq,ctd,II} = f_{eq,ctk,II} \cdot \alpha_c^f \cdot \alpha_{sys} / \gamma_{cf}^f \leq f_{eq,ctd,I}$ $\varepsilon_1 = \sigma_1/E_c$; $\varepsilon_2 = \varepsilon_1 + 0.1‰$; $\varepsilon_3 = \varepsilon_u = 10‰$	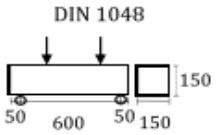	DBV
	$\sigma_1 = 0.7\, f_{ctm,fl}\,(1.6-d)$; $\sigma_2 = 0.45 \cdot \kappa_h \cdot f_{R,1}$; $\sigma_3 = 0.37 \cdot \kappa_h \cdot f_{R,4}$ $\varepsilon_1 = \sigma_1/E_c$; $\varepsilon_2 = \varepsilon_1 + 0.1‰$; $\varepsilon_3 = \varepsilon_u = 25‰$	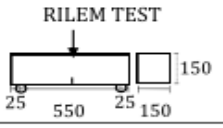	RILEM
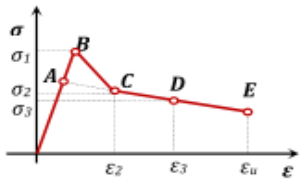	$\sigma_1 = f_{ct,d} = 0.6\, f_{ct,fl,d}$ $\sigma_2 = f_{ctR1,d} = 0.45 f_{R,1,d}$ $\sigma_3 = f_{ctR3,d} = k_1(0.5 f_{R,3,d} - 0.2\, f_{R,1,d})$ $\varepsilon_2 = 0.1 + 1000 \cdot f_{ct,d} / E_c$ $\varepsilon_3 = 2.5/l_{cs}$ (l_{cs}: characteristic length) ε_u=[20‰ bending; 10‰ pure tension]	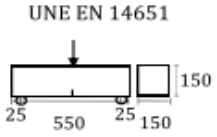	EHE-08
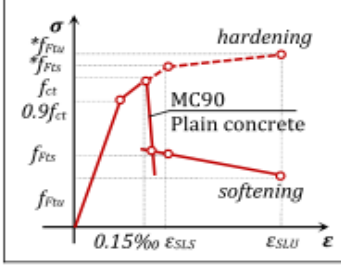	$f_{ctm} = 0.30 (f_{ck})^{2/3}$ $f_{Fts} = 0.45 f_{R1}$ $f_{Ftu} = k[f_{Fts} - (w_u/CMOD_3)(f_{Fts} - 0.5 f_{R3} + 0.2 f_{R1})]$ $\varepsilon_{SLS} = CMOD_1 / l_{cs}$ $\varepsilon_{SLU} = w_u/l_{cs} = \min(\varepsilon_{Fu}, 2.5/l_{cs} = 2.5/y)$ ε_{Fu} = [20‰ softening; 10‰ hardening]	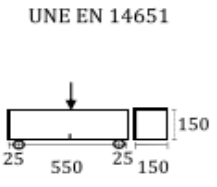	MC2010

2.7 Slabs Overview

A slab is a horizontal element of a structure, with a larger width than height (British Standard Institute, 2004, Engström, 2011). The principal distinction, when compared to a beam element, is that transverse action will be taken into consideration due to the bigger breadth. A slab carries the load in one or both directions supported by walls, beams or isolated columns/piles. A one-way slab [$l_y/l_x>2$] can be analysed as a wide beam and designed per unit width. However, a two-way slab [$l_y/l_x\leq2$] carries the load in two directions and will, therefore, require analysis in both directions to obtain proper reaction forces and deformations.

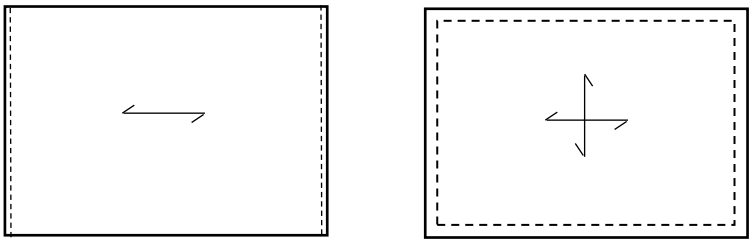

Figure 2.28: One and Two-way slabs

A slab is generally statically indeterminate, i.e. the static equilibrium equations are inadequate to define all the internal forces and reactions, which means that the material model will have much influence on the result. The material behaviour is similar to that of beam behaviour, but stresses exist in 3 directions [x, y, z].

2.7.1 Supports for slabs

The main supports for slabs are ground supported or suspended slabs [with free space underneath]. The research focuses mainly on suspended SFRC slabs with emphases on elevated and pile-supported SFRC slabs.

2.7.2 Methods of analysing and designing Elevated and Pile-supported slabs

Reinforced concrete slabs are complex to analyse, so their models are often simplified. There are three [3] methods for designing reinforced concrete slabs [plates] in the ultimate limit state. The most thorough is a non-linear finite element method which requires a non-linear finite element [NLFEA] software. The NLFEA solution explicitly models the reinforcement yielding and the concrete cracking. The other options are

elastic and yield line methods. These assume ideal plastic behaviour and the collapse load cannot be solved directly since there is no relationship between moment and curvature in the plastic state. It has to be approached from either upper bound or lower bound solutions

2.7.2.1 The Elastic Method

In the past, elastic design methods have been used for the design of slabs including elevated and pile-supported slabs. A linear elastic analysis is carried out to determine the moments and shear forces due to applied loads in each direction. It is possible to check whether cracking is likely to occur in the serviceability limit state (Concrete-Society, 2007). Some design methods adopt elastic design principles (The Concrete Society TR63, 2007, Thooft, 2000). The Dutch Code NEN 6720 (TGB NEN 6720, 1995) recommends an elastic design for that pile-supported floors, at the Ultimate Limit State (ULS). According to NEN 6720, the maximum design (support) moment that a pile-supported slab has to be designed for is given by the following expression:

$$M = \alpha q L^2 \qquad \text{Eqn. 2.41}$$

Where,

α is the moment coefficient [determined by the code]

q is the applied [action] load and

L is the span

Concerning the above equation, some proposals exist about the determination of the moment coefficient. The Dutch Code NEN 6720 recommends that:

0.132 for internal panels

0.178 for external panels and

0.190 for corner panels

The slab is divided into two edge strips, of width equivalent to L/4 and one middle strip of L/2. It allows the determination of the ultimate design moment from elastic or finite

element analysis as an alternative to the above design method. Furthermore, beam tests are used to obtain the material properties of the required SFRC

2.7.2.2 The Yield-Line Method

Yield Line Theory is an ultimate load analysis. It establishes either the moments in an element (e.g. a loaded slab) at the point of failure or the load at which a structural member will fail. It may be applied to many types of the slab, both with and without beams (Kennedy and Goodchild, 2004). A yield line is a line with plastic hinges where the deformation has reached the yield strain and the moment capacity cannot be further increased. It starts at the most stressed point and will, as in the theory of plastic hinges, eventually form a mechanism, and the slab will fail. Load increment hastens the formation of these hairline cracks; further increment of the load will increase the size of the cracks further and induce yielding of the reinforcement, initiating the development of large cracks originating from the point of maximum deflection. The development of a potential failure mechanism is shown in Figure 2.28 for a slab simply supported on four edges.

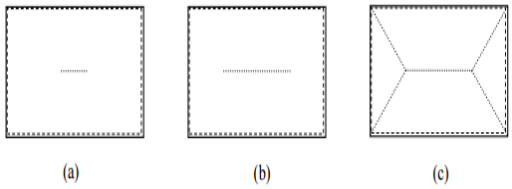

Figure 2.29: Yield line development in the 2-way slab

The yield line theory was developed by Johansen (Johansen, 1972), is a widely accepted method used for the design of pile-supported or suspended slabs (The Concrete Society TR34, 2014). The yield line theory is a plastic method of design. It is an upper bound analysis requiring the postulation of a failure mechanism. The principle of virtual work can be used to identify the failure load by equating the external work done by loads and the internal work done by the displacements.

The SFRC pile-supported or elevated slabs give rise to two significant failure modes (Kennedy and Goodchild, 2004, The Concrete Society TR34, 2014). The first of the failure is generally known as the Folded Plate Mechanism and is characteristic of flexural failure

[Figures 2.30]. The second is the conical collapse mechanism by which guidance is provided in (The Concrete Society TR34, 2014)Technical Report 34 regarding the calculation of both mechanisms, applying Classical Yield Line Theory.

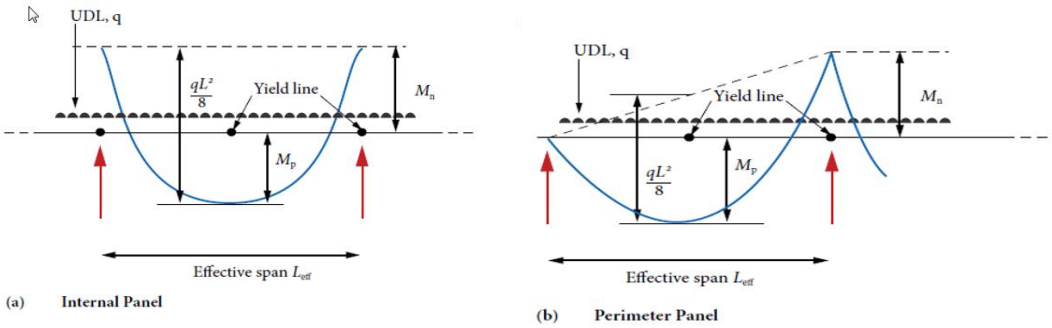

Figure 2.30: Folded plate yield line mechanism adapted from (The Concrete Society TR34, 2014)

Figure 2-29 illustrates the behaviour of the Folded Plate Failure Mechanism in the case of an exterior and interior panel under a UDL. The ultimate collapse load is found by equating the external and internal work.

In the case of an internal panel, the collapse load is given by:

$$M_p + M_n = \frac{q_u L_e^2}{8} \qquad \text{Eqn. 2.42}$$

Where,

M_p = Positive [sagging] moment

M_n = Negative [hogging] moment

q_u = UDL

L_e = effective span

L_e can be defined as $L - 0.7h_c$ (The Concrete Society, 2003)

The collapse load of the perimeter panel can be obtained from the following expression:

$$2Mp\left(1 + \sqrt{1 + \frac{M_n}{M_p}}\right)^2 = q_u L_e^2 \qquad \text{Eqn. 2.43}$$

Simplifying the equation further, assuming that

$$M_p = M_n \qquad \text{Eqn. 2.44}$$

Then,

$$M_p + M_n = \frac{q_u L_e^2}{5.83} \qquad \text{Eqn. 2.44}$$

The second load case is the concentrated loads, considered in the design of pile-supported SFRC slabs. Such loads could be from applications such as racking pallets and mezzanine supports.

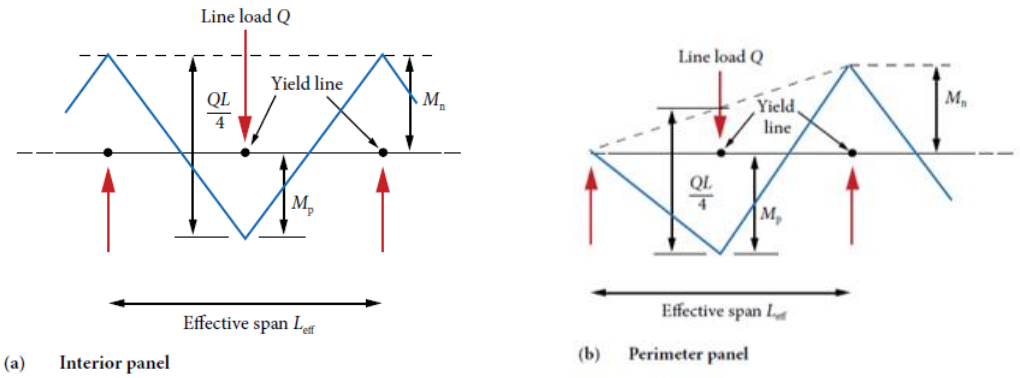

Figure 2.31: Folded plate yield line mechanism adapted from (The Concrete Society TR34, 2014)

The ultimate moment of resistance under a concentrated load in an interior panel is given by the following the equation (The Concrete Society TR34, 2014):

$$M_p + M_n = Q_t \frac{L_e}{4} + q_u \frac{L_e^2}{8} \qquad \text{Eqn. 2.44}$$

Where,

M_p = Positive [sagging] moment

M_n = Negative [hogging] moment

q_u = UDL

L_e = effective span

Q_t = Line load

q_u = Self weight of the pile supported slab

L_e can be defined as $L - 0.7h_c$ (The Concrete Society, 2003)

In the case of the exterior (perimeter) panels, this equation becomes:

$$M_p + M_n/2 = Q_t \frac{L_e}{4} + q_{sw} \frac{L_e^2}{8} \qquad \text{Eqn. 2.45}$$

The equation can be simplified further, assuming that

$$M_p = M_n$$

$$M_p + M_n = Q_t \frac{L_e}{3} + q_{sw} \frac{L_e^2}{6} \qquad \text{Eqn. 2.46}$$

The second yield line pattern is a fan of radius, r over the support pile

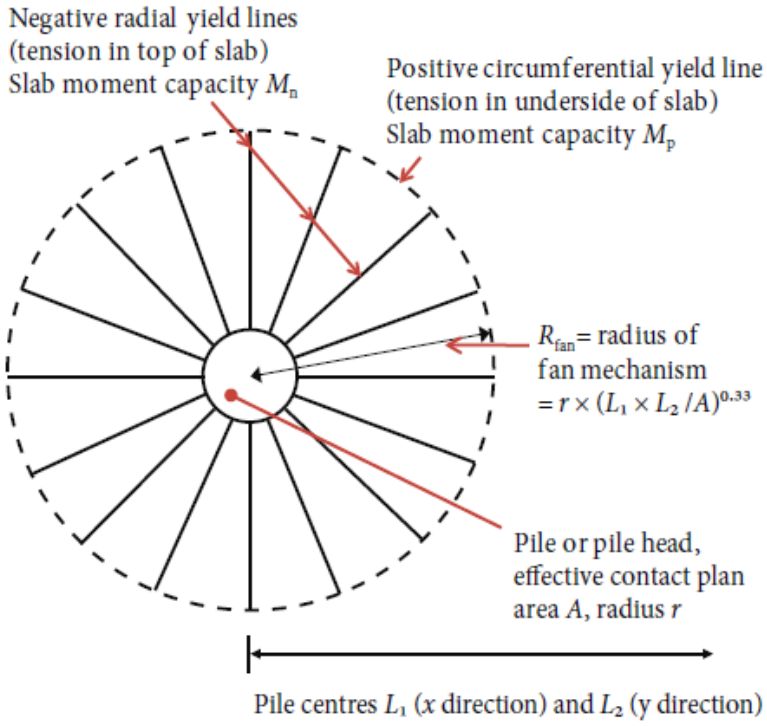

Figure 2.32: Fan yield line mechanism at pile adapted from (The Concrete Society TR34, 2014)

The ultimate moment capacity of a pile-supported slab failing with the circular fan mechanism is shown below (The Concrete Society TR34, 2014, Kennedy and Goodchild, 2003):

$$M_p + M_n = \frac{q_u L_1 L_2 \sqrt[3]{1 - \frac{A}{L_1 L_2}}}{2\pi} \qquad \text{Eqn. 2.47}$$

Where,

M_p = Positive [sagging] moment

M_n = Negative [hogging] moment

q_u = UDL

L_1 = pipe to pile centres in the x-direction

L_2 = pipe to pile centres in the y-direction

q_u = Self-weight of the pile-supported slab

A = cross-sectional area of the pile

Where there is no conventional steel reinforcement in a slab, M_p is typically assumed to be equal to M_n. Therefore the ultimate moment of resistance can be calculated with the following expression:

$$M = \frac{q_u L_1 L_2 \sqrt[3]{1-\frac{A}{L_1 L_2}}}{2\pi} \qquad \text{Eqn. 2.48}$$

In practice, the above checks are made at the location of the piles. However, according to the recommendations of the TR34 (The Concrete Society TR34, 2014), such checks should be repeated if any large point loads occur in the span as they may be critical. In order, to determine the ultimate moment of resistance in a structure, all the possible failure mechanisms must be evaluated. The lowest load obtained is the critical design load.

2.7.2.3 Modelling Pile-Supported SFRC Slabs

The model is made up of the slab and the piles. The two can be modelled with a 3D-brick, or the slab is modelled as 3D-brick and the pile as a spring. Adopting the 3D-brick model for both the slab and pile will see the pile being fixed at the base to connote a situation where it is assumed that there is no settlement in any pile. If the spring is used for the pile, the interaction between the pile and the surrounding soil would be considered. In this case, both the pile and the soil will be modelled as springs.

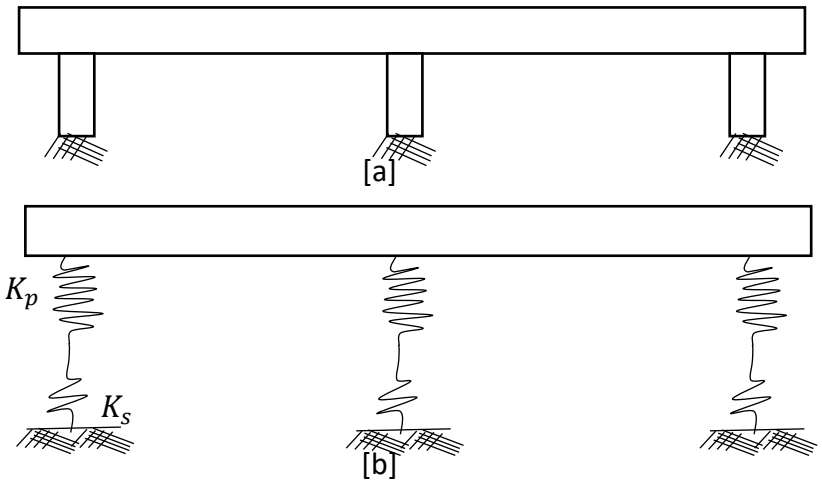

Figure 2.33: Diagrammatic Representation of Modelling Pile-Supported SFRC slabs in [a] 3D-Brick and [b] spring

The resistance from the pile is contributed by the pile skin and the tip at the base of the pile. The pile stiffness factor K_p and surrounding soil stiffness factor K_s are in series to one another. Therefore, the equivalent stiffness factor K_{eq} of the two springs is given as:

$$\frac{1}{K_{eq}} = \frac{1}{K_p} + \frac{1}{K_s} \qquad \text{Eqn. 2.49}$$

The pile-stiffness factor K_p

$$K_p = \frac{E_p R_a}{E_s} \qquad \text{Eqn. 2.50}$$

Where E_p= elastic modulus of pile material [MPa]

E_s= average value of secant modulus of soil along the pile shaft [MPa]

R_a= ratio of the area of pile section to the area bounded by pile outer circumference [-]

$$R_a = \frac{A_1}{A_2} \qquad \text{Eqn. 2.51}$$

A_1 = Average area of the cross-section of pile [m^2]

A_2 = area of pile shaft [m^2]

[For stiff piles R_a= 1]

The stiffness factor for the soil K_s at any depth

$$K_s = k_s \Delta_z Z \qquad \text{Eqn. 2.52}$$

Where

K_s – Equivalent spring stiffness

k_s - Coefficient of subgrade reaction [kN/m^3]

Δ_z- Spacing between the springs at a depth Z

The above shall be used to study the response of pile-supported SFRC in the serviceability limit state [SLS] using the Winkler's assumption.

$$\delta = \frac{P}{K_{eq}} \qquad \text{Eqn. 2.53}$$

Where P – Load on the pile [kN]

δ – Vertical displacement of pile [mm]

2.7.3 Flat Slabs

The flat slab is defined in BS8110: Part 1 [1.3.2.1] and EC2 [9.4 and Annex I.1] as a slab with or without drops, generally supported without beams by columns with or without column heads (British Standard Institute, 1997, British Standard Institute, 2004). The BS 8110 gave an in-depth insight into flat slabs. The code states that flat slab may be designed as a solid or have recesses formed at the soffit to give a waffle slab. Only solid slabs will be discussed

Flat slab arrangement in a floor is shown in Figure 2.34 for floors with square columns and drop panels. The slab is thicker than that required in T-beam floor slab construction, but the absence of beams gives a smaller storey height for a given clear height and simplification in construction and formwork.

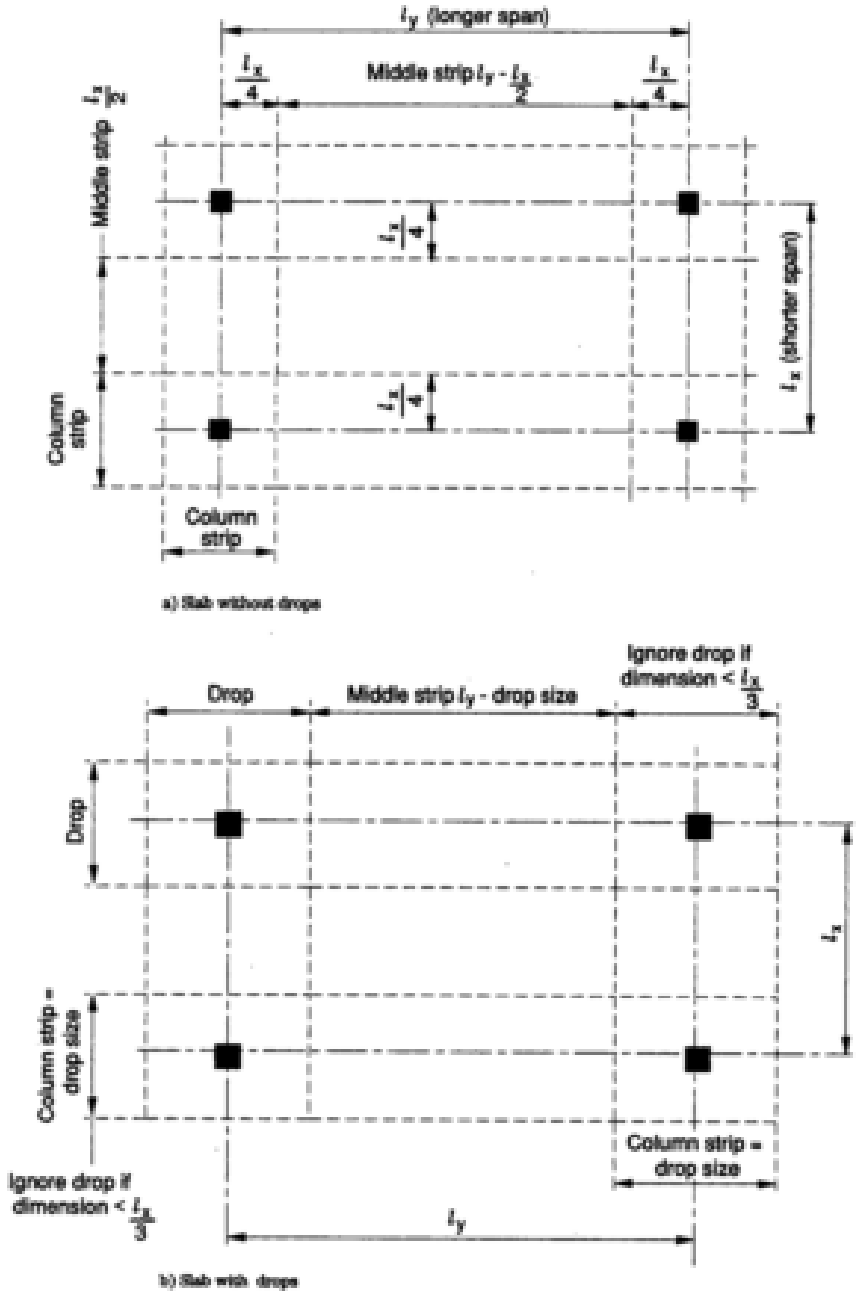

Figure 2.34: Flat slab arrangement for a floors with [a] square columns and [b] drop panels (British Standard Institute, 1997)

2.7.3.1 Analysis of Flat Slab

The BS 8110 states that it is usually sufficient to consider only the single load case of maximum design load, 1.35×dead load+1.5×imposed load [EC 2] on all spans. The following two methods of analysis are set out in section 3.7.2 of the code to obtain the moments and shears for design.

2.7.3.1.1 Frame analysis method

The structure is divided longitudinally and transversely into frames consisting of columns and strips of the slab. Either the entire frame or sub-frames can be analysed by moment distribution. This method is not considered further.

Table 2.3: Moments and shear forces for flat slabs for internal panels

	At first interior support	*At centre of interior span*	*At interior support*
Moment	$-0.063Fl$	$+0.071Fl$	$-0.055Fl$
Shear	$0.6F$		$0.5F$

$l = l_1 - 2h_c/3$, effective span; l_1, panel length parallel to the centre-to-centre span of the columns; h_c, effective diameter of the column or column head (section 8.7.2(d)); F, total design load on the strip of slab between adjacent columns due to 1.4 times the dead load plus 1.6 times the imposed load.

2.7.3.1.2 Simplified method

Moments and shears may be taken from Table 3.18 of the code for structures where lateral stability does not depend on slab-column connections. The following provisions apply:

1. The design is based on the single load case mentioned above;
2. The structure has at least three rows of panels of approximately equal span in the direction considered.

The design moments and shears for internal panels from Table 3.18 of the code are given in Table 2.3. Refer to the code for the complete table.

2.7.4 Difference between pile-supported and flat slabs

Sections 2.8.2 and 2.8.3 give an overview of the pile-supported and flat slabs. These include their anatomy, analysis and design methods. Some researchers treat the analysis and design of the two as the same (Thooft, 2000, Destrée, 2001, Cameron, 2002, Beton, 2004, Hedebratt and Silfwerbrand, 2004, Vollum, 2007, Destrée, 2007a, Hedebratt and Silfwerbrand, 2008, Destrée and Silfwerbrand, 2012, Barros et al., 2012, Hedebratt and Silfwerbrand, 2014, Salehian and Barros, 2015).

A critical look at pile-supported and flat slabs from design guidelines and experiences in the field (The Concrete Society TR63, 2007, Destrée, 2007a, Destrée and Silfwerbrand,

2012, Barros et al., 2012, The Concrete Society TR34, 2014) are expressed below and summarised in Table 2.4.

2.7.4.1 Slab Size and Depth

The span of pile-supported SFRC slab is presently limited to 4m (The Concrete Society TR63, 2007) while that of elevated [flat] SFRC slab has been taken to 8m (Destrée and Jürgen, 2008). The depth of the pile-supported SFRC slab ranges from 180mm to 400mm while the depth of elevated [flat] SFRC slab is maintained at a span-depth ratio of 15-20 (The Concrete Society TR63, 2007, Destrée and Jürgen, 2008, The Concrete Society TR34, 2014).

2.7.4.2 Support Systems

The support system for pile-supported SFRC slab includes a membrane in between the pile [or pile-head] and the slab. The membrane is to reduce the friction between the top of the pile and the slab. In an elevated slab, the slab is fixed to the columns

2.7.4.3 Deflection and Cracking

In pile-supported SFRC slab, cracking at the top surface is very critical. Punching shear is of importance to the pile-support and elevated slabs.

2.7.4.4 Analysis and design

The elevated and pile-supported SFRC slabs are analysed and designed with the yield-line method, elastic method and the FEA (Vandewalle et al., 2000, Hedebratt and Silfwerbrand, 2004, Destrée, 2007a, Oliveira, 2010, Destrée and Silfwerbrand, 2012, Barros et al., 2012)

Table 2.4: Differences between Pile-Supported and flat slabs

S/N	Description		Pile-Supported Slab	Elevated [Flat] Slab	Remarks
1	Support Span [m]		2.5-4.0	5.0-8.0	
2	FEA Modelling	Slab	3D-Brick	3D-Brick	
		Pile/Column	Spring	3D-Brick	
3	Slab thickness [mm]		200-400	180-250	For flat slabs, span/depth ratio of 15-20 is maintained
4	Support condition		Simply support	Fixed support	Membrane sheet is provided between the pile and the slab
5	Analysis and Design		Yield line Analysis, Elastic method, FEA	Yield line Analysis, Elastic method, FEA	

2.8 Punching shear

Punching shear occurs when a high localised force [load] applied to a small area of a slab or, most commonly, the reaction of a column against a slab causes a shear failure [cone like] which "punches" through the slab. The failure mechanism of punching shear in structural members like slabs and foundations is by shear under the influence of concentrated loads. One likely mode of failure is that the load punches through the slab or foundation.

2.8.1 Mechanism of Failure

The failure is because of shear. There are no visible signs shown prior to failure and this make this type of failure disastrous. In a slab system with a high localised force [load] or at a slab column [foundation column] connections, the loaded point is not really pushed through the slab as seen in Figure 2.35. The development of diagonal tension cracks around the loaded area initiates the punching shear failures, which produce a conical failure surface as shown in Figure 2.36

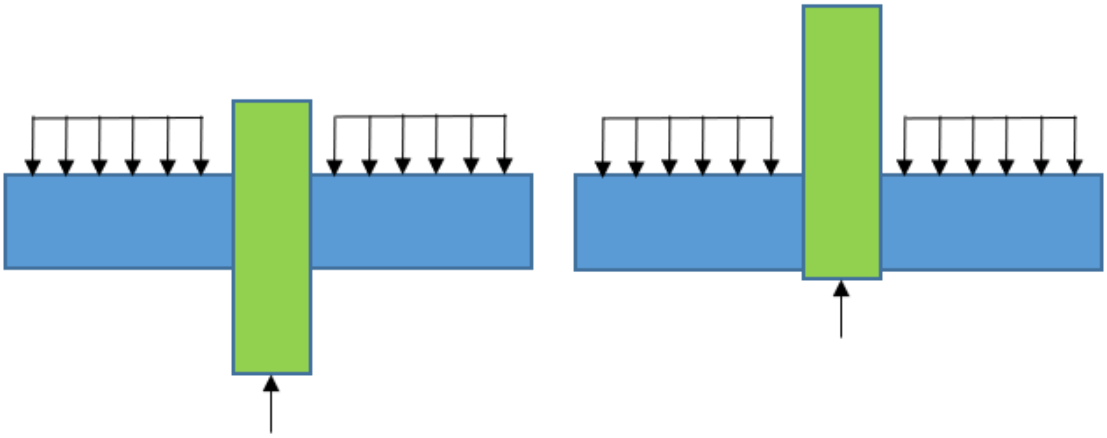

Figure 2.35: Punching Shear Failure Mechanism Misconception

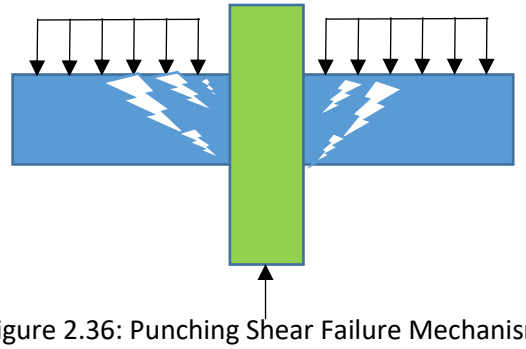

Figure 2.36: Punching Shear Failure Mechanism

Punching shear is a phenomenon in flat slabs triggered by concentrated support reactions bringing a cone shaped puncture beginning from the upper surface of the slab. Although usually followed by flexural failure, punching shear is a brittle failure mode and the risk of progressive collapse high and thus entails a higher safety measure in structural analysis and design.

2.8.2 Contribution of Steel Fibre

Several researchers have performed experiments on the contribution of steel fibres in slab-column connections (Bažant and Cao, 1987, Shaaban and Gesund, 1994, Labib, 2008, Nguyen-Minh et al., 2011, Maya et al., 2012, Choi et al., 2015, Caratelli et al., 2016, Nguyen et al., 2017). Their results show a substantial increase in the punching shear capacity and a significant enhancement of cracking behaviour as well as good structural integrity of slab-column connection of the slabs with fibres. The slabs without fibres failed unexpectedly in a brittle manner, whereas, the fibre reinforced slabs collapsed in more ductile manner.

Aside from experimental works, there are mechanical models used in understanding the punching share behaviour in slab-column connection. These models can be grouped into two, namely analytical and theoretical models. Analytical models include the finite element method [FEM] whereas the theoretical models include models based on different approaches such as, elastic, flexural capacity, plastic, and post-fractured (Desayi and Seshadri, 1996, Higashiyama et al., 2011, Neto et al., 2012, Metwally, 2013, Teixeira et al., 2015, Marčiukaitis and Šalna, 2017).

For the design of punching shear capacity in SFRC slabs, various design codes and guidance provide procedure which includes checking the shear at the face of the contact area and the critical perimeter distance [ranging from 0.5d to 2d, where d is the effective depth].

2.9 Design Guidelines for SFRC Slabs

The ever increasing in demand for the application of SFRC in structural flooring particularly its application in pile-supported and elevated slabs has led to a demand for a unified code of practice (The Concrete Society TR34, 2014). The inability for a worldwide design consensus among regulators and practitioners has led to manufacturers, associations and nations coming up with design guidelines and recommendations. Some of these are examined below.

2.9.1 RILEM TC 162-TDF (2002)

RILEM carried out extensive research on SFRC through the technical committee tagged RILEM TC 162-TDF. The work was mainly on SFRC beams. The proposed design has the same fundamentals as that of normal reinforced concrete and valid for SFRC with strength up to 60MPa. The proposed design method uses EC 2 for general framework.

2.9.1.1 Bending Moment

The design method was initially developed without size-dependent safety factors. A comparison of the predictions of the design method and the experimental results of structural elements of various sizes revealed a severe overestimation of the carrying capacity by the design method. To compensate for this effect, size-dependent safety factors have been introduced.

The moment at mid-span is gotten from

$$M_2 = \frac{F_2}{2}\frac{L}{2} = [\frac{D^f_{BZ,2}}{0.50}]\frac{L}{4}\,[\text{Nmm}] \qquad \text{Eqn. 2.54}$$

$$M_3 = \frac{F_3}{2}\frac{L}{2} = [\frac{D^f_{BZ,3}}{2.50}]\frac{L}{4}\,[\text{Nmm}] \qquad \text{Eqn. 2.55}$$

$$\text{Where } F_2 = \frac{D^f_{BZ,2}}{0.50}\,[\text{N}]$$

$$F_3 = \frac{D^f_{BZ,3}}{0.50}\,[\text{N}]$$

F_2 and F_3 are the mean forces under the shaded area $D^f_{BZ,2}$ and $D^f_{BZ,3}$ [Figure 2.12]

2.9.1.2 Shear Resistance

The provisions made for shear resistance is only applicable if provision is made for conventional flexural reinforcement. It concluded that as at the time of the publication, no acceptable method was provided for shear in fibre only section. Figure 2.37 is a schematic diagram of punching shear at the support or loading area for different guidelines. Figure 2.37 gave a summary of the provisions for Punching Shear at the support or loading area (IstructE, 1999, RILEM, 2002b, America Concrete Institute, 2002, British Standard Institute, 2004, British Standard Institute, 2006, The Concrete Society TR63, 2007, ArcelorMittal, 2010, The Concrete Society TR34, 2014)

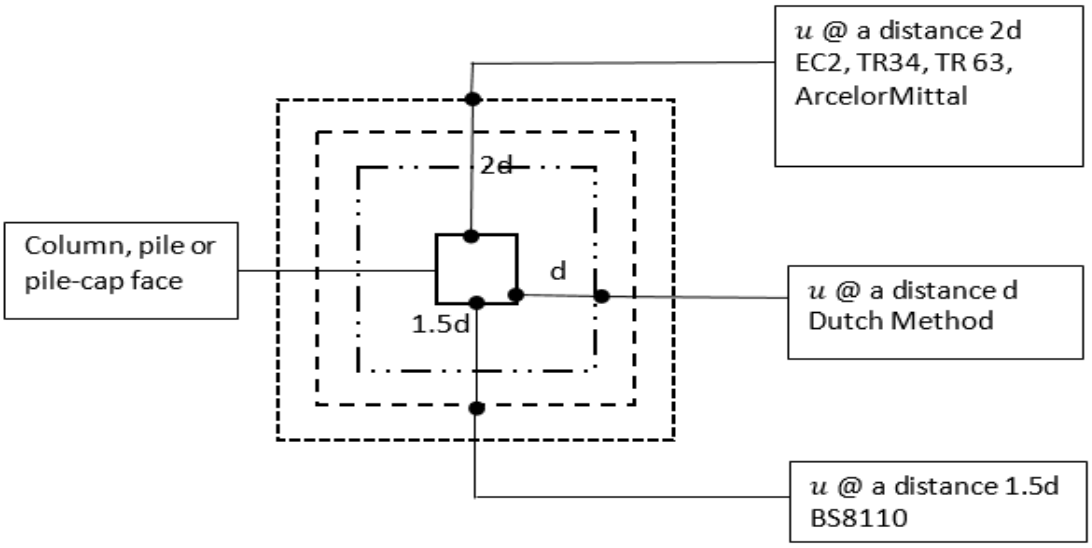

Figure 2.37: Punching Shear at the support or loading area

The designed shear resistance of a section of a beam with shear reinforcement and containing steel fibres is given by the equation:

$$V_{Rd,3} = V_{ed} + V_{fd} + V_{wd} \qquad \text{Eqn. 2.56}$$

Where:

V_{ed}= the shear resistance of the member without shear reinforcement

V_{fd}= contribution of the steel fibre shear reinforcement

V_{wd}= contribution of the shear reinforcement due to stirrups and/or inclined bars

2.9.1.3 Serviceability Limit State

The full SFRC section is assumed to be active when an uncracked section is used, and both concrete and steel are assumed to be elastic in tension as well as in compression. When a cracked section is used, the SFRC section is assumed to be elastic in compression, and capable of sustaining tensile stress equal to $0.45f_{R,1}$.

Maximum design cracked width allowed is 0.3mm under the quasi-permanent combination of loads. Notwithstanding the section analysis done, minimum conventional reinforcement shall be provided.

Minimum reinforcement $A_s = (k_c k k_p f_{fct,ef} - 0.45 f_{Rm,1}) \frac{A_{ct}}{\sigma_s}$ Eqn. 2.57

Where:

As = area of reinforcement within the tensile zone (mm^2). If As is smaller than zero only steel fibres are necessary

$f_{Rm,1}$ = the average residual flexural tensile strength of the steel fibre reinforced concrete at the moment when a crack is expected to occur (N/mm^2)

Act = area of concrete within the tensile zone (mm2). The tensile zone is that part of the section which is calculated to be in tension just before the formation of the first crack.

σ_s = the maximum stress permitted in the reinforcement immediately after formation of the crack (N/ram2). This may be taken equal to the yield strength of the reinforcement (fyk). However, a lower value may be needed to satisfy the crack width limits.

$f_{fct,ef}$ = the tensile strength of the concrete effective at the time when the cracks may first be expected to occur (N/mm2). In some cases, depending on the ambient conditions, this may be within 3 - 5 days from casting. Values of $f_{fct,ef}$ may be obtained from formula (1) by taking as f_{ck} the strength at the time cracking is expected to occur. When the time of cracking cannot be established with confidence as being less than 28 days, it is recommended that a minimum tensile strength of 3 N/mm 2 be adopted.

k_c= a coefficient which takes account of the nature of the stress distribution within the section immediately prior to cracking. The relevant stress distribution is that resulting from the combination of effects of loading and restrained imposed deformations.

$k =$ a coefficient which allows for the effect of non-uniform self-equilibrating stresses. The value can be taken as 0.8 as a first approximation. For further details, see ENV 1992-1-1.

k_p = a coefficient which takes account of the prestressing effect:

2.9.2 ArcelorMittal Design Guideline (2010)

In the proprietary guidelines on the usage of their products, different recommendations were given to certain types of steel fibres, their dosage and place of application. SFRC is defined as a concrete where the inter-granular mortar (the origin of all cracking) is controlled by steel fibres (ArcelorMittal, 2010).

The design method adopted by ArcelorMittal was the yield line method with a folding plate and Fan mechanisms for the slab and punching shear over support respectively.

For pile-supported SFRC floors (TAB-Structural), the following are recommended:

- A minimum fibre dosage of 40-50 kg/m³ is required
- Maximum span of 6m.
- The minimum size of the pile is 180mm in diameter
- Maximum unfactored live load on the floor area = 8.65kNm^{-2}
- Maximum ultimate load per pile = 300 kN

For elevated SFRC floors (TAB-Slab), the following are recommended

- A maximum dosage of 100 kg/m³ [TABIX 1.3/50]
- SFRC strength of C30-37
- Maximum span of 10m between columns
- Minimum slab depth of 100mm

2.9.2.1 Bending Moment

The design method for SFRC suspended slabs is based on the analysis of the shortest pattern of yield-lines where almost all deformations are concentrated due to the plastic rotation. The fibre dosage rate must be sufficient and high enough to ensure yielding of the section. The rupture mechanism to be considered is the least favourable for the proposed load and support, giving the minimum ultimate loading intensity Q_{ult}

Q_{ult} = 16.M_R [Middle panel] Eqn. 2.58

Q_{ult} = 12.M_R [Edge panel] Eqn. 2.59

Design condition for the middle span is given as

$$\gamma_p.P.\frac{l_n}{8.b} + \left(\gamma_g.G + \gamma_p.Q\right)\frac{l_n^2}{16} \leq \frac{M_R}{\gamma_M} \quad \text{Eqn. 2.60}$$

Design condition for edge span is given as

$$\gamma_p.P.\frac{l_n}{6.b} + \left(\gamma_g.G + \gamma_p.Q\right)\frac{L_n^2}{12} \leq \frac{M_R}{\gamma_M} \quad \text{Eqn. 2.61}$$

Where:

M_R = Radial Moment from round plate test

$$= 0.45 \cdot f_{ctu}^{f} \cdot h^2 \quad \text{Eqn. 2.62}$$

G = Self weight of slab

Q = Uniformly Distributed Loads

P = Point Loads

l_n = Effective length

γ_p= Safety factor for point loads

γ_g= Safety factor for self-weight

γ_M= Safety factor for the material

Note:

The slab is provided as well with anti-progressive collapse rebar, following an Elevated Slab Design Recommendation, and spanning from column to column at the bottom of the slab. These additional rebar are crossing over the columns and are mandatory regardless of the type of fibre-reinforcing used.

Area of additional rebar A_{sb}

$$A_{sb} = \frac{0.5G}{1000} \cdot l_2 \cdot l_n/[\Phi_s f_s] \quad \text{Eqn. 2.63}$$

Where

l_2 = length of the shorter longer side

Φ_s =

f_s = Characteristic strength in steel

2.9.2.2 Punching Shear

The final rupture pattern is the typical “FAN” pattern where the expression of the equilibrium of rotation of one circular sector gives. The critical area is taken as 2d from the face of the column or pile.

2.9.2.3 Serviceability Limit State

To control shrinkage in the concrete, a minimum fibre dosage of 20kg/m³ is required. Fibre dosages of below this will not provide effective control of shrinkage within the concrete.

2.9.3 Dramix by Bekaert Design Guideline (2012)

Bekaert has redesigned and expanded its Dramix® range of steel fibres for concrete reinforcement. The traditional range of steel fibres has been rebranded as the 3D series. Bekaert has adopted the TR 34 guidelines for their designs of SFRC suspended floors

2.9.4 Twintec (2012)

The proprietary guidelines given by Twintec was based on the design methodology for the fibre-only systems which combines the yield line theory (e.g. Johansson, Meyerhof) with other well-established design theories particularly the TR 63 (Eddy, 2008) to control the serviceability states. Section 2.9.5 discusses TR 63

2.9.5 The Concrete Society (2007) – TR 63

The Concrete Society came up with general guidance for the design of SFRC in Technical Report No. 63. The report included the beam tests [for residual flexural strength] and plate tests [for the determination of toughness]. TR 63 recognises the reasons why some manufacturers of steel-fibres prefer plate tests to beam tests. The design moment of resistance can be determined from plate tests by yield line analysis.

2.9.5.1 Bending Moment

The guidance made provisions for bending moments to be used in the design of SFRC to be derived from either elastic or plastic analysis. The residual tensile strengths derived in standard beam tests are used to calculate the design moment of resistance. Design equations are presented regarding residual strengths derived using both the BS EN 14651 $f_{R1}\ and\ f_{R4}$ and the Japanese beam test $R_{e,3}$. The simplified stress block in Figure 2.38 was adapted from Technical Report 63 (TR 63, 2007)

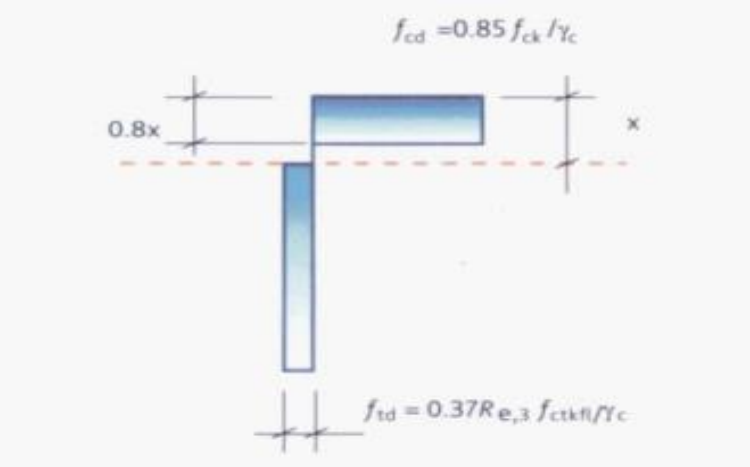

Figure 2.38: Simplified stress block adapted from (TR 63, 2007)

The design moment of resistance

$$M_p = 08 f_{cd} f_{td} bh^2 \left[0.5 + \frac{0.1 f_{td}}{0.8 f_{cd} + f_{td}}\right] / [0.8 f_{cd} + f_{td}] \quad \text{Eqn. 2.64}$$

Where:

f_{cd} = design compressive strength of concrete (cylinder)

f_{td} = design residual tensile strength of the concrete

$= 0.37 R_{e,3} f_{ctkfl} / \gamma_c$ Eqn. 2.65

2.9.5.2 Punching Shear

It is recommended that the design rules for punching shear given in Eurocode 2 should only be used for SFRC with conventional longitudinal reinforcement. The design shear stress (as defined in Clause 6.38 of Eurocode 2) should not exceed v_{max} at the face of the contact area irrespective of the amount of reinforcement in the slab.

$$v_{max} = 0.5 v f_{cd} \quad \text{Eqn. 2.66}$$

Where:

$$v = 0.6 \left(1 - \frac{f_{ck}}{250}\right) \quad \text{Eqn. 2.67}$$

f_{cd} = design concrete compressive strength (cylinder)

$= \frac{f_{ck}}{\gamma_c}$

Therefore, the maximum design punching shear resistance

$$P_{pmax} = v_{max} u_0 d \quad \text{Eqn. 2.68}$$

Where:

u_0 = perimeter of the loaded area

2.9.6 The Dutch Code [NEN 6720] (1995)

The Dutch code [NEN 6720] recommends that pile-supported SFRC slabs should be designed with the elastic method. It makes provisions for beam supported and pile-supported slabs. The bay is divided into two [2] edge strips with a width of a quarter [1/4] span and a middle strip just as obtainable in BS8110.

The slab is sized in a way that no conventional reinforcement is required in the bottom of the interior panels. The method is similar to the provisions made in BS8110 for the design of two-way spanning slabs where the requirement of punching shear determines the depth of the slab so that the moments at mid-span in internal panels are small thereby requires little or no reinforcement. With this, the elastic capacity of the SFRC section is adequate to carry the full mid-span moment [Figure 2.39].

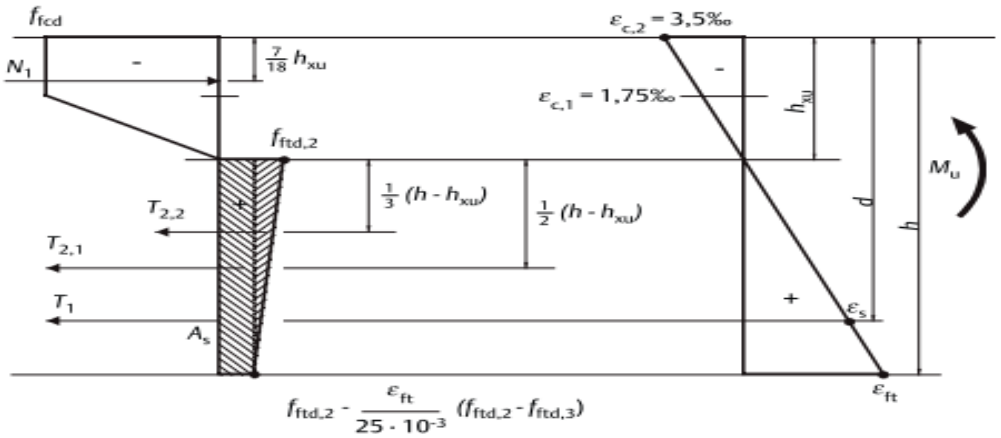

Figure 2.39: Simplified stress block at ULS adapted from (NEN 6720)

2.9.6.1 Bending Moment

Moment coefficients are provided for estimating moment at the edge strips and the middle strip.

$$M = \alpha n l^2 \qquad \text{Eqn. 2.69}$$

Where M= moment

α = moment coefficient

n = UDL

l = Span

Only UDL is used for final analysis in NEN 6720 to simplify the design process. Where point or line load exist, they are converted to UDL using the principle of virtual work.

Invariably, the internal piles or support would exhibit smaller hogging moments which are catered for by the introduction of reinforcement over the supports.

2.9.6.2 Punching Shear

Punching shear is checked along a perimeter at a distance d from the face of the column or pile. In order to prevent enhance shear resistance, additional steel bars are recommended to be integrated over the column in the design.

2.9.6.3 Serviceability Limit State

It recommends that the span-depth ratio should not exceed 21 in SLS. The crack widths over the pile can be predicted due to the presence of the conventional reinforcement [Figure 2.40].

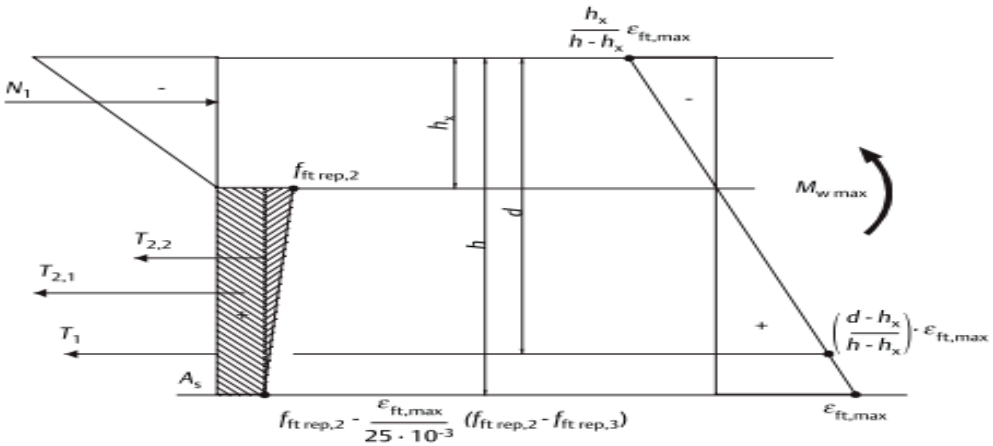

Figure 2.40: Simplified stress block at SLS adapted from (NEN 6720)

2.9.7 Eurocode 2 BS EN 1992 (2004)

Provisions are not made in EC2 for SFRC elevated or pile-supported slabs, but some researchers tend to refer or compare it for their designs.

2.9.7.1 Bending Moment

The design method in EC2 that suits SFRC slabs is the flat slab design. The flat slab design is as outlined in section 2.9.4.

2.9.7.2 Punching Shear

Punching shear is checked along a perimeter at a distance 2d from the face of the column, pile or pile-cap and loaded area. Also too, rebar is recommended to be incorporated over the column in the design to prevent punching shear.

Minimum Shear resistance $v_{c,min}$ due to plain concrete in SFRC is taken as

$$= 0.035k_1^{1.5}f_{ck}^{0.5} \qquad \text{Eqn. 2.70}$$

Where k_1 = 1 + $\sqrt{(200/d)}$ ≤ 2

Shear capacity V

$$V = v_{c,min}.ud \quad \text{Eqn. 2.71}$$

Where u = the critical perimeter at a distance of 2d from the column, pile or pile-head and loaded area face

d = effective depth of the slab

2.9.7.3 Serviceability Limit State

Cracking shall be limited to the extent that will not impair the proper functioning or durability of the structure or cause its appearance to be unacceptable. If crack control is required, a minimum amount of bonded reinforcement is required to control cracking in areas where tension is expected

2.9.8 The Swedish Proposal (2008)

The Swedish recommendations for SFRC design were first developed by the Swedish Concrete Association in 1995. The third edition published in 2008 covers plain concrete, conventionally reinforced concrete and SFRC concrete floors for ground and pile supported slabs.

2.9.8.1 Bending Moment

The Yield-Line method was used for the analysis of the slab section. Two types of flexural failure modes are possible; (a) straight and parallel lines above and between the pile lines [folding plate mechanism] and (b) circular and radial yield lines around the pile.

The flexural moment capacity [m_u] of the slab

$$m_u = \frac{f_{fld}.h^2}{6} \quad \text{Eqn. 2.72}$$

Where f_{fld} -

h - Slab thickness

2.9.8.2 Punching Shear

Punching failures are possible especially for piles with small cross section and thin slabs. The shear strength along the control section may be estimated by the equation

$$f_{v1} = \frac{\xi}{1.4}.C.\frac{f_{fld}}{\zeta} \quad \text{Eqn. 2.73}$$

Where ξ – size dependent factor

= 1.4 if h ≤ 0.2m

= 1.6-h if 0.2m < h ≤ 0.5m

= 1.3-0.4h if 0.5m < h ≤ 1.0m

= 0.9 if 1.0m < h

C –coefficient = 0.45

ζ – crack safety factor = 1-R_2/100

R_2 – Residual strength factor

2.9.8.3 Serviceability

The area above the piles is susceptible to wide cracks because of hogging moment. In order to limit the crack width the SFRC is recommended to be made with high residual strength factor or additional conventional reinforcement should be provided in this area.

2.9.9 ***fib*** Model Code 2010 (MC2010)

The fib Model Code for Concrete Structures is a set of recommendations for the design of reinforced and prestressed concrete which is intended to be a guiding document for future codes. It makes further provisions for the design of fibre-reinforced structures. The recommendations cover virtually all ranges of fibre from conventional fibre-reinforced concrete (FRC), with moderate strength and comparatively low volumes of coarse fibres, to ultra-high-performance FRC, with very high strength (180–200 MPa) and high volumes of fine steel fibres. The recommendation included the classification of FRC in respect to their mechanical properties. This implies that design parameters can be assumed in advance of carrying out the design, which is verified later by tests on control specimens.

The implication of this is that the design of FRC will follow the same way a reinforced concrete would be designed, where the concrete strength class is chosen in advance and later verified by cylinder or cube tests. This tends to be conservative. The methods by which the properties of FRC are tested should also be considered.

2.9.9.1 Bending Moment

A series of inverse analysis is used to derive the stress-crack opening relationship. The tests show mostly a considerable scatter in load-deflection relations. Figure 2.41 shows the simplified stress block adapted in the fib Model Code 2010

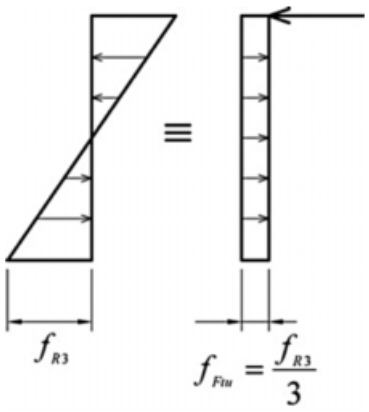

Figure 2.41: Simplified Stress block adapted fib Model Code 2010 (MC2010)

Equating the internal moment of resistance $M_{u,int}$ to the external applied moment $M_{u,ext}$

$$M_{u,int} = \frac{f_{R3} b h_{sp}^2}{6} = \frac{f_{Ftu} b h_{sp}^2}{2} = M_{u,ext} \qquad \text{Eqn. 2.74}$$

2.9.9.2 Punching Shear

MC2010 also adopts a rectangular perimeter for u but locates u at 0·5d from the column face, unless the loaded area is recessed into the slab, and u_{out} at $0.5d_v$ from the outer perimeter of the shear reinforcement.

Where d_v = the effective depth for shear

= d – 25mm (where 25mm is the cover to the shear studs).

MC2010 reduces the design shear resistance by k_e. At internal columns, in cases where lateral stability does not depend on the frame action, k_e as 0·9.

The punching shear resistance $V_{Rd} = V_{Rd,c} + V_{Rd,s}$ Eqn. 2.75

$$V_{Rd,c} = k_\psi \frac{{f_{ck}}^{0.5}}{\gamma_c} u d_v \qquad \text{Eqn. 2.76}$$

$$V_{Rd,s} = \sum_{d_v} A_{sw} k_e \sigma_{sw} \qquad \text{Eqn. 2.77}$$

Where f_{ck} = characteristic strength of concrete

γ_c = factor of safety

k_ψ = depends on the rotation of the slab around the support

$$= \frac{1}{1.5 + 0.9 k_{dg} \psi d} \leq 0.6 \qquad \text{Eqn. 2.78}$$

$$k_{dg} = \frac{32}{16 + d_g} \geq 0.75 \qquad \text{Eqn. 2.79}$$

d_g = maximum aggregate size

$\sum_{d_v} A_{sw}$=Cross-sectional area of all shear reinforcement

σ_{sw} = stress mobilised by shear reinforcement

2.9.10 The Concrete Society (2014) – TR 34

The guidance relates to internal concrete floors that are fully supported by the ground or supported on piles that are primarily found in industrial warehousing (both ambient and temperature controlled) and retail applications

2.9.10.1Bending Moment

The TR 34 uses the Yield-Line Method for the determination of the moments required for the design. The moments are obtained by folded plate mechanism for UDL and point load and fan yield line for punching shear. [See section 2.8.2]

2.9.10.2Punching Shear

The TR34 adopted the design process for punching shear from EC2. In addition to adopting the minimum shear resistance as the contribution of concrete and v_f as the contribution of the steel-fibres

Shear resistance $v_{c,min}$ due to concrete in SFRC is taken as the minimum shear resistance for slab made of plain concrete EC2

In the same vein, the punching resistance of SFRC slabs is taken as

$$V = (v_{c,min} + v_f)ud \qquad \text{Eqn. 2.80}$$

Where v_f = shear resistance provided by of steel-fibres

Taking v_f from RILEM (2002) recommendation

$$v_f = 0.12R_{e,3}f_{ctk,fl} \qquad \text{Eqn. 2.81}$$

Where $R_{e,3}$ = the flexural strength ratio

$f_{ctk,fl}$ = the flexural strength

The shear capacity of the SFRC slab is computed as

$$P_p = (0.035k_1^{1.5}f_{ck}^{0.5} + 0.12R_{e,3}f_{ctk,fl})\,ud \qquad \text{Eqn. 2.82}$$

The report also advised that punching shear should be checked at the pile or pile head and point loads. Pile-supported slabs are rarely provided with shear links, but if punching shear stresses are critical, the slab should be made thicker, top reinforcement over the pile increased or a larger pile head provided.

2.9.10.3Serviceability Limit State

For SLS, applying an upper limit on the elastic negative (hogging) moment over the pile can reduce the risk of flexural cracking at SLS in relation to the moment capacity of the plain, uncracked concrete section. Also, the sagging moment capacity in the span should not be higher than the hogging moment capacity over the pile.

For a pile-supported slab supported with at least six continuous spans on a regular grid of piles, carrying a uniformly distributed load, a minimum slab thickness, h_{min} applies

$$h_{min} = 21L_{eff}(\frac{q}{f_{ctd}})^{0.5} \quad \text{Eqn. 2.83}$$

Where:

L_{eff} = effective span

q = uniformly distributed load, including self-weight, in kN/m2 (unfactored)

f_{ctd}= design flexural strength of the concrete in N/mm2 (factored)

2.9.11 Deficiencies in Existing Design Methods for Elevated or Pile-supported Slabs

Having reviewed the different national, proprietary and association guidelines as well as the design methods for the analysis and design of elevated and pile-supported SFRC slabs, the need for a unified design approach has become apparent. At the moment, there is no provision for the design of SFRC in EC2. The Dutch Code NEN 6720 and ArcelorMittal that make provision for the design of pile-supported slabs limits it to cases when steel-fibres are used alongside conventional reinforcement. The below outline some of the deficiencies in the design guidelines.

2.9.11.1Elastic Design

The early analysis and design of elevated and pile-supported slabs were done by elastic design guidelines (Thooft, 2000, The Concrete Society TR63, 2007, Eddy, 2008). The effectiveness in the design of an SFRC section can be questioned [even though the design methods have been successfully used in designing structures that incorporates traditional reinforcement] as the useful contribution by fibres on the ductility of the

section are not recognised. According to TR 63, the inclusion of the steel-fibres is to control the crack widths at the SLS. Design of pile-supported SFRC slabs with elastic guidelines will produce an over-conservative design section (like the influence of the fibres is not taken into account).

2.9.11.2Yield Line Method [YLM]

As seen above [2.7.2], the elastic design methods disregard the post-cracking benefits of SFRC, thus leading to the load carrying capacity of SFRC slabs being underestimated. The yield line method has also been used in the design of soil supported SFRC slabs. The yield line method constitutes a theoretical upper bound design method for the design of pile-supported or elevated slabs since an elasto-plastic flexural response is assumed for the slab's cross section. Using the principle of virtual work, the ultimate failure load is found by equating the external and internal works.

The following limitations are seen when using the yield line method (The Concrete Society TR63, 2007)

- No information is given on support reactions or deflections.
- The adverse effects of pattern loading, such as uplift at piles, are not considered.
- The method is an upper bound one, which means that the design may be unsafe if not all the critical mechanisms have been investigated.
- The method is only valid if slabs have adequate ductility for the assumed yield lines to develop. It is not possible to authenticate whether this is the case since the analysis provides no information on slab deformations.
- Another drawback is that it does not give any information on the performance of the slab at the serviceability limit state.

The YLM is consensual when using conventional flexural reinforcement, but the discrete and the ''erratic'' nature of fibre reinforcement erases some concerns on the use of YLM unless fibre distribution and orientation are taken into account on the evaluation of the flexural capacity of an SFRC cross-section.

2.9.11.3Punching Shear

Earlier research has proven that steel-fibres increase the punching shear resistance of SFRC section (Beckett, 2004, Hedebratt and Silfwerbrand, 2004, Meda, 2005, Vollum, 2007, Dinh et al., 2010, Nguyen-Minh et al., 2011, Barros et al., 2013a, Abbas et al., 2014b, Ombres, 2015, Nguyen et al., 2017). However, the above research is somewhat restricted to certain load cases, slab geometry and fibre type (Labib, 2008). Likewise, the bulk of the tests have also been carried out on slabs with combined conventional reinforcement and steel fibres.

The RILEM (2002) recommendations were the first to take account of the positive effect of the fibres in punching shear that could be applied to structures encompassing steel fibres in addition to traditional reinforcement. As the RILEM recommendations are 'not supported by published research' (The Concrete Society, 2012), Technical Report 34 (2012 Final Draft) propose a reduction of 50% on the proposed value.

Eurocode 2 gives guidance on punching shear in slabs with conventional reinforcement. No recommendation is given for steel fibre only structures or even for the positive effects of the fibres in addition to the existing reinforcement. Concrete Society Technical Report 63 (The Concrete Society, 2007) claims that equation 3.13, which is based on the RILEM guidelines RILEM (2003), will yield over conservative results according to experimental research.

2.9.11.4Serviceability Limit States

There is a lack of authoritative design guidance regarding the serviceability limit state of SFRC slabs. TR34 (4th Edition) suggests that most of the practical problems regarding crack widths and shrinkage can be minimised at a material level by the appropriate selection of admixtures and cement. Available guidance on the calculation of crack width, such as the RILEM guidelines, applies to structural members that are reinforced with conventional reinforcement as well as fibres. None of the codes deals with the calculation of crack widths in SFRC only slabs.

2.9.12 Summary of Design Methods

Table 2.5 gives the summary of all the design methods described in section 2.9 above. It also provides a short remark on the design method.

Table 2.5 Summary of Design Methods

Design Guide	Bending	Punching Shear	Deflection [SLS]	Remarks
The Dutch Code NEN 6720 (1995)	Elastic design method used for analysis M= $\alpha n l^2$	Punching shear checked at distance d from the face of the support	s/d≤21	Rebar provided over supports
RILEM 162-TDF (2002)	$M_2 = \frac{F_2}{2}\frac{L}{2} = [\frac{D^f_{BZ,2}}{0.50}]\frac{L}{4}$ [Nmm] $M_3 = \frac{F_3}{2}\frac{L}{2} = [\frac{D^f_{BZ,3}}{2.50}]\frac{L}{4}$ [Nmm]	$V_{Rd,3} = V_{ed} + V_{fd} + V_{wd}$		Minimum reinforcement required $A_s = (k_c k k_p f_{fct,ef} - 0.45 f_{Rm,1})\frac{A_{ct}}{\sigma_s}$
Eurocode 2 BS EN 1992 (2004)	Flat slab design adopted	Punching shear checked at distance 2d from the face of the support Min shear resistance $v_{c,min} = 0.035 k_1^{1.5} f_{ck}^{0.5}$ Shear Capacity $V = v_{c,min}.ud$	For crack control, min amount of bonded reinforcement is provided in areas where tension is expected	No provision for SFRC in EC 2 but Some designers still refer to EC 2 for guidance
TR 63 (2007)	Elastic design method used for analysis $M_p = 08 f_{cd} f_{td} b h^2 \left[0.5 + \frac{0.1 f_{td}}{0.8 f_{cd} + f_{td}}\right] / [0.8 f_{cd} + f_{td}]$	Design shear stress $v_{max} = 0.5 v f_{cd}$ Max Punching Shear $P_{pmax} = v_{max} u_0 d$		f_{R1} and f_{R4} from BS EN 14651 and $R_{e,3}$ from the Japanese beam test

The Swedish Proposal (2008)	YLM used for analysis $m_u = \frac{f_{fld}.h^2}{6}$	Shear strength estimated as $f_{v1} = \frac{\xi}{1.4}.C.\frac{f_{fld}}{\zeta}$	To limit the crack width, the SFRC is recommended to be made with a high residual strength factor	Additional conventional reinforcement should be provided
ArcelorMittal (2010)	Q_{ult} = 16.M_R [Middle panel] Q_{ult} = 12.M_R [Edge panel]	FAN pattern The Critical area is 2d from the surface of the column	Minimum V_f=20kg/m^3 for SLS	Minimum V_f=40kg/m^3 for ULS
fib Model Code 2010 [MC 2010]	Inverse analysis used $M_{u,int} = \frac{f_{R3}bh_{sp}^2}{6} = \frac{f_{Ftu}bh_{sp}^2}{2} = M_{u,ext}$	The Critical area is 0.5d from the surface of the column The punching shear resistance $V_{Rd} = V_{Rd,c} + V_{Rd,s}$ $V_{Rd,c} = k_\psi \frac{f_{ck}^{0.5}}{\gamma_c} ud_v$ $V_{Rd,s} = \sum_{d_v} A_{sw}k_e\sigma_{sw}$		
Dramix by Bekaert (2012)				Adopts TR 34 design guidelines
Twintec (2012)				Adopts TR 63 design guidelines
TR 34 (2014)	YLM used for analysis For UDL, $M_p + M_n = \frac{q_u L_e^2}{8}$ [internal panel] For Point load, $M_p + M_n = Q_t \frac{L_e}{4} + q_u \frac{L_e^2}{8}$ For the pile-supported slab, ultimate moment capacity, $M_p + M_n = \frac{q_u L_1 L_2 \sqrt[3]{1-\frac{A}{L_1L_2}}}{2\pi}$	Adopts punching shear from EC2 The Critical area is 2d from the surface of the column Punching resistance of SFRC slabs, $V = (v_{c,min} + v_f)ud$	For at least six continuous spans on a regular grid of piles, min slab thickness h_{min} $h_{min} = 21L_{eff}(\frac{q}{f_{ctd}})^{0.5}$	

		The shear capacity of SFRC slab, $P_p = (0.035k_1^{1.5}f_{ck}^{0.5} + 0.12R_{e,3}f_{ctk,fl})ud$		

2.10 Summary

Numerous studies on the behaviour of SFRC were discussed in this chapter. Based on the work reviewed, some conclusions can be made as follows:

- There are several types of fibres [Figure 2.1] with the steel-fibres being the most used in the industry and researches. Also, the deformed shape [hook-end and crimped] steel-fibres are vastly used because of their high pull-out resistance with the straight fibre hardly used because of its low pull-out resistance. It was observed that steel fibres, provide better capability in increasing the stiffness, post-peak behaviour and energy absorption of the fibrous specimen (Barros and Figueiras, 1999). Likewise, steel fibres with higher aspect ratio provide higher energy absorption (Barros and Cruz, 1999, Bresler and Scordelis, 1963, Kooiman, 2000, Barros et al., 2005).
- The anchorage mechanism and pull-out resistance provided during crack propagation are the vital factors in the performance of SFRC. Some factors that affect the pull-out behaviour are a bond strength, the type of fibres, their shape and aspect ratio, fibre volume fraction, fibre orientation and embedment length.
- From previous research work (Lim et al., 1987, Barros and Cruz, 1999, Rossi, 1999, Lok and Xiao, 1999, Thooft, 1999, Bernard, 2000, Destrée, 2001, RILEM, 2002b, Barros, 2004, The Concrete Society TR63, 2007, Banthia and Sappakittipakorn, 2007, Barros et al., 2013c, The Concrete Society TR34, 2014, Abbas et al., 2014b, Salehian and Barros, 2017), it is mostly agreed that steel fibres have negligible impact on the compressive behaviour of RC. In most of the work, the behaviour of SFRC in compression and that of plain concrete are assumed to be the same [but with an improved ultimate strain value (Wahalathantri et al., 2011)].

- Several researchers (Lok and Xiao, 1999, RILEM, 2001, Barros and Antunes, 2003, Dupont, 2003, Tlemat et al., 2006a, Barros et al., 2005, Soranakom and Mobasher, 2009, Destrée, 2001) recommended that the inclusion of steel fibres enhance the concrete post-cracking behaviour from the sharp drop associated with plain concrete to either tension softening or tension stiffening. This enhancement in the stress-strain relationship is due to the pull-out resistance of the fibres by bridging the cracks and delaying crack propagation.
- The test methods general used to study the characteristic properties of SFRC elements are the uni-axial tension test and the beam [3-point and 4-point] bending tests and test methods for flexural properties is the plate test.
- The SFRC material constitutive models discussed in Part 2.7 can either be categorised as either generic (Lok and Pei, 1998, Loks and Xiao, 1999, RILEM, 2002b) or being applicable only for a specific type of steel fibres (Barros and Figueiras, 1999, Rossi, 1999).
- Slabs considered are flat [elevated] slab and pile-supported slab. The design of the pile-supported slabs are mainly by the elastic and yield-line methods. The flat slab is designed by the frame analysis and simplified methods.
- It was also concluded by some researchers (Lok and Xiao, 1999, Kooiman, 2000, Sukontasukkul, 2003, Barros et al., 2007, Døssland, 2008, Abbas et al., 2014b, Blanco et al., 2014b) that the increase in V_f resulted in increased strength and stiffness of the SFRC elements. Fibres shape and geometry have a substantial impact on the anchorage mechanism provided by the steel fibres.
- Various design guidelines were also examined. It was found that most of the designs are based on yield-line method YLM (RILEM, 2002b, America Concrete Institute, 2002, The Concrete Society TR63, 2007, The Concrete Society TR34, 2014, ArcelorMittal, 2010, Bekaert, 2012, Eddy, 2003) and the elastic method (Viney, 2007, TGB NEN 6720, 1995). Different punching areas where used ranging from d to 2d. It was also discovered, that most of the researchers used any of the two above, with the majority using the YLM for both the design of pile-supported and elevated slabs.

Consequently, it can be established from the investigation carried out that the SFRC exhibits considerable behaviour in which enhancement was observed in the ductility, cracking strength, stiffness and energy absorption. Also, steel fibres controlled the crack propagation, and the mode of failure changed from brittle to ductile one. The studies concluded that steel fibres were able to provide acceptable strength and ductility enhancement that can be compared with conventional structures even when the rebar were completely removed in SFRC structures (Mobasher and Destrée, 2010b, Destrée and Silfwerbrand, 2012, Singh, 2015, Singh, 2017). Moreover, the energy absorption of the SFRC structures showed improvement with more controlled crack propagation. Some of the crucial factors considered during the investigation are listed below:

- The range of fibre volume fractions
- Fibres shape and aspect ratio
- The extent of SFRC zone within the structure.
- Loading and boundary conditions

However, the present research work carried out so far was limited to specific amounts of steel fibres. The work carried out so far on suspended slabs are mainly experimental [with only point load used], and there is scarcely any numerical modelling executed. Hence, the present research work aims to expand this further using non-linear FE analysis and critically examine the potential of FEA to simulate the behaviour of suspended SFRC slabs correctly with UDL and Point-load and translate the results into design guidelines.

Chapter 3: FINITE ELEMENT METHOD

3.1 Introduction

The thrust of this research work is the FE analysis of pile-supported and suspended SFRC slabs. The methods used in this research work are outlined and explained in this chapter. The work includes:

- Examining and comparing the modelling tools in each software
- Collation and presentation of available experimental data and results on suspended slabs
- Running the models with FEA software
- Comparing the available experimental and FEA results
- Running parametric studies on models for pile-supported and suspended SFRC slabs both at the SLS and ULS.

Computational modelling of reinforced concrete structures has been used to understand the complex interaction of the reinforced concrete matrix. Over the years, the method has been extended to simulate and design the steel-fibre reinforced concrete [SFRC] elements. One of the computational modelling methods is the Finite Element Method [FEM]. The modelling of concrete using FEM covering linear [serviceability] and non-linear responses defined by proposed constitutive laws [concrete plasticity, cracking, tension stiffening and heat effect] has been covered extensively by many researchers (Hillerborg et al., 1976, Lim et al., 1987, Kotsovos, 1995, Lok and Xiao, 1998, Kooiman, 2000). This chapter contains a brief description of these constitutive models and a more detailed explanation of the preferred model.

3.2 Finite Element Analysis

The Finite Element Method [FEM] or Finite Element Analysis [FEA] is founded on the idea of building a complex object with simple blocks or dividing a complicated object into small and manageable pieces. The degree of freedom in the complex object [continuum system] is infinite. In many cases, their complexity does not allow for analytical solutions but often solved with FEM.

The FEM involves 'scaling down' the [object] structure into discrete [smaller isolated] elements, thus shifting the focus of consideration to a discrete domain from a continuum. The element consists of nodes, which are located at the inter-element

boundaries, and in some cases inside the element. The elements interconnect at a finite number of nodal points. The scaling down process is called discretisation. Nodal displacement is used to express the behaviour of each element. The displacement at the nodal points is assumed to have unknown values so that the difference within an element is described as a function of the nodal values using shape or interpolation functions.

$$\{u\} = [N]\{d\} \qquad \text{Eqn. 3.1}$$

In which {u} represent the matrix of displacement within the elements, [N] connotes the shape function matrix and {d} is the nodal displacement matrix. It also follows that the strain {ε} within the element can be derived from:

$$\{\varepsilon\} = [\delta]\{u\} = [B]\{d\} \qquad \text{Eqn. 3.2}$$

And $[B] = [\delta][N]$

The stress σ is given in relation to the strain ε by means of a matrix of constitutive relations [D]

$$\{\sigma\} = [D]\{\varepsilon\} \qquad \text{Eqn. 3.3}$$

Substituting Eqn. 3.2 into Eqn. 3.3 will give

$$\{\sigma\} = [D][B]\{d\} \qquad \text{Eqn. 3.4}$$

At this point, the local stiffness matrix is defined by the concept of virtual work. The stiffness matrix relates the external loads to the nodal displacement in Eqn. 3.4. When an external virtual force F is applied to a node, the internal work dissipated inside the element is computed as:

$$I_w = \int \{\varepsilon\}^T \{\sigma\} dV \qquad \text{Eqn. 3.5}$$

Putting Equations 3.2 and 3.4 into 3.5 will turn the internal work equation to:

$$I_w = \int ([B]\{d\}^T [D][B]\{d\} dV \qquad \text{Eqn. 3.6}$$

Moreover, the external work will be:

$$E_w = \{d\}^T [F] \qquad \text{Eqn. 3.7}$$

Where $\{d\}^T$ represents the nodal displacement matrix transpose and [F] represent the external force matrix applied to the element. For equilibrium to be attained in the element, the total potential energy within the element [system] must equal to zero [0]. Thus, combining the internal and external energy will give:

$$I_w = E_w$$

$$\{d\}^T [F] = \int ([B]\{d\}^T [D][B]\{d\} dV \qquad \text{Eqn. 3.8}$$

Solving Equation 3.8 by transforming $\int([B]\,[D][B]dV$ into global matrix [K] will give

$$[F] = [K]\{d\} \qquad \text{Eqn. 3.9}$$

The above provides the foundation for Linear Finite Element Analysis. For an in-depth study, specialised and relevant textbooks are to be consulted.

3.3 Non-Linear Finite Element Analysis

In concrete structures, where nonlinearity may occur due to geometry, material, kinematic, boundary and force, the overall behaviour tends to be non-linear during loading. Section 2.6 explains the constitutive models that depict the non-linearity behaviour. Non-linear problems are solved by a search process based on incremental, iterative method of the linear system until a definite degree of accuracy is achieved. The method comprises the load application in small increments.

The idea behind this method includes evaluating the load system from the stresses within the structure which are then compared with the applied load system. The variance between these two will lead to a set of residual forces. Therefore, to satisfy the equilibrium in the structure, the residual forces are applied. Moreover, the process of the equilibrium continues until the residual forces meet the specified convergence benchmarks.

3.4 Finite Element Analysis using ADINA and ABAQUS

The Finite Element Analysis shall be implemented using these two commercially available software in University of East London, ADINA and ABAQUS. They are both based on Finite Element Method of analysis. In ABAQUS, three concrete models [concrete smeared cracking CSC, concrete damaged plasticity CDP and concrete brittle cracking CBC] would be discussed and used in FEA while in ADINA, two concrete models were used [concrete and data-fitted concrete]. Chapter 4 contains the results and comparison of these models in the validation works.

3.5 ADINA

The Automatic Dynamic Incremental Nonlinear Analysis [ADINA] software founded by Dr K.J. Bathe [author of Finite Element Procedures] under the organisation called ADINA R & D, Inc. The mission of the organisation is the development of the ADINA analysis system based on FEM. The ADINA system consists of numerous modules which working together can simulate linear, multilinear and nonlinear [creep, crack and so on] analysis of solids and structures, thermo-mechanical coupled analysis, compressible and incompressible flow, soil-structure interaction, and fluid-structure interaction.

3.5.1 Elements in ADINA

Each component in a structure is regarded to as an element. The elements are in the different classes, which guides their modelling. It also comprises the materials that are compatible with each element type, their application to large strain and displacement problems.

The elements classification are truss [one-dimensional 1D], two-dimensional 2D [plane section] and three-dimensional 3D [solid elements]. The truss elements can be deployed as 2-node, 3-node and 4-node elements or as a 1-node ring element [Figure 3.1]. The force applied is transmitted as a longitudinal force in the element.

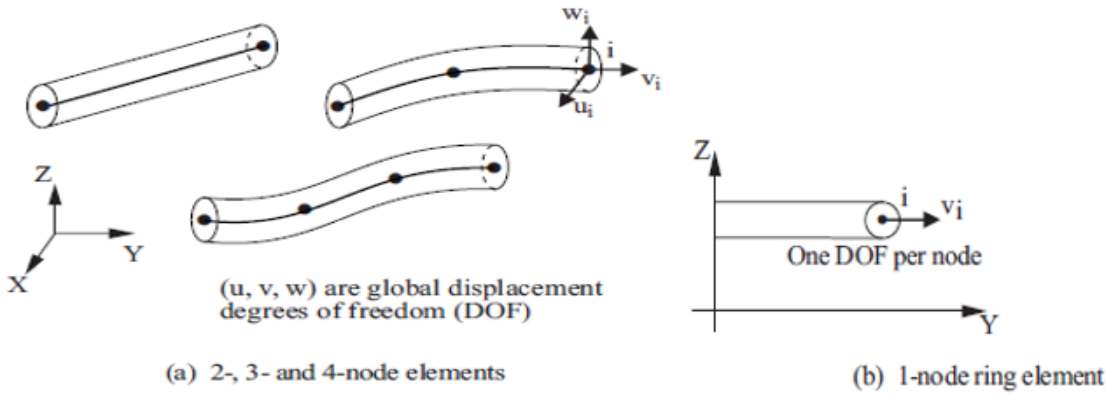

Figure 3.1: Truss Elements available in ADINA (adapter from ADINA 2012)

The force is constant in 2-node truss and ring element but may differ in the 3- and 4-node truss. A practical example of a truss is the rebar. The ADINA user interface AUI generate the truss element for rebar as an embedded 1-D element in 2-D or 3-D elements.

The two-dimensional solid elements in ADINA are available on the kinematic assumptions of plane stress, plane strain and membrane [3-D]. They are thin-plate elements. Two coordinates define each node on the 2-D element. Examples of 2-D solid elemens are given in Figure 3.2

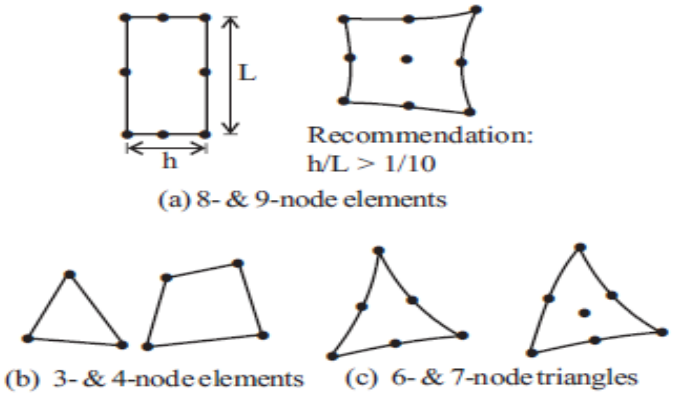

Figure 3.2: 2-D Solid Elements (adapter from ADINA 2012)

The plane stress and plane strain are defined in the Cartesian plane. The plain stress can have a uniform or varying thickness while the plain strain must maintain a unit thickness of the structure. The 2-D elements used isoparametric displacement-based finite elements. Several material models [elastic-isotropic, nonlinear-elastic, plastic-multilinear and so on] are compatible with 2-D elements.

The three-dimensional [3-D] solid elements have all the fields of variables dependants of x, y and z with 4- to 27-node. Figure 3.3 shows typical examples of 3-D solid elements. The stress and strain are expressed in the 3-D state. Apart from the displacement-based elements, mixed-interpolated elements are also available in which the displacement and pressure are interpolated.

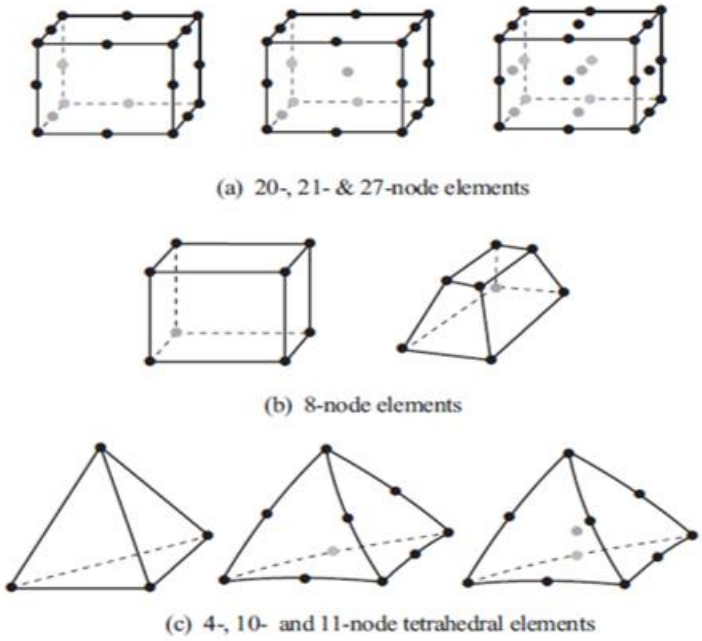

Figure 3.3: 3-D Solid elements adapted from (ADINA, 2012)

The 3-D solid element should be deployed for analysis in which the three-dimensional stress[or strain] is required. The 3-D elements can be used with small displacement/small strain, large displacement/small strain or large displacement/large strain. The following material models can be used with 3-D elements, and these are: elastic-isotropic, nonlinear-elastic, Drucker-Prager, creep gasket and so forth.

In conclusion, for the simulation and analysis of reinforced concrete [rebar and SFRC], 2-D or 3-D solid elements are used, but for this research work, only 3-D elements, having 8-node in ADINA shall be considered. The 8-node element has the feature of incompatibility mode.

3.5.2 Meshing

Meshing is the process of dividing the whole structure into smaller bits, called elements. It is the practice of generating a polygonal or polyhedral mesh that approximates a geometry domain. The accuracy of the output of the FEA is dependent on the mesh size used. Mesh sensitivity analyses were carried out on all the specimen used in this research work.

3.5.3 Material Model for Steel

There are two material models adopted for steel in this research work. A linear model of stress and strain for the loading plate and a bilinear model for rebar [Figure 3.4]. The linear model is adoted for the loading plate because the deformation expected is linear while the deformation in the rebar is nonlinear. The yield and ultimate stresses are has provided for in the experimental work.

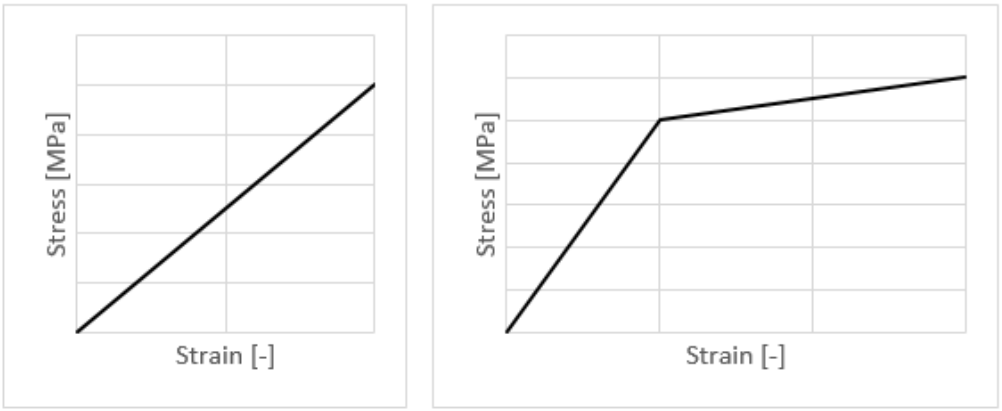

Figure 3.4: Linear and Bilinear Stress-Strain Models for Steel

The Young modulus E adopted is 200 GPa. The loading place deformation is within the elastic limit. Which means, it is not expected to deform permanently. The embedded rebar will undergo stretching beyond the elastic limit, and It is expected that the rebar should fail during the loading.

3.5.4 Material Models for Concrete

The most significant constitutive model for the SFRC suspended floors is a concrete material model for the tensile response under loading. There are also two concrete constitutive models in ADINA; the concrete and Data-Fitted [DF] models. The models can be used with 2D or 3D solid elements which assumes small strains irrespective of loading either with small or large displacement formulations. The two concrete material models are supported in implicit and explicit [dynamic] and static [standard] analyses. These material models allow three types of temperature effects: [i] no temperature effects, [ii] isotropic temperature independent effects; and [iii] isotropic temperature dependent effects. Detailed explanations are in sections 3.5.4.1 and 3.5.4.2.

3.5.4.1 ADINA Concrete Model

Concrete is a very complex material. The ‘concrete model’, is the primary model in ADINA for concrete but it can be used for other materials. The concrete model in ADINA

may not cover all the detailed material characteristics, but it is recognised that the model is beneficial in the modelling of concrete and rock materials, thereby satisfying the objective of the model in providing an effective model with adequate flexibility to model most of the frequently used material behaviours. The basic material characteristics are:

- Tensile cracking failure at a maximum, relatively small principal tensile stress
- Compression crushing failure at high compression
- Strain softening from compression crushing failure to an ultimate strain, at which the material totally fails.

The compression crushing and tensile cracking failure envelopes controlled the compression crushing and tensile cracking failures. The compression crushing fails at high compression. In compression, the concrete material model assumes a nonlinear stress-strain relation that includes softening behaviour. The tensile cracking fails at a maximum comparatively low principal tensile stress. The multiaxial stress-strain relations are expressed based on the uniaxial stress-strain relation displayed in Figure 3.5.

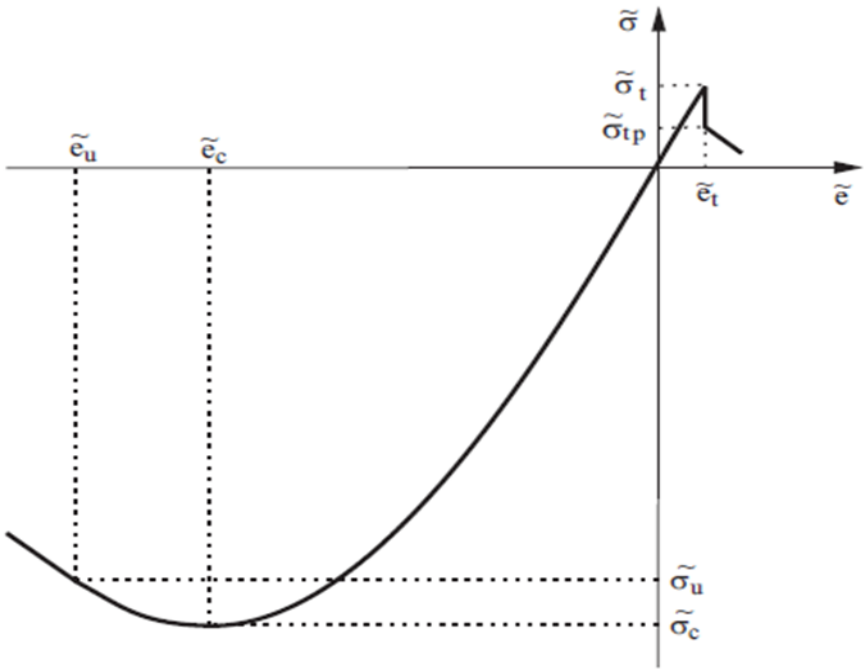

Figure 3.5 Uniaxial stress-strain relation adapted from (ADINA, 2012)

Where E_0 - Uniaxial initial tangent modulus

v - Poisson's ratio

α - Mean coefficient of thermal expansion

σ_t - Uniaxial cut-off tensile stress

σ_{tp} - Post-cracking uniaxial cut-off tensile stress

σ_c - Uniaxial maximum compressive stress

e_c - Uniaxial compressive strain at σ_c

σ_u - Uniaxial ultimate compressive stress u

e_u - Uniaxial strain at σ_u

G_f - Fracture energy

ξ – Constant for tensile strain failure

The features of the model are: [i] the nonlinear stress-strain relation that allows the weakening of the material under increasing compressive stresses; [ii] failure envelope that defines cracking failure in tension and crushing in compression and [iii] a strategy to model the post-cracking and crushing behaviour of the material. The model also includes material behaviour after failure [pots-tensile cracking, post-compression crushing and strain softening behavious].

Three basic features are used in the concrete model:

- A nonlinear stress-strain relation to allow for the weakening of the material under increasing compressive stresses
- Failure envelopes that define cracking failure in tension and crushing in compression
- A strategy to model the post-cracking and crushing behaviour of the material

The general multiaxial stress-strain relations are derived from a uniaxial stress-strain relation $\widetilde{\sigma_t}$ versus $\widetilde{e_t}$. A typical uniaxial stress $\widetilde{\sigma_t}$ to uniaxial strain $\widetilde{e_t}$ relation is shown in Figure 3.5. This stress-strain relation shows that there are three strain phases; namely,

$\widetilde{e_t} \geq 0$ Eqn. 3.10

$0 > \widetilde{e_t} \geq \widetilde{e_c}$ Eqn. 3.11

$$\tilde{e_c} > \tilde{e_t} \geq \tilde{e_u}$$ Eqn. 3.12

Where

$\tilde{e_c}$ is the strain corresponding to the minimum (crushing) stress $\tilde{\sigma_c}$ that can be reached, and $\tilde{e_u}$ is the ultimate compressive strain.

If $\tilde{e_t} > 0$, the material is in tension and the relation is linear until tensile failure at the stress $\tilde{\sigma_t}$. The ratio of the stress to strain before tensile failure gives the Young's modulus

$$E_0 = \tilde{\sigma}_t / \tilde{e}_t$$ Eqn. 3.13

When $\tilde{e_t} \leq 0$, the relationship between stress and strain it is assumed to be

$$\frac{{}^t\tilde{\sigma}}{\tilde{\sigma}_c} = \frac{\left(\frac{\tilde{E}_0}{\tilde{E}_s}\right)\left(\frac{{}^t\tilde{e}}{\tilde{e}_c}\right)}{1 + A\left(\frac{{}^t\tilde{e}}{\tilde{e}_c}\right) + B\left(\frac{{}^t\tilde{e}}{\tilde{e}_c}\right)^2 + C\left(\frac{{}^t\tilde{e}}{\tilde{e}_c}\right)^3}$$ Eqn. 3.14

And hence,

$${}^t\tilde{E} = \frac{\tilde{E}_0\left[1 - B\left(\frac{{}^t\tilde{e}}{\tilde{e}_c}\right)^2 - 2C\left(\frac{{}^t\tilde{e}}{\tilde{e}_c}\right)^3\right]}{\left[1 + A\left(\frac{{}^t\tilde{e}}{\tilde{e}_c}\right) + B\left(\frac{{}^t\tilde{e}}{\tilde{e}_c}\right)^2 + C\left(\frac{{}^t\tilde{e}}{\tilde{e}_c}\right)^3\right]^2}$$ Eqn. 3.15

Where

$$A = \frac{\left[\frac{\tilde{E}_0}{\tilde{E}_u} + \left(p^3 - 2p^2\right)\frac{\tilde{E}_0}{\tilde{E}_s} - \left(2p^3 - 3p^2 + 1\right)\right]}{\left[\left(p^2 - 2p + 1\right)p\right]}$$

$$B = \left[\left(2\frac{\tilde{E}_0}{\tilde{E}_s} - 3\right) - 2A\right]$$

$$C = \left[\left(2 - \frac{\tilde{E}_0}{\tilde{E}_s}\right) + A\right]$$

the following parameters were obtained from the uniaxial tests:

$$\tilde{E}_0, \tilde{\sigma}_c, \tilde{e}_c, \tilde{E}_s = \frac{\tilde{\sigma}_c}{\tilde{e}_c}, \tilde{\sigma}_u, \tilde{e}_u, p = \frac{\tilde{e}_u}{\tilde{e}_c}, \tilde{E}_u = \frac{\tilde{\sigma}_u}{\tilde{e}_u}$$

The stress-strain relation in Eqn. 3.15 assumes monotonic loading conditions. The initial Young's modulus E_0 is used for unloading conditions and loading back to the stress state from which unloading occurred. To describe loading and unloading conditions, the loading scalar is defined as ${}^t g$ for each integration point, and ${}^t g = {}^t\sigma_e$ where ${}^t\sigma_e$ is the effective stress at time t. During unloading, the material is assumed to be isotropic and the initial Young's modulus, E_0, is used to form the incremental stress-strain matrix, both for stiffness and stress calculations.

The failure envelopes shown in Figures 3.6 to 3.8 are employed to establish the uniaxial stress-strain law accounting for multiaxial stress conditions, and to identify whether tensile or crushing failure of the material has occurred.

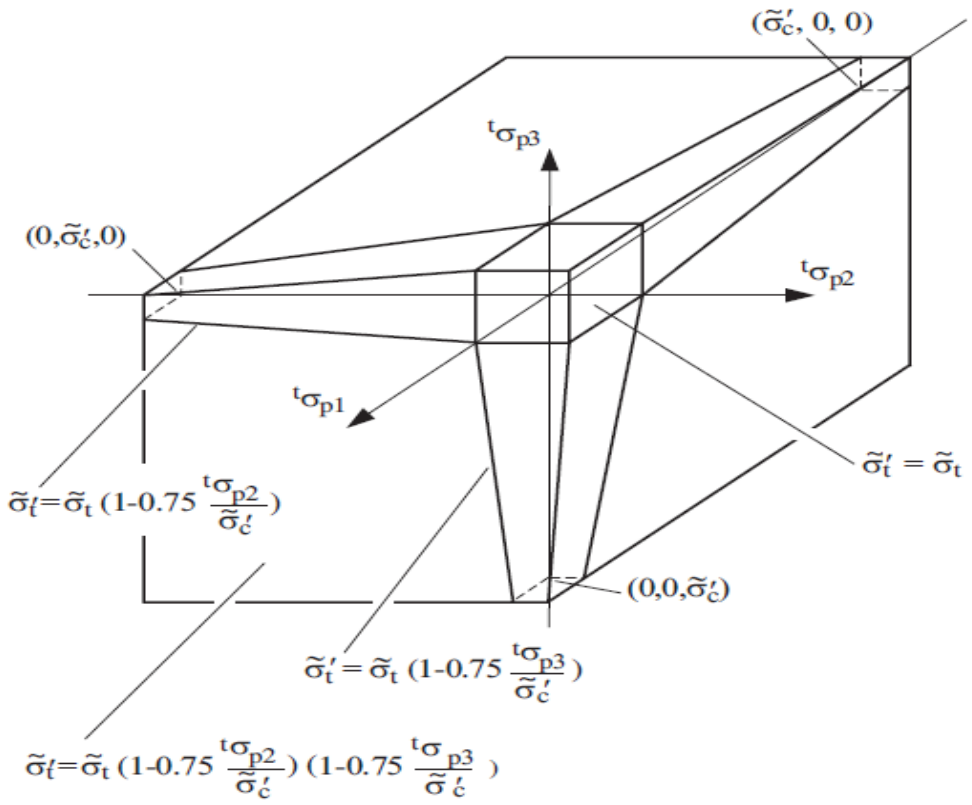

Figure 3.6: Three-dimensional tensile failure envelope of concrete model (ADINA 2012)

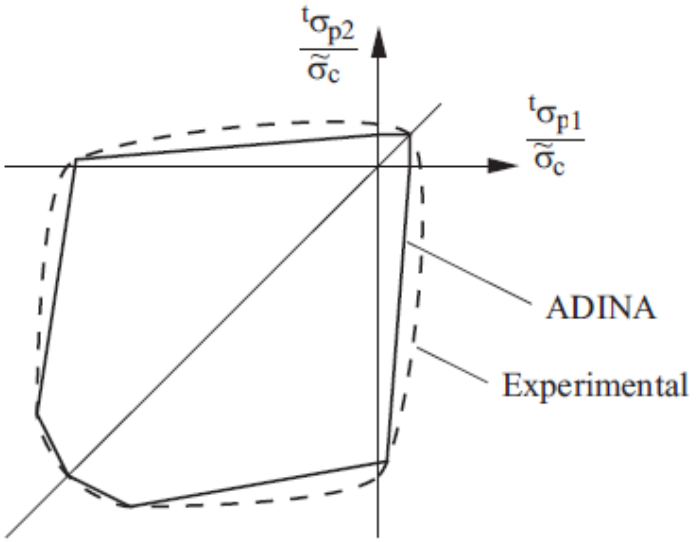

Figure 3.7: Biaxial concrete compressive failure envelope (adapter from ADINA 2012)

A smeared cracking approach is used in which tensile response can be built on either fracture energy or tension stiffening.

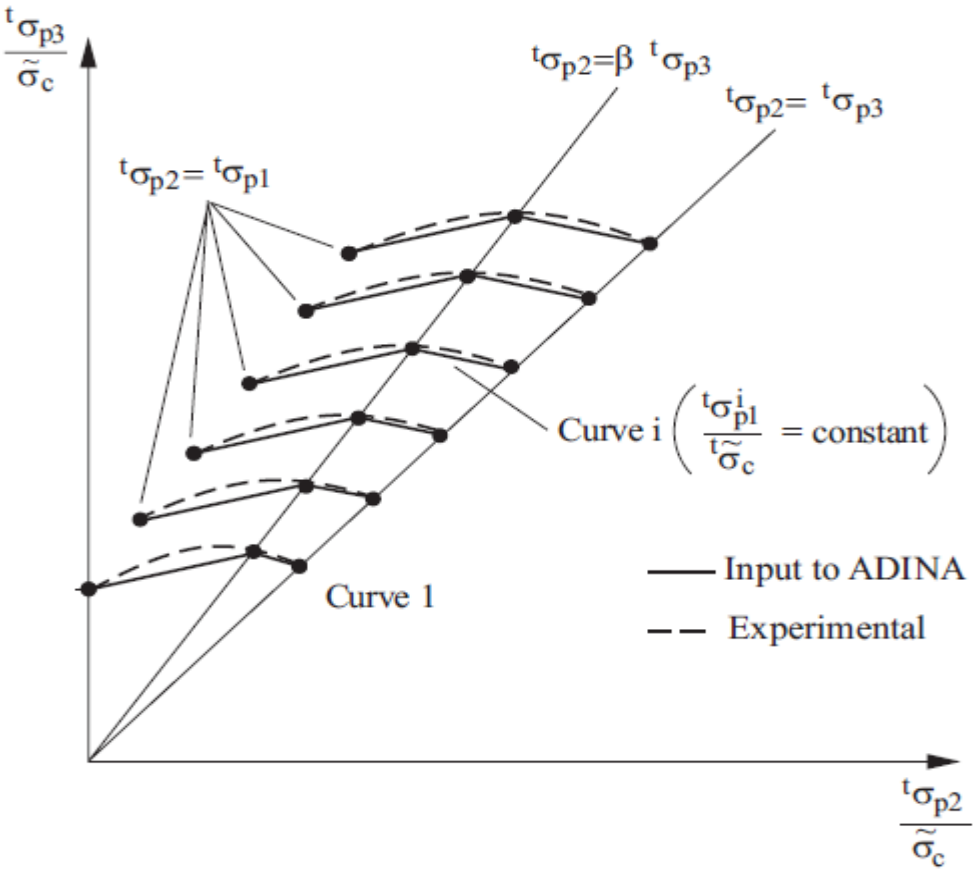

Figure 3.8: Triaxial compressive failure envelope (adapter from ADINA 2012)

Under multiaxial stress conditions, the stress-strain relations are estimated differently depending on whether the material is loading or unloading. Poisson's ratio is presumed to be constant under tensile stress conditions and can vary in the compressive region

3.5.4.1.1 Tensile failure envelope

Figure 3.6 shows the tensile failure envelope used in the concrete model. To determine whether the material has failed, the principal stresses are used to locate the current stress state. The tensile strength of the material in a principal direction depends on compressive stresses in the other directions. but does not depend on tensile stresses in the other principal stress directions

Tensile failure arises if the tensile stress in a principal stress direction surpasses the tensile failure stress. In this circumstance, it is assumed that a plane of failure develops perpendicular to the corresponding principal stress direction. The consequences of this material failure are the reduction in the normal and shear stiffnesses and stresses across the plane of failure and plane stress conditions are assumed to exist at the plane of tensile failure.

Figure 3.9(a) adopts loading from zero stress directly into the tensile region. The strain normal to the tensile failure plane is measured from the specific strain value at which the stress is zero when the tensile stress is reached by unloading from a compressive stress. Strain softening may give nonunique solutions if ξ is chosen to be greater than 1.0, thereby special care should be taken in the analysis. For a mesh independent solution, the fracture energy G_f is provided instead of ξ. In doing so, ξ is estimated at each integration point, based on the finite elements size. At this point, ADINA overwriting the user input by internally calculating η_s.

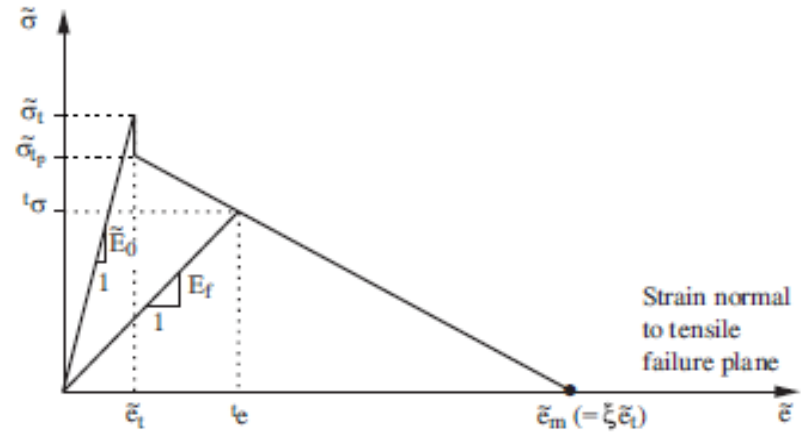

a) Calculation of Young's modulus E_f, normal to tensile failure plane. $\tilde{\sigma}_{t_p}$ is the post-cracking uniaxial cut-off tensile stress.

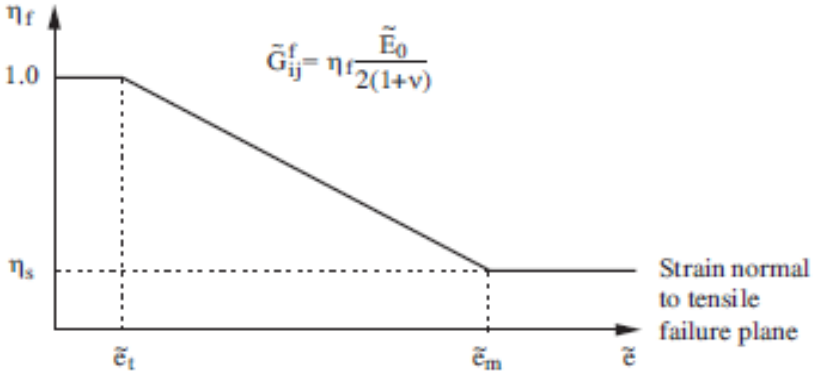

b) Calculation of shear modulus in tensile failure plane

Figure 3.9: Material Moduli for Stress Calculation after Tensile Failure (adapter from ADINA 2012)

3.5.4.1.1 Compressive failure envelope

Figure. 3.8 shows the triaxial failure envelope used for the concrete model. the biaxial failure envelope in Fig. 3.7 is curve 1 of the triaxial failure envelope. Likewise, the flexibility of the biaxial and triaxial envelope curves makes it possible to represent a large number of concrete and rock materials. A vital criterial is choosing the appropriate values for the input of the failure surfaces and other parameters. These may differ significantly for diverse materials and structures and must be gotten from experimental data.

Once a tensile plane of failure has formed, the activeness of the failure is checked in each subsequent solution step. The post failure material behaviours considered in the concrete model in ADINA include post tensile cracking, post compression crushing, and strain-softening.

3.5.4.2 *Data-Fitted concrete model*

The data fitted concrete material model present a simpler modelling alternative in ADINA. It is a pragmatic material model, exclusively described by its uniaxial cylinder compressive strength (i.e., the maximum axial compressive stress that a right-cylindrical sample of concrete can withstand before failing) and it identifies concrete as a brittle material, which behaves nonlinearly in compression. The model is based on the work of M.D. Kotsovos and other researchers (Kotsovos, 1995, Kotsovos and Spiliopoulos, 1998). From their experimental works, the following were reported which formed the basis for the data-fitted model for concrete: The concrete material

- can be considered an isotropic material with nonlinear compressive behaviour followed by a brittle post-peak behaviour which is characterised by a complete and immediate loss of load-carrying capacity after the ultimate strength is reached as shown in Figure 3.10.
- after the peak load value, the material is not considered to be a continuum since Poisson's ratio measured near and around the peak load level were greater than 0.5

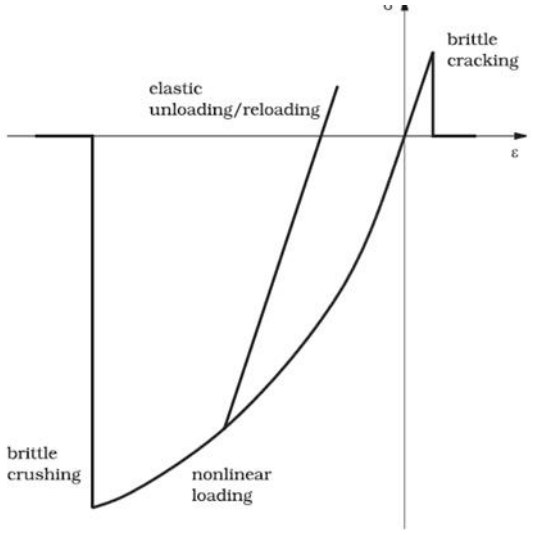

Figure 3.10: Stress-strain behaviour of DF-concrete adapted from (ADINA, 2012)

- the microcracking, and macrocracking processes describe the compressive behaviour of concrete up to failure and the fracture processes occurring during failure.
- during unloading and reloading, no appreciable stress-strain hysteresis loop occurs;

- Failure is captured in the stress space via a three-dimensional failure surface [Figure 3.11].
- The general mechanical properties are free of the loading rate.

Considering the test results and analytical work by Kotsovos et al., the data fitted concrete model consist of the following:

  - the behaviour in compression and tension is based on a nonlinear stress-strain law from an experimental work that combined linear behaviour when concrete unloads/reloads and is in tension as shown in Figure 3.10
  - an experiment-based stress failure surface function that dictates when either cracking or crushing occurs in concrete as shown in Figure 3.11 and

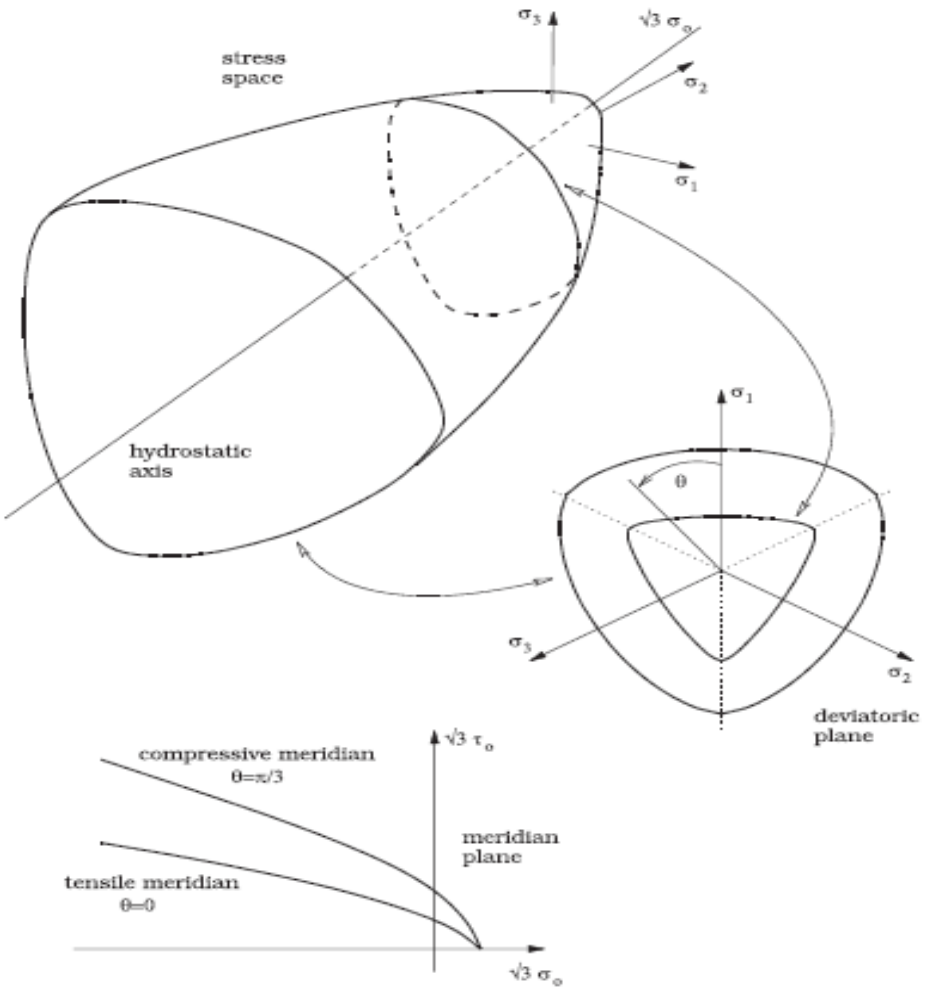

Figure 3.11: Failure Surface of the Data Fitted Concrete Material Model (adapter from ADINA 2012)

- a post-failure response for cracking based on a smeared crack approach that allows cracks to close and reopen as shown in Figures 3.12-3.14 .

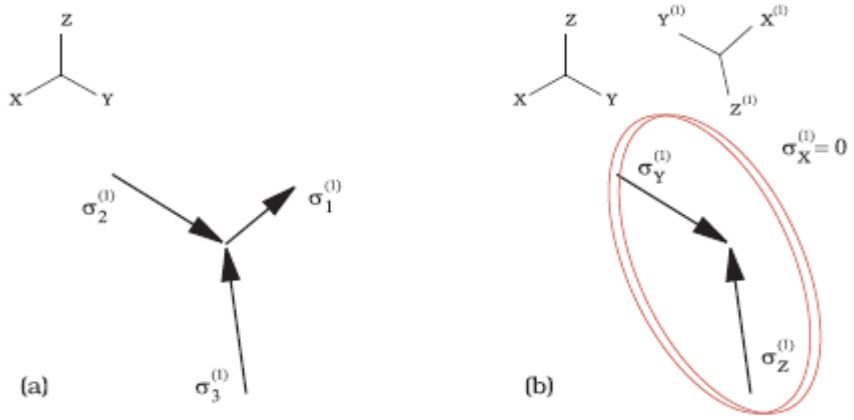

Figure 3.12: First crack formation of the data fitted concrete material model (a) before, and (b) after

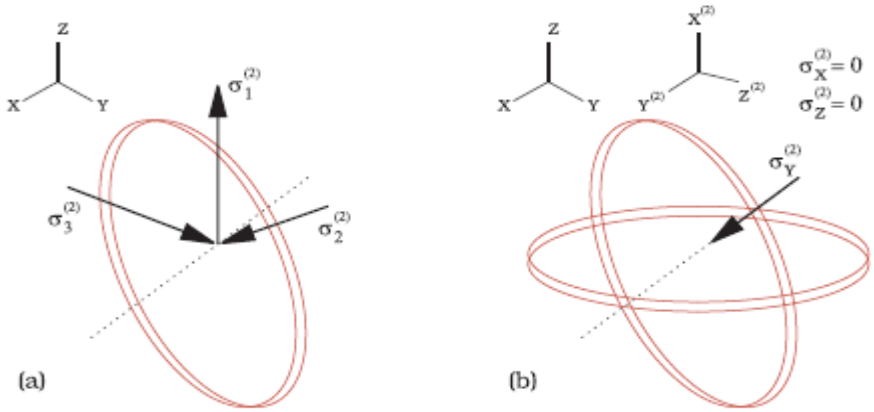

Figure 3.13: Second crack formation of the data fitted concrete material model (a) before, and (b) after

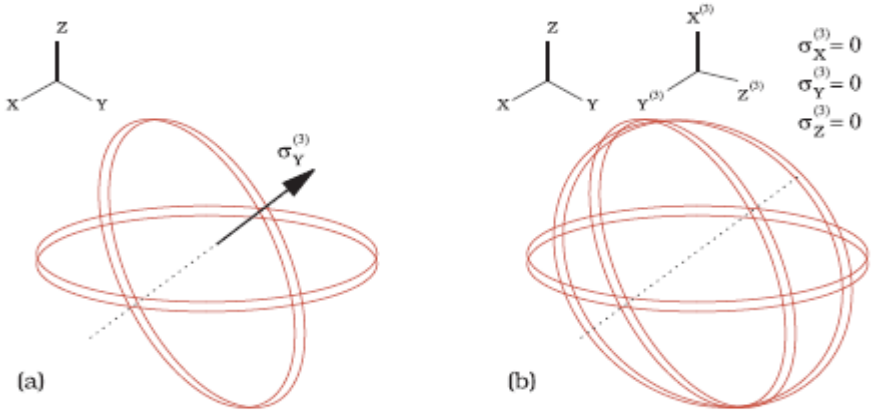

Figure 3.14: Third crack formation of the data fitted concrete material model (a) before, and (b) after

Kotsovos et al. (1995, 1998) presented the experimental data in a compact way in terms of the octahedral normal and shear stresses (σ_0 , τ_0), their corresponding octahedral strains (ε_0 ,γ_0) and the material constant, uniaxial cylinder compressive strength (f_{cu}). The following material parameters [*Ke*, *Ge*, *A*, *b*, *C*, *d*, *k*, *l*, *m* and *n*] are derived for values of f_{cu} in the range of 16–65 N/mm^2. These parameters are the same for f_{cu} ≤ 16 N/mm^2 and same for f_{cu} ≥ 65 N/mm^2. The expressions of these material parameters are:

$$K_e = 11000 + 3.2 f_c^2,$$

$$G_e = 9224 + 136 f_c + 3296 \cdot 10^{-15} f_c^{8.273},$$

$$A = \begin{cases} 0.516 & \text{for } f_c \le 31.7 \text{ N/mm}^2, \\ \dfrac{0.516}{1 + 0.0027 \left(f_c - 31.7 \right)^{2.397}} & \text{for } f_c > 31.7 \text{ N/mm}^2, \end{cases}$$

$$b = 2 + 1.81 \times 10^{-8} f_c^{4.461},$$

$$C = \begin{cases} 3.573 & \text{for } f_c \le 31.7 \text{ N/mm}^2, \\ \dfrac{3.573}{1 + 0.0134 \left(f_c - 31.7 \right)^{1.414}} & \text{for } f_c > 31.7 \text{ N/mm}^2, \end{cases}$$

$$d = \begin{cases} 2.12 + 0.0183 f_c & \text{for } f_c \le 31.7 \text{ N/mm}^2, \\ 2.7 & \text{for } f_c > 31.7 \text{ N/mm}^2, \end{cases}$$

$$k = \frac{4}{1 + 1.087 \left(f_c - 15 \right)^{0.23}},$$

$$m = \begin{cases} -2.415 & \text{for } f_c \le 31.7 \text{ N/mm}^2, \\ -3.531 + 0.0352 f_c & \text{for } f_c > 31.7 \text{ N/mm}^2, \end{cases}$$

$$n = \begin{cases} 1 & \text{for } f_c \le 31.7 \text{ N/mm}^2, \\ 0.3124 + 0.0217 f_c & \text{for } f_c > 31.7 \text{ N/mm}^2. \end{cases}$$

The expressions are unit dependent where *Ke* and *Ge* are the elastic bulk and shear moduli, N/mm^2. The remaining material parameters are either exponents or coefficients so they do not have units.

A supplementary feature of the data fitted concrete material model is the inclusion of tension softening after cracking necessitated by the addition of reinforcement into the concrete. The tension softening behaviour follows a linear stress-strain curve (see Figure. 3.15) which connote he response of the concrete when reinforcement is added and, therefore, will replace the default brittle cracking behaviour.

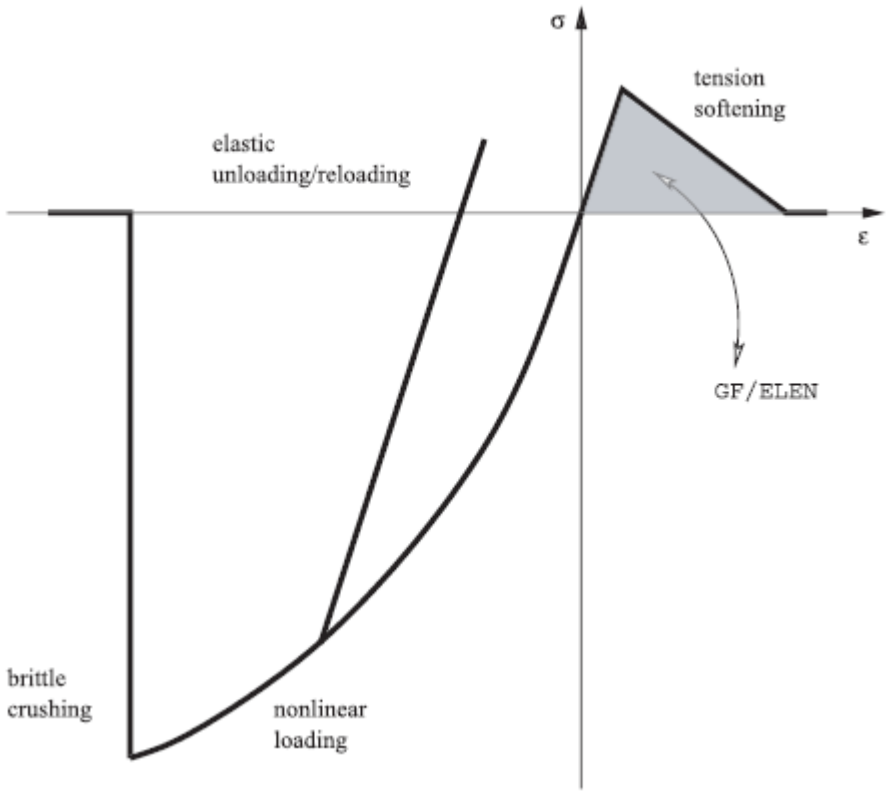

Figure 3.15: Stress-strain behaviour of the data fitted concrete material model

The fracture energy value and the characteristic length of the concrete model define the tension softening behaviour so that the numerical solution is not dependent on the mesh size of the concrete's finite element.

The data fitted DF concrete material model is proposed for modelling reinforced concrete structures. The DF concrete model is recommended when the available material parameters of concrete cannot fully describe complex stress-strain laws and/or failure surfaces. The merit of the DF concrete material model is that it is wholly described by a single material parameter, which is the uniaxial cylinder compressive strength. The model is only valid with SI units [Force=N, Length=m, Pressure= MPa]

3.6 ABAQUS

ABAQUS is a general purpose, versatile, highly sophisticated simulation finite element method software that can be explored for a variety of modelling applications of civil engineering and other acoustics structures. ABAQUS has two essential analysis products; ABAQUS/Standard, and ABAQUS/Explicit. The ABAQUS/Standard has four special-purpose products as add-ons.

ABAQUS has a materials library that has several models of the elastic and inelastic behaviour of various materials which include concrete, cast iron, metals, rock and soils. There are models embedded in it that can be used to model concrete and masonry structures. ABAQUS/Standard utilises the FEM to indirectly solve a system of equations at each solution “increment” for the analysis of framework, shell, and, solid models.

3.6.1 Elements in ABAQUS

The Abaqus element library makes available the capacity to model the complete geometry of any structure. Thus, any blend of components can be utilised to make up any model. At times, multi-point constraints are necessary for the application of the essential kinematic relations to produce the model. Each component in a structure is taken as an element [Figure 3.16]. The elements are in the distinctive classes, which controls their modelling. It also involves the materials that are in harmony with each element type, their application to large strain and displacement problems.

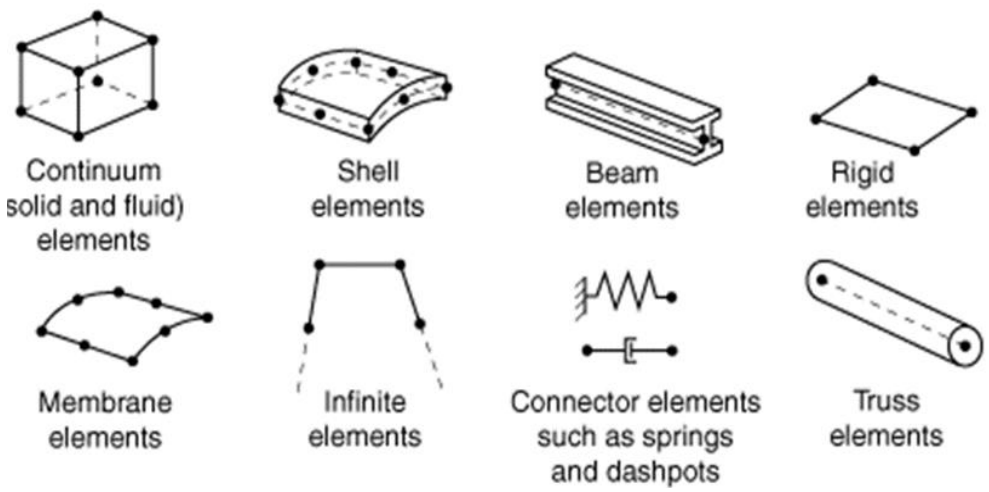

Figure 3.16: Element models in ABAQUS adapted from ABAQUS (2009)

The Abaqus element library contains several types of beam elements. A “beam” in this perspective is an element in which the model is reduced to one dimension [1-D] mathematically along the axis of the beam. The reduction to a one-dimensional problem depends on several levels of complexity in the assumptions, and different assumptions for different beam elements in Abaqus. The classical Euler-Bernoulli assumption is the most straightforward approach to beam theory, and it assumes that plane cross-sections initially perpendicular to the beam's axis remain plane, and undistorted after loading.

Abaqus has a library of solid elements for applications in two-dimensional [2-D] and three-dimensional [3-D] elements. The two-dimensional elements permit the modelling of the plane and axisymmetric problems and comprise extensions to generalised plane strain. They come in triangular and quadrilateral continuum elements with 3- to 8-node as shown in Figure 3.17.

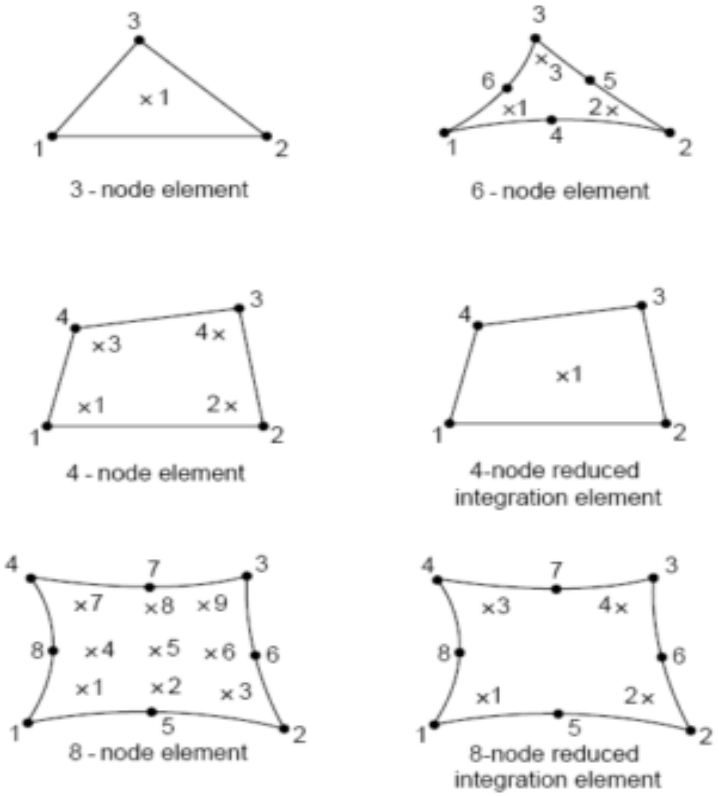

Figure 3.17: ABAQUS 2-D Solid Elements (adapter from ABAQUS 2012)

The 2-D element types can be used to solving structural applications such as the plane strain, plane stress and generalised plane strain. The elements' nodes have two degrees of freedom per node.

The material description of the 3-D solid elements may comprise numerous layers of diverse materials, in different orientations, particularly for the modelling and analysis of laminated composite solids. It consists of 4- to 20-node shapes as shown in Figure 3.18. For every node, there is a minimum of 3 degrees of freedom.

Other elements available are cylindrical solids, axisymmetrical solids, infinite elements, membrane elements, shell elements, and wrapping elements.

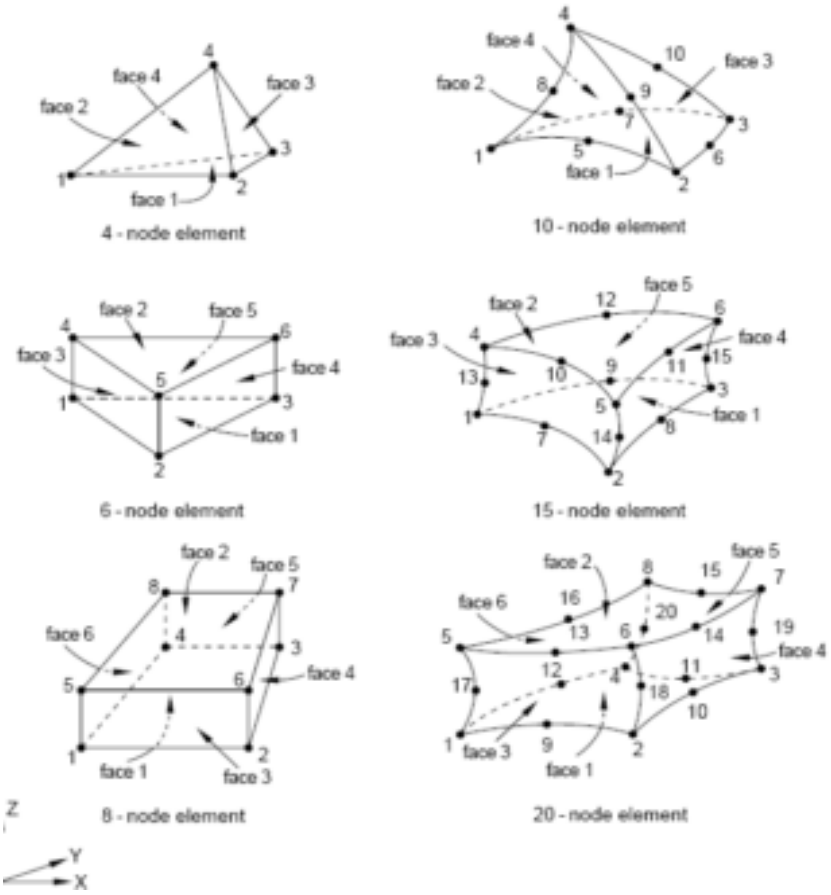

Figure 3.18 ABAQUS 3-D Solid Elements (adapter from ABAQUS 2012)

For this research work, to model the concrete slab and columns, a combination of 3-D eight-node reduced integration brick element [C3D8R] and 3-D six-node wedge elements [C3D6] were deployed in all the modelling and analyses. The ABAQUS/Standard element libraries are used for the static analysis. The ABAQUS/Standard uses either linear or quadratic elements for stress/displacement analyses.

The rate of convergence and computational time are better in the solution offered by the brick elements than the other elements. Consequently, the brick elements are used in most of the sections of the flexural test and where the geometry of the section required their use, the wedge elements are employed.

3.6.2 Concrete Material Models

The most significant model for the SFRC beam and slab simulations is the concrete material model. The accuracy of the FEA is dependent on the selection of a suitable material model for concrete. Diverse concrete material models are examined and presented together with the material properties. Three commonly used concrete constitutive models in ABAQUS are considered and discussed in details. Each can be used for modelling concrete at low confining pressures in all types of elements. In each of the models, ABAQUS permits the user to define mechanical material behaviour. There are other models which can be used for concrete, mainly if studying at Serviceability limit state [SLS] and these include the linear-plastic model and Drucker-Prager Hardening model.

3.6.2.1 Concrete Elastic Properties

Concrete elastic properties mainly depend on its component materials particularly the aggregates. The modulus of elasticity of concrete, E_{cm}, for all beams and slabs is from the experimental result, and when it is not in the literature, it is calculated using the BS EN 1992-1-1 provisions as given in Equations 3.16 and 3.17. Poisson's ratio and of normal weight concrete were taken from the report of the experiments or assumed to be 0.2 and 2400 kg/m^3 respectively for all concrete grades.

$$E_{cm} = 22\left[\frac{f_{cm}}{10}\right]^{0.3} \qquad [f_{cm} \text{ in MPa}] \qquad \text{Eqn. 3.16}$$

$$f_{cm} = f_{ck} + 8 \qquad [\text{MPa}] \qquad \text{Eqn. 3.17}$$

Where

f_{cm} is the mean compressive strength

f_{ck} is the Characteristic compressive cylinder strength of concrete at 28 days

These elastic properties are the same for all material models of concrete considered in this research work.

3.6.2.2 Concrete smeared cracking model

The Concrete Smeared Cracking model in ABAQUS/Standard provides an all-purpose ability for modelling all types of concrete structures, including beams, trusses, shells, and solids. it is intended for applications in which concrete is subjected to mainly monotonic straining and the material displays either compressive crushing or tensile cracking. In the model, elastic properties are defined by linear elastic behaviour and the reversible part of the material's response after cracking failure is described by the

smeared cracking. The model “comprises of an isotropically hardening active yield surface that is when the stress is predominantly compressive and an autonomous “crack detection surface” that regulates if a point fails by cracking”. Principally, it is intended for reinforced concrete structures, but it can be used for plain concrete as well. The uniaxial concrete behaviour of concrete is described by Figure 3.19.

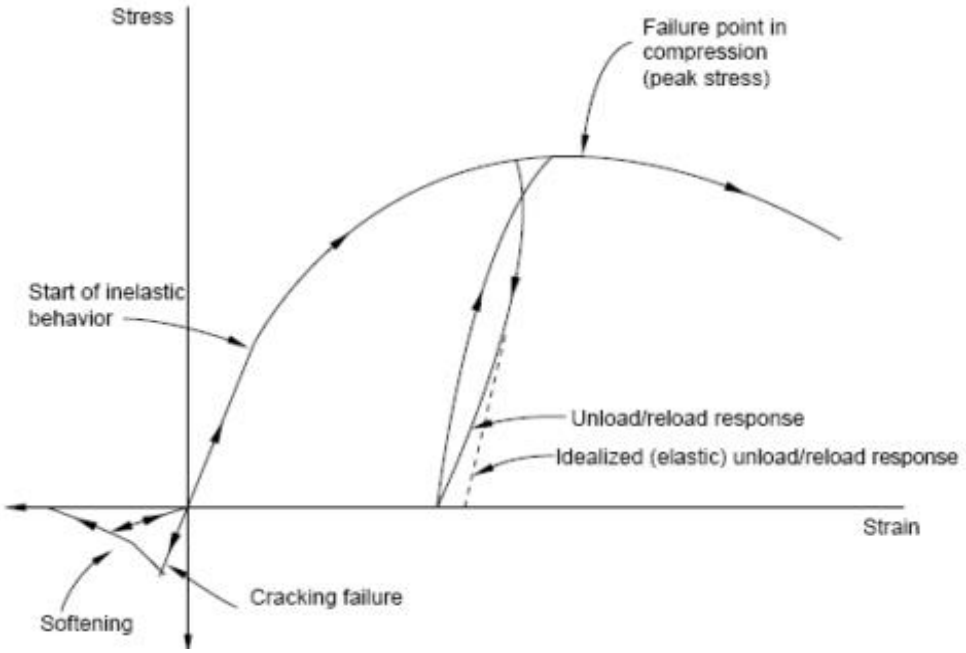

Figure 3.19: Uniaxial concrete behaviour adapted from (ABAQUS, 2009)

The cracking is a vital component of this model, which is assumed to occur when the stress extends a failure surface termed as “crack detection surface”. Once a crack has been detected, the direction of the crack is stored for subsequent calculations. The tension stiffening is defined in Figure 3.12. It also shows the influence of adding fibres to the concrete matrix. The plain concrete fails abruptly in tension, but with the introduction of fibres, it is extended to a higher strain value, thus making a brittle material ductile

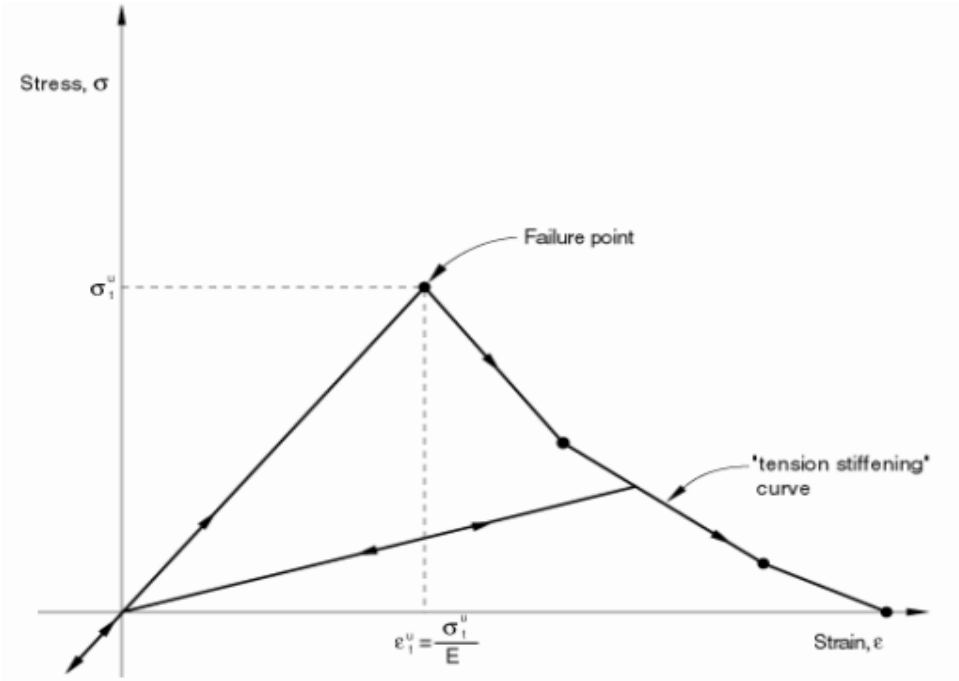

Figure 3.20: Tension Stiffening Model (adapter from ABAQUS 2012)

Table 3.1: Failure Ratios for Concrete Smeared Cracking Model

Ratio 1	Ratio 2	Ratio 3	Ratio 4
1.16	0.09	1.28	0.3333

Where:

Ratio 1 is the ratio of the ultimate biaxial compressive stress to the uniaxial compressive ultimate stress.

Ratio 2 is the absolute value of the ratio of uniaxial tensile stress at the failure to the uniaxial compressive stress at failure.

Ratio 3 is the ratio of the magnitude of a principal component of plastic strain at ultimate stress in biaxial compression to the plastic strain at ultimate stress in uniaxial compression.

Ratio 4 is the ratio of the tensile principal stress value at cracking in plane stress, when the other nonzero principal stress component is at the ultimate compressive stress value, to the tensile cracking stress under uniaxial tension.

3.6.2.3 *Concrete damaged plasticity CDP model*

The Concrete Damaged Plasticity model is available in the ABAQUS/Standard and ABAQUS/Explicit and has the capacity of modelling concrete and other quasi-brittle materials in a variety of structures [beams, shells, trusses, and solids]. This model "takes into account the degradation of the elastic stiffness prompted by plastic straining both in tension and compression. It also accounts for stiffness recovery effects under cyclic loading." The compressive behaviour is elastic until the initial yield and then is characterised by stress hardening followed by strain softening after the ultimate point (ABAQUS, 2009). The concrete Damaged Plasticity Model permits for stiffness recovery effects. It is designed for applications in which concrete is exposed to monotonic, cyclic, and/or dynamic loading under low confining pressures.

Two main failure mechanisms [compressive crushing and tensile cracking of concrete], depict the concrete damaged plasticity model. The evolution of the yield (or failure) surface is controlled by two hardening variables, ε_c^{pl} and ε_t^{pl}, connected to failure mechanisms under compression and tension loading, respectively. The ε_c^{pl} and ε_t^{pl}, are referred to as tensile and compressive equivalent plastic strains, respectively.

Post-cracking behaviour can be accounted for by specifying a post-crack stress-strain relation or by applying a fracture energy criterion. The unloading response is characterised by a weakening of the material and degradation of the elastic stiffness in both the tensile and compressive stress-strain curves. The damage plasticity parameters define these phenomena.

3.6.2.3.1 Plasticity Parameters

The CDP models follow a non-associated flow rule, where there is no overlap between the potential plastic function and yield surface. Concrete can demonstrate a significant volume change, commonly referred to as dilation, when subjected to severe inelastic stress states. An appropriate plastic potential function can represent the dilation. On the other hand, the hardening rule can be used to define the yield surface. For this research work, the dilation angle was taken from 25^0 to 40^0 depending on the type of slabs, beams and case study, while default values were assumed for all other plasticity

parameters as shown in Table 3.2. 0 – 100% damaged were used for calibration with 80% damaged providing he closes result o he experimental results. Therefore, he 80% damaged was used for all the simulations.

Table 3.2: Plasticity Parameters for Concrete Damaged Plasticity Model

Dilation Angle ψ	Eccentricity ε	f_{b0}/f_{c0}	K	Viscosity Parameter μ
25, 35 & 40^0	0.1	1.16	0.6667	0.003 – 0.006

Where:

Dilation Angle ψ — is defined in the p-q plane at high confining pressure, and value is entered in degrees

Eccentricity ε — The flow potential eccentricity a small positive number that defines the rate at which the hyperbolic flow potential approaches its asymptote.

f_{b0}/f_{c0} — σ_{b0}/σ_{c0} is the ratio of initial equi-biaxial compressive yield stress to the initial uniaxial compressive yield stress

K — K_c is the ratio of the second stress invariant on the tensile meridian, q(TM), to that on the compressive meridian, q(CM), at initial yield for any given value of the pressure invariant p such that the maximum principal stress is negative, $\sigma_c < 0$. It must satisfy the condition $0.5<K_c\leq1.0$.

Viscosity Parameter — is used for the visco-plastic regularisation of the concrete constitutive equations in Abaqus/Standard analyses.

3.6.2.3.2 Compression Behaviour

The stress-strain behaviour of plain concrete [used for SFRC] in uniaxial compression was from BS EN 1992-1-1 and expressed in Equation 3.18. The graphic presentation of the stress-strain relationship for nonlinear structural analysis of concrete is presented in Figure 3.13.

$$\frac{\sigma_c}{f_{cm}} = \frac{k\eta-\eta^2}{1+(k-2)\eta} \qquad \text{Eqn. 3.18}$$

Where

σ_c - Compressive stress in the concrete

η - $\frac{\varepsilon_c}{\varepsilon_{cl}}$

ε_c - Compressive strain in the concrete

ε_{cl} - Compressive strain in the concrete at the peak stress f_c

$$\varepsilon_{cl} = 0.7\, f_{cm}^{0.31} \leq 2.8$$

k - $\frac{1.05 E_{cm}\, x\, |\varepsilon_{cl}|}{f_{cm}}$

Equation 3.12 is valid for 0 < | ε_c| < | ε_{cu1}| where ε_{cu1} is the nominal ultimate strain

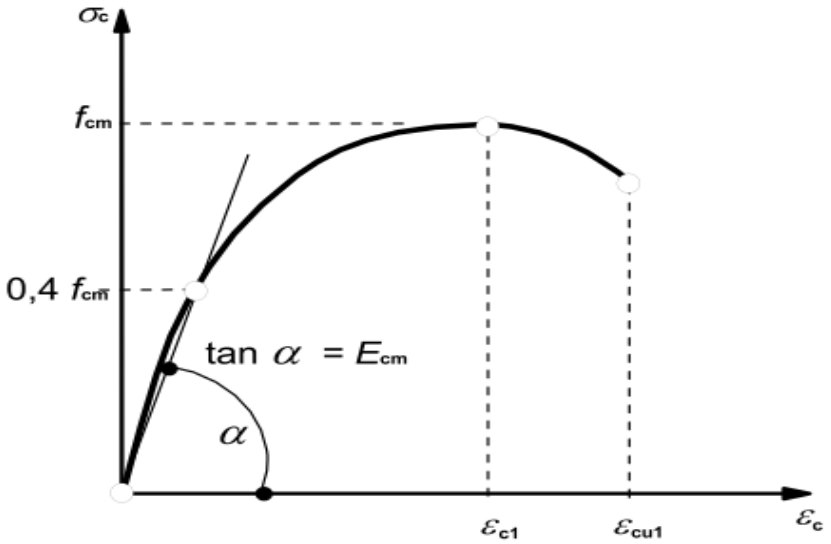

Figure 3.21: Stress-Strain Relation of Concrete in compression adapted from (BS EN 1992-1-1)

BS EN 1992-1-1 stipulates the nominal ultimate strain, ε_{cu1} for concrete characteristic compressive cylinder strength, f_{ck} ≤ 50 MPa can be taken as 0.0035. For the characteristic compressive strength, f_{ck} > 50 MPa, the ultimate compressive strain, ε_{cu1} can be calculated from Equation 3.19.

$$\varepsilon_{cu1} = 2.8 + 2.7 \left[\frac{(98 - f_{cm}}{100}\right]^4 \qquad \text{Eqn. 3.19}$$

The Compressive stress data are provided as a tabular function of inelastic (or crushing) strain, ε_c^{in}, which is outside the elastic range. The compressive stress and strain have Positive (absolute) values and can be defined beyond the ultimate stress, into the strain-softening regime.

Hardening data are given in terms of an inelastic strain, ε_c^{in}, instead of plastic strain, ε_c^{pl}. The compressive inelastic strain is defined as the total strain minus the elastic strain corresponding to the undamaged material, $\varepsilon_c^{in} = \varepsilon_c - \varepsilon_{0c}^{el}$,

where

$\varepsilon_{0c}^{el} = \sigma_c / E_0$, as illustrated in Figure 3.22.

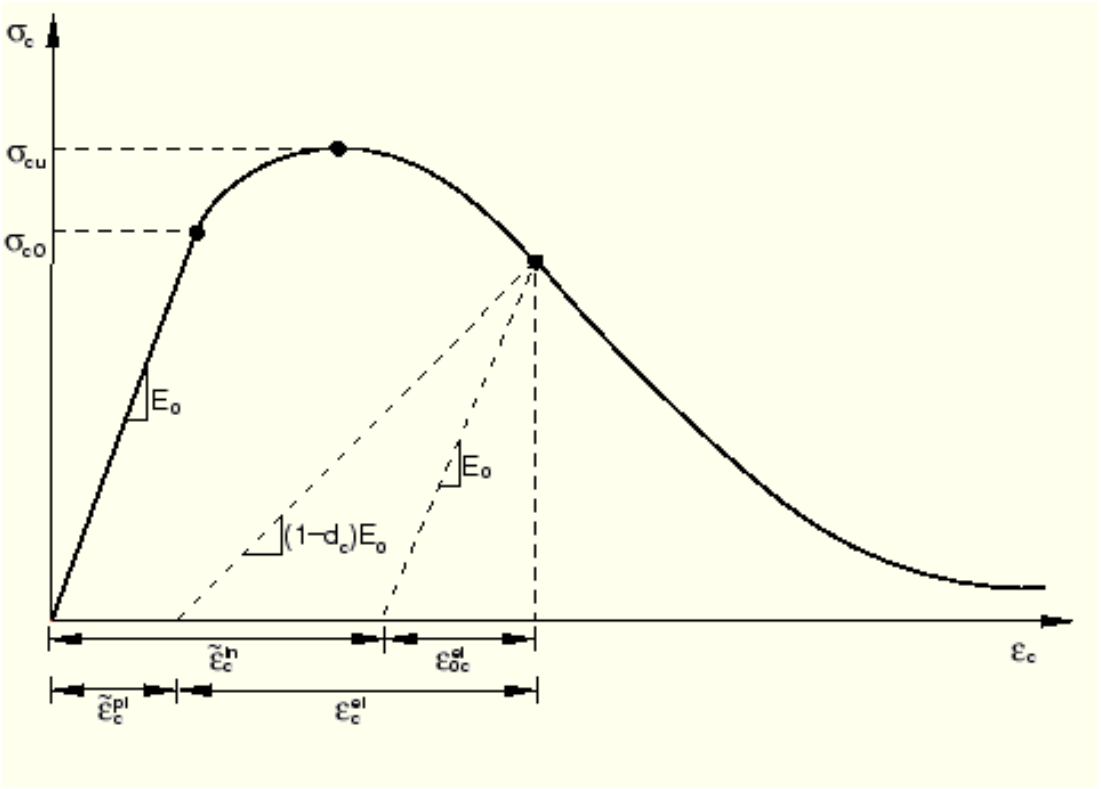

Figure 3.22: Compressive inelastic (or crushing) strain defining compression hardening data.

Under loading, the uniaxial compressive response of concrete is linear up to initial yield stress, σ_{c0}. After the yield stress, the material response becomes plastic with stress

hardening and followed by strain softening beyond the peak compressive stress σ_{cu} as shown in Figure 3.23.

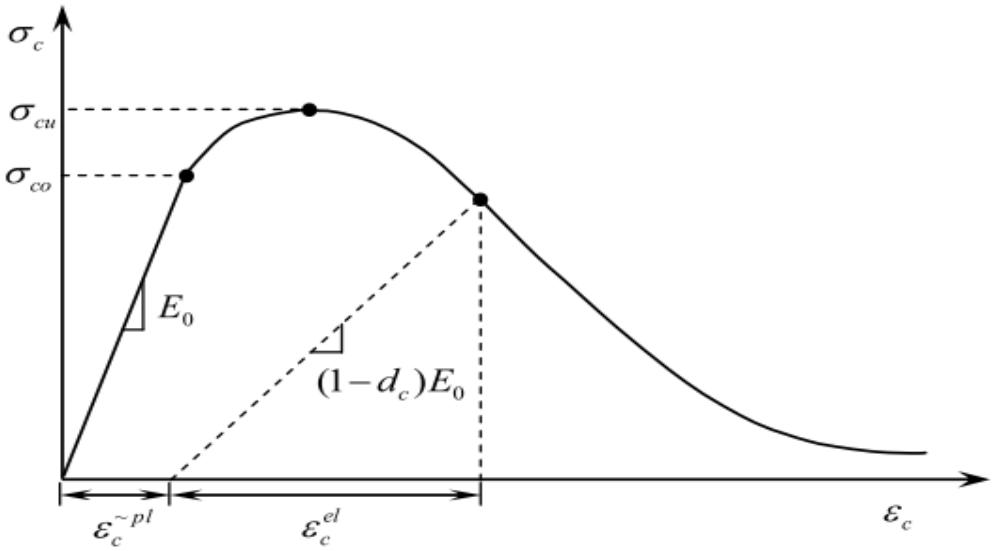

Figure 3.23: Response of Concrete to Uniaxial Loading in Compression adapted from ABAQUS (2012)

The elastic stiffness of the material becomes damaged at any point on the softening branch of the stress-strain curve that the concrete specimen is unloaded. The compressive damage variable, d_c characterise the damage.

$$\sigma_c = (1 - d_c)E_0(\varepsilon_c - \varepsilon_c^{-pl}) \qquad \text{Eqn. 3.20}$$

Where

ε_c^{-pl} – Compressive equivalent plastic strain.

Likewise, the CDP model requires the inelastic strain curve, and this is defined as:

$$\varepsilon_c^{-in} = \varepsilon_c^{-pl} + \frac{d_c}{1-d_c}\frac{\sigma_c}{E_0} \qquad \text{Eqn. 3.21}$$

A typical uniaxial compressive stress against inelastic strain curve for a bending test for SFRC slab with a mean compressive cylinder strength, f_{ck} = 45.0MPa is shown in Figure 3.24. The curve stars from non-zero stress point against inelastic strain which is from the yield point of the specimen.

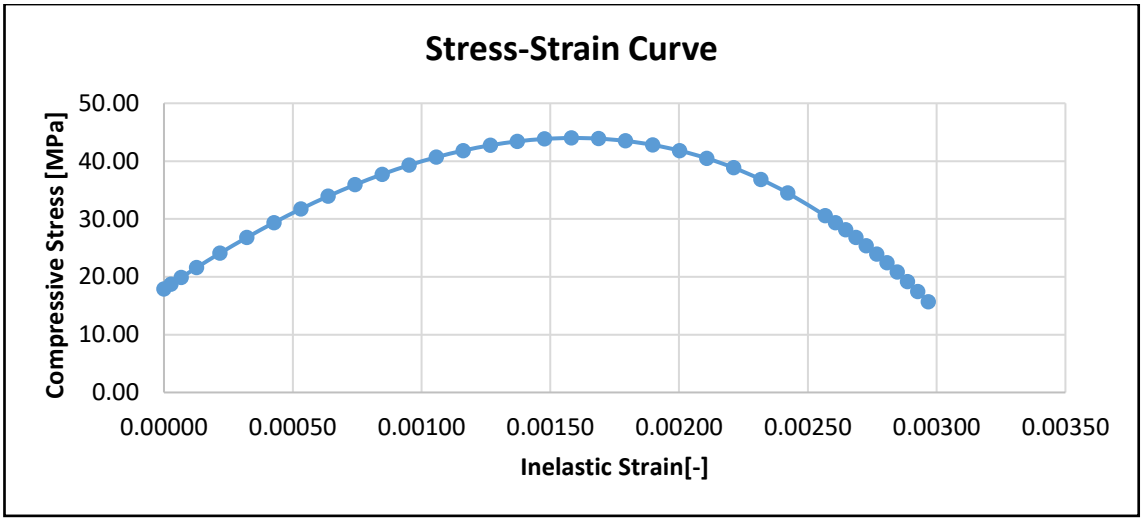

Figure 3.24: Compressive Stress-Strain Curve

3.6.2.3.2 Tensile Behaviour

The model assumes that damaged plasticity also characterises the uniaxial tensile response of the concrete. It is a continuum, plasticity-based, damaged model for concrete. The uniaxial tension stress-strain response follows a linear elastic relationship until the value of the failure stress, σ_{t0}, is reached.

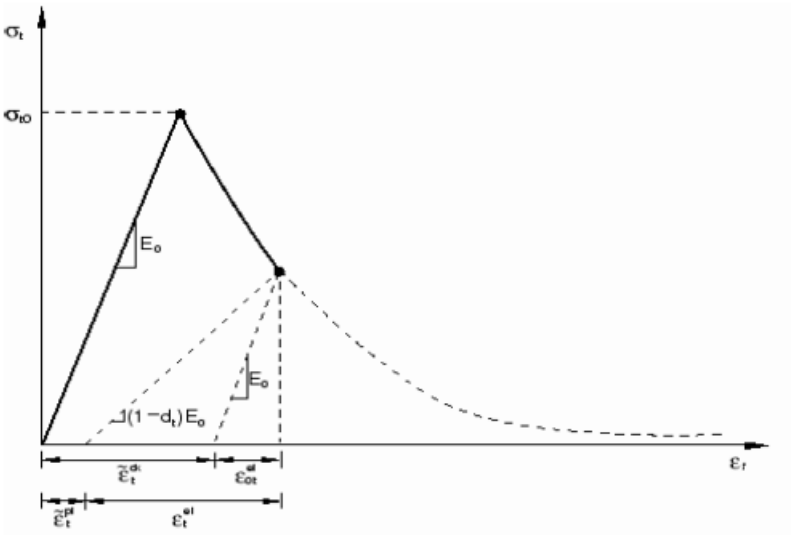

Figure 3.25: Response of Concrete to Uniaxial Loading in tension adapted from ABAQUS (2012)

The failure stress corresponds to the beginning of micro-cracking in the concrete material. After the failure stress, the micro-cracks formation is macroscopically denoted with a softening stress-strain response, which induces strain localisation in the concrete

structure. With the introduction of steel-fibres, the tensile response of SFRC under the impact of the flexural strength is shown in Figure 3.25

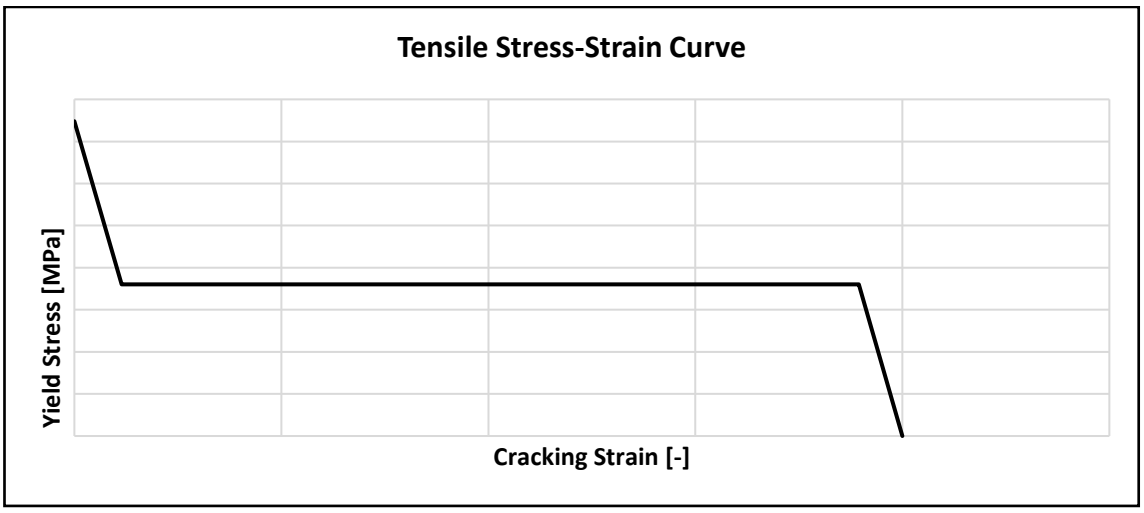

Figure 3.26: Tensile Stress-Strain Curve based on Lok and Xiao (1999)

The tensile behaviour constitutive model proposed by Lok and Xiao (1999) is adopted for the interpretation of the tensile behaviour of the SFRC material as resenyed in Figure 3.26. The ultimate tensile strain is taken as 0.02.

3.6.3 Brittle cracking model

This model is only accessible in ABAQUS/Explicit. It has the capability to model any types of concrete structures. It assumes that the compressive behaviour of concrete is always linear elastic, so it must be used with the linear elastic material model. The compressive behaviour of the model does not represent the actual behaviour of the concrete material and is a significant disadvantage of this model.

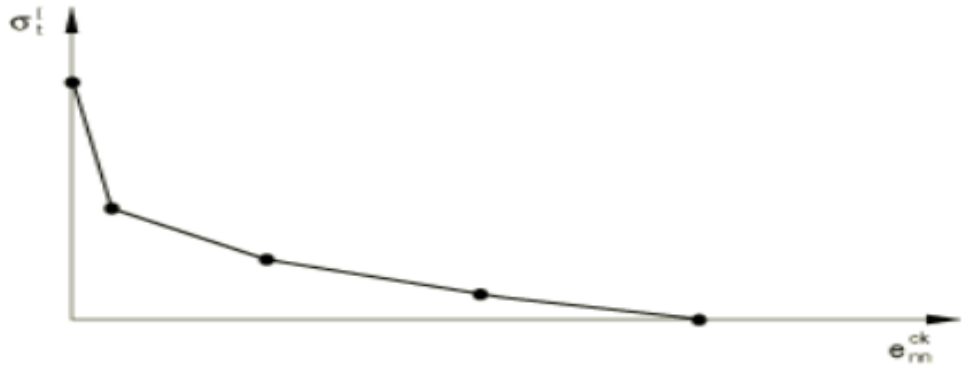

Figure 3.27: Post-Failure Stress-Strain Curve adapted from ABAQUS (2012)

This model also models cracks in a smeared manner and the tension stiffening post-cracking behaviour can be accounted for by specifying a post stress-strain relation or by applying a fracture energy criterion. The post-cracked shear modulus is reduced as the crack opens and is a function of the opening strain across the crack and uncracked shear modulus. Additionally, a brittle failure criterion can be defined as the point the material as reached the number of cracks that are the user-specified value (default is one). The associated element is then removed.

$$\rho_{nn}^{ck} = \left(1 - \frac{e_{nn}^{ck}}{e_{max}^{ck}}\right)^{p} \qquad \text{Eqn. 3.22}$$

Where ρ is the shear retention factor, e_{max}^{ck} is the crack opening strain at which the post-cracking shear modulus is equal to zero and complete loss of aggregate interlock occurs. The exponent p equivalent to one represents the linear loss and having a value greater than one indicates the exponential loss of the shear stiffness [Figure 3.28].

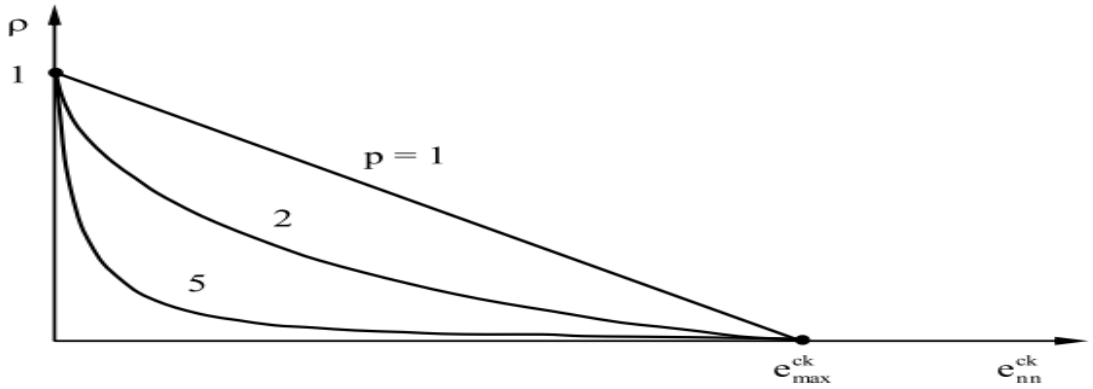

Figure 3.28: Power Law Form of the Shear Retention Model adapted from ABAQUS (2012)

3.7 Material Model for Rebar

A bilinear stress-strain model was adopted for rebar used in validation of the experimental works on reinforced concrete [RC] beams [without steel-fibre] by (Bresler and Scordelis, 1963) and (Hughes and Speirs, 1982). The rebar behaves as linear elastic materials up to the point of yielding, followed by plastic behaviour. The material properties for the rebar [longitudinal bars and stirrups] are given in respective research work and explained in Chapter 4. The density of all steel components was taken as 7800 kg/m^3.

3.8 Philosophies of Constitutive Models

The benefits obtained by the introduction of steel-fibres in reinforced concrete has led to a sharp increase in its usage in a variety of practical applications (Swamy, 1974, CHANH, 1990, Zollo, 1997, Loks and Xiao, 1999, Destrée, 2001, Cameron, 2002, Beddar, 2004, Døssland, 2008, Eddy, 2008, Hedebratt and Silfwerbrand, 2008, ArcelorMittal, 2011, Ghaffar et al., 2014) .

The introduction of steel-fibres posed a research challenge to introduce and produce a constitutive model to emulate the structural behaviour of SFRC. All the constitutive models discussed in chapter 2 falls under the following research philosophies, vis-à-vis stress-strain and stress-crack width philosophies

3.8.1 Stress-Strain Constitutive model

The σ-ε method can be used to describe the softening behaviour of SFRC and is based on the same principles of the design of normal reinforced concrete in Euro-code 2 (British Standard Institute, 2004). The general framework for this design method proposed. It is valid for concrete with a compressive strength of up to C50/60. The identification of crack width and its corresponding structural characteristic length (l_{cs}) of the structural element, is the basis for the definition of the stress-strain law (RILEM, 2003, RILEM, 2000). To this end, smeared crack models and discrete crack models can be translated into each other with the use of l_{cs}. The interaction can be seen in Figure 3.20, which shows a schematic depiction of an SFRC constitutive diagram using the σ-ε.

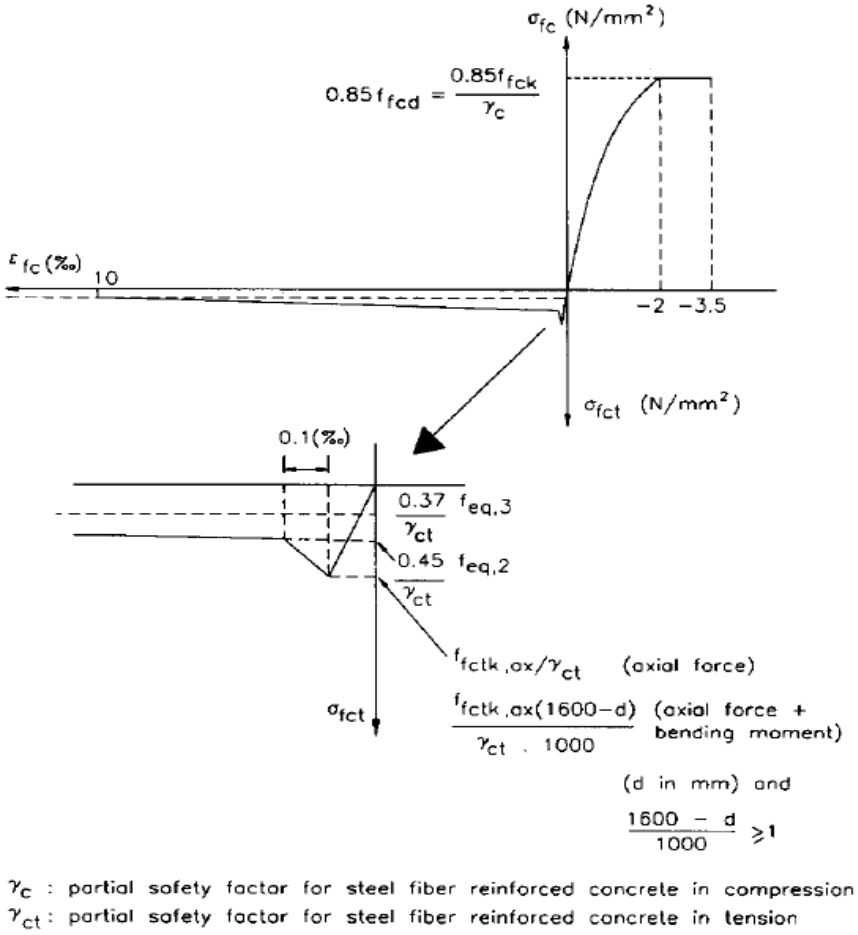

Figure 3.29: Stress-strain graph Adapted from (RILEM, 2000)

3.8.2 Stress-crack width [σ-w] constitutive model

When unreinforced concrete fails in uniaxial tension, the failure is governed by the formation of a single crack. The promulgation of a crack through plain concrete can be represented by a region of micro-cracking incorporating a 'process zone and a localised crack' (Hillerborg et al., 1976, Kotsovos and Spiliopoulos, 1998, RILEM, 2002a). The localised crack zone is sub-divided into a traction-free crack [also termed as a macro-crack] and a zone where aggregate interlock occurs. The mechanical behaviour of the so-called fictitious crack is characterised by the stress-crack opening relationship, σ_w-w, where σ_w is the traction applied to the crack surface as a function of crack opening w. This concept is illustrated in Figure 3.30.

(Hillerborg et al., 1976) Proposed the so-called Fictitious Crack Model (FCM) which initially was intended for use in combination with FEM. However, as it will be shown

here, the approach can simply be adopted in other numerical and analytical models, but it relies on some assumptions.

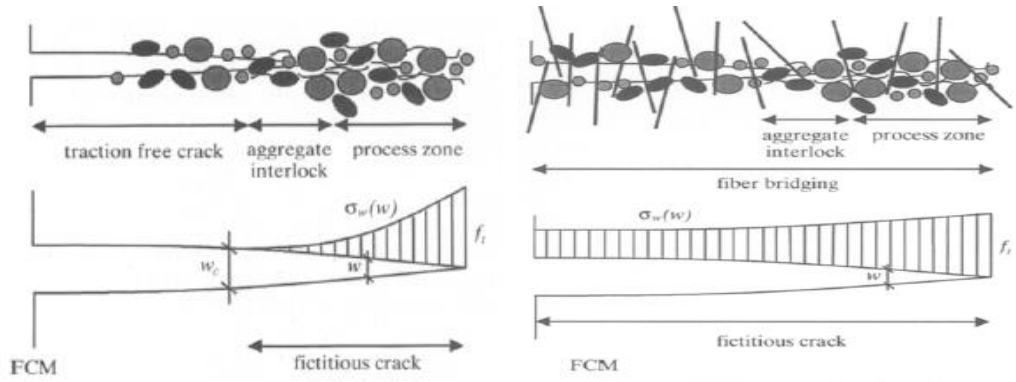

Figure 3.30: Schematic diagrams of crack opening without and with fibres adapted from (RILEM, 2002a)

At the formation of a crack in fibre reinforced concrete, the fibres will naturally stay unbroken within the matrix. The fibres crossing a crack will then resist further crack opening and impose what is called crack bridging or crack closing effect on the crack surfaces. Different failure modes can be the outcome, depending on the effectiveness of the fibres in providing crack bridging [Figure 3.31]

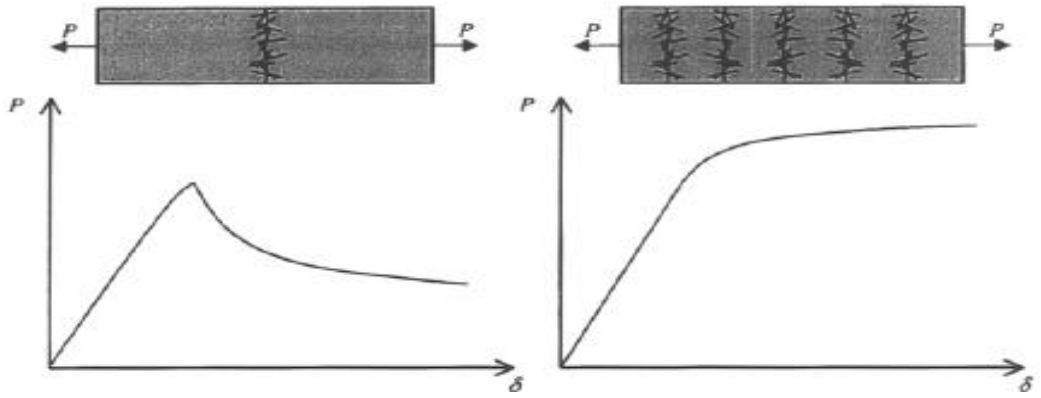

[a] [b]

Figure 3.31: The principle of [a] single cracking and [b] multiple cracking adapted from (RILEM, 2002a)

3.8.3 Review of Philosophies of Constitutive Models

The stress-strain relationship captures the requirement for inverse analysis of a plate, unlike the stress-crack width relationship which is mesh dependent (Bernard, 2000, Kooiman et al., 2000, di Prisco et al., 2013). Using both the σ-w and σ-ε in the

implementation of the inverse analysis does produce some form of the result, but the most realistic relation would be adopted.

The main challenges in any pile-supported or suspended slab are cracks and punching. These would be examined by relating the applied load and deformation obtained in determining the crack widths in pile-supported SFRC slabs using the σ-ε.

A summary of the constitutive models for SFRC both at the material and structural level and related models for non-linear FE analysis in the FEA software have been presented in sections 2.7 and 3.2 respectively. The results of the calibration work carried out to validate the predictions of the different models, and the corresponding existing experimental data is also presented in Chapter 4.

3.9 Scope of Parametric/Case Studies

The research work is focused on the FE modelling of SFRC suspended slab considering both pile-supported and elevated slabs. Three cases that were studied comprised of (1) single panels with (a) continuous support and (b) isolated supports (2) 4-panel pile-supported slab and (3) 9-panel elevated slab. For case 1, a parametric study was carried out considering two parameters: the diameter of the panel and the fibre volume fraction. For case 2, two situations were considered, SFRC slab with and without conventional reinforcement. For the two situations, the fibre volume fraction and slab depths was varied. For case 3, the depth and fibre volume were varied. The fibre volume fractions (V_f) considered were 0.50%, 1.00%, 1.50%, 1.75, 2.00% and 2.50%. The approved span/depth ratio was used to determine the depth of the slab in case 3.

The purpose of the case studies and the accompanying parametric inquiries was to (a) determine the effect of the addition of steel fibres on both the load carrying capacity and ductility and (b) determine the potential reduction in depth of the slabs. The research work examined key structural behaviour and design parameters such as load-deflection curves, strength (i.e. shear force and bending moment capacities), stiffness (which is relevant to storey drift), ductility (i.e. ratio of ultimate displacement to the displacement at yield), plastic hinges formation and cracking patterns

3.9.1 Case Study 1: Round Plate SFRC Slab under Point Load

Case Study 1 focused on the behaviour of SFRC simply supported round plates with (a) isolated, (b) continuous supports and square plate supported along the edges (i.e. statically determinate slabs). The two round plates considered are loaded monolithically using displacement loading system [Figure 3.32].

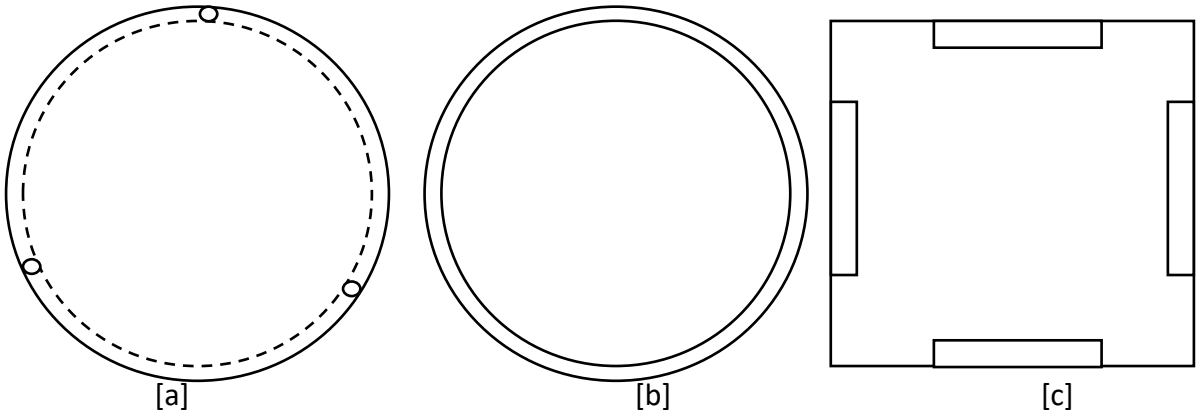

Figure 3.32 Round-Plate simply supported over (a) Isolated, (b) Continuous Supports and (c) Square-Panel with Edge supports

Case Study 1(a) was based on the R. de Montaignac, B. Massicotte, JP Charron & A. Nour (de Montaignac et al., 2011) experimental work on SFRC round plate with three supports at angle 120^0 apart with 1% volume fraction of steel-fibres used. The hook-end steel fibres were used. Their results were used to calibrate and validate the FE model used in this parametric analysis (section 4.3.3.3). The round plates were tested under static monotonic loading. The round panels were used for characterisation tests and to understand the post-cracking tensile properties of SFRC. In this particular case, the fibre volume fractions (V_f) considered for this case studies were 1.00%, 1.25%, 1.50%, 1.75%, 2.00% and 2.50%.

Case study 1(b) was based on the experimental works on round plates conducted by Soranakom C., Mobasher B. and Destree X (Soranakom et al., 2007). The SFRC round plate was placed on simple continuous support along its perimeter. The fibre volume fraction used was 1.25%. The test was for characterisation to determine the properties of SFRC. The round plates were tested under monotonic loading. Their results were used to calibrate and validate the FE model used in this parametric analysis (section 4.3.3.2).

For this case study, the fibre volume fractions (V_f) considered were 1.00%, 1.25%, 1.50%, 1.75%, 2.00% and 2.50%.

In Case study 1(c), tests were performed on square panels by Blanco, A., Cavalaro, S., De La Fuente, A., Grünewald, S., Blom, CBM & Walraven, JC (Blanco et al., 2014a) to confirm the provisions made by RILEM on SFRC testing. The supports are half the length of each side and place at the centre of the edges. 0.5% fibre volume fraction was used in the experiment. Their results were used to calibrate and validate the FE model used in this parametric analysis (Part 4.3.3.4). For this case study, the fibre volume fractions (V_f) considered were 0.50%, 1.00%, 1.25%, 1.50%, 1.75%, 2.00% and 2.50%.

3.9.2 Case study 2: Four Panel Pile Supported SFRC Slab

The four-panel pile-supported slab has nine [9] piles as supports, and it was chosen because experimental data on the behaviour of statically-indeterminate SFRC slabs is limited in comparison to that of simply supported single structural panelled-slabs [Figure 3.33]. Also, studying statically-indeterminate structural elements gives an ample opportunity to understand the structural behaviour of SFRC slabs, since it allows the investigation of important parameters such plastic hinge formation, internal forces redistribution, ductility characteristics and the structural modelling of points of contra-flexure, which cannot be investigated by only considering statically determinate structures.

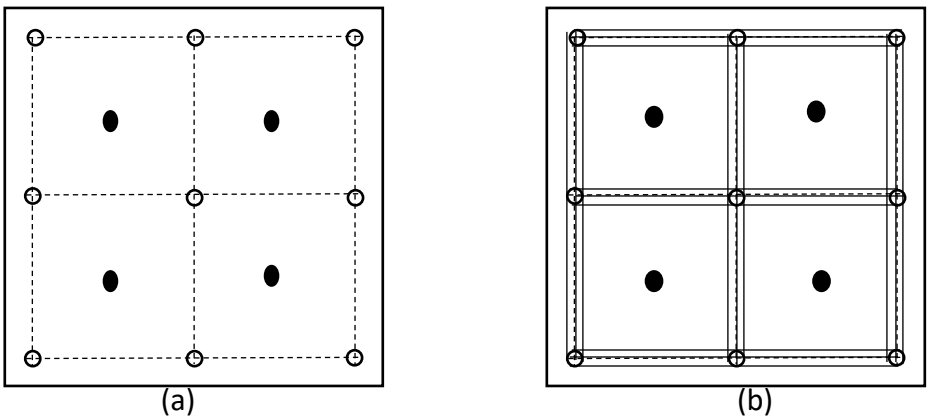

Figure 3.33: 4-Panel SFRC Slab (a) without rebar and (b) with rebar

Case Study 2 was based on the research work of (Thooft, 2000) with tests on the pile-supported four-panel SFRC slab. Two set of slabs were examined (a) SFRC slab without rebar and (b) SFRC slab with rebar along the pile supports. The general layout of the

slabs is shown in Figure 3.24, where an axial load (P) will be applied simultaneously at the middle of each panel. Case study 2(a) has no rebar across the pile supports. The case study 2(b) is used to understudy progressive collapse of the slab. The SFRC was made with 40kg/m3 (0.50%) of steel-fibre. Their results were used to calibrate and validate the FE model used in this parametric analysis (Part 4.4.3). For this case study, the fibre volume fractions (V_f) considered were 0.50%, 1.00%, 1.50%, 2.00% and 2.50%.

3.9.3 Case study 3: Nine-Panel SFRC Elevated Slab

The experimental works of testing to design and construct of nine (9) panel SFRC elevated slab by Destree (Destrée, 2006) was adopted for Case study 3 [Figure 3.34]. The elevated SFRC slab contains nine panels placed on sixteen circular supports. The response of the slab in the serviceability limit state [SLS] was determined by placing containers of water over the panels in different patterns. The slabs were tested to determine their response at the ultimate limit state [ULS] at the centre, edge and corner panels.

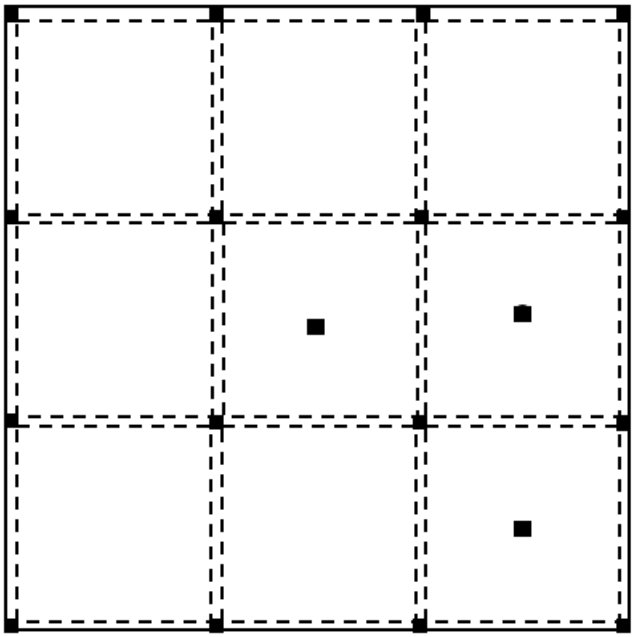

Figure 3.34: 9-Panel SFRC Slab

The slab was chosen to examine the failure mechanism in the elevated slab under point load and UDL. The results will be used later to compare with existing design methods. The results obtained from the experimental works were used to calibrate and validate

the FE model used in this parametric analysis (Part 4.4.4). For this case study, the fibre volume fractions (V_f) considered were 1.00%, 1.25%, 1.50%, 1.75%, 2.00% and 2.50%.

3.10 Analysis Process

The inverse analysis process was deployed to produce a suitable tensile stress-strain $\sigma - \varepsilon$ relationship for each experimental result considered using both ABAQUS and ADINA. This involves the testing of the constitutive models until an agreement with the experimental result is obtained.

3.6 Summary

The review of the NLFEA software used (ABAQUS and ADINA) including their concrete models, the philosophies of constitutive models (stress-strain and stress-crack width) and the case studies for initial calibration works was presented in this chapter. Three [3] models were considered in ABAQUS and two [2] in ADINA for SFRC. Linear and bilinear stress-strain model were adopted for loading plate and rebar respectively. the two philosophy of models [stress-strain and stress-crack width] were also considered.

The calibration and validation works (Chapter 4) were carried out to select the most suitable models for the case studies and related parametric investigations. From the results of the calibration work, it was decided that the SFRC constitutive model proposed by (Lok and Xiao, 1999) be adopted, in conjunction with the concrete damaged plasticity model of ABAQUS. The case studies were carried out using quasi-static analyses in ABAQUS/Standard. The scope of the parametric/case studies is also presented in this Chapter.

Chapter 4: Validation of Numerical Models using Available Experimental Results

4.1 Introduction

The essence of validating the numerical models using the available experimental work is to test the reliability of the software to be used to model the research work correctly, that is, the suspended SFRC slabs. The verification process involves the accurate determination or prediction of the experimental process using computer simulation in achieving an acceptable degree of resemblance. Modelling and simulations have helped in creating the exact happening in a process which has led to a better understanding of that same process.

Using the constitutive models of ADINA, ABAQUS and SFRC discussed in Chapters 2 and 3, a set of analyses were carried out. The analyses were carried out to choose and calibrate the most suitable SFRC constitutive model (section 2.7) and ADINA and ABAQUS numerical models (section 3.2) to be adopted in the subsequent parametric studies for Case Studies 1, 2 and 3. This Chapter 4 discusses all the validation and calibration works executed, including a comparative study between numerical and experimental results.

At first, validation and calibrations on RC beams (i.e. without fibres) were carried out using experimental data on beams undergoing brittle and ductile responses (Bresler and Scordelis, 1963, Hughes and Speirs, 1982), respectively. These analyses were carried out to ensure that the FE analysis software and associated constitutive model adopted for concrete (fully described in Chapters 2 and 3) is capable of producing right predictions for RC beams. Because these beams include rebar, a constitutive model for reinforcement was adopted for modelling as discussed in section 3.2.3.

Afterwards, additional analyses were carried out to calibrate the SFRC constitutive models considered to numerically validate existing experimental data at the material and structural levels. At the material level investigations were carried out on the experimental works by (Barros et al., 2005), (de Montaignac et al., 2011), (Tlemat et al., 2006b), (Olivito and Zuccarello, 2010), (Hadi, 2008), (Blanco et al., 2015), (Soranakom and Mobasher, 2007) and (Bernard, 2000) as presented in sections 4.3.1, 4.3.2 and 4.3.3. Similarly, full-scale testing done on SFRC slabs by (Destrée and Jürgen, 2008), (Thooft,

1999), (Barros et al., 2012) and (Destrée, 2006) were analysed for cases at the structural level as discussed in section 4.4.

In the application of load, it was done based on displacement and force-controlled tests. Applying displacement-controlled test give the system the leverage of continuing even after the specimen has collapsed. This is because a non-zero displacement constraint is used. The solution can switch back to force control through the use of a null load step. Other types of loading that can be used are velocity, pressure and so forth.

4.2 Reinforced Concrete Beams Cases [No Fibres]

The proficiency of the two commercially available software [ABAQUS and ADINA] were verified by using them to model and simulate two classical beams (Bresler and Scordelis, 1963) and (Hughes and Speirs, 1982) using the models on ABAQUS (Concrete Damaged Plasticity, CDP and Concrete Brittle Cracking, CBC) and ADINA (ADINA-Concrete and Data-Fitted, DF). It should be noted that sensitivity analyses were performed on each beam to determine which mesh size would accurately predict the experimental results.

4.2.1 Bresler and Scordelis (1963) Beam – Brittle Failure

Twelve [12] beams were tested for various purposes and with a varying configuration which resulted in having a different amount of longitudinal reinforcement. The beam, labelled OA1, was 310 by 556mm in dimension and has 4-T28.7mm bars without shear reinforcement was picked for modelling [Figure 4.2]. It was an over-reinforced beam that resulted in brittle failure. It was simply supported at the span of 3660mm. The total length of the beam is 4100mm. Figure 4.2 shows the set-up of the experiment. The compressive strength of concrete, characteristic strength in steel and other properties of the beam and materials are presented in Table 4.1.

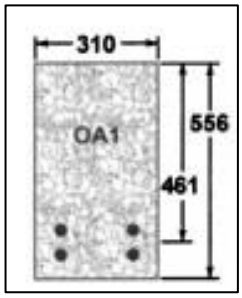

Figure 4.1: Cross-section of the Bresler-Scordelis (1963) beam

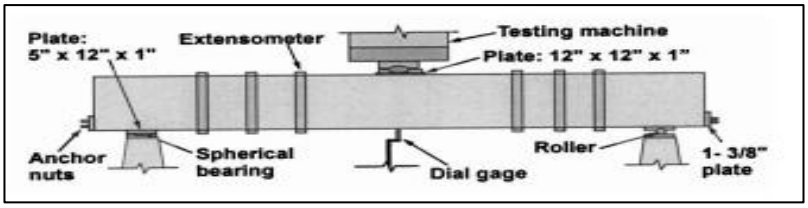

Figure 4.2: Test setup for Bresler-Scordelis (1963) beam

Table 4.1: Geometrical details and material properties of the beam.

Beam Number	*b* [mm]	*h* [mm]	d [mm]	Reinforcement				Concrete	
				Area [mm2]	f_y [MPa]	f_u [MPa]	E_s [MPa]	σ_c [MPa]	σ_t [MPa]
OA1	310	556	461	645	555	933	218,000	22.5	2.25

4.2.1.1 Sensitivity Analysis

The beam was modelled into ABAQUS and ADINA using different mesh sizes. Different meshes [15, 30, 60mm] were used to see the response of the beam to mesh sensitivity. The FE Model and results obtained are shown in Figures 4.3 – 4.5. In all, 10% of the compression strength [2.25MPa] was used for the tensile strength.

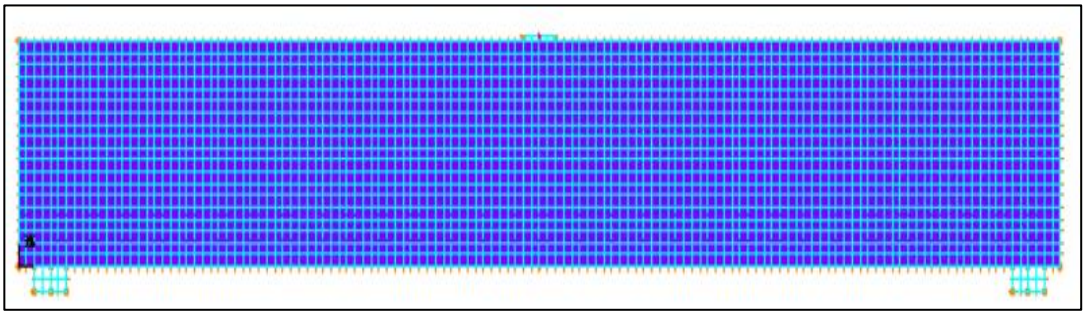

Figure 4.3: FE Model of Bresler-Scordelis (1963) beam

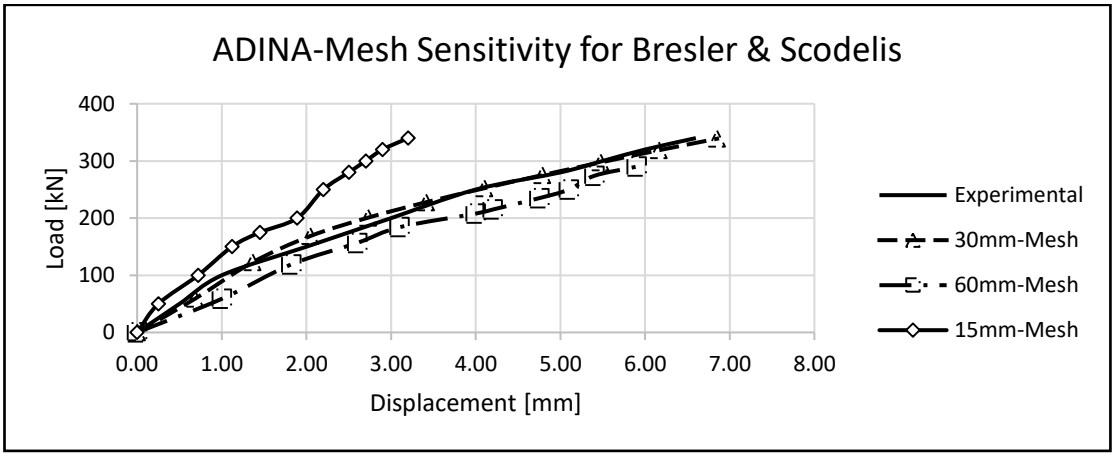

Figure 4.4: Load-Deflection Graph for Sensitivity Analysis Bresler-Scordelis (1963) beam [ADINA]

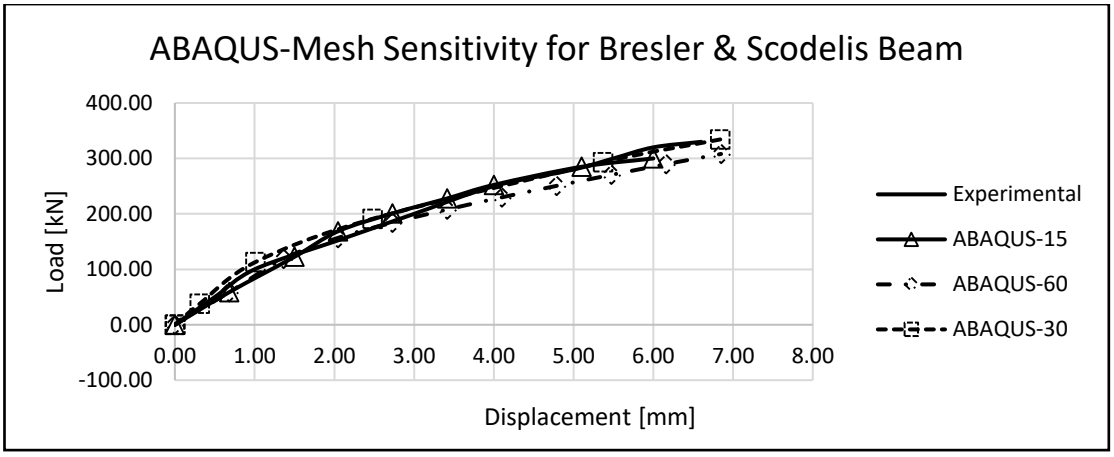

Figure 4.5: Load-Deflection Graph for Sensitivity Analysis Bresler-Scordelis (1963) beam [ABAQUS]

For Bresler-Scordelis beam, the 30mm-mesh using 8-nodes solid element produces a result favourably comparable to the experimental result. The result was less than 3% of the one gotten through the experiment. The 30mm mesh shall be used for further works with the FEA both in ABAQUS and ADINA. For ABAQUS, the tensile damage parameter for CDP was placed at 80%.

4.2.1.2 Bresler-Scordelis (1963) beam FE Model and Load-Deflection Curve

The specimen was set up to investigate the effect of the absence of shear links in over-reinforced beams. The experimental result shows a diagonal-tension failure, and this can be attributed to the absence of shear reinforcement. The two software was used to model the geometry of the full beam [This was made possible due to the High-Performance Computer provided by University of East London]. The analyses were done in static mode, which allows the time function in ADINA and time step in ABAQUS to regulate the rate at which load are added over the given period. The FE model is made up the concrete beam, modelled as 3D-brick, the reinforcing bars, modelled as a truss (rebar in ADINA) and the steel supports and loading point as 3D-brick, all assembled (in ADINA, the assembling process is explained in Appendix A) to represent the actual experimental setup. [Figures 4.6].

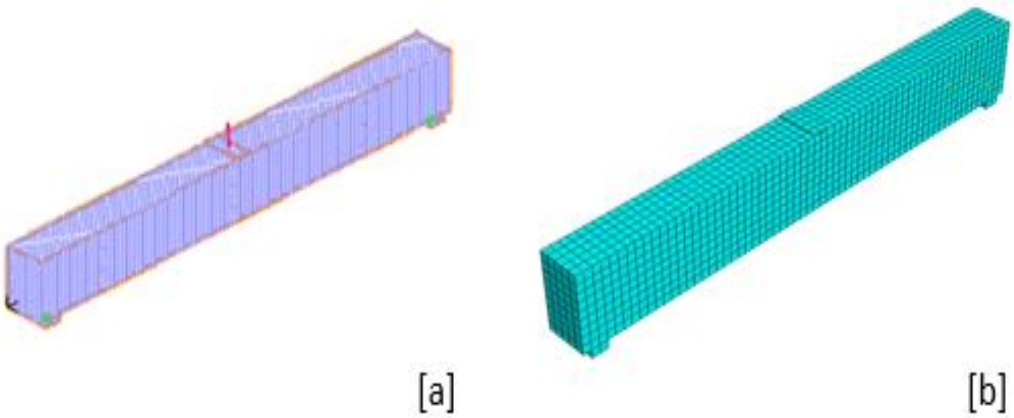

Figure 4.6: FE Model of Bresler-Scordelis (1963) Beam [a] ADINA and [b] ABAQUS

The beam was modelled a full scale with a pin [restrain in x and y directions] and roller [restrain in y-direction only] boundary conditions at the supports. To imitate experimental conditions and avoid untimely localised failure, steel plates of 10 mm thickness were added at the supports and loading points. The specified coefficient of friction 0.5 in Eurocode 2 (British Standard Institute, 1994) was used for the contact faces between the concrete and steel members for beam and supports respectively. The reinforcement is treated as an embedded member in the concrete beam using the embedded constraint method. The beam was placed on two supports with the first support restrained in the X and Y directions (pin support) and the second in the Y direction (roller). Vertical loadings (higher than what was used in the experiment) were applied in the form of displacement and force at the centre of the steel loading plate. Figures 4.7-4.9 show he failure patterns in the experiment, ADINA and ABAQUS

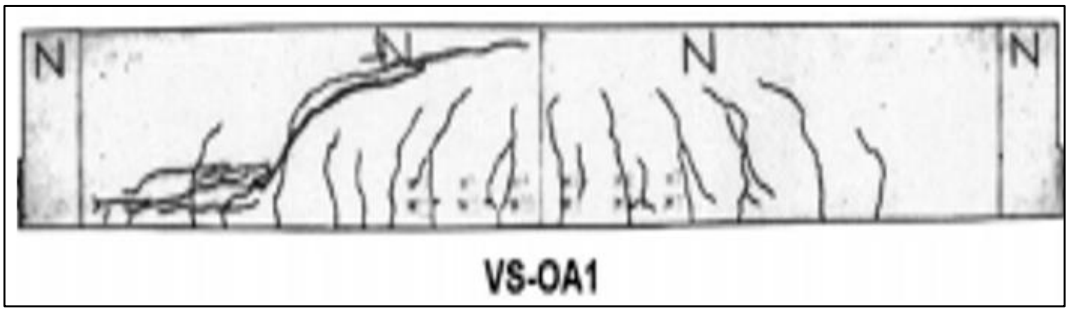

Figure 4.7: Crack pattern in Bresler-Scordelis (1963) beam [Experiment]

The uniaxial stress-strain relationship of the reinforced concrete beam deployed in this analysis using ADINA-Concrete is shown in Figure 3.5, where σ_c and ε_c are the maximum uniaxial compressive stress and uniaxial strain corresponding to σ_c; σ_u and ε_u are the

ultimate uniaxial compressive stress and ultimate uniaxial compressive strain corresponding to σ_u; σ_t and ε_t are uniaxial cut-off tensile strength and uniaxial strain corresponding to σ_t; σ_{tp} is post-cracking uniaxial cut-off tensile strength, E_{ct} uniaxial tangent modulus at zero strain [must be greater than σ_c/ε_c]. For this analysis σ_u was gotten from the experiment or taken as $0.8\sigma_c$. All material parameters used in ADINA concrete are gotten from the experiment and are as follows:

σ_c = - 22.5 MPa	ε_c = -0.002
σ_u = - 18.0 MPa	ε_u = -0.0035
σ_t = 2.25 MPa	ε_t = 0.002
σ_{tp} = 2.25 MPa	E_0 = 21.3 GPa

Whereas, in data-fitted concrete model, only the σ_c and the percentage of the σ_t to σ_c [0.1%] are specified and inputted into the model.

The displacement loading of 10mm was applied at the centre of the beam at an incremental rate of 0.1mm. This is to minimise challenges associated with convergence. The convergence criteria based on the residual forces tolerance is 5%.

Whereas, in the ABAQUS-CDP, the plasticity parameters are given as follows: ψ=25^0, ε= 0.1, f_{b0}/f_{c0}= 1.16, K=0.667 and μ= 0.003. The compression and tensile stresses and damaged parameters [as given in equations 3.12 and 3.13] are given in the Table 4.2 below with concrete cracking failure strain taken as $25\varepsilon_{cr}$ and $\varepsilon_{cr} = \sigma_t/E_t$ (Hassan, 2016).

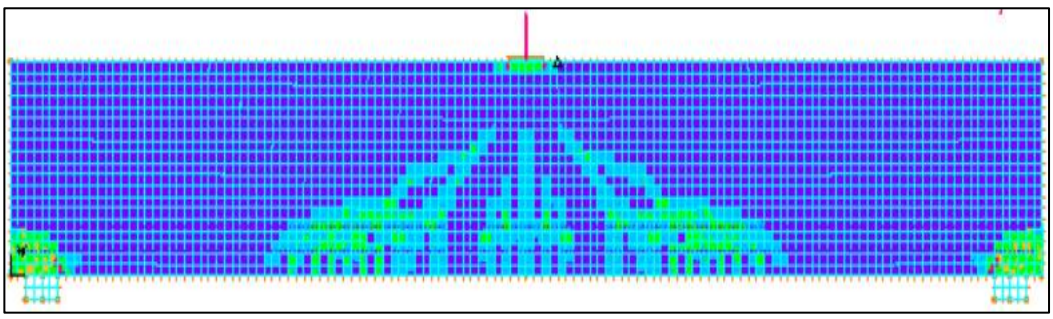

Figure 4.8: Crack pattern for Bresler-Scordelis (1963) beam [ADINA]

Table 4.2: Compression and Tensile Parameters

	Yield Stress σ_c MPa	Compressive Damage Variable d_c	Inelastic Strain	Tensile Stress 'σ_t' MPa	Tensile Damage Variable d_t	Cracking Strain
1	12.9	0.00	0.00000	2.25	0.00	0.000000
2	17.3	0.00	0.00024	1.32	0.41	0.000080
3	20.8	0.00	0.00049	0.83	0.63	0.000162
4	23.3	0.00	0.00074	0.59	0.74	0.000243
5	25.0	0.00	0.00099	0.45	0.80	0.000324
6	25.8	0.00	0.00124	0.37	0.84	0.000405
7	26.0	0.00	0.00149	0.30	0.87	0.000486
8	25.3	0.00	0.00178	0.24	0.89	0.000567
9	24.3	0.07	0.00205	0.19	0.92	0.000648
10	22.5	0.13	0.00236	0.14	0.94	0.000729
11	20.3	0.22	0.00268	0.09	0.96	0.000810
12	17.5	0.33	0.00303	0.06	0.98	0.000891
13	14.3	0.45	0.00339	0.02	0.99	0.000972

In-built in ABAQUS are the failure criteria connected with each concrete model [damaged plasticity smeared cracking, and brittle cracking]. The convergence criteria based on the residual forces tolerance is 5%. In other to minimise problems associated with convergence criteria, the displacement-loading of 10mm was applied at an incremental rate of 0.01mm at the centre of the beam.

Stress-strain value for reinforcement follows a bilinear material behaviour of steel and based on the yield and ultimate strength of the bar used in both ADINA and ABAQUS is given in Table 4.3:

Table 4.3: Stress-Strain Value for Reinforcement

Stress MPa	Strain
0.00	0.00
460.00	0.001
560.00	0.01

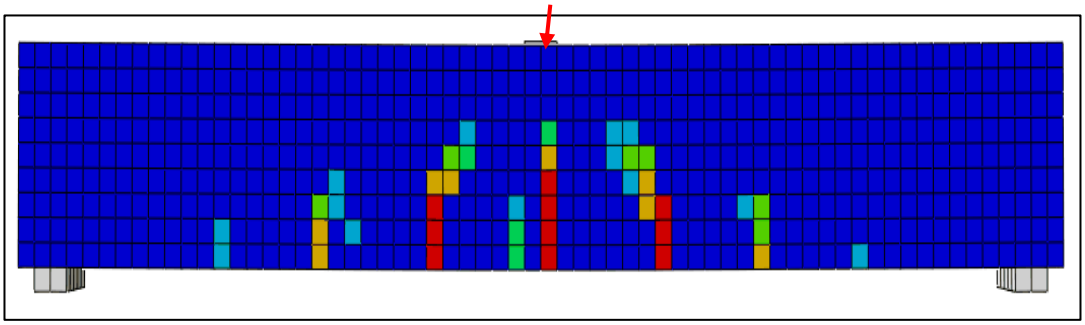

Figure 4.9: Crack pattern for Bresler-Scordelis (1963) beam [ABAQUS]

The accuracy of the results from the simulations of the models is influenced mainly by the following: mesh [element] size, material properties, boundary conditions, application of loading [displacement or force controlled] and time-function (ABAQUS, 2009, ADINA, 2012). A 30 x 30mm mesh, displacement-controlled loadings and a time function of 10 used for the FE analysis of the Bresler-Scordelis beam executed with the earlier models identified in ABAQUS and ADINA gave the results in Table 4.4 and figures 4.10 - 4.12.

Table 4.4: Result from FEA for Bresler-Scordelis (1963)

Model	Max Load [kN]	Displacement at Max Load [mm]	percentage of	
			Load	Disp
Experiment	330	6.60		
ADINA-Conc [Load]	245	2.33	74.2	35.3
ADINA-Conc [Disp]	314	5.21	95.2	77.6
ADINA-DF [Load]	240	2.10	72.7	31.8
ADINA-DF [Disp]	235	5.70	71.2	86.4
ABAQUS CDP [Load]	350	8.00	106.1	121.2
ABAQUS CDP [Disp]	334	6.80	101.2	103.0
ABAQUS CSC [Disp]	252	4.10	76.4	62.1

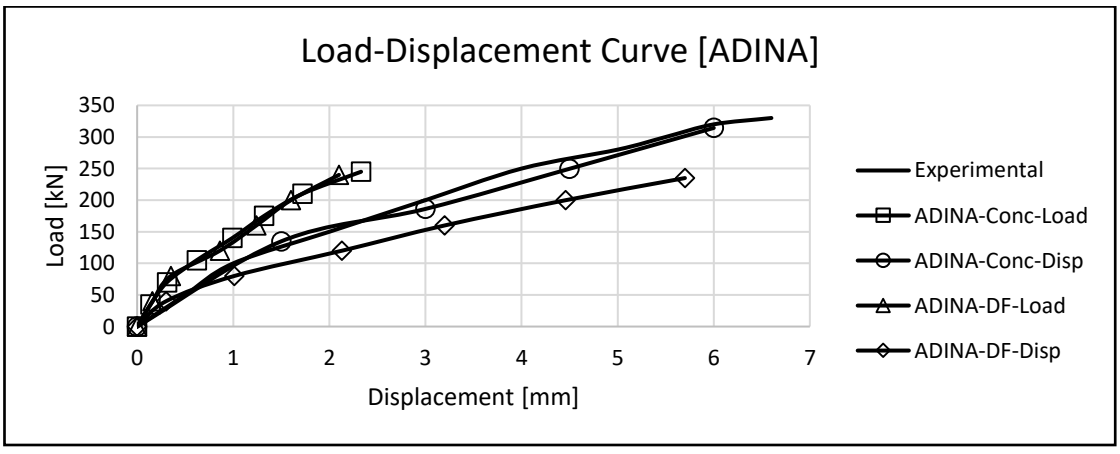

Figure 4.10: Load-Deflection curve for Bresler-Scordelis (1963) beam

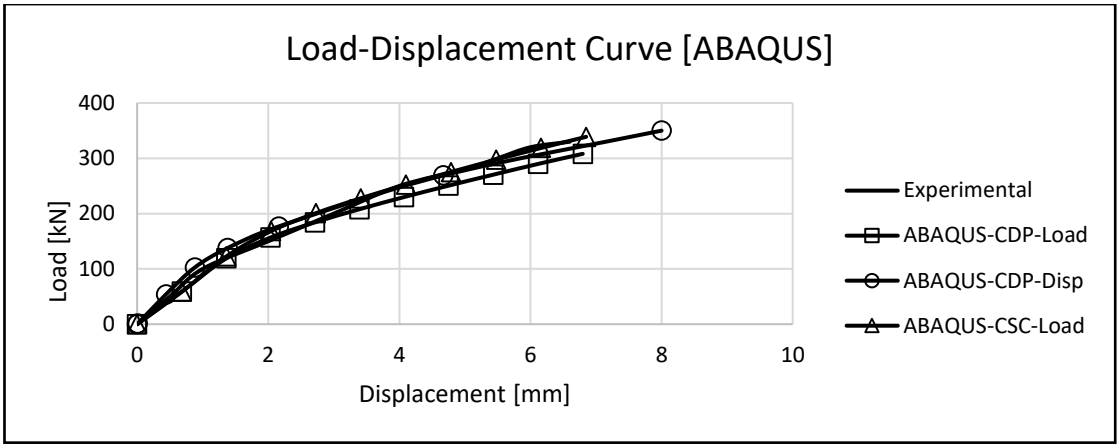

Figure 4.11: Load-Deflection curve for Bresler-Scordelis (1963) beam

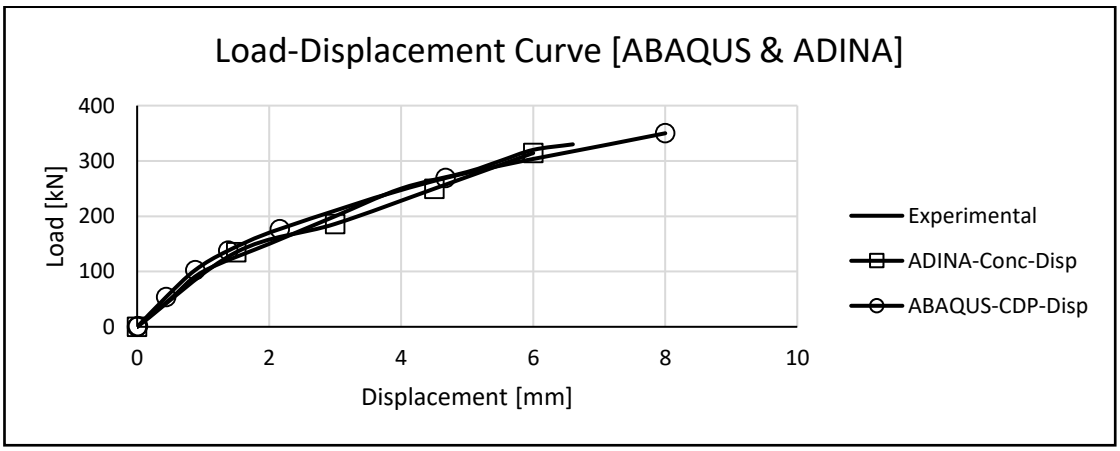

Figure 4.12: Load-Deflection curve [Best Fits] for Bresler-Scordelis (1963) beam

The FEA results show that the mode of failure is diagonal tension, and these are in total agreement with the experimental result. The results show that the two software predicted the behaviour as a brittle failure.

The results also show that the ABAQUS CDP using displacement-controlled loading agrees with the experimental results with a variance of 1.1% in loading at peak and 3% in displacement. The ADINA-Concrete produces a loading that is 6% lower at 22% lower mid-span displacement. Also, the graphs follow the same path as that of the experimental results.

It could be seen that all the models that ran with displacement-based loading gave about the same result, this is due to the fact the Bresler-Scordelis beam is a brittle beam that fails a little above the elastic limit causing the beam to fail in shear at about 330kN with mid-span displacement of about 6.6mm without yielding of the reinforcing bars. This is

also due to the absence of shear reinforcement. The results clearly show that the two software can model comfortably any section that is subject to brittle failure.

The results also show that the displacement-controlled loading is better for this kind of simulation as they continued even after the model has collapsed. From henceforth, only the 'displacement controlled' loading shall be used for further simulations.

4.2.2 Hughes and Speirs (1982) Beam

A series of tests were executed on different types of beams of which twelve [12] specimens were labelled C2, 100mm wide by 200mm deep and spans 2.7m over simple supports [Figure 4.13]. It has 2-T12 and 2-T06 tension and compression reinforcement respectively. In addition to these reinforcement, 6mm shear reinforcement was provided in the beam. The geometric details and material properties of the beam and reinforcing bars are shown in Table 4.3. The specimen is subjected to a centre loading of the reinforced concrete beam. From the result of the experiment, the failure experienced was that of ductile failure in which the reinforcement yielded before the concrete.

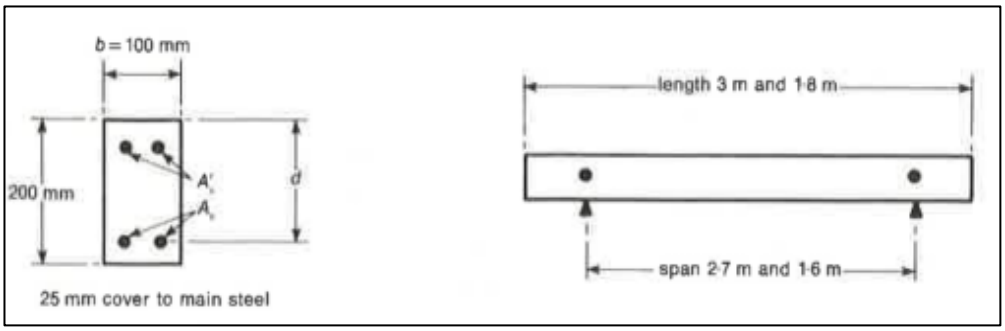

Figure 4.13: Set-up for Experiment for Hughes and Speirs (1982) Beam

Table 4.5: Geometrical details and material properties of the beam.

Beam Number	*b* [mm]	*h* [mm]	d [mm]	Reinforcement						Concrete	
				As	As'	Link	f_y [MPa]	f_u [MPa]	E_s [MPa]	f'_c [MPa]	f_t [MPa]
C2	100	200	175	2-T12	2-T06	14-T06	460	560	206,000	44.4	3.04

4.2.2.1 Hughes and Speirs beam FE Model and Load-Deflection Curve –Ductile Failure

The FEA was done using the ADINA [Concrete and Data-Fitted] and ABAQUS [Concrete Damaged Plasticity CDP and Concrete Smeared Cracking CSC]. The FEA was modelled using the full beam. The concrete beam, supports and loading point were modelled as 3D-brick. The reinforcing bars (compression, tensile and links) were embedded into the concrete beam using the embedded constraint. The supports were modelled as pin and roller with restraining in X, Y directions and Y direction respectively. A 0.5 coefficient of friction, in accordance to EC 4 was provided at the contact faces between concrete and steel.

The material parameters used in ADINA concrete are taken from the experiment and are as follows:

σ_c = - 44.4 MPa	ε_c = -0.002
σ_u = - 28.13 MPa	ε_u = -0.0035
σ_t = 3.04 MPa	ε_t = 0.002
σ_{tp} = 3.04 MPa	E_0 = 34.2 GPa

And in the data-fitted concrete model, the σ_c and the ratio of the σ_t to σ_c [0.07] are provided and inputted into the model.

Displacement controlled loading of 10mm was applied at the centre of the loading plate. (It should be noted that sensitivity analysis done on the beam has a more favourable result with 30mm mesh). The crack pattern from the experiment and FEA modelling are shown in Figures 4.14 - 4.16 while the load-displacement curves are in Figures 4.17 - 4.19.

However, in the ABAQUS-CDP, the plasticity parameters are given as follows: ψ=35^0, ε= 0.1, f_{b0}/f_{c0}= 1.16, K=0.667 and μ= 0.003. The compression and tensile stresses and damaged parameters [as specified in equations 3.12 and 3.13] are given in the Table 4.6 below with concrete cracking failure strain taken as 25ε_{cr} and $\varepsilon_{cr} = \sigma_t/E_t$ (Hassan, 2016) and the displacement-loading of 10mm was applied at an incremental rate of 0.1mm at the centre of the beam.

Table 4.6: Compression and Tensile Parameters

	Yield Stress σ_c MPa	Compressive Damage Variable d_c	Inelastic Strain	Tensile Stress 'σ_t' MPa	Tensile Damage Variable d_t	Cracking Strain
1	16.6	0.00	0.00000	3.04	0.00	0.00000
2	23.2	0.00	0.00024	1.79	0.41	0.00009
3	29.2	0.00	0.00049	1.13	0.63	0.00019
4	34.2	0.00	0.00074	0.79	0.74	0.00028
5	38.1	0.00	0.00099	0.61	0.80	0.00037
6	41.1	0.00	0.00124	0.50	0.84	0.00046
7	42.9	0.00	0.00149	0.41	0.87	0.00056
8	43.5	0.00	0.00178	0.33	0.89	0.00065
9	42.9	0.01	0.00201	0.25	0.92	0.00074
10	41.0	0.06	0.00231	0.19	0.94	0.00083
11	37.7	0.13	0.00266	0.13	0.96	0.00093
12	32.9	0.24	0.00305	0.07	0.98	0.00102
13	26.6	0.39	0.00349	0.03	0.99	0.00111

The bilinear stress-strain value for rebar [adopted for the material behaviour of steel and based on the yield and ultimate strength of the bar] used in both ADINA and ABAQUS is given in Table 4.7:

Table 4.7: Stress-Strain Value for Reinforcement

Stress MPa	Strain
0.00	0.00
460.00	0.001
560.00	0.01

To reproduce experimental conditions in the FEA and avoid untimely localised failure, 10 mm thick steel plates were added at the supports and loading points.

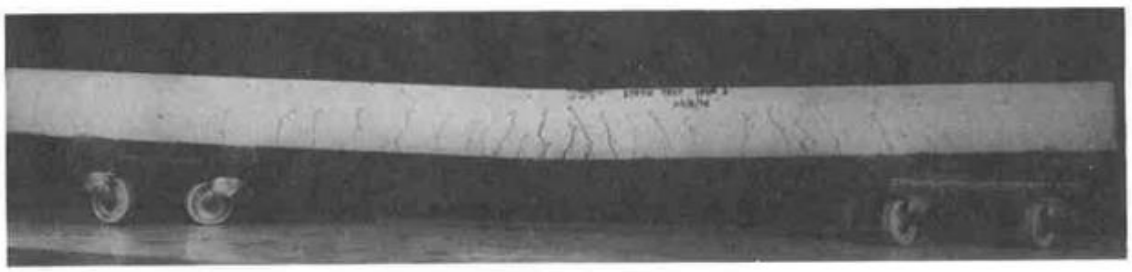

Figure 4.14: Crack pattern in Hughes and Speirs (1982) Beam [Experiment]

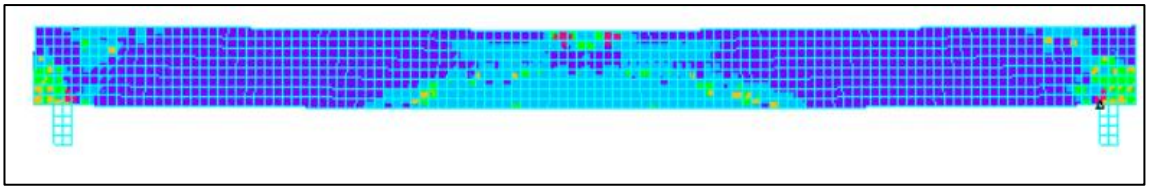

Figure 4.15: Crack pattern in Hughes and Speirs (1982) Beam [ADINA]

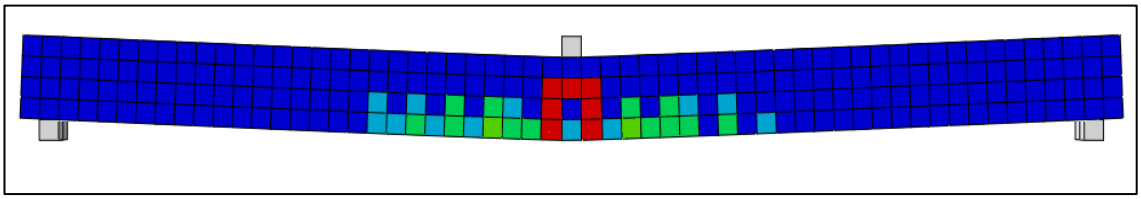

Figure 4.16: Crack pattern in Hughes and Speirs (1982) Beam [ABAQUS]

The provision of links restrained the beam from failing diagonally. The FE models for ductile beam like Hughes and Speirs produces about the same curve as the experimental curve but with stiffer results than the experimental one.

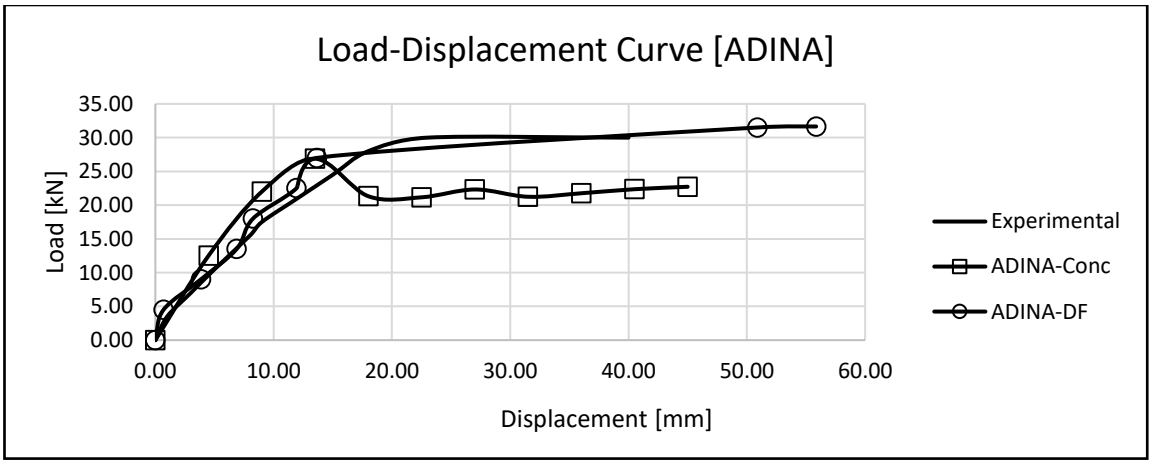

Figure 4.17: Load-Deflection curve of Hughes and Speirs (1982) Beam [ADINA]

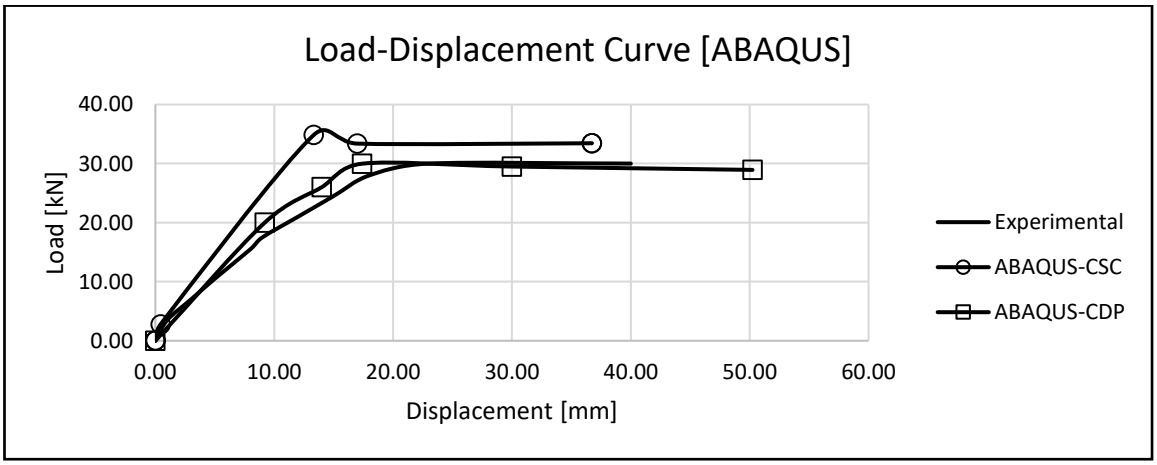

Figure 4.18: Load-Deflection curve of Hughes and Speirs (1982) Beam [ABAQUS]

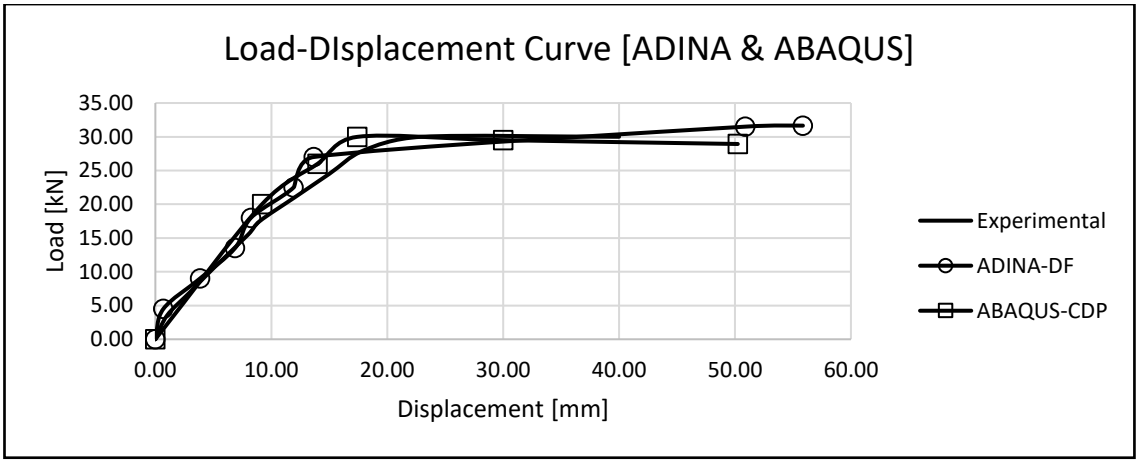

Figure 4.19: Load-Deflection curve [Best Fits]

Table 4.8: Results from FEA for Hughes and Speirs (1982)

Model	Yield Load [kN]	Displacement at Yield Load [mm]	percentage of	
			Load	Disp
Experiment	30.0	23.00		
ADINA-Conc [Disp]	26.9	13.50	89.7	58.7
ADINA-DF [Disp]	27.0	13.70	90.0	59.6
ABAQUS CDP [Disp]	29.9	17.40	99.7	75.7
ABAQUS CSC [Disp]	34.9	13.33	116.3	58.0

The Table 4.8 shows he results from both ADINA and ABAQUS. ABAQUS CDP produced a peak load that is 0.3% lower than the experiment while ADINA Concrete and DF behave about the same way with results that are about 10% lesser than the experiment. The CDP results are good thereby economical to use in design. All in all, the FE models have demonstrated in no small means that if the input parameters were correct, a good result would be obtained.

4.3 Steel-Fibre Reinforced Concrete Experimental Works

The core focus of this research work is aimed at investigating the behaviours of pile-supported and elevated steel-fibre reinforced concrete [SFRC] slabs at material and structural levels using the commercially available structural engineering software ADINA and ABAQUS [linear and non-linear finite element analysis (FEA)].

SFRC can be tested for flexural properties using the notched beams, 3 and 4 points system (Japanese Concrete Institute, 1984, RILEM, 2000, British Standard Institute, 2005, Institute, 2007) and square or round plates (America Concrete Institute, 1999, Bernard, 2000, Kooiman et al., 2000) as explained earlier in the literature review. The earlier works done on the reinforced concrete beams (with rebar) has shown that the ABAQUS CDP agrees with the experimental results.

4.3.1 3-Point Bending Beam Tests

4.3.1.1 Barros J.A.O., Cunha V.M.C.F, Ribeiro A.F. & Antunes JAB Beam (2005)

Steel Fibre Reinforced Concrete [SFRC] beams and panels modelling for FEA requires the use of a constitutive model as discussed in the literature review for the tensile response of the specimen. Two constitutive models (Lok and Xiao, 1998, Lok and Pei, 1998) were used to model the experimental work (Barros et al., 2005) of a beam specimen with 150mm square cross section and 500mm clear span, simply supported and 25mm deep notch at the centre [Figure 4.20].

The beam was modelled in full scale using 3-D brick model [3D3R] for the beam, loading plate and the supports. Boundary conditions at the supports are pin [restrain in x and y directions] and roller [restrain in y-direction only]. To avoid untimely localised failure, a steel plates of 10 mm thickness were added at the loading point.

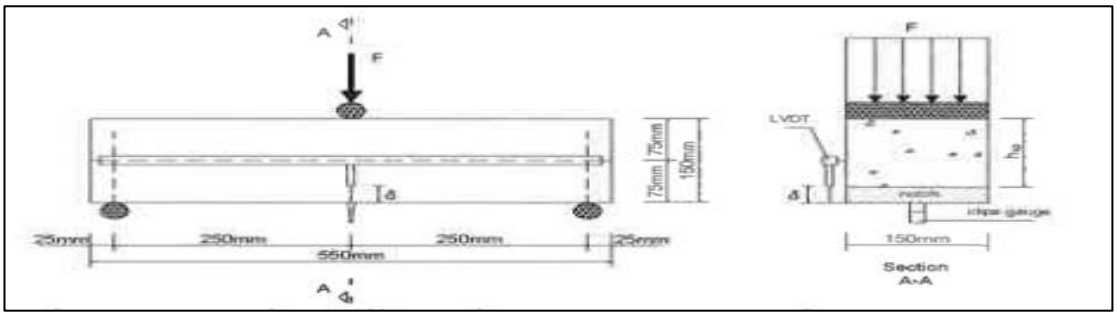

Figure 4.20: Experiment Setup for Barros et al. SFRC Beam 2005

The 3-point bending test used for the validation of these constitutive models was based on the proposal by RILEM TC 162-TDF (RILEM, 2002b). Dramix RC 80/60 BN steel-fibres were used having a 60mm nominal length and equivalent diameter of 0.75mm. A 0.4%

fraction volume of steel-fibre was mixed with the concrete. The elastic modulus [E_c] and compressive strength [f_c] of the concrete beam are 29250 MPa and 25 MPa respectively.

The concrete material properties used in ADINA concrete are obtained from the experiment and are as follows with the effect of the fibres seen on the flexural strength [σ_{tp}] of the SFRC matrix while, in data-fitted concrete model, the σ_c and the proportion of the σ_t to σ_c [0.1%] are specified and inputted into the model:

σ_c = - 25.0 MPa	ε_c = -0.002
σ_u = - 20.0 MPa	ε_u = -0.0035
σ_t = 2.5 MPa	ε_t = 0.02
σ_{tp} = 0.544 MPa	E_c = 29.25 GPa

For the ABAQUS-CDP, the plasticity parameters are given as follows: ψ=40^0, ε= 0.1, f_{b0}/f_{c0}= 1.16, K=0.667 and μ= 0.006. The compression and tensile stresses and damaged parameters are given in the Table 4.10 below with 80% tensile damaged. The Lok and Pei (1998) and Lok & Xiao (1999) models were used to interpret and represents the tensile behaviour of the SFRC beam inputted into ABAQUS-CDP and ADINA-Concrete as shown in Table 4.9 and Figure 4.21.

The displacement loading of 4mm was applied at the centre of the beam at a slow incremental rate of 0.04mm. This is to reduce convergence challenges. The convergence criteria based on the residual forces tolerance is maintained at 5%.

Table 4.9: Tensile Stress-Strain Relationship for Constitutive Models Barros et al. SFRC Beam 2005

	Lok and Xiao (1999)		Lok and Pei (1998)	
Point	Strain [$^0/_{00}$]	Stress [MPa]	Strain [$^0/_{00}$]	Stress [MPa]
Peak Tensile Stress	0	2.500	0	2.500
Point II	0.06	0.544	0.06	0.544
Point III	17.8	0.544	11.0	0.300
Point IV	20.0	0.000	20.0	0.000

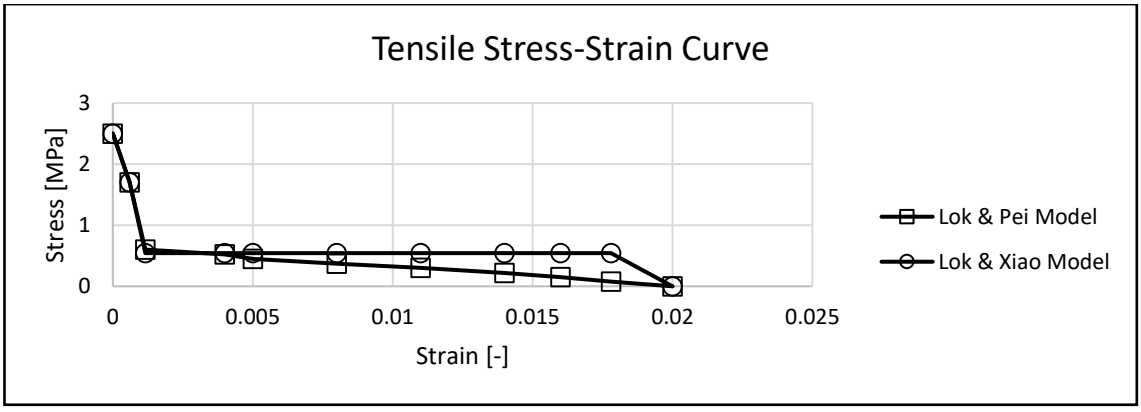

Figure 4.21: Tensile Stress-Strain Curve for Constitutive Models Barros et al. SFRC Beam 2005

The ABAQUS [Concrete Damage Plasticity CDP and Concrete Smeared Cracking CSC] and ADINA [ADINA-Concrete and Data-Fitted] were used to compare and assess the performance of the constitutive models (Lok and Xiao, 1998, Lok and Pei, 1998). The two constitutive models both present a multi-linear descending curve to simulate the tension softening of the concrete after cracking [Figure 4.21]. The bond stress used for this analysis is 3.0MPa and 25mm mesh size.

Table 4.10: Compression and Tensile Parameters for Barros et al. SFRC Beam 2005

	Yield Stress σ_c MPa	Compressive Damage Variable d_c	Inelastic Strain	Lok and Pei (1998)			Lok and Xios (1999)		
				Tensile Stress 'σ_t' MPa	Tensile Damage Variable d_t	Cracking Strain	Tensile Stress 'σ_t' MPa	Tensile Damage Variable d_t	Cracking Strain
1	14.6	0.00	0.00000	2.50	0.00	0.000	2.50	0.00	0.000
2	19.9	0.00	0.00024	0.54	0.08	0.002	0.54	0.08	0.002
3	24.5	0.00	0.00049	0.48	0.16	0.004	0.54	0.16	0.004
4	28.0	0.00	0.00074	0.42	0.24	0.006	0.54	0.24	0.006
5	30.6	0.00	0.00099	0.36	0.32	0.008	0.54	0.32	0.008
6	32.3	0.00	0.00124	0.30	0.40	0.010	0.54	0.40	0.010
7	33.0	0.00	0.00149	0.24	0.48	0.012	0.54	0.48	0.012
8	32.7	0.00	0.00178	0.18	0.56	0.014	0.54	0.56	0.014
9	31.7	0.04	0.00203	0.12	0.64	0.016	0.54	0.64	0.016
10	29.7	0.10	0.00234	0.06	0.72	0.018	0.54	0.72	0.018
11	27.0	0.18	0.00268	0.00	0.80	0.020	0.00	0.80	0.020
12	23.4	0.29	0.00305						
13	18.9	0.43	0.00344						

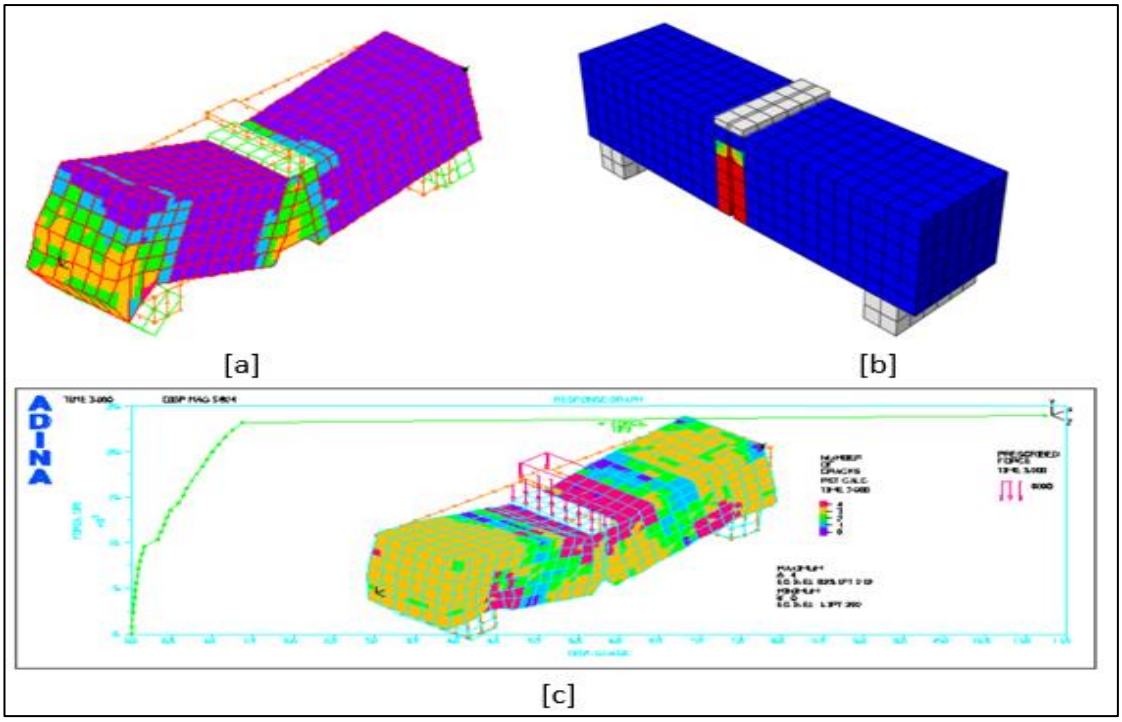

Figure 4.22: Crack-Pattern in [a] ADINA-Conc, [b] ABAQUS and [c] ADINA-DF for Barros et al SFRC Beam 2005

The results obtained are presented in Figures 4.22, 4.23 and 4.24. The models after failure are seen in Figure 4.22. It can be seen that the CSC had a localised failure as it exhibited a softening behaviour in post cracking. The ADINA-Conc uses the tensile and flexural strengths to depict the behaviour of SFRC in tension while the ADINA-DF uses the energy absorbed [area of the under tensile graph] [Figure 4.25]. The ADINA-Conc model has punching around one of the supports which should not be due to simple support arrangement of the supports.

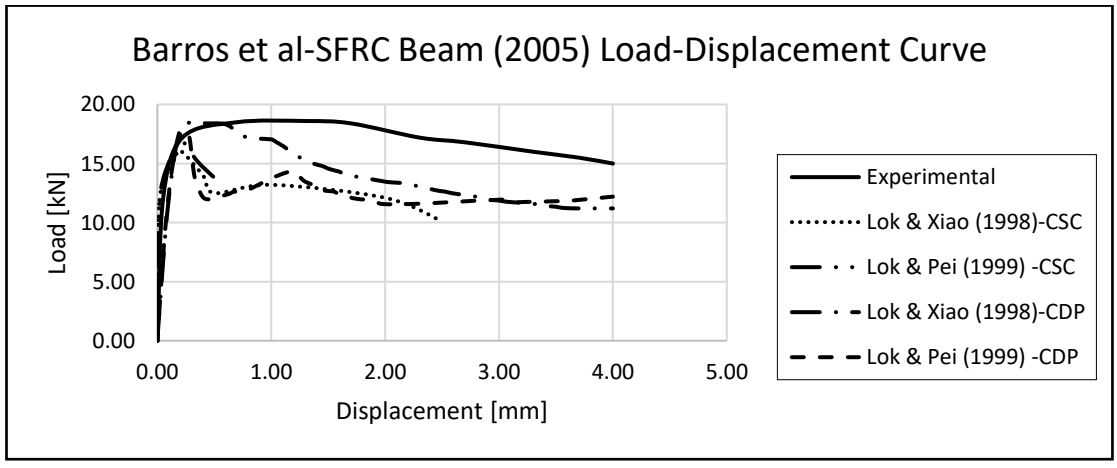

Figure 4.23: Barros et al. SFRC Beam (2005) Load-Displacement Curve [ABAQUS]

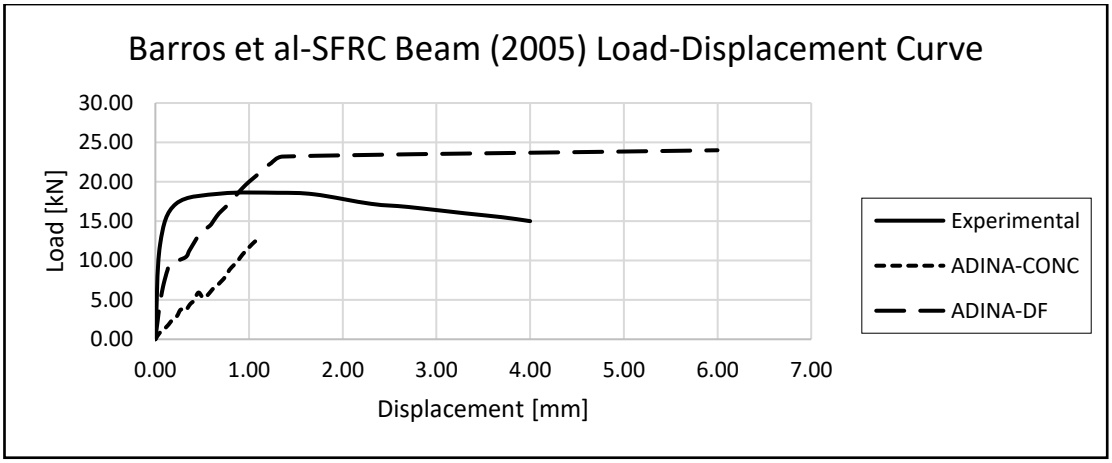

Figure 4.24: Barros et al. SFRC Beam (2005) Load-Displacement Curve [ADINA]

The ADINA-Conc and DF produce a stiffer section with the ADINA-Conc failing after the elastic limit. The ADINA-DF failed at a load 31% higher than the experimental value. Also too, the cracks that appears to form close to the supports makes the ADINA-Conc model no suitable for his present research.

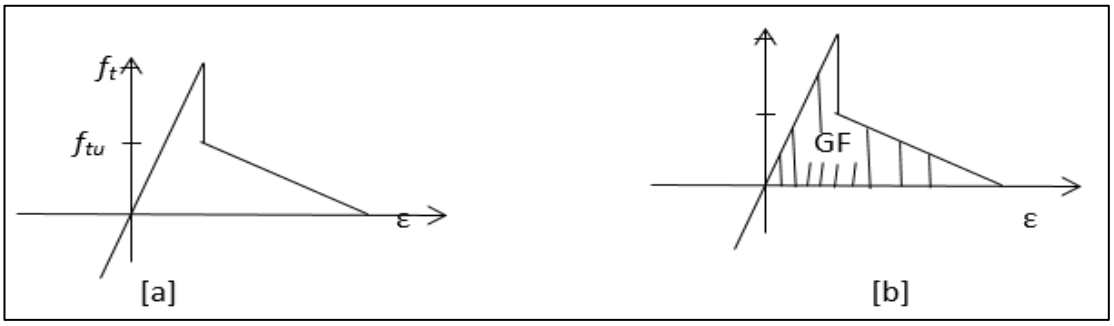

Figure 4.25: SFRC tensile Modelling in [a] ADINA-Conc and [b] ADINA-DF

From the above results, it could be seen that the ABAQUS CDP using Lok and Xiao (1999) constitutive model produces a better result than all other models. It reaches a peak load 2% greater than the experiment and then undergoes a softening behaviour. The result is good and within acceptable limits. For all other SFRC Beam validation, the CDP shall be used.

4.3.1.2 R. de Montaignac, B. Massicotte, JP Charron & A. Nour Beam (2011)

In their research work on the post-cracking behaviour of SFRC in structural elements, they experimented on notched beam based on EN 14651 (British Standard Institute, 2005) test. The experimental work consists of a minimum of six [6] specimens for each

mix with varying amount of steel fibres [0.75-1.25%]. Two linear vertical displacement transducers [LVDT] were placed by the sides [Figure 4.26]. In the overall tests for post-cracking tensile strength of the SFRC structural beams, the fibre content was between 0.75 to 1.25% which makes Lok and Xiao (1999) a preferred model.

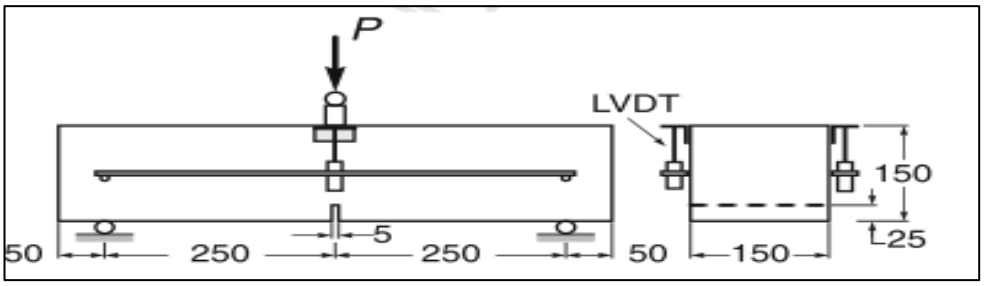

Figure 4.26: Experiment Setup for de Montaignac et al. (2011) SFRC Beam

The mechanical properties of the SFRC beam in compression made from 1% volume fraction of fibres are compressive strength 46.9MPa, modulus of elasticity 33.5GPa and the Poisson ratio of 0.23 while the post-cracking tensile strength is 2.6MPa. The hooked-end steel-fibre used in the concrete matrix is 37mm long with 0.55mm equivalent diameter.

The 3-point bending test used for the validation of these constitutive models was based on the works of (de Montaignac et al., 2011). The experimental work consists of a minimum of six [6] specimens for each mix with varying amount of steel fibres [0.75-1.25%]. Two linear vertical displacement transducers [LVDT] were placed by the sides. The findings of the experimental works demonstrate that the characterisation tests [uniaxial tensile test, inverse analysis of notched beam and round panel test] can be used to derive the stress-crack opening $[\sigma - w]$. In the overall tests for post-cracking tensile strength of the SFRC structural beams, the fibre content was between 0.75 to 1.25%.

Table 4.11: Tensile Stress-Strain Relationship for Constitutive Models de Montaignac et al SFRC Beam (2011)

	Lok and Xiao (1999)		de Montaignac et al (2011)	
Point	Strain [$^0/_{00}$]	Stress [MPa]	Strain [$^0/_{00}$]	Stress [MPa]
Peak Tensile Stress	0	2.60	0	2.60
Point II	0.06	1.17	2.00	1.80
Point III	17.8	1.17	2.40	2.00
Point IV	20.0	0.00	40.0	0.00

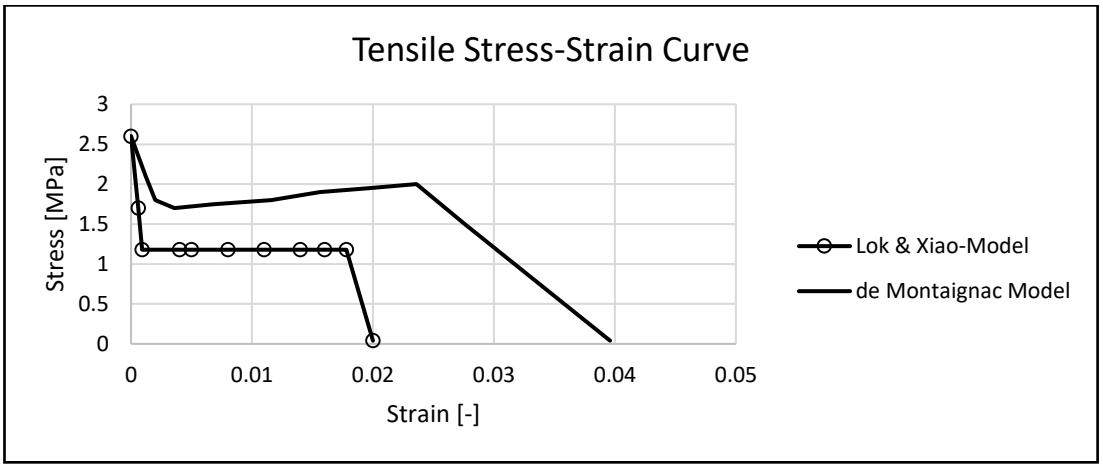

Figure 4.27: Tensile Stress-Strain Curve for de Montaignac et al SFRC Beam (2011)

Their entire works was based on the stress-crack opening design $[\sigma - w]$ model which was proposed by the researchers in their report and was derived from experimental works carried out by them. For comparison with Lok and Xiao (1999), the $[\sigma - w]$ is converted to$[\sigma - \varepsilon]$. The $[\sigma - w]$ is mesh dependent. The relationship between the cracked width and the strain is given as and the resulting strain used in Table 4.11 and Figure 4.27:

$$l_{cs} = \frac{w}{\varepsilon}$$

Where:

l_{cs} - Structural characteristic length

.

The plasticity parameters used in the ABAQUS-CDP are given as follows: ψ=40^0, ε= 0.1, f_{b0}/f_{c0}= 1.16, K=0.667 and μ= 0.006 with 80% tensile damaged. The compression and tensile stresses and damaged parameters are given in Table 4.12.

Table 4.12: Compression and Tensile Parameters for de Montaignac et al SFRC Beam 2011

	Yield Stress σ_c MPa	Compressive Damage Variable d_c	Inelastic Strain	Lok and Pei (1998)			de Montaignac et al (2011)		
				Tensile Stress 'σ_t' MPa	Tensile Damage Variable d_t	Cracking Strain	Tensile Stress 'σ_t' MPa	Tensile Damage Variable d_t	Cracking Strain
1	18.4	0.00	0.00000	2.60	0.00	0.000	2.60	0.00	0.000
2	26.0	0.00	0.00024	1.18	0.08	0.002	2.10	0.08	0.001
3	33.3	0.00	0.00049	1.18	0.16	0.004	1.80	0.16	0.002
4	39.7	0.00	0.00074	1.18	0.24	0.006	1.70	0.24	0.004
5	45.1	0.00	0.00099	1.18	0.32	0.008	1.75	0.32	0.007
6	49.5	0.00	0.00124	1.18	0.40	0.010	1.80	0.40	0.012
7	52.7	0.00	0.00149	1.18	0.48	0.012	1.90	0.48	0.016
8	54.7	0.00	0.00178	1.18	0.56	0.014	1.95	0.56	0.020
9	54.8	0.00	0.00199	1.18	0.64	0.016	2.00	0.64	0.024
10	53.4	0.03	0.00228	1.18	0.72	0.018	1.50	0.72	0.028
11	49.9	0.09	0.00262	0.00	0.80	0.020	0.00	0.80	0.040
12	44.2	0.20	0.00303						
13	35.7	0.35	0.00351						

The displacement loading of 10mm was applied at the centre of the beam at an incremental rate of 0.1mm in order to minimise problems related with convergence. The Time-Frequency value ranges from 0.00 – 10.00 and 0.00 – 1.00 at 0.1 and 0.01 intervals respectively. The convergence criteria based on the residual forces tolerance is 5%. The crack patterns and Load-Displacement Curve for de Montaignac et al SFRC Beam (2011) are presented in Figures 4.28 and 4.29 respectively.

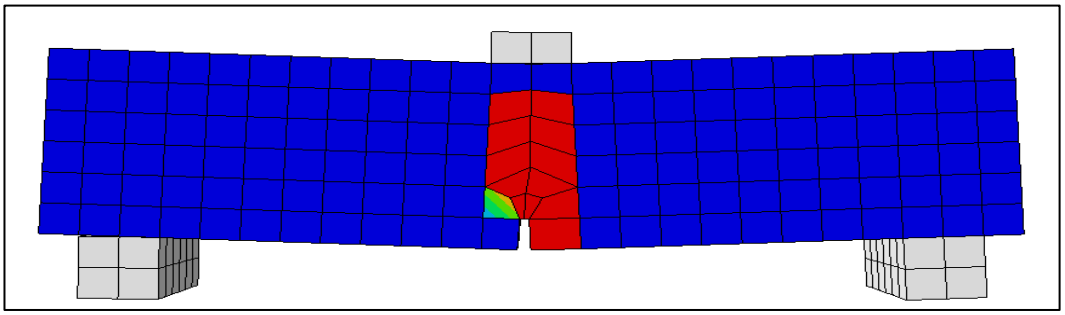

Figure 4.28: Crack Pattern for de Montaignac et al. SFRC Beam (2011)

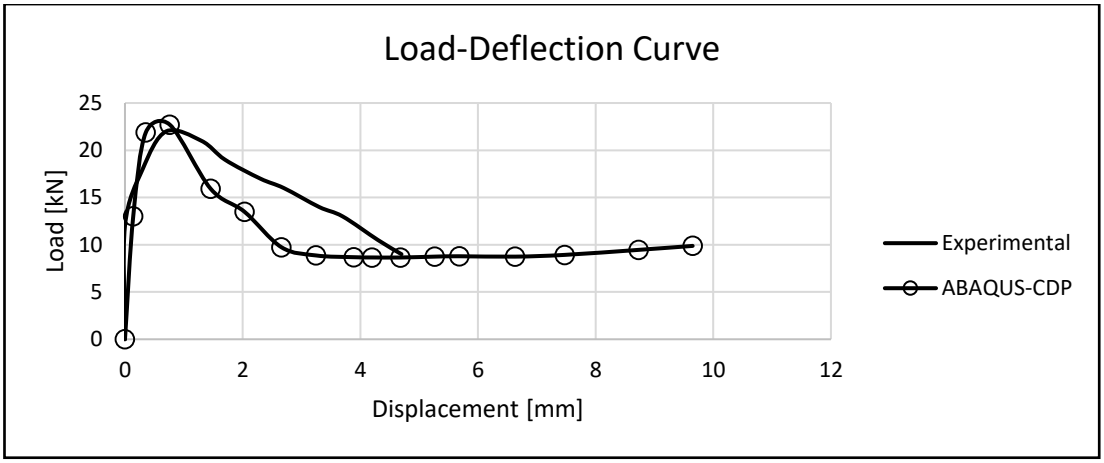

Figure 4.29: Load-Displacement Curve for de Montaignac et al SFRC Beam (2011)

The experimental and FEA [ABAQUS-CDP] results of loads and the corresponding displacements at the centre of the beam is presented in Figure 4.29. The beam was loaded slowly at an increment of 0.1mm which resulted in the first crack observed at a displacement of 0.14mm with to 13.00kN load took place at the notch. The peak load of 22.71kN occurred at a central displacement of 0.76mm.

It can be observed that the FEA predictions overestimates the peak load by 3.2% when compared with the experimental results. The results show that Lok and Xiao (1999) which is based on the stress-strain relationship has the capacity for the high volume of fibres and produces a result within ±5% of the experimental results and RILEM recommendation.

4.3.2 4-Point Bending Tests

The 4-point bending test has a load application at two [2] points on the beam in between the two supports [always equidistant from the supports].

4.3.2.1 H. Tlemat, K. Pilakoutas and K. Neocleous SFRC Beam (2006)

In this work on a compressive study of a flexural framework for SFRC, an inverse FEA was used to determine the tensile behaviour of SFRC beam with a 25mm notch at the centre in a 4-point bending test [Figure 4.30]. The compressive strength and tensile strength of the composite material were 54.1 MPa and 2.68MPa respectively for a volume fibre fraction of 1.5% and fibre parameters of 50mm length, 1.55mm diameter and a modulus of elasticity of 210GPa. This was modelled using ABAQUS CDP.

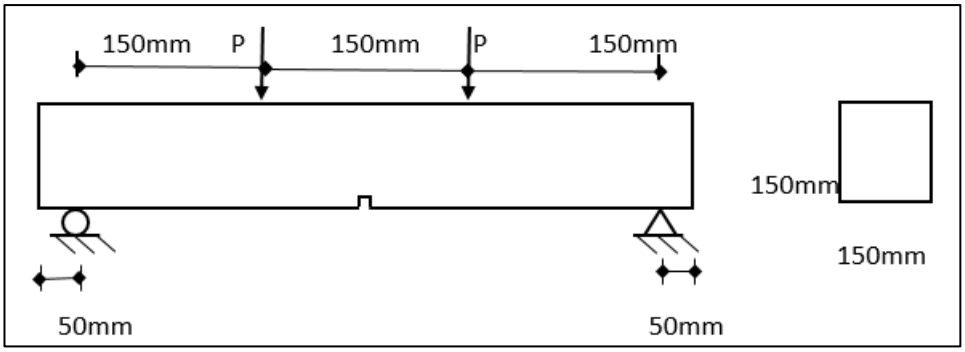

Figure 4.30: Experimental Set-up for Tlemat et al (2006) SFRC Beam

The tensile stress-strain relationship is presented in Table 4.13 and Figure 4.31. The Tlemat et al. (2006) Model is compared to that of Lok and Xiao (1999) Model. The Tlemat et al. (2006) cracking strain reaches 0.040 while that of Lok and Xiao (1999) reaches 0.02. 3.5MPa was adopted for the bond stress. A mesh size of 25mm was used for the analyses. The displacement-controlled loading was applied at the two loading points.

Table 4.13: Tensile Stress-Strain Relationship for Constitutive Models Tlemat et al SFRC Beam (2006)

	Lok and Xiao (1999)		Tlemat et al (2006)	
Point	Strain [$^0/_{00}$]	Stress [MPa]	Strain [$^0/_{00}$]	Stress [MPa]
Peak Tensile Stress	0.00	2.68	0.00	2.68
Point II	0.60	1.94	1.40	1.50
Point III	17.8	1.94	2.40	0.60
Point IV	20.0	0.00	40.0	0.00

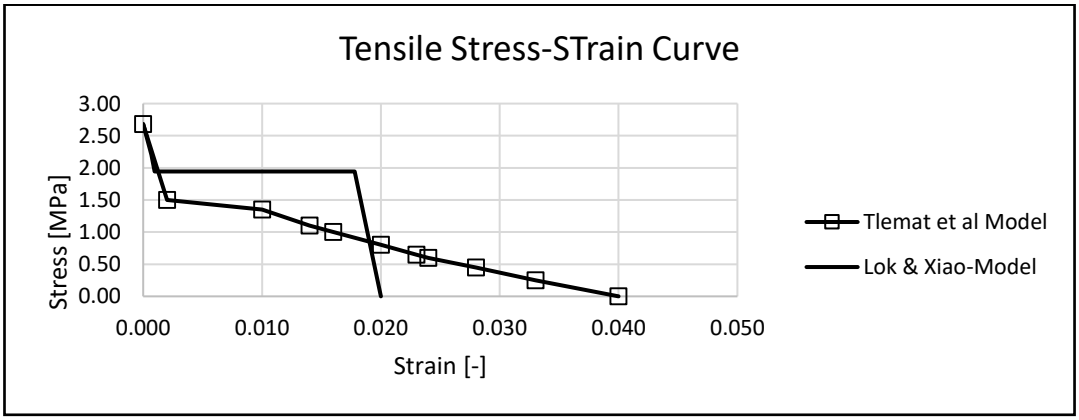

Figure 4.31: Tensile Stress-Strain Curve for Tlemat et al. SFRC Beam (2006) with V_f= 1.5%

The plasticity parameters [ψ=40^0, ε= 0.1, f_{b0}/f_{c0}= 1.16, K=0.667 and μ= 0.006] and 80% tensile damaged were used in the ABAQUS-CDP. Tlemat et al proposed a constitutive model for post-cracking behavior of SFRC section which is presented in Figure 4.31 and Table 4.14 alongside Lok and Xiao (1999) constitutive model. The compression and tensile stresses and damaged parameters values are also stated in Table 4.14.

Table 4.14: Compression and Tensile Parameters for Tlemat et al SFRC Beam 2005

	Yield Stress σ_c MPa	Compressive Damage Variable d_c	Inelastic Strain	Lok and Xiao (1999)			Tlemat et al (2005)		
				Tensile Stress 'σ_t' MPa	Tensile Damage Variable d_t	Cracking Strain	Tensile Stress 'σ_t' MPa	Tensile Damage Variable d_t	Cracking Strain
1	17.9	0.00	0.00000	2.68	0.00	0.0000	2.68	0.00	0.000
2	25.2	0.00	0.00024	2.20	0.08	0.0007	1.50	0.08	0.002
3	32.1	0.00	0.00049	1.94	0.16	0.0010	1.35	0.16	0.010
4	38.0	0.00	0.00074	1.94	0.24	0.0040	1.10	0.24	0.014
5	43.0	0.00	0.00099	1.94	0.32	0.0050	1.00	0.32	0.016
6	46.9	0.00	0.00124	1.94	0.40	0.0080	0.80	0.40	0.020
7	49.7	0.00	0.00149	1.94	0.48	0.0110	0.65	0.48	0.023
8	51.2	0.00	0.00178	1.94	0.56	0.0140	0.60	0.56	0.024
9	51.1	0.00	0.00200	1.94	0.64	0.0160	0.45	0.64	0.028
10	49.4	0.04	0.00229	1.94	0.72	0.0178	0.25	0.72	0.033
11	46.0	0.10	0.00264	0.00	0.80	0.0200	0.00	0.80	0.040
12	40.5	0.21	0.00304						
13	32.7	0.36	0.00351						

The beam was loaded slowly at two points, 150mm apart, on the beam at an incremental rate of 0.04mm which resulted in the first crack observed at the notch at displacements of 0.01mm and 0.04mm with to 10.00kN and 9.98kN loads for Tlemat et al and FEA prediction respectively. The peak loads of 30.00kN and 29.40kN for the two models occurred at a central displacement of 0.09mm and 0.20mm respectively.

The results in the form of crack patterns and load-displacement curves are presented in Figures 4.32 and 4.33 respectively. The crack pattern is similar to that of any beam with a notch. The formation of cracks takes place around the notch [the weakest point].

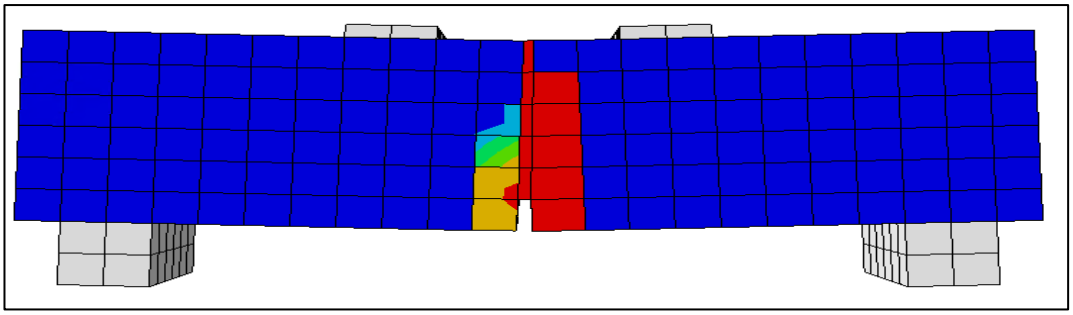

Figure 4.32: Crack patterns for Tlemat et al. (2006) [ABAQUS]

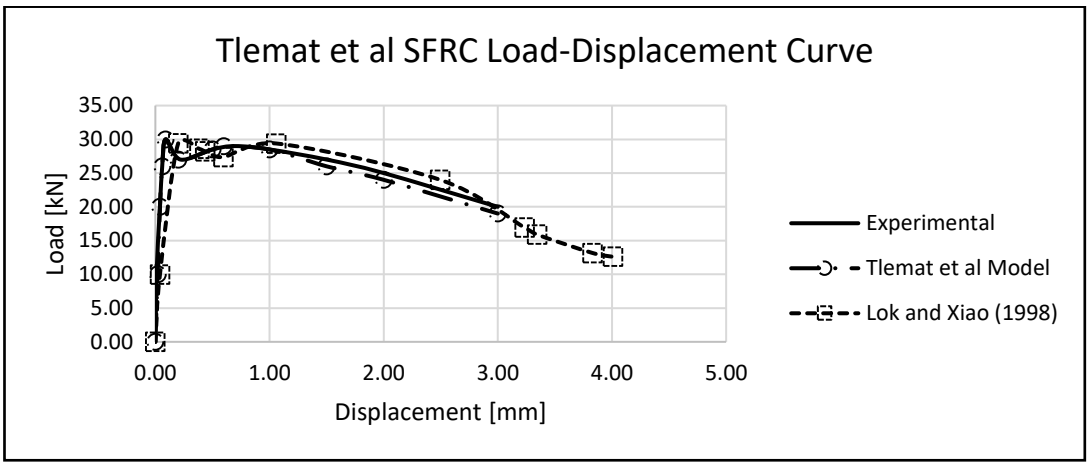

Figure 4.33: Load-Displacement Curve for Tlemat et al. SFRC Beam (2006)

The model proposed by Tlemat et al. (2006) was in good agreement and is the nearest to the experimental result. Likewise, the result shows that using the Lok and Xiao proposed model in ABAQUS CDP, a compatible agreement with the experimental result was achieved. The FEA model was a bit less stiff (5%) than the experimental result. They both achieve a maximum load of 30kN though the post-cracking load along the curve is marginally overestimated. This further attest that the ABAQUS CDP can model an SFRC beam.

4.3.2.2 R.S. Olivito and F.A. Zuccarello (2010) SFRC Beam

In the experimental works of Olivito and Zuccarello (2010) on the notched beam for the determination of the static mechanical behaviour (including the tensile response) of SFRC beam. The grove of the notch is 45mm deep, making it slightly different from others. The SFRC beam is 600mm long over a clear distance of 450mm with a 150mm square cross-section. The steel-fibre properties are 30mm length, 0.6mm equivalent diameter, 210GPa modulus of elasticity and 1% volume fibre fraction. The test was a 4-

point bending test conducted over 24 samples with different fibre sizes and concrete properties.

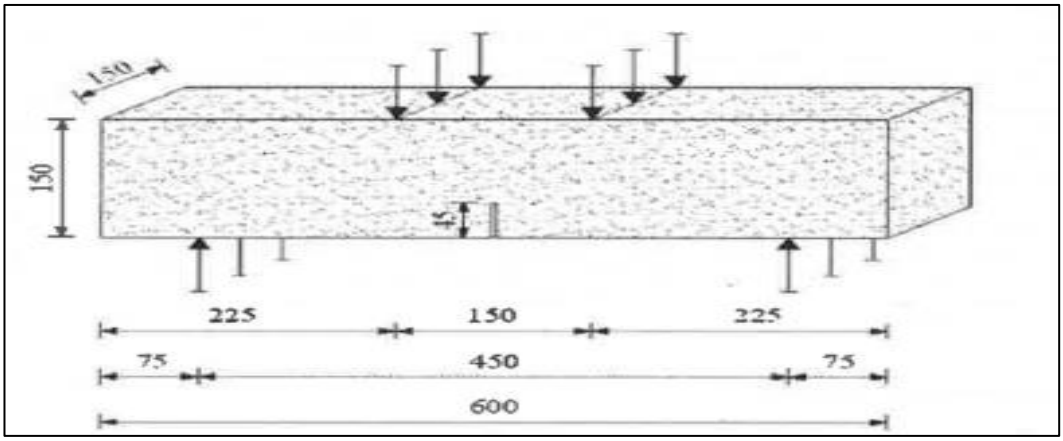

Figure 4.34: Experiment Setup for R.S. Olivito and F.A. Zuccarello (2010) SFRC Beam

A sketch of the beam model is given in Figure 4.34 and due to the size of the beam, a full scale was modelled. The supports are modelled as a roller [restrained in x and y directions] and pin [restrained in y direction] boundary conditions provided at 75mm to the edge of the beam. The loads were applied 150mm apart. To avoid early localised failure, steel plates of 10 mm thickness were added at the support and loading points.

Table 4.15 and Figure 4.35 describe the relationship of the tensile stress and strain using the Lok and Xiao (1999) Model. The bond stress of 3.5MPa was adopted for the simulation. A mesh size of 25mm was used for the analyses. The displacement-controlled loading was applied at a slow rate of 0.01mm simultaneously at the two loading points.

Table 4.15: Tensile Stress-Strain for R.S. Olivito and F.A. Zuccarello (2010) SFRC Beam

	Lok and Xiao (1999)	
Point	Strain [$^{0}/_{00}$]	Stress [MPa]
Peak Tensile Stress	0.00	1.70
Point II	0.70	0.88
Point III	17.8	0.88
Point IV	20.0	0.00

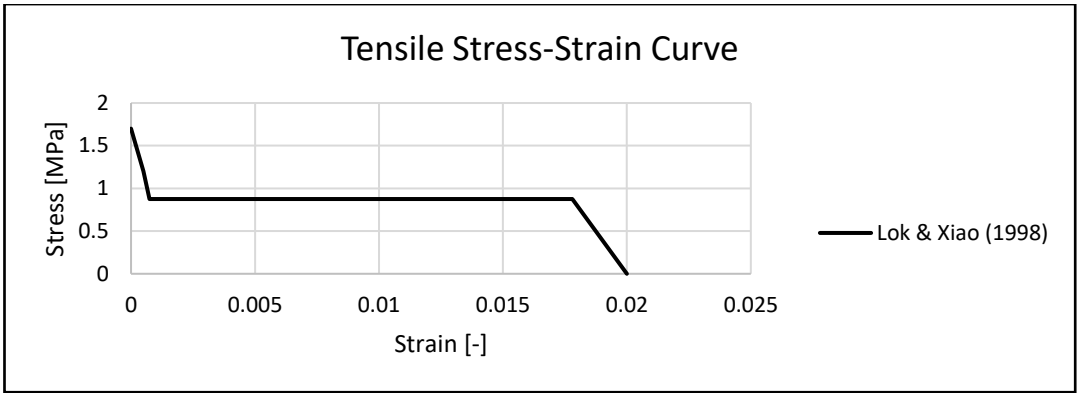

Figure 4.35: Tensile Stress-Strain Curve for Olivito and Zuccarello (2010) SFRC Beam

Their works was purely an experimental one with no model proposed. The bean labelled B1 was chosen for verification and calibration. The experiment arrived at a compressive strength of 47.80MPa after taking into consideration all the factors that may affect the mechanical behaviour of SFRC. The tensile strength of 1.7MPa was gotten from the direct tensile test, representing 3.6% of compressive strength.

For the ABAQUS-CDP, 80% tensile damaged was adopted and the plasticity parameters values are provided as follows: ψ=40^0, ε= 0.1, f_{b0}/f_{c0}= 1.16, K=0.667 and μ= 0.006. Table 4.16 gives the compression and tensile stresses and damaged parameters.

Table 4.16: Compression and Tensile Parameters for Olivito and Zuccarello (2010) SFRC Beam

	Yield Stress σ_c MPa	Compressive Damage Variable d_c	Inelastic Strain	Lok and Xiao (1999)		
				Tensile Stress 'σ_t' MPa	Tensile Damage Variable d_t	Cracking Strain
1	18.5	0.00	0.00000	1.70	0.00	0
2	26.2	0.00	0.00024	1.20	0.08	0.0005
3	33.6	0.00	0.00049	0.88	0.16	0.0007
4	40.1	0.00	0.00074	0.88	0.24	0.002
5	45.6	0.00	0.00099	0.88	0.32	0.005
6	50.1	0.00	0.00124	0.88	0.40	0.008
7	53.4	0.00	0.00149	0.88	0.48	0.011
8	55.5	0.00	0.00178	0.88	0.56	0.014
9	55.7	0.00	0.00199	0.88	0.64	0.016
10	54.4	0.03	0.00228	0.88	0.72	0.018
11	50.9	0.09	0.00262	0.00	0.80	0.020
12	45.1	0.19	0.00303			
13	36.5	0.35	0.00351			

The results are presented in the form of crack patterns and load-displacement curves in Figures 4.36 and 4.37 respectively. The crack formation starts around the notch and spread ward. The crack pattern is similar to that of any beam with a notch. The first crack detected was at a displacement of 0.07mm with a 12.82kN load while the peak load of 21.38kN [2.80% less than experimental vale] occurred at a central displacement of 0.72mm. The model finally collapsed at 16.03kN load.

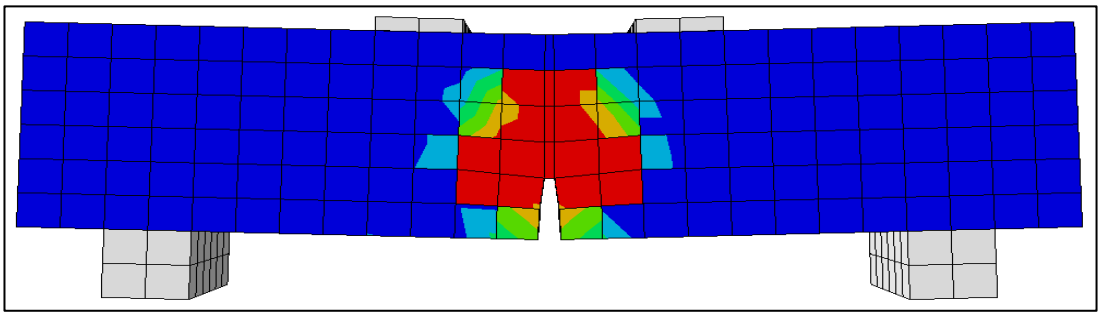

Figure 4.36: Crack patterns for Olivito and Zuccarello (2010) SFRC Beam

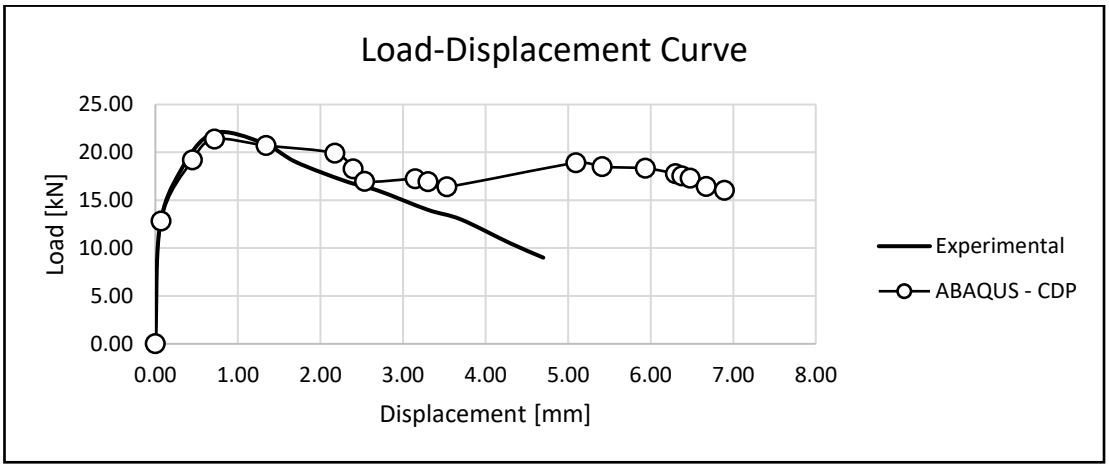

Figure 4.37: Load-Displacement Curve for Olivito and Zuccarello (2010) SFRC Beam

The ABAQUS CDP was used to simulate the response of the section to displacement-controlled loading. The cracked mouth opening displacement CMOD was plotted against the load [Figure 4.36]. The result shows significant agreement in the elastic state and then a combination of softening and hardening behaviour [Figure 4.37].

4.3.3 SFRC Slabs [Plates]

Performance assessment of panel-based SFRC is more desirable to beam-based SFRC performance assessment in consideration for slabs [suspended or ground supported] analysis and design through FEM because panels fail through a combination of stress action that reflects the true behaviour of an in-situ slab (Bernard, 2000, Destrée, 2006, Hadi, 2008, Barros et al., 2013c).

4.3.3.1 Hadi (2008) Square Plate

The study was undertaken to compare the response of two types of fibres, but for this validation work, the result for the SFRC square panel shall be used. The SFRC attains a compressive strength of 13.9MPa with a tensile strength of 2.5MPa for a 0.5% volume fraction of steel-fibre. Hooked end steel-fibres of length 35mm and equivalent diameter of 0.55 were used. The dimension of the panel is 820mm x 820mm x 80mm. It was loaded centrally with a piston, 75mm x 75mm x 50mm [Figure 4.38].

Figure 4.38: Panel Testing in the Lab

The panel was simply placed on metal supports [50mm square] at the corners. The panel was constrained on two sides to guide against lateral displacement and thus panel-supports boundary conditions were modelled as pinon one support and rollers on the other three supports.

The material properties used in ADINA-concrete model are obtained from the experiment with the effect of the steel-fibres reflecting on the flexural strength [σ_{tp}] of the SFRC matrix and given as follows:

σ_c = - 13.9 MPa ε_c = -0.002

σ_u = - 11.12 MPa ε_u = -0.0035

σ_t = 2.5 MPa ε_t = 0.02

σ_{tp} = 1.11 MPa E_c = 36.85 GPa

The Lok & Xiao (1999) model [being the most suitable constitutive model] was used to construe the tensile behaviour of the SFRC panel in the ABAQUS-CDP and ADINA-Concrete as shown in Table 4.17 and Figure 4.39.

Table 4.17: Tensile Stress-Strain Relationship for Hadi's SFRC Square Panel (2008)

	Lok and Xiao (1999)	
Point	Strain [$^0/_{00}$]	Stress [MPa]
Peak Tensile Stress	0.00	2.50
Point II	2.00	1.11
Point III	17.8	1.11
Point IV	20.0	0.00

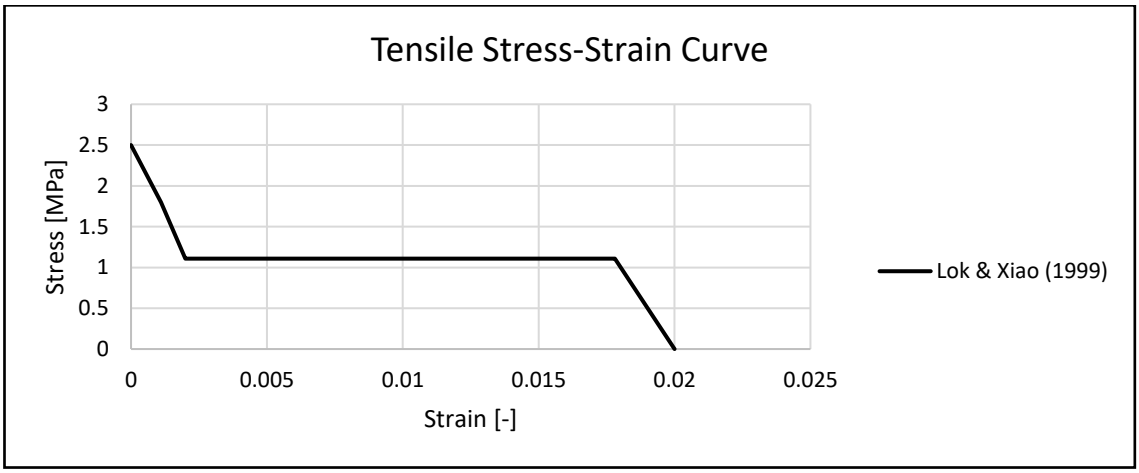

Figure 4.39: Tensile Stress-Strain Curve for Hadi's SFRC Square Panel (2008)

The ABAQUS-CDP plasticity parameters are given as follows: ψ=40^0, ε= 0.1, f_{b0}/f_{c0}= 1.16, K=0.667 and μ= 0.006. The compression, tensile stresses and damaged parameters are given in the Table 4.18 with tensile damaged taken as 80%. The displacement loading of 50mm was placed at the centre of the panel at a slow incremental rate of 0.50mm from 0.00mm. This is to reduce problems connected with convergence.

Table 4.18: Compression and Tensile Parameters for Hadi's SFRC Square Panel (2008)

	Yield Stress σ_c MPa	Compressive Damage Variable d_c	Inelastic Strain	Lok and Xiao (1999)		
				Tensile Stress 'σ_t' MPa	Tensile Damage Variable d_t	Cracking Strain
1	11.8	0.00	0.00000	2.50	0.00	0.000
2	15.5	0.00	0.00024	1.80	0.08	0.001
3	18.3	0.00	0.00049	1.11	0.16	0.002
4	20.2	0.00	0.00074	1.11	0.24	0.004
5	21.4	0.00	0.00099	1.11	0.32	0.005
6	21.9	0.00	0.00124	1.11	0.40	0.008
7	21.8	0.00	0.00149	1.11	0.48	0.011
8	21.0	0.00	0.00178	1.11	0.56	0.014
9	20.0	0.09	0.00206	1.11	0.64	0.016
10	18.5	0.16	0.00236	1.11	0.72	0.018
11	16.6	0.24	0.00268	0.00	0.80	0.020
12	14.3	0.35	0.00301			
13	11.8	0.46	0.00335			

The Figure 4.40 shows the crack patterns based on ABAQUS and ADINA and Figure 4.41 the experimental and FEA [ABAQUS-CDP and ADINA-Conc] results of loads and the corresponding displacements at the panel's centre. It is necessary to use ADINA for the validation work on slab [panel], since it has not been used for FEA on slab in this research work.

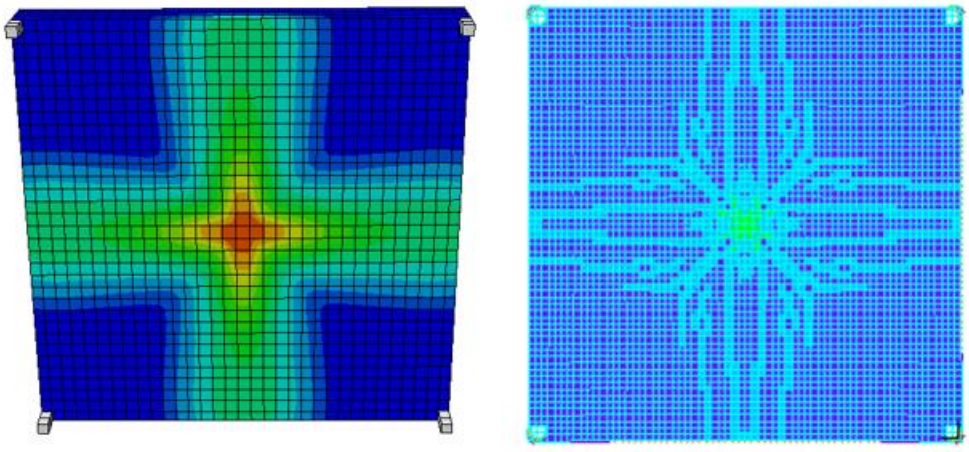

[a] [b]

Figure 4.40: Crack patterns in Hadi's SFRC Slab (2008) [a] ABAQUS and [b] ADINA

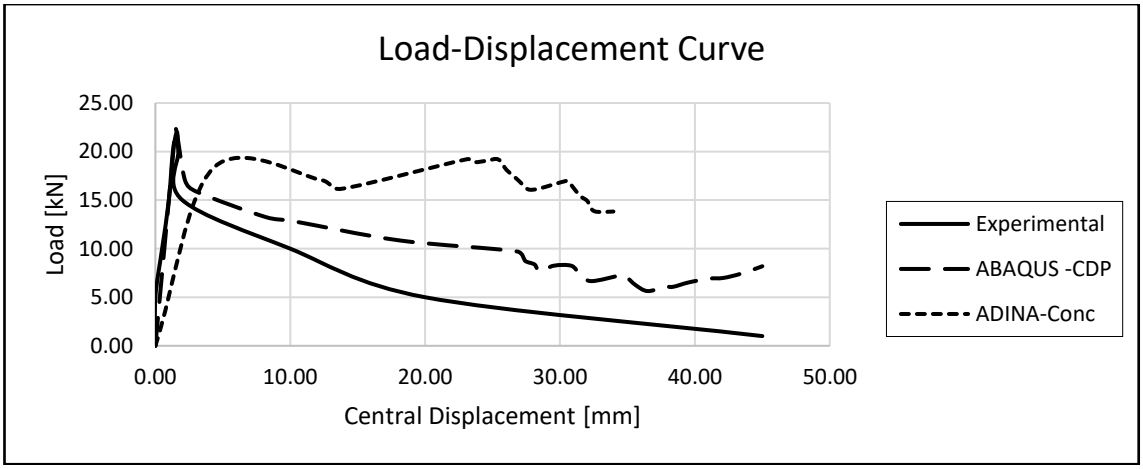

Figure 4.41: Load-Displacement Curve for Hadi's SFRC Slab (2008) [a] ABAQUS and [b] ADINA

As a result of the continuous loading to destruction on the square-panel, the first crack observed at the centre of the panel was at a displacement of 1.30mm in ABAQUS-CDP and 4.30 in ADINA-Conc with 19.53kN and 18.31kN loads respectively. The peak loads of 22.71kN [ABAQUS-CDP] and 18.31kN [ADINA-Conc] occurred at a central displacement of 1.50mm and 4.30mm. The ADINA-DF gave a stiffer result with softening and hardening response after failure while the ABAQUS CDP gave a response similar to the experimental result. The crack patterns from CDP and ADINA-Conc show collapse from the centre point in which the load was applied moving towards the free edges and very similar to one another. Comparing the pattern with the load-displacement curve, it shows that the slab collapsed after the elastic state with a post-cracking softening behaviour.

The load-displacement curves in Figure 4.41 reveal that the ABAQUS concrete damaged plasticity give a higher response in post-cracking behaviour than the experiment. The result from ADINA-Data fitted is much higher [>150%] that the experiment. The CDP is better in modelling the Hadi's SFRC Slab.

4.3.3.2 Blanco, A., Cavalaro, S., De La Fuente, A., Grünewald, S., Blom, CBM & Walraven, JC Square Plate (2014)

The experimental work, which was also validated with numerical analysis was set-up to confirm the provisions made by RILEM for testing SFRC (RILEM, 2002a). Three different slabs were tested and modelled. The panels, 1500mm x 750mm x 200mm, 1500mm x 1000mm x 200mm and 1500mm x 1500mm x 200mmm were used. The largest one was

used for this validation and calibration work. The slab was simply supported at the edge with support equal to the half of the length of the side and placed at the centre. Provisions were made for a 20mm neoprene membrane placed in between the slab and the supports. It was loaded centrally with a square ram.

The SFRC has a compressive strength of 46.7MPa, tensile strength of 5.6MPa and modulus of elasticity of 29GPa. 40kg/m3 of Dramix® hooked end steel fibres, 50mm long and 0.625mm equivalent diameter. The percentage of volume fibre used was 0.5%.

The relationship of the stress and strain in tension is presented in Table 4.19 and Figure 4.42 in which the RILEM (2002) Model is compared to that of Lok and Xiao (1999) Model. The RILEM (2002) cracking strain reaches 0.022 and with descending values of stress while that of Lok and Xiao (1999) reaches 0.02 with a constant value of stress from the flexural strength. 4.5MPa was adopted for the bond stress and 25mm mesh size was used for the FE analyses. The displacement-controlled loading was applied at the centre of the panel.

Table 4.19: Tensile Stress-Strain Relationship for Blanco et al SFRC Square Panel (2015)

	Lok and Xiao (1999)		RILEM (2002)	
Point	Strain [$^0/_{00}$]	Stress [MPa]	Strain [$^0/_{00}$]	Stress [MPa]
Peak Tensile Stress	0.00	5.60	0.00	5.60
Point II	1.40	2.50	0.50	2.50
Point III	17.8	2.50	17.8	2.24
Point IV	20.0	0.00	22.0	0.00

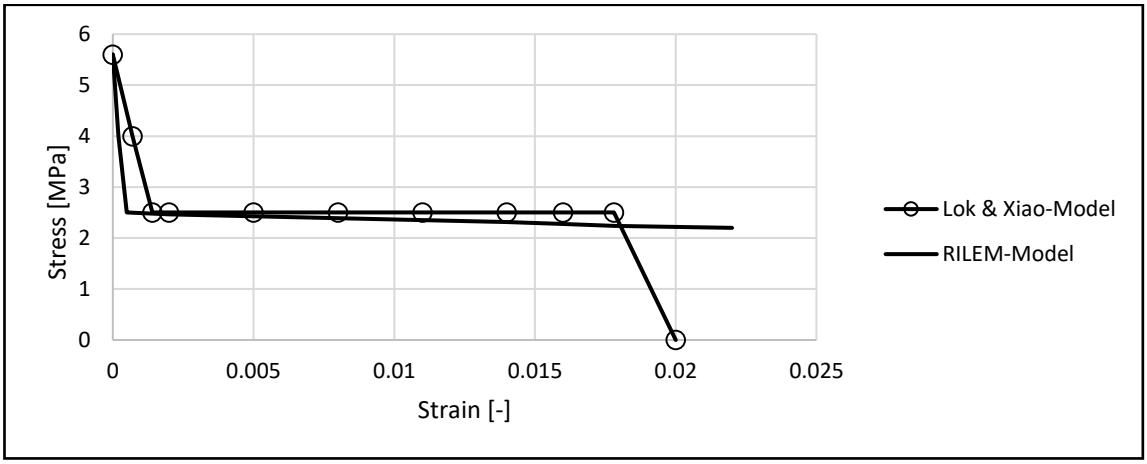

Figure 4.42: Tensile Stress-Strain Curve for Blanco et al SFRC Square Panel (2015)

80% tensile damaged and the SFRC plasticity parameters [ψ=40^0, ε= 0.1, f_{b0}/f_{c0}= 1.16, K=0.667 and μ= 0.006] were used for the ABAQUS-CDP. The compression and tensile stresses and damaged parameters values for both models are stated in Table 4.20.

Table 4.20: Compression and Tensile Parameters for Tlemat et al SFRC Beam 2005

	Yield Stress σ_c MPa	Compressive Damage Variable d_c	Inelastic Strain	Lok and Xiao (1999)			RILEM (2002)		
				Tensile Stress 'σ_t' MPa	Tensile Damage Variable d_t	Cracking Strain	Tensile Stress 'σ_t' MPa	Tensile Damage Variable d_t	Cracking Strain
1	18.4	0.00	0.00000	5.60	0.00	0.000	5.60	0.00	0.000
2	26.0	0.00	0.00024	4.00	0.08	0.0007	4.00	0.08	0.0002
3	33.2	0.00	0.00049	2.50	0.16	0.0014	2.50	0.16	0.0005
4	39.6	0.00	0.00074	2.50	0.24	0.002	2.46	0.24	0.002
5	45.0	0.00	0.00099	2.50	0.32	0.005	2.43	0.32	0.005
6	49.4	0.00	0.00124	2.50	0.40	0.008	2.39	0.40	0.008
7	52.5	0.00	0.00149	2.50	0.48	0.011	2.35	0.48	0.011
8	54.5	0.00	0.00178	2.50	0.56	0.014	2.31	0.56	0.014
9	54.6	0.00	0.00199	2.50	0.64	0.016	2.28	0.64	0.016
10	53.2	0.03	0.00228	2.50	0.72	0.018	2.24	0.72	0.018
11	49.7	0.09	0.00263	0.00	0.80	0.02	2.20	0.80	0.022
12	44.0	0.20	0.00303						
13	35.6	0.35	0.00351						

To curtail the problems connected with convergence, incremental loading rate of 0.5mm was applied through the displacement-loading up to 35mm at the centre of the panel. The Time and Frequency values adopted for the research work are from 0.00 – 10.00 and 0.00 – 1.00 at 0.1 and 0.01 intervals respectively. The crack patterns and Load-Displacement Curve of the experimental work and FEA for Blanco et al SFRC Square Panel (2015) are presented in Figures 4.43 and 4.44 respectively.

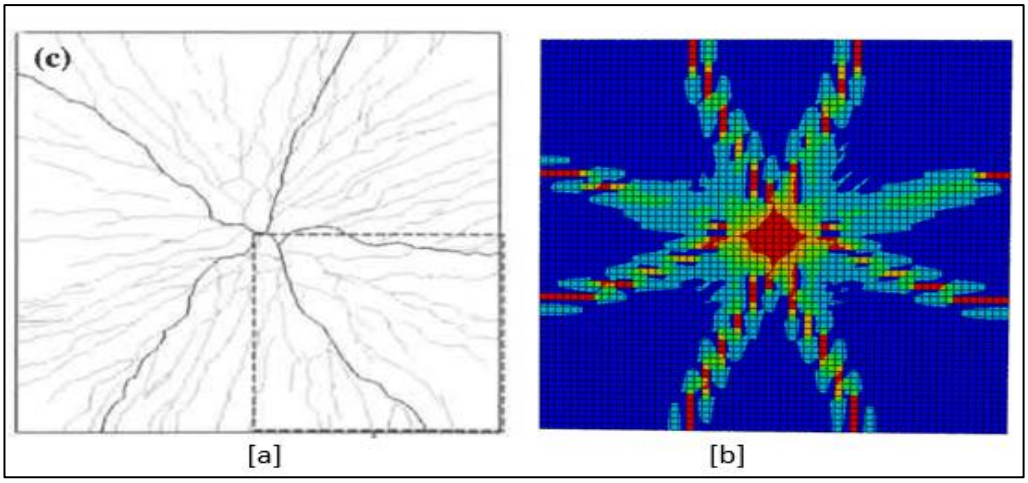

Figure 4.43: Crack Pattern Results [a] Experiment and [b] ABAQUS CDP of Blanco et al SFRC Square Panel (2015)

The crack pattern from the FEA agreed with the test results. The cracks started at the point of the application of load. The cracks radiate from the point of load application towards the corners at approximately 45^0. The first crack occurred at the centre of the panel at 271.17kN load with central displacement of 3.10mm. Due to continuous testing to destruction on the square-panel, the peak loads of 435.25kN was attained at a central displacement of 11.89mm. The panel finally collapsed at a load of 355.60kN with central displacement of 30.00mm.

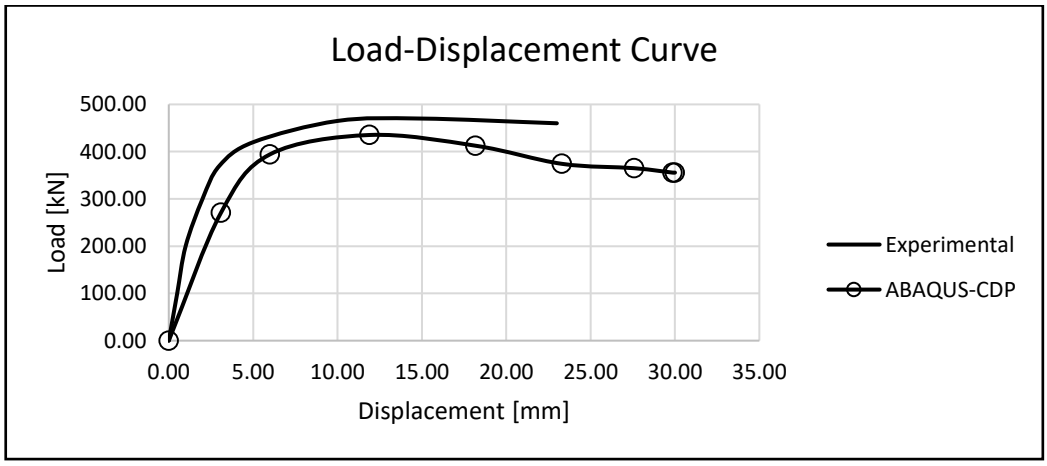

Figure 4.44: Load-Displacement Curve for Blanco et al. 's SFRC Square Panel (2015)

The FEA model is in good agreement with the experimental result. Similarly, the result shows that the Lok and Xiao proposed constitutive model in ABAQUS CDP produces acceptable result which is compatible with the experimental result. The FEA model was

less stiff (15%) than the experimental result. The maximum load from the FEA is 20% lesser than the experimental value.

4.3.3.3 R. de Montaignac, B. Massicotte, JP Charron & A. Nour Round Plate (2011)

Part of their research work was the testing of round plates, 800mm diameter supported by three supports at angle 120^0 with a clear space of 750mm diameter. The input parameter is as shown in Figure 4.27, Tables 4.11 and 4.12 on pages 153 and 154. The setup shown in Figure 4.45 shows an LVDT fixed to the base of the panel to measure the central displacement. The supports are placed at 120^0 to each other. Five mixes were used to produce the SFRC using hooked-end fibres.

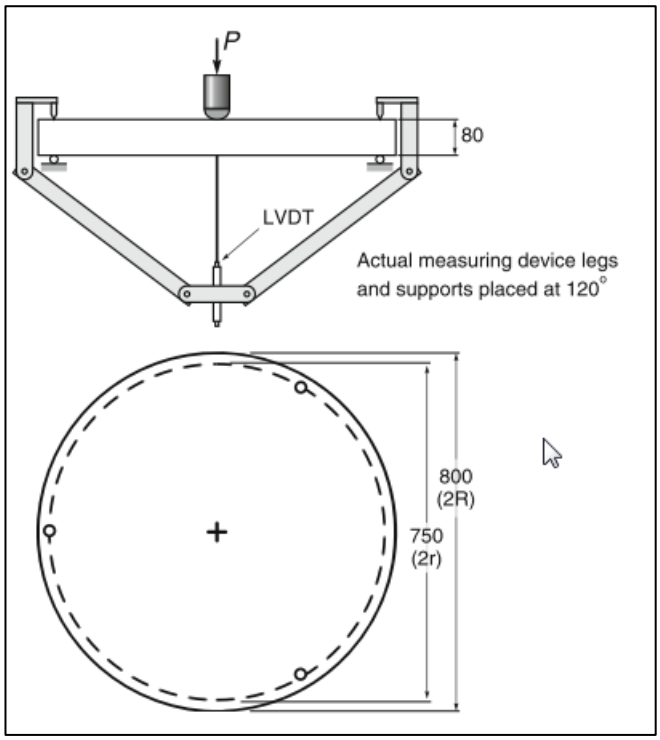

Figure 4.45: Experiment Set-up of Montaignac et al. RP (2011)

The hook-end steel fibre is 35mm long, 0.375mm in diameter, the aspect ratio of 80, a tensile strength of 2300MPa and a fibre dosage of 1.00%. The steel-fibre was added to the concrete matrix to form an SFRC with 46.9 MPa characteristic strength. The displacement loading of 40mm was applied at the centre of the panel at an incremental rate of 0.4mm. The Time-Frequency value was the same as that of 4.3.1.3.

Figures 4.46 and 4.47 show the crack patterns and Load-Displacement Curve from ABAQUS CDP. The crack pattern from the FEA agreed with the test results. The cracks started at the point of the application of load and moves at angle 120^0 to each other and in between two supports. Each leg of the cracks at the top of the panel [compression face] radiates to about half the radius of the panel while the legs at the soffit [tension face] radiates from the centre to the edge covering approximately 40^0.

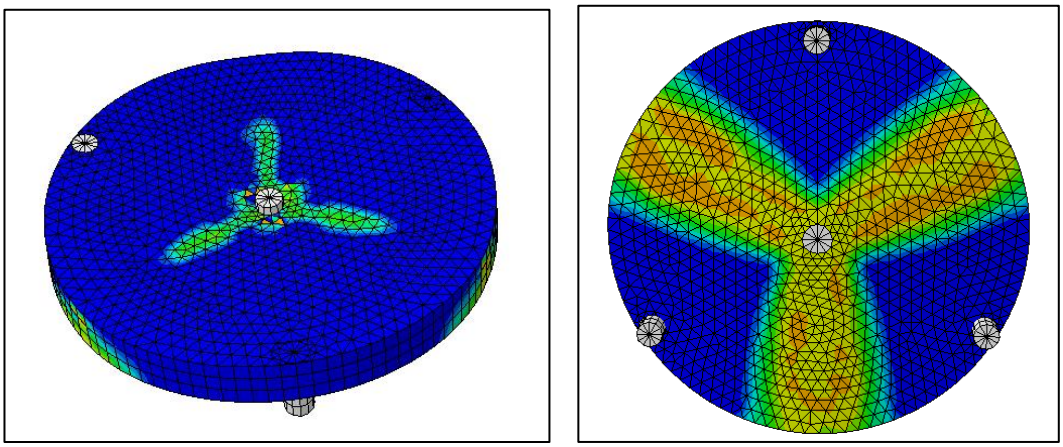

Figure 4.46: NLFEA Crack Patterns Top and Bottom [ABAQUS] Montaignac et al. Round Plate (2011)

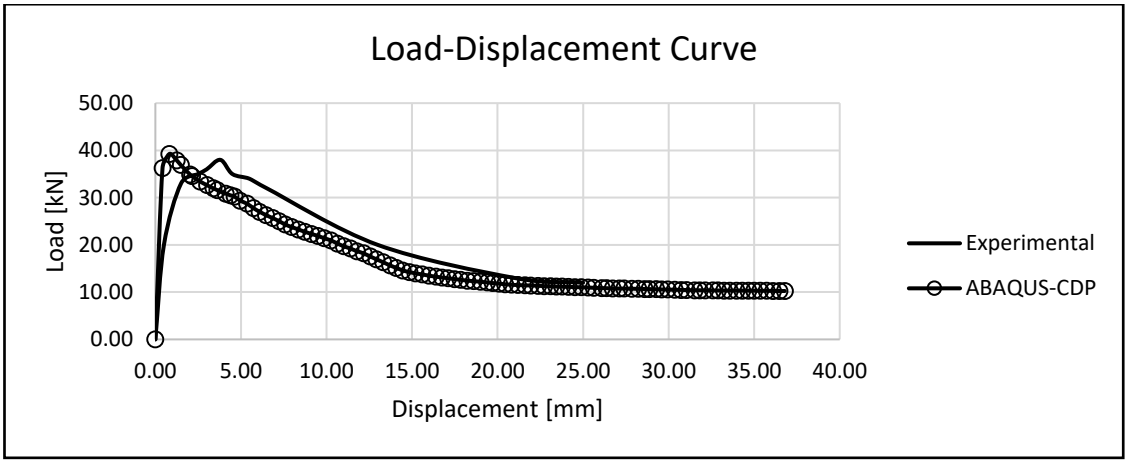

Figure 4.47: Load-Displacement Curve for Montaignac et al. Round Plate (2011)

The first crack appeared at the centre of the panel at 36.29kN load with central displacement of 0.42mm. As the loading continues slowly, the peak loads of 39.25kN was reached at a central displacement of 0.82mm. The panel finally collapsed at a central displacement of 36.79mm with 10.24kN load. The response of ABAQUS CDP [39.25kN at peak] agreed with the experimental results [38.00kN at peak], though

stiffer. At the peak load, the concrete cracked, and the fibre held the composite together while undergoing to softening behaviour.

4.3.3.4 Soranakom C., Mobasher B. and Destree X. Round Plate (2007)

The researchers used the response [load-displacement] of the tests on SFRC round panels with 1500mm span and 150mm thick, in the inverse analysis to determine the properties of material [Young modulus, tensile stress, Poisson's ratio]. The round panel was placed on a continuous simple support. The panel test was mainly for the characterisation of the materials. One cubic meter of the SFRC was made of 350kg Cement (type I), aggregate grading of 0-16mm, 60kg fly ash, 1.25% superplasticiser by volume, Undulated steel wire, TABIX 13/50 steel-fibres [1.3mm diameter, 50mm length and 900MPa tensile strength and 0.50 water-cement ratio.

Figure 4.48: Experimental Setup of Soranakom et al. Round Plate (2007)

The experimental setup is as displayed in Figure 4.48. The round panel tests involve flexure testing with the central loading of twelve [12] panels. At 28days, the average crushing strength of cube test was 43.7MPa. The panels were loaded to failure. Their crack patterns are shown in Figure 4.49 [a-c]

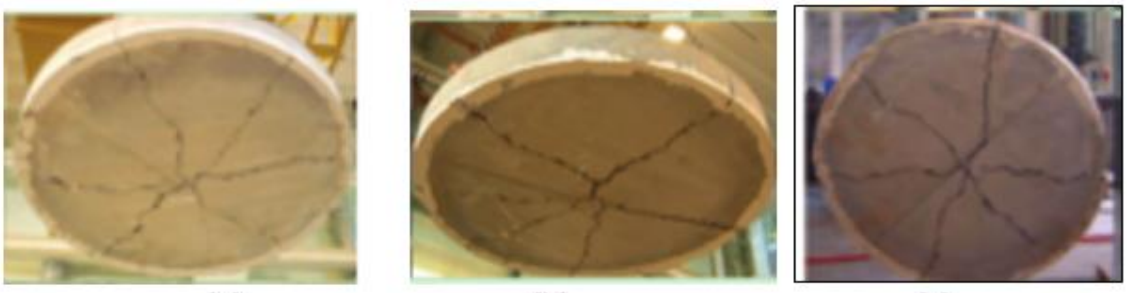

[a] [b] [c]

Figure 4.49: Crack Patterns of Soranakom et al. Round Plate (2007)

From the test results [Figure 3.49 a-c], it was observed that the crack pattern was different from one another [unpredicted regarding orientation and number of cracks] and this was attributed to the effect of the continuous supports. This is different from round panels with three [3] isolated supports that produces consistent three [3] symmetrical crack patterns.

Table 4.21 and Figure 4.50 describe the tensile stress and strain using the Lok and Xiao (1999) Model. A mesh size of 25mm and bond stress of 3.5MPa was were used for the analyses.

Table 4.21: Tensile Stress-Strain for Soranakom et al. Round Plate (2007)

	Lok and Xiao (1999)	
Point	Strain [$^0/_{00}$]	Stress [MPa]
Peak Tensile Stress	0.00	2.40
Point II	0.90	1.25
Point III	17.8	1.25
Point IV	20.0	0.00

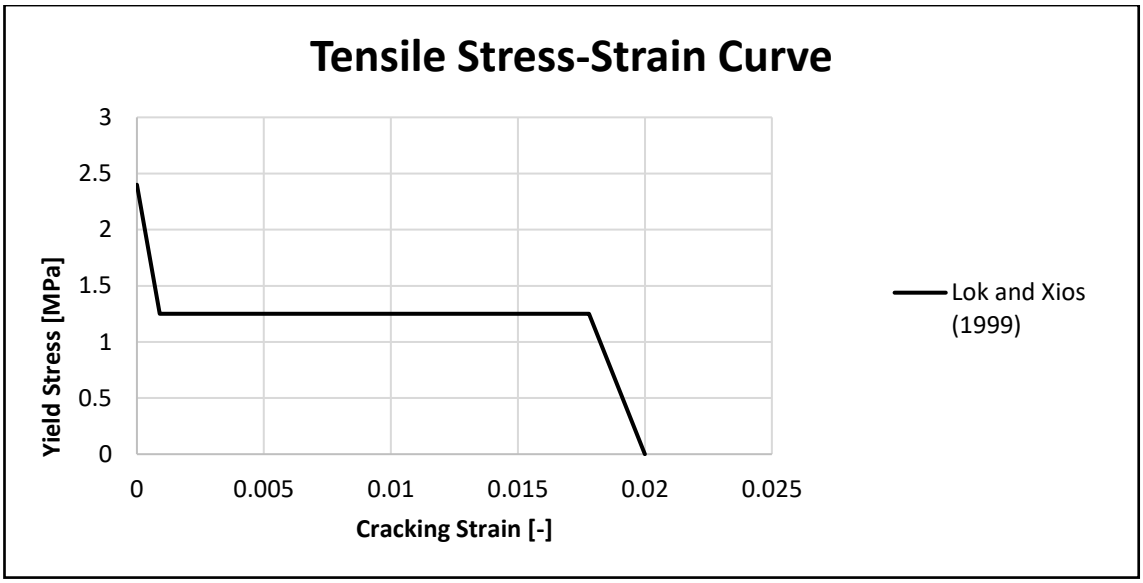

Figure 4.50: Tensile Stress-Strain Curve for Soranakom et al. Round Plate (2007)

The ABAQUS-CDP has 80% tensile damaged with the plasticity parameters taken as: ψ=40^0, ε= 0.1, f_{b0}/f_{c0}= 1.16, K=0.667 and μ= 0.006. The compression and tensile stresses and damaged parameters are provided in Table 4.22.

Table 4.22: Compression and Tensile Parameters for Soranakom et al. Round Plate (2007)

	Yield Stress σ_c MPa	Compressive Damage Variable d_c	Inelastic Strain	Lok and Xiao (1999)		
				Tensile Stress 'σ_t' MPa	Tensile Damage Variable d_t	Cracking Strain
1	16.5	0.00	0.00000	2.40	0.00	0.000
2	23.0	0.00	0.00024	1.25	0.08	0.001
3	28.9	0.00	0.00049	1.25	0.16	0.003
4	33.9	0.00	0.00074	1.25	0.24	0.006
5	37.8	0.00	0.00099	1.25	0.32	0.008
6	40.6	0.00	0.00124	1.25	0.40	0.010
7	42.4	0.00	0.00149	1.25	0.48	0.012
8	42.9	0.00	0.00178	1.25	0.56	0.014
9	42.3	0.01	0.00201	1.25	0.64	0.016
10	40.4	0.06	0.00232	1.25	0.72	0.018
11	37.1	0.14	0.00266	0.00	0.80	0.020
12	32.4	0.25	0.00305			
13	26.1	0.39	0.00348			

The flexural behaviour of the round panel was modelled using ABAQUS-CDP in the nonlinear state. To capture the panel [and due to the use of the high-performance computers available in UEL], the full panel was modelled using a 3-D brick model with 25mm mesh. The loading on the round panel was modelled using static analysis using displacement-based loading. To vary the amount of the loading, time-frequency of 0-10 [at 0.1 increment] with an amplitude of 0-1 [at 0.01 increment].

The compressive and shear stresses are assumed to develop within the elastic range thus guided by the elastic properties of the material [young's modulus and Poisson's ratio]. The tension behaved elastically until it cracks and then conform to the tensile-strain (Loks and Xiao, 1999) relationship afterwards. The pictorial results are shown in Figure 4.51.

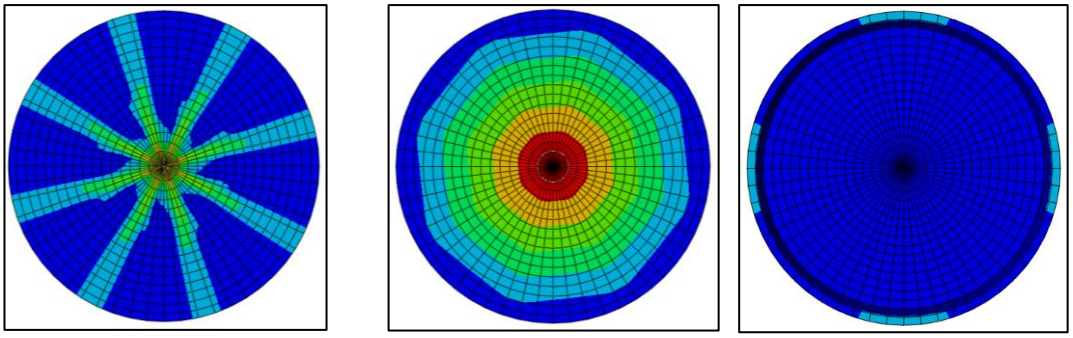

[a] [b] [c]

Figure 4.51: NLFEA Results of Soranakom et al Round Plate (2007) [a] Crack Pattern [b] Displacement and [c] Reaction at the support

The first crack appeared at the tension face directly under the point of load application with 130.29kN load and central displacement of 1.22mm. As the loading continues gradually, the peak load of 140.09kN was attained at a central displacement of 2.20mm.

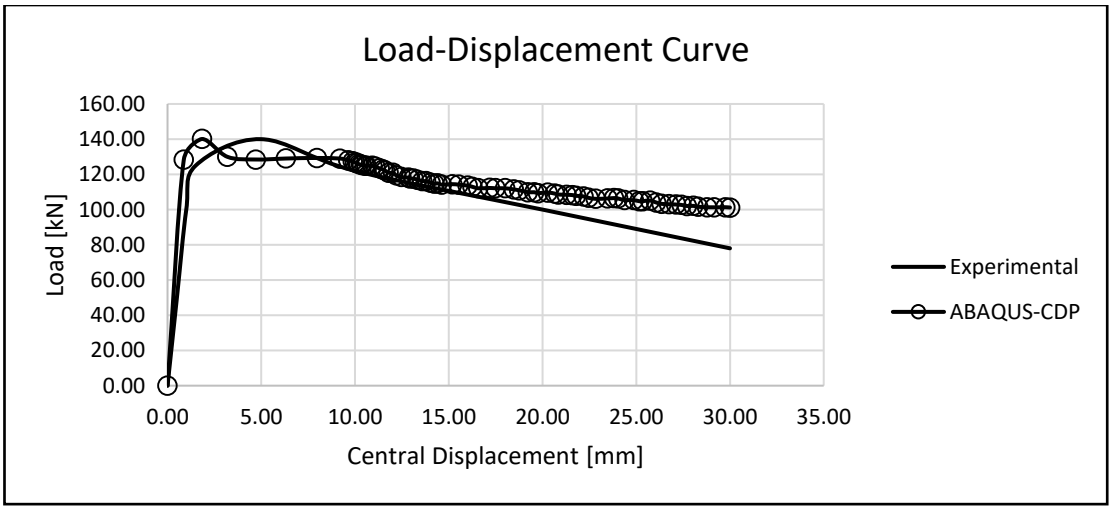

Figure 4.52: Load-Displacement Curve for Soranakom et al. Round Plate (2007)

The Young's modulus controls the rising elastic response of the curve from the origin up to the first crack. The point that the load-displacement curve diverges from the linear elastic response correlates with the tensile strength parameter f_t. The maximum load is governed by the first softening of the slope and the f_t while the post cracking response is governed by the tensile stress-strain parameters (Loks and Xiao, 1999). The load-displacement curve was plotted [Figure 4.52] which shows the experimental result with an ultimate load of 138.6kN. The NLFEA gave an ultimate load of 140.09kN. This is 1.08% higher than the experimental value.

4.3.3.5 Bernard E.S (2000) Round Plate

One of the earliest works on SFRC round plate was undertaken by Bernard (2000). The primary aim of the work was to examine the methods of testing round SFRC panels in order to acquire the empirical estimates of post-crack load capacity due to the application of point loads. Several [60 for each specimen] round plates [500, 800 and 980mm diameter] with 25, 50 and 75mm thickness respectively were cast and tested. The plates considered in this report were simply supported along the perimeter with a clear span of 300, 600 and 850mm respectively [Figure 4.53].

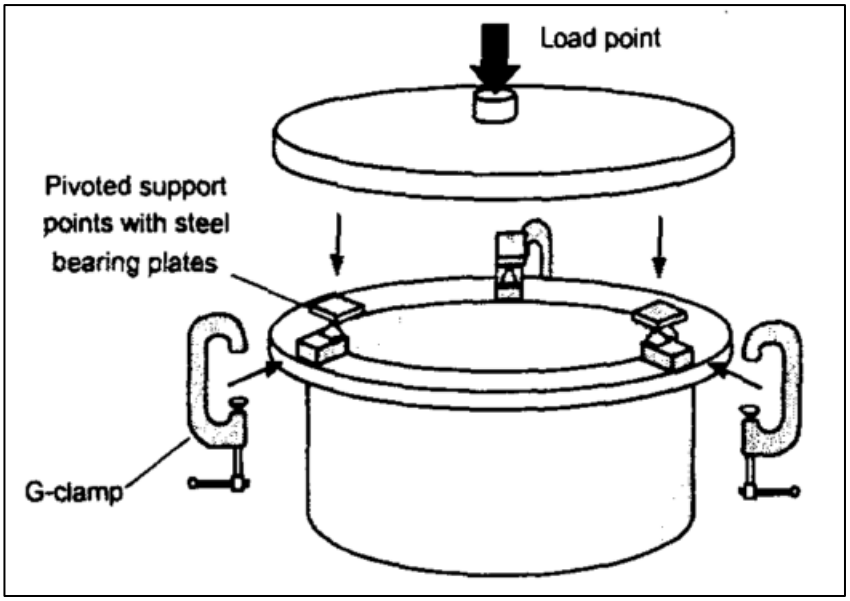

Figure 4.53: Experimental set-up for Bernard (2000) Round Plate

The setup involves three types of restraints; clamped in 3 points at angle 120^0, simply supported and quasi-continuous edge restraint. The restraint considered in this report is that of simple support. The results from the cylindrical uni-axial compression tests have an average compressive strength of 68MPa, concrete modulus of elasticity of 38700MPa with average energy absorption of 1160J.

The tensile stress and strain behaviour is depicted using the Lok and Xiao (1999) Model and provided in Table 4.23 and Figure 4.54. A mesh size of 25mm and 4.5MPa bond stress were used for the analyses.

Table 4.23: Tensile Stress-Strain for Bernard (2000) Round Plate

	Lok and Xiao (1999)	
Point	Strain [$^0/_{00}$]	Stress [MPa]
Peak Tensile Stress	0.00	4.50
Point II	1.00	2.45
Point III	17.8	2.45
Point IV	20.0	0.00

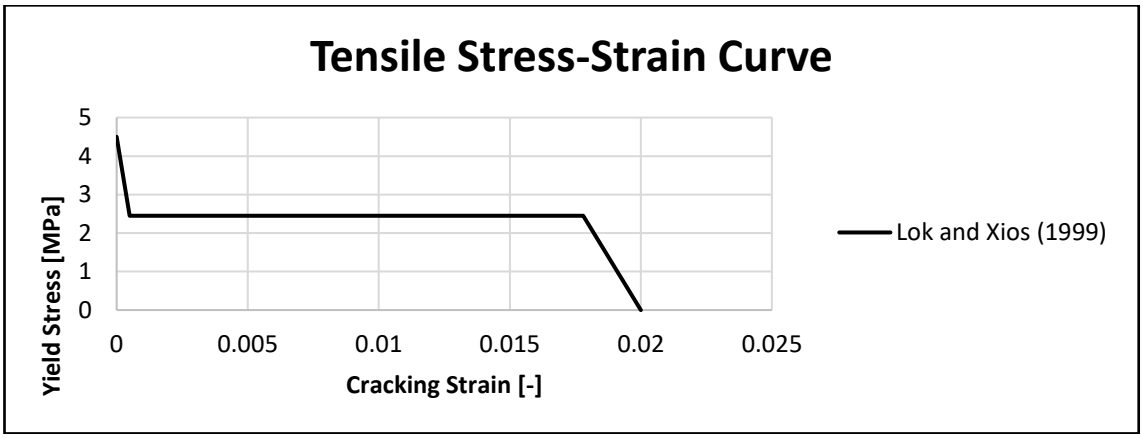

Figure 4.54: Tensile Stress-Strain Curve for Bernard (2000) Round Plate

The analysis was carried out using ABAQUS-CDP with 80% tensile damaged and the plasticity parameters taken as: ψ=40^0, ε= 0.1, f_{b0}/f_{c0}= 1.16, K=0.667 and μ= 0.006. The compression and tensile stresses and damaged parameters are provided in Table 4.24.

Table 4.24: Compression and Tensile Parameters for Bernard (2000) Round Plate

	Yield Stress σ_c MPa	Compressive Damage Variable d_c	Inelastic Strain	Lok and Xiao (1999)		
				Tensile Stress 'σ_t' MPa	Tensile Damage Variable d_t	Cracking Strain
1	20.9	0.00	0.00000	4.50	0.00	0.000
2	30.1	0.00	0.00024	2.45	0.08	0.0005
3	39.2	0.00	0.00049	2.45	0.16	0.0007
4	47.7	0.00	0.00074	2.45	0.24	0.002
5	55.5	0.00	0.00099	2.45	0.32	0.005
6	62.4	0.00	0.00124	2.45	0.40	0.008
7	68.2	0.00	0.00149	2.45	0.48	0.011
8	73.2	0.00	0.00178	2.45	0.56	0.014
9	**75.4**	**0.01**	0.00201	2.45	0.64	0.016
10	**75.9**	**0.00**	0.00224	2.45	0.72	0.0178
11	**73.5**	**0.03**	0.00255	0.00	0.80	0.020
12	**67.2**	**0.12**	0.00296			
13	**55.3**	**0.27**	0.00350			

Using the Universal Testing Machine [UTM] under displacement-controlled loading, the panels were tested to failure. A 100mm diameter ram imposed the load at an average rate of 7.5mm/min. This continued until the load capacity of slab dropped significantly. Since the flatness of the specimen cannot be completely flat, the failure pattern varies. However, on the average, 4-8 cracks radial from the centre towards the circumference [Figure 4.55].

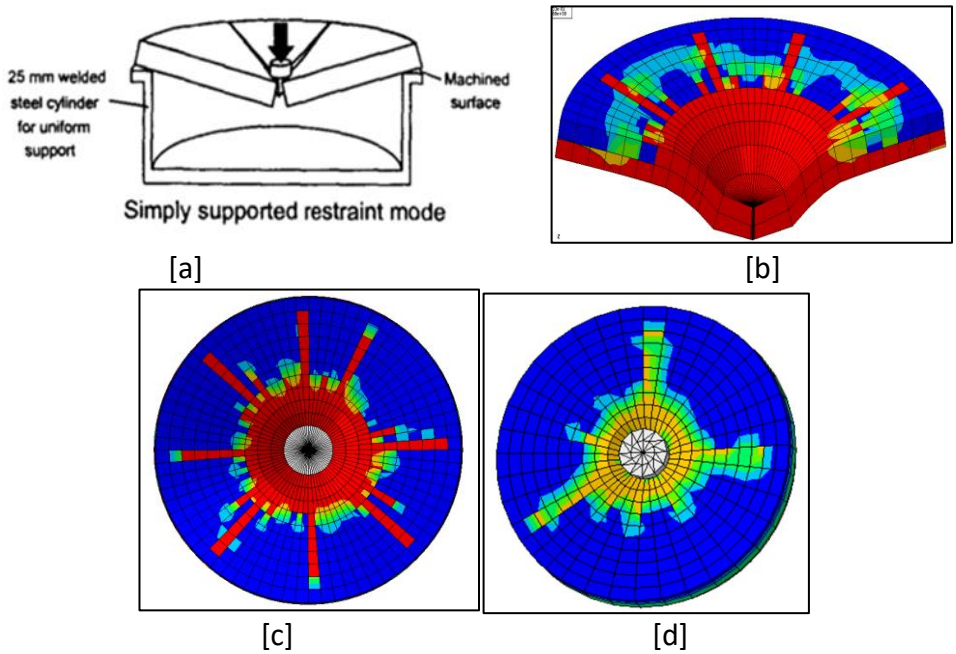

Figure 4.55: Crack Patterns in Bernard (2000) Round Plate [a] pictorial diagram of collapse mechanism [b] x-z section of the damaged panel through the centre [c] FEA crack pattern at full damage [d] FEA crack propagation at early stage

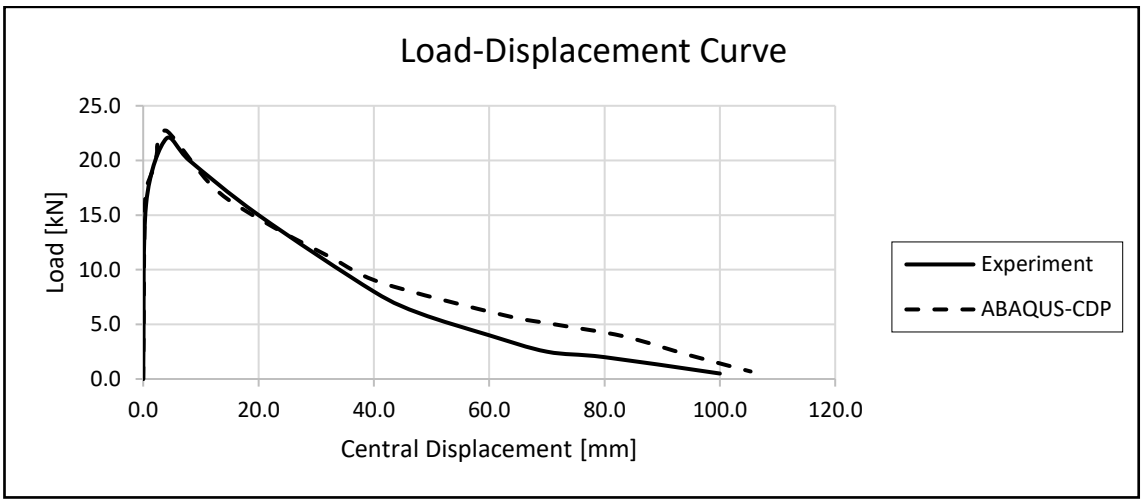

Figure 4.56: Load-Displacement Curve for Bernard (2000) Round Plate

The load-displacement history for the simply supported round-plate was characterised by a less rapid rate of unloading after the first crack. This resulted in higher residual loading capacity at the centre of the panel. The crack patterns reported by the researcher in the experiment shows a great level of inconsistencies, which was also noticed in the FEA output. This also shows that there is some amount of friction between the upper surface of the round panel and the loading ram. The load-displacement curve in Figure 4.56 shows an agreement between the experiment and the FEA. The ABAQUS CDP prove to be compatible in modelling Bernard's round-plate.

4.4 Full-Scale Testing

This section is based on tests performed on slabs detailed to the actual size of what is obtainable on the field. This is necessary to compare the response of the test cases to expectations and guidelines on the field.

4.4.1 Destree X and Mandl J. (2008) Square Slab

In a series of testing to destruction spanning over 15 years and in the bid to understand the mechanism of total replacement of rebar with steel-fibres in a slab, the research work was undertaken. It investigated the structural behaviour of a structural SFRC slab. The 3100mm square slab and 160mm thick were supported at the four corners with square columns 210mm wide to depict typical pile-supported slab [Figure 4.55]. The span/depth ratio is 19. The concrete matrix contains a 45kg/m3 dosage of steel fibres [0.56%].

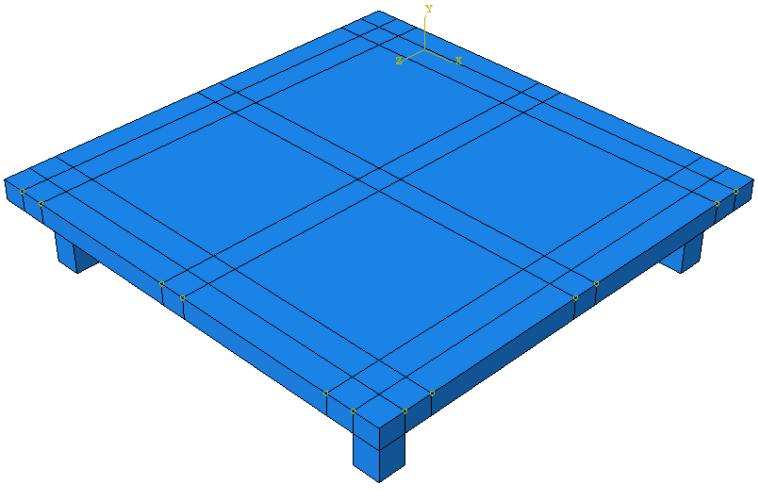

Figure 4.57: FE representation of the Test set-up for Destree and Mandl (2008)

To determine the response of the slab under the serviceability limit state, the slab was then loaded with water barrels up to service loads. From the test, it was noticed that there were no cracks. For the ultimate limit state test, the slab was loaded centrally.

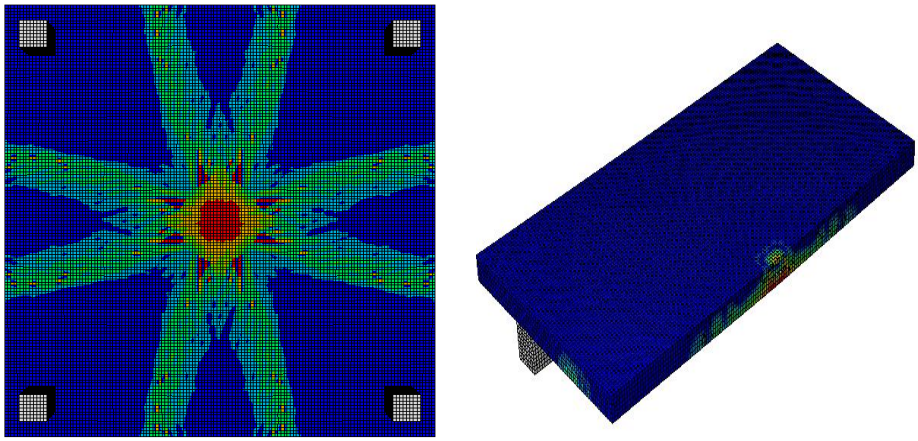

Figure 4.58: FEA Results showing Cracking Pattern at (a) bottom and (b) internal

The crack pattern radiates from the point of the application of loading and moves gradually towards the edges [Figure 4.56]. This is the characteristic of plates supported at the corners. Table 4.5 shows the comparison of test results with FEA for Destree and Mandl (2008)

Table 4.25: Comparison of Test results with FEA for Destree and Mandl (2008)

Experiment			FEA		Cal
	Load at First Crack [kN]	ULS Load [kN]	Load at First Crack [kN]	ULS Load [kN]	SLS Load [kN]
Mid span	110	450	105	446	85
Corner	80	180	75	178	58

4.4.3 Thooft (1999) Pile supported slabs

In the works on the design of steel fibre reinforced floors on foundation piles, pile caps were avoided mainly because of the possibility of restraining due to horizontal soil interaction. The test was aimed at investigating the load bearing capacity and deformation of a suspended floor made from Dramix fibre. The 5000mm square slab was supported by nine [9] columns, 200mm diameter and 2000mm apart. The thickness of the slab was put at 140mm [Figure 4.57]. The loading ram, 300mm square, was placed

at the centre of each span of the slab. The columns settlement was also monitored for uneven settlement.

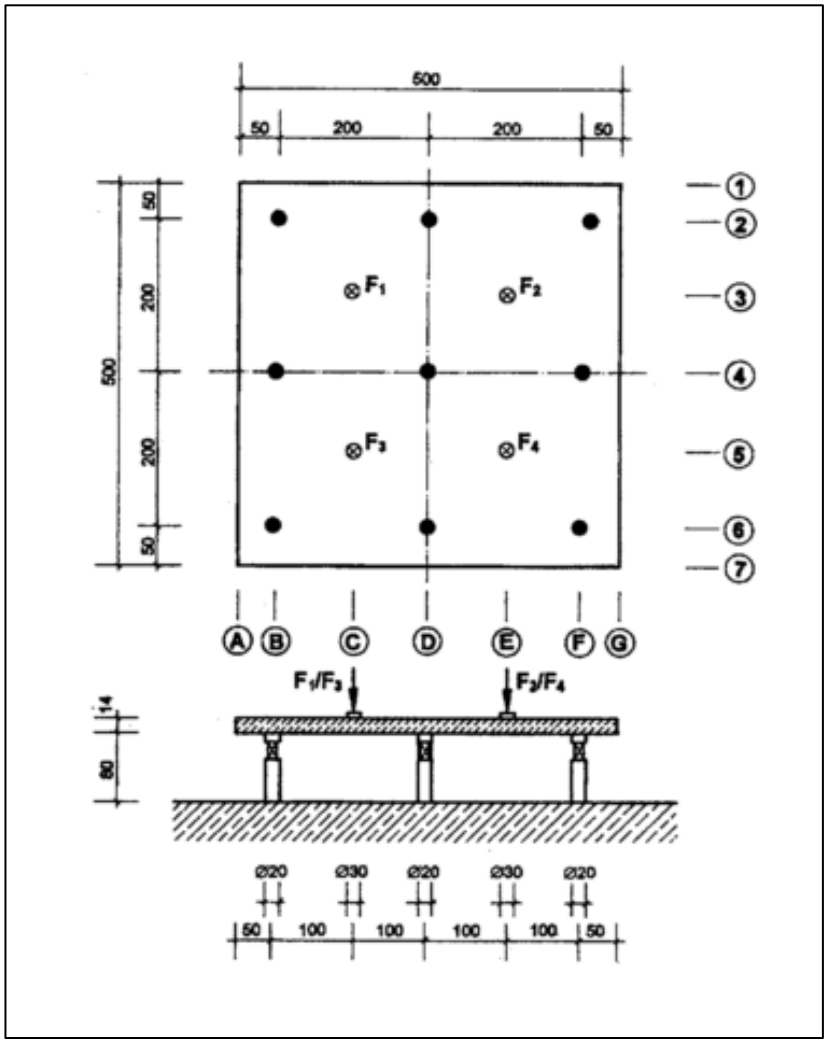

Figure 4.59: Experimental Set-up of Thooft (1999) 4-Panels Slab

The SFRC matrix is made of 360kg/m^3 of cement, 1748kg/m^3 of aggregates [sand and gravel], 100kg/m^3 fly ash and 0.5% plasticizer. The Dramix 80/60-BN was added in the batching plant to achieve a compressive strength of 45MPa. The steel-fibre is 60mm long and 0.75mm in equivalent diameter. The test was monitored by the use of equipment which is computer controlled.

25mm mesh and 4.5MPa bond stress were used in this analysis. The tensile stress and strain behaviour as described by the Lok and Xiao (1999) constitutive Model are provided in Table 4.26 and Figure 4.60.

Table 4.26: Tensile Stress-Strain for Thooft (1999) Pile-Supported Slab

	Lok and Xiao (1999)	
Point	Strain [$^0/_{00}$]	Stress [MPa]
Peak Tensile Stress	0.00	5.60
Point II	1.00	1.25
Point III	18.0	1.25
Point IV	20.0	0.00

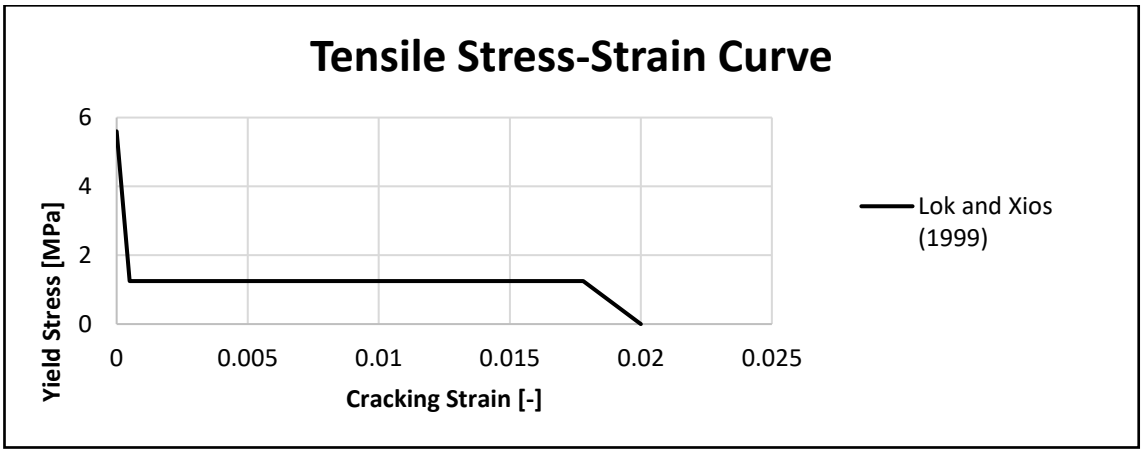

Figure 4.60: Tensile Stress-Strain Curve for Thooft (1999) Pile-Supported Slab

The analysis was carried out with ABAQUS-CDP using the same plasticity parameters as in section 4.3.3.5. The compression and tensile stresses and damaged parameters are provided in Table 4.27.

Table 4.27: Compression and Tensile Parameters for Thooft (1999) Pile-Supported Slab

	Yield Stress σ_c MPa	Compressive Damage Variable d_c	Inelastic Strain	Lok and Xiao (1999)		
				Tensile Stress 'σ_t' MPa	Tensile Damage Variable d_t	Cracking Strain
1	16.7	0.00	0.00000	5.60	0.00	0.000
2	23.3	0.00	0.00024	1.25	0.08	0.001
3	29.3	0.00	0.00049	1.25	0.16	0.001
4	34.4	0.00	0.00074	1.25	0.24	0.006
5	38.5	0.00	0.00099	1.25	0.32	0.008
6	41.5	0.00	0.00124	1.25	0.40	0.010
7	43.3	0.00	0.00149	1.25	0.48	0.012
8	44.0	0.00	0.00178	1.25	0.56	0.014
9	43.4	0.01	0.00201	1.25	0.64	0.016
10	41.5	0.06	0.00231	1.25	0.72	0.018
11	38.2	0.13	0.00266	0.00	0.80	0.020
12	33.4	0.24	0.00305			
13	26.9	0.39	0.00349			

The load was applied at intervals of 5kN. The peak load of 81.6kN was reached at a displacement of 3mm. In the FEA, the peak load of 74.09kN was reached after cracking at 3.99mm. The first cracking occurred at 2.54mm with a cracking load of 70.33kN [Figure 4.60]

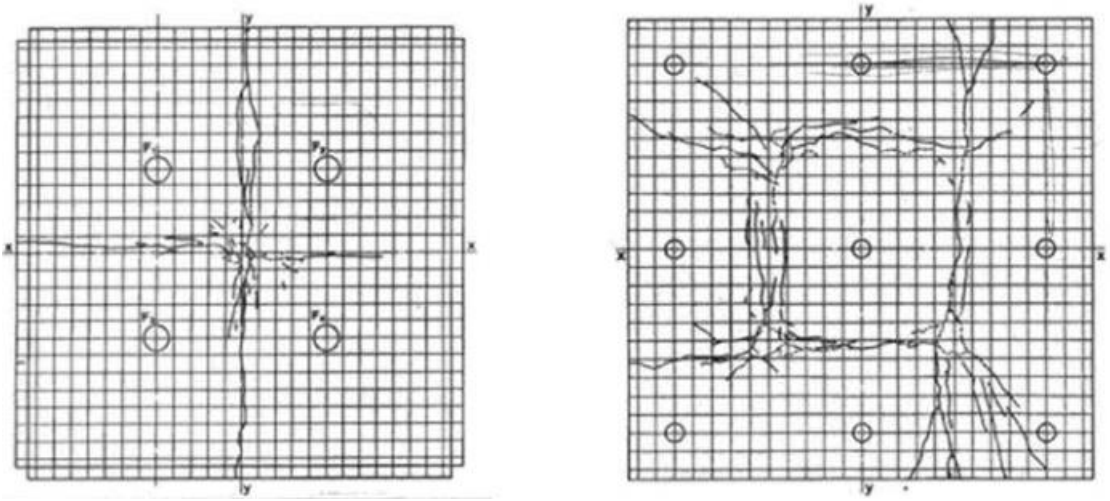

Figure 4.61: Top and Bottom face after cracking in Experimental work (Thooft, 1999)

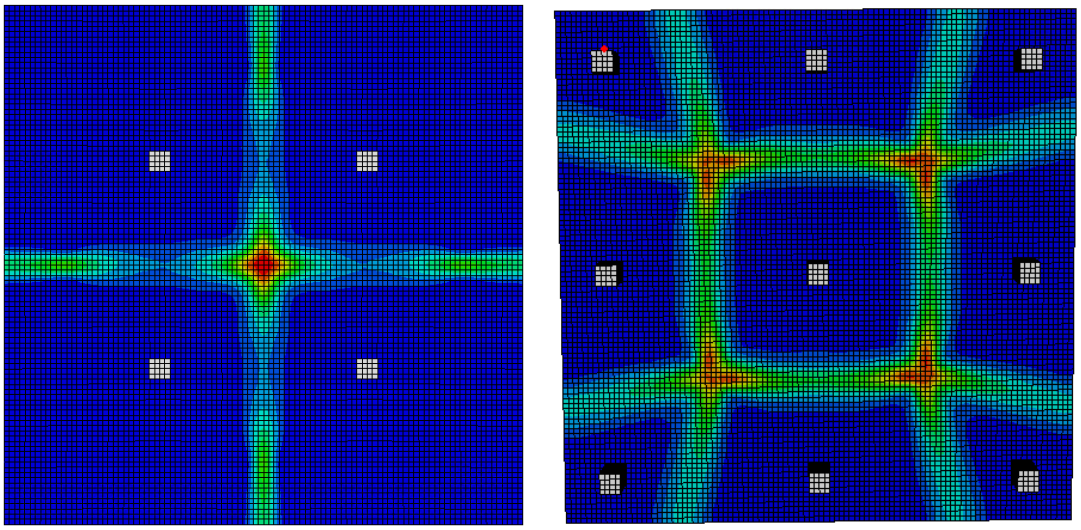

Figure 4.62: FEA Results showing Cracking Pattern at (a) Top and (b) Bottom

The crack patterns of the test are shown in Figures 4.61 and 4.62. This shows crack lines at the top from one middle column at the edges to the other end passing through the column at the centre. At the bottom of the slab, the pattern was a fan like around the central column and radiating out to all the edges. A theoretical calculation done by Thooft gave an ultimate load of 72.8kN which is 1.5% lower than the NLFEA result and 10.8% lesser than the experimental result.

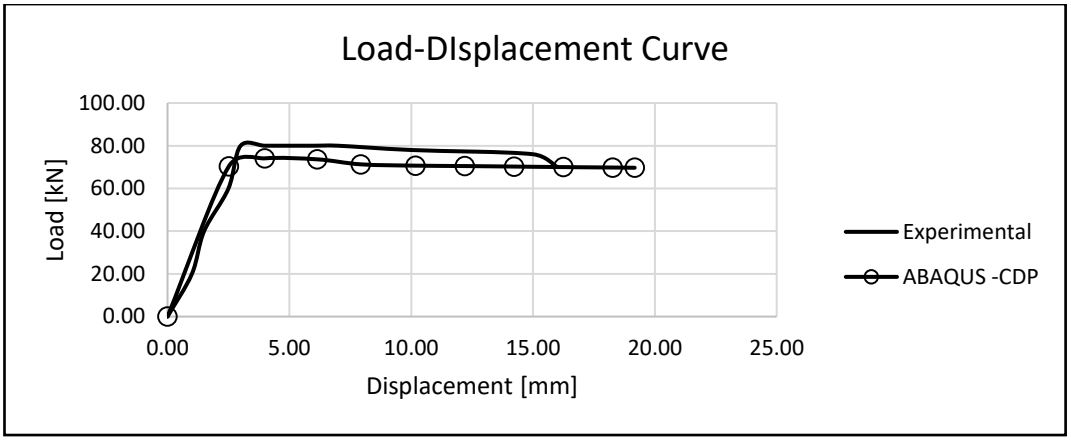

Figure 4.63: Load-Displacement Curve for Thooft (1999) Pile-Supported Slab

It was seen that the NLFEA results conform greatly to the experimental results. The peak load of the NLFEA was 9.2% lower than the experimental result while the displacement is 24.8% higher. The crack pattern of the NLFEA follows the same mode as that of the experimental test.

4.4.4 Barros J.A.O., Salehian H., Pires N.M.M.A and Goncalves D.M.F (2012)

In their research work, steel fibre reinforced self-compacting concrete [SFRSCC] was developed to guide against the use of vibrators as this can make the steel-fibres pull downward because of their higher weight compared to other concrete materials. This resulted in the construction of elevated steel fibre reinforced concrete [ESFRC] slab. An ESFRC structural system, 14.8 x 8.4 x 0.3m [L x B x h], supported by 12 columns [Figure 4.61] was modelled to a ¼ scale [Figure 4.64]. The columns are 1.2m and 1.0m centres apart in Y and X directions respectively in the model. The columns are anchored at the base by a ground supported slab.

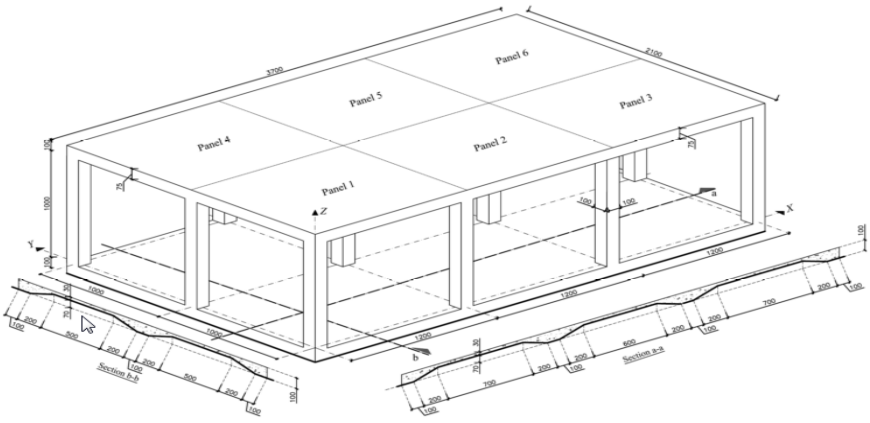

Figure 4.64: Geometry of the built prototype (Barros et al. 2012)

The developed SFRSCC was used to build the prototype for testing. The columns have four bars of diameter 6mm. The developed SFRSCC was made up of the materials shown in Table 4.28.

Table 4.28: Composition of SFRSCC per m^3 of concrete

Cement (kg)	Water (kg)	Super plasticiser (kg)	Limestone Filler (kg)	Fly ash (kg)	Fine river sand (kg)	Coarse river sand (kg)	Crushed granite (kg)	Fibres (kg)
408	150	6.26	395	73	263	658	446	90

The hooked-end steel fibres, 37mm long, 0.5mm equivalent diameter were used. The tensile strength is 1100MPa. The compression test results after 28 days using the cylindrical tests give a mean compressive strength of 65.96MPa and Young's modulus of 40400MPa.

The prototype [Figure 4.65] was first loaded with uniform distributed load [UDL] over panels in the serviceability limit state. A total of 3.5kN/m^2 load was placed on the panels in different load cases using water tanks.

Figure 4.65: Prototype model of Barros et al. (2012)

The ABAQUS was used for the FEA analysis. The simulation produces a strong alignment with the experimental results. Figures 4.66 and 4.67 show the crack patterns from FEA.

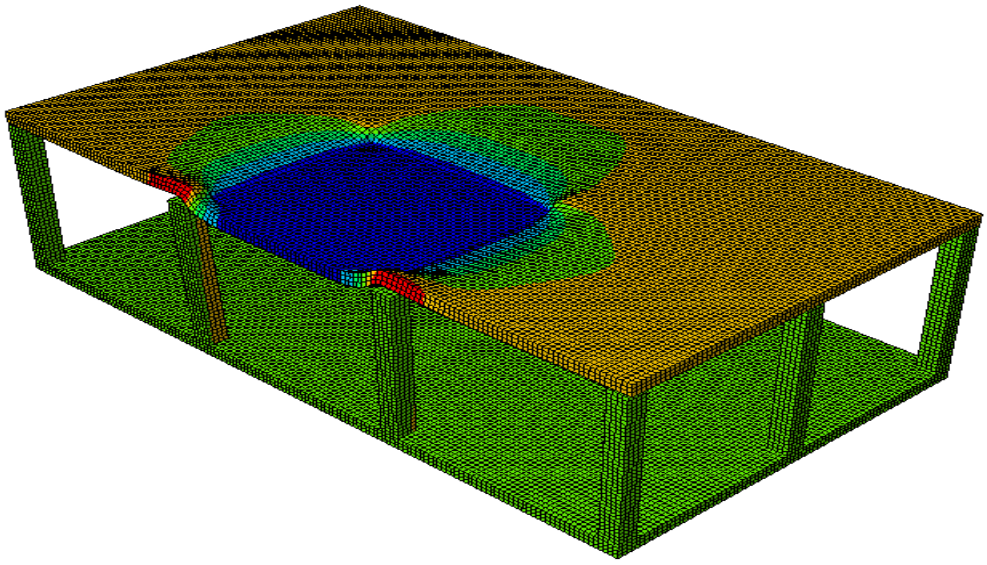

Figure 4.66: FEA Modelling of Barros et al. (2012) slab

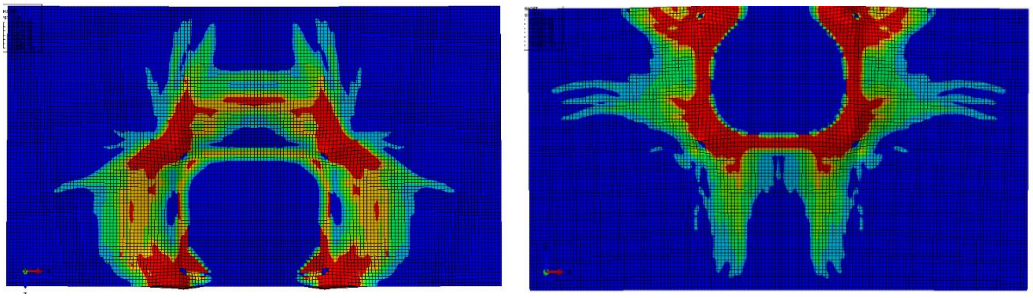

[a] [b]

Figure 4.67: FEA Crack pattern of Barros et al. slab [a] top and [b] bottom

4.5 Summary of Validation works

The Table 4.29 gives the summary of the validation works done with FEA. The ratio between the experiment and FEM displacement and peak load show the validation of the material model adopted for this research work.

Table 4.29: Comparison of FEM and Experimental Results

Name of Researchers	Type	f_c MPa	L [m]	b [mm]	d [mm]	δ_{exp}	δ_{FEM}	$\frac{\delta_{FEM}}{\delta_{exp}}$	P_{exp}	P_{FEM}	$\frac{P_{FEM}}{P_{exp}}$
Bresler & Scordelis 1963	RC Beam	22.5	4.1	310	556	6.6	6.8	1.03	330.0	334.0	1.01
Hughes & Speirs 1982	RC Beam	44.4	3.0	100	200	23.0	17.4	0.76	30.0	29.9	0.99
Barros et al 2005	SFRC Beam	25.0	0.6	150	150	0.70	0.33	0.47	18.5	18.55	1.00
de Montaignac et al 2011	SFRC Beam	46.9	0.6	150	150	0.70	0.85	1.21	22.0	20.07	0.91
Tlemat et al 2006	SFRC Beam	54.1	0.55	150	150	0.09	0.20	2.22	30.0	29.4	0.98
Olivito et al 2010	SFRC Beam	47.8	0.6	150	150	0.07	0.13	1.85	24.0	22.93	0.96
Bernard (2000)	SFRC RP	38.7		600	50	4.0	4.2	1.05	22.0	22.66	1.03
Hadi 2008	SFRC SP	13.9	0.82	820	80	1.60	1.50	0.94	22.0	22.42	0.89
Blanco et al 2015	SFRC SP	46.7	1.5	1500	200	12.3	10.5	0.85	427.0	423.3	0.99
de Montaignac et al 2011	SFRC RP	46.4	0.8	800	150	3.8	0.51	0.13	38.0	38.20	1.01
Destree et al 2007	SFRC RP	43.7	1.5	1500	150	5.0	1.83	0.37	140.0	140.0	1.00
Thooft 1999	SFRC 4-P	45.0	5.0	5000	140	4.0	3.98	0.99	84.0	85.80	1.02

Note: *SP – Square Panel *RP – Round Panel *4-P – 4 Panels

4.6 Summary

FEAs are computer-based numerical methods for demonstrating the behaviour [performance and capacity] of any engineering structures. In this thesis, the FEAs are used to determine the responses [yield and ultimate load capacity, central displacement, stress distributions, deflected shapes and crack patterns] of the whole test specimen [beams and slabs]. Several FE models different modelling assumptions, parameters, boundary conditions, and different loading conditions were used to represent the SFRC elements at material and structural levels. This chapter highlights the significance of selecting an appropriate and effective finite element type, the constitutive model and adequate mesh size. The primary purpose is to achieve an accurate result when compared with the experimental studies. The FEA results were sensitive to the material constitutive models and mesh sizes, which validate the impartiality of the modelling method used in this research work.

Considering the FE modelling results for the validation and calibration work presented in this Chapter, it can be observed that both the numerical predictions and their corresponding experimental results are in good agreement with one another (even in cases where there were some slight differences, the FE-based results are within 15% of the experimental data). Concrete damaged plasticity CDP model and the SFRC model proposed by Lok and Xiao (1999) incorporated into it gave the best results and in good agreement with experimental data, confirming the ability of the two models to effectively capture the critical features of concrete tensile behaviour, namely brittleness and cracking. Therefore, the SFRC tensile model by Lok and Xiao (1999) and the ABAQUS CDP models were adopted for successive parametric studies in the present research work.

Chapter 5: CASE STUDY 1: SIMPLY SUPPORTED SINGLE SLABS UNDER POINT LOAD

5.1 Introduction

Case study 1 deals with three number single SFRC panel slabs. The results of these cases as examined using NLFEA using ABAQUS [the description of the models used are presented in Chapter 3]. The first two were based on the experimental works on round plates with isolated and continuous supports (de Montaignac et al., 2011, Soranakom et al., 2007). Case study 1A centred on an SFRC round plate with three [3] isolated footings under monotonic loading. The initial FE models were calibrated based on the experimental works of (de Montaignac et al., 2011) on round SFRC plates. Case study 1B centred on SFRC round plate with continuous support along the edge under monotonic loading initially calibrated with the works of (Soranakom et al., 2007). They were used to study SFRC round plates [slabs] at the material level under central static monotonic loading. The third part of the Case Study 1, [C] was based on the SFRC square slab initially calibrated based on the experimental work of (Blanco et al., 2015) under monotonic loading. The experimental work examined the effect of adding fibres to suspended panels up to 1.5%. This case study extended the fibre volume ratio to full range as practically obtainable in the industry.

5.2 Case Study 1A: R. de Montaignac, B. Massicotte, JP Charron & A. Nour Round Plate (2011)

The post-cracking behaviour of SFRC structural elements was the thrust of their research works. The experimental work involves simply supported beams and round-plates consisting of six [6] specimens for each SFRC mix with varying amount of steel fibres [0.75-1.25%]. The mechanical properties of the SFRC round-plate [labelled F35-1.0] chosen for this study in compression made were made from 1% volume fraction of fibres are compressive strength 46.9MPa, modulus of elasticity 33.5GPa and Poisson ratio of 0.23 while the post-cracking tensile strength of 2.6MPa was gotten from the uniaxial test. The hooked-end steel-fibre used in the concrete matrix has an aspect ratio of 67.2 and a length of 35mm. The strength of the steel fibre is 1200MPa.

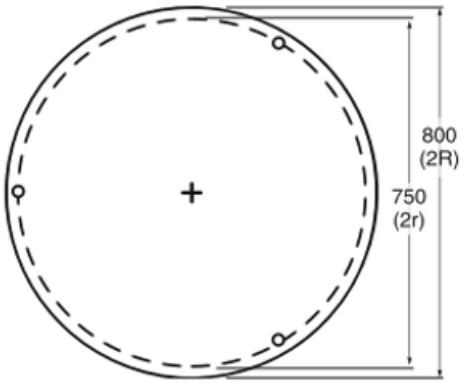

Figure 5.1: Dimensions of Round-Plate adapted from (de Montaignac et al., 2011)

NLFEA were carried out in 3D using the ABAQUS model and Lok and Xiao constitutive models [as discussed in Chapter 3]. Taking advantage of the high-performance computer in UEL, the full size of the round-plate was modelled (i.e. 800 mm in diameter, 750 mm clear distance and 80 mm thick). Round steel sections were used to mimic the supports to prevent localised failure. A representation of the plate model is shown in Figure 5.1. The calibrated work on the validation of the numerical model using the respective experimental data was presented in Section 4.3.3.3. The parametric study involves only the fibre volume being changed. The experiment was conducted with 1% fibre volume. The case at hand was modelled using V_f values of 1%, 1.25%, 1.50%, 1.75%, 2.00% and 2.5%. Also too, the concrete strength used in the experiment was 46.9MPa and for this parametric study f_{cu} used are 30MPa, 40MPa, 50MPa and 60MPa.

Table 5.1: Tensile Stress-strain Values for Parametric Study of SFRC Round Plate

Point	Strain $^0/_{00}$	Stress [MPa]					
		Vf= 1.00%	Vf = 1.25%	Vf = 1.5%	Vf = 1.75%	Vf = 2.00%	Vf = 2.5%
Peak Tensile Stress	0	2.600	2.600	2.600	2.600	2.600	2.600
Point II	0.9	1.177	1.472	1.766	2.060	2.350	2.940
Point III	17.8	1.177	1.472	1.766	2.060	2.350	2.940
Point IV	19.1	0.040	0.040	0.040	0.040	0.040	0.040

The key points on the tensile stress-strain diagram used for the round plate are shown in Table 5.1 and represented in Figure 5.2. The value of V_f was limited to 2.50% because after this value, the SFRC workability will be very low and may require large water-cement ratio and also, it has passed the practically available limit. Point I correspond to the tensile strength, which based on the result from the experiment, while points II and III represent the beginning and end of the flexural strength, which is determined by the pull-out effects of the steel-fibres and point IV the position of the ultimate tensile strain of the matrix.

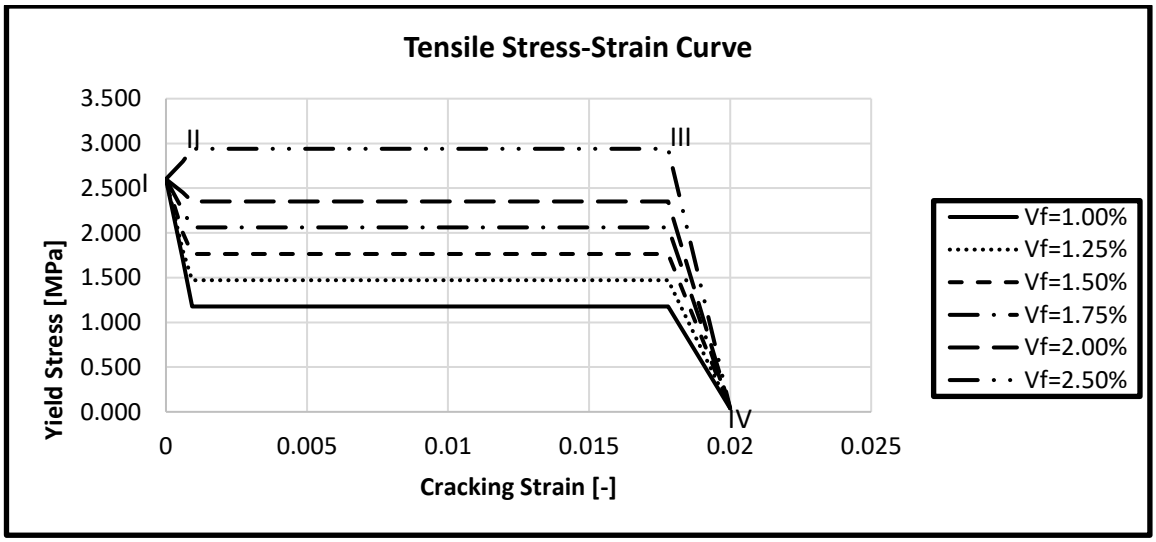

Figure 5.2: Tensile Stress-strain Values for Parametric Study of SFRC Round Plate

For a wider range of the strength of concrete, the input parameters are given in Table 5.2 and Figure 5.3. These cover the practical range of concrete strength used in the industry. It also provides the platform for comparison and checks for dependencies of one parameter on the other in this research work. The input parameters are as shown in Figure 4.27, Tables 4.11 and 4.12 on pages 153 and 154.

Table 5.2: Tensile Stress-strain Parameters for SFRC at f_{cu} with Different fibre volume ratios

Point	f_{cu} MPa	Strain $^0/_{00}$	Stress [MPa]					
			Vf= 1.00%	Vf = 1.25%	Vf = 1.50%	Vf = 1.75%	Vf = 2.00%	Vf = 2.50%
Peak Tensile Stress	30	0	1.665	1.665	1.665	1.665	1.665	1.665
	40	0	2.220	2.220	2.220	2.220	2.220	2.220
	50	0	2.775	2.775	2.775	2.775	2.775	2.775
	60	0	3.330	3.330	3.330	3.330	3.330	3.330
Point II		0.9	1.177	1.472	1.766	2.060	2.350	2.940
Point III		17.8	1.177	1.472	1.766	2.060	2.350	2.940
Point IV		19.1	0.040	0.040	0.040	0.040	0.040	0.040

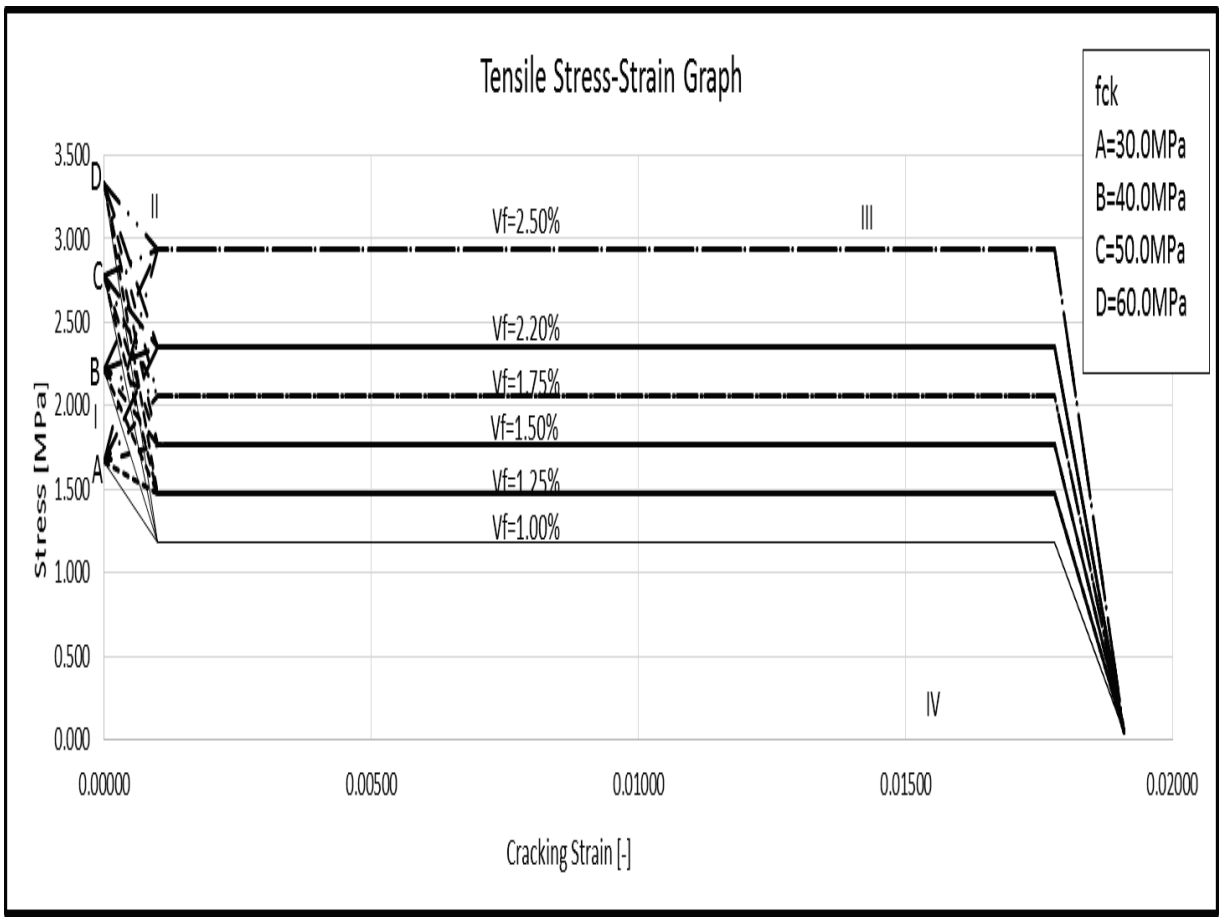

Figure 5.3: Tensile Stress-strain Parameters for SFRC at f_{cu} with Different fibre volume ratios

Figure 5.3 shows all the tensile stress-strain input, and it could be seen that Points II, III and IV are the same for all the values of f_{cu}, this is because all those points are dependent on flexural strength of the SFRC. The flexural strength f_{tu}, [Point II] is dependent on the amount of fibres and its properties and largely independent of the strength of concrete. The flexural strength is expressed as:

$$f_{tu}. = \frac{1}{2} V_f \, \tau_d \, \frac{L}{d} \qquad \text{Eq. 5.1}$$

The Point I correspond with the direct tensile stress, and the values are dependent on the characteristic strength of concrete. A, B, C and D represent the direct tensile stress for the characteristic strength of 30, 40, 50 and 60MPa respectively. Obviously, the higher the value of f_{cu}, the higher the value of f_t. The f_t is the tensile strength of the SFRC. Likewise, the SFRC plasticity parameters are as provided for in 4.3.3.3 on page 153

As earlier stated, the displacement-based loading was applied at the centre of the round plate. To guide against localised failure, a steel plate, 10mm thick was modelled for the loading rig. The monolithic loading type input data is shown in Figure 5.4. A mesh elements size of 25 mm width was adopted based on the early sensitivity analysis done, which produces the most suitable agreement with experimental data. To avoid distortion in the meshing, the wedge was used to restrain an uneven mesh pattern.

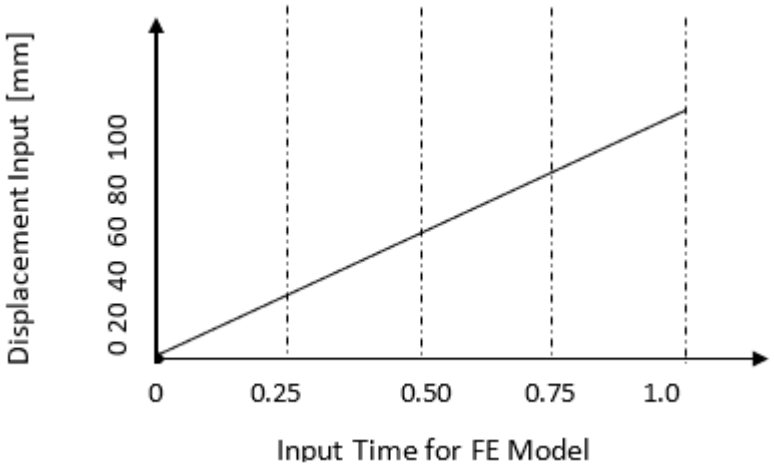

Frequency-Time input Data for Loading

The loading was applied gradually until failure using the displacement-based control loading data defined in Figure 5.4. The following NLFEA results are at this moment discussed in the following sections.

5.2.1 The Load-Displacement Curves

The load-displacement curves for the varying volume fibre fraction are shown in Figure 5.5. These are also interpreted in Table 5.3, namely: the load at first crack [P_y] signifying the yield load and its associated displacement [δ_y] the maximum load [P_{max}] signifying the load-carrying capacity and associated displacement [δ_{max}], the ultimate load [P_u] signifying the residual strength (taken as the lesser of the load at failure or 85% of the maximum load to ensure its practical usefulness) and associated displacement [δ_u] and the ductility ratio [μ] defined as $\mu = {\delta_u}/{\delta_y}$. For comparison purposes, the SFRC with V_f=1.00% is taken as the control specimen. The maximum load is the measure of the strength of the slab while the ultimate load is a measure of the residual strength. Likewise, the displacement at yield and ultimate loads are δ_y and δ_u respectively. The ductility of the slab is measured as the ratio of δ_y to δ_u.

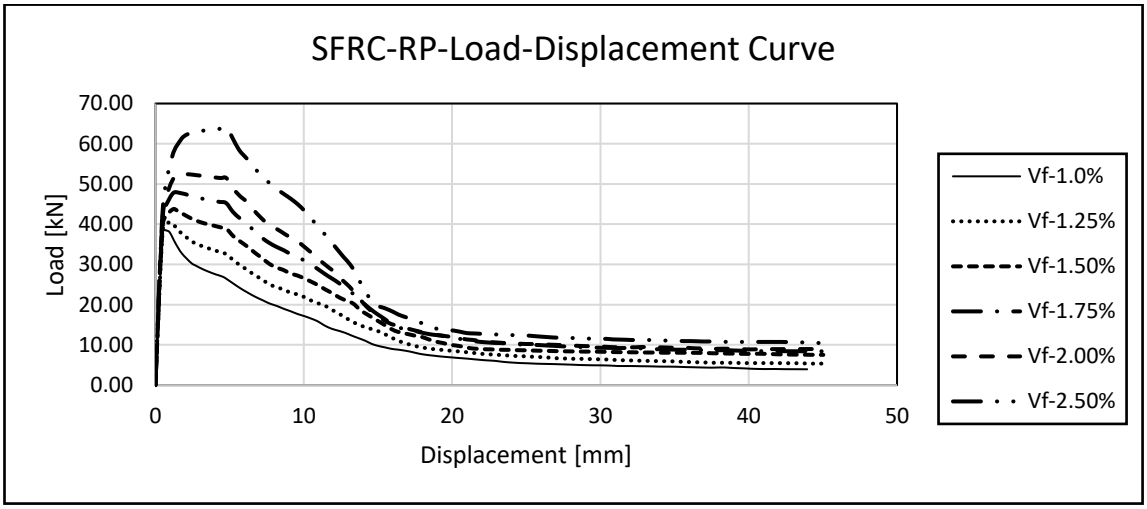

Figure 5.5: Load-Displacement Curve for a range of V_f

Figure 5.5 shows the Load-displacement curve for various values of V_f given that the f_{cu} for the experimental work was used. It clearly shows that as the fibre volume ratio increases, the peak load also increases. To further examined the response of the round-plate to apply loads, different amount of characteristic strength of concrete are considered. This is to determine the

dependency of peak load with characteristic strength of concrete. Figures 5.6 [a-f] shows the relationship between the load-displacement curves for various values of V_f.

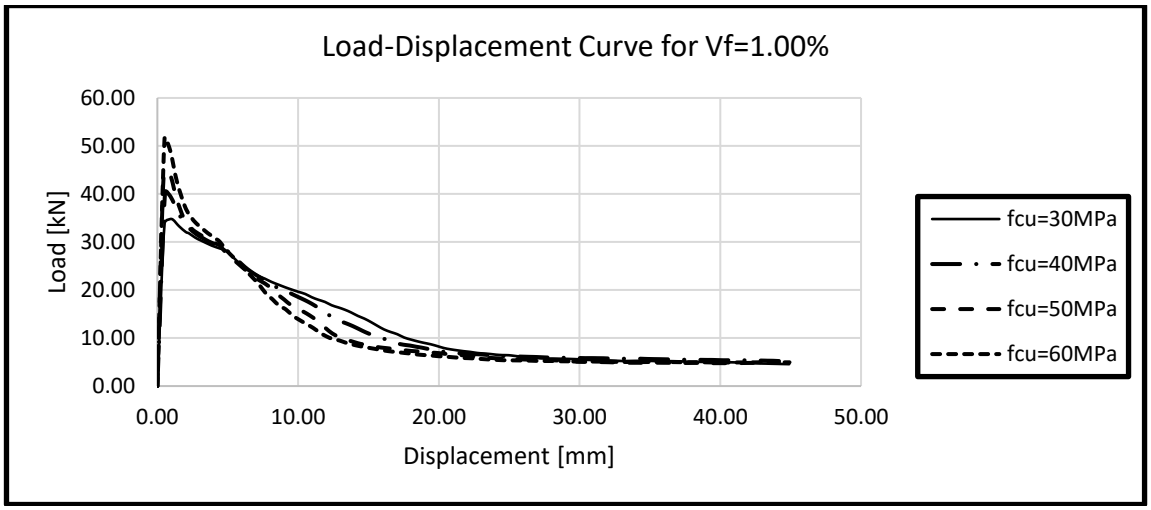

Figure 5.6[a]: Load-Displacement Curve for range of V_f = 1.00%

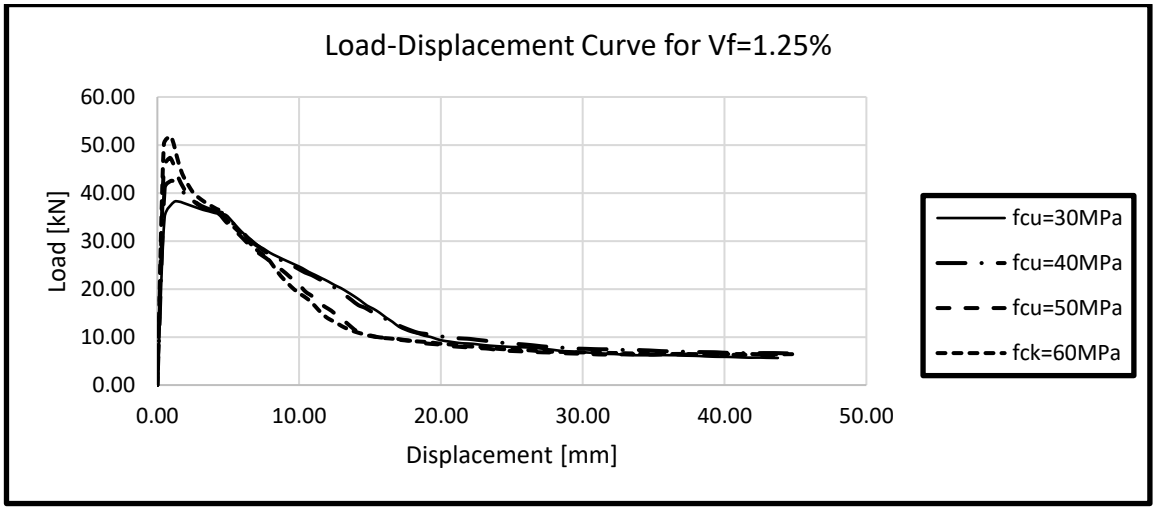

Figure 5.6[b]: Load-Displacement Curve for range of V_f = 1.25%

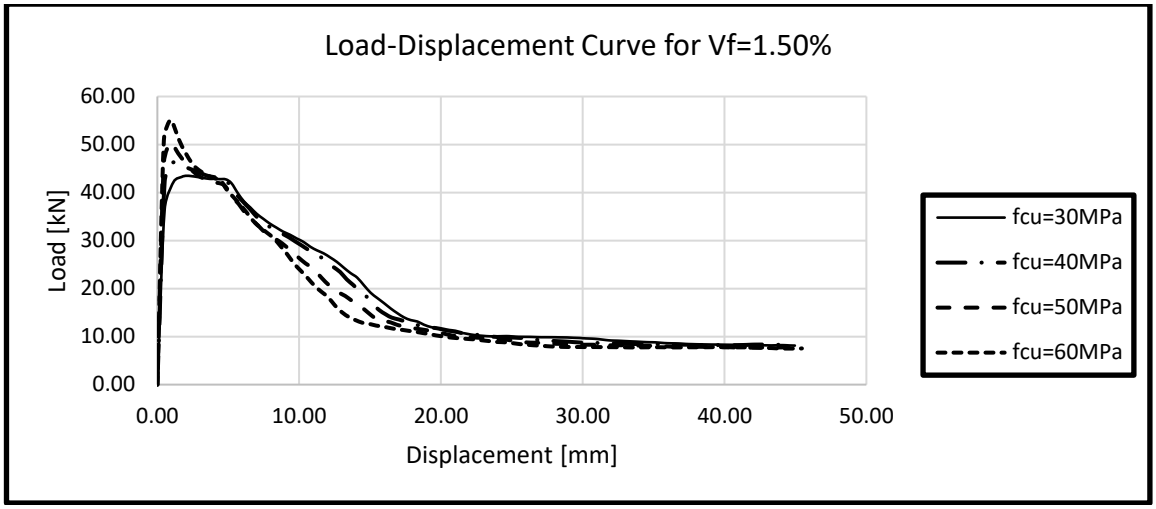

Figure 5.6[c]: Load-Displacement Curve for range of V_f =1.50%

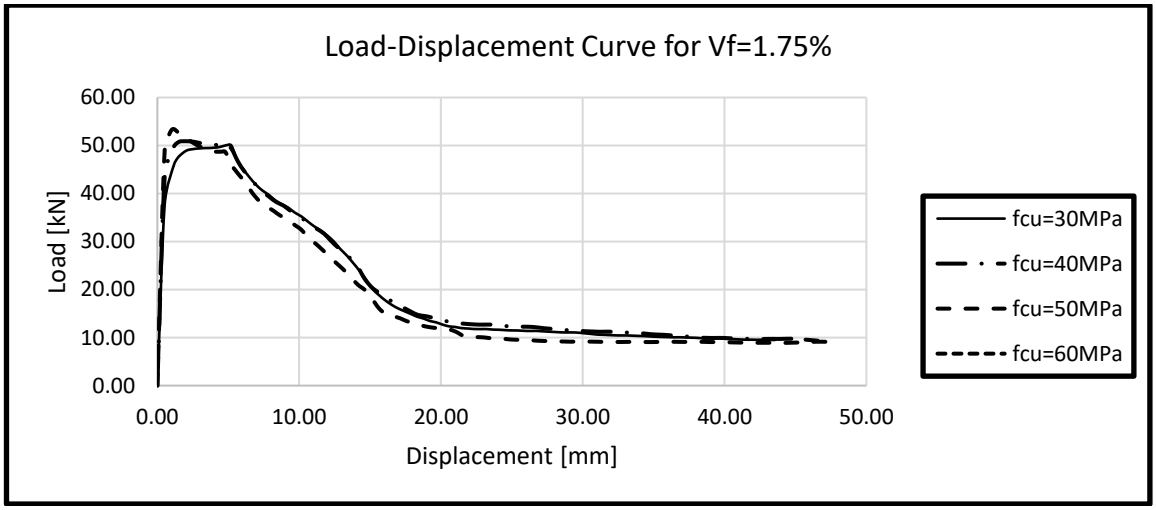

Figure 5.6[d]: Load-Displacement Curve for range of V_f = 1.75%

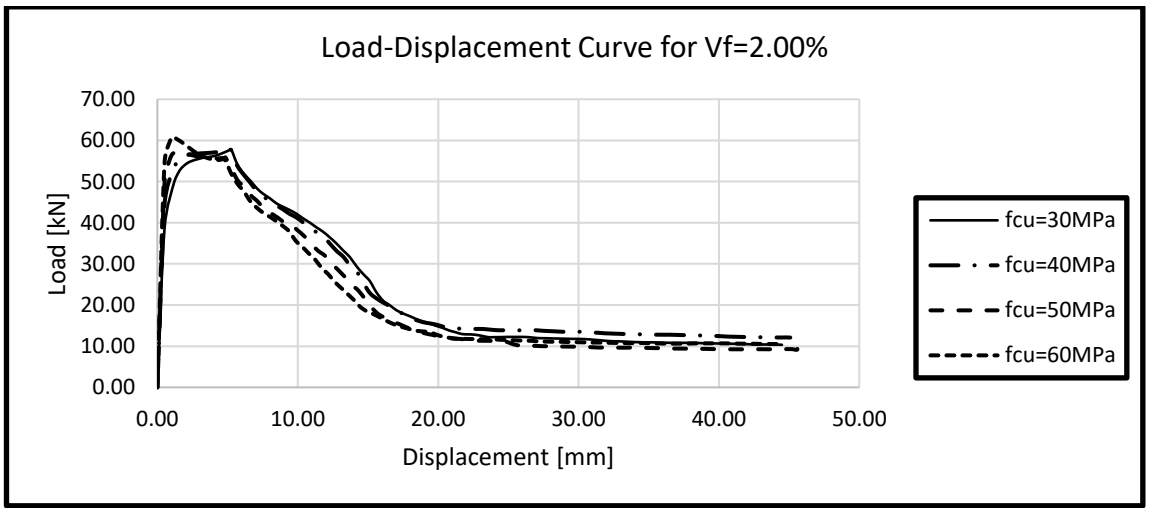

Figure 5.6[e]: Load-Displacement Curve for range of V_f =2.00%

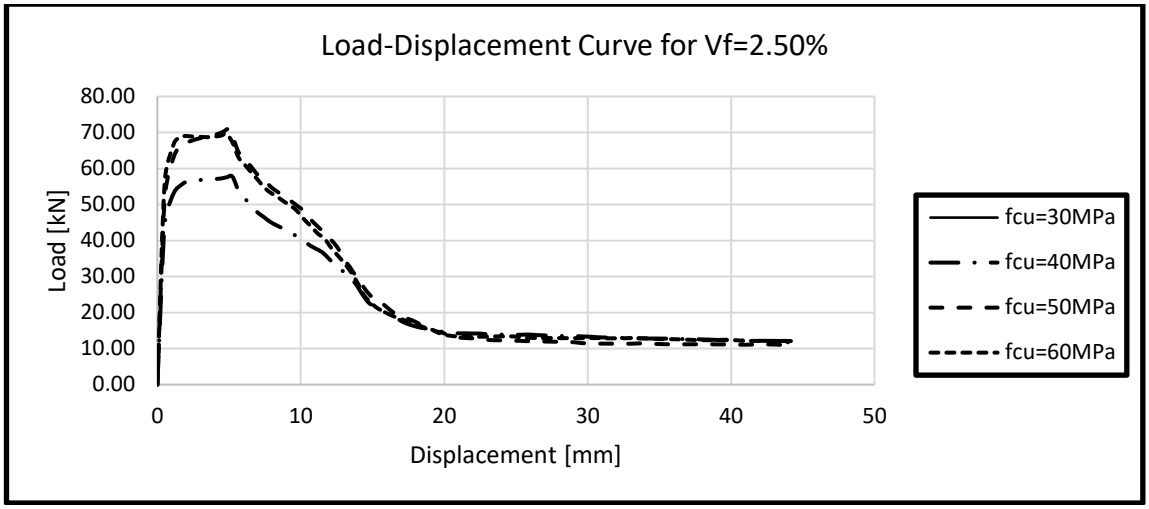

Figure 5.6[f]: Load-Displacement Curve for range of V_f = 2.50%

The graphs show that there was a significant increase in load resistance at V_f below 1.75% as the f_{cu} increases. These became nearly the same at V_f less than 2.50% as the peak loads for various f_{cu} tends to be the same. But as the fibre volume ratio increases, the peak load increases and this can be attributed to more fibres bridging the cracks as fibre volume increases. These can be further observed in Figures 5.7[a-d] which clearly show the load-displacement curves at different f_{cu} for various V_f.

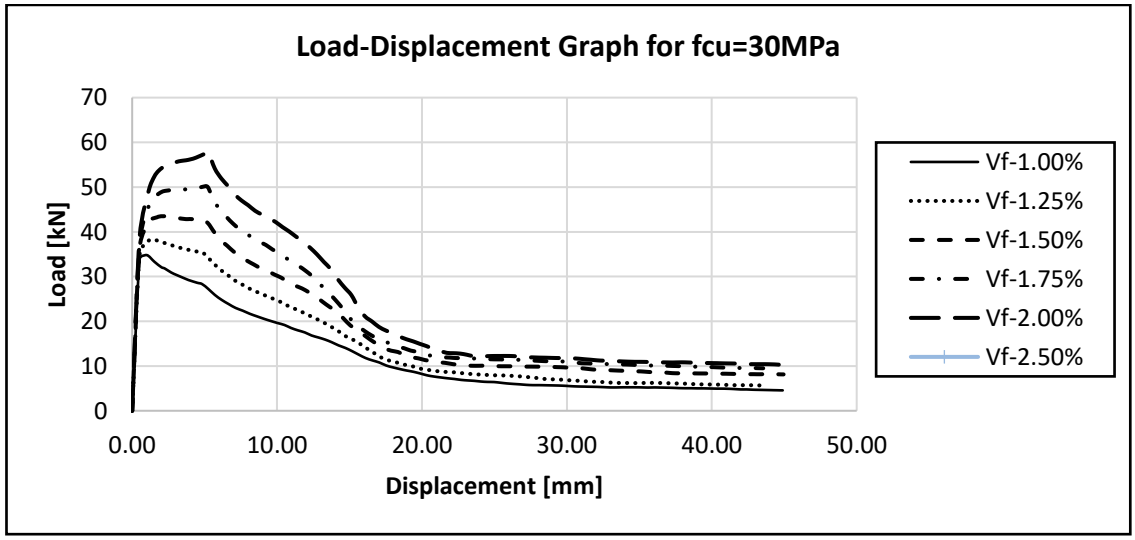

Figure 5.7[a]: Load-Displacement Curve for range of V_f at f_{cu}= 30MPa

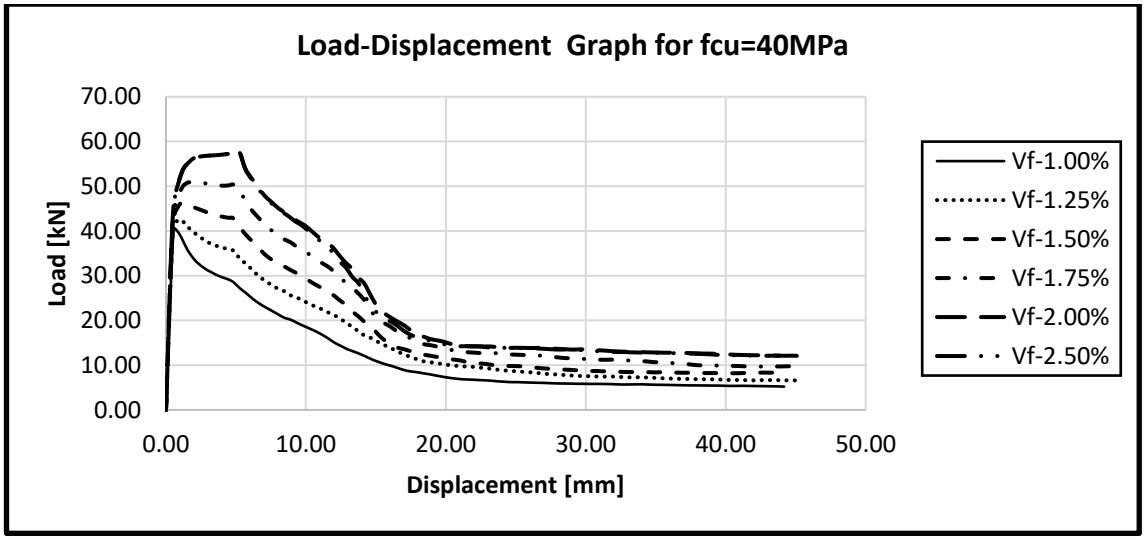

Figure 5.7[b]: Load-Displacement Curve for range of V_f at f_{cu}= 40MPa

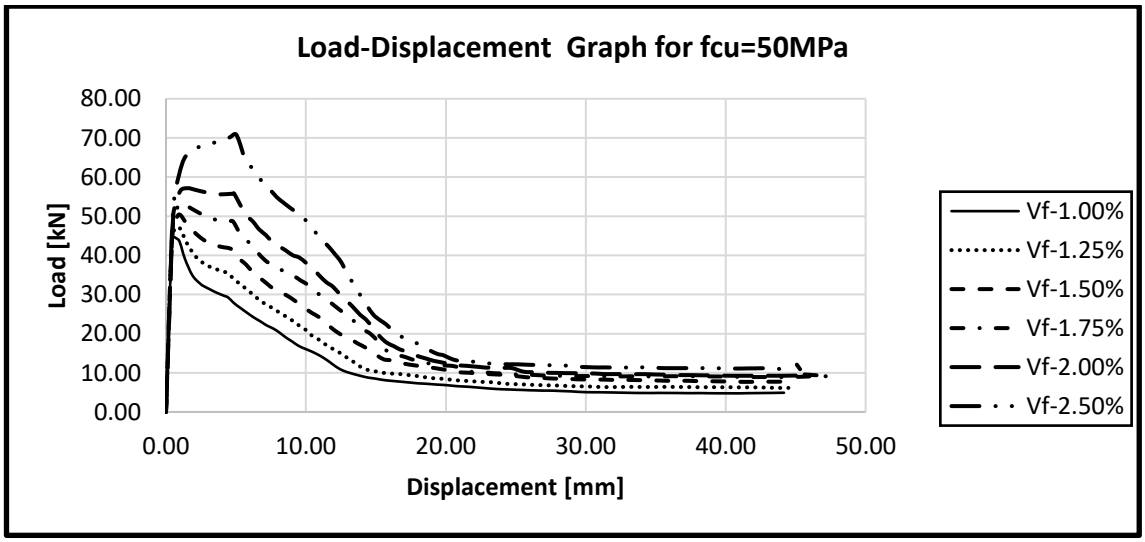

Figure 5.7[c]: Load-Displacement Curve for range of V_f at f_{cu}= 50MPa

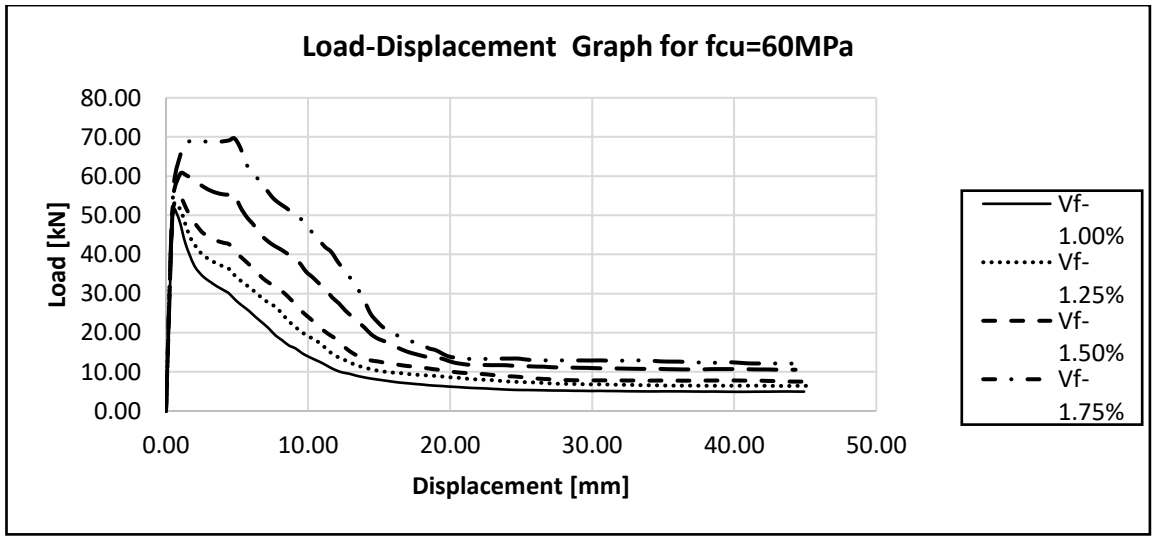

Figure 5.7[d]: Load-Displacement Curve for range of V_f at f_{cu}= 60MPa

5.2.2 Strength

The results show the panels after cracking occurred to demonstrate a sharp but controlled load reduction followed immediately by a post-cracking hardening phase which then changed gradually to smooth load reduction. After the matrix has cracked, a hardening response occurred when the peak load was approaching, followed by a gradual reduction in load as the crack width increases. The load-displacement curve and extract from it are presented in Figures 5.6 and 5.7, and Table 5.3 respectively. The fibre volume ratios influence can be observed clearly as the fibre content increases.

Table 5.3: Results for SFRC Round Plate

	V_f %	P_y [kN]	δ_y [mm]	P_{max} [kN]	$\frac{P_{max}}{P_{maxe}}$	δ_{max} [mm]	Pu [kN]	δ_u [mm]	$\frac{P_y}{P_{ye}}$	$\mu = \frac{\delta_u}{\delta_y}$	$\frac{\mu}{\mu_e}$
Control	1.00	38.21	0.51	38.21		0.51	32.48	1.75		3.43	
	1.00	38.21	0.51	38.21	1.00	0.51	32.48	1.75	1.00	3.43	1.00
	1.25	39.08	0.51	40.51	1.06	1.01	34.43	3.28	1.02	6.43	1.87
	1.50	40.31	0.51	43.24	1.13	1.53	36.75	3.22	1.05	6.31	1.84
	1.75	41.68	0.52	47.73	1.25	1.71	40.57	6.15	1.09	11.83	3.45
	2.00	42.77	0.52	52.44	1.37	2.13	44.57	6.32	1.12	12.15	3.54
	2.50	57.11	1.16	63.91	1.67	4.82	54.32	6.62	1.49	5.71	1.66

*P_{maxe} represent the control peak load

Likewise, for a better understanding, the extracts are presented for different values of f_{cu} in Table 5.4.

Table 5.4: Results for SFRC Round Plate at f_{cu}

f_{cu} MPa	V_f %	P_y [kN]	δ_y [mm]	P_{max} [kN]	δ_{max} [mm]	$\frac{P_{max}}{P_{maxc}}$	P_u [kN]	δ_u [mm]	$\frac{P_y}{P_{yc}}$	$\mu = \frac{\delta_u}{\delta_y}$	$\frac{\mu}{\mu_c}$
30	1.00	33.90	0.51	34.80	1.01	1.00	29.31	3.82	1.00	7.49	1.00
40		40.39	0.55	40.39	0.55	1.00	33.98	1.94	1.00	3.52	1.00
50		44.41	0.46	44.41	0.46	1.00	37.75	1.54	1.00	3.35	1.00
60		51.50	0.51	51.50	0.51	1.00	42.70	1.38	1.00	2.71	1.00
30	1.25	34.99	0.51	38.22	1.50	1.10	32.70	5.69	1.03	11.16	1.49
40		41.06	0.52	42.56	1.01	1.05	36.27	4.03	1.02	7.75	2.20
50		45.32	0.46	47.32	0.90	1.07	39.23	2.24	1.02	4.87	1.45
60		50.14	0.46	51.83	0.95	1.01	43.41	1.85	0.97	4.02	1.48
30	1.50	36.53	0.51	43.49	2.21	1.25	36.90	5.67	1.08	12.37	1.65
40		42.32	0.52	46.07	1.01	1.14	39.28	5.68	1.05	10.92	3.10
50		46.16	0.46	50.41	0.90	1.14	42.45	3.63	1.04	7.89	2.36
60		50.88	0.46	55.12	0.91	1.07	46.85	2.25	0.99	4.89	1.80
30	1.75	37.66	0.52	50.07	4.87	1.44	43.36	6.50	1.11	12.50	1.67
40		43.49	0.52	50.90	1.83	1.26	43.27	6.48	1.07	12.46	3.54
50		48.96	0.52	53.28	1.01	1.20	45.91	5.25	1.10	10.10	3.01
60											
30	2.00	38.85	0.52	57.82	5.25	1.66	50.21	6.62	1.15	12.73	1.70
40		44.61	0.52	57.79	5.23	1.43	49.84	6.52	1.10	12.54	3.56
50		49.96	0.52	57.16	1.54	1.29	48.72	6.19	1.12	11.90	3.55
60		54.79	0.52	60.64	1.01	1.18	51.99	5.25	1.06	10.10	3.96
30	2.50	53.88	0.52	57.83	0.92	1.66	48.81	4.28	1.59	8.24	1.10
40		44.61	0.52	57.79	5.23	1.43	49.84	6.52	1.10	12.54	3.56
50		51.83	0.52	71.00	4.97	1.60	60.47	6.55	1.17	12.60	3.76
60		56.48	0.52	69.02	1.83	1.34	58.78	6.57	1.10	12.63	4.66

P_{maxc} represent the peak load from the control [V_f = 1.00%]

In the SFRC with f_{cu}=30MPa, the result shows that round-panel with 1% fibre volume ratio yielded 38.21kN, while that of 2.50% fibre volume is 57.11kN in control. As the fibre volume is increased, there is a gradual increase in the yield load. There is also an increase in the stiffness as the fibre volume increases. The strength of the slab was also enhanced as the fibre volume increases. An 18% and 22% increment in strength was obtained in the slab when the fibre was increased to 1.25% and 1.5% respectively. Incidentally, all the FEA results for the displacement at the yield load give 0.51mm.

The load-carrying capacity of the slab was enhanced as the fibre volume is increased as shown in the load-displacement curves. This simply translates into, the higher the fibre volume, the higher the strength of the round plate to resist applied load. Both the experiment and FEA with 1% volume fibre failed at 38kN. As the fibre increases, the maximum load also increases. This can be attributed to the stiffness in the FEA results. The strength and ductility ratios were also measured. There is a significant increase in the strength ratio and a decrease in the ductility ratio.

Table 5.5: Comparison of Yield Load and Peak Load against Fibre Volume Ratio

V_f %	P_y [kN]	P_{max} [kN]	P_y [kN]	P_{max} [kN]	P_y [kN]	P_{max} [kN]	P_y [kN]	P_{max} [kN]
	f_{cu}= 30MPa		f_{cu}= 40MPa		f_{cu}= 50MPa		f_{cu}= 60MPa	
1.00	33.90	34.80	40.39	40.39	44.41	44.41	51.50	51.50
1.25	34.99	38.22	41.06	42.56	45.32	47.32	50.14	51.83
1.50	36.53	43.49	42.32	46.07	46.16	50.41	50.88	55.12
1.75	37.66	50.07	43.49	50.90	48.96	53.28	52.25	58.35
2.00	38.85	57.82	44.61	57.79	49.96	57.16	54.79	60.64
2.50	42.52	60.25	50.61	62.79	51.83	71.00	56.48	69.64

Also, as the fibre volume fraction content increases (from 1.75% - 2.50%) a gentle plateau was observed that is relative to the peak load. The “plateau” was more obvious in beams with higher fibre volume ratio than in ones with small fibre dosage. This is due to the influence of the amount of fibre in the post-cracking phase of the slab.

A further illustration of the yield loads, peak loads and the corresponding displacement against the fibre volume ratios for the various characteristic strength of the SFRC are shown in Figures 5.8 and 5.9. The yield and peak loads increase gradually as the f_{cu} increases and as V_f increases. Figures 5.8 and 5.9 show the graphs of the variation of yield strength (connected with the SLS) and peak-load depicting load-bearing capacity (connected with the ULS) of the specimens with increasing fibre dosage respectively.

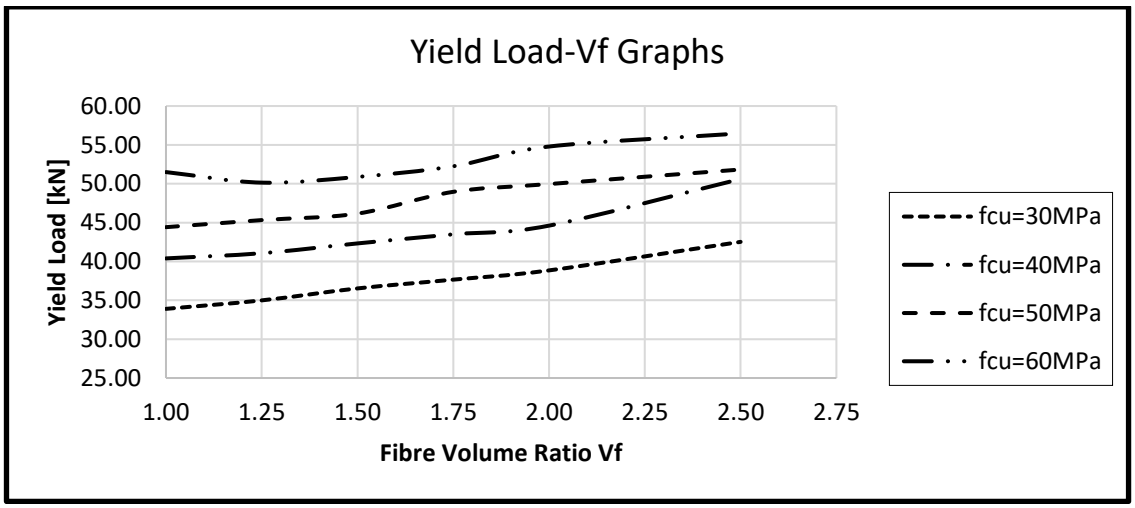

Figure 5.8: Yield load and Fibre Volume Ratio Graphs for f_{cu}

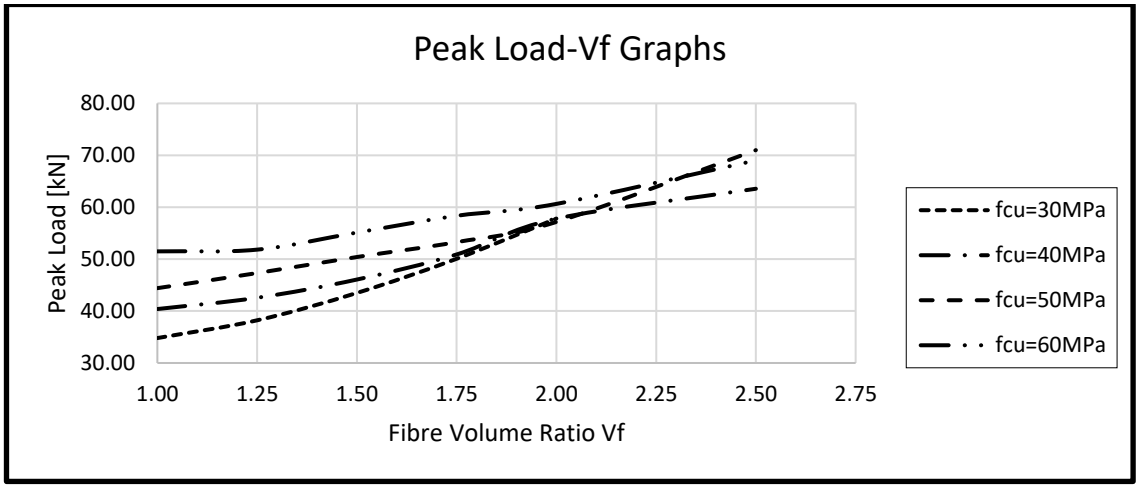

Figure 5.9: Peak load and Fibre Volume Ratio Graphs for f_{cu}

At the peak load, the graphs crossed at V_f=2.0% for f_{cu}=30MPa and 40MPa, meaning that the optimum value has been reached and that at this fibre dosage, any of the two f_{cu} can be used to obtain the same result. The same is what is obtainable at V_f=2.25% for f_{cu}=50 MPa and 60 MPa.

Table 5.6: Comparison of Displacement at Yield Load and Peak Load against Fibre Volume Ratio

V_f %	δ_y [mm]	δ_{max} [mm]	δ_y [mm]	δ_{max} [mm]	δ_y [mm]	δ_{max} [mm]	δ_y [mm]	δ_{max} [mm]
	f_{cu}= 30MPa		f_{cu}= 40MPa		f_{cu}= 50MPa		f_{cu}= 60MPa	
1.00	0.51	1.01	0.55	0.55	0.46	0.46	0.51	0.51
1.25	0.51	1.50	0.52	1.01	0.46	0.90	0.46	0.95
1.50	0.51	2.21	0.52	1.01	0.46	0.90	0.46	0.91
1.75	0.52	4.87	0.52	1.83	0.52	1.01	0.48	1.00
2.00	0.52	5.25	0.52	5.23	0.52	1.54	0.52	1.01
2.50	0.52	6.10	0.52	5.22	0.52	4.97	0.52	4.82

The displacements at yield loads are about the same for all the fibre volume ratios of different characteristic strengths. This can be attributed to the fact that the linear part of the load-displacement graph [from zero to the point of yield load] is guided by the material properties of the SFRC matrix. In this part, the steel fibres place little or no role in the resistance of the load. They are resisted by the concrete matrix.

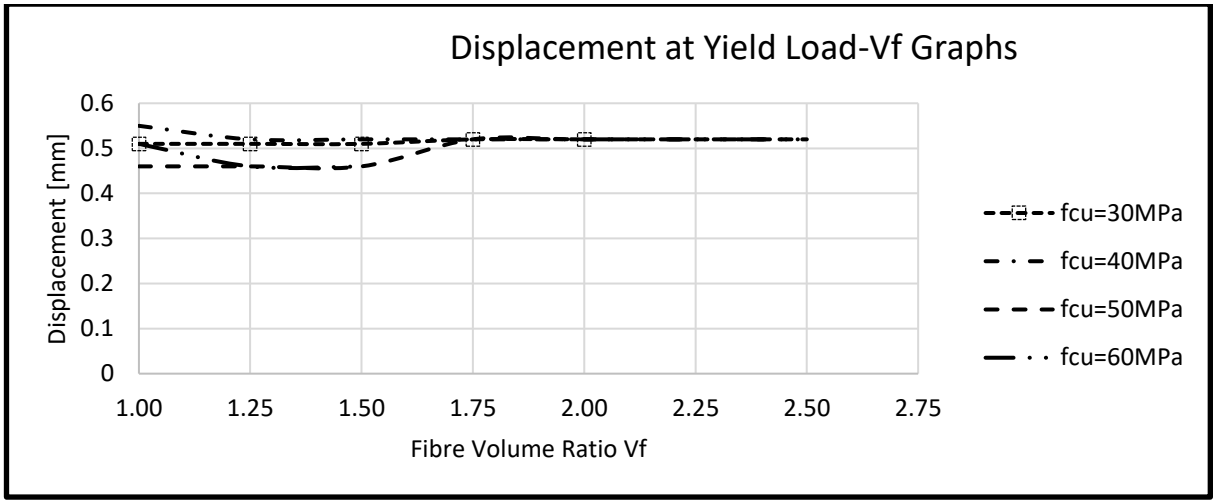

Figure 5.10: Displacement at Yield load and Fibre Volume Ratio Graphs for f_{ck}

At the peak load, the steel-fibre improves the resistance to load. There was a jump in the displacement from 1.50% to 2.00% in f_{cu} less than 50MPa. The peak load in 60MPa strength was a gentle slope from 1.00% to 2.50% fiber volume ratio.

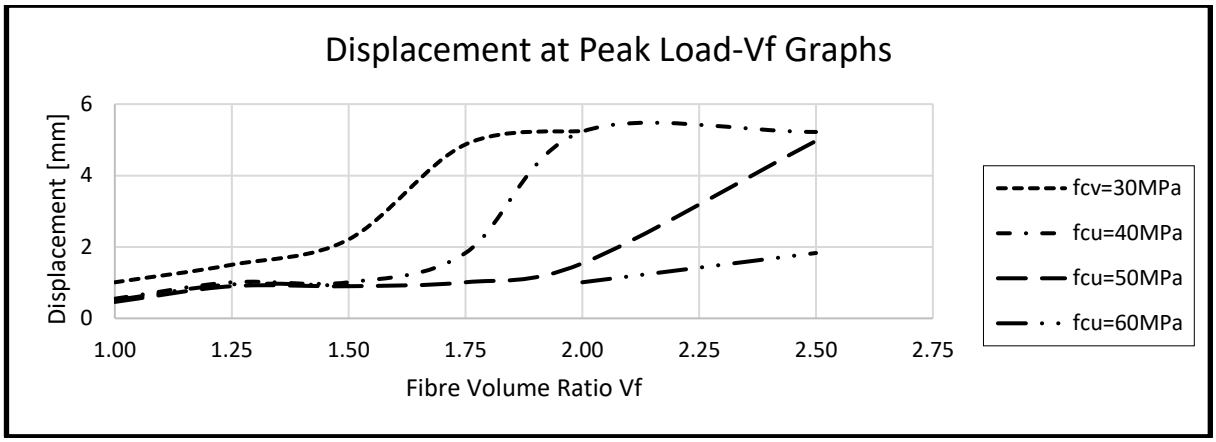

Figure 5.11: Displacement at Peak load and Fibre Volume Ratio Graphs for f_{cu}

For this behaviour to be understood further plots regarding the tensile strains versus deflection, taken at the centre of the panel at the tension face were constructed as illustrated in Figures 5.12. The strain values were taken at the crack opening region at the bottom of the panel.

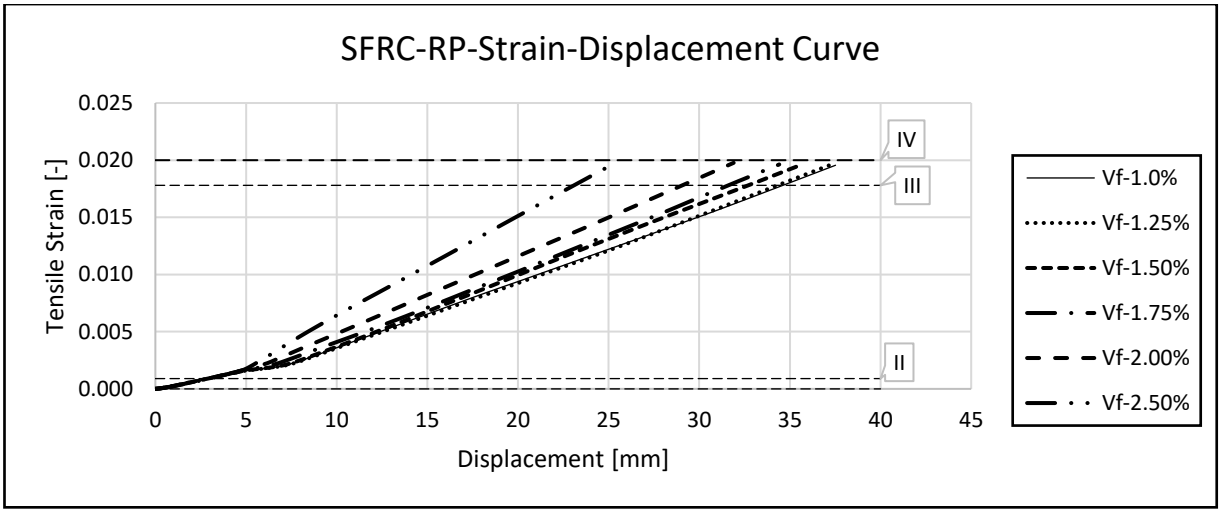

Figure 5.12: Tensile Strain-Displacement Curve for a range of V_f

The crucial points [I, II, III and IV] on the tensile stress-strain curve [at cracking strain 0.0, 0.0009, 0.0178 and 0.02 in Figure 5.1] are indicated on Figure 5.12 [horizontal lines at each strain level are indicated in the graph]. With these values, a new load-displacement curve is constructed using the corresponding displacements identified in Figures 5.12, and this is represented in Figure 5.13.

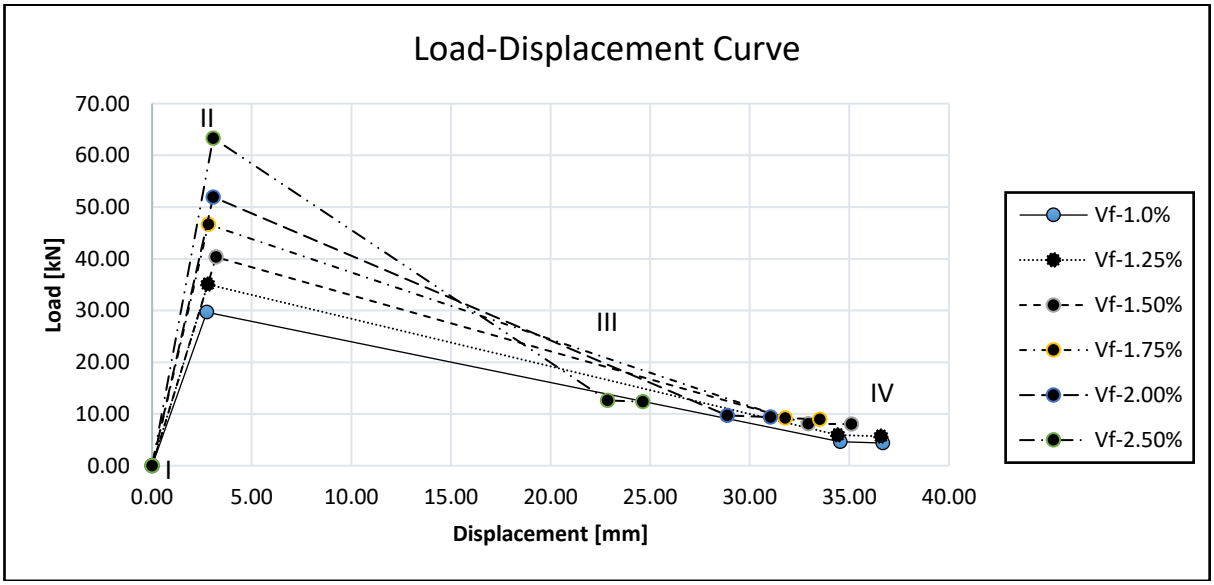

Figure 5.13: Load-Displacement Curve for a range of V_f up to 35mm displacement

The SFRC Panel with $V_f = 1\%$ fibres, the ultimate tensile strain of the matrix is the lowest and this can be attributed to the amount of the steel-fibres. After the initial crack, the steel-fibre yields before the ultimate tensile (i.e. pull-out) strain of fibrous concrete

(Point IV) is reached. The deformation of the steel fibres continue beyond the yield point while the residual stresses were maintained by the SFRC between Points II, III and IV (Figure 5.13). This leads to more stresses in the tension zone being sustained by steel-fibres and concrete matrix (the more the fibres, the higher the stresses in the tension zone). Therefore, it will also lead to an increase in the stresses in the compression zone in order to maintain an equilibrium. As Point III is reached, the stresses in the SFRC panel drop instantaneously to zero at Point IV (tensile stress-strain constitutive model described in Figure 5.2). This rapid drop from III to IV is more prominent for panels with a high fibre volume ratio (1.75% - 2.5%), which are described by "strain hardening" behaviour. Afterward, there is a significant drop in the stresses in tension and likewise in compression, a substantial amount of stresses is lost, and this change is responsible for the plateau behaviour observed for on the load-deflection curves (Figure 5.5).

Round-panels with smaller fibre volume ratio (1.0% - 1.5%) exhibit "strain softening" behaviour and thus the drop from point III to IV is not as high leading to a "gentle" response contrary to that of high V_f which has a "plateau" response. Figure 5.5 shows the load-deflection with the steel-fibres acting without concrete contribution from points II to III and from III to IV (an ultimate strain of fibres representing pull-out failure. For all the SFRC Round-Plates points III and IV are at the failure load confirming that fibres at the bottom of the RP are active [bridging the cracks and thus resisting the stresses induced by the applied load] in the pull-out stage. These was repeated for different values of f_{cu} as shown in Figures 5.14 [a-f]

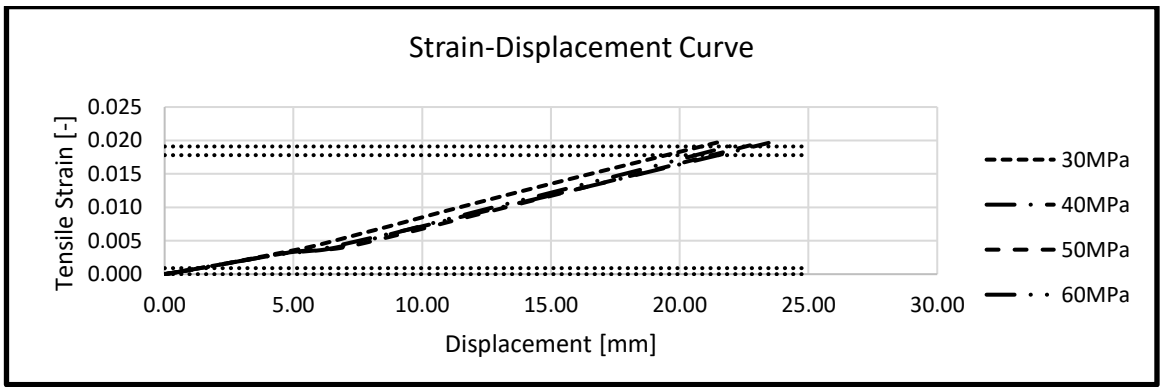

[a]

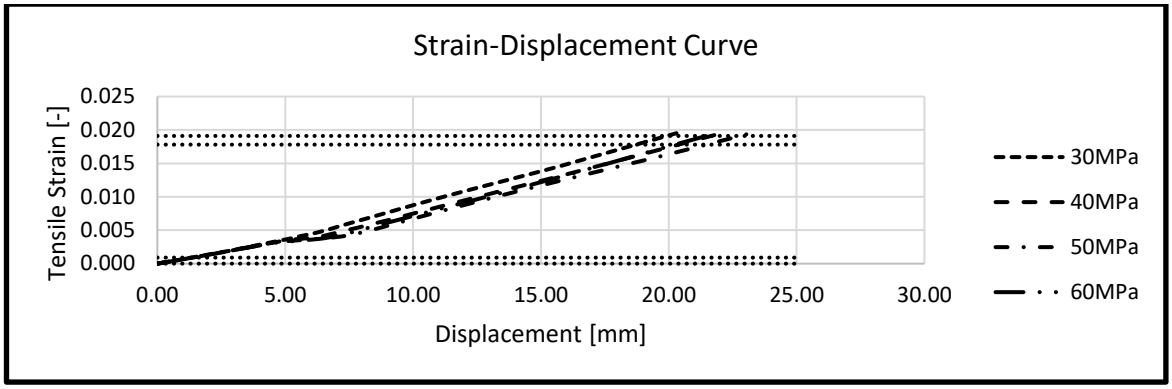
Strain-Displacement Curve
Tensile Strain [-]
0.025
0.020
0.015
0.010
0.005
0.000
0.00
5.00
10.00
15.00
20.00
25.00
30.00
Displacement [mm]
30MPa
40MPa
50MPa
60MPa

[b]

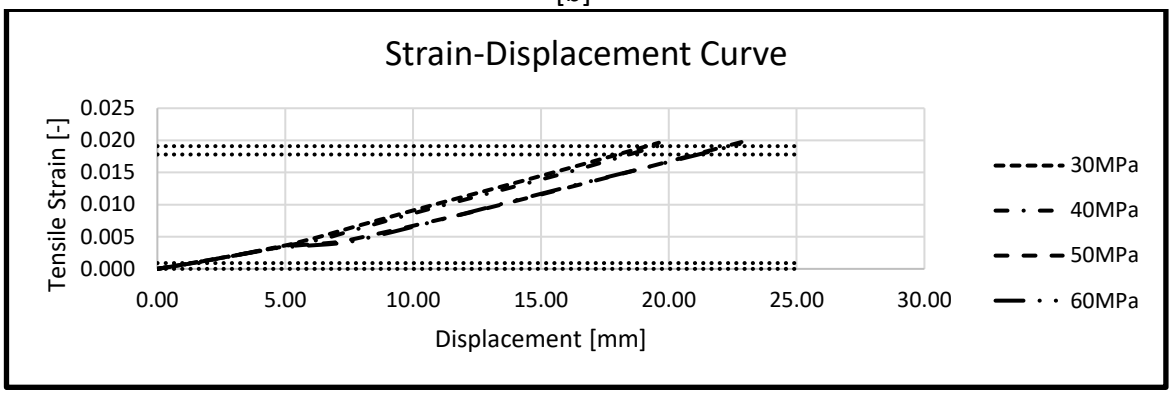
Strain-Displacement Curve
Tensile Strain [-]
0.025
0.020
0.015
0.010
0.005
0.000
0.00
5.00
10.00
15.00
20.00
25.00
30.00
Displacement [mm]
30MPa
40MPa
50MPa
60MPa

[c]

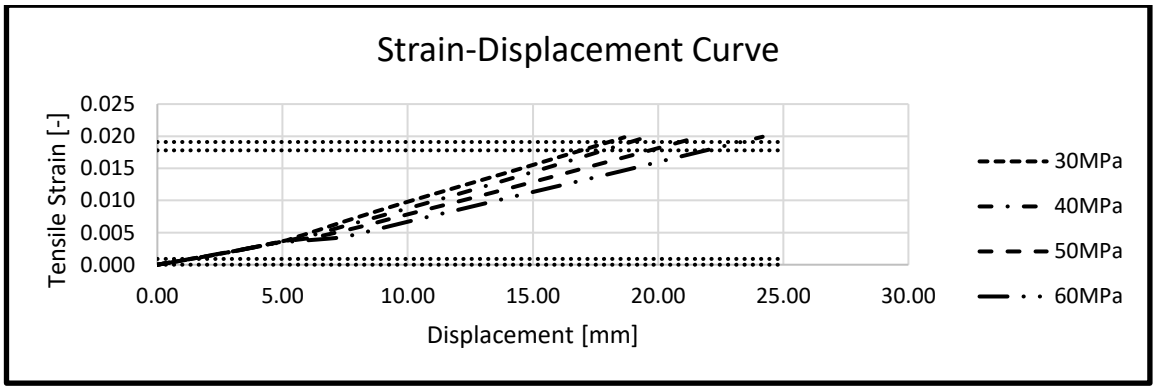
Strain-Displacement Curve
Tensile Strain [-]
0.025
0.020
0.015
0.010
0.005
0.000
0.00
5.00
10.00
15.00
20.00
25.00
30.00
Displacement [mm]
30MPa
40MPa
50MPa
60MPa

[d]

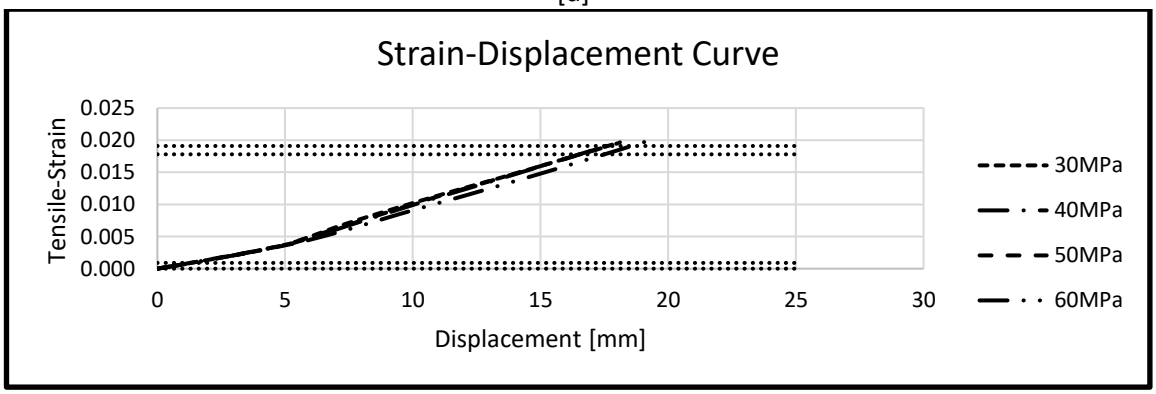
Strain-Displacement Curve
Tensile-Strain
0.025
0.020
0.015
0.010
0.005
0.000
0
5
10
15
20
25
30
Displacement [mm]
30MPa
40MPa
50MPa
60MPa

[e]

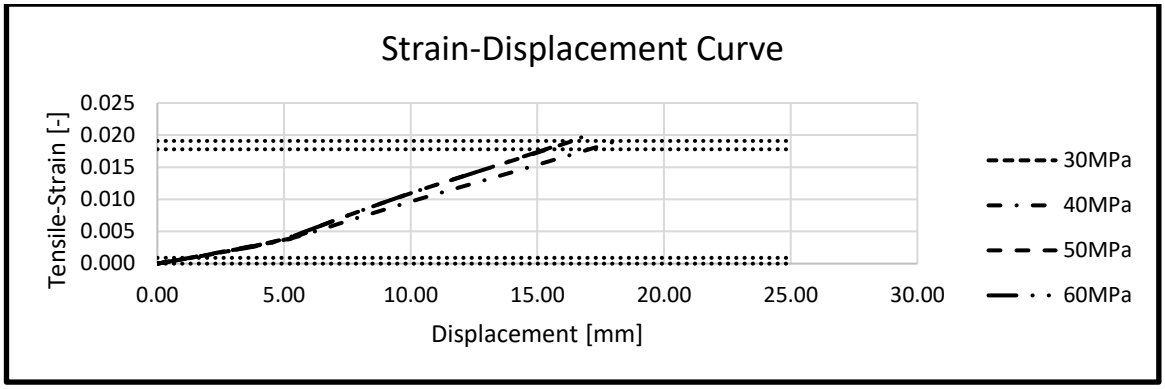

[f]

Figure 5.14: Tensile Strain-Displacement Curve for range of V_f [a=1.00, b=1.25, c=1.50, d=1.75, e=2.00 and f=2.5%]

5.2.3 Ductility

The ultimate displacement [δ_u] taken at the ultimate load [P_u] is used to measure the ductility of the Round-plate panels. The ultimate load [P_u] represents the (post-peak) residual strength at failure. A softening behaviour of the load-deflection response accompanies the rise in ductility. The residual strength was found to be sufficiently low (<85%) in all cases studied, suggesting that the softening is very significant. Consequently, to ensure practicality of these ductility levels, the residual strength was limited to a minimum of 85% of the load-carrying capacity [P_{max}]. To truly utilise the resulting increase in ductility for the design purposes, it is vital to maintain the residual strength at a tolerable level.

The ductility of the Round-Plate panels can be determined based on the ductility ratio $\mu = {\delta_u}/{\delta_y}$ which shows that the addition of fibres leads to enhanced ductility ratio of the SFRC RP panels significantly. However, as the fibre volume fraction exceeds a crucial value, the addition of fibres beyond this value does not increase the ductility of the RP panel. A further comparative study of the RP panels' response and that of the experimental RP panel is provided in a subsequent section of this Chapter 5.

5.2.4 Cracking Pattern

In the test of round plate on three supports, the three governing cracks are initiated before entering the post-cracking behaviour. This makes the onset of cracking a bit

difficult to perceive. This observation is credited to the redundant structural behaviour that takes place in round panels. Multiple cracking follows as experienced in SFRC members with high fibre volume dosage. This section presents the cracking patterns-based on FE for deflected shapes, principal strain contours and vectors under monotonic loading. The results depicted in the figures were taken at failure and indicated crack formation and patterns.

5.2.4.1 Principal Strain Contours

The principal strain contours for the round-plate examined in Case Study 1A at failure are shown in Figures 5.15 [a-f]. The principal strain range was picked between the ultimate tensile strain of 0.02 (i.e. pull-out strain for SFRC round-plate) and an ultimate compressive strain of -0.0035. The tensile failure was represented by regions where the ultimate tensile strain is exceeded, highlighted in red, while blue depicts the regions where there is a compressive failure.

Figures 5.15 [a] shows the principal strain contour [observed at the bottom] in the round plate with fibre volume ratio of 1.00%. It was observed that the cracks move from the centre, at the point of load application, to the edge. The failure of the round-plate was dominated by tensile-cracking at the middle of the round-plate. The Plate collapse in three regions with each failure line radiating from the centre to mid-point in between two supports, following the experimental results.

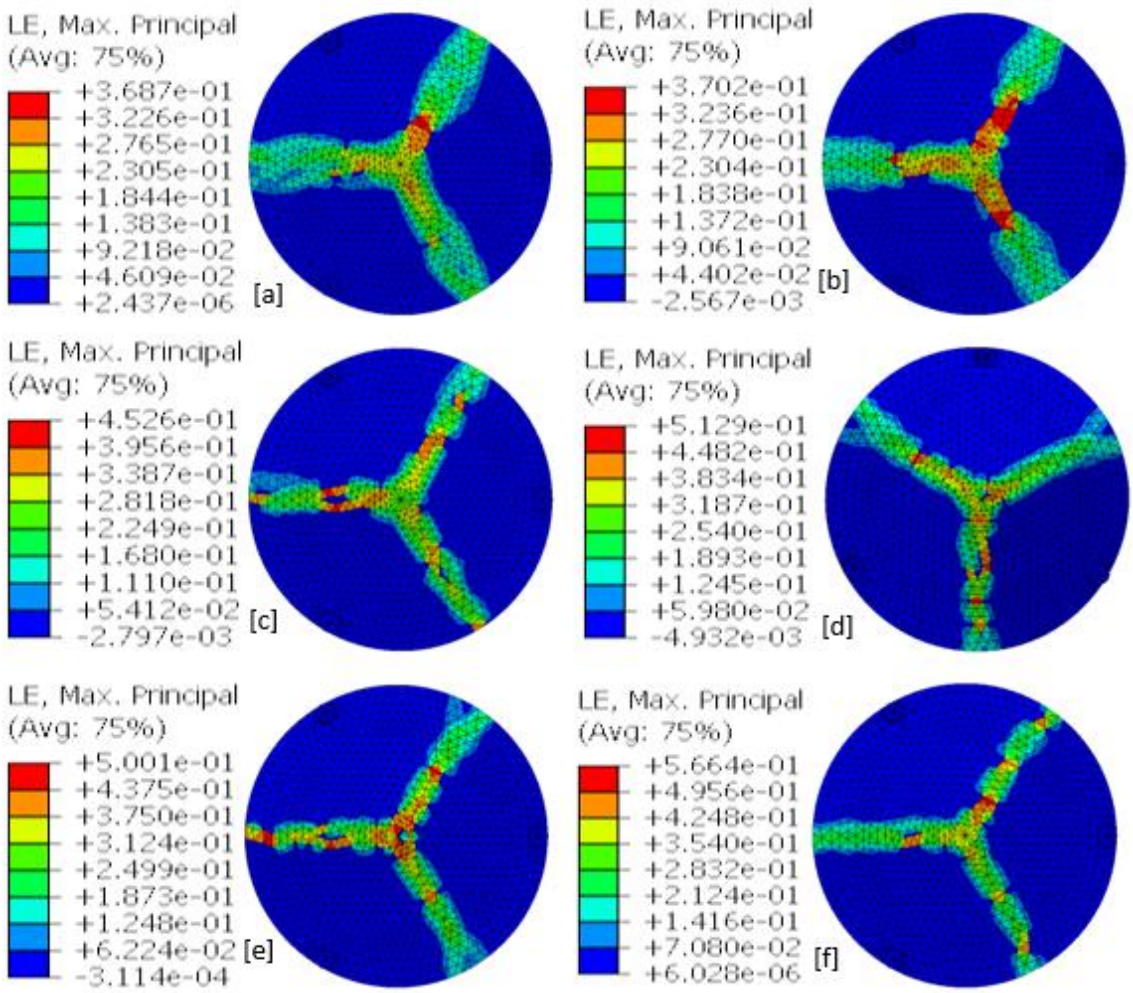

Figure 5.15: Principal strain contour [bottom] for Case Study 1A with V_f [a= 1.00, b=1.25, c=1.50, d=1.75, e=2.00 and f=2.50%]

Figures 5.15 [b-d] show the principal strain contour in the round plate with fibre volume ratio of 1.25-1.75%. It was observed that the cracks still moves from the centre and dominated by tensile-cracking in the middle of the round-plate. The Plate collapse along three lines [c] with each failure line radiating from the centre to mid-point in between two supports. Figures 5.15 [e & f] show the principal strain contour in the round plate with fibre volume ratio of 2.00-2.50%. It could be seen that at the point of load application, the cracks propagate from the centre to the edge. The failure of the round-plate was controlled by tensile-cracking at the middle of the round-plate.

A close observation of the strain contours for various fibre volume ratios shows that the strain at the compression face [top] of the round-panel was decreasing as the fibre

volume increases, and this can be attributed to the fibres, the restraint at the compression face becomes tougher. In the tension [bottom] face of the round-plate, the stain decreased as the fibre volume increases, and thus the load resisted at failure increases. The failure patterns are at about angle 120^0 to one another.

5.2.4.2 Principal strain vectors

For the study of the principal strain vectors, only the tension [bottom] face and section y-y of the slab shall be considered. The principal strain vectors for the round-plates are presented in Figure 5.16 below.

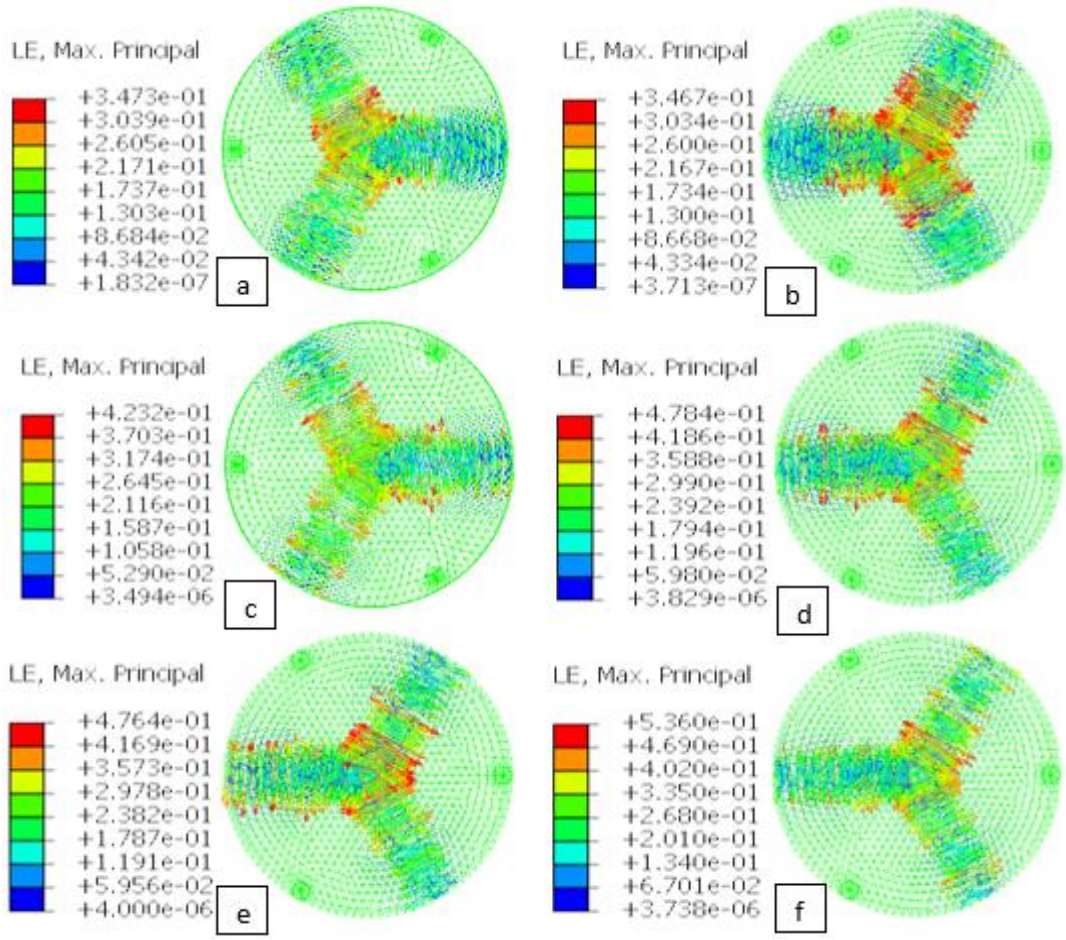

Figure 5.16: Principal strain vector for Case Study 1A with V_f = [a] 1.00% [b] 1.25% [c] 1.50% [d] 1.75% [e] 2.00% and [f] 2.50%

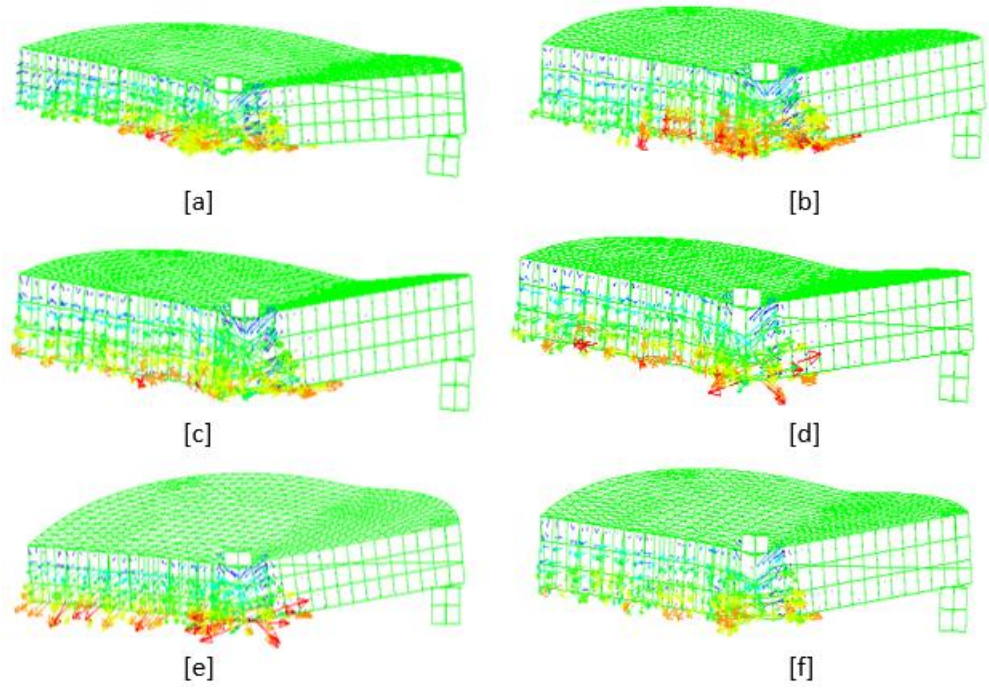

Figure 5.17: Principal strain vector [section y-y] for Case Study 1A with V_f = [a] 1.00% [b] 1.25% [c] 1.50% [d] 1.75% [e] 2.00% and [f] 2.50% and the same numerical values as Figure 5.16

From the vectors diagrams in Figures 5.16 and 5.17, it is observed that failure occurred at the centre of the round-panels. The concentration of the vectors can be seen at the bottom of the round-plate and decrease gradually towards the edge. The concentration of the vectors is at the bottom of the point of the application of load. Considering the cracking patterns in Figure 5.16 and from the section y-y [Figure 5.17], the analysed round plates can be concluded to have failed in bending mode.

5.2.4.3 Deformed [Compressive and Tensile] Shapes

The next set of figures [5.18-5.21] shows the compressive and tensile damaged patterns at the bottom and top of the round-plate. The cracks are more significant at the bottom than at the top. This confirms that the round-plates failed in tension.

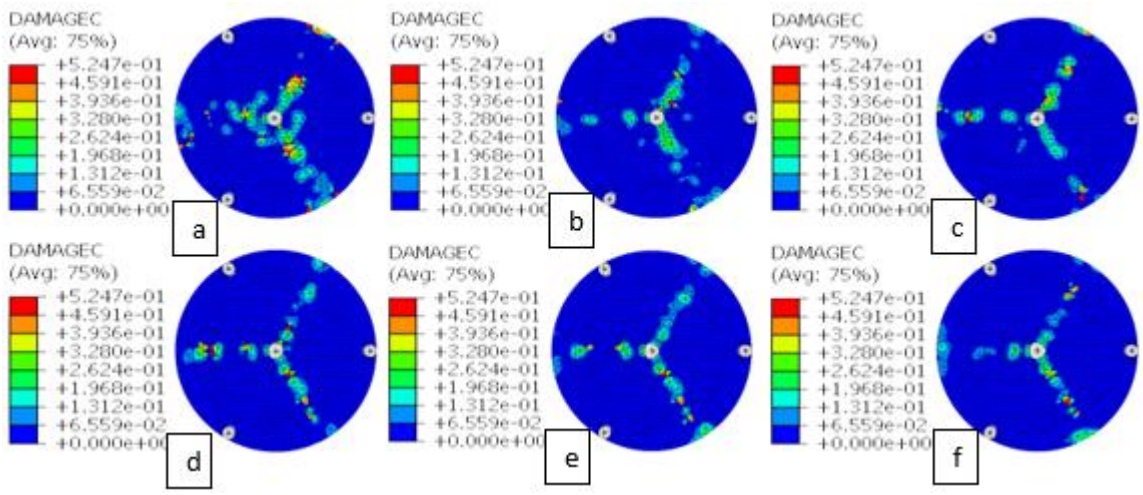

Figure 5.18: Compressive Damaged patterns at the bottom of the round-plate with V_f = [a] 1.00% [b] 1.25% [c] 1.50% [d] 1.75% [e] 2.00% and [f] 2.50%

Figures 5.18 and 5.19 show the damaged compressive behaviour of SFRC round-plates on isolated supports. The top shows significant resistance to cracking because concrete is good at compression [Figure 5.18]. There is little compressive resistance at the bottom provided by the concrete matrix [Figure 5.19].

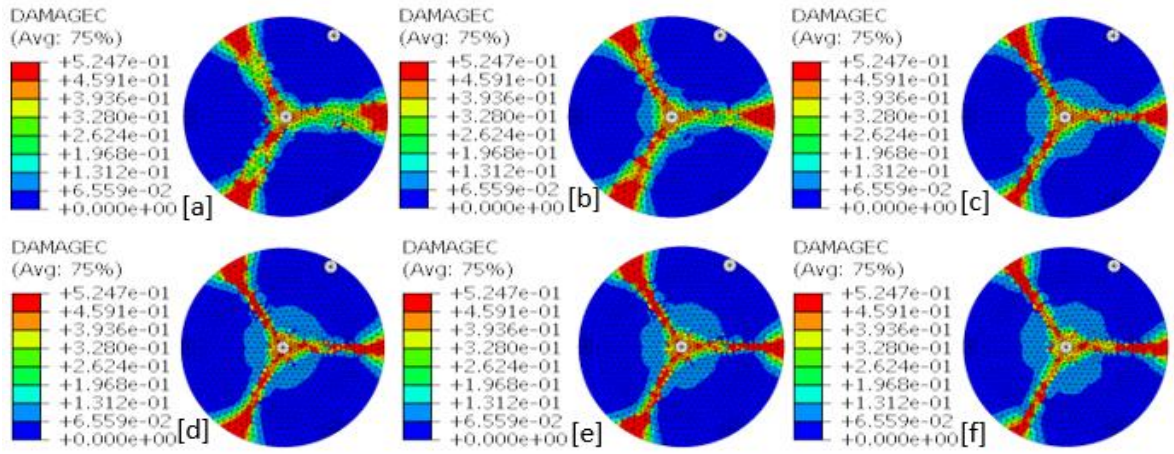

Figure 5.19: Compressive Damaged patterns at the top of the round-plate with V_f = [a] 1.00% [b] 1.25% [c] 1.50% [d] 1.75% [e] 2.00% and [f] 2.50%

The tensile damaged behaviours are presented in Figures 5.16 and 5.17. The tensile damage at the bottom started with lines failure radiating from the point of application of load at angle 120^0 to one another, along with the three weakest planes to the edge [circumference] of the round-plate. This is followed by multiple cracking along and around the initial lines.

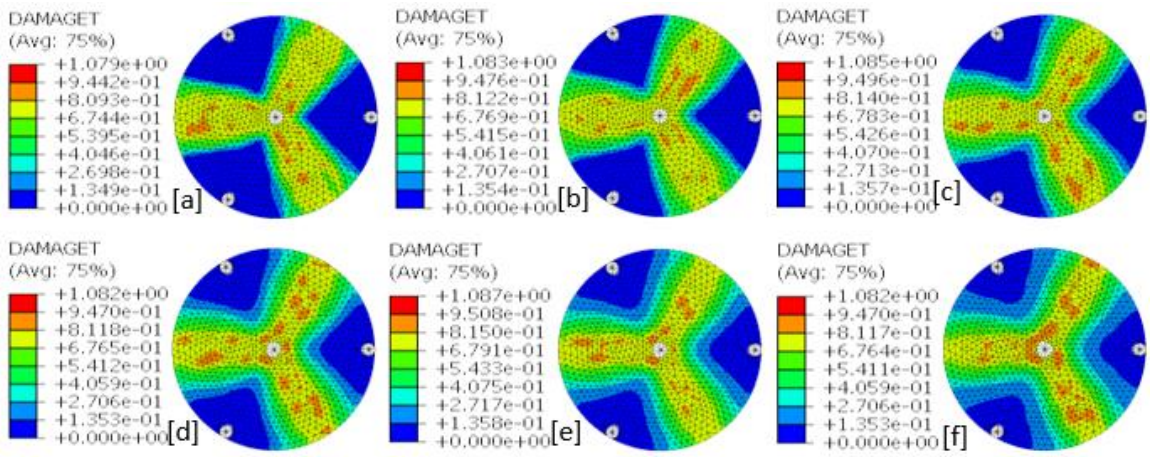

Figure 5.20: Tensile Damaged patterns at the bottom of the round-plate with V_f = [a] 1.00% [b] 1.25% [c] 1.50% [d] 1.75% [e] 2.00% and [f] 2.50%

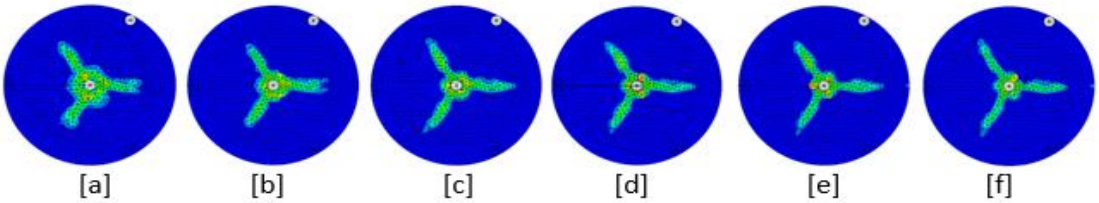

Figure 5.21: Tensile Damaged patterns at the bottom of the round-plate with V_f = [a] 1.00% [b] 1.25% [c] 1.50% [d] 1.75% [e] 2.00% and [f] 2.50% and the same numerical values as Figure 5.20

The tensile damage is insignificant at the top of the round-panel, thou visible around the point of the application of the load. This is expected because of the interface between the loading, and the round plate that give rise to tensile damage at the point of contact between the surfaces.

5.2.4.4 Deflected Shapes

A graphic presentation of the deflected shapes for the round-plate analysed in Case Study 1A at failure are given in Figure 5.22 below. The results are in agreement and have similar patterns with a substantial deflection at the round-plates' mid-span and a collapse along the weakest plane. The deformations observed are identical to the cracking patterns discussed earlier. While there is central displacement at the points of applications of loads, punching did not take place at these points and at the points the supports touched the panels [the panels actually lifted above the supports].

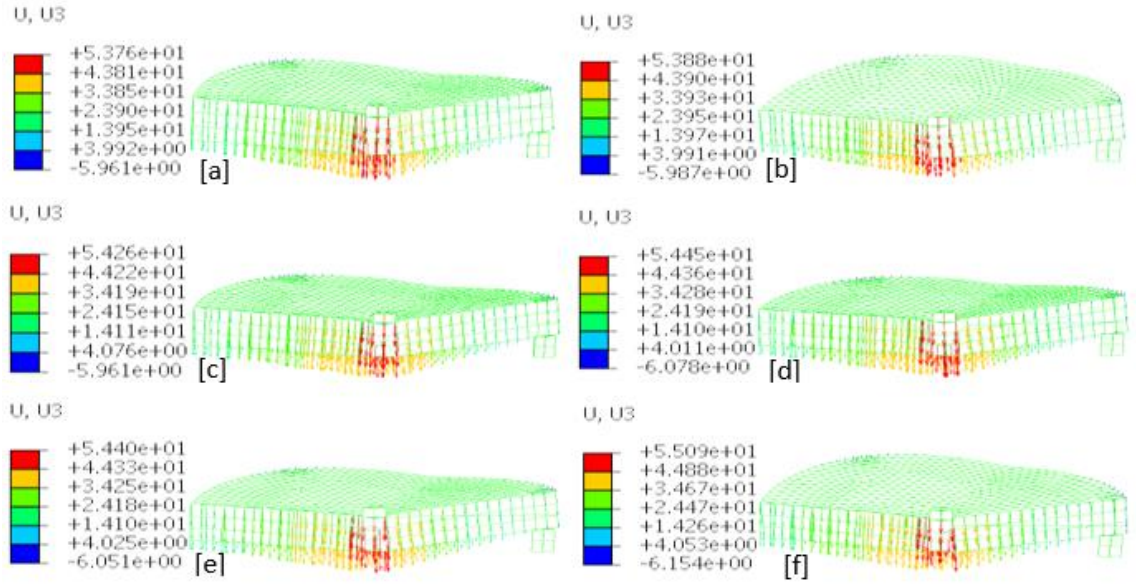

Figure 5.22: Deflected Shapes [y-y] for the round-plate with V_f = [a] 1.00% [b] 1.25% [c] 1.50% [d] 1.75% [e] 2.00% and [f] 2.50%

5.2.5 Comparative Study with Experimental Results Using Non-Dimensional Ratios

Comparisons are made between the round-plates analysed with various fibre volume and the experimental result serving as a control in this part. The normalisation of strength, ductility and energy absorption were obtained by dividing their values with the corresponding values of the experimental results. This will create a better understanding of the SFRC round-plates on isolated supports. Thus, conclusions were made on the potential of increase in fibres volume to be used for higher load bearing capacity in round-plates.

5.2.5.1 Strength Ratio

Figure 5.23 shows the ratio between each round-plate maximum load and that of the round-plate used in the experiment [$^{P_{max}}/_{P_{maxc}}$]. The graph shows that there is an enhancement in the strength of the round-plate as the fibre volume ratio increases.

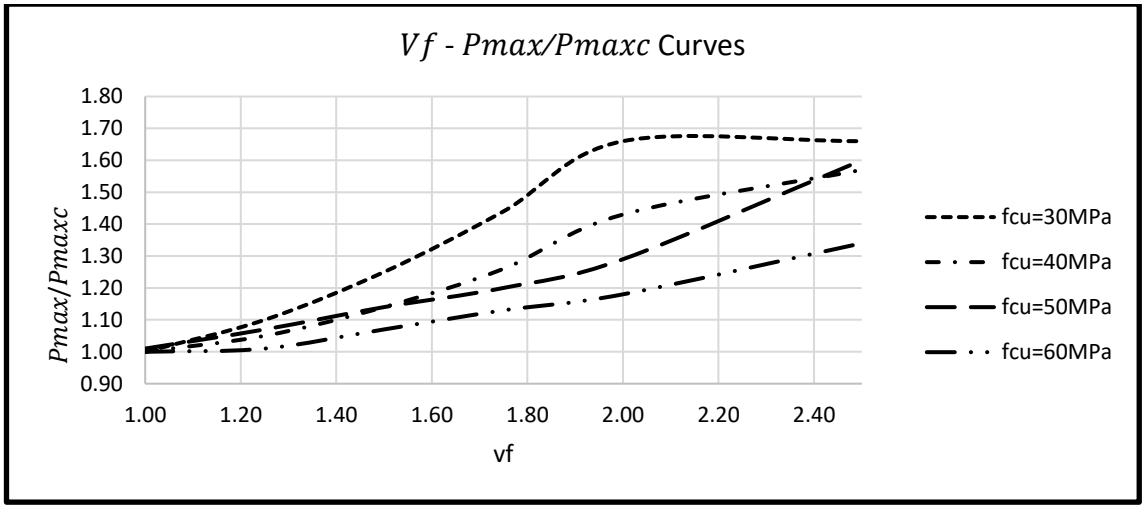

Figure 5.23: Graph of V_f against P_{max}/P_{maxc} for f_{cu} for Case Study 1A

The ratio between each round plate's yield load and that of the experimental round-plate $[{P_y}/{P_{ye}}]$ is represented in Figure 5.23. The upward trend of the graph was consistent in this figure, meaning that as the fibre increases, the yield load also increases.

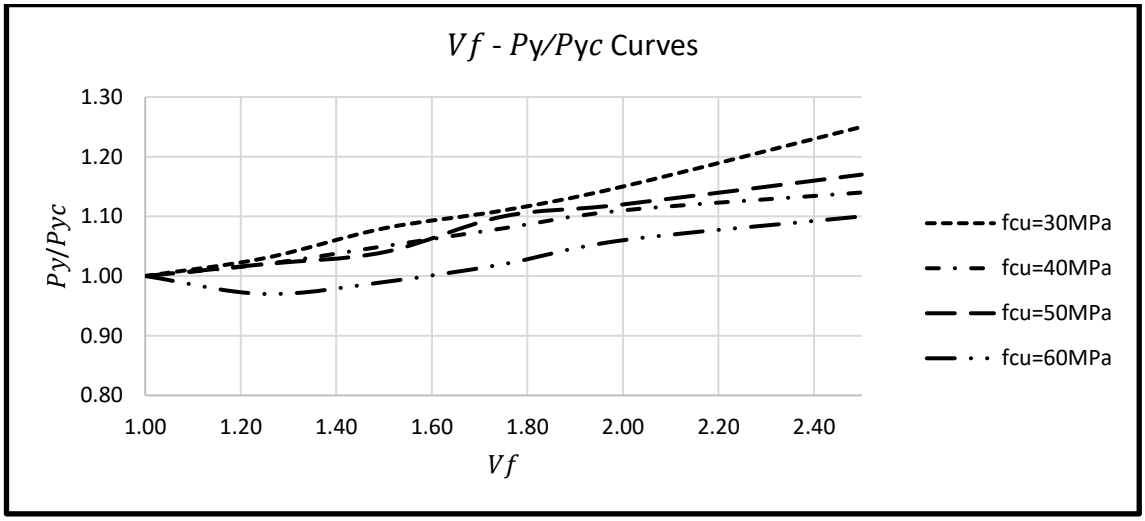

Figure 5.24: Graph of V_f against P_y/P_{yc} for f_{cu} for Case Study 1A

5.2.5.2 Ductility Ratio

The ductility ratios of the round-panels analysed were normalised by dividing them by the corresponding ratio of the control round plate (i.e. $\mu/\mu e$) and the results were plotted against the fibre volume fraction as shown in Figure 5.25. For the round plate with f_{cu}=30MPa, the ductility ratio reaches a maximum with fibre volume fraction of 1.75%. As the strength of SFRC matrix increase, the ductility ratio also increases.

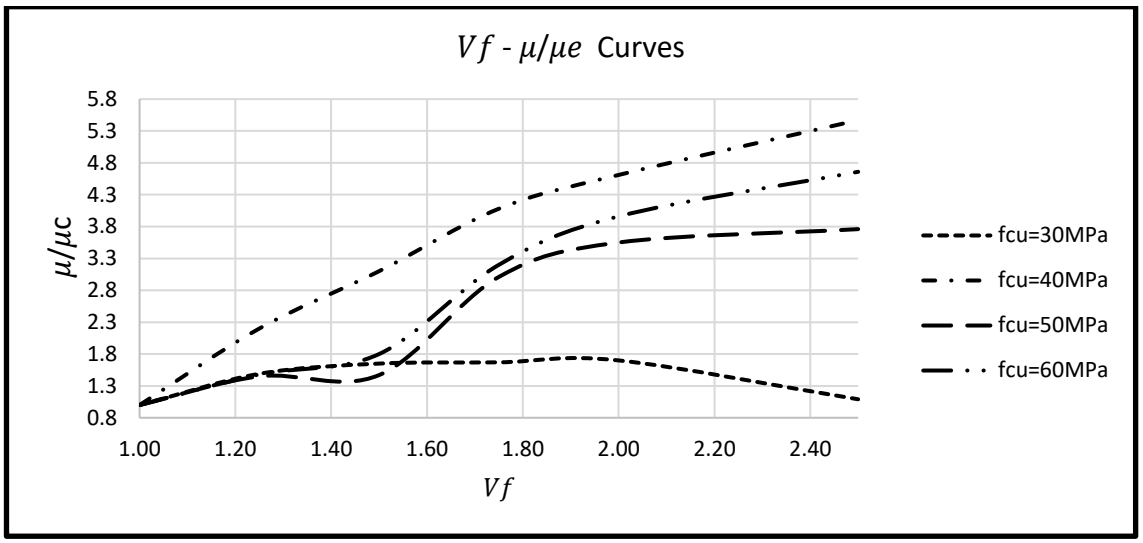

Figure 5.25: Graph of V_f against $\mu/\mu c$ for f_{cu} for Case Study 1A

5.3 Case Study 1B: Soranakom, C., Mobasher, B. and Destrée, X. (2007) Round Plate

The research work was based on using inverse analysis to confirm the material properties of steel-fibre reinforced concrete [Young's modulus, Poisson's ratio and tensile stress crack width parameters] from the load-deflection response from the round-plate test. Two sets of SFRC mixes with 1.00% and 1.25% of fibre volume ratio [TABIX 13/50] were used. The round panel is on simple continuous support. This is taken by some researchers as a convenient method for the determination of the biaxial flexural capacity of steel-fibre reinforced concrete slabs. The load-displacement response is the main essence of the round panel tests, which is generally used for material characterisation purposes. The FE result of the SFRC with V_f= 1.00% was used as a control.

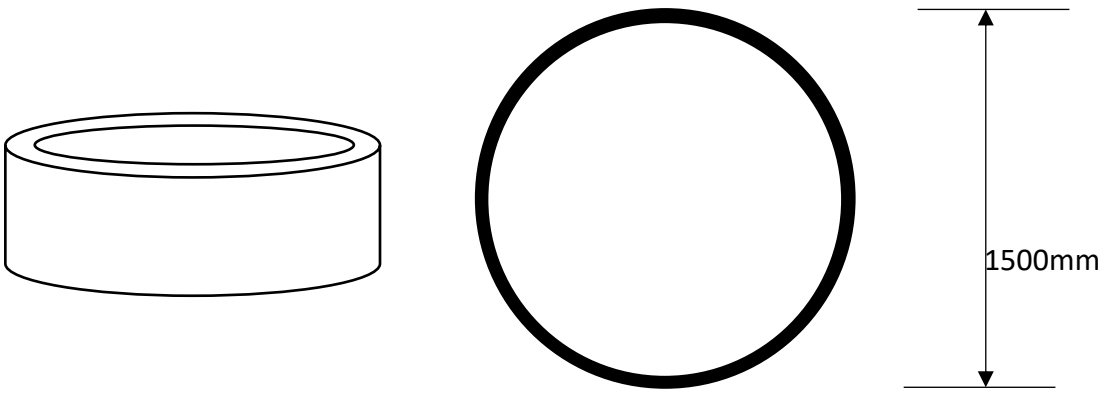

Figure 5.26: Schematic representation of experimental set-up for Case Study 1B

As in Case Study 1A, the full size of the round-plate was modelled (i.e. 1500 mm in diameter, 1400 mm clear distance and 150 mm thick). The parametric studies were carried out using the constitutive models (with models described in Chapters 2 and 3). The schematic illustration of the set-up is shown in Figure 5.26. The calibrated work on the validation of the numerical model using the respective experimental data was presented in section 4.3.3.4. Only the V_f and f_{cu} were changed in this parametric study. This study-case was modelled using V_f values of 1%, 1.25%, 1.50%, 1.75%, 2.00% and 2.5%.

Table 5.7: Tensile Stress-strain Parameters for SFRC for Case Study 1B

Point	Strain $^0/_{00}$	Stress [MPa]					
		Vf= 1.0%	Vf = 1.25%	Vf = 1.5%	Vf = 1.75%	Vf = 2.0%	Vf = 2.5%
Peak Tensile Stress	0	2.400	2.400	2.400	2.400	2.400	2.400
Point II	0.9	1.250	1.563	1.875	2.188	2.500	3.125
Point III	17.8	1.250	1.563	1.875	2.188	2.500	3.125
Point IV	19.1	0.040	0.040	0.040	0.040	0.040	0.040

The key points on the tensile stress-strain diagram used for the round plate are shown in Table 5.7 and represented in Figure 5.27. The value of V_f was limited to 2.50% because at this point, the flexural strength is greater the tensile strength.

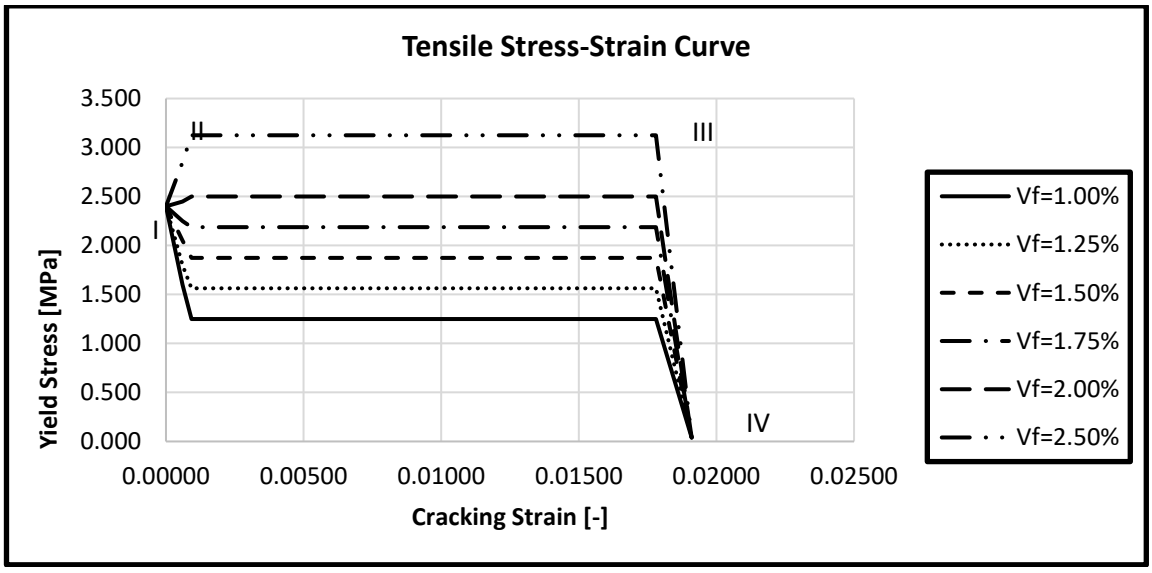

Figure 5.27: Tensile Stress-strain Parameters for SFRC round-Panel in Case Study 1B

As earlier stated, the displacement-based loading was applied at the centre of the round-plate. To guide against localised failure, a steel plate, 10mm thick was modelled for the loading rig. The monolithic loading type input data is shown in Figure 5.4. A mesh elements size of 25 mm width was adopted based on the early sensitivity analysis done, which produces the most suitable agreement with experimental data. The loading was applied gradually until failure using the displacement-based control loading data defined in Figure 5.4. The following NLFEA results are at this moment discussed next.

5.3.1 The load-Displacement Curves

The load-displacement curves for the varying fibre volume fractions are shown in Figure 5.28. These are also interpreted in Table 5.8, namely: the load at first crack [P_y], its displacement [δ_y], the maximum load [P_{max}], its displacement [δ_{max}], the ultimate load [P_u], its displacement [δ_u] and the ductility ratio [μ] are as defined in section 5.2.1.1. The load-displacement curves of the slab with different amount of fibre volume ratio shows that the maximum loads were reached for vf= 1.00-1.50% before 3mm central displacement while for vf=1.75-2.50%, they were reached after 3mm. These resistances are due to the amount of fibres in the concrete matrix. For all the specimens in case study 1B, the first crack was noticed before 5mm displacement.

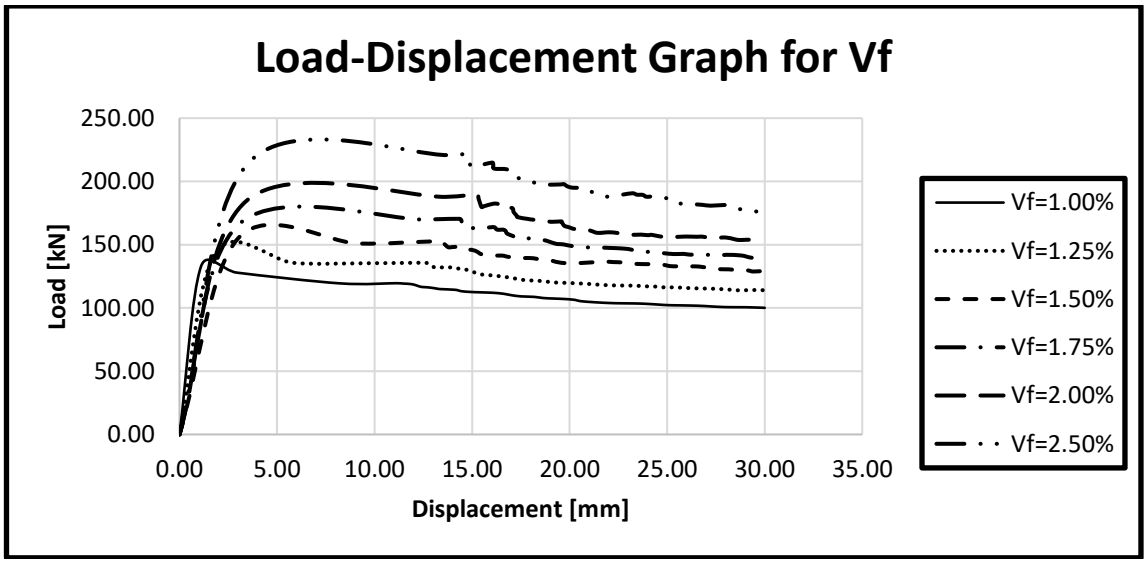

Figure 5.28: Load-Displacement Curve for a range of V_f for Case Study 1B

5.3.2 Strength

The results show the panels after cracking occurred to demonstrate a gentle but controlled load reduction followed immediately by a post-cracking softening phase which then changed gradually to smooth load reduction. After the matrix has cracked, a hardening response occurred when the peak load was approaching, followed by a gradual reduction in load as the crack width increases. The load-displacement curve and extract from it are presented in Figure 5.28 and Table 5.8 respectively.

The fibre volume ratios influence can be observed clearly as the fibre content increases. It can be seen that the load-carrying capacity [P_{max}] of the round-panels were improved by the increment in steel fibres. The enhancement was evident in all the round-panels as the values of fibre volume increases which lead to higher strength. The curves also show that stiffness was enhance with fibres between 1.00-1.50%. The round-panels deflects more with 1.750-2.50% fibre volume.

Table 5.8: Results for SFRC Round Plate

	V_f %	P_y [kN]	δ_y [mm]	P_{max} [kN]	δ_{max} [mm]	$\frac{P_{max}}{P_{maxc}}$	$\frac{P_y}{P_{yc}}$	Pu [kN]	δ_u [mm]	$\mu = \frac{\delta_u}{\delta_y}$	$\frac{\mu}{\mu_c}$
Control	1.00	132.91	1.11	132.9	1.11			113.0	14.5	13.06	
	1.00	132.91	1.11	132.9	1.11	1.00	1.00	113.0	14.5	13.06	1.00
	1.25	143.79	1.85	143.8	1.85	1.08	1.08	122.2	17.5	9.46	0.72
	1.50	155.51	3.03	155.5	3.03	1.17	1.17	132.2	26.8	8.84	0.68
	1.75	166.82	3.10	170.4	14.36	1.28	1.26	144.8	23.7	3.05	0.23
	2.00	184.19	3.40	189.7	15.24	1.43	1.39	161.2	21.1	2.36	0.18
	2.50	215.64	3.60	221.8	14.74	1.67	1.62	188.5	22.1	2.42	0.19

*P_{maxc} represent the peak load from the control results

In a similar vein, the yield load [P_y] present a pattern that was observed to increase in the SFRC round-panels when the fibre dosage was increased.

5.3.3 Ductility

Ductility in case study 1B [round-panel with continuous support] does not follow the pattern that was observed in round-panels with isolated supports [case study 1A]; that is, it decreases as more fibres are added. This is due to multiple cracks exhibited in the panel with continuous support.

5.3.4 Cracking Patterns

The deflected shapes, the principal strain contours and vectors of the round-panels with continuous supports analysed under monotonic loading are presented in this section. All the data herein were taken at failure. The cracking patterns are also presented.

5.3.4.1 The Deflected Shapes

The FE-based deflected shapes, taken at failure, of the round-panels analysed in Case Study 1B are illustrated in Figures 5.29 [a-f]. The deformations were related to the direction of the load (i.e. downward) and depicted bending at failure.

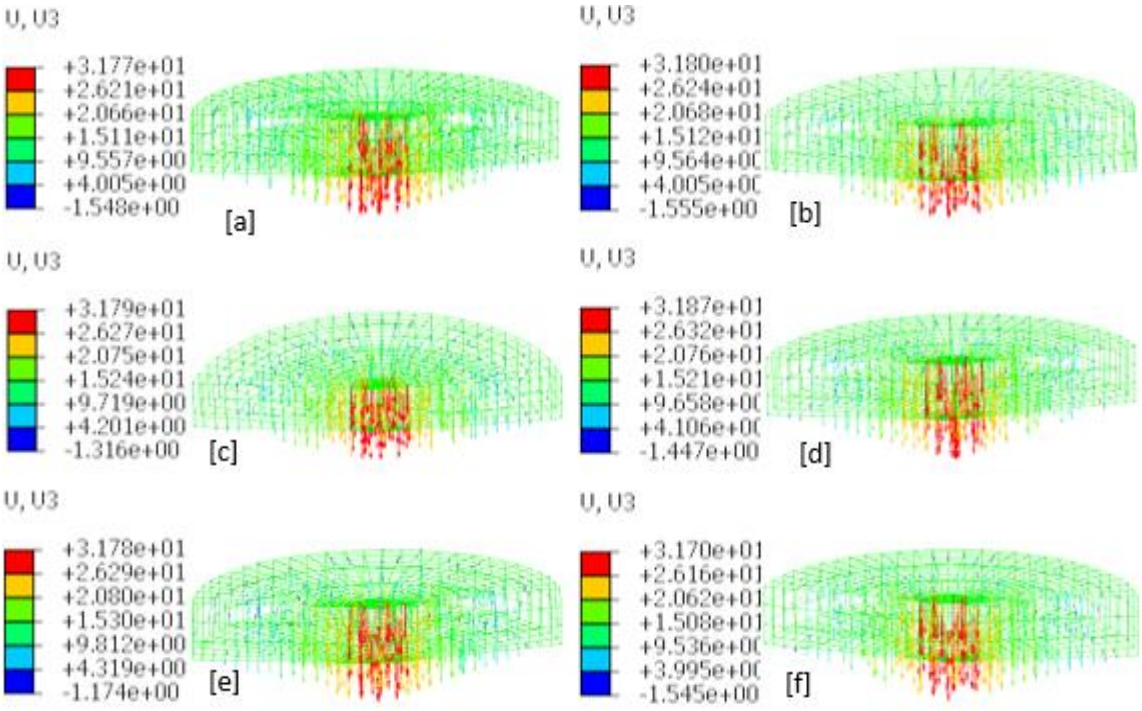

Figure 5.29: Deflected Shapes [y-y] for the Case Study 1B round-plate with V_f = [a] 1.00% [b] 1.25% [c] 1.50% [d] 1.75% [e] 2.00% and [f] 2.50%

5.3.4.2 The Principal Strain Contours

Figures 5.30 [a-f] show Case Study 1B round-panel's Principal strain contours. These were characterised by tensile cracking at the point of the application of the load due to

the failure of the round-panel. The strained were formed along the cracked line. The panel with V_f =1.00% exhibit multiple strain contours [eight] and as the fibre volume increases, the stain contours reduces. At V_f =2.50% the strain contours have reduced to four. Punching was noticed at the point of the application of load for V_f=1.0%, but as the fibre volume increases, the effects of punching diminished.

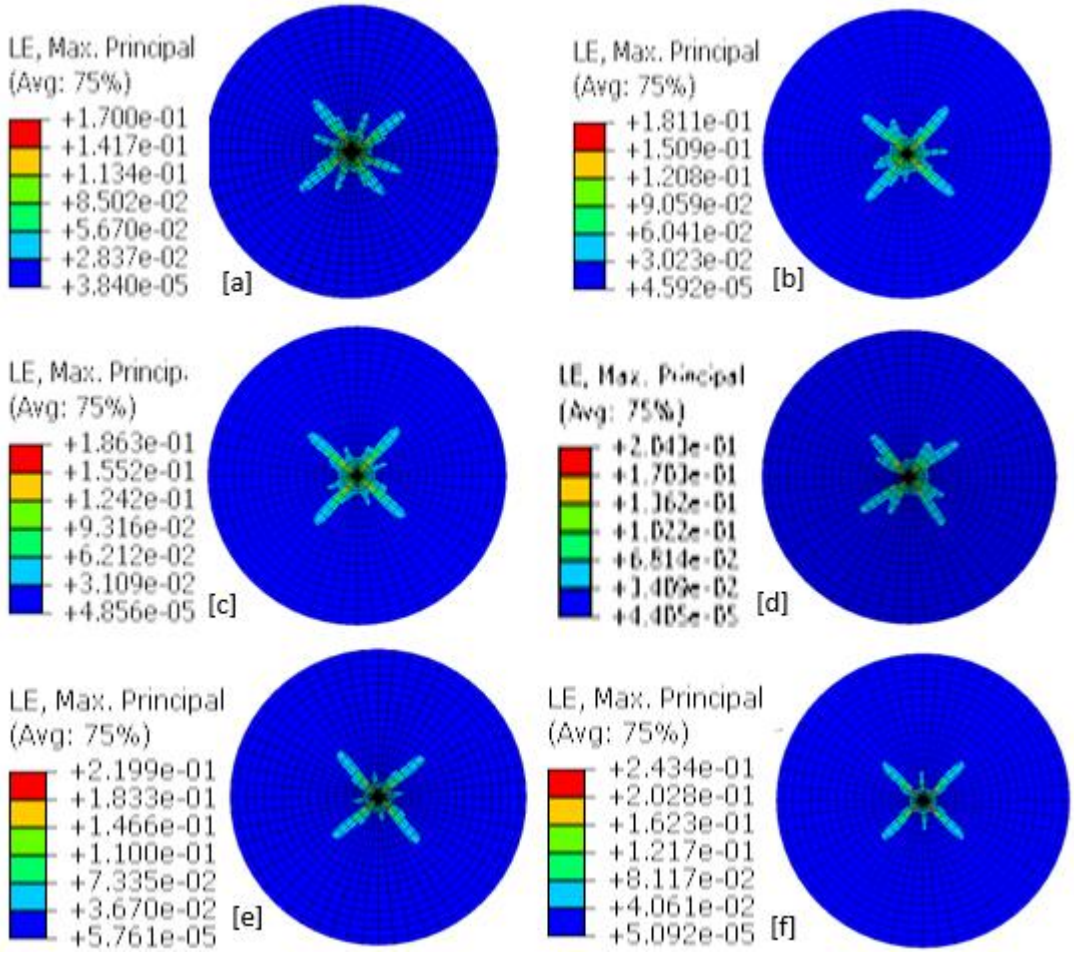

Figure 5.30: Principal strain contour for Case Study 1B with V_f [a= 1.00, b=1.25, c=1.50, d=1.75, e=2.00 and f=2.50%]

As the steel fibres increases, there is a reduction in the areas affected by failure at pull-out as shown in Figures 5.30 above. This implies that the fibres aid crack propagation control. It also shows the effectiveness of fibres in crack control.

5.3.4.3 The Principal Strain Vectors

The principal strain vectors for the round-panels are given in Figure 5.31, which shows a reduction of cracks in the panels as the fibres volume increases. The round-panel with 1.00% fibres volume failed with higher strain around the point of application of load on panel span, whereas the panel with 2.50% fibre volume failed with reduced strains. The strains are concentrated at the mid-span of the panels.

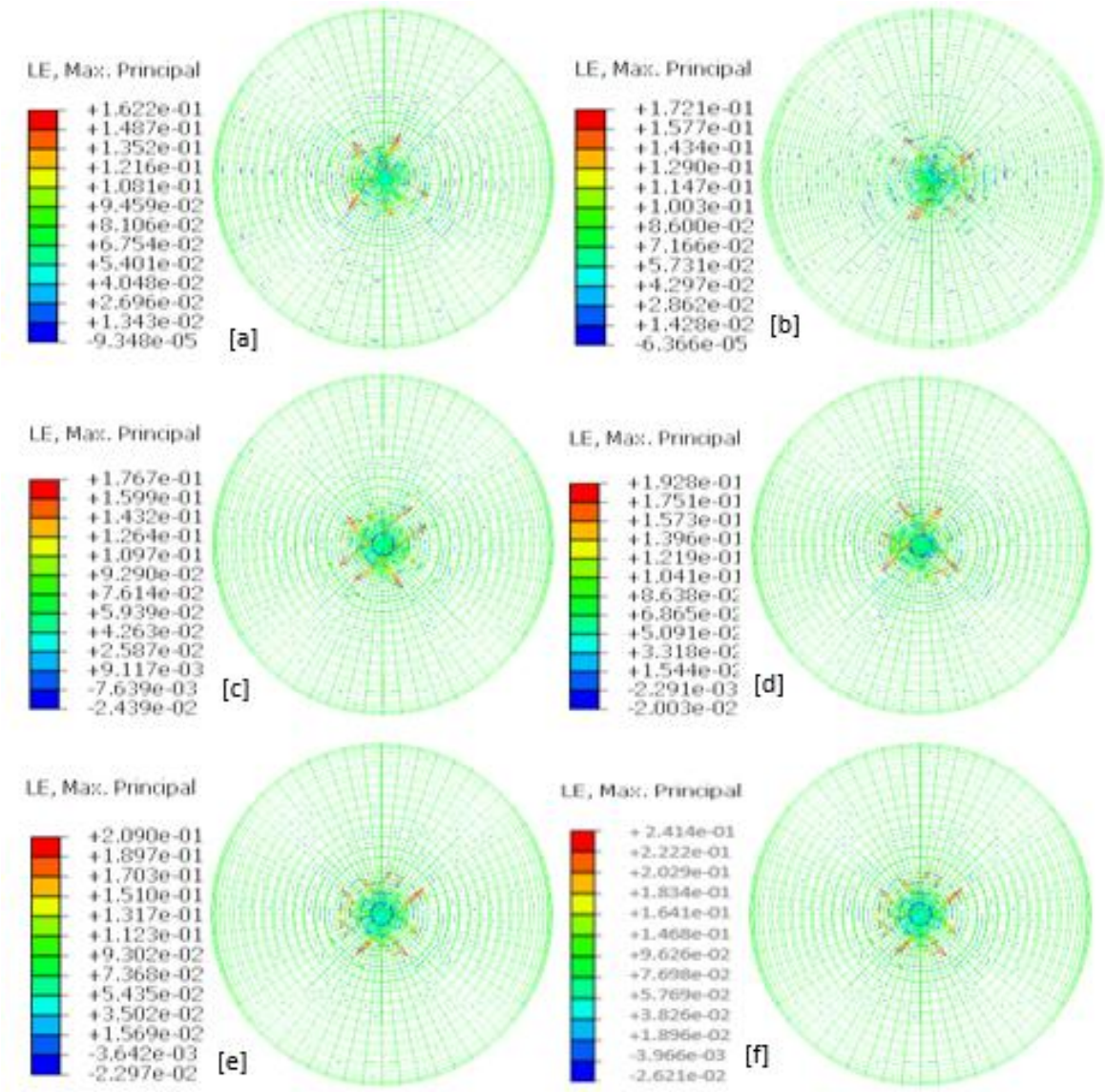

Figure 5.31: Principal strain vector for Case Study 1B with V_f = [a] 1.00% [b] 1.25% [c] 1.50% [d] 1.75% [e] 2.00% and [f] 2.50%

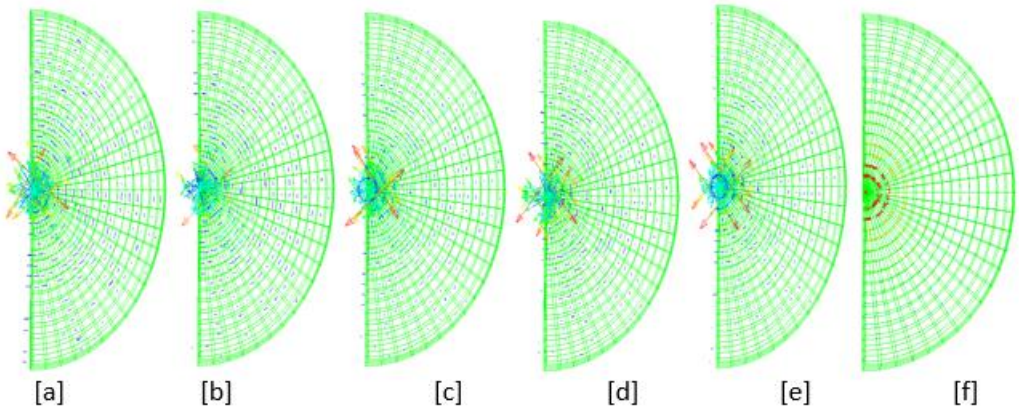

Figure 5.32: Principal strain vector for Case Study 1B [section y-y] with V_f = [a] 1.00% [b] 1.25% [c] 1.50% [d] 1.75% [e] 2.00% [f] 2.50% and the same numerical values as Figure 5.31

Figures 5.31[a] and 5.32 [a] depicts the strains vectors in a round-panel with V_f =1.00%. There is a concentration of the strains vectors from the mid-span and towards the circumference representing that the cracks cover a wide area. As the fibre volume increases, the stains vectors reduces and at V_f = 2.50%, the strains vectors reduces, signifying the reduction in crack area as shown in Figures 5.31 [b-f] and 5.32 [b-f].

5.3.4.4 Deformed [compressive and tensile] shapes

Figures 5.33 – 5.36 show the tensile and compressive damaged patterns at the top and bottom of the round-plate. The round-plates failed in tension evident by the significant cracks at the bottom which are more than that at the top.

Figures 5.33 and 5.34 depict the damaged tensile behaviours. The tensile damage at the top follows the pattern of the strain contours thou insignificant. The pattern at the bottom is wider and radiates from the point of application of load, along with the three weakest planes to the edge [circumference] of the round-plate. These are followed closely by multiple cracking along and around the initial lines.

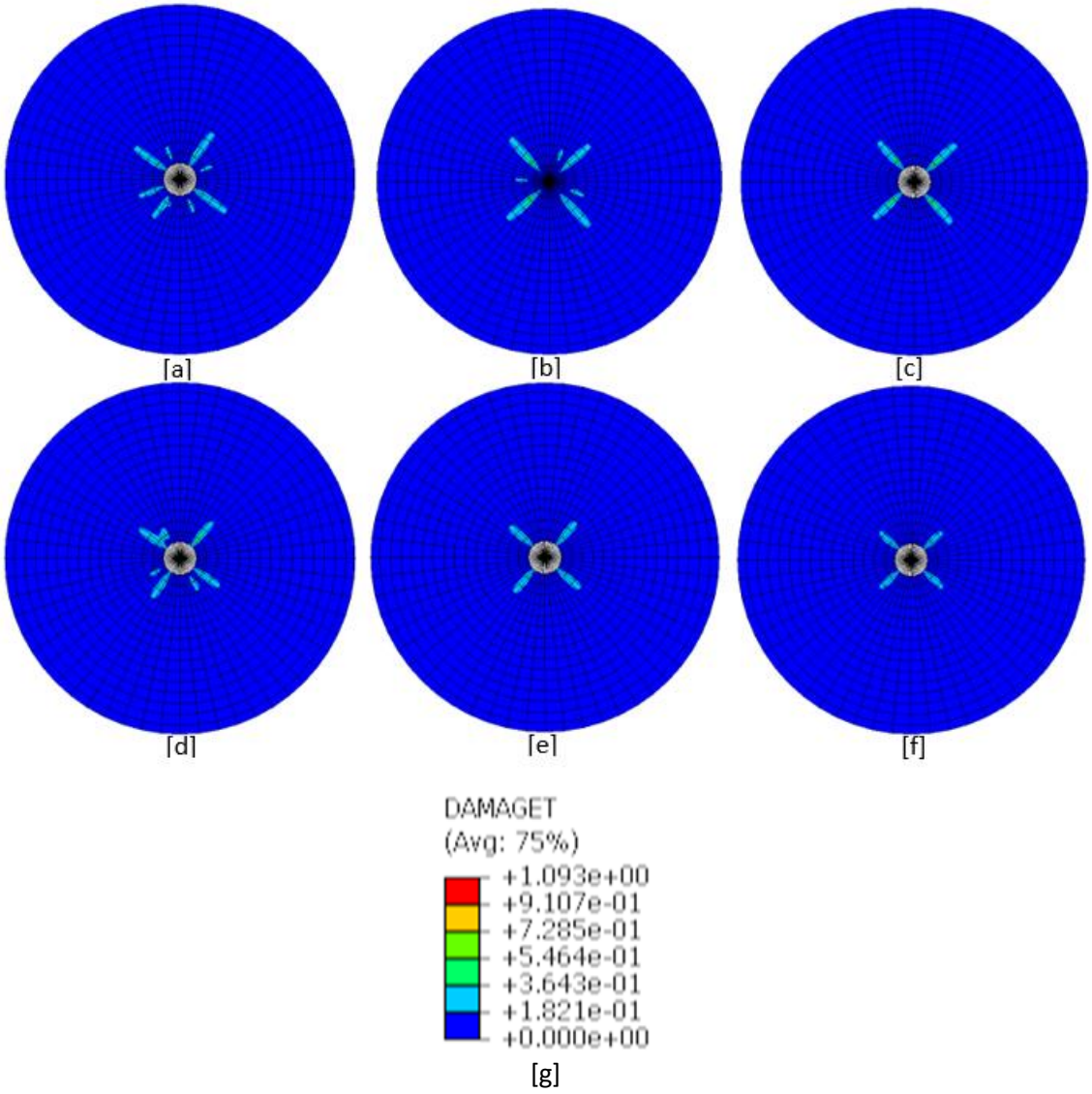

Figure 5.33: Tensile Damaged patterns at the top of the round-plate with V_f = [a] 1.00% [b] 1.25% [c] 1.50% [d] 1.75% [e] 2.00% [f] 2.50% and [g] Legend for Figures 5.33 [a-f]

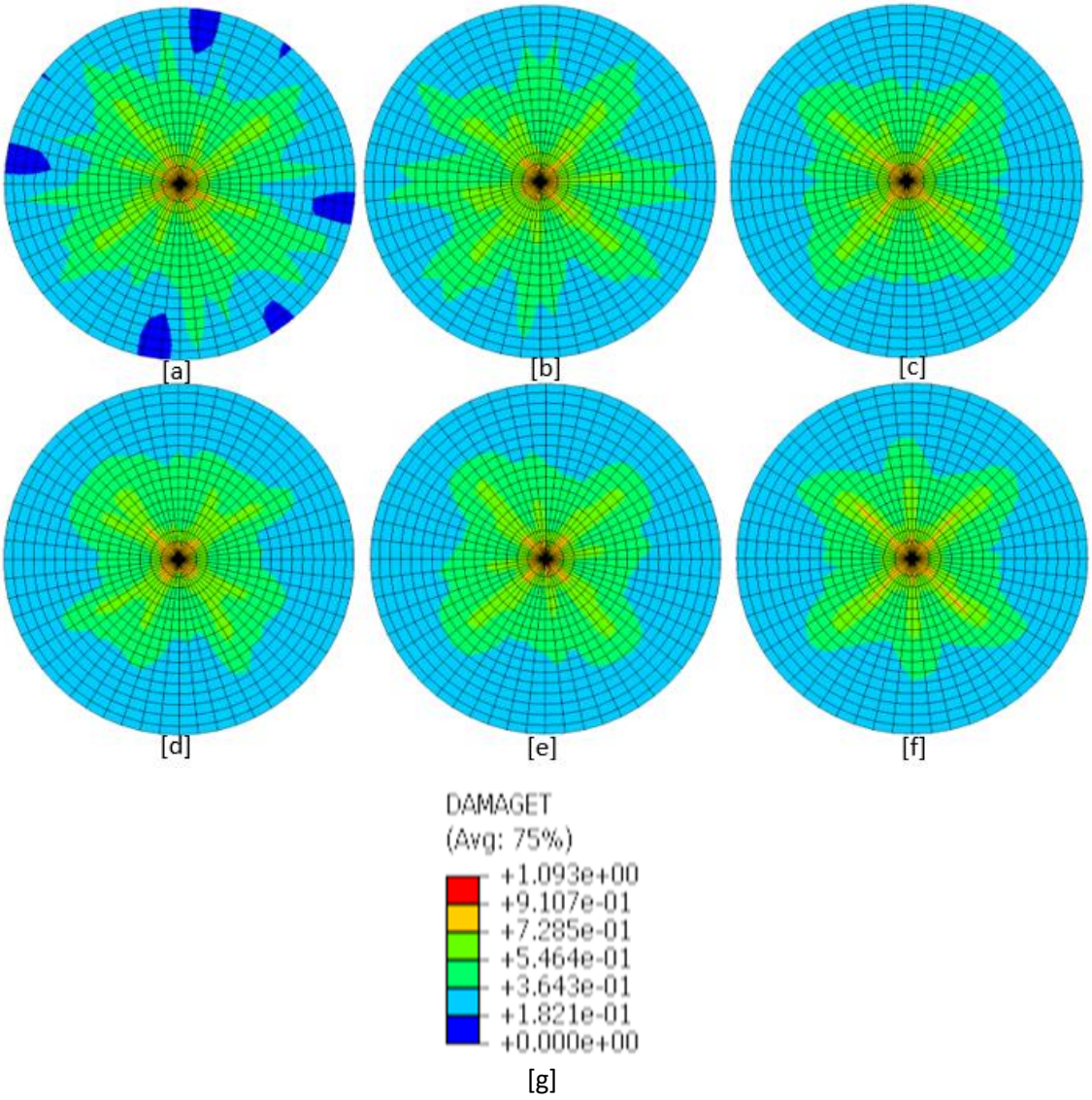

Figure 5.34: Tensile Damaged patterns at the bottom of the round-plate with V_f = [a] 1.00% [b] 1.25% [c] 1.50% [d] 1.75% [e] 2.00% [f] 2.50% and [g] Legend for Figures 5.34 [a-f]

Figures 5.35 and 5.36 show the damaged compressive behaviour of SFRC round-panels resting on continuous supports. The top shows a substantial resistance to cracking traceable to the fact that concrete is good at compression [Figure 5.35]. There is more damaged at the bottom because concrete provides little resistance at the tension face [Figure 5.36].

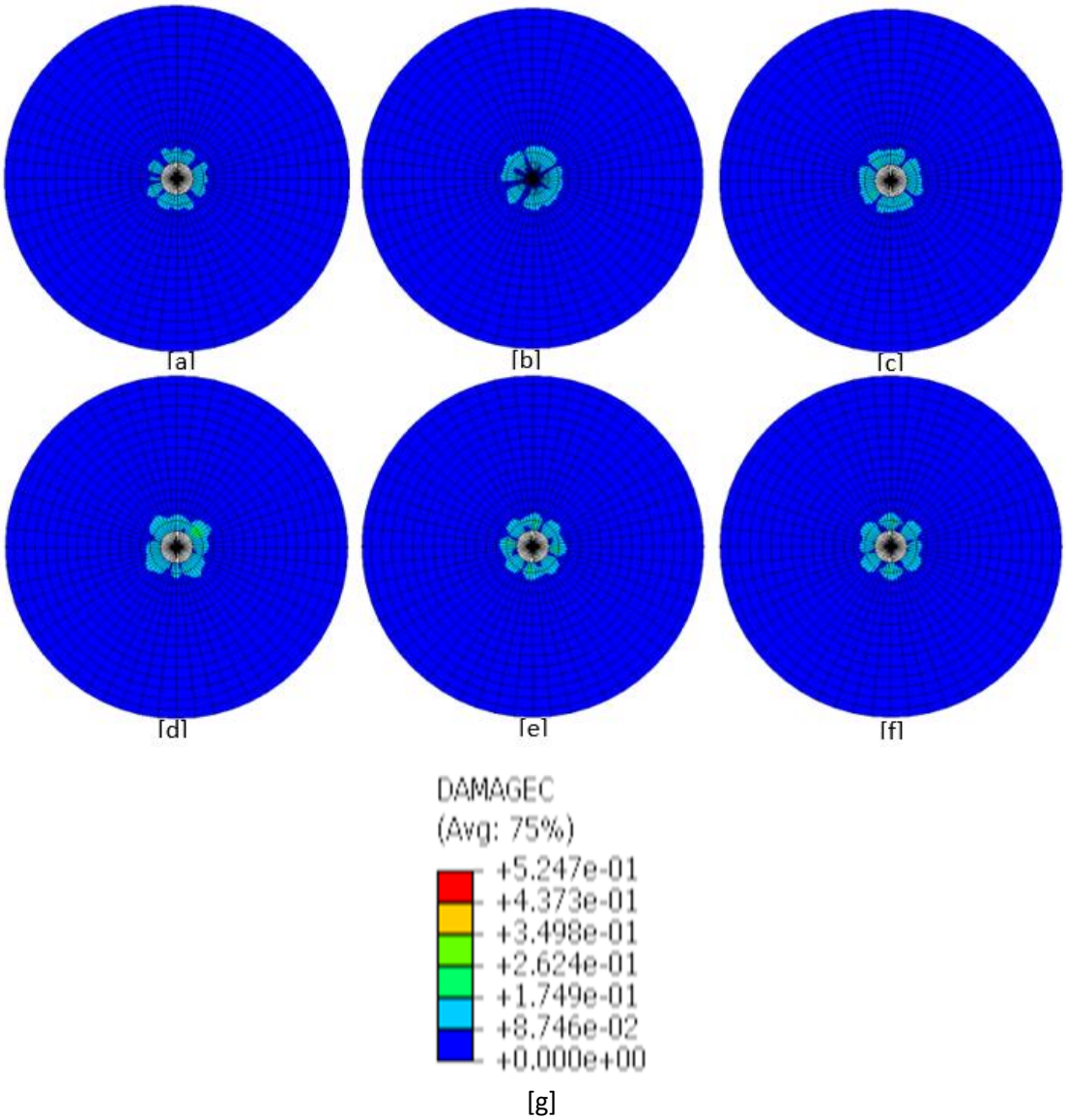

[g]

Figure 5.35: Compressive Damaged patterns at the top of the round-plate with V_f = [a] 1.00% [b] 1.25% [c] 1.50% [d] 1.75% [e] 2.00% [f] 2.50% and [g] Legend for Figure 5.35 [a-f]

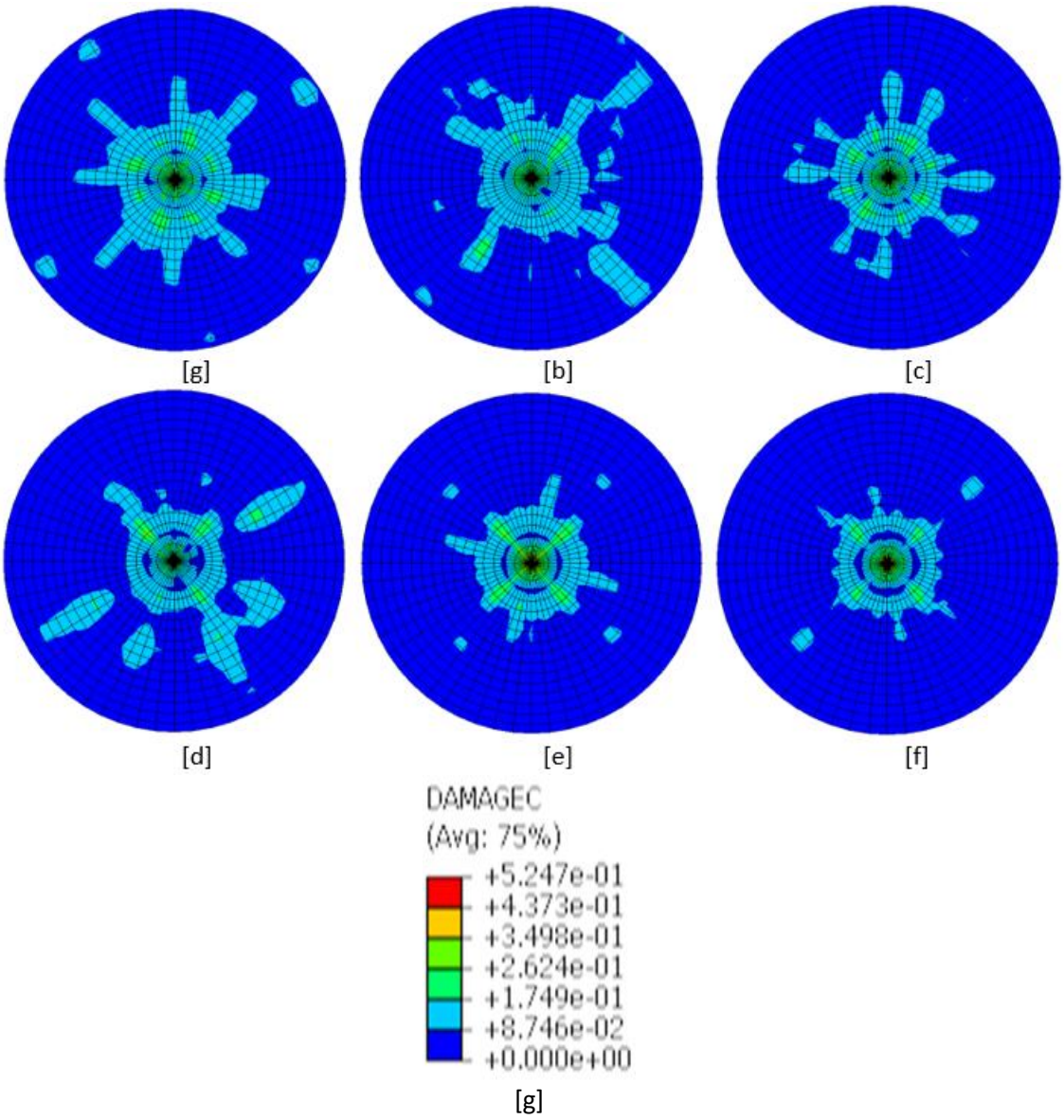

Figure 5.36: Compressive Damaged patterns at the bottom of the round-plate with V_f = [a] 1.00% [b] 1.25% [c] 1.50% [d] 1.75% [e] 2.00% [f] 2.50% and [g] Legend for Figure 5.36 [a-f]

5.3.5 Comparative Study with Experimental Results Using Non-Dimensional Ratios

The round-panels analysed with various fibre volume were compared with the control specimen [the experimental results served as a control]. The values of strength and ductility were normalised by dividing them with their corresponding values of the control. Like in Case Study 1A, increase in fibres volume leads to higher load bearing capacity in round-plates on continuous supports.

5.3.5.1 Strength Ratio

Figure 5.37 shows the ratio between round-panel with different V_f's maximum load and that of control [$^{P_{max}}/_{P_{maxc}}$]. The graph shows that there is an enhancement in the strength ratio as the fibre volume ratio increases.

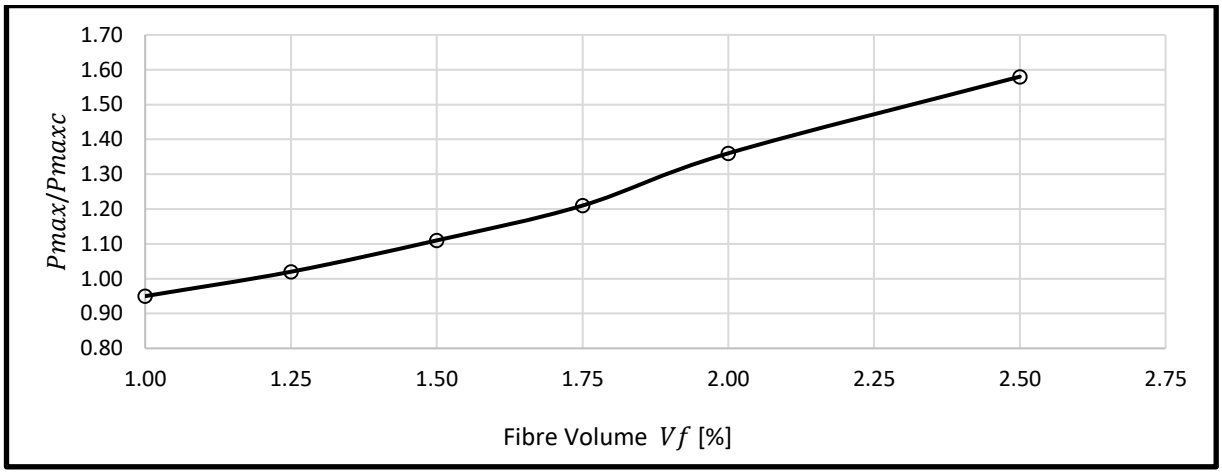

Figure 5.37: Graph of V_f against P_{max}/P_{maxc} for Case Study 1B

5.3.5.2 Ductility Ratio

The ductility ratio is taken as the ratio of the ductility of the round-panel with different V_f to that in the control round-panel and is shown in Figure 5.34. A reduction in the ductility ratio is noticed as the fibre increases.

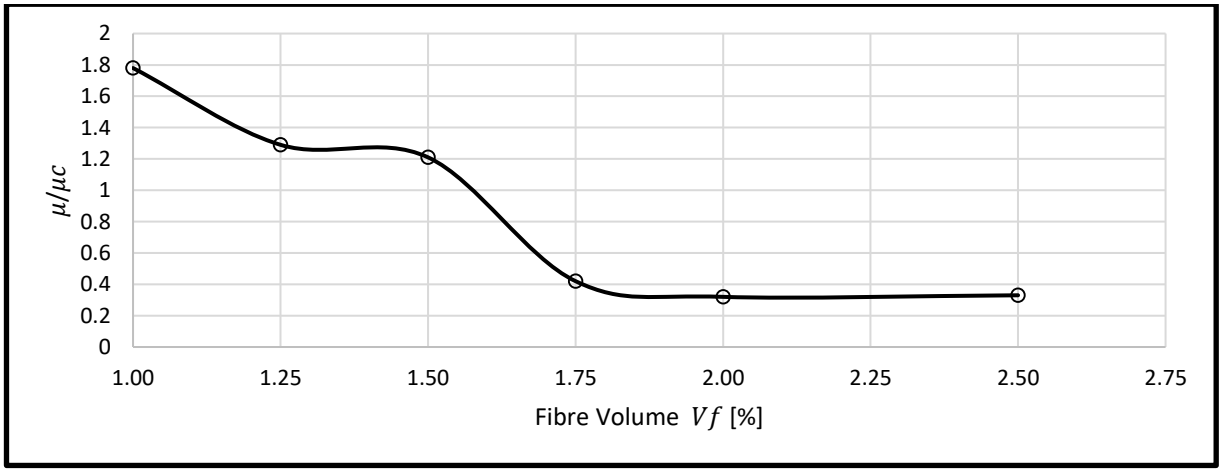

Figure 5.38: Graph of V_f against $\mu \ /\mu_c$ for Case Study 1B

5.4 Case Study 1C: Blanco, A., Cavalaro, S., De La Fuente, A., Grünewald, S., Blom, CBM & Walraven, JC Square Plate (2014)

The experimental work, which they also validated with numerical analysis was set-up to confirm the provisions made by RILEM for testing SFRC (RILEM, 2002a). Three different slabs were tested and modelled. The panels, 1500mm x 750mm x 200mm, 1500mm x 1000mm x 200mm and 3000mm x 3000mm x 200mmm were used. The largest one was used for this validation, calibration and Case Study 1C.

The SFRC has a compressive strength of 46.7MPa, tensile strength of 5.6MPa and modulus of elasticity of 29GPa. 40kg/m3 of Dramix® hooked end steel fibres, 50mm long and 0.625mm equivalent diameter. The percentage of volume fibre used was 0.5%. The slab was supported at the edge with support equal to the half of the length of the side and placed at the centre. Provisions were made for a 20mm neoprene membrane placed in between the slab and the supports. It was loaded centrally with a square ram.

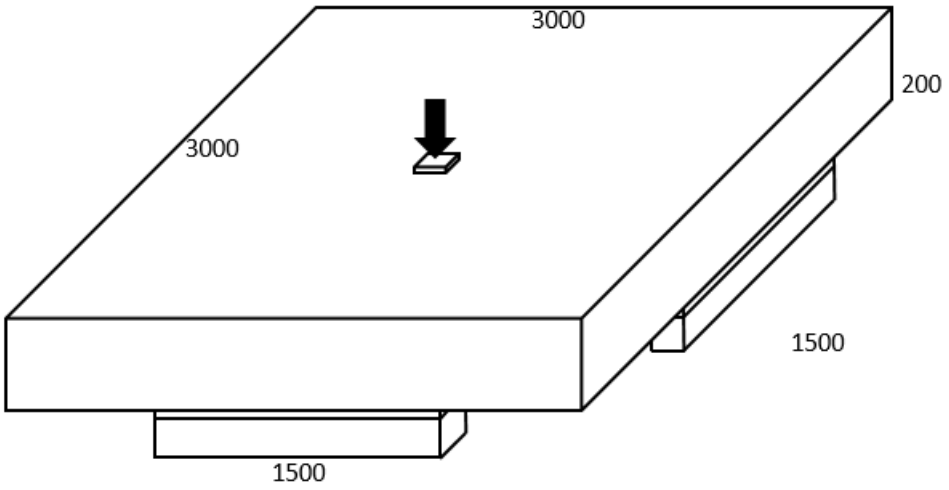

Figure 5.39: Schematic representation of the experimental set-up for Case Study 1C

The displacement-based method was used in applying the load gradually with the input data given in Figure 5.4. The constitutive model used to interpret the tensile stress-strain relationship is given in Table 4.19 and Figure 5.40 with the input parameters as outlined in Table 4.20.

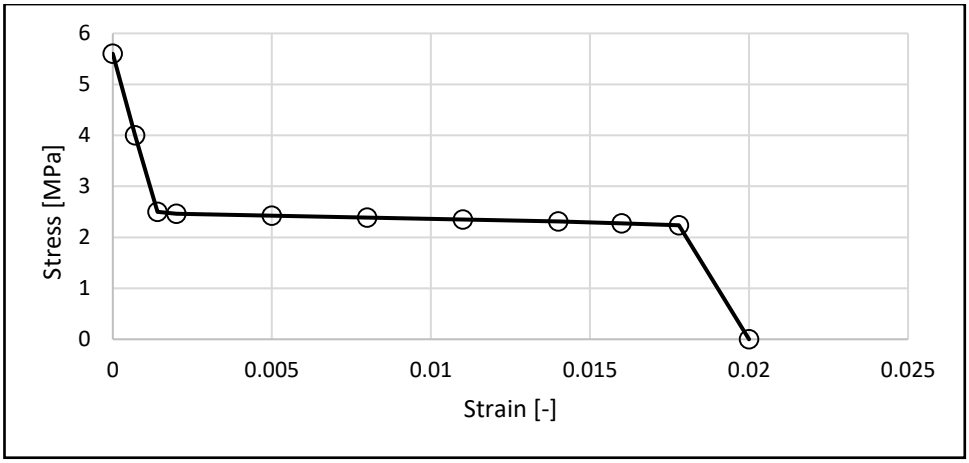

Figure 5.40: Tensile stress-strain diagram

The results of the response of the square-panel to loading is given in Figure 5.51. The FEA with V_f = 0.50% produces a result with is less than 5% of the experimental works at peak load. This shall be used as a control in the Case Study 1C.

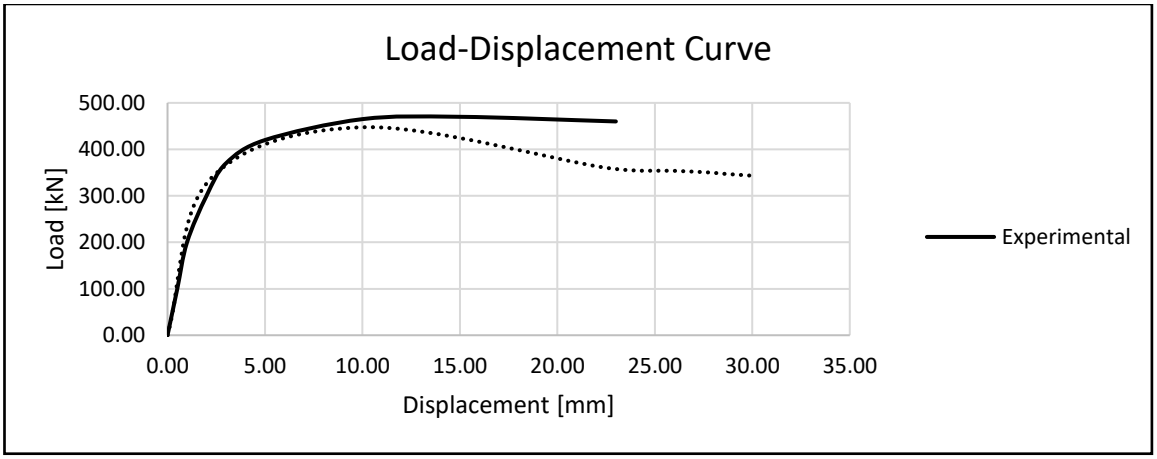

Figure 5.41: Load-Displacement Curves of Experiment and FEA

The V_f was the main parameter that was change in this Case Study 1C after the validation and calibration work were concluded. The square-panels were modelled with fibre volume ratio ranging from 1.00%, 1.25%, 1.50%, 1.75%, 2.00% and 2.50%. The input parameter [tensile stress-strain] for the square-panels are presented in Table 5.9 and Figure 5.42

Table 5.9: Tensile Stress-strain Parameters for SFRC for Case Study 1C

Point	Strain $^0/_{00}$	Stress [MPa]					
		V_f=1.0%	V_f= 1.25%	V_f = 1.5%	V_f= 1.75%	V_f = 2.0%	V_f = 2.5%
Peak Tensile Stress	0	5.60	5.60	5.60	5.60	5.60	5.60
Point II	0.9	2.50	3.13	3.75	4.38	5.00	6.25
Point III	17.8	2.50	3.13	3.75	4.38	5.00	6.25
Point IV	19.1	0.04	0.04	0.04	0.04	0.04	0.04

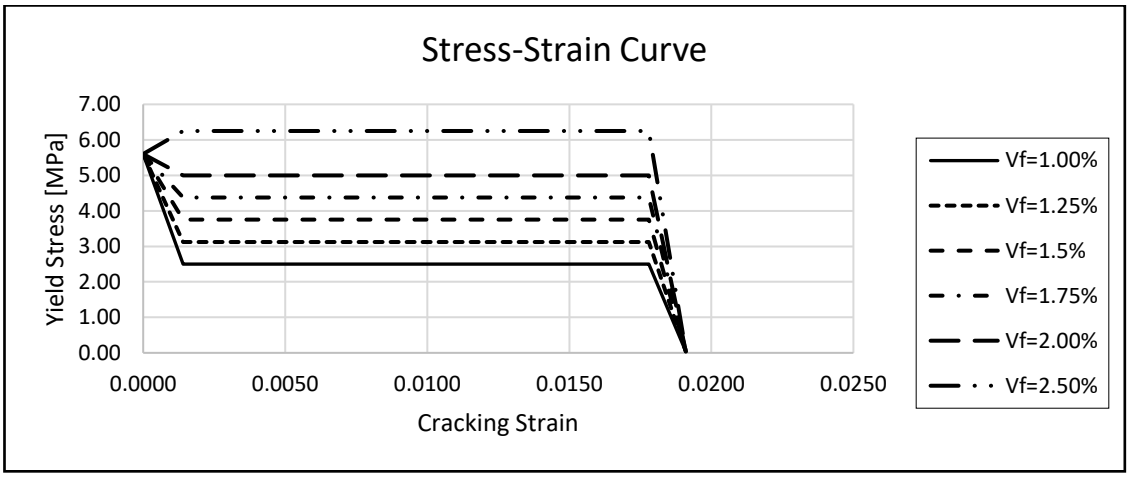

Figure 5.42: Tensile Stress-Strain Curve for Input Parameters for V_f

5.4.1 Load-Displacement Curves

The load-deflection curves for Case Study 1C is presented in Figure 5.43. Also, a summary of the vital load values and their corresponding displacements is given in Table 5.10. From the load-displacement curves, it can be seen that there is a marginal difference in the values of the yield load for various values of fibre volume ratio. In similarity, there is a gradual increase in strength and ductility as the fibres volume ratio is increased. The ductility ratio [μ] is defined as the ratio of the displacement corresponding to the ultimate load to that of displacement corresponding to the yield load [μ_u/μ_y]. There was a noticeable increment in the stiffness up to V_f= 2.00% compared to the control specimen, indicating that SFRC square-panel deflect less as the fibre volume increases. Signifying that there are strong advantages of additional fibres at both the serviceability and ultimate limit states, which are vital in design considerations.

5.4.2 Strength

Judging from the load-displacement curves in Figure 5.43, a marginal increase can be seen in the load-carrying capacity of the square-panel as more fibres were added. The square-panel with V_f =1.00% with yield load [P_y] of 336.33 kN and corresponding displacement [δ_y] of 2.20mm is taken as the control square-panel. It is used to compare other square-panels for the parametric studies. The marginal increase was about 1% from V_f =1.25% to V_f =2.50% for the yield load P_y.

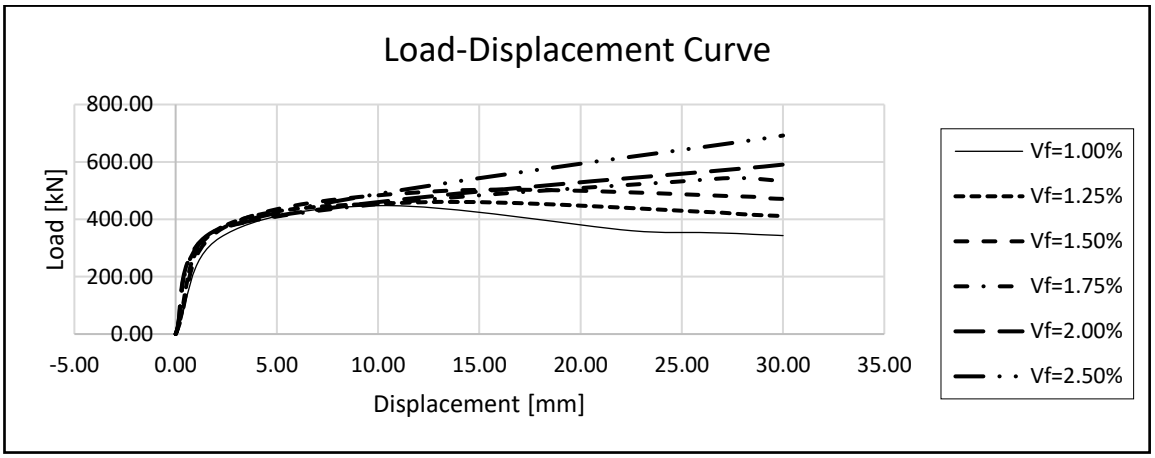

Figure 5.43: Load-Displacement Curve for V_f

Table 5.10: Results for SFRC Square Plate

V_f %	P_y [kN]	δ_y [mm]	$\frac{P_y}{P_{yc}}$	P_{max} [kN]	δ_{max} [mm]	$\frac{P_{max}}{P_{max,c}}$	P_u [kN]	δ_u [mm]	$\mu = \frac{\delta_u}{\delta_y}$	$\frac{\mu}{\mu_c}$
1.00	336.33	2.20	1.000	447.61	10.10	1.00	380.47	3.50	1.59	1.00
1.25	369.88	2.20	1.100	459.33	12.20	1.03	390.43	3.00	1.36	0.86
1.50	371.80	2.40	1.105	498.12	13.00	1.11	423.40	4.20	1.75	1.10
1.75	373.47	2.50	1.111	541.28	26.73	1.21	460.01	11.80	4.72	2.97
2.00	374.92	2.50	1.115	590.65	30.00	1.32	502.03	15.80	6.08	6.32
2.50	377.41	2.55	1.122	691.82	30.00	1.55	588.05	19.20	7.53	4.74

*$P_{max,c}$ represents the peak load from the control results

The maximum load P_{max}, saw an increment of by 3% - 55% for V_f =1.25% to V_f =2.50% over the control specimen with an average of 10% over consecutive ones. The increase in fibre volume ratio has led to an enhancement in load resistance of the square-panel.

5.4.3 Ductility

The ultimate displacement at failure [δ_u] corresponding to the ultimate load [P_u] is used to determine ductility of the square-slabs. The P_u was taken as the least of the 85% of the maximum load or load at failure [$0.85P_{max} \leq P_u$]. There is a significant increase in the ultimate displacement as the fibre volume increases. From the results, it clearly shows that the increase in fibres volume enhances the ductility of the square-panels.

5.5.4 Crack Patterns

In this section, further insight into cracking formation and patterns are gotten from the data from the principal strain contours and vectors and deflected shapes at failure.

5.5.4.1 Principal Strain Contours

The principal strain contours for the square panels in Case Study 1C are presented in Figures 5.44[a-f] and 5.45[a-f]. The contour intervals for SFRC panels were selected so that the tensile strains beyond 0.02 [i.e. fibres pull-out strain] were highlighted in grey and compressive strains beyond ultimate concrete strain [i.e., 0.0035] were represented in black.

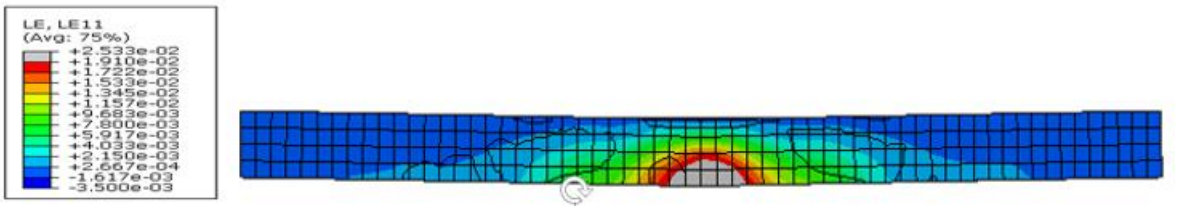

[a]

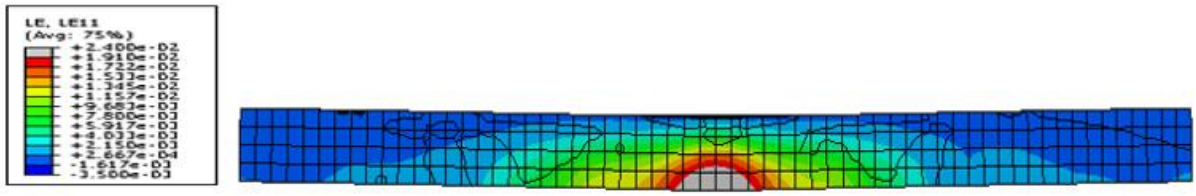

[b]

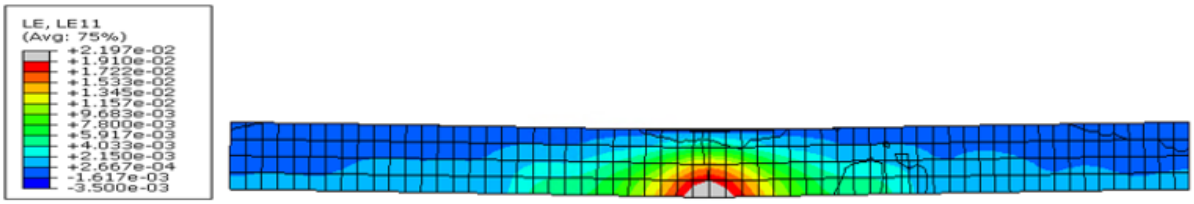

[c]

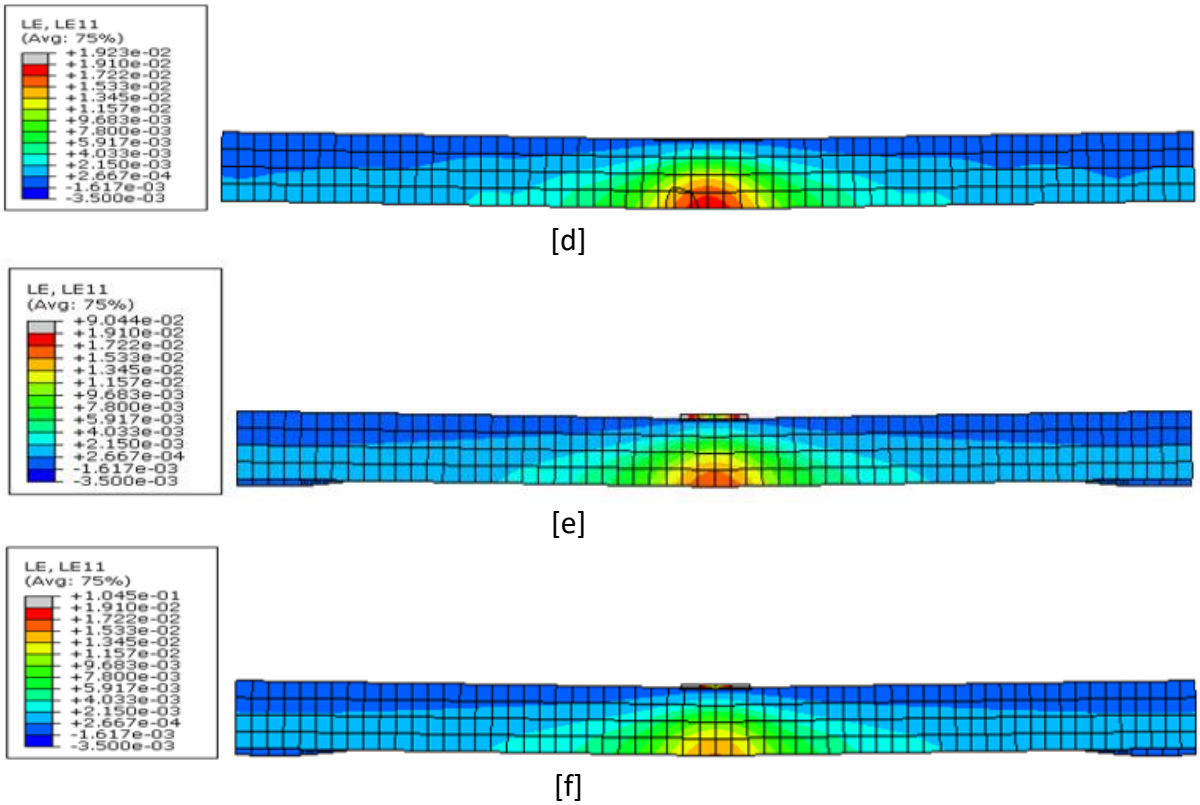

Figure 5.44: Principal Strain Contours [section y-y] for Case Study 1C with V_f = [a] 1.00% [b] 1.25% [c] 1.50% [d] 1.75% [e] 2.00% and [f] 2.50%

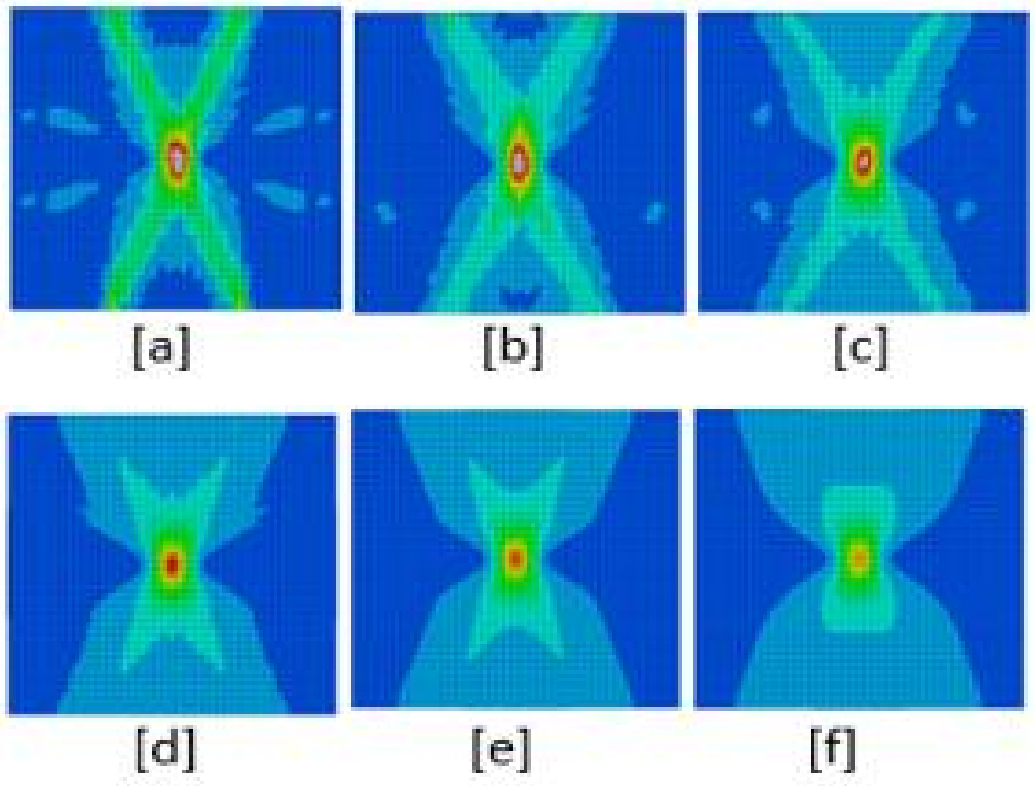

Figure 5.45: Principal Strain Contours for Case Study 1C with V_f = [a] 1.00% [b] 1.25% [c] 1.50% [d] 1.75% [e] 2.00% and [f] 2.50% and the same numerical values as Figure 4.44

The contours show that as the fibre volume increases, there was a reduction in the grey area that depicts the areas affected by the pull-out failure. The area got smaller at the mid-span until it fizzles out at V_f=1.75% and thereafter. This indicates that control crack propagation was reduced as the fibre volume increase.

5.5.4.2 Principal Strain Vectors

Figures 5.46 [a-f] show the principal strain vectors for case study 1C's square-panel. The addition of fibres has led to the reduction in the cracks in the single square-panels. The panel with a low fibre volume of 1% failed with greater strain along the panel mid-span and these decreases gradually but concentrated at the mid-span of the panel as the fibre volume increases. The preceding results establish the impact of cracking under monotonic central loading and the possibility of steel-fibres to control crack propagation and opening.

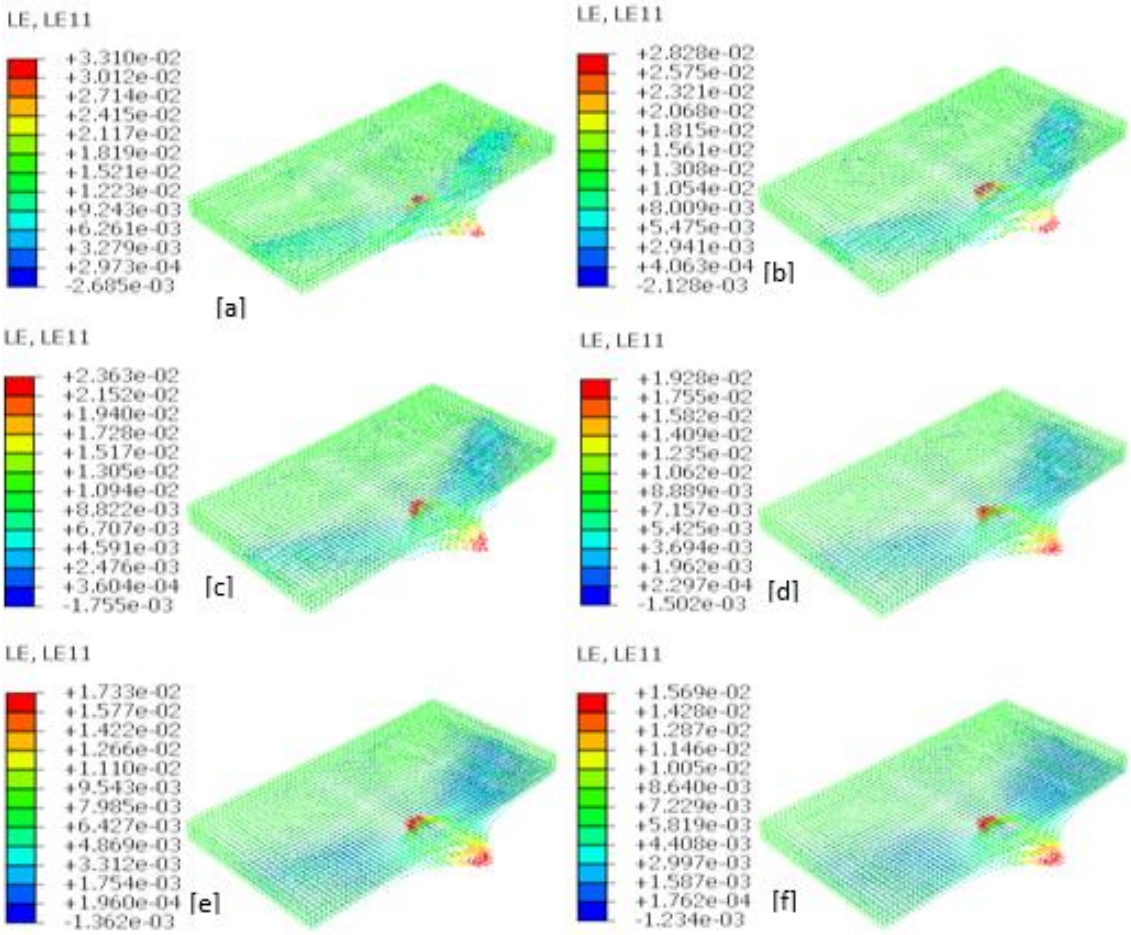

Figure 5.46: Principal Strain Vectors for Case Study 1C with V_f = [a] 1.00% [b] 1.25% [c] 1.50% [d] 1.75% [e] 2.00% and [f] 2.50%

5.5.4.3 Deformed [compressive and tensile] shapes

The tensile and compressive damaged patterns at the bottom of the square-panels are shown Figures 5.47 and 5.48. The square-panels failed in bending manifested by the cracks at the bottom.

The tensile damaged behaviours are depicted in Figures 5.47. The tensile damage at the bottom of the square panels shows the crack pattern. The pattern radiates from the point of application of load, along with the weakest planes to the edge [circumference] of the panel. These are reduced as the fibre volume increase with the concentration of the cracks at the centre at 2.50% fibre volume ratio.

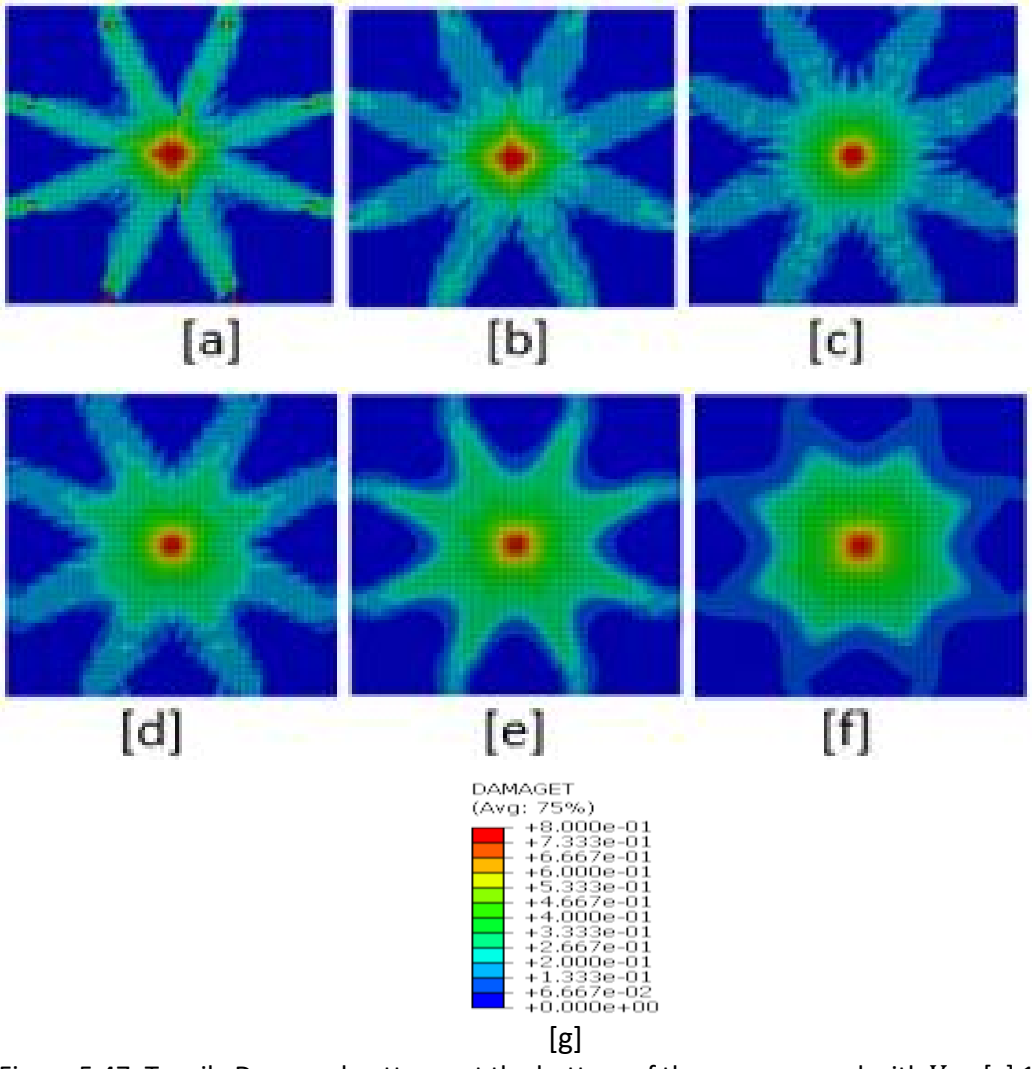

Figure 5.47: Tensile Damaged patterns at the bottom of the square-panel with V_f = [a] 1.00% [b] 1.25% [c] 1.50% [d] 1.75% [e] 2.00% [f] 2.50% and [g] Legend for Figure 5.47 [a-f]

Figures 5.48 [a-f] present the compressive damaged behaviour of square-panels. There is some traces of compressive damaged at the bottom noticeable in panels with low fibre volume at the tension face [Figures 5.48a and b]. From higher volume contents [Figures 5.48c-f], the effect of compressive resistance of the concrete faded away in the tension zone.

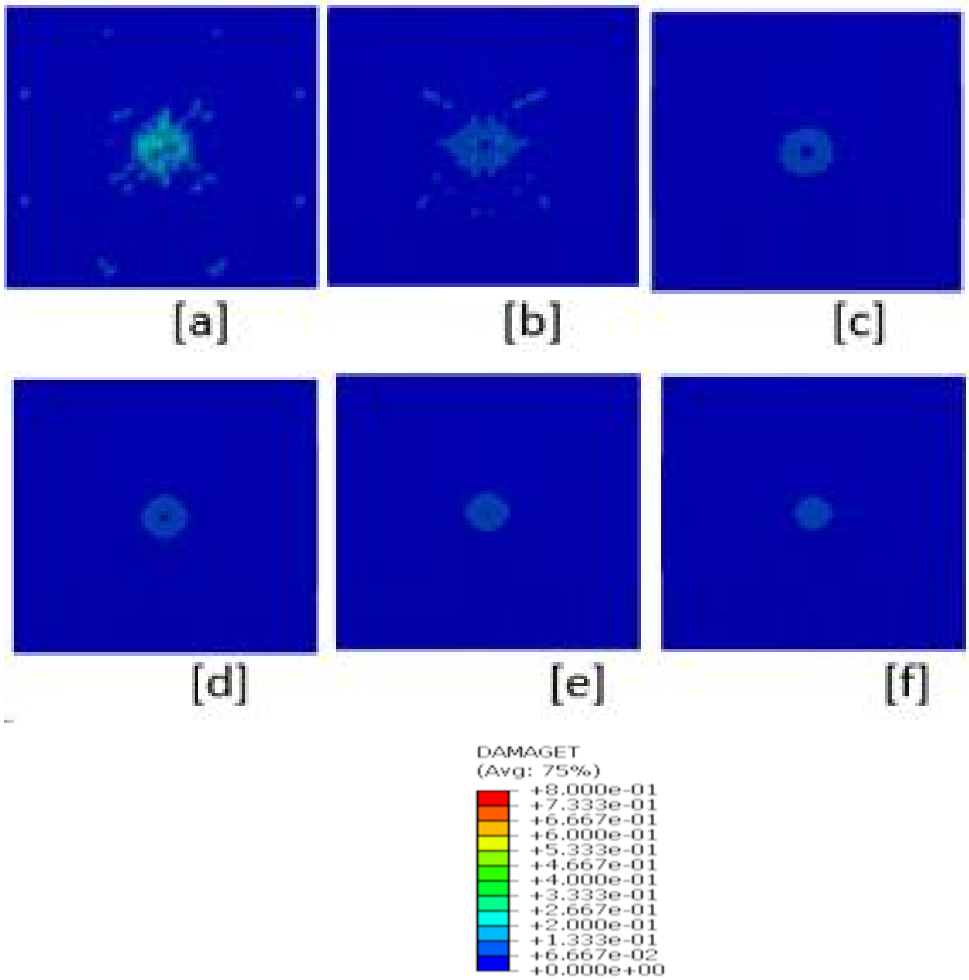

Figure 5.48: Compressive Damaged patterns at the bottom of the square-panel with V_f = [a] 1.00% [b] 1.25% [c] 1.50% [d] 1.75% [e] 2.00% and [f] 2.50% and [g] Legend for Figure 5.48 [a-f]

5.5.4.4 Deflected shapes

The deformed shapes [x-y plane], taken at failure, of the square-panels considered in Case Study 1C are presented in Figures 5.49 [a-f]. The panel deformed by bending at the mid-span and uplifting at the edges due to the central loading and the simple supports.

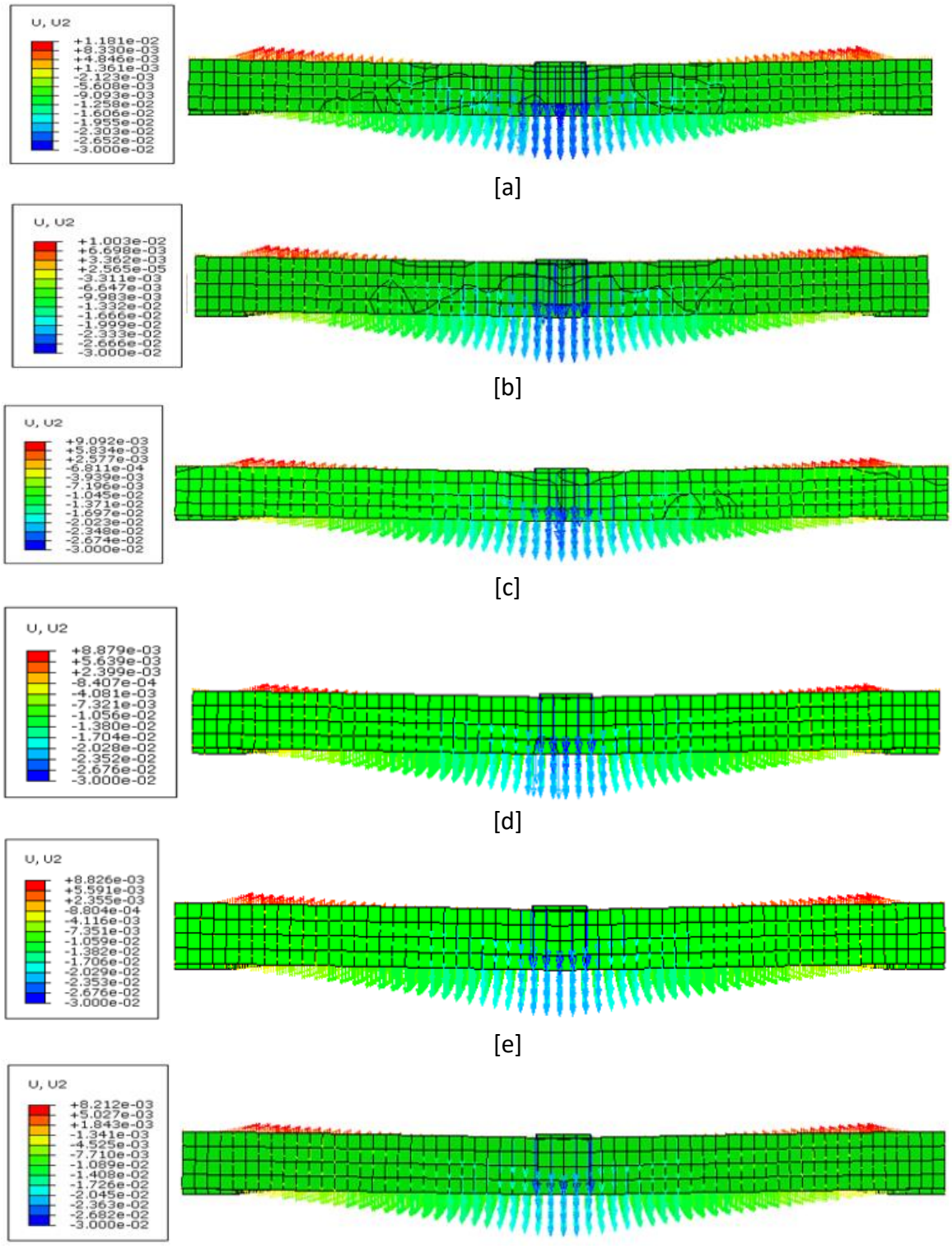

Figure 5.49: Deflected Shapes [x-y plane] for the Case Study 1C square-panel with V_f = [a] 1.00% [b] 1.25% [c] 1.50% [d] 1.75% [e] 2.00% and [f] 2.50%

5.5.5 Using Non-Dimensional Ratios for Comparative Study with Control Specimen

Comparison was made between the square-panels analysed with various fibre volume ratios and the control specimen. The square panel used for validation of the

experimental work served as the control specimen. The values of strength and ductility were normalised by dividing them with their corresponding values of the control.

5.5.5.1 Strength Ratio

It can be seen from Figure 5.50 that there is an upward movement in the strength ratio for all the square-panels considered.

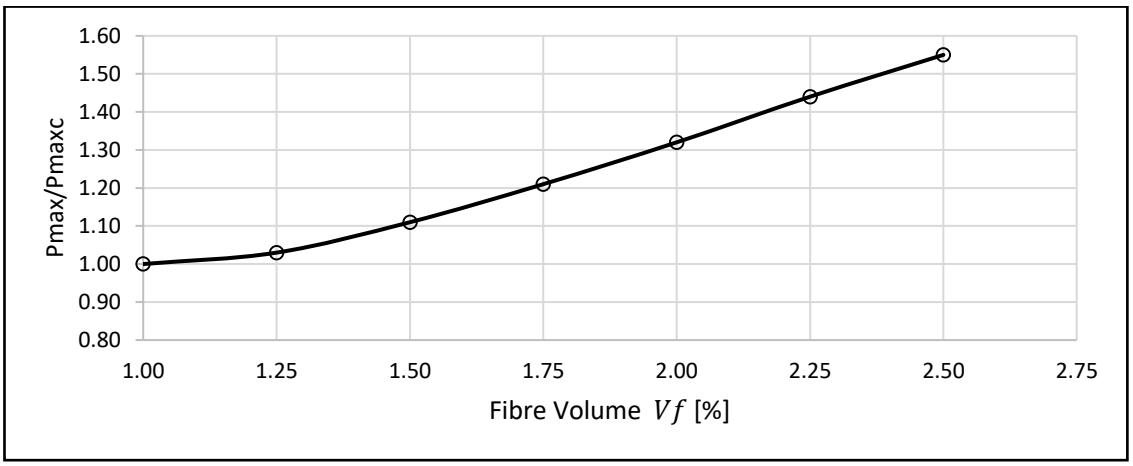

Figure 5.50: Graph of V_f against P_{max}/P_{maxc} for Case Study 1C

The increase in fibre volume ratio in the square-panels has led to strength enhancement of over 10% of the latter slabs.

5.5.5.2 Ductility Ratio

The ductility ratio is given as the ratio of the ductility of the square-panel [with different V_f] to that in the control and is shown in Figure 5.51. There is an improvement in the ductility ratio up to a threshold and then it declines [this as attributed to an excess of fibres in the panel]. Additional simulation was carried out with V_f=2.25%.

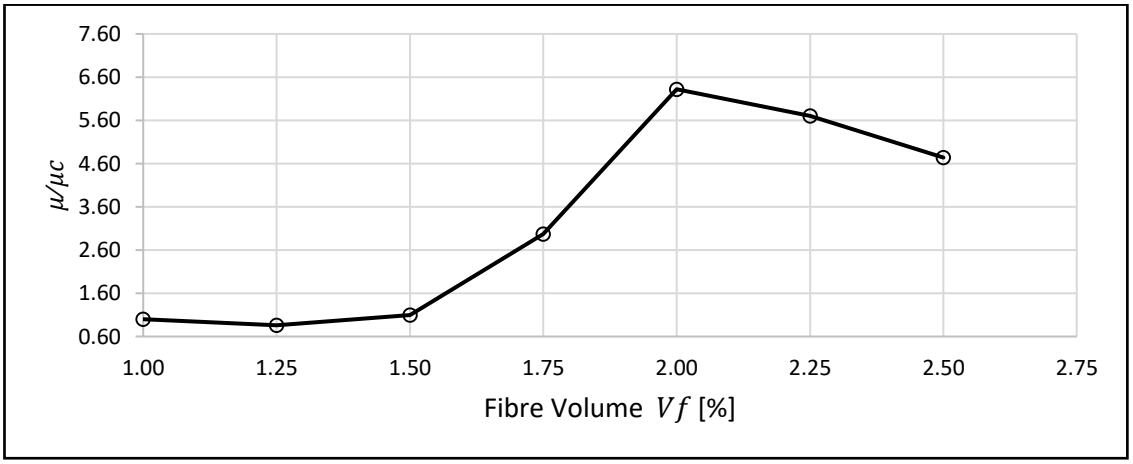

Figure 5.51: Graph of V_f against μ/μ_c for Case Study 1C

The possibilities of fibres to improve the structural response under monotonic loading is established for the square-panel in case study 1C.

5.5.6 Comparison between FE-Based Predictions and Design Guidelines

A comparison is made in this section between the FE-based results and those calculated according to the existing design guidelines. From the results in Table 5.11, it could be seen clearly that the values from these guidelines are either too much [overestimation] or too small. The FEA provides the best results with the experimental results. This further confirms that the FEA can predict accurately the responses in a single-panel slab to an acceptable limit.

Table 5.11: Comparison between Experiment, FEA-Based Predictions and Design Guidelines

		R. de Montaignac et al. Round Plate	Soranakom et al. Round Plate	Blanco et al. Square Panel	Remark
		Load [kN]			
Experiment		38.00	140.0	427.0	
FE-Based		39.25	140.0	423.3	Within limits
TR 34	$M = \frac{q_u L_1 L_2 \sqrt[3]{1 - \frac{A}{L_1 L_2}}}{2\pi}$	50.5	62.4	509.0	
Swedish	$m_u = \frac{f_{fld} . h^2}{6}$	11.1	20.8	520.0	Outside the limits
fib MC 2010					
ArcellorMittal	$M = 0.45 \cdot f_{ctu}^{f} \cdot h^2$	30.0	56.16	704	Outside the limits
RILEM TC 162					No provision
Dutch Code NEN 6720	M= $\alpha n l^2$	34.4	79.6	638	Outside the limits

5.6 Summary

Three case studies on SFRC simply supported plates were examined using NLFEA. The first Case Study [1A] investigated was on round-plates with three [3] isolated supports under monotonic loads. The flexural behaviour of the round-panels was studied with fibre volume ratio V_f =1.00%. Case Study 1B, centered on round-plates with continuous supports under monotonic loads. Cases 1A and 1B are for study at the material levels.

Case Study 1A comprises of change in fibre volume ratios and the characteristic strength of the SFRC. It was observed that the characteristic strength f_{ck} has no effect on the flexural strength f_{tu} of the matrix. This is because the flexural strength is based on certain parameters [fibre volume ratio, bond stress, length and equivalent diameter of fibre]. While Case Study 1B was examined with varied fibre volume ratios.

Discoveries from Case Studies 1A & 1B show that the load-carrying capacity of the round-plates was enhanced as the volume of steel fibres increases. Likewise, the strength increases by ~7% over the previous result of the round-panel with isolated supports and ~11% for the round-plates with continuous support under monotonic loading. Also, additional fibres lead to increase stiffness which resulted in a reduction to deflections of the round-panels. The benefits of adding steel fibres are seen both at the serviceability and ultimate limit states. Reduction in crack formation was also achieved. Structurally, increase in fibres changes the failure mode to ductile failure from brittle failure, which is required in the structural design.

In Case Study 1A, as the fibres volume increases, ductility was improved. Interestingly, the different characteristic strengths produce an increase in ductility and strength, which shows that the higher the characteristic strength of the SFRC matrix, the higher the ductility and strength. Three cracks formed along the weakest plane, from the point of load application, which are the spaces in-between two adjacent supports. Case Study 1B shows a different pattern in ductility as an increase in fibre volume led to a decrease in ductility. On the other hand, there was an increase in the strength as the fibre volume increases. Multiple cracks [4-8] were formed, radiating from the centre towards the

circumference. The lower the fibre volume, the higher the number of cracks and vice-versa.

Punching was noticed in Case Study 1B at the point of the application of load for V_f=1.0% which signifies that punching shear needs to be provided for [but punching shear is not within the objectives of this research], but as the fibre volume increases, the effects of punching diminished.

Case Study 1C present a square-panel simply supported at the centre of the four-edges by a support half the length of the edge, under monotonic loading. The test was based on the structural response of a full-scale SFRC square-panel, 3m wide. The parametric study shows that all the square-panels cracked at the mid-span of the panel indicating flexural failure. There is an average increment of 10% in the strength of the square-panel as the fibre increases. The same happened in the ductility up to a certain threshold [V_f=2.00%] when the ductility falls. This can be attributed to excess fibres in the SFRC matrix.

Conclusively, it can be established that the load-carrying capacity of the plates are enhanced by the addition of steel fibres and ensures a more ductile structural response (thus avoiding a brittle failure mode), which is preferred in design. This also leads to a rise in ductility and strength enhancement.

Chapter 6: CASE STUDY 2 - 4-PANEL PILE-SUPPORTED SLABS WITH AND WITHOUT REBAR OVER SUPPORTS

6.1 Introduction

The case studies 2 present the use of steel-fibres in structural pile-supported ground floors. The study is on the works done at the University of Braunschweig, Germany and reported by Thooft H. (1999). Two models were considered vis-à-vis pile-supported floor without and with rebar in the panel across the pile positions. Pile-caps were not provided for in the experimental works to avoid restraints due to horizontal soil interactions. The purpose of the work was to study the load-bearing capacity and deformation of a pile-supported suspended floor reinforced with steel-fibres. The slab was 5m by 5m and 140mm in depth, supported by nine [9] piles, 200mm in diameter, and 2m apart [Figure 6.1]. The span-depth ratio was 14.3

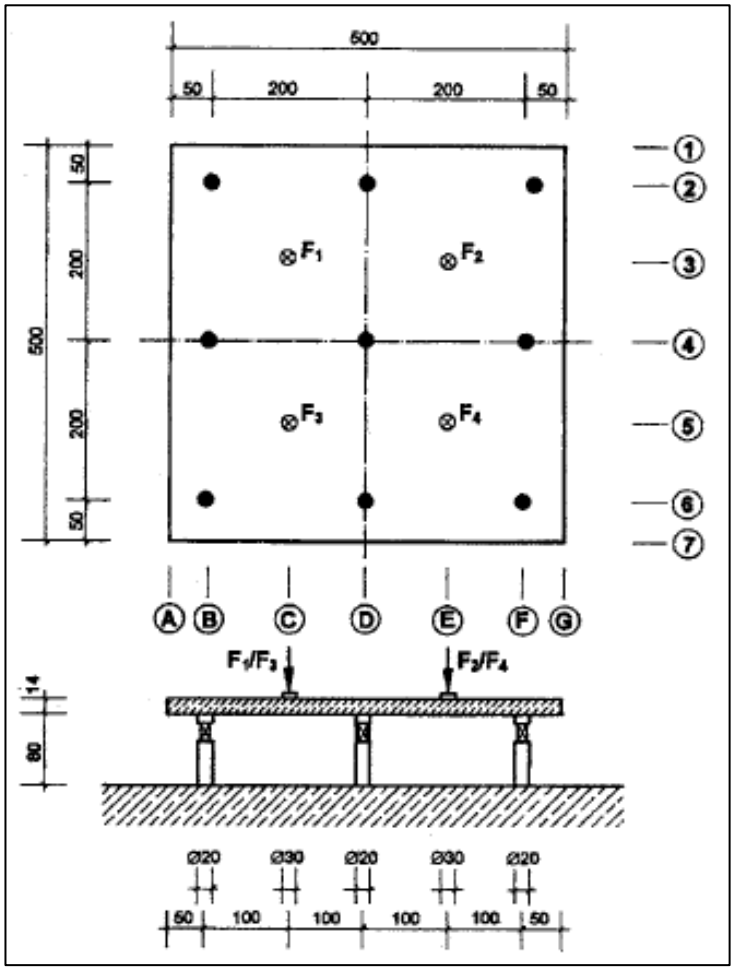

Figure 6.1: Experimental Set-up (Thooft 1999)

The loads were applied simultaneously at the midspan of the four panels. The loading rig was 300mm in diameter. This testing was under point loads [Figure 6.1]. The concrete

mix contains 40kg/m^3 [0.5%] of steel-fibres [DRAMIX® RC-80/60-BN] with 50mm length and 0.75mm diameter. The strength of the mix was 45N/mm^2. Table 6.1 comprises other materials in 1m^3 of the concrete mix.

Table 6.1: Material Constituents of SFRC Per m^3

Steel-fibre [DRAMIX® RC-80/60-BN]		Materials	Slab without Rebar	Slab with Rebar
Length [mm]	60.0	Cement [kg]	360	360
Diameter [mm]	0.75	Fly ash [kg]	100	100
Volume [kg]	40.0	w/c ratio	0.46	0.53
Aspect ratio [L/d]	80.0	Sand 0/2 [kg]	703	681
Rebar		Gravel 2/8 [kg]	279	280
Diameter [mm]	10.0	Gravel 8/16 [kg]	766	748
f_y	460.0	Plasticizer [%]	0.5	0.5

6.2 Sensitivity Analysis

The section considers the calibration of the numerical model for suitability in modelling the experimental results. The model deployed to simulate the pile-supported SFRC slab was eight-node 3D brick [C3D8R] elements. The comparison of the results from the mesh sizes 25mm, 50mm, and 100mm in Figure 6.3 was to determine the optimised mesh. The tensile behaviour of ABAQUS Concrete Damaged Plasticity [CDP] was with Lok and Xiao (1999) constitutive model. The compressive behaviour of plain concrete is used to describe the SFRC in compression. Table 6.2 and Figure 6.2 show the input parameter of the tensile stress and strain.

Table 6.2: Tensile Stress-Strain Input

	Tensile Strain [-]	**Tensile Stress [MPa]**
Origin/Peak Tensile Stress	0.000	3.74
Flexural Strength	0.001	0.60
Flexural Strength	0.180	0.60
Ultimate Tensile Strain	0.200	0.00

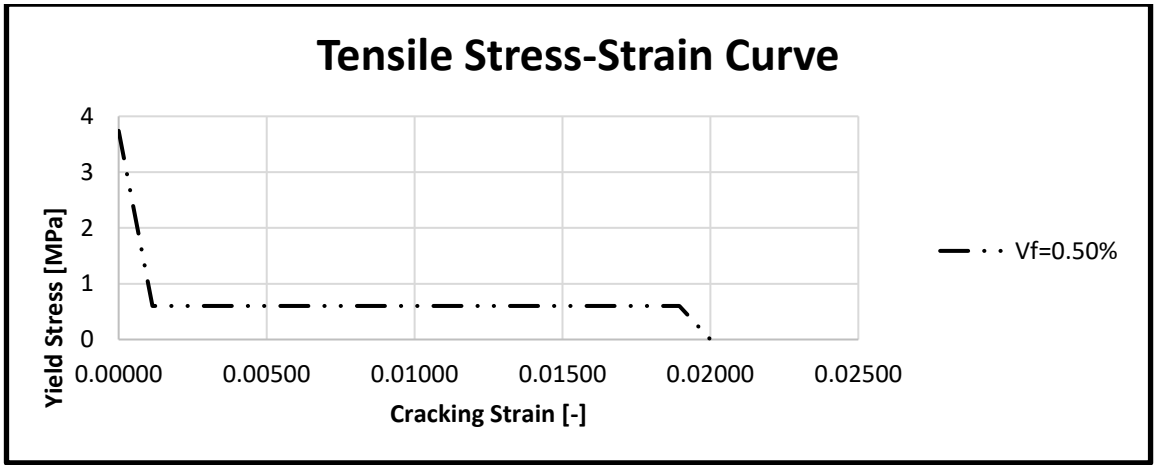

Figure 6.2: Tensile Stress-Strain Curve

The Load-Displacement curves from the different mesh sizes are presented in Figure 6.3. The 50mm mesh size is well-suited to the experimental result. The 75mm mesh produces a result lower than experimental work while that of 100mm was much lower. The displacement at yield load for the experiment, 50mm mesh and 75mm mesh are about the same. The yield loads for the three is also within 10% to one another. The 50mm mesh is most suitable for the NLFEA of this 4-Panel SFRC pile-supported slab.

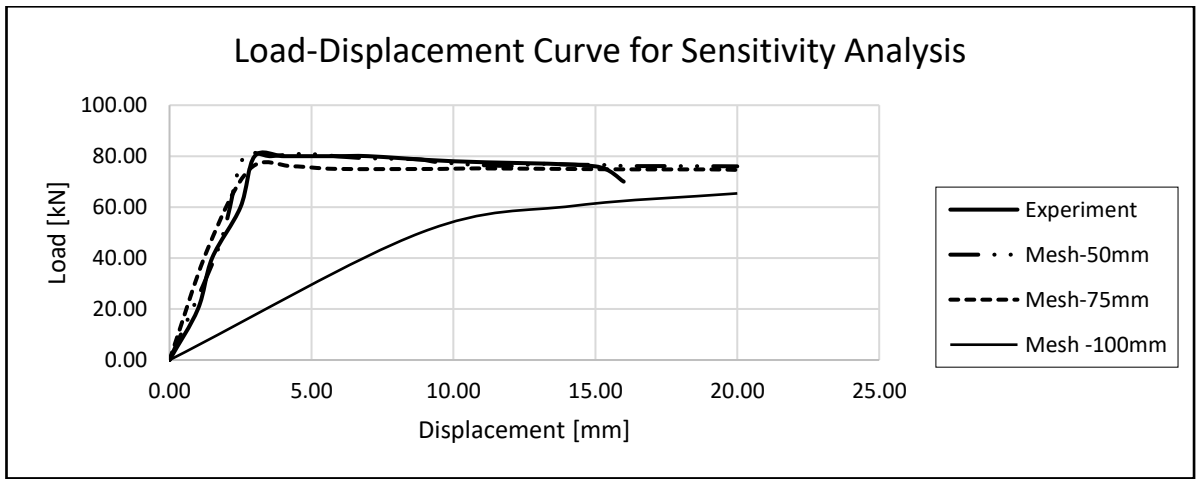

Figure 6.3: Load-Displacement Curve for Sensitivity Analysis

The quarter-size and full-size of the slab was modelled to determine which will be preferable for the research work considering time and accuracy. Using all the four-processors for optimisation of results, the time expended to complete each analysis favours a quarter-size slab. The time is taken for each mesh size in a quarter, and full-size slabs are given in Table 6.3

Table 6.3: Mesh-Sizes and Time of Execution

	Full-Size			Quarter-Size		
Mesh Size [mm]	50.0	75.0	100	25.0	50.0	100.0
Time taken [hrs]	84.0	13.4	4.2	38.2	3.2	1.10
Accuracy [%]	92.0	97.3	84.2	90.1	98.0	85.6

6.3 Parametric Study

Parametric study permit for the nomination of parameters for assessment, determination of range and ability to put design constraints. The FEA offers an economical and reliable substitute for full-scale testing in getting acceptable results. The validation work shows that the behaviour of the pile-supported SFRC slab (Thooft 1999) was efficiently captured by FEA thus allowing further simulation using the parametric data. In general, the parametric study was carried out by varying one parameter [at first, V_f and after that f_{ck}] while all other parameters [particularly, the plasticity factors of CDP] remain the same and unchanged as in the validation work.

For the full parametric study, fibre volume ratio was varied [V_f= 0.50, 1.00, 1.25, 1.50, 1.75, 2.00 and 2.50%]. Figure 6.4 and Table 6.4 show the tensile stress-strain input data. As earlier discussed in case study 1, changes in fibre volume ratios only affect the flexural strength of the SFRC.

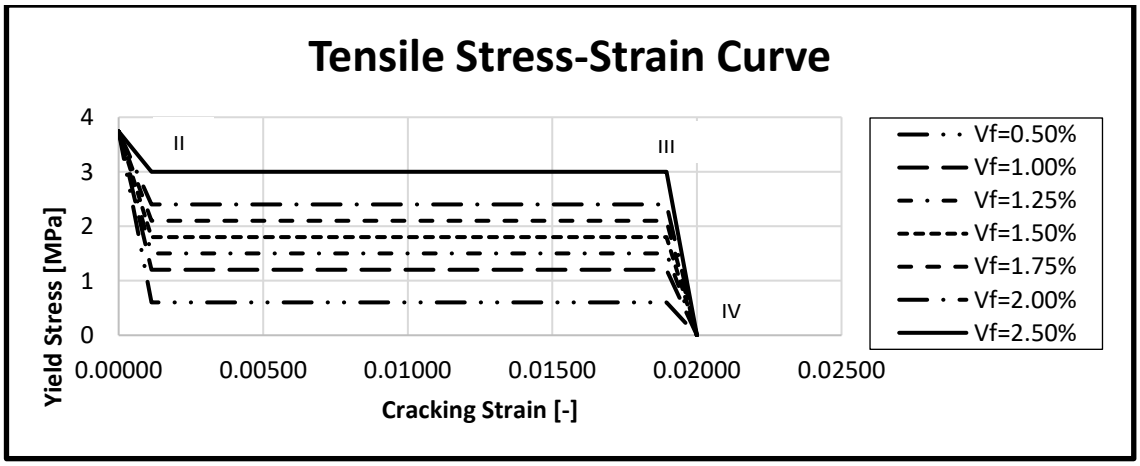

Figure 6.4: Tensile Stress-Strain Curves for different fibre volume ratios [V_f]

Table 6.4: Tensile Stress-Strain Parameters for different fibre volume ratios [V_f]

	Strain [-]	Stress [MPa]						
		V_f [%]						
		0.50	1.00	1.25	1.50	1.75	2.00	2.50
Origin/Peak Tensile Stress [I]	0.000	3.74	3.74	3.74	3.74	3.74	3.74	3.74
Flexural Strength [II]	0.002	0.60	1.20	1.50	1.80	2.10	2.40	3.00
Flexural Strength [III]	0.018	0.60	1.20	1.50	1.80	2.10	2.40	3.00
Ultimate Tensile Strain [IV]	0.020	0.00	0.00	0.00	0.00	0.00	0.00	0.00

The detailed parametric study is to examine the effect of changes in fibre volume ratios and characteristic strength and response of SFRC slabs. The displacement-based loading was the mode of load application.

6.4 Slab without Rebar

The clear distance between the piles is 2000mm centre to centre, measured in x-x and z-z directions. The loading rig, 300mm in diameter, is placed at the centre of each panel. Every panel rest on four piles. In the quarter-size model, 2500 by 2500mm, the loading-rig remains 300mm in diameter. The shadowed sides indicate the continuity of those sides.

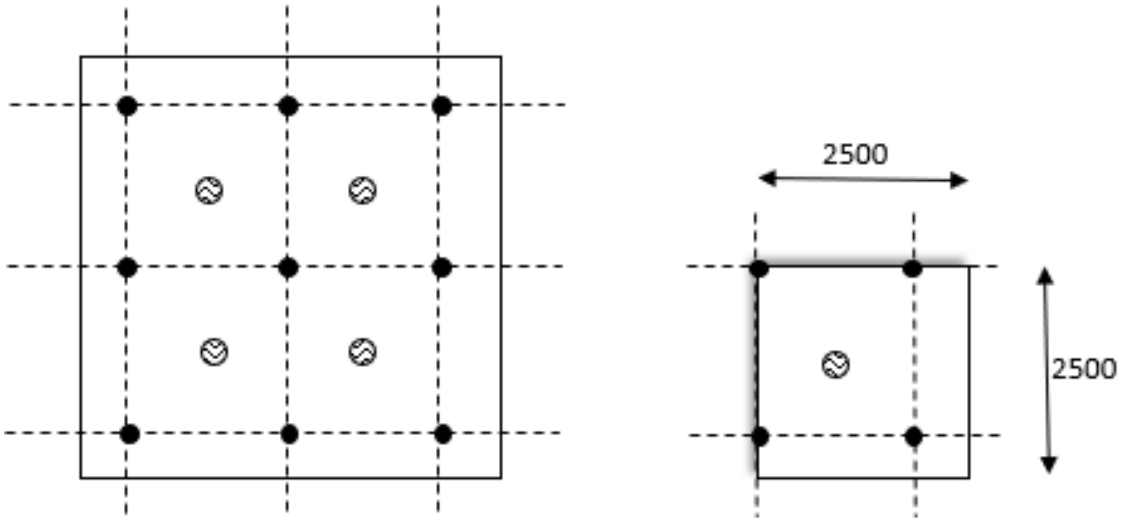

Figure 6.5: Loading Pattern of Slab without Rebar [Full and Quarter-Size]

The interaction between the panel and the piles was a simple one [restraint on one axis, x]. This was to significantly emulate the actual interaction between the panel and the piles but for stability of the model, the central pile was fixed [restraint on all three axes, x, y and z]. The pile at the joint of the two continuous sides is model a quarter, the two piles on the continuous sides modelled as half-piles while the last pile was modelled a full-pile. The continuous sides x-x and z-z were restrained in their plane to show the continuity.

For the analysis of the quarter panel, 50mm mesh and 4.5MPa bond stress were used. The tensile stress and strain behaviour as described by the Lok and Xiao (1999) constitutive Model are as shown in Table 6.4 and Figure 6.4. The analysis plasticity parameters as detailed in section 4.3.3.5 were inputted into ABAQUS-CDP with the compression and tensile stresses and damaged parameters as provided in Table 4.27.

The slab was fully loaded at the mid-span of the four panels simultaneously starting with serviceability load [50kN and 20kN representing maximum and minimum respectively]. To imitate the experimental process, the loading on the quarter slab was modelled with static analysis using displacement-based loading. To vary the amount of the loading, time-frequency of 0-10 [at 0.1 increment] with an amplitude of 0-1 [at 0.01 increment]. The displacement was applied slowly at the rate of 0.2mm until deformation and crack propagation.

6.4.1 Load-Displacement Curves [Slab without Rebar]

Figure 6.6 displays the load-displacement curves between the experimental result and that of NLFEA. The FEA agrees with the experiment with an accuracy of 99%. There is an agreement between the estimated values from the NLFEA and that of the experiment for the yield and maximum load carrying capacity. The load-displacement curves of the NLFEA and the experimental test are very similar. The response of the simulated FE model is as ductile as the experimental results.

When compared together, there is a similarity between the experimental and NLFEA results, especially on the load-displacement behaviour [Figure 6.6 and Table 6.5]. Strain softening response was gradual in this full-scale FEA of the SFRC slabs. The gradient of the curve before failure is small. The slab failed in a flexural mode with a warning [bending]. The curve does not show structural toughness. The predicted load carrying capacity of the FE model is 99.8% of the experimental work. For additional parametric studies, the FEA parameters that produce this result remains unchanged.

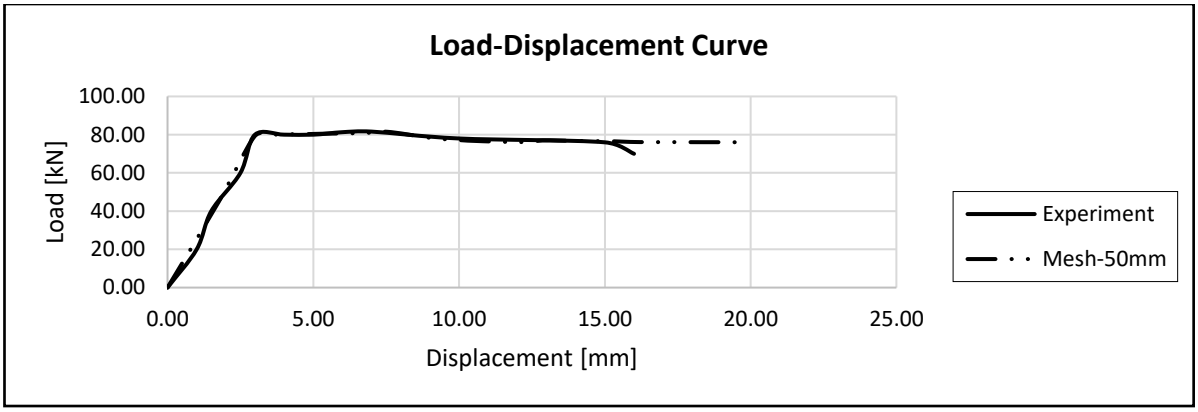

Figure 6.6: Load-Displacement Curves for Experiment and FEA

Table 6.5: Comparison of Experimental and FEA Validation Results

	Slab without Rebar		% Variance
	Experiment	FEA	
Load at First Crack [kN]	80.0	79.0	1.25
Displacement at First Crack [mm]	3.0	2.98	0.67
Maximum Load [kN]	81.6	81.5	0.12
Displacement at Maximum Load [mm]	7.6	7.5	1.32

Taking a quarter of the slab analysed by FEA, the crack pattern due to experimental testing is comparable to the one NLFEA produces both at the initial and the failure [final] stages. The NLFEA further demonstrates the capacity to capture the influence of steel-fibres on the concrete strength [yield and maximum loads and their respective displacement] and its bridging impact in arresting crack propagation adequately.

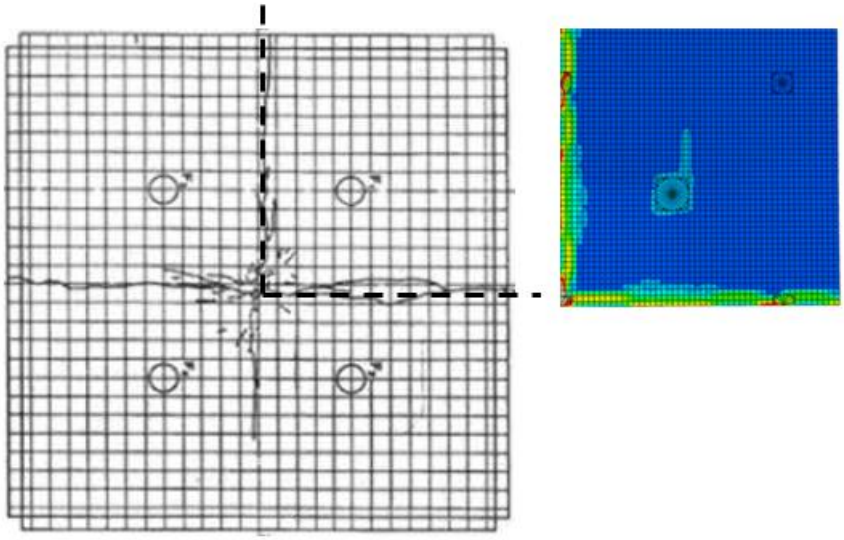

Figure 6.7: Comparison between Experimental and FEA Crack Pattern [Top]

At the top of the slab, the cracks developed from the point above the centre pile and moved at a right angle to the middle piles on the edges. This shows the impact [punching] of the supports on crack propagation.

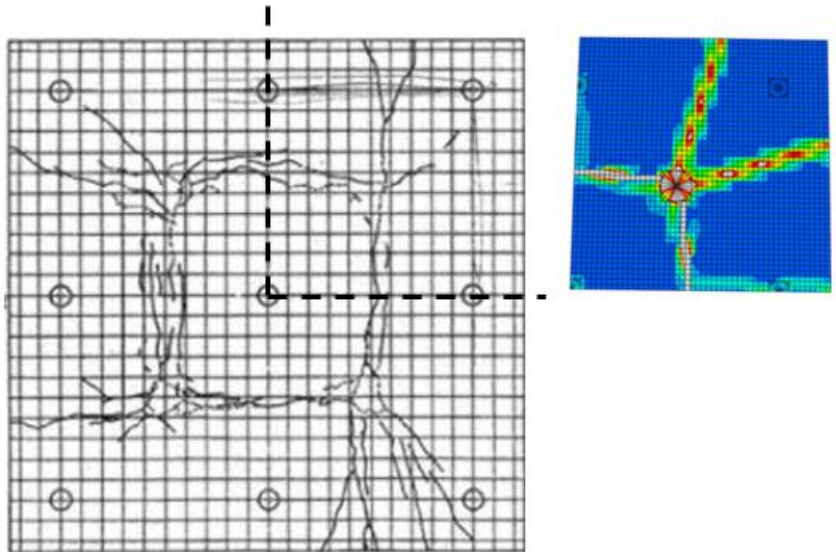

Figure 6.8: Comparison between Experimental and FEA Crack Pattern [Soffit]

At the soffit, the crack developed linearly from on the point of load application to another and the spread at an equal angle towards the piles at the corner. The cracks formed a square pattern [2000mm by 2000mm] captured by the FEA quarter model as 1000mm long across the soffit of the slab at the point of load applications. This interaction was imitated rightly by the FEA. It establishes that the constitutive models

of ABAQUS concrete damaged plasticity [CDP], Lok and Xiao (1999) and correct material properties can realistically predict the behaviour of pile-supported SFRC slabs regarding maximum load capacity, displacement and cracking patterns using either full or quarter slab.

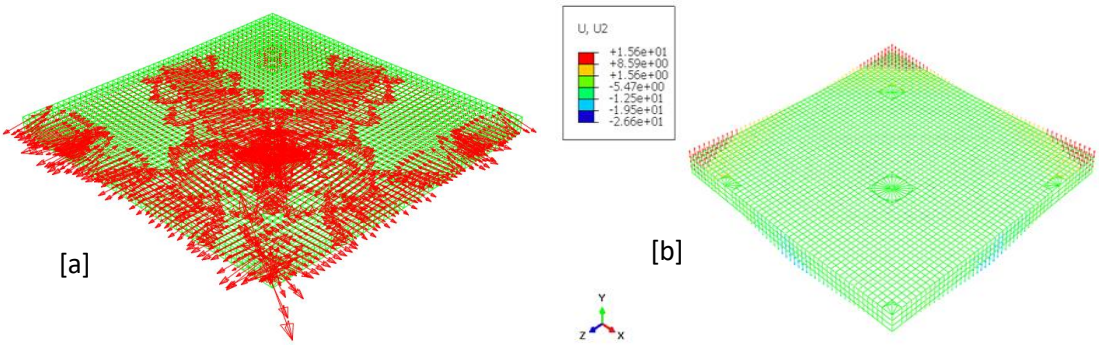

Figure 6.9: Principal Strain Vector and Deflected Shape of FEA Model

The principal strain vector and deflected shape of the validation model is shown in Figure 6.9. The strain vector [Figure 6.9a] shows the internal deformation of the quarter slab. The Figures also represent the failure mechanism within the slab. It also follows the crack pattern. As the load increases, the binding force of the SFRC becomes weaker, thus making the steel-fibres to carry the stresses induced by the loads. This causes strain to develop along the path that forms the cracks.

The foremost structural response indicators, concerning the yield load [P_y] with its displacement [δ_y], the maximum load [P_{max}] signifying the load-carrying capacity with its displacement [δ_{max}], ultimate load [P_u] representing the residual strength [which is the lesser of the load at failure and 85% maximum load] with its displacement [δ_u] and the ductility ratio [μ] expressed as δ_u/δ_y [Table 6.6].

6.4.2 The Strength [Slab without Rebar]

In this first part of the parametric study, only the fibre volume ratio [V_f] is varied. An increase in the value of V_f leads to enhanced strength and higher resistance [i.e. there is an increment in load carrying capacity] demonstrating that stiffness rises as V_f increases [Table 6.6 and Figure 6.10]. This enhancement is visible as V_f rises leading to more strength. As the loading increases, radial cracks spread. As the micro-cracks

emerged due to continuous loading, the steel-fibres bridge these cracks as they appear. [CDP does not illustrate actual cracking, by sections falling off, like CBC but these are defined by boundaries based on the cracking strain at tension and compression zones]

Table 6.6: Strength Parameters for f_{cu}=45MPa

V_f [%]	P_y [kN]	δ_y [mm]	P_{max} [kN]	δ_{max} [mm]	P_u [kN]	δ_u [mm]	$\mu = \delta_u/\delta_y$
Control	79.0	2.98	81.5	7.53	76.2	15.28	5.13
0.50	79.0	2.98	81.5	7.53	76.2	15.28	5.13
1.00	59.0	2.50	88.0	3.80	82.6	15.54	6.22
1.25	101.7	1.78	103.9	5.03	89.3	16.66	9.36
1.50	102.3	1.78	104.8	5.80	100.8	16.68	9.37
1.75	110.7	2.24	107.7	7.14	106.9	15.31	6.83
2.00	114.4	2.52	114.5	9.92	113.3	15.34	6.09
2.50	125.8	4.05	127.1	12.61	126.8	15.41	3.80

However, as the V_f increases towards 2.50%, more fibres are available to bridge the openings leading to a decrease in displacement at V_f =1.00% and increase from 1.25% to 2.50%. (Which denotes that to have the same central displacement as in slab with V_f =0.50% in the slab with V_f > 1.00%, greater loads would be needed). Improved stiffness is observed in the curves as fibres are increasing then a fall at V_f = 2.50%; this can be attributed to more fibres than necessary. Too much fibres can lead to low workability and insufficient bond between the concrete matrix and the fibres. As fibres volume increases in the concrete matrix, a greater number of fibres bridging the cracks are available and controlling their opening, but when the fibres are more than necessary, it reduces ductility. This enhancement is important for structural design at ULS and SLS.

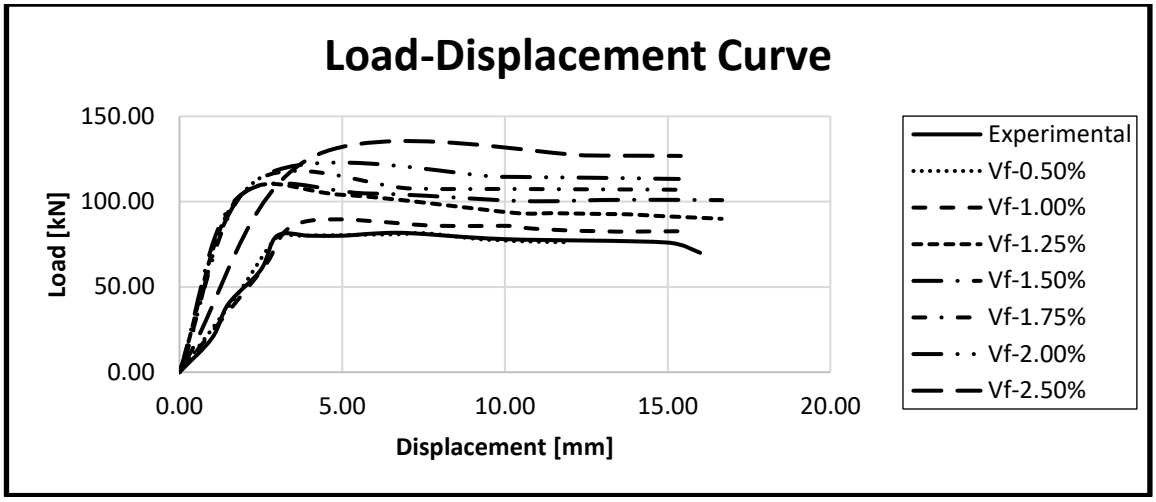

Figure 6.10: Load-Displacement Curves for various V_f under Dual Loading

6.4.3 Ductility

The ductility of the slab can be evaluated by examining the ultimate displacement at ultimate load δ_u, and the ductility ratio μ. This a measure of slab's capability to undergo enormous deformations without shattering [or strength reduction] at a tensile strength that exceeds its yield strength. After a certain threshold, the ductility reduces. The highest ductility ratio is when the V_f=1.50%. The ductility factor is expressed as δ_u/δ_y, where δ_y and δ_u are the displacement at yield and failure loads respectively.

6.4.4 Crack Shapes [Slab without Rebar]

Figures 6.11 – 6.14 show the cracking shapes of the 4-panel pile-supported SFRC slab. These comprise of the principal strain contours, principal strain vectors, deflected shapes and tensile damaged shapes. All these are to describe the failure mechanism of the slab and also compare it with the cracking patterns from the experimental works. Graphical visualisation of the cracking patterns in the concrete structure which represent crack direction (Lubliner et al., 1989) is used in concrete damaged plasticity [CDP] model. The CDP model does not display actual cracks opening unlike concrete smeared cracking [CSC] at the material integration. The cracks are presented in colour patterns.

6.4.4.1 Crack Patterns [Principal Strain Contours] of Slab without Rebar

The principal strain contours at failure for the pile-supported SFRC slab [without rebar across supports] in the analysed quarter-slab are shown in Figure 6.11. Colours and boundaries define the damage pattern in CDP with 0.02 representing fibres pull-out strain for SFRC slab depicted in grey and -0.0035 for compressive strains beyond SFRC ultimate strain in black. As anticipated in a ductile behaviour of the suspended slab, the cracks propagate throughout the soffit of the slab directly under the point of load application and increase in penetration with load increment.

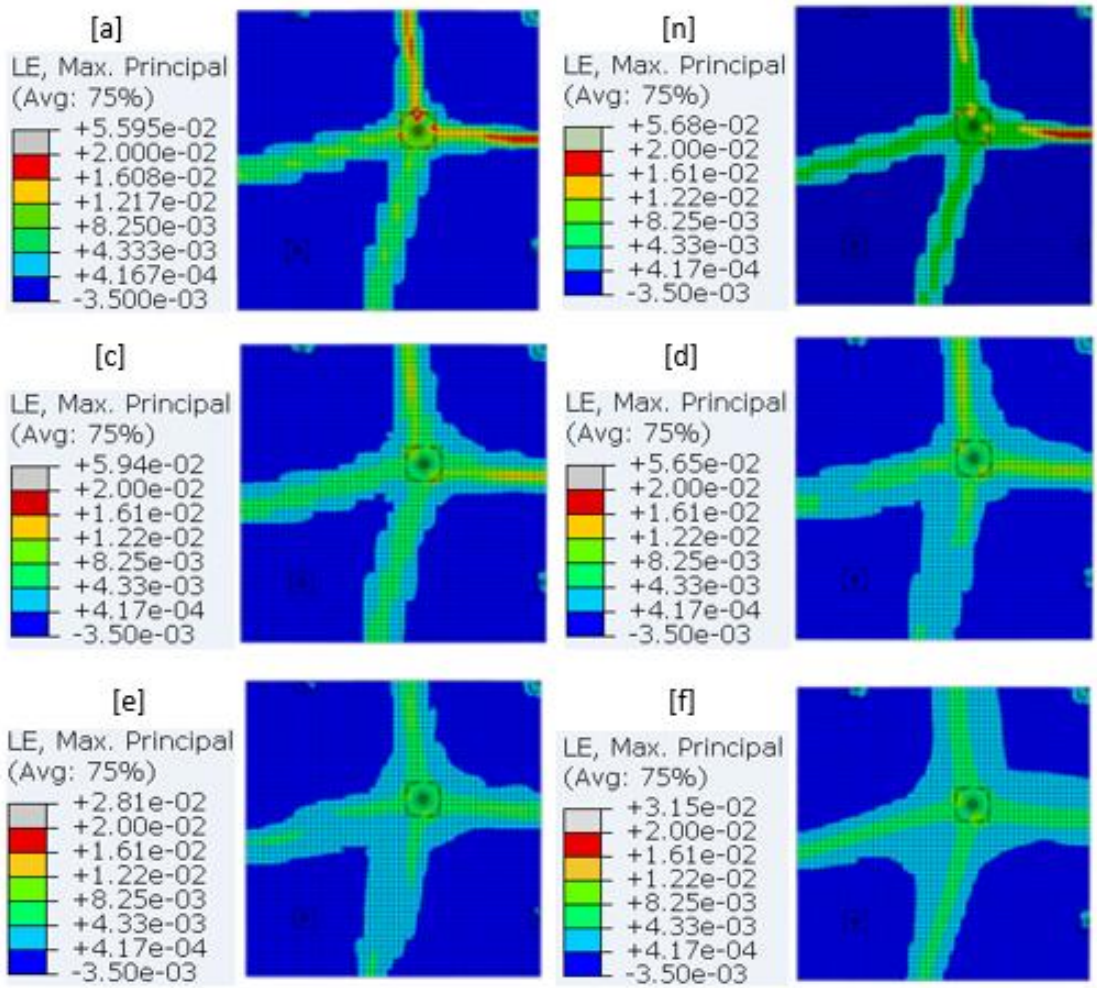

Figure 6.11: Principal Strain Contours for Pile-Supported SFRC Slab without Rebar with V_f [a]= 1.00%, [b]= 1.25%, [c]= 1.50%, [d]= 1.75%, [e]= 2.00% and [f]= 2.5%

In Figures 6.11 [a-f], the red patches show the critical-crack formation. The red patches continue to diminish as the fibre volume increases from Figure 6.12[a] to Figure 6.12[f] signifying that crack formation and propagation reduces as V_f increases. The strain,

indicating crack locations, spread in two legs at a right angle from the point of load application to another. In all the slabs analysed, the failure mode was bending at the mid-span. The severe cracks occur in the slabs with low V_f [0.50%, 1.00% and 1.25%] at the points of load application. Small cracks developed upon continuous loading, and these cracks continue to link together to form crack lines, which are yield lines for the slab. As V_f increases, the crack openings are reduced. At every point of crack formation, the fibres bridge the cracks. This is followed by the pull-out failure of the fibres when the stresses exceeded that of the bond between the concrete and embedded fibres. From V_f≥1.25%, tensile strain is lower than 0.02, which shows that the fibres are enough to bridge the cracks, thus no grey areas.

6.4.4.2 Crack Patterns [Principal Strain Vectors] of Slab without Rebar

Figures 6.13 [a-f] further exemplify the crack patterns using principal strain vectors for the 4-panel pile-supported SFRC slab with varying V_f. The failure is due to crack opening at the points of application and on top of the piles. The cracks can be seen as the concentration of the vector at the points of contacts between the slab and loading point and top of the piles.

For slab with V_f=0.50%, the strain vector [cracking] is broader at the point of vertical load application while it is smaller in the slab with V_f=2.50%. As the V_f increases, the crack propagation reduces, facilitating moment redistribution, thereby allowing the slab to develop a second plastic hinge at the piles at the edges and at the middle. The intensity of the vectors changes as the V_f. The shape of the cracks appears to be the same in all the slabs, what differ is the extent of the cracks. ABAQUS visualisation module provides these graphical patterns.

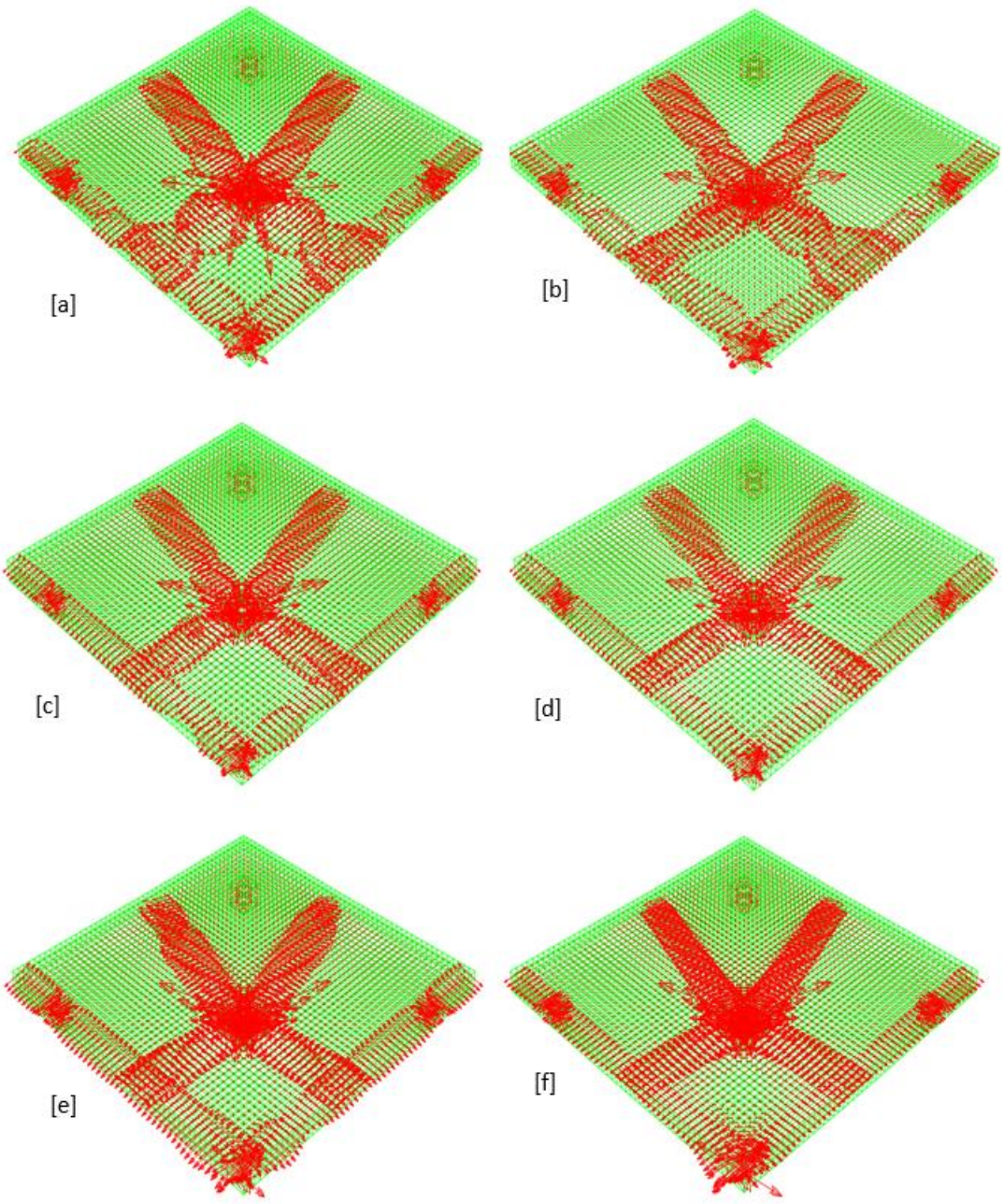

Figure 6.12: Principal Strain Vectors for Pile-Supported SFRC Slab without Rebar with V_f [a]= 1.00%, [b]= 1.25%, [c]= 1.50%, [d]= 1.75%, [e]= 2.00% and [f]= 2.5%

The crack patterns in all the slabs look very similar, concentrating at the point of load application in the mid-span of the panel, which is a flexural (and ductile) failure mode. The spread of the vectors at the panel's mid-span decreases as the V_f increases. This affirms improvement in ductility as the V_f rises.

6.4.4.3 Crack Patterns [Deflected Shapes] of Slab without Rebar

The effect of loading on displacement is considered in these deflected shapes of the slabs [Figures 6.13 (a-f)]. The deformed slabs sag at mid-span showing a failure in bending and a hog after the support [cantilever].

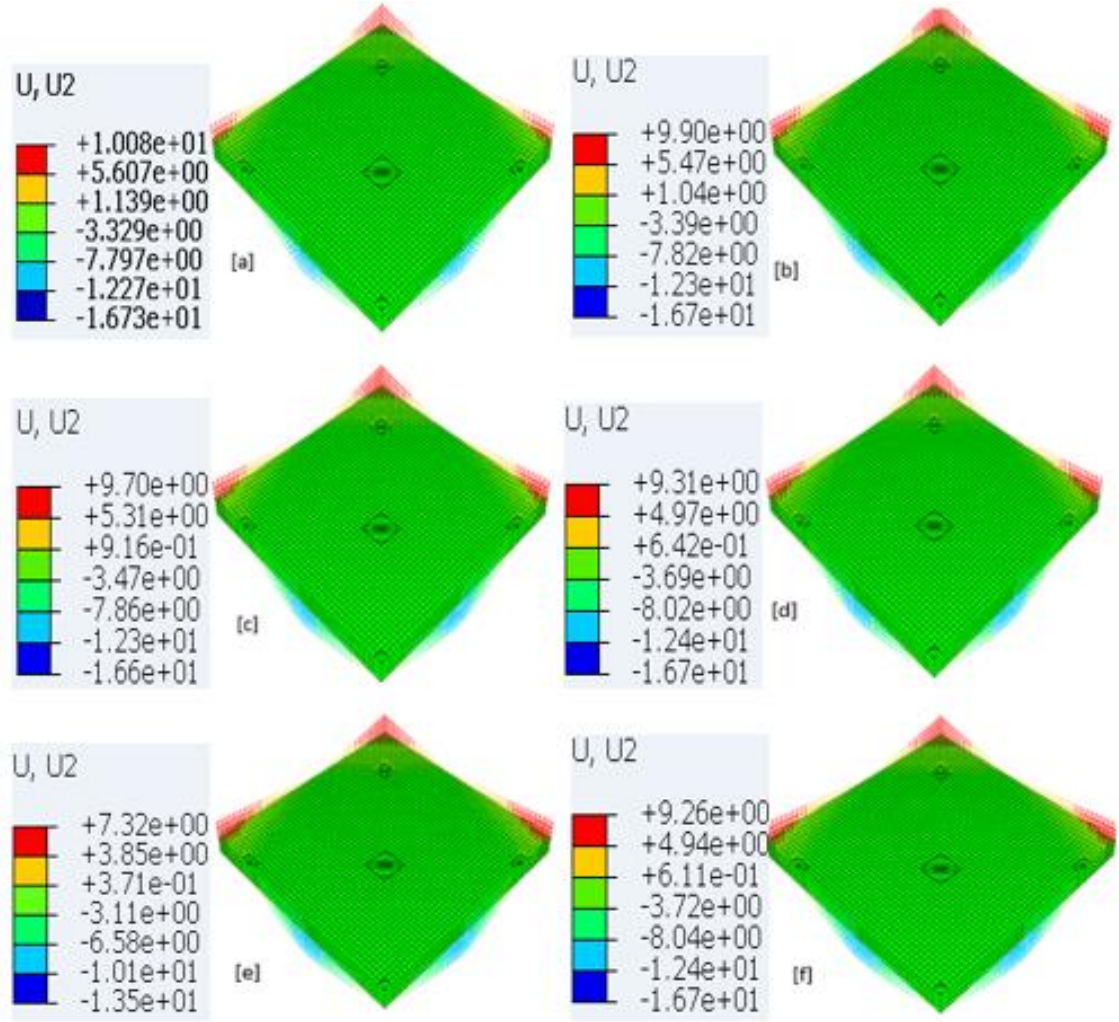

Figure 6.13: Deflected Shapes for Pile-Supported SFRC Slab without Rebar with V_f [a]= 1.00%, [b]= 1.25%, [c]= 1.50%, [d]= 1.75%, [e]= 2.00% and [f]= 2.5%

The deflected shapes also show the influence of an increase in V_f. At a displacement of 3mm [signifying the threshold of linearity (SLS) of material and determined by the elastic properties of the SFRC], the load resisted by the slab increases from 80kN inV_f=1.00% to 125kN in V_f=2.50%. Additional steel-fibres leads to higher load carrying capacity and ultimately, bridging the cracks that emerged.

6.4.4.4 *Crack Patterns [Tensile Damaged Shapes] of Slab without Rebar*

Figures 6.14 [a-f] depict the crack patterns based on FE-tensile damaged shapes. The grey area shows tensile damage above a maximum strain of 0.02. The figures show the impact of the application of loads that give rise to tensile damage at the soffit and top of the slabs. The cracks start to develop when the peak stress is reached. The tensile cracking is examined both at soffit and two sides of the slabs. In the slab with V_f=1.00% and 1.25%, the steel-fibre covers the crack [sparcely] as they appear but for V_f≥1.50% the impact is more felt as the coverage is greater.

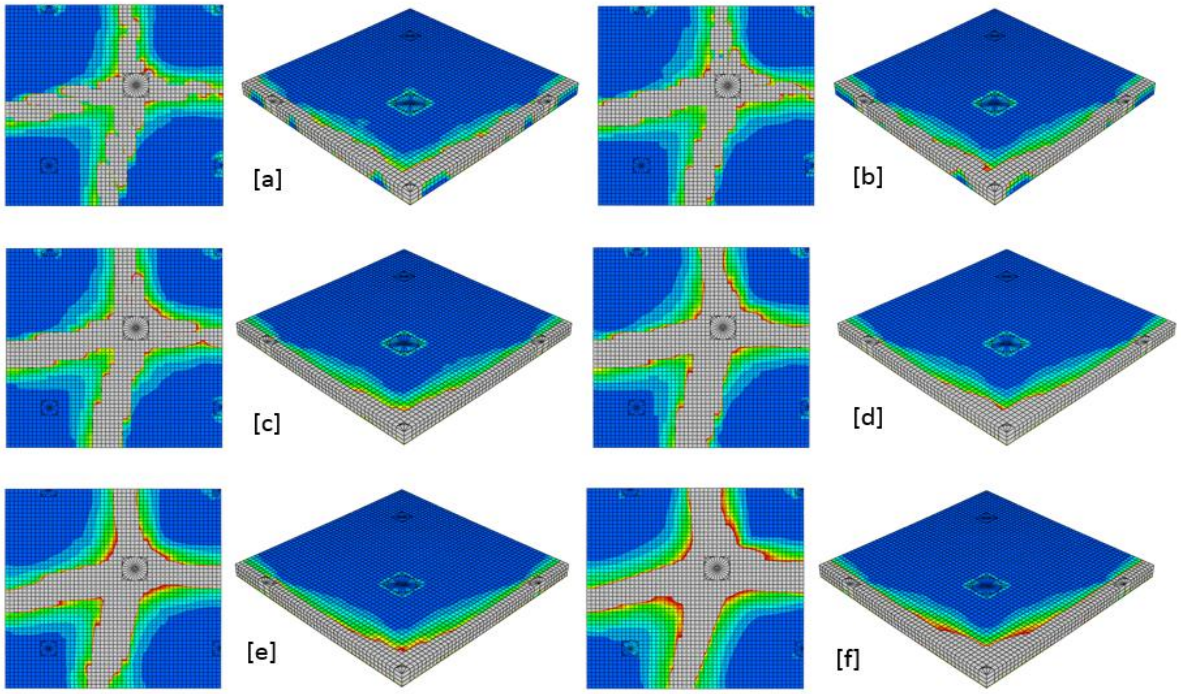

Figure 6.14: Tensile Damaged Shapes for Pile-Supported SFRC Slab without Rebar with V_f [a]= 1.00%, [b]= 1.25%, [c]= 1.50%, [d]= 1.75%, [e]= 2.00% and [f]= 2.5%

As the V_f increases, the uneven legs [cracks] merge gradually until the legs were smoothened. Likewise, there was a gradual internal coverage [a, b] of these cracks until the entire section was covered [c-f]. the width of this coverage at the soffit also increases as the V_f increases.

6.4.5 Comparative Study with Experimental Specimen using Non-Dimensional Ratios [Slab without Rebar]

A general comparison between the FE-based SFRC slabs with different V_f and the experimental result [taken as control specimen] are made in this section. They are

described by using non-dimensional ratios [dividing their values of strength and ductility by the values in the control]. The resulting figures helps to make concluding remarks on the practicality of using various dosages of steel-fibres in pile supported slabs.

6.4.5.1 Strength Ratio [Slab without Rebar]

Table 6.7 contains the strength and ductility ratios. Figure 6.15 shows the graph of the ratio of the maximum load obtained [P_{max}] to that of the control [$P_{max,c}$] from experimental work against V_f. There is an increase in the strength ratio as V_f increases. There is a good agreement in terms of strength, particularly the P_y and P_{max} between the FEA predicted values and the experimental data.

Table 6.7: Strength and Ductility Ratios

V_f [%]	P_y [kN]	$\frac{P_y}{P_{y,c}}$	P_{max} [kN]	$\frac{P_{max}}{P_{max,c}}$	P_u [kN]	μ	$\frac{\mu}{\mu_c}$
Control	79.0		81.5		76.2	5.13	
0.50	79.0	1.00	81.5	1.00	76.2	5.13	1.00
1.00	79.0	1.00	88.0	1.08	82.6	5.27	1.02
1.25	101.7	1.29	103.9	1.27	89.3	5.37	1.04
1.50	102.3	1.29	104.8	1.28	100.8	5.38	1.05
1.75	110.7	1.40	107.7	1.32	106.9	5.47	1.06
2.00	114.4	1.45	114.5	1.40	113.3	5.48	1.07
2.50	125.8	1.59	127.1	1.56	126.8	5.48	1.07

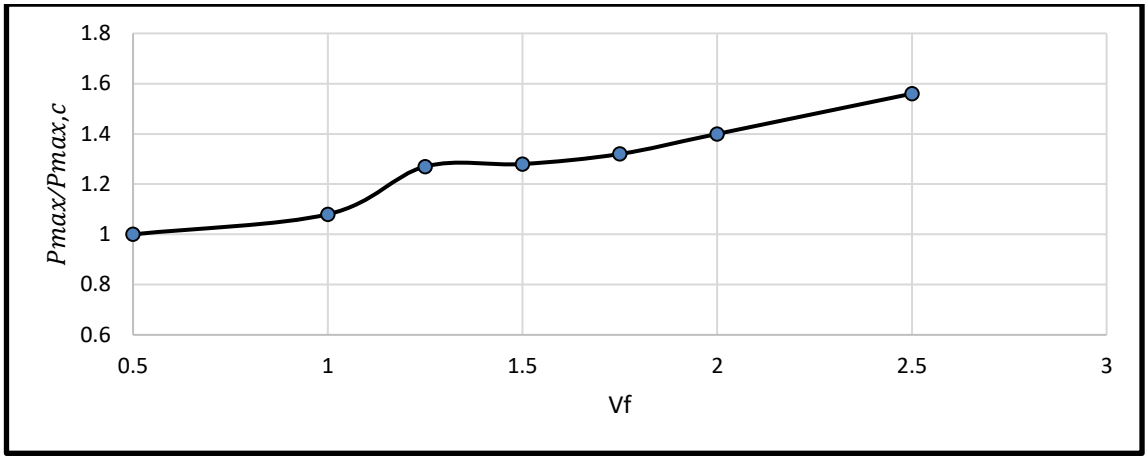

Figure 6.15: Graph of V_f against $P_{max}/P_{max,c}$

A further comparison is made between the yield-load [P_y] of each slab against that of the control [$P_{y,c}$] and presented in Figure 6.16. As the V_f increases, an ascending inclination is noticed in the loading. This also validate that an increase in V_f ultimately leads to increase in strength and load-carrying capacity of the slab. There is a rise in strength ratio of up to 56% in both the $P_y/P_{y,c}$ and $P_{max}/P_{max,c}$ as the V_f increases.

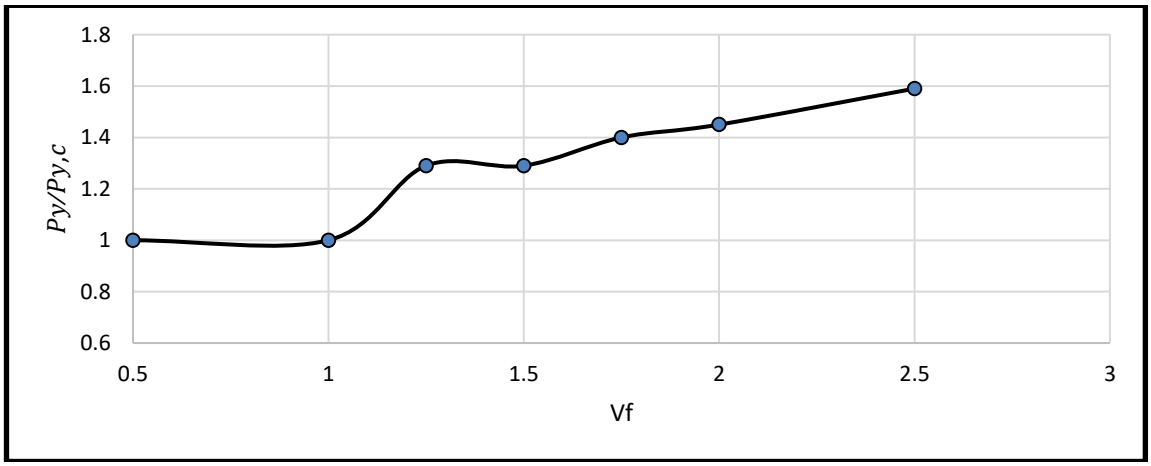

Figure 6.16: Graph of V_f against $P_y/P_{y,c}$

6.4.5.2 Ductility Ratio [Slab without Rebar]

The ductility [μ] of the slab-derived as a response of the SFRC slab to ultimate load [in central displacement, δ_u] and the displacement at yield load. These were normalised for every slab with varying V_f [μ/μ_c]. There is a considerable improvement in the ductility as V_f increase. [Figure 6.17] up till V_f=1.75%. The ductility remains the same from V_f=1.75% to 2.5%. The ductility achieved in the experiment at V_f=0.50% is higher than

what is produced by FEA at V_f = 0.50%. This is attributed to the stiffness matrix of the FEA model.

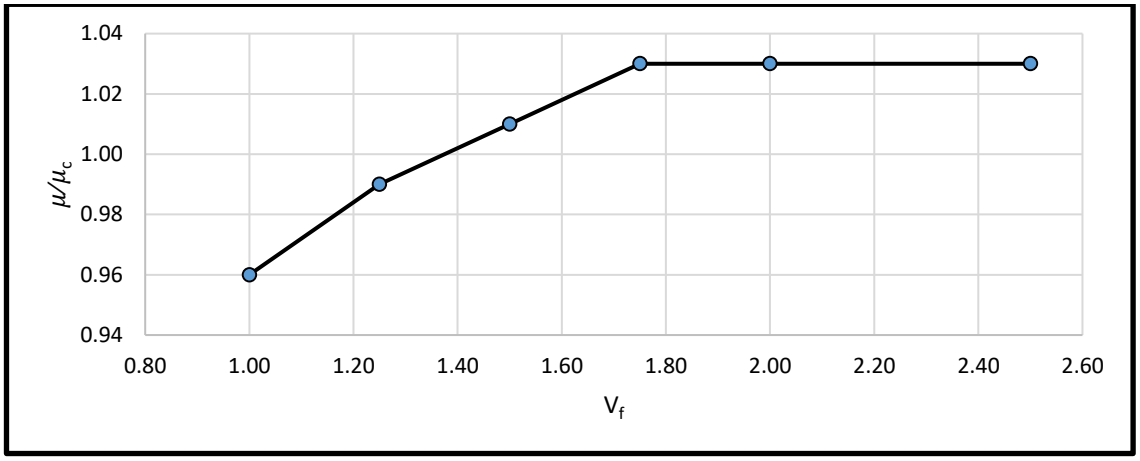

Figure 6.17: Graph of V_f against μ/μ_c

6.4.6 Additional Analysis with Different f_{cu} [Slab without Rebar]

Additional analyses involving different characteristic strength [30MPa, 40MPa and 50MPa] of pile-supported SFRC slabs with varying V_f [1.00%, 1.25%, 1.50%, 1.75%, 2.00% and 2.50%] were carried out with the results of load-displacement graphs in Table 6.8 and Figures 6.18 – 6.20. These additional analyses are essential for the derivation of a formula for the maximum load carrying capacity through regression analysis in order to obtain a reliable result with multiple variables. All other material and plasticity properties remain the same.

6.4.6.1 The Influence of the Characteristic Strength [f_{cu}] of Concrete [Slab without Rebar]

The results from the simulation of the pile-supported SFRC slabs having varying f_{cu} with different V_f shows an increase in the strength ratios. These are considered in terms of the yield load [load at first crack], maximum load [load carrying capacity] and the ultimate load [load at failure] and their respective displacements.

Table 6.8: Strength and Ductility Ratios for various V_f [Slab without Rebar]

V_f [%]	f_{cu} [MPa]	P_y [kN]	$\frac{P_y}{P_{y,c}}$	P_{max} [kN]	$\frac{P_{max}}{P_{max,c}}$	P_u [kN]	μ	$\frac{\mu}{\mu_c}$
Control	30.0	65.22		69.65		62.80	8.48	
0.50		65.22	1.00	69.65	1.00	62.80	8.48	1.00
1.00		73.21	1.12	75.59	1.08	66.75	8.43	0.99
1.25		78.00	1.20	79.35	1.14	73.74	7.76	0.92
1.50		83.36	1.28	84.90	1.22	83.48	7.07	0.83
1.75		92.35	1.42	93.09	1.34	91.15	5.80	0.68
2.00		96.65	1.48	97.52	1.40	95.11	4.82	0.57
2.50		103.20	1.58	103.84	1.49	103.60	3.15	0.37
Control	40.0	76.58		77.79		72.45	11.17	
0.50		76.58	1.00	77.79	1.00	72.45	11.17	1.00
1.00		82.54	1.08	83.99	1.08	72.91	9.21	0.82
1.25		88.50	1.16	90.11	1.16	78.89	7.97	0.71
1.50		96.25	1.26	99.52	1.28	91.86	8.04	0.72
1.75		104.55	1.37	105.28	1.35	103.21	6.65	0.60
2.00		110.84	1.45	111.61	1.43	110.14	5.51	0.49
2.50		120.07	1.57	123.70	1.59	121.24	3.87	0.35
Control	50.0	87.00		89.84		86.44	11.31	
0.50		87.00	1.00	89.84	1.00	86.44	11.31	1.00
1.00		96.90	1.11	98.00	1.09	87.34	10.50	0.93
1.25		109.00	1.25	113.91	1.27	96.44	10.46	0.92
1.50		118.00	1.36	120.64	1.34	103.57	8.90	0.79
1.75		134.00	1.54	135.57	1.51	124.46	7.76	0.69
2.00		141.07	1.62	147.07	1.64	145.04	6.33	0.56
2.50		160.41	1.84	163.41	1.82	161.15	5.81	0.51

As envisaged, the strength results continue to increase as the f_{cu} and V_f increases. Also, there is an increment in the ductility of the slabs as f_{cu} increases and a decrease as V_f increase. This decrease is attributed to the number of steel-fibres bridging the cracks as they emerged, thus leading to a decrease in the central displacement of the slabs.

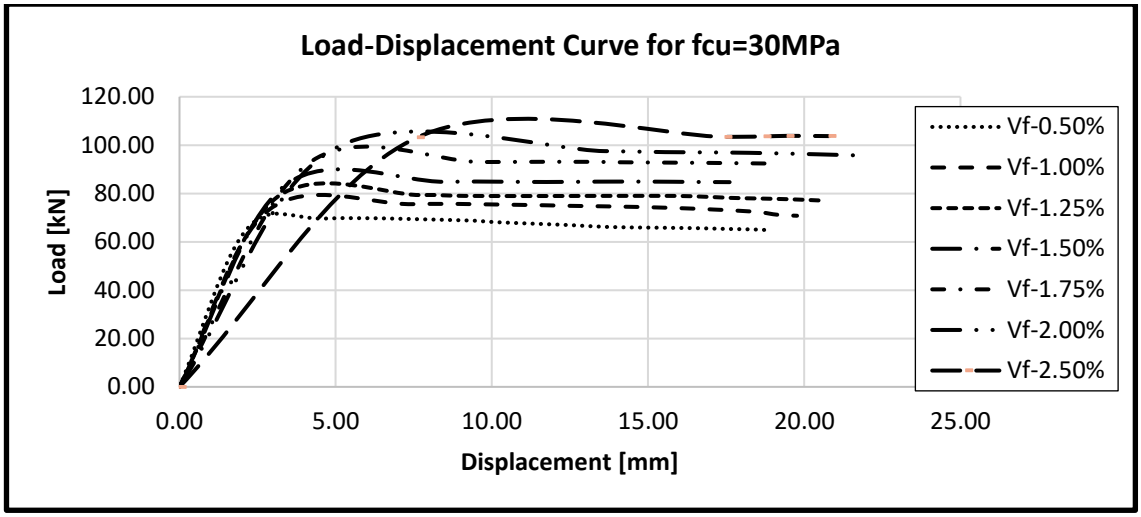

Figure 6.18: Load-Displacement Curves for various V_f with f_{cu}=30MPa [Slab without Rebar]

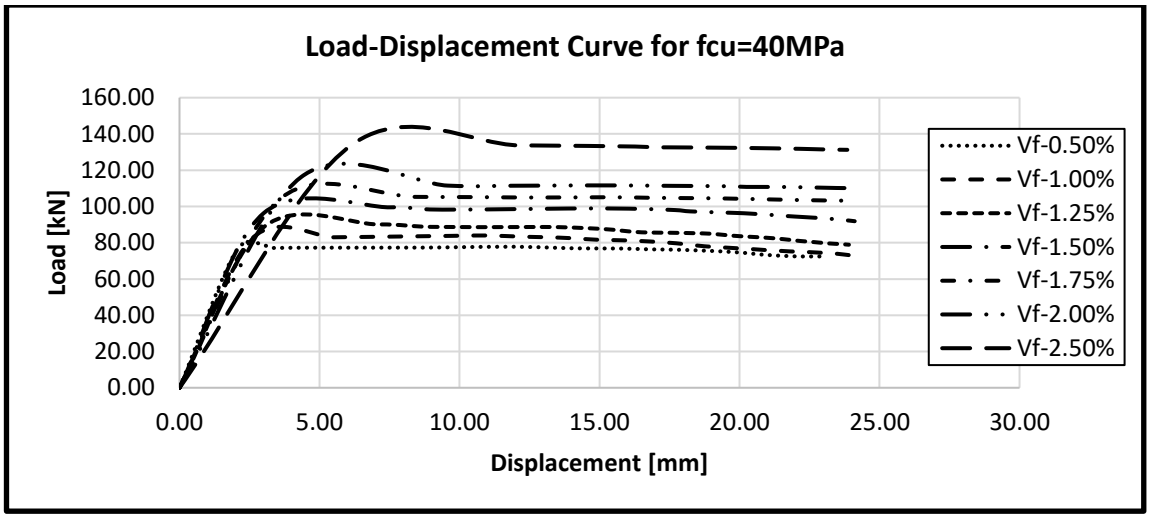

Figure 6.19: Load-Displacement Curves for various V_f with f_{cu}=40MPa [Slab without Rebar]

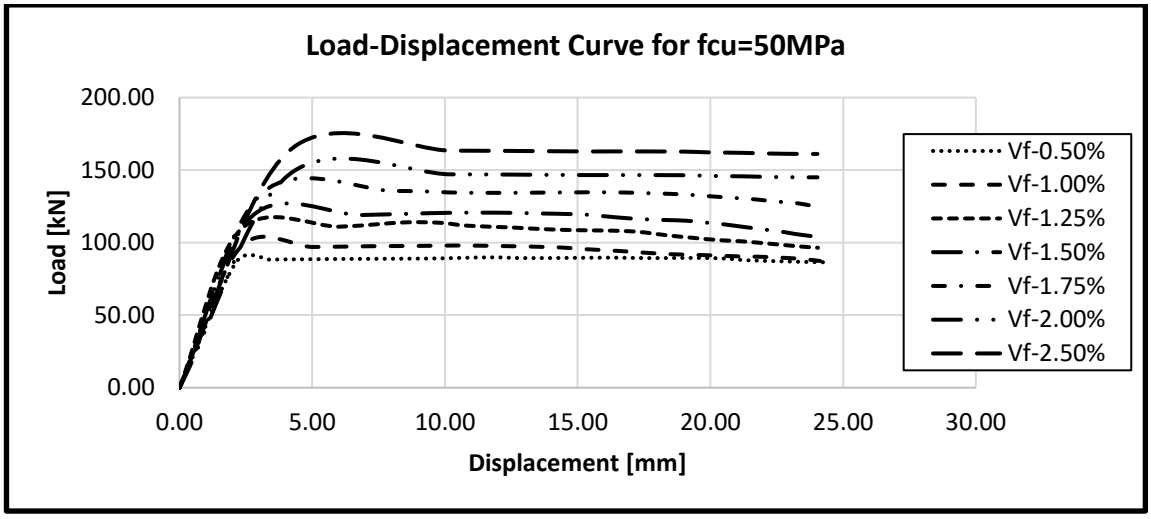

Figure 6.20: Load-Displacement Curves for various V_f with f_{cu}=50MPa [Slab without Rebar]

Figures 610, 6.18 -6.20 show the Load-Displacement curves for different V_f with various f_{cu} and considering the consequences on the pile-supported SFRC slabs load carrying capacity and central displacement. The f_{cu} of 30MPa, 40MPa, 50MPa and that of the experiment, 45MPa were used. All other parameters and the material properties were kept the same as in the validation analysis. The characteristic compressive strength of the SFRC has no significant impact on the post cracking behaviour of the slab. The post-cracking behaviour is influenced by the tensile and flexural strengths, f_t and f_{tu}, which leads to an improvement in the load carrying capacity of the slab by 20% and 84%.

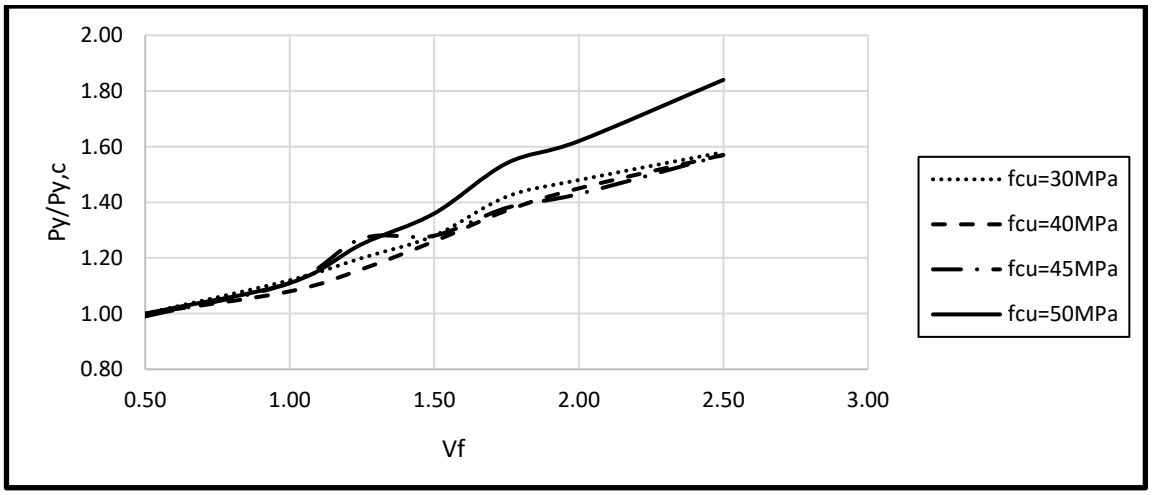

Figure 6.21: Graph of V_f against $P_y/P_{y,c}$ with varying f_{cu} [Slab without Rebar]

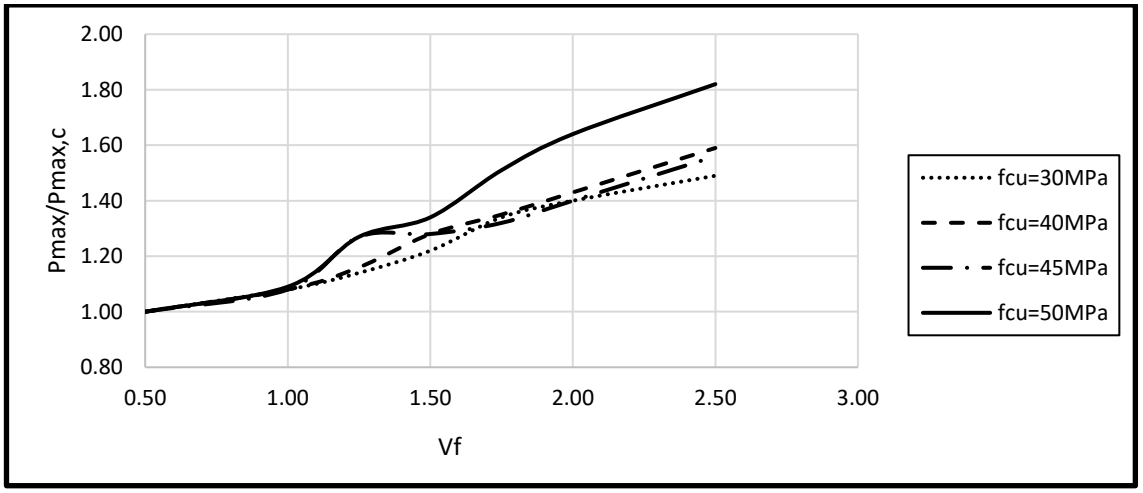

Figure 6.22: Graph of V_f against $P_{max}/P_{max,c}$ with varying f_{cu} [Slab without Rebar]

The curves in Figures 6.21 and 6.22 depict the response of the slab when compared with non-dimensional parameters. The figures above also revealed that as V_f increases,

there is a consistent upward movement in the yield and maximum load ratios. Both the $P_y/P_{y,c}$ and $P_{max}/P_{max,c}$ increase relatively to the value of f_{cu}

The results from FEA are used to generate formulae for the yield and maximum load bearing capacity and their corresponding displacement. To develop an equation that has a wide range of variables [f_{cu}, V_f, L/d, δ, and P_y, or P_{max}], more analyses were carried out with the depth increased to 160mm. This gives the span/depth ratio of 12.5. The values of the f_{cu} and V_f are varied with all other plasticity parameters and concrete properties remaining the same. Bending was the mode of failure at the middle of the panel. The summary of the additional analyses is in Table 6.9.

Table 6.9: Strength and Ductility Ratios for various V_f [Slab without Rebar]

V_f [%]	f_{cu} [MPa]	P_y [kN]	δ_y [mm]	P_{max} [kN]	δ_{max} [mm]
0.50	30	78.26	3.06	83.58	4.92
1.00		87.85	3.08	90.71	7.67
1.25		93.60	3.30	95.23	7.89
1.50		100.03	3.60	101.88	13.56
1.75		110.82	4.32	111.70	13.53
2.00		115.98	5.18	117.02	13.81
2.50		123.84	7.85	124.60	19.69
0.50	40	88.83	2.25	90.24	12.16
1.00		95.75	2.79	97.42	11.15
1.25		102.66	3.00	104.52	7.08
1.50		111.65	3.19	115.44	7.27
1.75		121.28	3.81	122.12	8.67
2.00		134.84	4.54	134.84	4.54
2.50		139.28	6.38	143.49	12.36
0.50	50	108.75	2.16	110.99	6.73
1.00		121.13	2.30	122.25	9.57
1.25		136.25	2.30	142.38	8.44
1.50		147.50	2.72	150.80	11.08
1.75		167.50	3.11	169.46	8.09
2.00		176.33	3.80	183.83	10.21
2.50		200.51	4.14	204.26	10.21

6.4.7 Proposed Equation for Peak and Maximum Load [Slab without Rebar]

The proposed equations for estimating the peak load and the maximum load carrying capacity when a 4-panel pile-supported SFRC suspended floor is loaded simultaneously in the middle of the panels [with the fibre volume ratio [V_f], characteristic strength [f_{cu}], span depth ratio [L/d] and acceptable displacement [δ] as dependent variables] are derived using the regression analysis of the MS-Excel as:

$$P_y = 2.04f_{cu} + 30.43V_f - 13.52\,{}^{L}/_{d} + 163.88 \quad \text{- Eqn. 6.1}$$

$$P_y = 5.43\delta_y + 90.93 \quad \text{- Eqn. 6.2}$$

$$P_{max} = 2.13f_{cu} + 29.58V_f - 13.49\,{}^{L}/_{d} + 163.71 \quad \text{- Eqn. 6.3}$$

$$P_{max} = 1.01\delta_{max} + 102.63 \quad \text{- Eqn. 6.4}$$

Where L – Span of the panel

d – Overall depth of the panel

The data used in developing these equations are taken from Tables 6.7 – 6.9 and are stated in Appendix B1

6.5 Case Study 2[b]: 4-Panel Slab with Rebar

The second part of this case study is the inclusion of six 10mm bars [three in both directions] running over each of the supports [Figure 6.23]. All other properties, parameters, details and dimensions remain the same as Case Study 2[a]. In the quarter-size model, 2500 by 2500mm, the loading-rig is 300mm in diameter, but the rebar along the cut-sides are one and a half [though two were provided, one has a diameter of 10mm and the second has a diameter of 7.07mm whose area is half that of 10mm bar]. The shaded edges show the continuity of the sides.

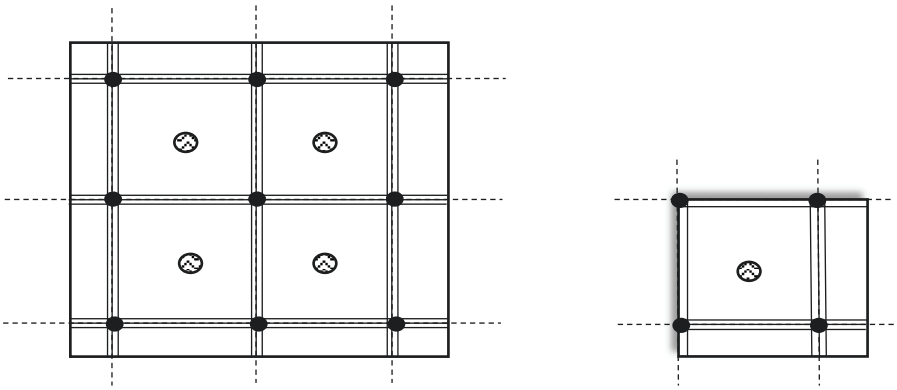

Figure 6.23: Loading Pattern of Slab with Rebar [Full and Quarter-Size]

The rebars are modelled as trusses and embedded in the slab 3D model. This guides against the rebar slipping away from the panel. At FEA, the quarter-slab was loaded at the mid-span with displacement-based loading. To vary the loadings, time-frequency of 0-10 [at 0.1 increment] with an amplitude of 0-1 [at 0.01 increment] was deployed. The displacement was applied slowly at the rate of 0.2mm until crack propagation and final deformation. A bilinear material behaviour of steel is given in the Stress-Strain Value for Reinforcement

Table 6.10: Stress-Strain Value for Reinforcement

Stress MPa	Strain
0.00	0.00
460.00	0.001
560.00	0.01

6.5.1 Load-Displacement Curves of Slab with Rebar

The load-displacement curves of the NLFEA and experimental results are shown in Figure 6.24. The FEA was able to capture the experiment up to 97.4% accuracy. The yield load and maximum load carrying capacity of both the NLFEA and that of the experiment are in agreement. The ductility response of the experimental results is the same as that of the simulated FE model [Figure 6.24 and Table 6.11]. Strain hardening response was sharp unto the peak load in this full-scale FEA of the SFRC slabs and the FEA model. The gradient increased steadily before failure. The mode of failure in the slab was bending [flexural]. The presence of the rebar has prevented progressive collapse with the curve

showing structural toughness. Additional parametric studies using the same FEA parameters was carried out.

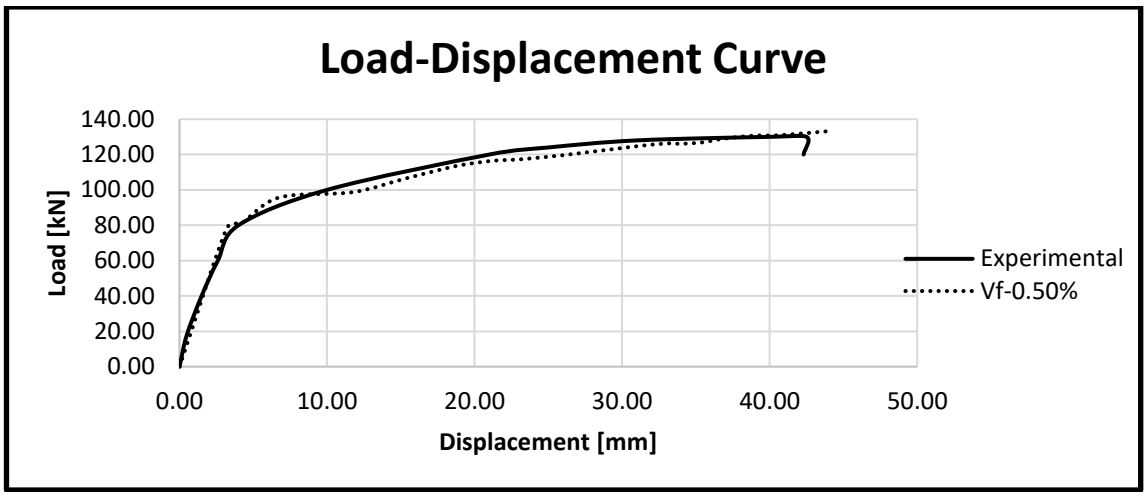

Figure 6.24: Load-Displacement Curves for Experiment and FEA [Slab with Rebar]

Table 6.11: Comparison of Experimental and FEA Validation Results [Slab with Rebar]

	Slab with Rebar		% Variance
	Experiment	FEA	
Load at First Crack [kN]	80.0	81.2	1.50
Displacement at First Crack [mm]	4.0	4.2	5.00
Maximum Load [kN]	130.0	133.2	2.46
Displacement at Maximum Load [mm]	40.0	44.1	10.2

The crack patterns at first crack and final [failure] stages of the experimental testing and the NLFEA simulated images are alike [Figure 6.25]. The NLFEA further exhibits the ability to capture the changes in SFRC slab with rebar on the concrete strength [yield and maximum loads and their respective displacement] and arresting the crack propagation by steel-fibres bridging the openings.

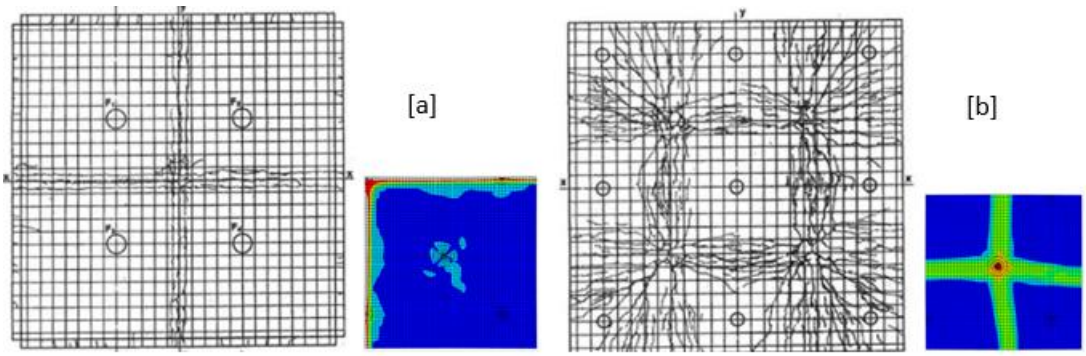

Figure 6.25: Comparison between Experimental and FEA Crack Pattern [a] Top and [b] soffit [Slab with Rebar]

The crack patterns from the FEA further reinforced the adequacy of the Lok and Xiao (1999) constitutive models integrated into the concrete damaged plasticity [CDP] of ABAQUS with correct material properties to predict the behaviour of pile-supported SFRC slabs with rebar across supports vis-à-vis maximum load capacity, displacements and cracking patterns in either quarter or full slab.

The damaged plasticity and principal strain vector shapes of the validation model are presented in Figure 6.26a. The strain vector [Figure 6.27b] shows the internal distortion of the quarter slab in transparent visualisation mode, which indicates the mode of failure in the slab. The presence of the rebar is felt as the slab was able to carry more loads. The slab also was able to deflect more without collapse. The rebar makes the slab more ductile. As the load increases, progressive collapse of the slab was averted as the rebar over the piles act against the moment across the pile support.

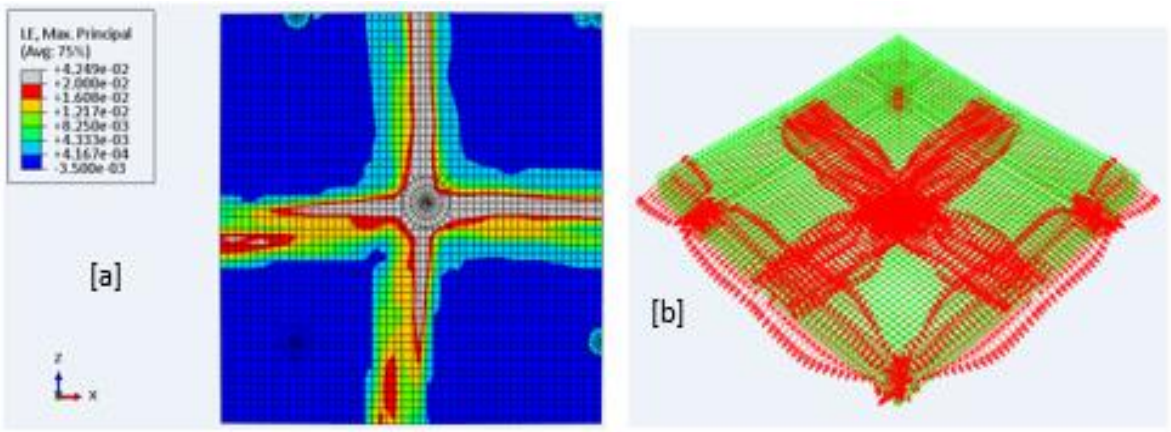

Figure 6.26: Damaged Plasticity and Principal Strain Vector Shape of FEA Model [Slab with Rebar]

As done earlier, the critical structural response indicators, the yield load [P_y], the maximum load [P_{max}], the ultimate load [P_u] and their respective displacements [δ_y, δ_{max}, δ_u] and the ductility ratio [μ] expressed as δ_u/δ_y [Table 6.12].

6.5.2 The Strength of Slab with Rebar

Change in the fibre volume ratio [V_f] is the subject of the initial parametric study. An enhanced strength and higher increment in load carrying capacity is observed as there is an increment in the value of V_f indicating that stiffness increases as V_f rises [Table 6.12 and Figure 6.27]. The value of the load-carrying capacity increased by 9.7% from V_f=1.00% to V_f=1.25% and went as much as an increment of 9.6% from V_f=2.00% to V_f=2.50%. As the loading increases, the cracks spread but as V_f increases, the cracks reduce thus signifying that the micro-cracks that emerged due to continuous loading, are being bridged by several steel-fibres.

Table 6.12: Strength Parameters for f_{cu}=45MPa [Slab with Rebar]

V_f [%]	P_y [kN]	δ_y [mm]	P_{max} [kN]	δ_{max} [mm]	P_u [kN]	δ_u [mm]	$\mu = \delta_u/\delta_y$
0.50	81.2	4.2	133.2	44.1	133.2	44.1	10.5
1.00	112.7	3.6	174.0	44.6	174.0	44.6	12.4
1.25	131.2	3.7	190.8	44.7	190.8	44.7	12.1
1.50	151.0	4.0	207.0	44.5	207.0	44.5	11.1
1.75	163.9	4.3	221.1	45.7	221.1	45.7	10.6
2.00	178.2	4.9	240.7	45.4	240.7	45.4	9.3
2.50	203.7	7.3	263.7	44.5	263.7	44.5	6.1

At the maximum load, higher load carrying capacity is achieved as V_f increases. To obtain the same displacement in all the slabs with different V_f, a more significant load will be required as the fibre dosage increases. The slabs become stiffer as the V_f increases as can be seen in the curves [Figure 6.27]. The stiffness is attributed to additional fibres in the slabs. The yield load P_y of the slabs also increases as fibres volume increases in the concrete matrix. The increase in P_y shows the capability of steel-fibres bridging the available cracks and controlling the openings. The behaviour of the slabs with rebar has been consistent in the FE analyses.

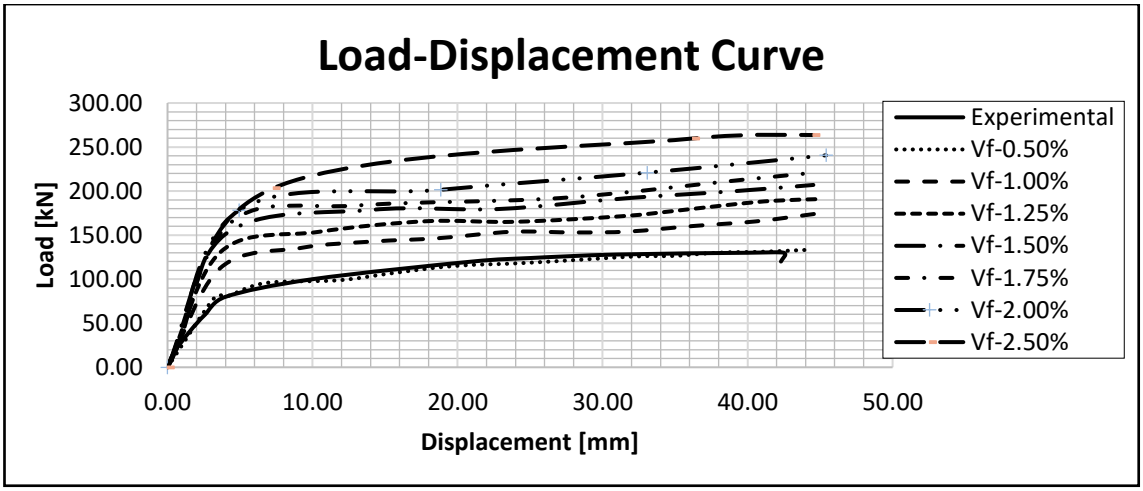

Figure 6.27: Load-Displacement Curves for various V_f [Slab with Rebar]

The strength at the failure of each pile supported SFRC slabs when compared to that of the experiment with V_f=0.50% shows a substantial increase in their ultimate load. From a slab with 0.50% V_f to that of 1.00% V_f, an increase of 41.2kN [a rise of 30.6% in P_u].

6.5.3 Ductility of Slab with Rebar

The ductility of the slab is the capability of the slab to experience large plastic deformation without substantial loss of load carrying capacity, and it can be calculated by dividing the displacement at ultimate load δ_y by the displacement at ultimate load δ_u. There is a reduction in the ductility after a certain threshold. The threshold is at V_f=1.00%. It should be noticed that the slab failed at the peak load, thus making the ultimate load the same as the peak load.

6.5.4 Crack Shapes of Slab with Rebar

This section presents and discusses the cracking shapes [the principal strain contours, principal strain vectors, deflected shapes and tensile damaged shapes] of the 4-panel pile-supported SFRC slab with rebar across the top of the pile [Figures 6.27 – 6.30]. All the cracking patterns are used to describe and compare the failure mechanism of the slab at the FEA and the experimental works.

6.5.4.1 Crack Patterns [Principal Strain Contours] of Slab with Rebar

Figures 6.28 [a-f] show the FE-modelled quarter-slabs' principal strain contours at failure for the pile-supported SFRC slabs [with rebar across supports]. The tensile cracking

strain of the slabs is 0.02 denoted with grey and -0.0035 for compressive cracking strains in black.

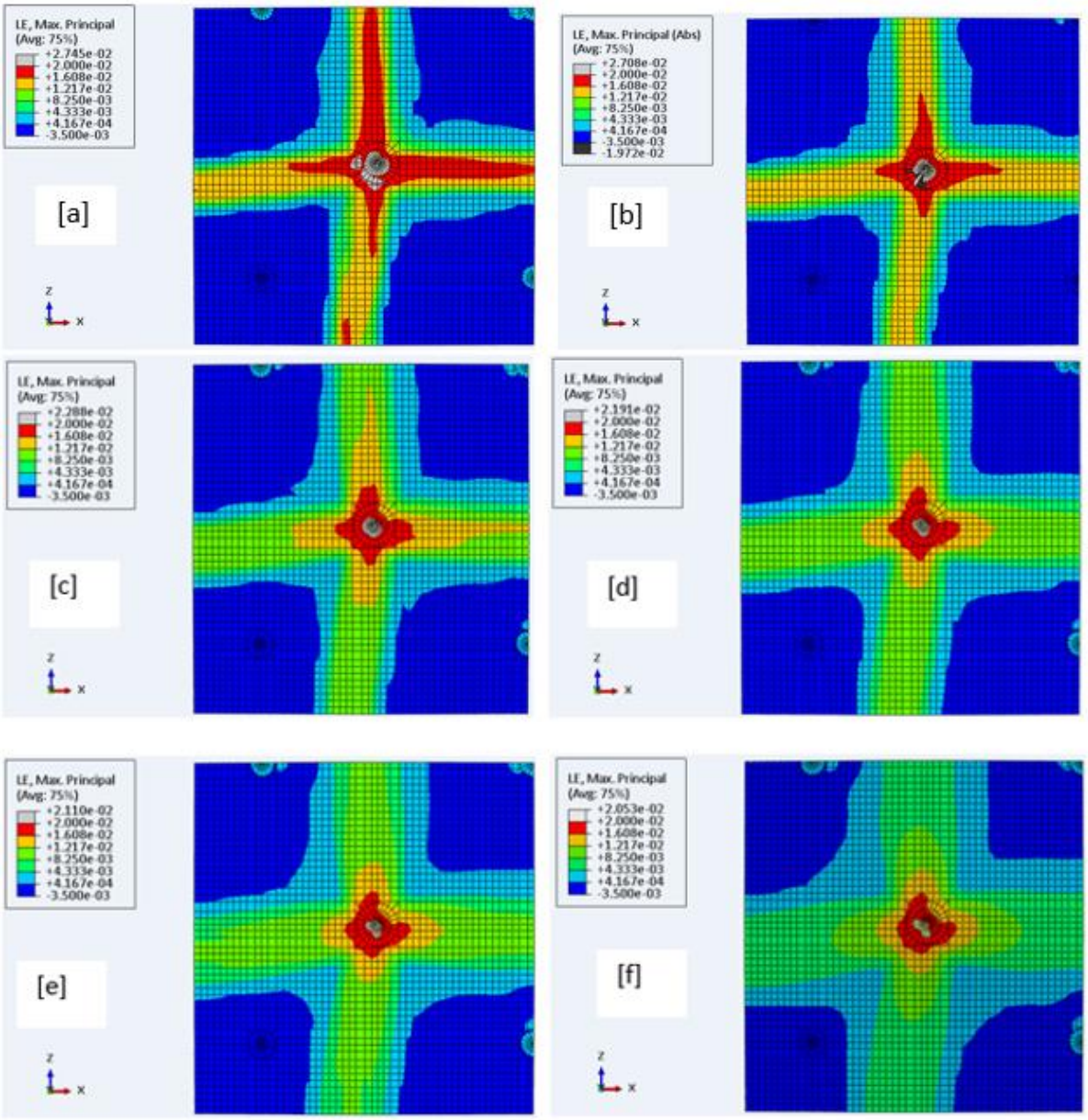

Figure 6.28: Principal Strain Contours for Pile-Supported SFRC Slab with Rebar with V_f [a]= 1.00%, [b]= 1.25%, [c]= 1.50%, [d]= 1.75%, [e]= 2.00% and [f]= 2.5%

In all the FE analyses on the slabs, the cracks formation at the soffit starts at the point of load application. It is formed in four [4] legs with the intensity of the cracks going between two edge supports. The tensile strain did not reach the ultimate value due to the presence of rebar [colour denoting strain ends in red]. From each of the slabs, the crack patterns are severe and broad, especially at the location where the load is applied. The addition of more steel fibres reduces the crack openings, thus narrowing down the

cracks propagation. In the slab with V_f=2.50%, the strain has reduced considerably signifying the reduction in the crack opening at the soffit of the slab.

6.5.4.2 Crack Patterns [Principal Strain Vectors] of Slab with Rebar

The principal strain vectors are used to understand the crack formation in the slabs at the failure point with the slabs viewed in transparent mode [Figures 6.29 (a-f)]. This mode allows viewing the top and soffit of the slabs simultaneously. The concentration of the vectors can be seen at the centre [point of loads application] with the four [4] legs and along the continuous edges. As the fibre dosage increase, the strain vectors become scanty [i.e. reduces significantly]

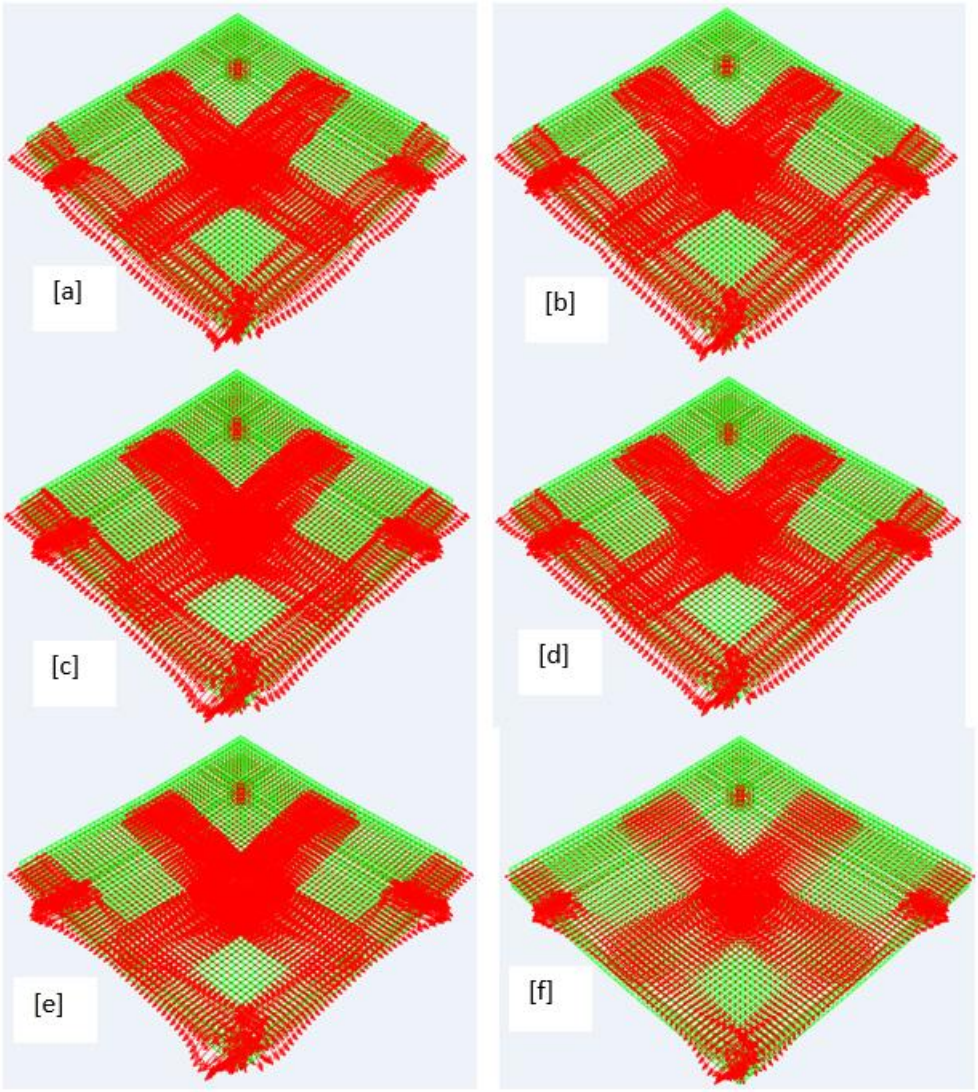

Figure 6.29: Principal Strain Vectors for Pile-Supported SFRC Slab with Rebar with V_f [a]= 1.00%, [b]= 1.25%, [c]= 1.50%, [d]= 1.75%, [e]= 2.00% and [f]= 2.5%

The slab with V_f=0.50% fails with severe cracking at the mid-span, and as the fibre dosage increase, the intensity of the cracking reduced drastically. These show that the steel-fibres control the crack openings by bridging he cracks as they are propagated.

6.5.4.3 Crack Patterns [Deflected Shapes] of Slab with Rebar

The deformation of the slabs showing the influence of loading just before the final collapse is presented in deflected shapes [Figures 6.30 (a-f)]. The deformation occurs in the direction of the applied load with the slabs sagging at mid-span showing a failure in bending and hogging over the support.

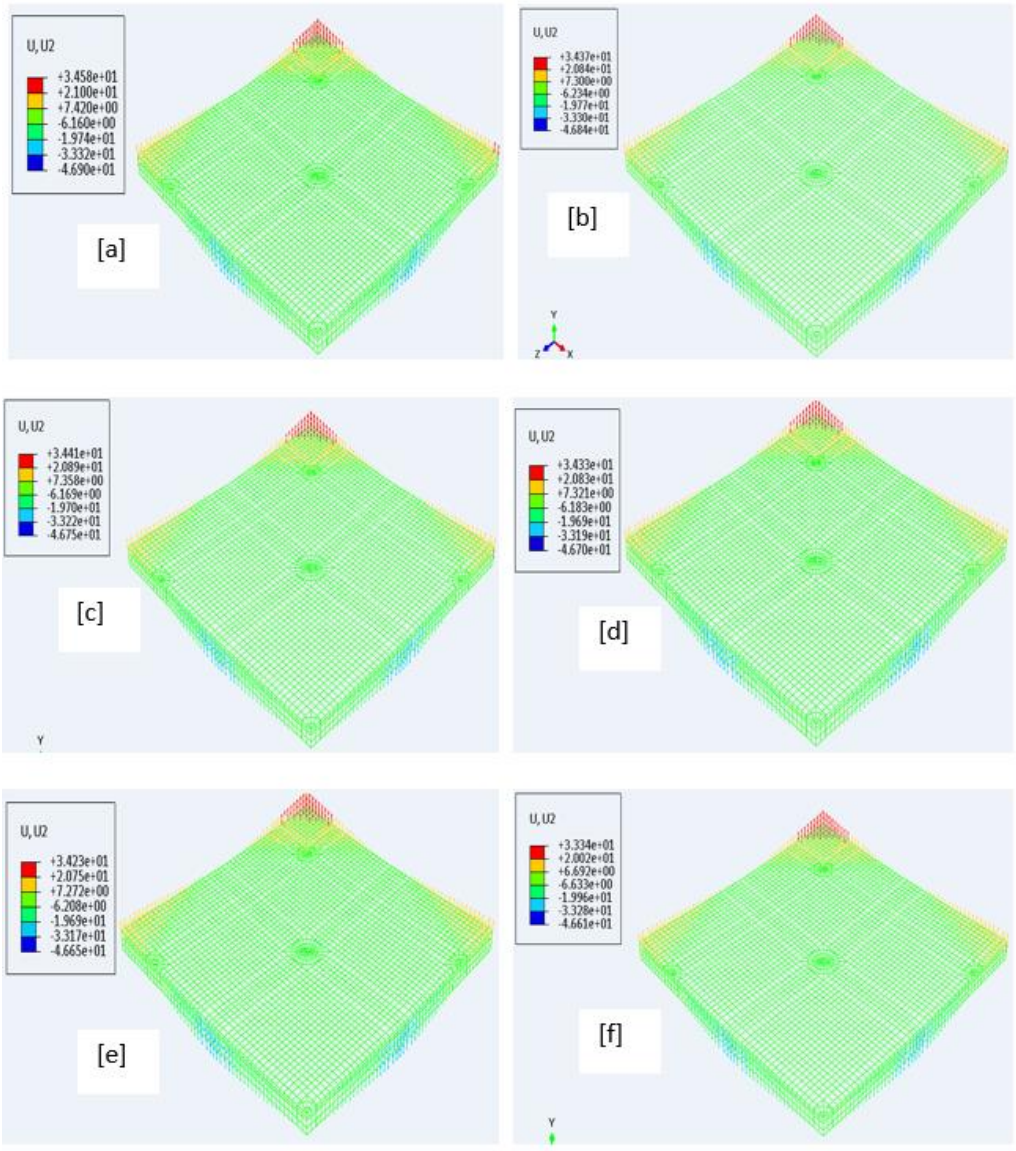

Figure 6.30: Deflected Shapes for Pile-Supported SFRC Slab with Rebar with V_f [a]= 1.00%, [b]= 1.25%, [c]= 1.50%, [d]= 1.75%, [e]= 2.00% and [f]= 2.5%

6.5.4.4 Crack Patterns [Tensile Damaged Shapes] of Slab with Rebar

The crack pattern of the slabs [soffit and top] are finally presented in the damaged tensile shapes [Figures 6.31 (a-f)]. The impact of the rebar can also be seen in the shapes as additional strain develops along the path of he rebar. The loading at mid-span triggered cross-damaged pattern at the soffit and two adjacent damage patterns at the top edge-line. The damage is introduced when the principal strain in the material reaches the peak. Cracks start to develop at this peak strain. The tensile cracking patterns are observed both at the soffit and top of the slabs. The grey area gets broader as the V_f increase. Likewise, the two adjacent legs get wider along the edges, signifying the influence of the rebar and the continuity of the slabs. The strain distribution at the top also reduces as fibre dosage increases.

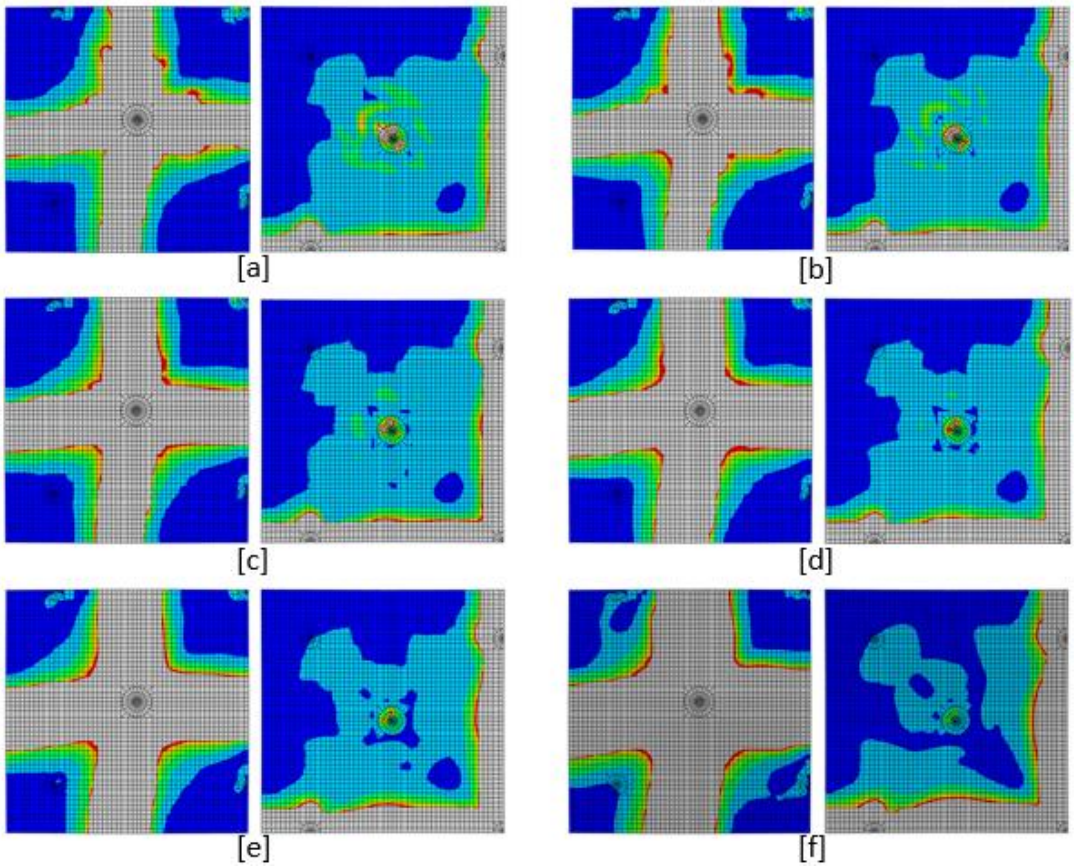

Figure 6.31: Tensile Damaged Shapes for Pile-Supported SFRC Slab with Rebar with V_f [a]= 1.00%, [b]= 1.25%, [c]= 1.50%, [d]= 1.75%, [e]= 2.00% and [f]= 2.5% [Left=bottom, right = top]

6.5.5 Comparative Study with Experimental Specimen using Non-Dimensional Ratios [Slab with Rebar]

The slabs are described using non-dimensional ratios in this section with comparison made between experimental and FEA results. Concluding remarks are made from the ensuring results.

6.5.5.1 Strength Ratio [Slab with Rebar]

Table 6.13 and Figures 6.32-34 display the strength and ductility ratios of the pile-supported SFRC slabs with rebar across the support. A substantial increase in the $\frac{P_y}{P_{y,c}}$ and $\frac{P_{max}}{P_{max,c}}$ are obtained as V_f increases.

Table 6.13: Strength and Ductility Ratios of Slab with Rebar

V_f [%]	P_y [kN]	$\frac{P_y}{P_{y,c}}$	P_{max} [kN]	$\frac{P_{max}}{P_{max,c}}$	P_u [kN]	μ	$\frac{\mu}{\mu_c}$
Control	81.2		133.2		133.2	10.5	
0.50	81.2	1.00	133.2	1.00	133.2	10.5	1.00
1.00	112.7	1.39	174.0	1.31	174.0	12.4	1.18
1.25	131.2	1.62	190.8	1.43	190.8	12.1	1.15
1.50	151.0	1.86	207.0	1.55	207.0	11.1	1.06
1.75	163.9	2.02	221.1	1.66	221.1	10.6	1.01
2.00	178.2	2.19	240.7	1.81	240.7	9.3	0.89
2.50	203.7	2.51	263.7	1.98	263.7	6.1	0.58

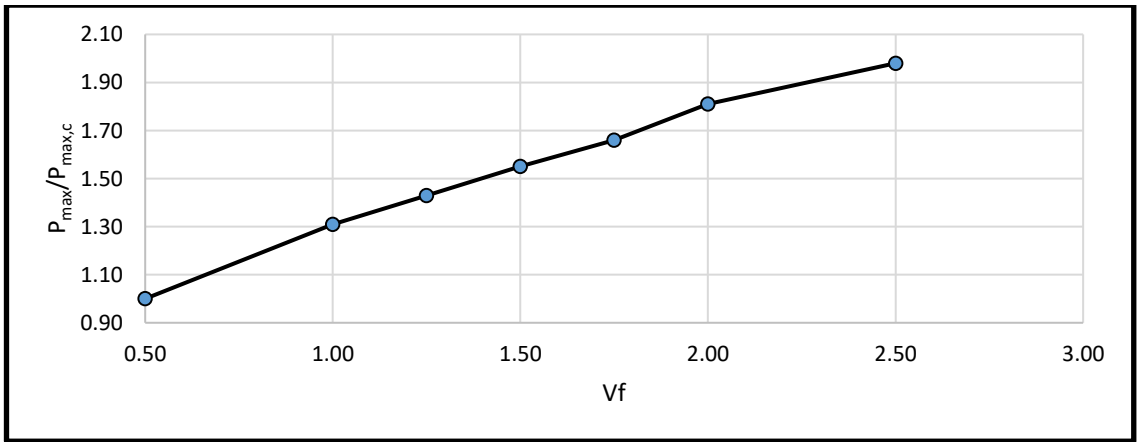

Figure 6.32: Graph of V_f against $P_{max}/P_{max,c}$ [Slab with Rebar]

Figures 6.31 and 6.32 present additional evaluation made between the yield-load [P_y] and maximum load [P_{max}] of each slab against that of the control [$P_{y,c}$ and $P_{max,c}$]. There is a continuous increase in the strength ratio as the V_f increases.

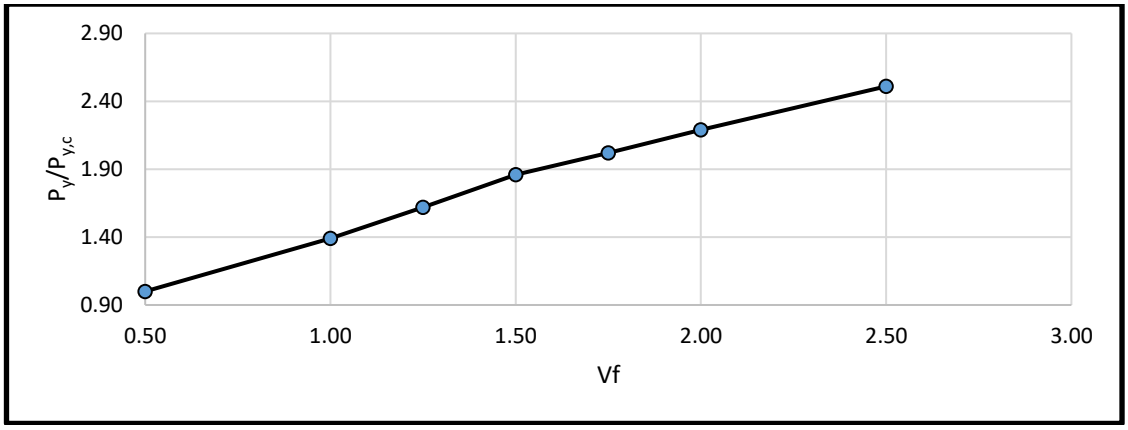

Figure 6.32: Graph of V_f against $P_y/P_{y,c}$ [Slab with Rebar]

6.5.5.2 Ductility Ratio [Slab with Rebar]

The ductility ratio [μ/μ_c] of the slab with rebar is measured by the dividing the ductility [μ] of the slab by the ductility of the control [experiment] slab [μ_c]. These repeated for every slab with varying V_f. There is a sizable improvement in the ductility ratio from V_f=0.50% to 1.00% and after that a steady decline to V_f=2.50%.

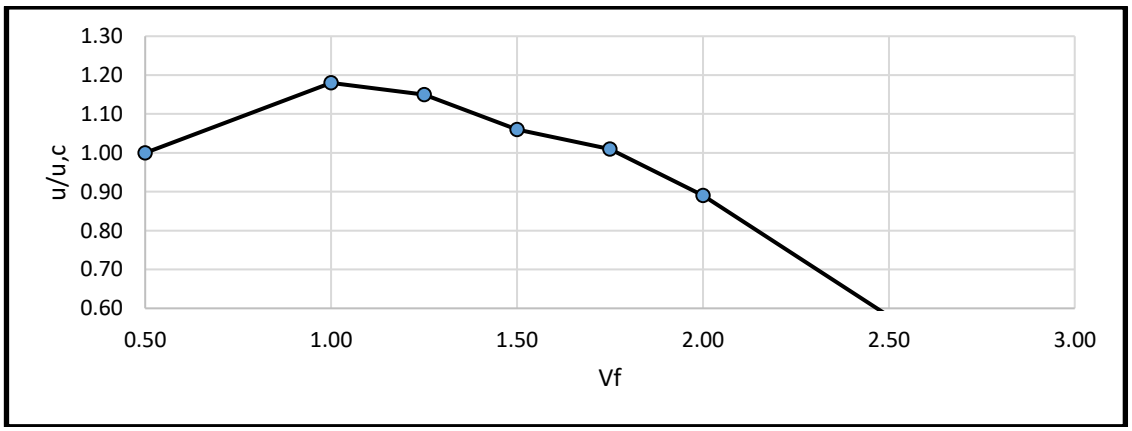

Figure 6.34: Graph of V_f against μ/μ_c [Slab with Rebar]

6.5.6 Additional Analysis with Different f_{cu}

Table 6.14 and Figures 6.35 – 6.37 contain the results of additional analyses involving different f_{cu} [30MPa, 40MPa and 50MPa] of pile-supported SFRC slabs with rebar. The V_f values [1.00%, 1.25%, 1.50%, 1.75%, 2.00% and 2.50%] were used for each f_{cu}. These analyses are necessary in order to understand the behaviour of the SFRC slab with rebar and to have multiple variables essential for regression analysis.

6.5.6.1 The Influence of the Characteristic Strength [f_{cu}] of Concrete

The maximum carrying capacity is derived regression analysis. The regression analysis consists of the results [yield load, maximum load carrying capacity and their respective displacements] from the simulation of the pile-supported SFRC slabs with varying f_{cu}, V_f and span/depth ratios.

Table 6.14: Strength and Ductility Ratios for various V_f [Slab with Rebar]

V_f [mm]	f_{cu} [MPa]	P_y [kN]	$\frac{P_y}{P_{y,c}}$	P_{max} [kN]	$\frac{P_{max}}{P_{max,c}}$	P_u [kN]	μ	$\frac{\mu}{\mu_c}$
Control	30.0	71.4		102.6		102.6	8.00	
0.50		71.4	1.00	102.6	1.00	102.6	8.00	1.00
1.00		80.6	1.13	145.1	1.42	145.1	12.1	1.50
1.25		104.9	1.47	159.2	1.56	159.2	10.7	1.33
1.50		119.2	1.67	175.3	1.72	175.3	9.70	1.21
1.75		136.0	1.90	193.3	1.89	193.3	8.10	1.01
2.00		147.7	2.07	209.4	2.05	209.4	7.30	0.91
2.50		185.7	2.60	244.0	2.39	244.0	4.80	0.59
Control	40.0	79.2		126.1				
0.50		79.2	1.00	126.1	1.00	126.1	10.0	1.00
1.00		82.3	1.04	155.8	1.24	155.8	12.2	1.22
1.25		106.0	1.34	170.3	1.35	185.5	11.2	1.12
1.50		121.3	1.53	185.5	1.47	203.1	11.1	1.11
1.75		143.6	1.81	203.1	1.61	221.8	9.70	0.97
2.00		158.5	2.00	221.8	1.76	254.1	7.70	0.77
2.50		198.2	2.50	254.1	2.02	254.1	5.40	0.54
Control	50.0	83.5		142.2		142.2		
0.50		83.5	1.00	142.2	1.00	142.2	13.78	1.00
1.00		120.2	1.44	185.7	1.31	185.7	12.39	0.90
1.25		140.0	1.68	203.6	1.43	203.6	12.08	0.88
1.50		161.1	1.93	220.8	1.55	220.8	11.13	0.81
1.75		174.9	2.09	235.9	1.66	235.9	10.40	0.75
2.00		190.1	2.28	256.8	1.81	256.8	9.27	0.67
2.50		216.9	2.60	281.3	1.98	281.3	6.10	0.44

As seen in the table 6.14 above, there is an appreciable increment in strength as the f_{cu} and V_f increases. Both the P_y and P_{max} rose in value as V_f increases. In contrary, there is a rise in the ductility of the slabs as V_f value gets to 1.00% and them a downward trend till 2.50% for f_{cu} ≤ 50MPa while for f_{cu} = 50MPa, ductility decreases as V_f increase.

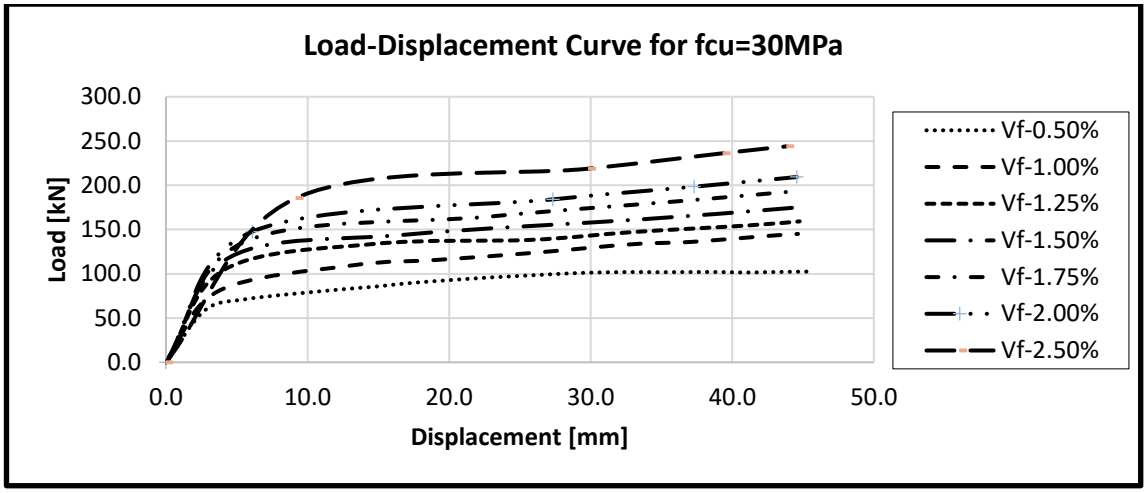

Figure 6.35: Load-Displacement Curves for various V_f with f_{cu}=30MPa [Slab with Rebar]

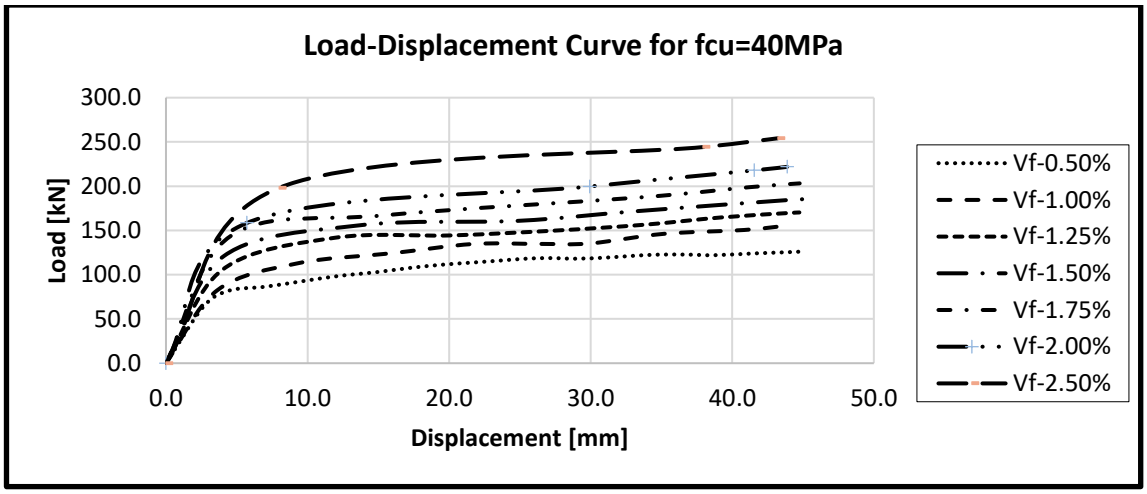

Figure 6.36: Load-Displacement Curves for various V_f with f_{cu}=40MPa [Slab with Rebar]

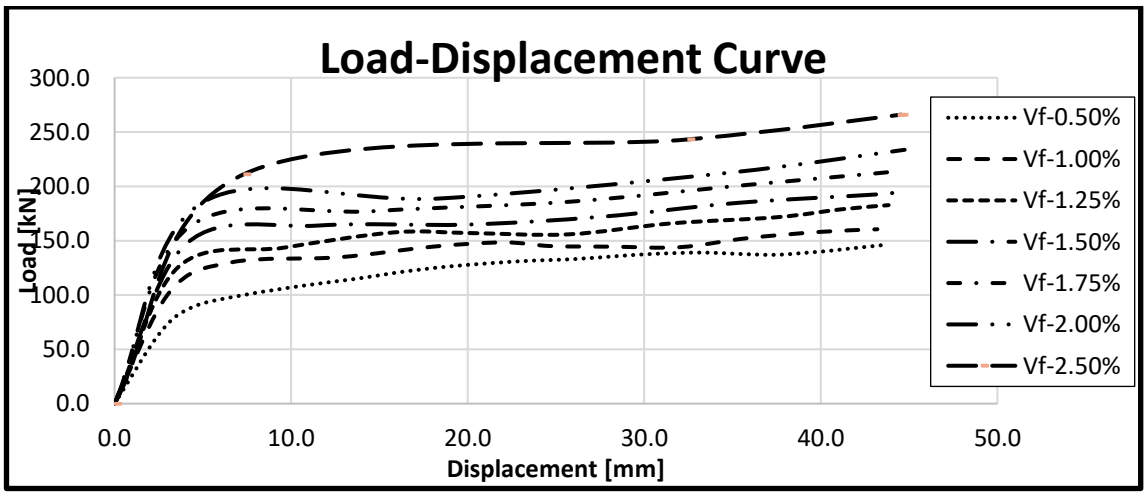

Figure 6.37: Load-Displacement Curves for various V_f with f_{cu}=50MPa [Slab with Rebar]

Figures 6.35-6.37 show the graphs of the load and corresponding displacement of different f_{cu} [30MPa, 40MPa, and 50MPa] with various V_f [0.50% - 2.50%]. The plasticity parameters and the material properties were the same as the ones in the validation analysis. The tensile strength f_t and flexural strength f_{tu} of the SFRC have an impact on the post-cracking behaviour rather than the characteristic compressive strength. The loading carrying capacity is enhanced as both the V_f and f_{cu} increases while the ductility has a downward trend.

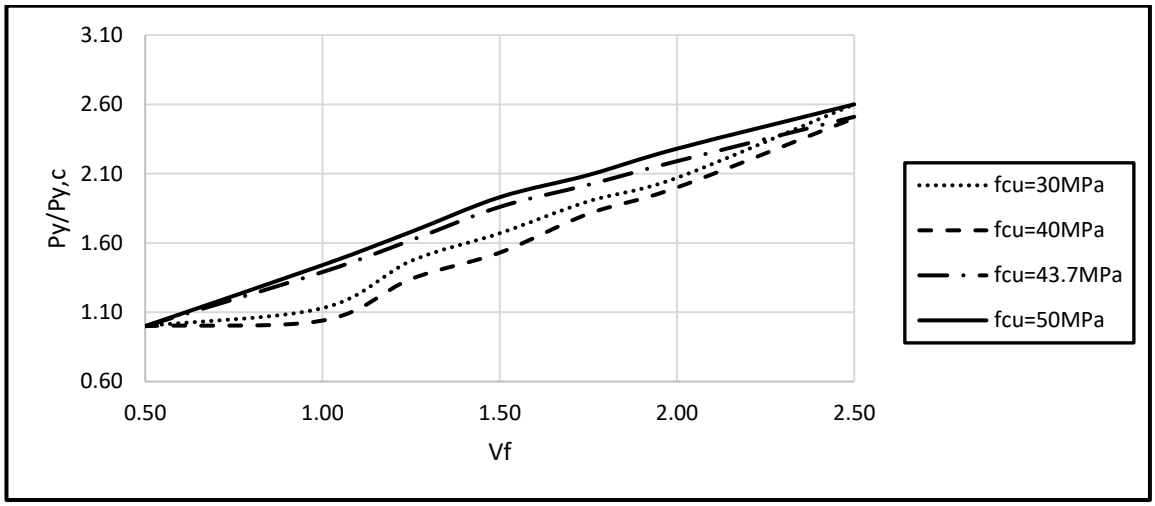

Figure 6.38: Graph of V_f against $P_y/P_{y,c}$ with varying f_{cu} [Slab with Rebar]

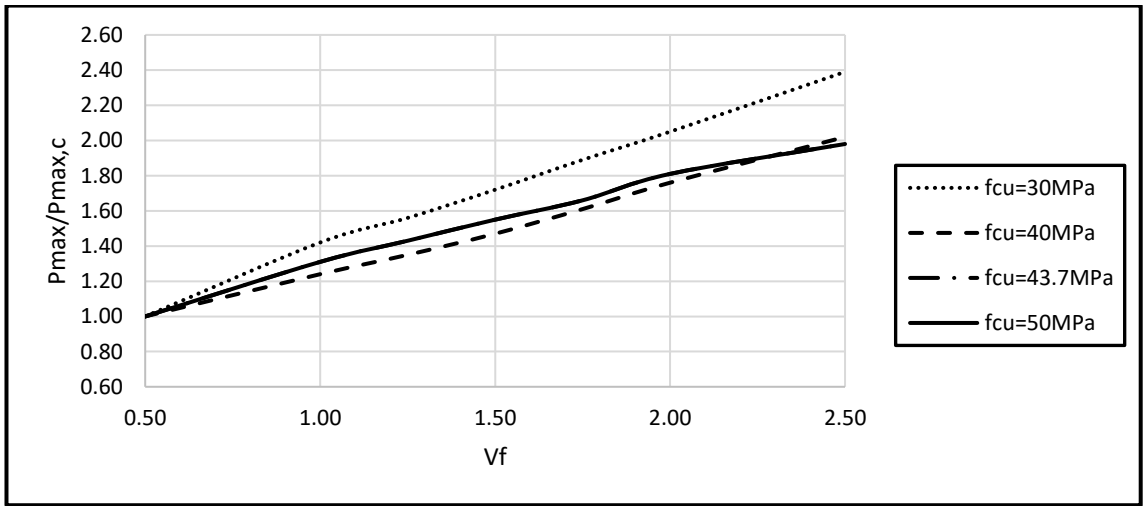

Figure 6.39: Graph of V_f against $P_{max}/P_{max,c}$ with varying f_{cu} [Slab with Rebar]

The curves in Figures 6.38 and 6.39 depict the comparison with non-dimensional parameters and the response of the slab with regards to strength. The figures above also revealed that as V_f increases, there is a consistent upward movement in the yield

and maximum load ratios. Both the $P_y/P_{y,c}$ and $P_{max}/P_{max,c}$ increase relatively to the value of f_{cu}.

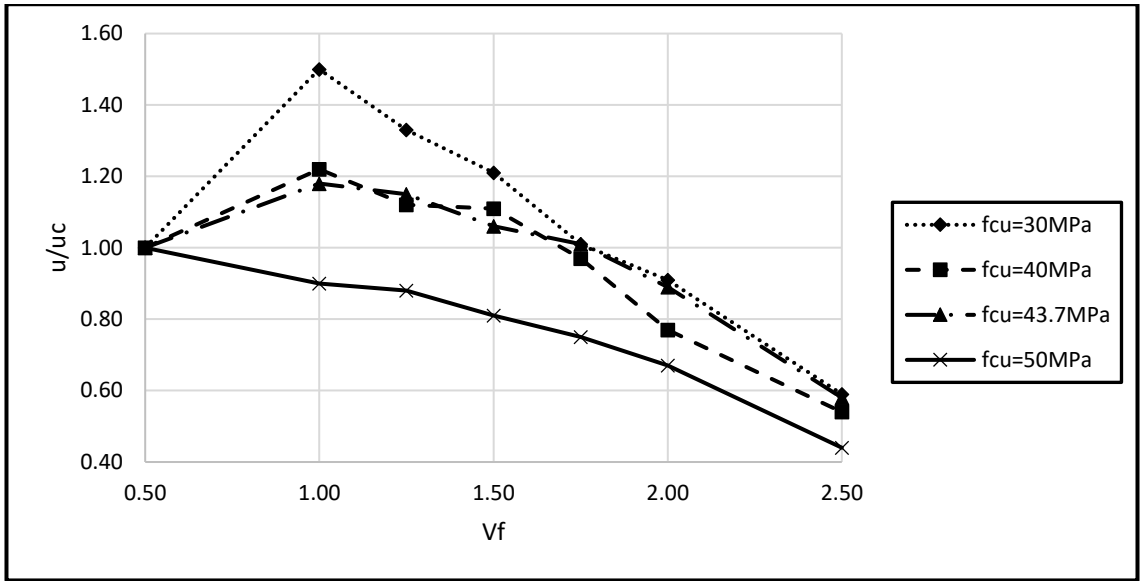

Figure 6.40: Graph of V_f against μ/μ_c with varying f_{cu} [Slab with Rebar]

Figure 6.40 shows the slabs response in ductility when compare with non-dimensional ratios. There is a rise in ductility ratios for f_{cu} ≤ 50MPa from V_f of 0.50% to 1.00% and after that, a fall in value till V_f = 2.50%. In the slab with f_{cu} = 50MPa, there was a decrease in the ductility ratio throughout the whole V_f.

Additional simulations were run for a slab depth of 160mm and 200mm. This gives the span/depth ratio of 12.5 and 10 respectively. The results from FEA presented in Table 6.15. The values of the f_{cu} and V_f are varied with all other plasticity parameters and concrete properties remaining the same. For a depth of 200mm, the f_{cu} was retained at 40 MPa. The mode of failure was bending at the middle of the panel.

Table 6.15: Strength and Ductility Ratios for various V_f

V_f [%]	f_{cu} [MPa]	P_y [kN]	δ_y [mm]	P_{max} [kN]	δ_{max} [mm]
0.50	30	84.1	2.9	142.8	45.1
1.00		103.0	3.6	191.1	42.8
1.25		129.7	4.5	212.7	44.5
1.50		142.3	4.1	234.1	45.0
1.75		166.3	5.6	261.2	44.2
2.00		187.5	7.9	282.7	44.5
2.50		205.7	9.0	354.8	44.3
0.50	40	94.6	1.8	144.7	45.4
1.00		129.1	3.3	202.7	43.3
1.25		131.6	3.5	227.7	42.8
1.50		132.8	4.0	248.2	42.8
1.75		135.8	4.4	269.7	43.6
2.00		145.6	4.7	293.2	42.9
2.50		160.2	4.8	310.2	43.1
0.50	50	99.9	2.2	157.1	43.0
1.00		114.2	2.9	214.3	44.5
1.25		138.3	3.3	239.2	43.7
1.50		162.5	3.7	259.9	43.6
1.75		181.1	4.3	283.9	44.5
2.00		207.7	4.5	305.0	44.5
2.50		251.0	5.6	351.2	42.9
0.50	40 [200mm]	136.6	2.3	227.3	43.9
1.00		201.3	2.9	340.5	44.2
1.25		239.0	3.4	382.4	44.4
1.50		250.3	3.5	420.3	43.2
1.75		286.8	4.5	464.0	41.7
2.00		323.4	4.7	504.7	42.8
2.50		358.9	7.3	584.2	43.3

6.5.7 Proposed Equation for Peak and Maximum Load

The regression analysis of the MS-Excel is used in proposing equations for estimating the peak load and the maximum load carrying capacity in the 4-panel pile-supported SFRC floor with rebar at the top of the piles and loaded simultaneously in the middle of the panels with the following variables (characteristic strength [f_{cu}], fibre volume ratio [V_f], acceptable displacement [δ], and span depth ratio [L/d]). The data used in developing the equations are taken from Tables 6.13 – 6.15 and are stated in Appendix B2.

The equations are given below:

$$P_y = 1.56f_{cu} + 65.1V_f - 25.13\,{}^{L}/_{d} + 324.74 \quad \text{- Eqn. 6.5}$$

$$\delta_y = 16.65\delta_y + 80.1 \quad \text{- Eqn. 6.6}$$

$$P_{max} = 1.76f_{cu} + 85.66V_f - 50.14\,{}^{L}/_{d} + 700.87 \quad \text{- Eqn. 6.7}$$

$$P_{max} = 2854.09 - 59.12\delta_{max} \quad \text{- Eqn. 6.8}$$

Where L – Span of the panel

d – Overall depth of the panel

6.6 Comparison between SFRC Slab with and without Rebar

Figure 6.40 shows the load-displacement curves of pile-supported SFRC slab with and without rebar. The results show a 35% increase in load carrying capacity. The SFRC slab without rebar fails at a central displacement of 15.5mm while that with rebar was able to reach 44.1mm before failure.

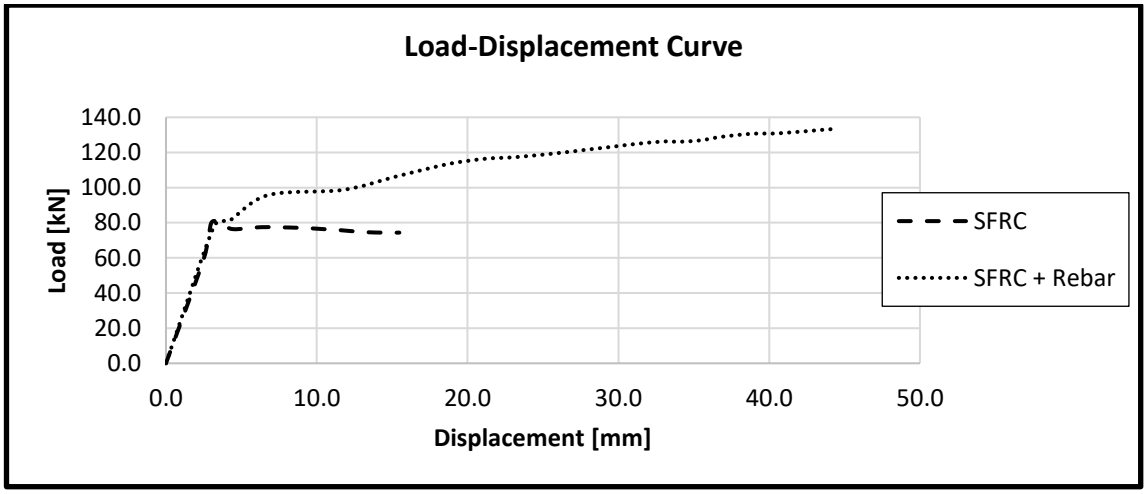

Figure 6.41: Load-Displacement Curve for SFRC with and without Rebar

6.7 Comparison with Existing Guidelines

At the limit state, there are provisions for point load and UDL in the design procedure of SFRC pile-supported slabs in existing guidelines and codes. The Table 6.15 provides a summary of the results of these guidelines, the FEA yield load and the experimental work using the slab with rebar.

Table 6.15: Comparison with Existing Guidelines

Design Guideline	Formula for Moment	Load [kN]	Remarks
TR 34	$Q_t \frac{L_e}{4} + q_u \frac{L_e^2}{8}$	6.52	Underestimated
Swedish	$\frac{f_{fld}.h^2}{6}$	5.88	Underestimated
fib MC 2010	$\frac{f_{Ftu} b h_{sp}^2}{2}$	35.28	Underestimated
TR 63	$08 f_{cd} f_{td} b h^2 \left[0.5 + \frac{0.1 f_{td}}{0.8 f_{cd} + f_{td}}\right] / [0.8 f_{cd} + f_{td}]$	34.85	Underestimated
Dutch Code NEN 6720	$\alpha n l^2$	21.36	Underestimated
RILEM TC 162	$\frac{F_2}{2} \frac{L}{2}$	10.80	Underestimated
Proposed FEA Equation	$1.56 f_{cu} + 65.1 V_f - 25.13 {}^{L}/_{d} + 324.74$	68.49	Underestimated
Experiment	[Yield Load]	80.00	

The FEA, thou produce an underestimated value, but it is the closest to the experimental result [17.99%]. The FEA is much better than the existing guidelines.

6.8 Summary

The results of the parametric studies carried out on the pile-supported SFRC 4-panel slab (i.e. statically indeterminate) with and without steel fibres under point load are presented and discussed in this chapter. The input parameters of the models are the same as that of the material properties [fibre geometry, fibre and concrete matrix tensile strengths), boundary conditions (simple support for piles and slab and fibre-steel embedded in the concrete matrix) and loading direction. The parameters play a significant role at each stage of the tensile stress-strain response through an easy and straightforward multi-linear diagram. Thus, this model provides relevant guidelines in manipulating the fibre or concrete matrix property to determine the load-displacement response of the slab. From the FEA results on the parametric studies, it can be

established that the strength of the slabs increases with the increase in fibre dosage. From observations, there is an improvement in stiffness and ductility of the SFRC slabs with the addition of fibres up to an optimum fibre dosage. The ductility of the SFRC slabs without rebar is observed to remain the same after the fibres added exceed this optimum fibre dosage. Also, as the f_{cu} increases in the slab without rebar, the strength ratio also increases. Likewise, there is an effective crack control as the fibre dosage increases. This is because of the amount of steel-fibre crossing the emerging cracks.

For slabs with rebar, three-6mm rebar were provided over the pile in addition to the SFRC matrix. A strain hardening post-cracking behaviour is observed. The more the fibre dosage, so also the higher the strength, stiffness and ductility up to a certain threshold. After the threshold, there is a decrease in strength, signifying that the additional fibre after this will not enhance the strength of the slab. The inclusion of rebar over the piles [supports] increases the load carrying capacity of the slab and also guide against the progressive collapse of the slab. In the same vein, positive change in f_{cu} leads to increases in the strength of the slabs.

All the cracks propagate at the area under the load application at the soffit of the slab and radiate at right-angle passing through the mid-span of adjacent supports. At the top of the slab, the crack propagates at the right-angle passing through the internal boundaries of the panels [Figure 6.26]. As the fibre dosage increases, the fibres help in controlling the cracks and minimise crack width opening especially in the area between the supports and the area under the point of load application. Consequently, considering the work carried out and presented in this chapter, it can be established that steel fibres can enhance the strength and ductility of the pile-supported slabs [with or without rebar] under concentrated loading condition. Thus, the use of steel fibres enhances the post-cracking behaviour of the slabs [with or without rebar] and provides higher strength and ductility, as well as mitigating against crack propagation.

Chapter 7: CASE STUDY 3 - 9-PANEL

ELEVATED SLAB UNDER POINT LOAD

7.1 Introduction

The case studies 3 present an elevated slab with nine-panels fully reinforced with steel fibres [without rebar]. The experiment took place in Aachen, Germany [Figure 7.1]. The experimental work includes understudying the SFRC at the material level. The floor slab examined under ultimate and serviceability limit states [ULS and SLS]. The loadings considered under ULS were centrally loaded at the middle, edge and corner panels as shown in Figure 7.5. These are point load from a piston with 200mm square head. The elevated floor was 200 mm in thickness, supported on 16 square columns [300mm x 300mm] in three spans of 6m each in both directions, built to full scale. The span-depth ratio was 30. Choosing a proper boundary condition that will represent the actual experimental work has an important role in the results of the FEA. Adequate consideration for continuity of each rotational and translational component of displacement are essential in modelling of support conditions. For this static analysis, the use of simpler assumption for supports (pinned) without considering the foundation/soil stiffness was adopted. The supports are modelled as simply supported at the contact surface with the slab and fixed at the base to depict the interaction between soil and pile.

This testing was under point loads [Figures 7.5, 7.6, 7.24 and 7.40] to final rupture. The SFRC is made up of 100kg/m^3 [1.25%] of steel-fibres which has a length of 50mm and diameter of 1.3mm. The strength is 750N/mm^2. Other materials in 1m^3 of concrete are listed below in Table 7.1, and the entire mix produces a cube crushing strength of 43.7MPa at 28 days. The tensile strength was 3.2N/mm^2.

Table 7.1: Material Constituents of SFRC Per m^3

Cement [kg]	Fly Ash [kg]	W/C	Aggregate [mm]	Super Plasticizer [%]	Steel-fibre			
					Length [mm]	Diameter [mm]	Strength [N/mm^2]	Volume [%]
350	60	<0.50	0-16	1.25	50	1.3	750	1.25

Figure 7.1: Picture of the full-scale testing of the 9-Panel slab (Destrée, 2001)

7.2 Sensitivity Analysis

The numerical model was calibrated against the experimental results. The SFRC elevated slab was modelled with 3D brick [C3D8R] elements having eight-nodes. For optimised mesh, a mesh sensitivity analysis was carried out with mesh sizes of 50mm, 75mm, 100mm and 200mm. The Concrete Damaged Plasticity of ABAQUS with Lok and Xiao (1999) constitutive model was used to interpret the tensile behaviour in this analyses. The compressive behaviour of the SFRC is taken as the same as that of plain concrete. The input parameter of the tensile stress and strain is presented in Table 7.2 and Figure 7.2 below.

Table 7.2: Tensile Stress-Strain Input

	Tensile Strain [-]	**Tensile Stress [MPa]**
Origin/Peak Tensile Stress	0.000	3.200
Flexural Strength	0.001	1.563
Flexural Strength	0.189	1.563
Ultimate Tensile Strain	0.200	0.000

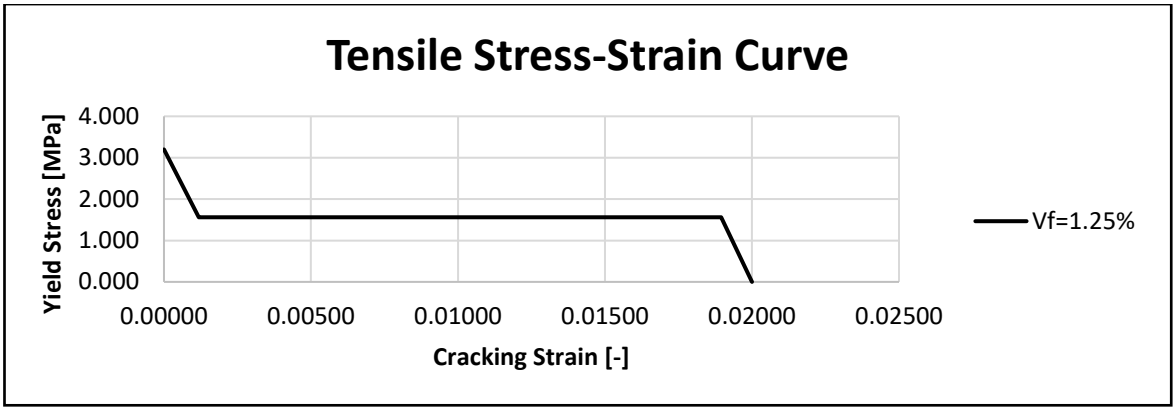

Figure 7.2: Tensile Stress-Strain Curve

The sensitivity analysis was carried out using the centrally loaded middle panel. The results from the different mesh sizes are given in the Load-Displacement curve of Figure 7.3. From the result, the mesh size 75mm is the most compatible with the experimental result. The 50mm mesh collapsed at a displacement of 42mm while that of 100mm was continuously increasing. The 200mm mesh produces a much higher value of load while the 75mm delivered a slightly bigger load at 35mm displacement but failed at 63mm. The mesh, 75mm, is at this point adopted for the FE analysis of this 9-Panel SFRC floor.

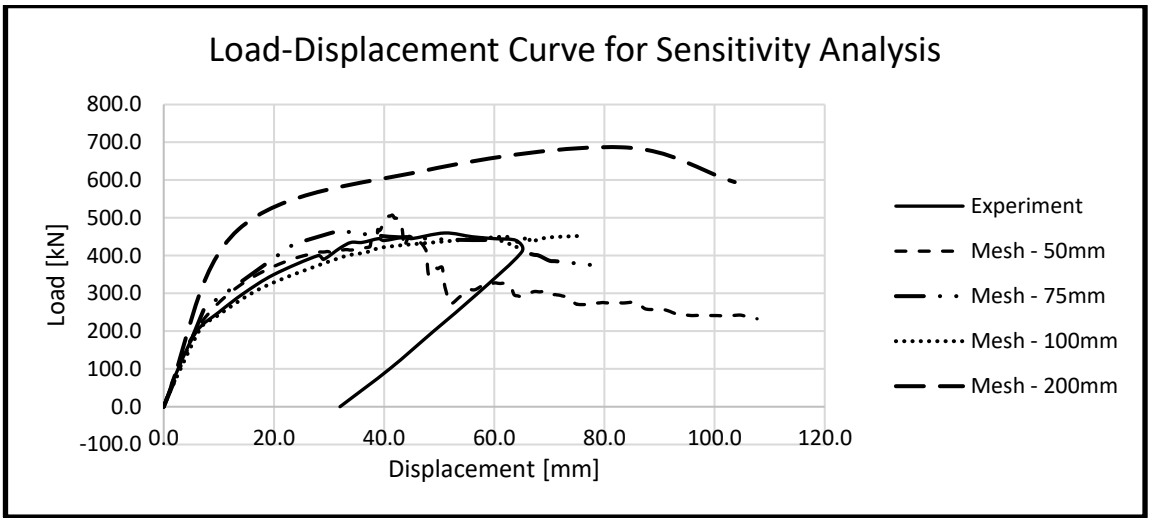

Figure 7.3: Load-Displacement Curve for Sensitivity Analysis

The slab was considered under full-size and quarter-size for FEA and to determine which will be best for the research work. Apart from taking advantage of the symmetrical nature of the floor, the time used to complete each analysis favours a quarter-size slab. With the high-performance computer [HPC] in UEL and using all the four-processors for

optimisation of results, the time taken for each mesh size in full and quarter size slabs is given in Table 7.3

Table 7.3: Mesh-Sizes and Time of Execution

	Full-Size				Quarter-Size			
Mesh Size [mm]	50	75	100	200	50	75	100	200
Time taken [hrs]	84.0	13.4	4.0	1.2	38.2	3.2	1.1	0.25
Accuracy [%]	92.0	92.3	80.2	188.2	90.1	98.6	85.6	175.0

7.3 Parametric Study

The FEA offers a very dependable and cost-effective alternative to full-scale testing as a way of producing results. The behaviour of the SFRC suspended slabs were successfully simulated thus allowing the running of the parametric analysis. The FE model used in the parametric studies for the SFRC slabs show the impact of changes in compressive strength [f_{ck}] and fibre volume ratios [V_f], tensile strength, slab span and thickness. In overall, the FEA was carried out by changing one parameter [at first, V_f and after that f_{ck}] while all other parameters remain the same and unchanged as in the experiment.

For the full parametric study with different fibre volume ratio [V_f= 1.00, 1.25, 1.50, 1.75, 2.00 and 2.50%], the tensile stress-strain input data are given in Figure 7.4 and Table 7.4. It should be noted as stated earlier, that the fibre volume ratios only affect the flexural strength of the SFRC matrix.

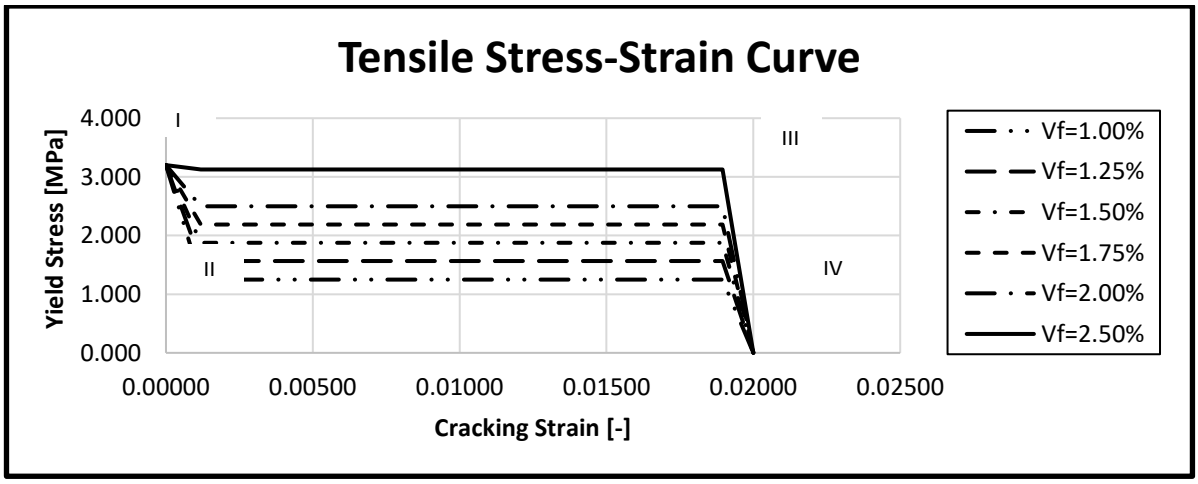

Figure 7.4: Tensile Stress-Strain Curves for different fibre volume ratios [V_f]

Table 7.4: Tensile Stress-Strain Parameters for different fibre volume ratios [V_f]

	Strain [-]	Stress [MPa]					
		V_f = 1.00%	V_f = 1.25%	V_f = 1.50%	V_f = 1.75%	V_f = 2.00%	V_f = 2.50%
Origin/Peak Tensile Stress [I]	0.000	3.200	3.200	3.200	3.200	3.200	3.200
Flexural Strength [II]	0.001	1.250	1.563	1.875	2.188	2.500	3.125
Flexural Strength [III]	0.189	1.250	1.563	1.875	2.188	2.500	3.125
Ultimate Tensile Strain [IV]	0.200	0.000	0.000	0.000	0.000	0.000	0.000

The full-parametric study is to examine the response of full-scale slab to changes in fibre volume ratios and characteristic strength of SFRC. The load were applied using the displacement-based loading. This discussion is made under the ULS and SLS with different loading patterns.

7.4 Loadings under Ultimate Limit State [ULS]

The Parametric studies were carried out under different loading conditions at the ultimate limit state. Three panels were used to understand the response of the slab in ULS with various loading conditions. This loading patterns [Figure 7.5] are for middle, edge and corner panels. They were all centrally loaded with a 200mm square rig [Figure 7.1]. The results of the FEA are discussed further in the following sections.

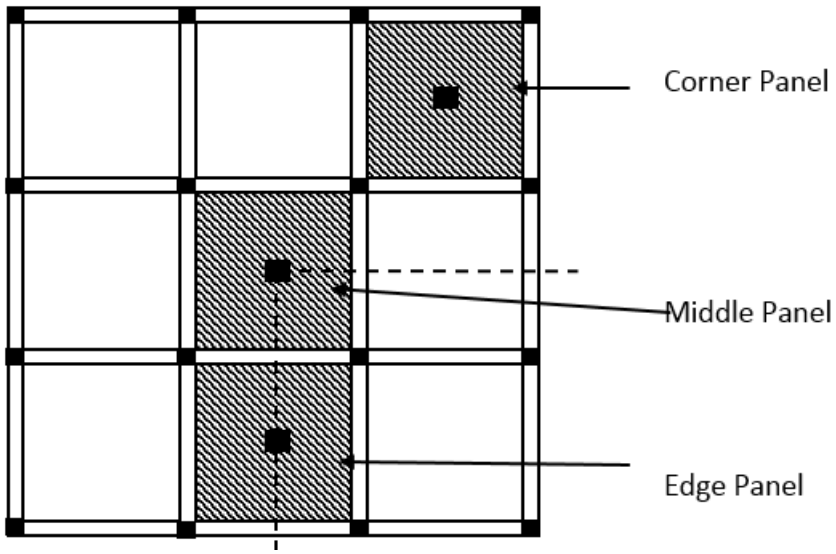

Figure 7.5: Loading Patterns at ULS [Full-Size]

7.5 Part I: Middle Panel

A quarter of the slab [Figure 7.6] was modelled due to its symmetrical nature and to save time of the analysis. A loading rig of 200mm square deployed at the centre of the panel was used to test for destruction. In the quarter-size model, the loading-rig becomes 50mm square for the FEA. The result of the analysis [load components] is multiplied by 4. In the experiment, the slab was unloaded at a point when the load drops in value.

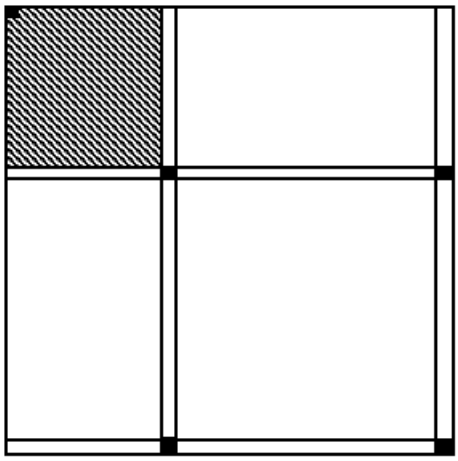

Figure 7.6: Loading Pattern at ULS [Quarter-Size] for Middle Panel

The two adjacent sides to the loading rig were fixed in their plane to give the software a sense of continuity of the slab in both directions. The quarter model also outlines one of the advantages of using a FEM in that a section of the model can be analysed to get the response of the whole model.

7.5.1 Load-Displacement Curves

The simulated FE model is slightly less brittle than the experimental results. The comparative analysis of the experimental and the FEA results revealed a functional similarity between the experimental and the NLFEA data, particularly on the level of load-displacement behaviour.

Figure 7.7 and Table 7.5 show the load-displacement curves and comparison between the experimental result and that of FEA. The FEA agrees with the experimental outcome with 99% accuracy. In this case, the yield and maximum load carrying capacity estimated

by FEA diligently concur with the experimental results and the load-displacement curve obtained from the FEA was also near to the same results. This full-scale FEA suggests that SFRC slabs demonstrate a strain hardening response unlike notched beams and round plates of the same material which exhibit a strain softening response [Chapter 5]. It also ascertains why the notched beam test cannot be used to predict the load-carrying capacity of a full-scale SFRC slab. The FEA parameters that produce these results are further used in complete parametric studies below.

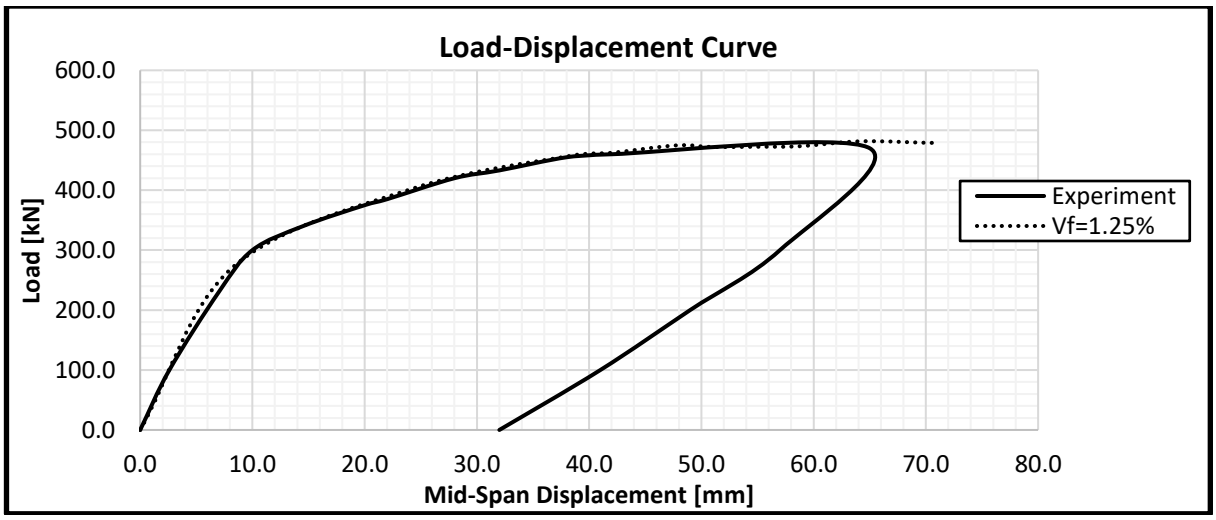

Figure 7.7: Load-Displacement Curves for Experiment and FEA for Middle Panel

Table 7.5: Comparison of Experimental and FEA Validation Results for Middle Panel

	Middle Panel		% Variance
	Experiment	FEA	
Load at First Crack [kN]	230.0	237.8	3.39
Displacement at First Crack [mm]	7.0	7.15	2.14
Maximum Load [kN]	470.0	475.3	1.13
Displacement at Maximum Load [mm]	65.0	46.92	(27.8)

The NLFEA produces a crack pattern both at the initial and the failure [final] stages which were close in agreement with the experiment results. The NLFEA demonstrated that the effect of steel-fibres on the concrete strength [yield and maximum loads] and ductility [ratio of displacement at yield and ultimate load] and its bridging influence in arresting crack propagation are captured satisfactorily.

It establishes that the use of the concrete damaged plasticity model, Lok and Xiao (1999) constitutive model and appropriate material properties can credibly predict the behaviour of SFRC suspended slabs in response to loading, displacement and cracking patterns using quarter slab.

The leading structural response indicators, vis-à-vis, the yield load [P_y] with corresponding displacement [δ_y], the maximum load [P_{max}] indicating the load-carrying capacity with corresponding displacement [δ_{max}], ultimate load [P_u] indicating the residual strength [which is the lesser of load at failure and 85% of the maximum load] with the corresponding displacement [δ_u] and the ductility ratio [μ] expressed as δ_u/δ_y [Table 7.5].

7.5.2 The Strength

An increase in the fibre volume ratio [V_f] leads to the load carrying capacity increasing indicating that stiffness increases as V_f increases [Figure 7.8]. This clearly revealed that increase in the amount of fibre volume ratio improved its load-carrying capacity of the slab. This improvement is noticeable as V_f increases are leading to higher strength. As the loading increases, cracks are propagated. The cracks are controlled by the steel-fibres which bridge them as they appear. The strength parameters are given in Table 7.6

Table 7.6: Strength Parameters of Middle Panel for fcu=43.7MPa for Middle Panel

V_f [%]	P_y [kN]	δ_y [mm]	P_{max} [kN]	δ_{max} [mm]	P_u [kN]	δ_u [mm]	$\mu = \delta_u/\delta_y$
1.00	225.2	7.15	472.9	57.8	429.0	72.4	10.13
1.25	237.8	7.15	475.3	46.9	457.7	70.7	9.89
1.50	242.5	7.15	482.1	44.5	470.4	70.6	9.87
1.75	246.3	7.15	512.3	70.2	512.3	70.2	9.82
2.00	255.4	7.15	513.1	54.0	502.1	70.3	9.83
2.50	250.5	7.15	590.7	69.1	581.0	70.8	9.90

However, as the V_f increases towards 2.50%, more fibres are available to bridge the openings leading to a decrease in displacements compared to the slab with V_f =1.00%. (Which implies that to get the same displacement as in slab with V_f =1.00% in the slab with V_f > 1.00%, higher loads would be required). Enhance stiffness is noticed in the curves as fibres are increasing. The more the fibres volume in the concrete matrix, the more the number of fibres bridging the cracks and controlling their opening. This improvement is essential for structural design at ULS and SLS.

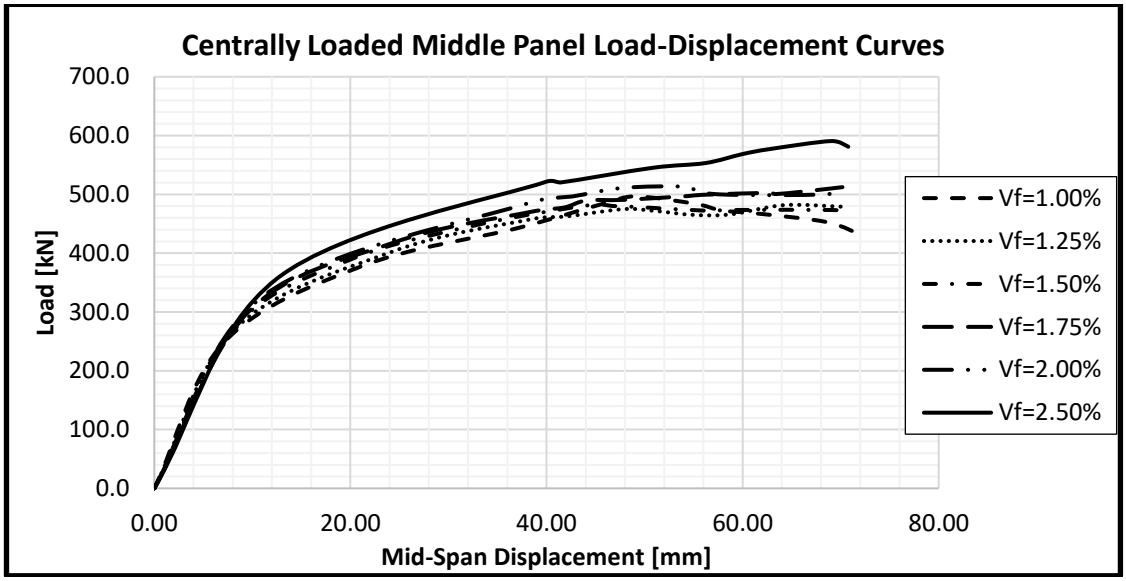

Figure 7.8: Load-Displacement Curves for various fibre volume ratio V_f for Middle Panel

7.5.3 Ductility

Ductility is the measure of material [in this case, SFRC] ability to undergo large deformations without rupturing [or significant reduction in strength] when positioned beneath a tensile strength that surpasses its yield strength. The ductility factor is expressed by the equation δu/δy, where δu and δy are the displacement at ultimate and yield load respectively. The displacement at ultimate load is taken as the displacement of the lesser of the failure load and 15% less the maximum load [i.e. $P_u \geq 0.85P_{max}$].

7.5.4 Crack Shapes

The cracking shapes of the 9-panel SFRC suspended slab is studied using the crack patterns in Figures 7.9 – 7.12 [principal strain contours, principal strain vectors,

deflected and damaged tensile shapes] to describe the mechanism of the failure experienced.

7.5.4.1 Crack Patterns [Principal Strain Contours]

The principal strain contours for the middle-panel within quarter-slab analysed is illustrated in Figure 7.9. The contour intervals selected were 0.02 (i.e. fibres pull-out strain) for SFRC slab highlighted in grey and compressive strains exceeding concrete ultimate strain (i.e., -0.0035) coloured in black.

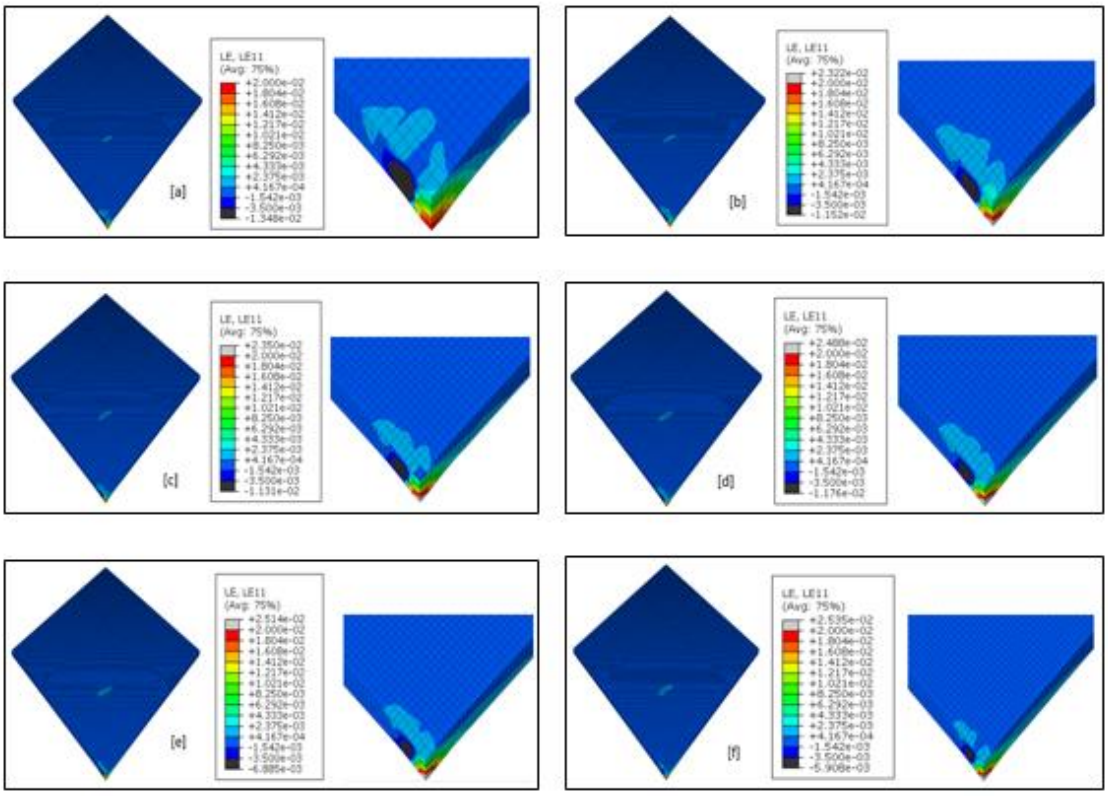

Figure 7.9: Principal Strain Contours for Middle Panel with V_f [a]= 1.00%, [b]= 1.25%, [c]= 1.50%, [d]= 1.75%, [e]= 2.00% and [f]= 2.5% [Top on the left and soffit on the right]

Figures 7.9 [a-f] show that as the fibre volume increases, there is a reduction in crack formation and propagation. The slab failed in bending at the mid-span. The Pull-out failure of fibres occurred at mid-span area and this same area in all the SFRC slabs. The occurrence of the pull-out failure at the mid-span is also traceable to the impact of the point of load application. In the slab with V_f=1.00%, the tensile strain did not exceed 0.02, which indicates that the volume of fibres was not sufficient to carry the tensile strain developed after cracking of the concrete. From V_f≥1.25%, tensile strain exceeded 0.02, which shows that there were adequate fibres to bridge the cracks, thus the grey

areas. The crack propagation starts with a small crack, which upon continuous loading develops into a bigger one. This eventually led to the failure of the slabs.

7.5.4.2 Crack Patterns [Principal Strain Vectors]

Concrete models based on the concrete damaged plasticity [CDP] model does not incorporate cracks development at the material integration point unlike the ones formed on smeared cracking approach. Nonetheless, the concept of an effective crack direction is used to obtain a graphical image of the cracking patterns in the concrete structure (Lubliner et al., 1989). After the first crack formation, the path is fixed and remains continuous during entire loadings. The crack direction is at right angles to the direction of opening of the principal strain.

Figures 7.10 [a-f] illustrate the principal strain vectors for the 9-panel SFRC slab with varying values of steel-fibres. The maximum principal strains and the vector plot diagram are used to represent the crack patterns. These directions are viewed in the visualisation module of ABAQUS. The changes in the vectors can be seen to be changing as the fibre volume ratio increases. The plots illustrate the extension of the radial and tangential crack across the section. The radial cracks appear to have spread in a triangular shape from the slab centre at the point of load application towards the internal supports of the slab.

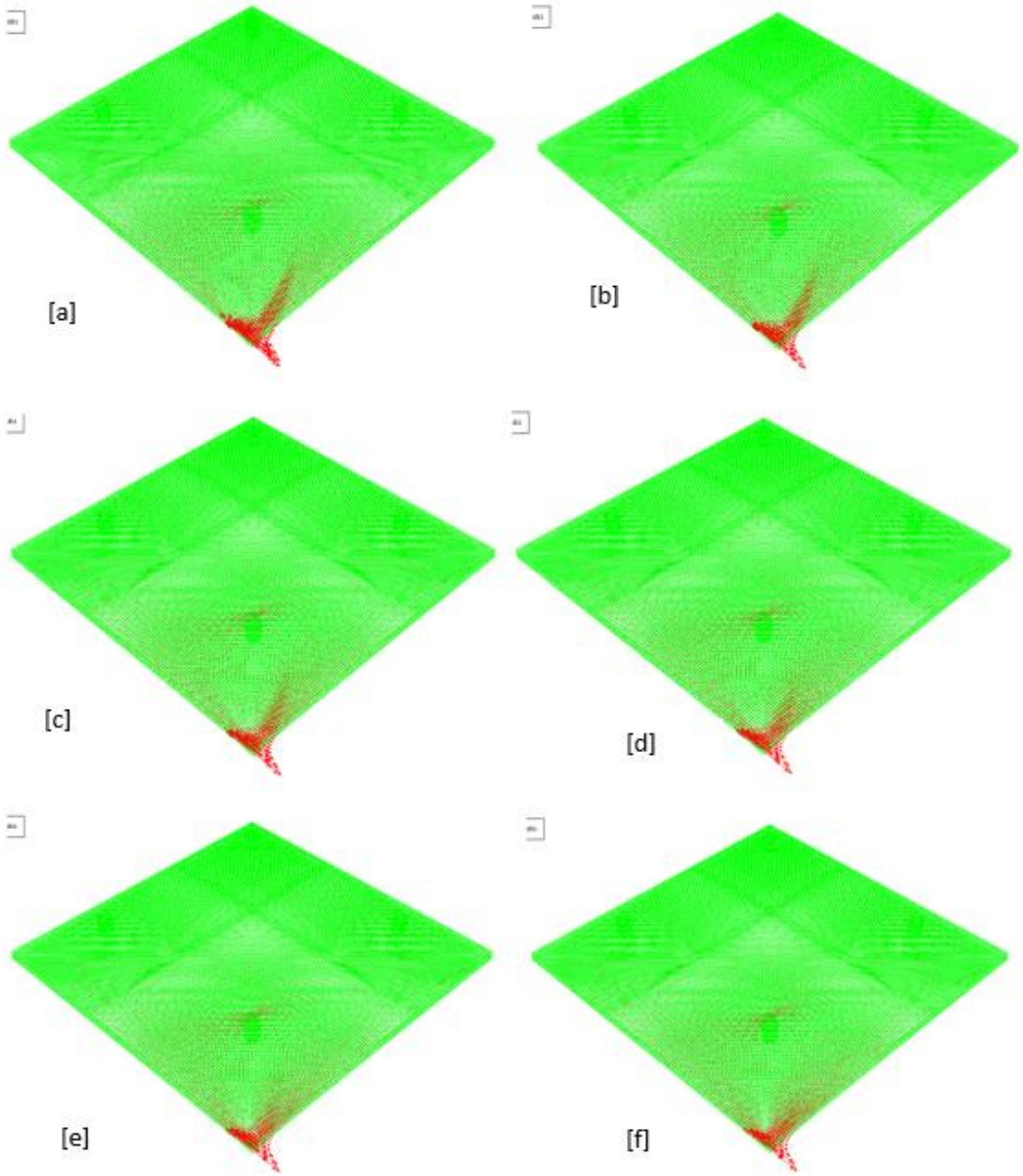

Figure 7.10: Principal Strain Vectors for Middle Panel with V_f [a]= 1.00%, [b]= 1.25%, [c]= 1.50%, [d]= 1.75%, [e]= 2.00% and [f]= 2.5%

The crack patterns in all the slabs follow the same form, concentrating in the panel mid-span, which specifies a flexural (and ductile) failure mode. The intensity of the vectors at the mid-span of the panel decreases as the fibre volume ratio increases. The crack propagation at the slab centre stopped at about half the depth. In the plots, short lines indicate the tangential cracks discovered, which also specify the direction of the cracks. This point out that ductility improves as the V_f increases. The strain vector around the point of load application get smaller as V_f increases.

7.5.4.3 Crack Patterns [Deflected Shapes]

The deflected shapes of the slabs are considered in this session [Figures 7.11 (a-f)]. It shows that the slabs failed in bending as the thrust of the shape is downward in the direction of the applied load. These directions are consistent with the location of the loading and the supports.

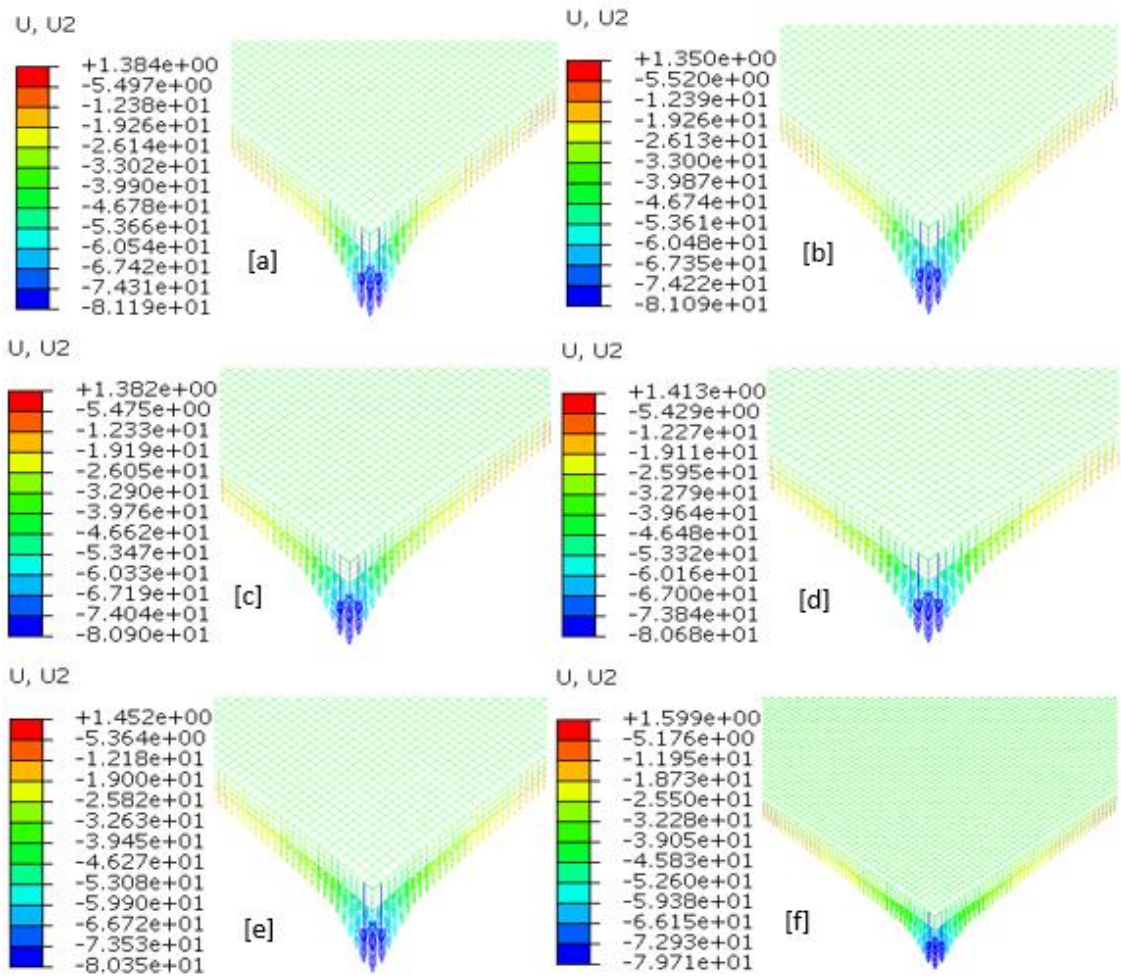

Figure 7.11: Deflected Shapes for Middle Panel with V_f [a]= 1.00%, [b]= 1.25%, [c]= 1.50%, [d]= 1.75%, [e]= 2.00% and [f]= 2.5%

The impact of an increase in fibre volume can also is seen in the deflected shapes. The mid-span displacement was higher in the slab with V_f=1.00% and least in the one with V_f=2.50%. The more the steel-fibres, the more the adequacy in bridging the micro-cracks that developed due to the applied load. This invariably led to resistance to the applied load, thus reducing the displacement. It also translates to a higher load resistance.

7.5.4.4 Crack Patterns [Tensile Damaged Shapes]

The crack patterns are also examined under tensile damaged shapes. These show the crack formation at the top and soffit of the slabs at the point of the application of loads. The damaged tensile pattern at the tension [soffit] side of the panel with V_f=1.00% spread from the point of load application. It spreads on two legs at an angle of 45^0 to one another. Each leg is measuring 1947.1mm.

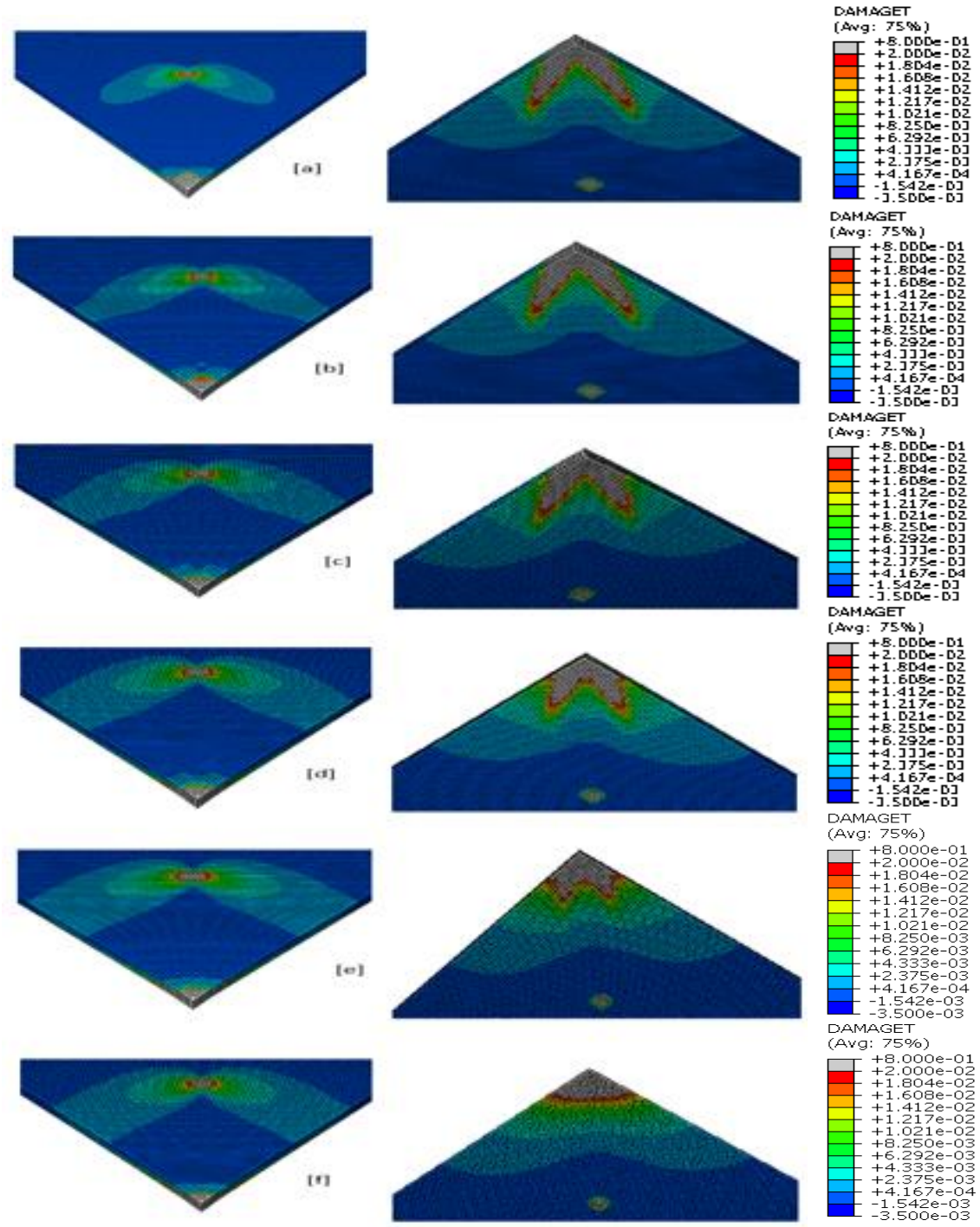

Figure 7.12: Tensile Damaged Shapes for Middle Panel with V_f [a]= 1.00%, [b]= 1.25%, [c]= 1.50%, [d]= 1.75%, [e]= 2.00% and [f]= 2.5% [Top on the left and soffit on the right]

As the fibre volume increases, the legs decrease gradually until the legs merged and turned to an oval shape with a 1050mm radius for a slab with V_f=2.50%. The impact of the cracking has been bridged as the fibre volume increases. This shows the effectiveness of the steel-fibres in bridging the micro cracks.

7.5.5 Comparative Study with Experimental Specimen using Non-Dimensional Ratios

The comparison between the slabs analysed with various fibre volume ratios and the experimental result [which serve as the control specimen] are made in this session using non-dimensional ratios.

7.5.5.1 Strength Ratio

The strength ratios are considered by dividing the yield load [P_y] and the maximum load [P_{max}] of the slabs with various V_f by their corresponding values in control. These are shown in Table 7.7, Figures 7.13 and 7.14 respectively.

Table 7.7: Strength and Ductility Ratios for Middle Panel

V_f [%]	P_y [kN]	$\frac{P_y}{P_{y,c}}$	P_{max} [kN]	$\frac{P_{max}}{P_{max,c}}$	P_u [kN]	μ	$\frac{\mu}{\mu_c}$
Control	225.2		472.9			10.13	
1.00	225.2	1.00	472.9	1.00	402.0	10.13	1.000
1.25	237.8	1.06	475.3	1.01	404.0	9.89	0.976
1.50	242.5	1.08	482.1	1.02	409.8	9.87	0.974
1.75	246.3	1.09	512.3	1.08	435.5	9.82	0.969
2.00	255.4	1.13	513.1	1.09	436.1	9.83	0.970
2.50	250.5	1.11	590.7	1.25	502.1	9.90	0.977

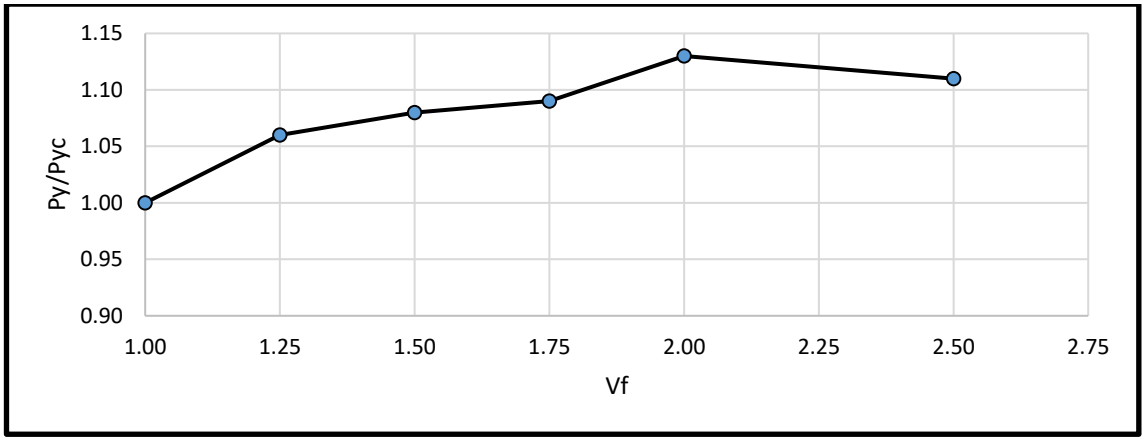

Figure 7.13: Graph of V_f against $P_y/P_{y,c}$ for Middle Panel

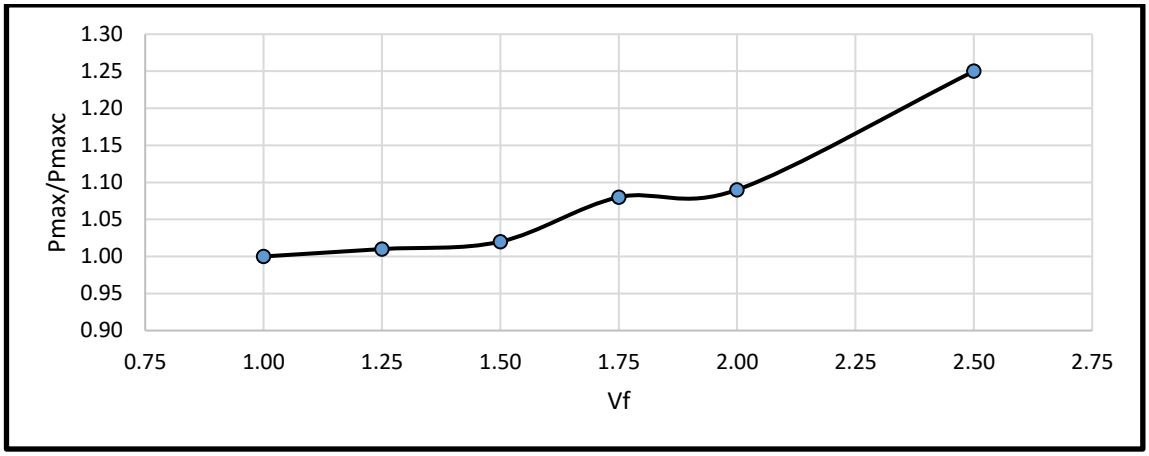

Figure 7.14: Graph of V_f against $P_{max}/P_{max,c}$ for Middle Panel

There is an increase of between 10-25% in the $P_y/P_{y,c}$ as the V_f increases while for $P_{max}/P_{max,c}$ it decreases from V_f=1.00% to V_f=1.25% and the increase steadily to V_f=2.50%. This also shows that SFRC slab with V_f=1.00% can reach the same maximum load as the experimental value of V_f=1.25%.

7.5.6 Further Analysis with Different f_{cu}

Further analyses were carried out with different characteristic strength [30MPa, 40MPa and 50MPa] of SFRC slabs with varying dosage of steel-fibres [1.00%, 1.25%, 1.50%, 1.75%, 2.00% and 2.50%] and results of load-displacement graphs presented in Table 7.8 and Figures 7.15 - 7.20.

7.5.6.1 The Influence of the Characteristic Strength of Concrete

The primary concrete parameters in a hardened state for structural use are the compressive and tensile strengths which are related. Nevertheless, for further parametric analysis, their effects on the failure process as it affects the yield load, and maximum load carrying capacity and their respective displacements are considered.

Table 7.8: Strength Ratios for various V_f for Middle Panel

V_f [%]	f_{cu} [MPa]	P_y [kN]	$\frac{P_y}{P_{y,c}}$	P_{max} [kN]	$\frac{P_{max}}{P_{max,c}}$
Control	30.0	200.4		384.0	
1.00		200.4	1.00	384.0	1.00
1.25		210.0	1.05	400.9	1.04
1.50		216.8	1.08	409.0	1.07
1.75		225.0	1.12	422.6	1.10
2.00		233.0	1.16	462.0	1.20
2.50		238.2	1.19	489.4	1.27
Control	40.0	212.0		448.0	
1.00		212.0	1.00	448.0	1.00
1.25		220.2	1.04	463.5	1.03
1.50		225.0	1.06	489.9	1.09
1.75		232.5	1.10	492.8	1.10
2.00		238.1	1.12	561.0	1.25
2.50		242.0	1.14	579.3	1.29
Control	43.7	225.2		472.9	
1.00		225.2	1.00	472.9	1.00
1.25		237.8	1.06	475.3	1.01
1.50		242.5	1.08	482.1	1.02
1.75		246.3	1.09	512.3	1.08
2.00		255.4	1.13	513.1	1.09
2.50		250.5	1.11	590.7	1.25
Control	50.0	317.7		522.4	
1.00		317.7	1.00	522.4	1.00
1.25		328.4	1.03	521.9	1.00
1.50		344.9	1.09	534.6	1.02
1.75		367.4	1.16	543.3	1.04
2.00		372.6	1.17	541.6	1.04
2.50		380.6	1.20	647.2	1.24

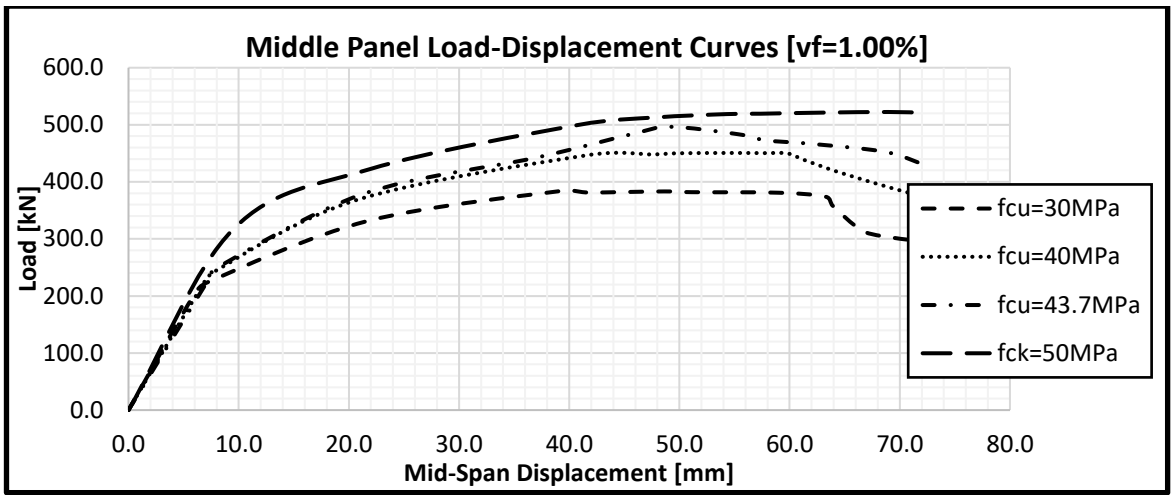

Figure 7.15: Load-Displacement Curves for various f_{cu} with fibre volume ratio V_f =1.00% for Middle Panel

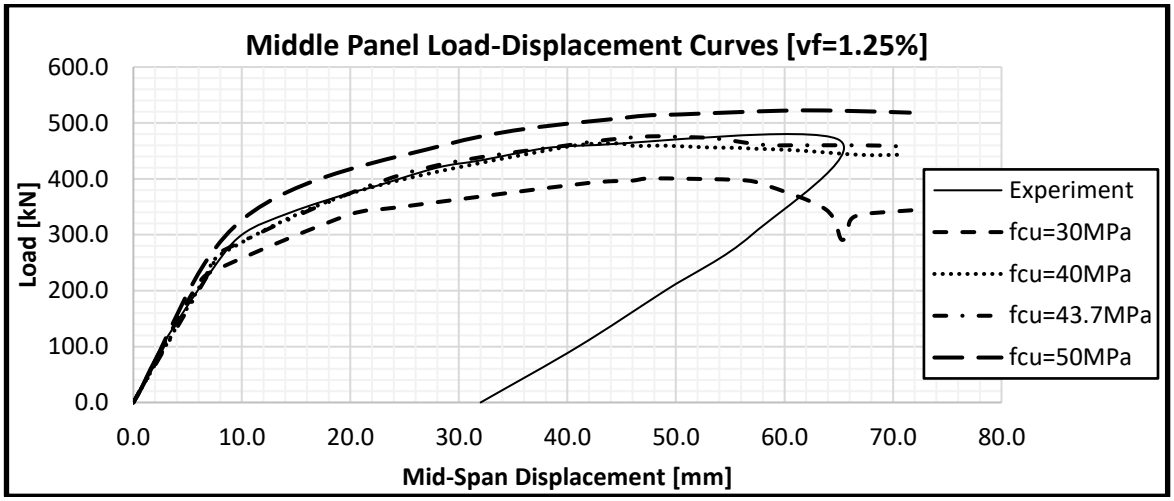

Figure 7.16: Load-Displacement Curves for various f_{cu} with fibre volume ratio V_f =1.25% for Middle Panel

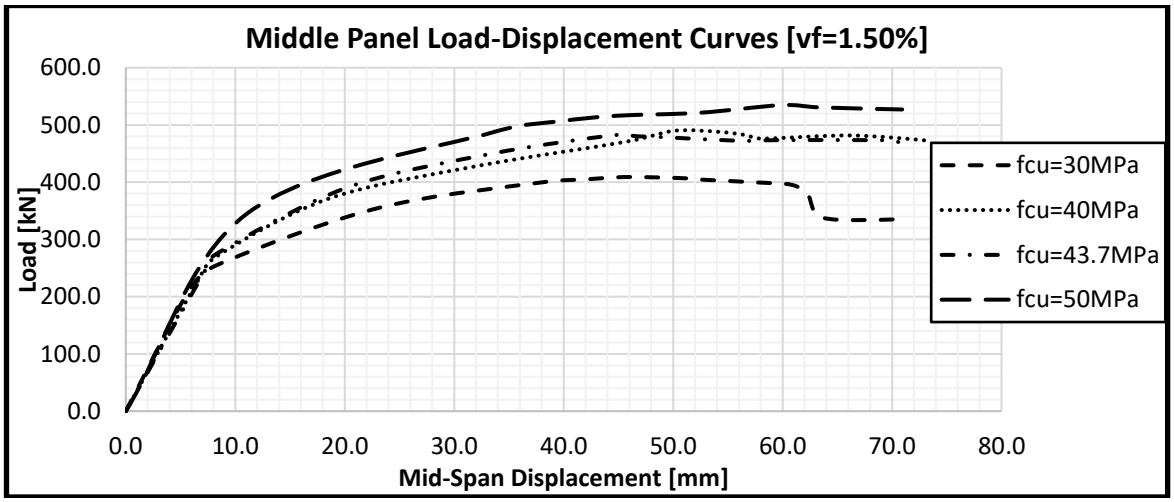

Figure 7.17: Load-Displacement Curves for various f_{cu} with fibre volume ratio V_f =1.50% for Middle Panel

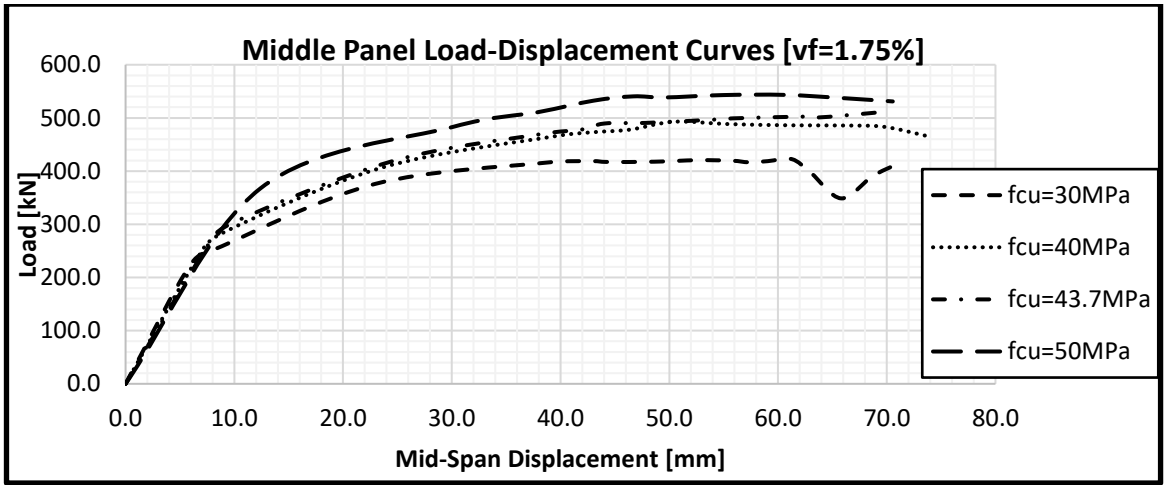

Figure 7.18: Load-Displacement Curves for various f_{cu} with fibre volume ratio V_f =1.75% for Middle Panel

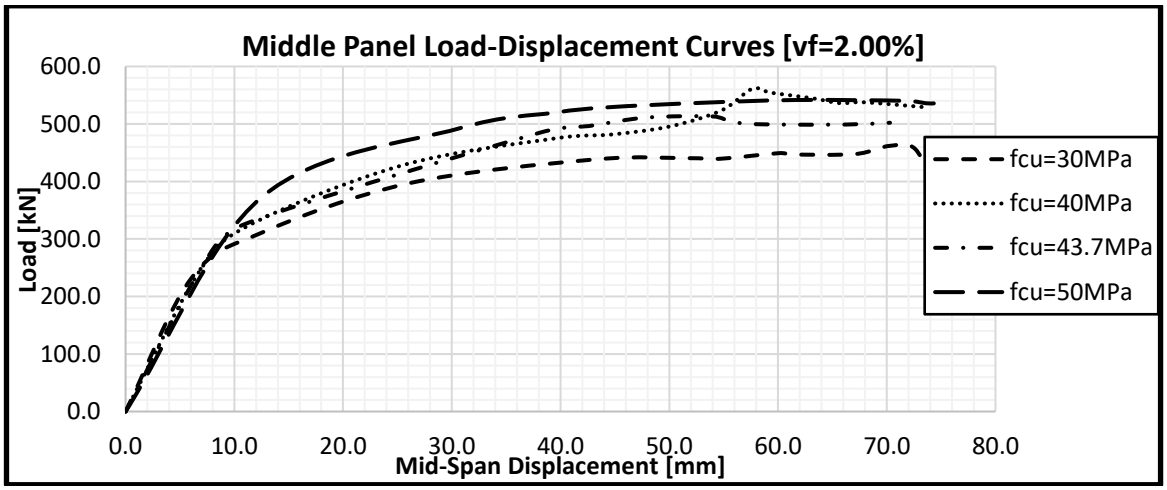

Figure 7.19: Load-Displacement Curves for various f_{cu} with fibre volume ratio V_f =2.00% for Middle Panel

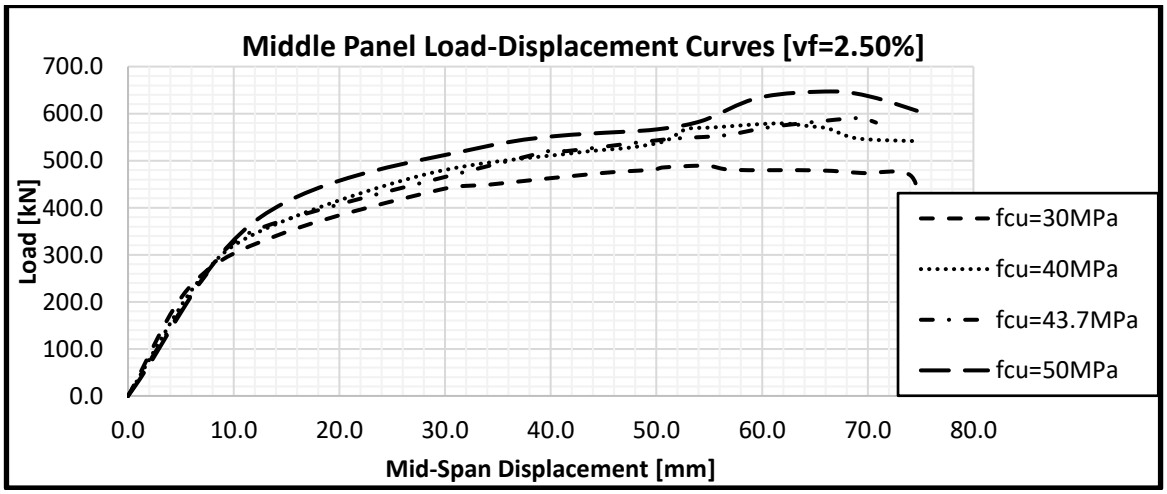

Figure 7.20: Load-Displacement Curves for various f_{cu} with fibre volume ratio V_f =2.50% for Middle Panel

Figures 7.15-7.20 show the effect of the characteristic strength of SFRC on the response of the suspended slabs load carrying capacity and central displacement of the middle panel. The f_{cu} of 30MPa, 40MPa and 50MPa were used in addition to that of the experiment, 43.7MPa. The material properties and all other parameters had the same values as in the validation analysis.

It could also be noticed from Figures 7.15 – 7.20 that the load fails at around 60mm - 75mm central displacement for f_{cu} =30MPa for all models analysed at different V_f. These also indicate that the fibre dosage is not enough and thus fails to bridge the ensuring cracks effectively. There is an upward movement in the load resisting capacity of the slabs as both f_{cu} and V_f increases.

The figures show the load-deflection curves. The effect of the characteristic compressive strength of the SFRC is not significant. All the curves have about the same linear part [which is influenced by f_{cu}]. The influence of the tensile strength f_t is more visible [all the slabs failed in bending] as it produces between 10% and 20% enhancement on the load carrying capacity of the slab. The cracking patterns are also about the same.

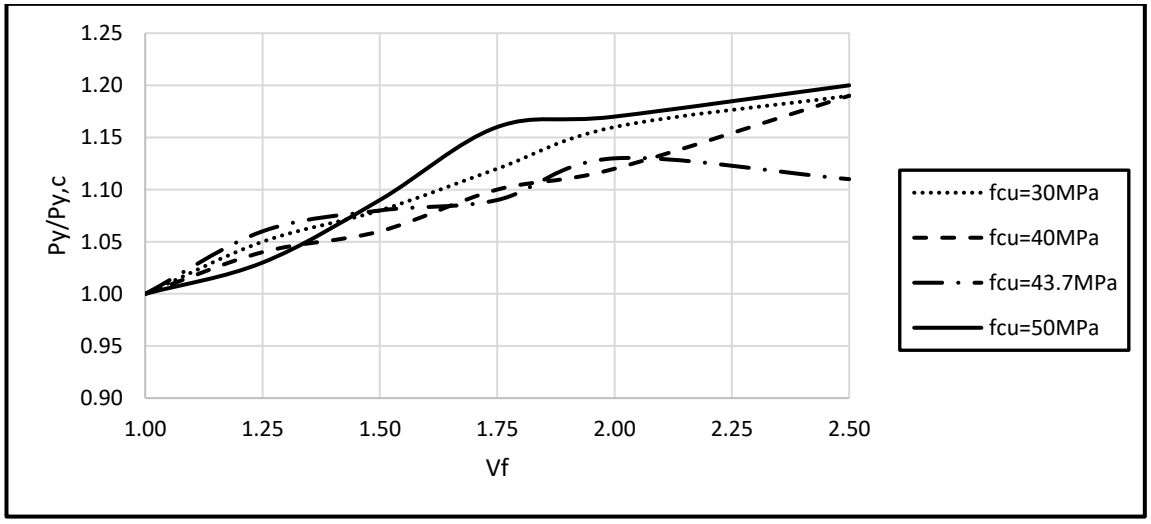

Figure 7.21: Graph of V_f against $P_y/P_{y,c}$ with varying f_{cu} for Middle Panel

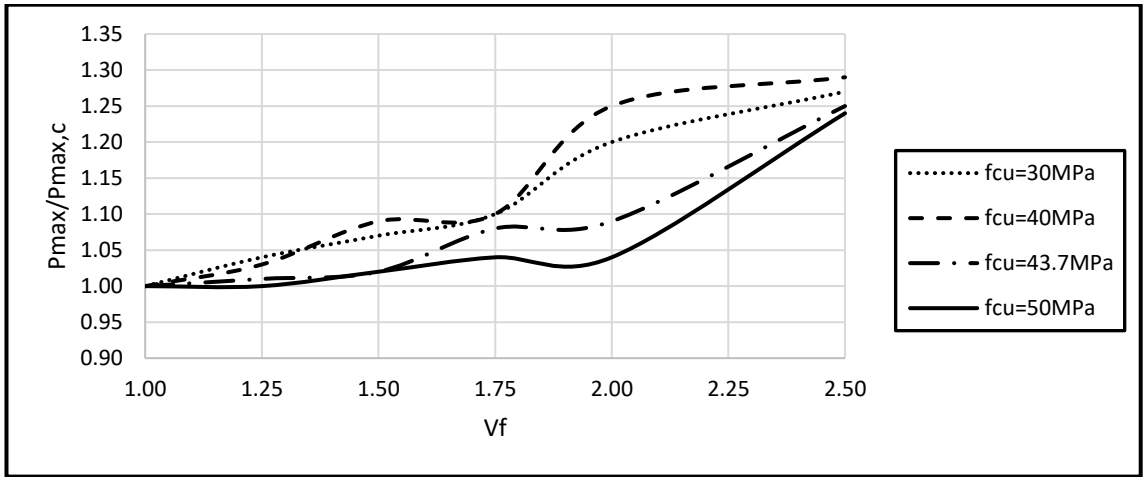

Figure 7.22 Graph of V_f against $P_{max}/P_{max,c}$ with varying f_{cu} for Middle Panel

Figures 7.21 and 7.22 display the response when compared to non-dimensional parameters. An upward trend is seen in the curves of $P_y/P_{y,c}$ and $P_{max}/P_{max,c}$ as the V_f increases. From the Figures, there is a consistent increase in the yield and maximum load ratios with the increase of the fibre volume ratios. The $P_y/P_{y,c}$ is high as the value of f_{cu} increases but it is a reversal in $P_{max}/P_{max,c}$ which is high when f_{cu} is low as V_f increases. This indicates that V_f compensate the strength ratio in lower value of f_{cu}.

Further analyses were carried out with the span/depth ratio taken as 33.3 and 27.3 while varying the f_{cu} and V_f [all other parameters remains the same]. This is aimed at generating an equation for maximum load carrying capacity of the slab. The summary of the analyses is in Tables 7.9 and 7.10. The mode of failure at the centre of the panel remains bending, signifying a consistence with slab's span/depth ratio of 40.

Table 7.9: Strength Ratios for various V_f for Middle Panel for 180mm depth

V_f [%]	f_{cu} [MPa]	P_y [kN]	δ_y [mm]	P_{max} [kN]	δ_{max} [mm]
1.00	30.0	178.7	12.3	263.2	54.1
1.25		191.2	13.8	272.2	50.4
1.50		200.1	14.8	282.5	52.4
1.75		230.6	20.6	296.0	51.0
2.00		250.3	23.7	310.2	52.0
2.50		300.1	34.6	336.4	52.6
1.00	40.0	182.7	10.2	292.9	54.2
1.25		208.1	13.4	301.1	54.0
1.50		221.4	15.0	312.0	52.5
1.75		236.4	17.1	321.3	53.6
2.00		252.2	19.2	336.2	54.2
2.50		308.6	30.2	360.2	53.8
1.00	50.0	241.2	15.7	330.2	54.0
1.25		251.3	16.9	346.4	54.0
1.50		252.5	16.3	351.0	54.3
1.75		262.0	17.2	357.2	54.3
2.00		296.9	24.4	366.1	54.4
2.50		331.1	29.7	387.6	54.2

Table 7.10: Strength Ratios for various V_f for Middle Panel for 220mm depth

V_f [%]	f_{cu} [MPa]	P_y [kN]	δ_y [mm]	P_{max} [kN]	δ_{max} [mm]
1.00	30.0	279.4	7.0	390.4	54.5
1.25		286.6	7.2	496.9	45.5
1.50		310.1	8.2	494.1	44.6
1.75		325.5	8.8	505.1	41.6
2.00		354.1	10.1	552.1	51.8
2.50		450.8	15.7	617.6	51.6
1.00	40.0	291.2	6.4	538.2	55.9
1.25		311.7	7.1	573.9	51.4
1.50		340.1	8.2	579.8	51.1
1.75		344.5	8.2	602.6	46.9
2.00		403.3	11.0	613.9	47.6
2.50		440.5	12.4	665.1	50.8
1.00	50.0	384.7	8.8	631.5	47.0
1.25		388.0	8.8	642.7	56.5
1.50		415.8	10.1	664.3	43.7
1.75		436.6	10.9	665.8	53.0
2.00		443.0	11.0	689.8	52.9
2.50		477.4	12.4	782.8	45.1

7.5.6 Proposed Equation for Maximum Load Carrying Capacity

A general equation is proposed for evaluating the maximum load carrying capacity of the middle panel in a 9-panel SFRC suspended floor with the fibre volume ratio [V_f], characteristic strength [f_{cu}], span depth ratio [L/d] and acceptable displacement [μ] as dependent variables.

The yield load [Py] and the maximum load carrying capacity [Pmax] with the corresponding central displacements [δy and δmax respectively] of the panel obtained through regression analysis of the MS-Excel are:

$$P_y = 4.09f_{cu} + 61.09V_f - 20.37\,{}^{L}/_{d} + 636.89 \qquad \text{- Eqn. 7.1}$$

$$P_y = 1.26\delta y + 274.2 \qquad \text{- Eqn. 7.2}$$

$$P_{max} = 5.98f_{cu} + 75.45V_f - 45.26\,{}^{L}/_{d} + 1473.01 \qquad \text{- Eqn. 7.3}$$

$$P_{max} = 0.80\delta max + 432.22 \qquad \text{- Eqn. 7.4}$$

Where L – Span of the panel

d – Overall depth of the panel

The input data used in deriving Equations 7.1 – 7.4 were obtained from the results of loads and corresponding central displacements and are presented in Appendix B4.

7.6 Part II: Edge Panel

This section considered the response of the SFRC suspended slab at the edge panel with the point load acting at the centre. As in the middle panel, a loading rig on a portal frame placed diagonally across the panel resting on columns supporting the slab. As done in section 7.5, a quarter-size of the experiment was modelled to full scale. The simulation was to destruction/collapse of the structure. In the quarter-size model [Figure 7.23], the loading-rig becomes 100 by 200mm square for the FEA. The result [loads only] of the analysis is multiplied by 2.

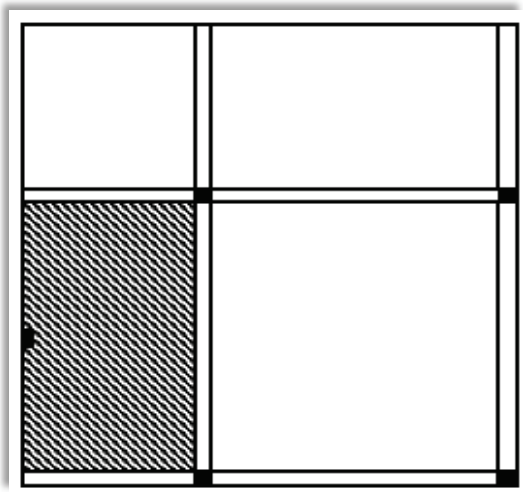

Figure 7.23: Loading Pattern at ULS [Quarter-Size] for Edge Panel

The two continuous adjacent sides were assigned asymmetry boundary conditions in their plane which signifies that the continuity of the slab in both directions. Further discussion on the responses of the quarter slab is in the following sections.

7.6.1 Load-Displacement Curves

Figure 7.24 displays the load-displacement curves between the experimental result and the validation model of NLFEA. Inverse analysis of the bending tests was performed to validate the experimental work by determining the best fitting curve using the concrete damage plasticity [CDP] of ABAQUS with (σ-ε) constitutive model of Lok and Xiao (1999). There is a good agreement between the NLFEA and experimental data. The load-displacement curve obtained from the FEA was near perfect to the curve from the experiment with the yield and maximum load carrying capacity estimated by FEA are close to the experimental results.

Like the middle panel, the response of the full-scale FEA suggests that SFRC slabs demonstrate a strain hardening. It also collaborates that the notched beam test cannot be used to predict the response of a full-scale SFRC slab under a central loading point. The response curve was bilinear with the near vertical part from the origin being associated with [unconnected] microcracking, mainly due to the effect of the properties of SFRC [Young's modulus, characteristic strength and Poisson's ration] while the second part represents the fibre bridging and pull out.

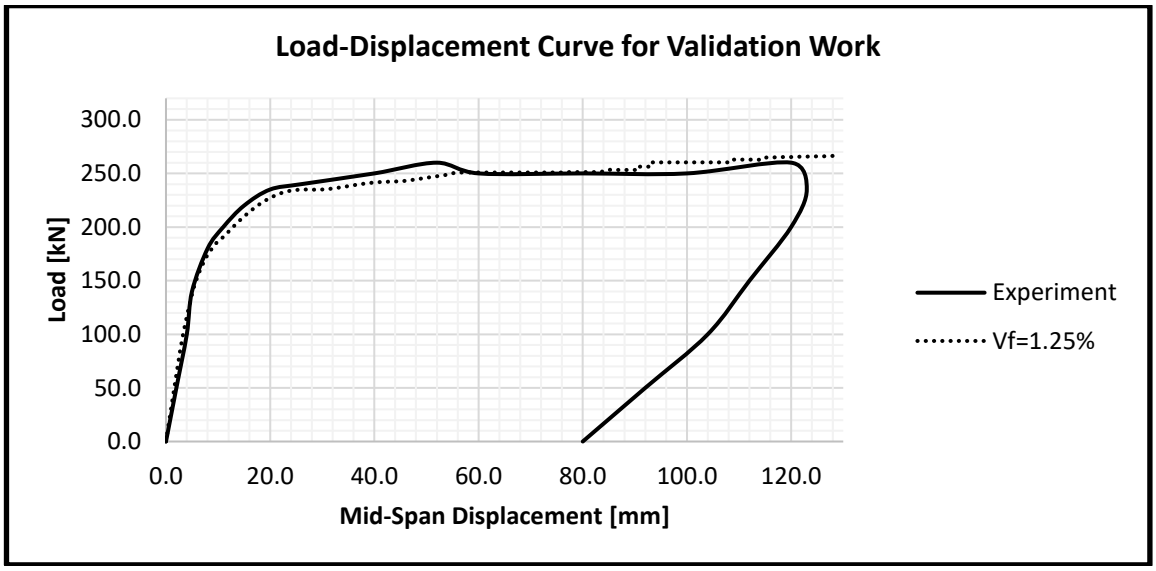

Figure 7.24: Load-Displacement Curves for Experiment and FEA for Edge Panel

The numerical analysis based on NLFEA captures the overall structural behaviour of the SFRC suspended slab. This result further confirms the suitability of using an NLFEA approach to analyse SFRC suspended structures.

Table 7.11: Validation Results for Edge Panel

	Edge Panel		% Variance
	Experiment	FEA	
Load at First Crack [kN]	160.0	164.9	3.06
Displacement at First Crack [mm]	6.0	7.4	23.3
Maximum Load [kN]	260.0	266.3	2.42
Displacement at Maximum Load [mm]	52.0	64.7	6.83

Table 7.11 displays a summary of the critical structural parameters in respect to the yield, the maximum, and ultimate loads [P_y, P_{max}, and P_u] with corresponding displacements [δ_y, δ_{max}, and δ_u] the respectively and the ductility ratio [μ] expressed as δ_u/δ_y. Further simulations for the complete parametric studies use the same NLFEA parameters that produced the validated result.

7.6.2 The Strength

The preceding Table 7.12 and Figure 7.25 show the results of parametric studies on the edge panel with varying values of V_f. The increment in the fibre volume ratio leads to increases in the load carrying capacity of the SFRC suspended slab specifying that stiffness increases as V_f increases. 10 – 35% increment in the load carrying capacity of the slab is noticeable as V_f increases are leading to greater strength. The yield strength also increases as the V_f increase thus proving a higher load before the propagation of the first crack. The propagation of the cracks continue as the loading exceeds the yield load. The flexural strength of the SFRC matrix come into play by preventing the sudden collapse of the slab. These cracks are bridged by the steel-fibres.

Table 7.12: Strength Parameters for Edge Panel

V_f [%]	P_y [kN]	δ_y [mm]	P_{max} [kN]	δ_{max} [mm]
1.00	157.0	6.9	240.8	58.2
1.25	160.9	6.9	264.0	64.7
1.50	162.8	6.9	284.0	76.1
1.75	170.6	6.9	298.3	69.3
2.00	176.4	8.0	328.9	58.5
2.50	180.5	8.0	354.3	60.9

Conversely, the increase in the fibre volume ratio considerably enhanced the values of P_y and P_{max}. There is an increase of at least 1.50% in P_y as V_f increases. Comparing a V_f of 1.50% to that of 2.50%, an increase of 52.55% was recorded. Addition of steel-fibres bridges the micro-cracks as they appear, thus reducing the cracks formation and control the crack width. There was a steady increase in the displacement at yield load as more

steel-fibres were added. This is different in what is obtainable in the displacement at maximum and ultimate loads. The displacement at maximum load saw an increase to a threshold before a decrease while displacement at ultimate load maintains a gradual decrease as the V_f decreases. Stiffness is enhanced in the curves as V_f are increasing.

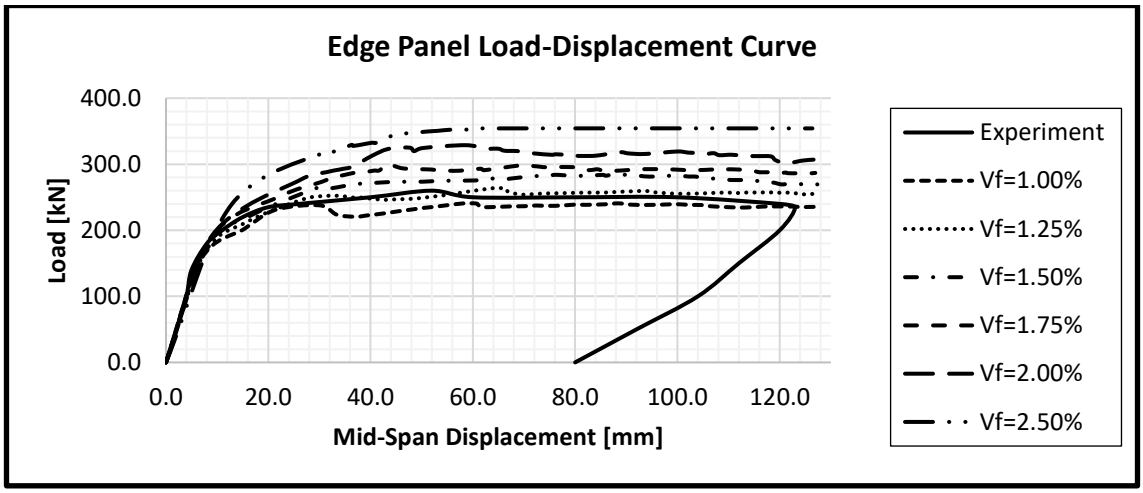

Figure 7.25: Load-Displacement Curves for various fibre volume ratio V_f for Edge Panel

7.6.2.1 Crack Patterns [Principal Strain Contours]

Principal strain contours for the analysed quarter-size edge-panel and compared with experimental work is presented in Figure 7.26 while that of the parametric study is presented in Figures 7.27 [a-f]. The deformed shapes are picked at the point when the slab failed under bending. The contour intervals adopted were 0.02 for SFRC slab which is highlighted in grey representing the steel-fibres pull-out strain and 0.0035 for compressive strains exceeding concrete ultimate strain is presented in black.

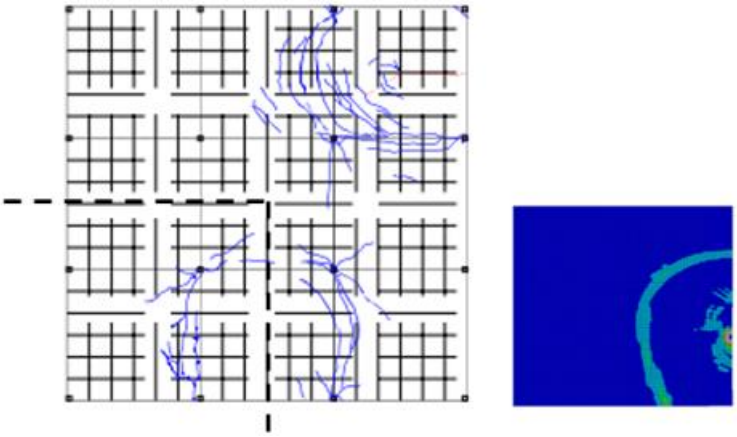

Figure 7.26: Comparison between Crack Patterns in Experiment and FEA for Edge Panel

In the quarter-size model slabs analyses, there is radial crack propagation at a radius R [Figure 7.27]. This was identical to what was obtained in the experimental work. Thus, further indicating the suitability of the ABAQUS software for this present research work.

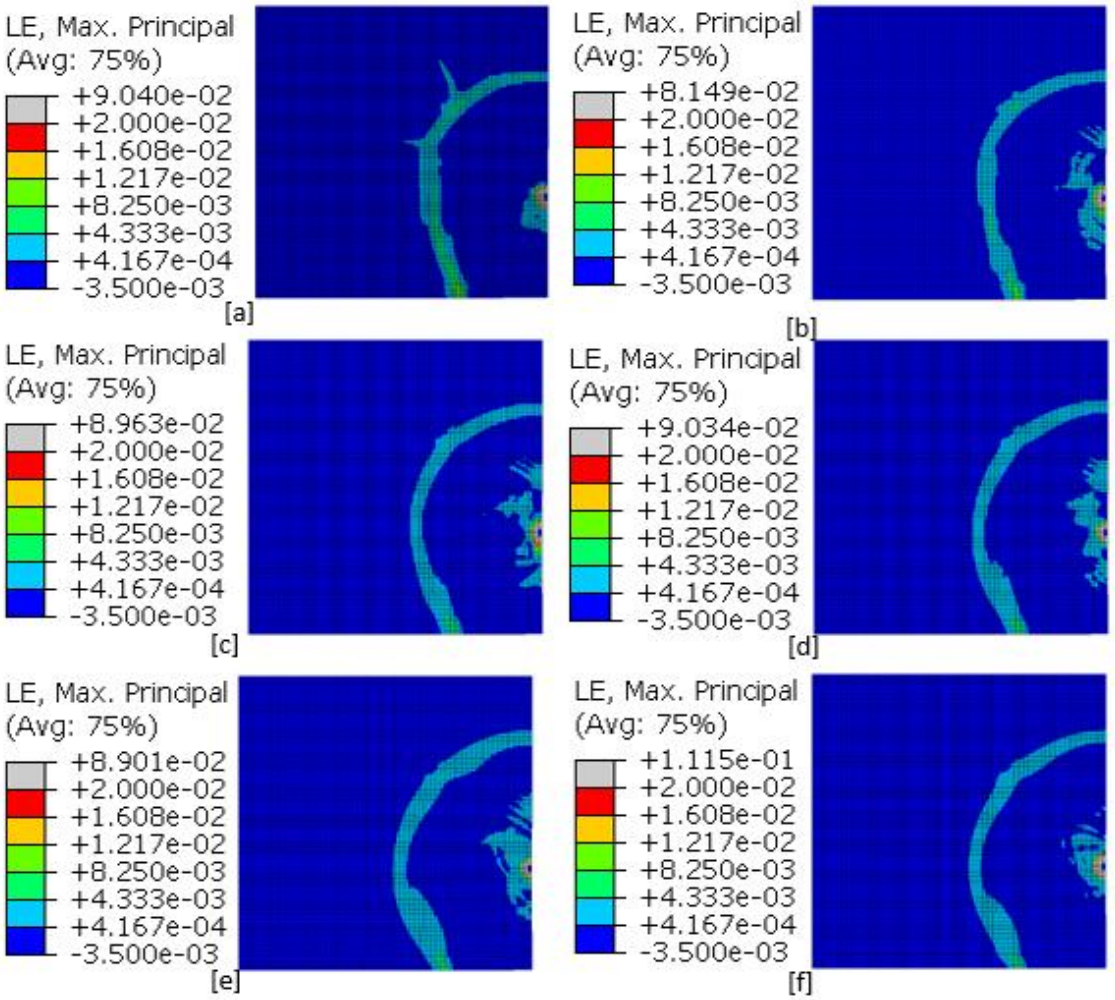

Figure 7.27: Principal Strain Contours for Edge Panel with V_f [a]= 1.00%, [b]= 1.25%, [c]= 1.50%, [d]= 1.75%, [e]= 2.00% and [f]= 2.5%

All the quarter-size slabs analysed have the same failure pattern with radial cracks at radius R and concentrated cracks at the point of load application. The radial crack is a tensile crack on the top of the slabs. The mode of failure is bending at the point of load application. There is a hog around the radial arc.

7.6.2.2 Crack Patterns [Principal Strain Vectors]

To further understand the cracks at failure with strain vectors, the crack patterns are illustrated in Figures 7.28 [a-f]. The vectors were viewed in the z-z axis. The strain vectors appropriately indicate the cracking pattern in the slabs. From observations, in all the

slabs analysed, failure occurs due to crack propagation in two areas: [i] area under the load application and [ii] immediate four [4] columns that surround the edge panel.

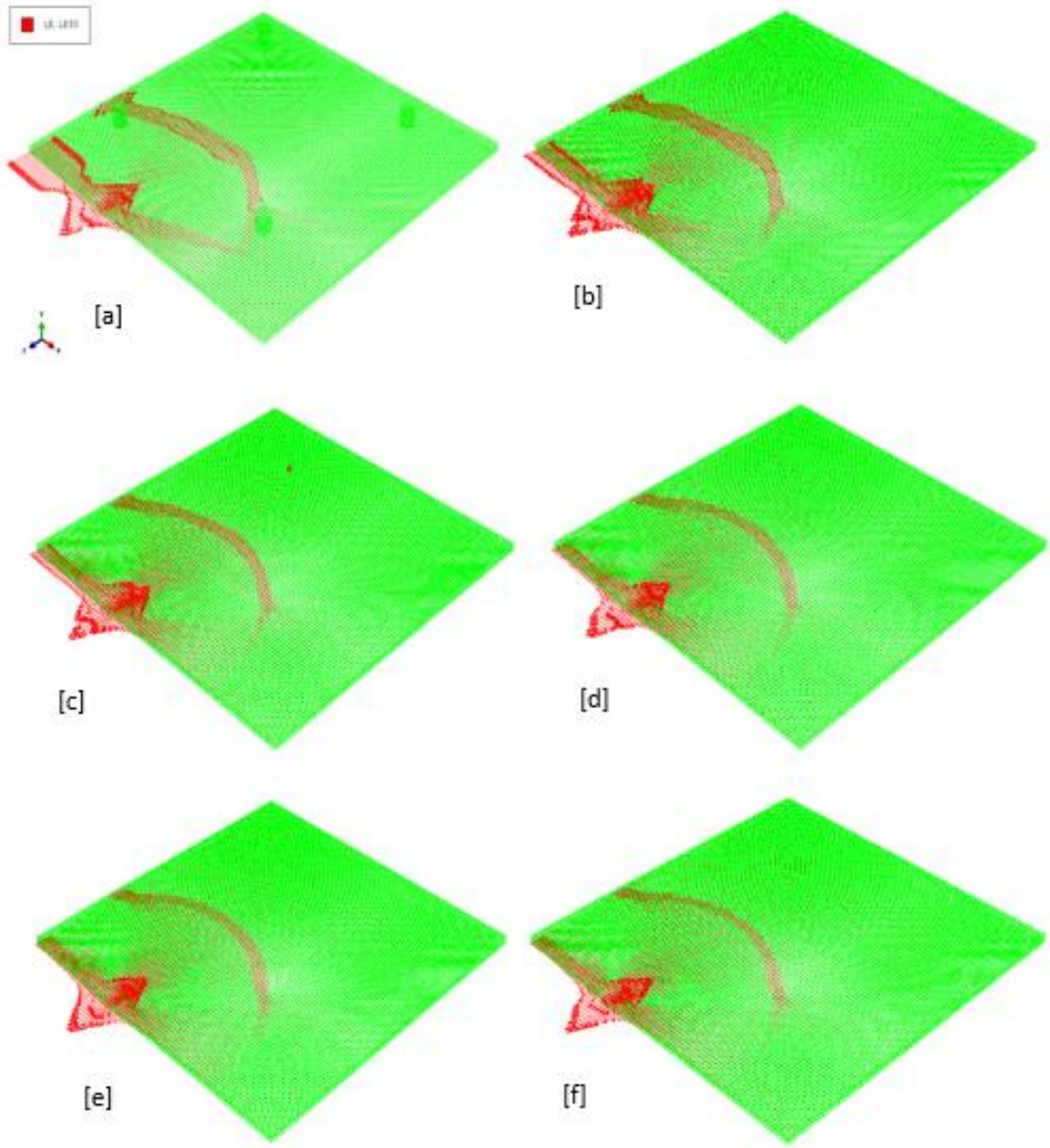

Figure 7.28: Principal Strain Vectors for Edge Panel with V_f [a]= 1.00%, [b]= 1.25%, [c]= 1.50%, [d]= 1.75%, [e]= 2.00% and [f]= 2.5%

The radial cracks transcend from the support at the edge to the internal one and from there towards the second internal support. The extent of the strain vectors marks the magnitude of the cracks. These cracks follow the pattern seen in the experimental works. In the slab with V_f=1.00%, the vector extends significantly to the continuous side, and this continues to reduce as the steel-fibres increase. The slabs failed in bending at the mid-span of the panel, with radial cracks around the supports.

7.6.2.3 Crack Patterns [Deflected Shapes]

Figures 7.29 [a-f] shows the deformation of the slab expressed in deflected shapes. The deformation is associated with the direction of the load application. The slabs sag at the mid-span due to load-application. These indicate bending failure. The effect is a radial one at a radius from the point of application of loads. The displacement at the maximum load continues to decrease steadily as V_f increases. The load causing this diaplacement also increases as the V_f increases. This shows that the more the steel-fibres, the greater the stiffness of the slabs.

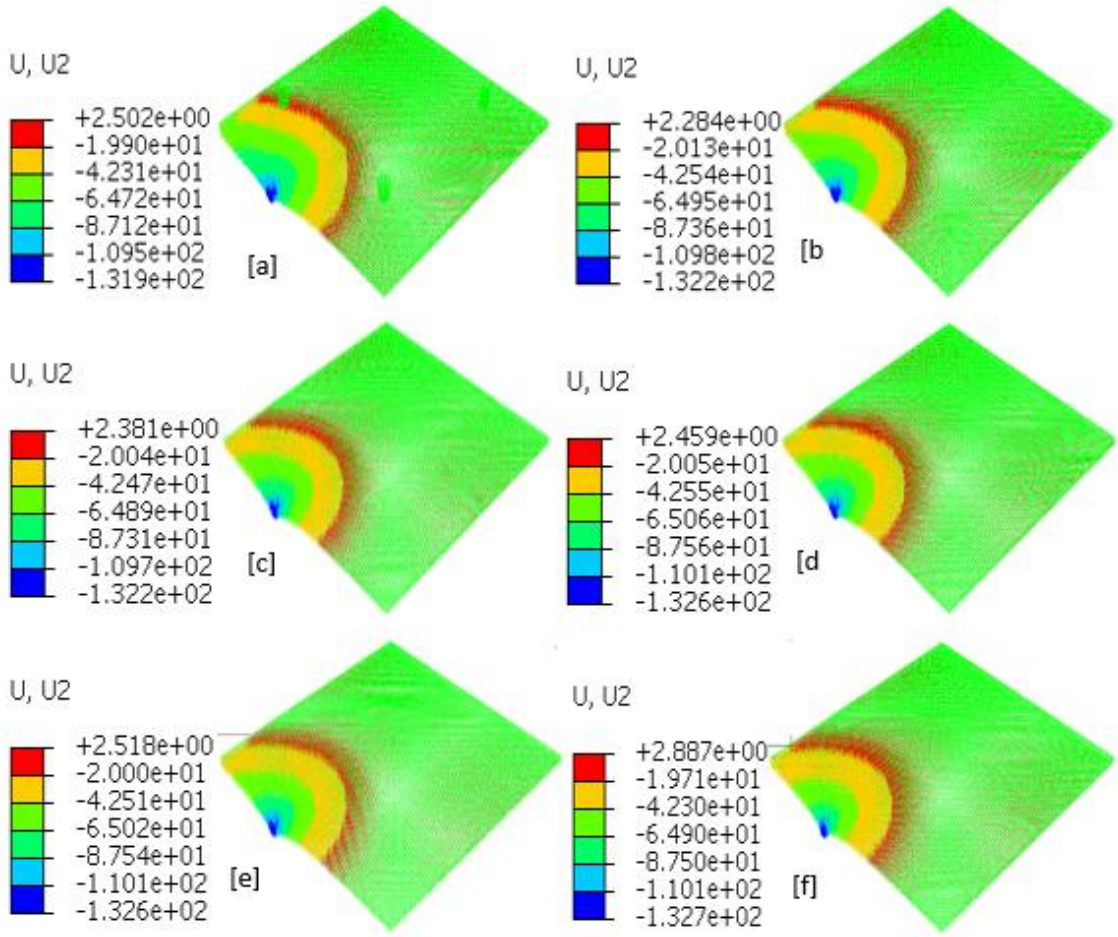

Figure 7.29: Deflected Shapes for Edge Panel with V_f [a]= 1.00%, [b]= 1.25%, [c]= 1.50%, [d]= 1.75%, [e]= 2.00% and [f]= 2.5%

7.6.2.4 Crack Patterns [Tensile Damaged Shapes]

Additional figures showing the crack patterns expressed in tensile damaged shapes are shown in Figure 7.30. The effect of the loading at the mid-span of the slab is viewed from the top and soffit of the slabs. The formation of the crack is at the top and soffit of the slabs around the point where the loads are applied. The damaged tensile pattern at the

tension face of the panel with V_f=1.00% spread from the point of load application in three legs. The size kept decrease and merging into a wider but shorter one as V_f increases.

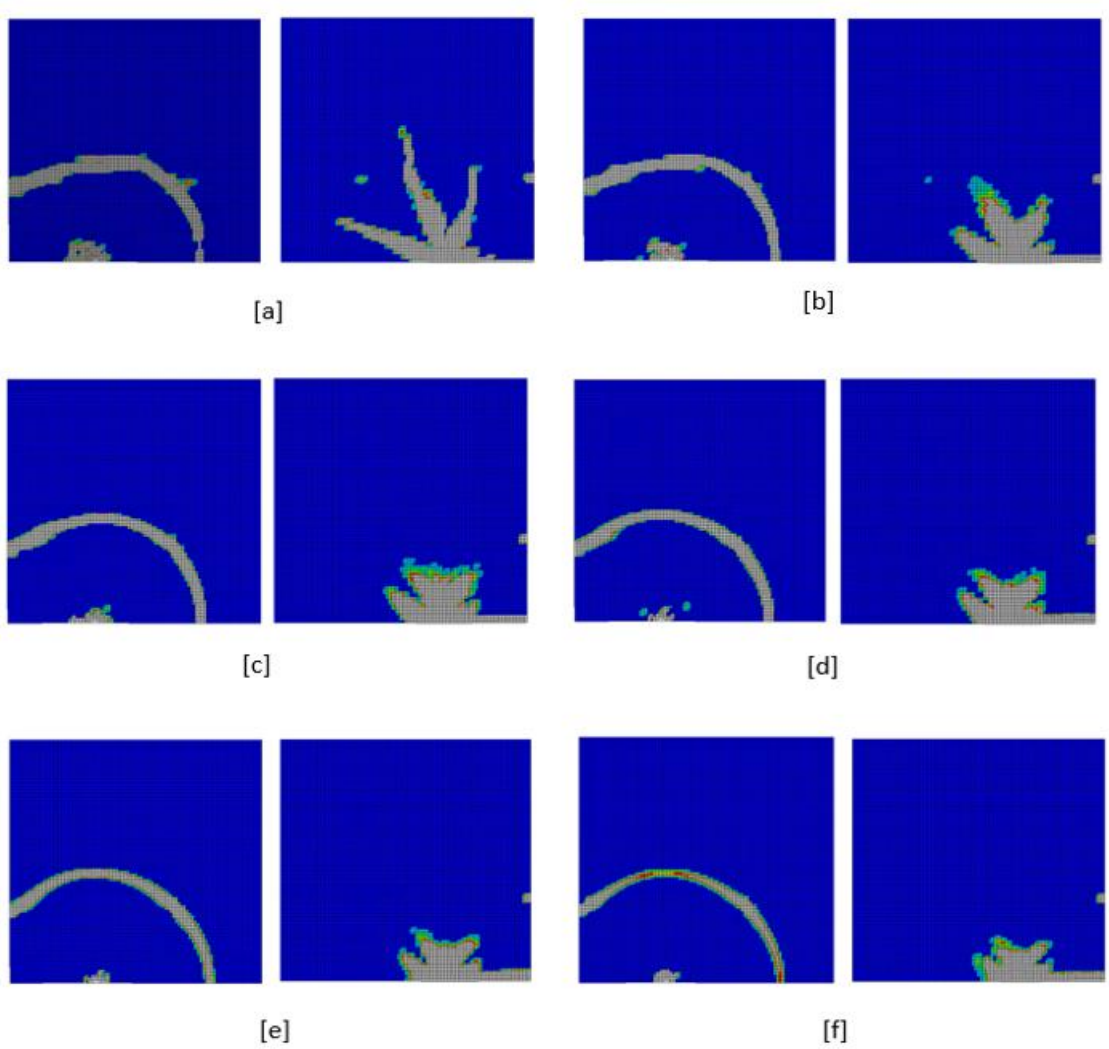

Figure 7.30: Tensile Damaged Shapes [Top and Soffit] for Edge Panel with V_f [a]= 1.00%, [b]= 1.25%, [c]= 1.50%, [d]= 1.75%, [e]= 2.00% and [f]= 2.5% [top surface on right, soffit on left]

The cracks at the soffit of the panel occur directly under the point of load application. In the slab with V_f=1.0%, the cracks emerged in three legs [with the longest 3874mm in length]. As the V_f increases, the crack legs reduce [1590mm in V_f=2.50%] and becomes more concentrated at the point of load application. This shows the positive effect of additional V_f in arresting crack propagation. The crack pattern at the top of the panel is in the form of a radial arc which is similar and consistent in all the slabs with different

V_f. The failure patterns in these tensile damaged shapes confirms that the slabs failed in bending.

7.6.3 Comparative Study with Experimental Specimen using Non-Dimensional Ratios

This section presents a comparison between the experimental result [control specimen] and the results of the slabs examined with various V_f using non-dimensional ratios.

7.6.3.1 Strength Ratio

The strength ratios are measured by dividing the yield load [P_y] and the maximum load [P_{max}] of the slabs with various V_f by $P_{y,c}$ and $P_{max,c}$ respectively [$P_{y,c}$ and $P_{max,c}$ are from the experimental results]. These are presented in Table 7.13, Figures 7.31 and 7.32.

Table 7.13: Strength Ratios for Edge Panel

V_f [%]	P_y [kN]	$\frac{P_y}{P_{y,c}}$	P_{max} [kN]	$\frac{P_{max}}{P_{max,c}}$
Control	157.0		240.8	
1.00	157.0	1.00	240.8	1.00
1.25	160.9	1.02	264.0	1.10
1.50	162.8	1.04	284.0	1.18
1.75	170.6	1.09	298.3	1.24
2.00	176.4	1.12	328.9	1.37
2.50	180.5	1.15	354.3	1.47

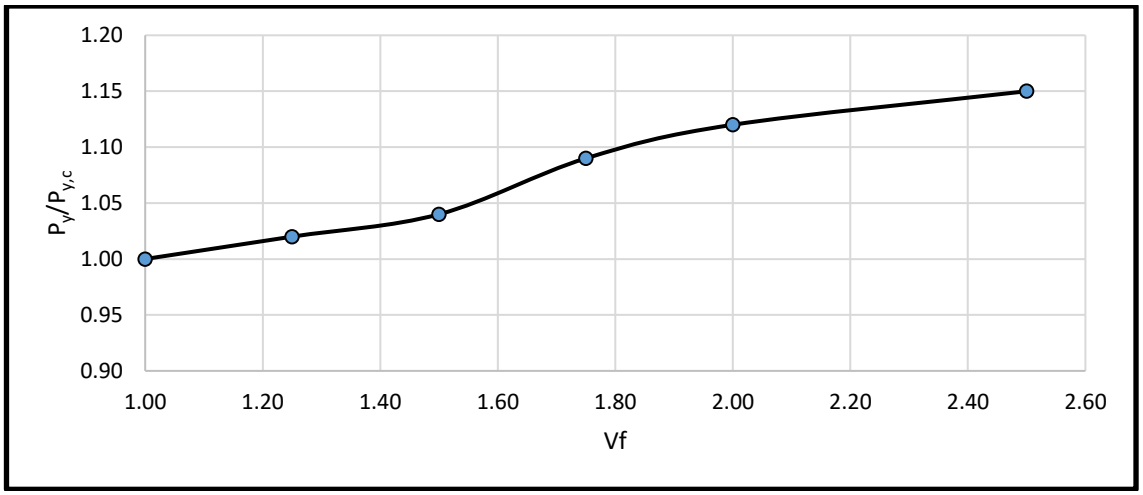

Figure 7.31: Graph of V_f against $P_y/P_{y,c}$ for Edge Panel

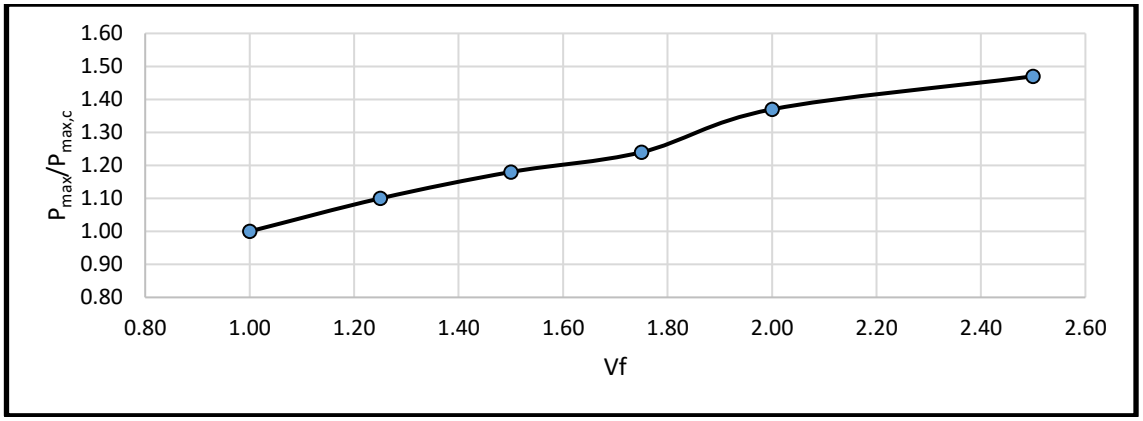

Figure 7.32: Graph of V_f against $P_{max}/P_{max,c}$ for Edge Panel

There is a considerable increase in the strength ratio $P_y/P_{y,c}$ up to 50.0% as the V_f increases while for $P_{max}/P_{max,c}$ an increase of 36.0% was attained. These reveal that the responses of the edge panel centrally loaded consistently rise in strength as V_f increases.

7.6.4 Further Analysis with Different f_{cu} for Edge Panel

The responses of the slab were understudy with different characteristic strength f_{cu} [30MPa, 40MPa and 50MPa] with varying volumes of steel-fibres V_f [1.00%, 1.25%, 1.50%, 1.75%, 2.00% and 2.50%] and the results are presented in Table 7.14 with load-displacement curves in Figures 7.33 - 7.35.

7.6.4.1 The Influence of the f_{cu} for Edge Panel

As done in section 7.5.6.1, further parametric analyses were carried out with different f_{cu} and the reports on their effects on the yield load, and maximum load carrying capacity and their respective displacements presented below. All other parameters [concrete and damaged plasticity] remain unchanged.

Table 7.14: Strength Ratios for various V_f for Edge Panel

V_f [%]	f_{cu} [MPa]	P_y [kN]	$\frac{P_y}{P_{y,c}}$	P_{max} [kN]	$\frac{P_{max}}{P_{max,c}}$
Control	30.0	132.8		228.1	
1.00		132.8	1.00	228.1	1.00
1.25		144.2	1.09	233.2	1.02
1.50		157.1	1.18	255.5	1.12
1.75		165.2	1.24	285.6	1.25
2.00		176.9	1.33	305.4	1.34
2.50		190.3	1.43	351.9	1.54
Control	40.0	130.5		240.6	
1.00		130.5	1.00	240.6	1.00
1.25		156.5	1.20	263.0	1.09
1.50		166.9	1.28	284.1	1.18
1.75		178.9	1.37	304.5	1.27
2.00		182.2	1.40	320.2	1.33
2.50		193.7	1.48	365.3	1.52
Control	43.7	157.0		240.8	
1.00		157.0	1.00	240.8	1.00
1.25		164.9	1.02	264.0	1.10
1.50		176.8	1.04	284.0	1.18
1.75		190.6	1.09	298.3	1.24
2.00		193.4	1.12	328.9	1.37
2.50		239.5	1.15	354.3	1.47
Control	50.0	165.5		255.9	
1.00		165.5	1.00	255.9	1.00
1.25		167.0	1.01	283.8	1.11
1.50		175.3	1.06	303.6	1.19
1.75		196.5	1.18	323.2	1.26
2.00		206.3	1.24	344.6	1.35
2.50		249.5	1.49	375.1	1.47

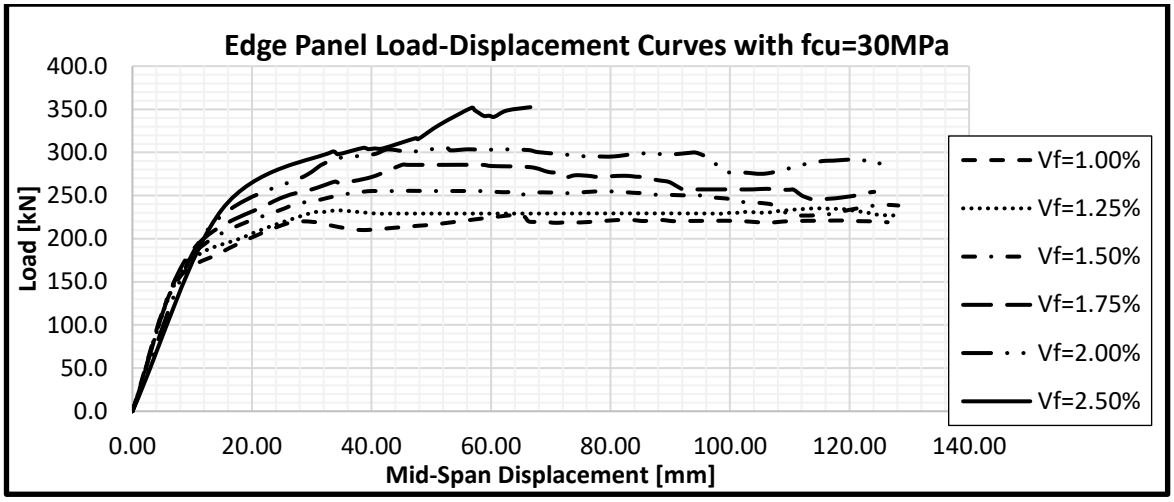

Figure 7.33: Load-Displacement Curves for various V_f with f_{cu}=30MPa for Edge Panel

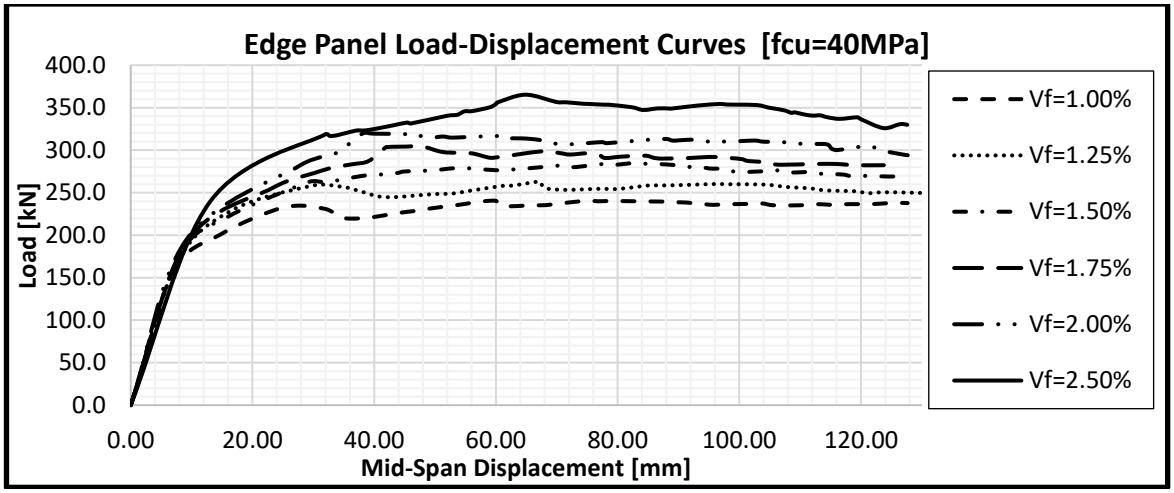

Figure 7.34: Load-Displacement Curves for various V_f with f_{cu}=40MPa for Edge Panel

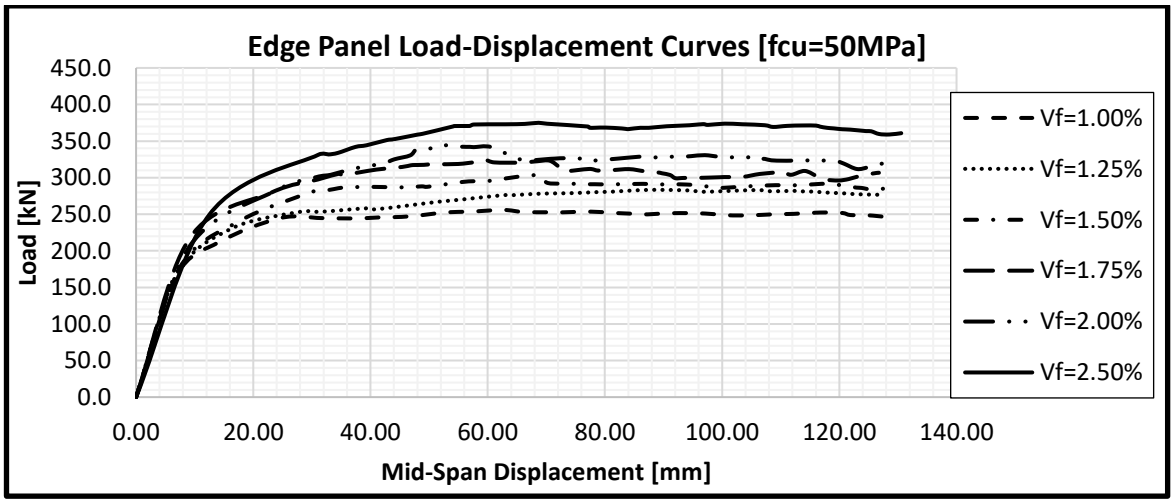

Figure 7.35: Load-Displacement Curves for various V_f with f_{cu}=50MPa for Edge Panel

The influence of a change in characteristic strength f_{cu}, and fibre volume ratio V_f of a 9-panel SFRC suspended slab [centrally loaded on the edge panel] are shown in Figures 7.33-7.35. The figures show the load-displacement curves, where the load capacity and the corresponding central displacement are gotten. The f_{cu} of 30MPa, 40MPa and 50MPa were used in the additional analyses. In the slab with f_{cu},=30MPa the model failed before the applied displacement is reached. This is due to excessive steel-fibre [over reinforcement] thus making the concrete to reach the limiting values of strain before that of steel-fibre.

The impact of the tensile strength f_t is first on the yield load [point of the first crack] followed by the impact of the flexural strength f_{tu} with make the curves to experience strain hardening or softening as the case may be. The overall response is a failure in bending. The load carrying capacity of the edge panel in the slab was enhanced by over 18%. The cracking shapes follows the same pattern in all the slabs.

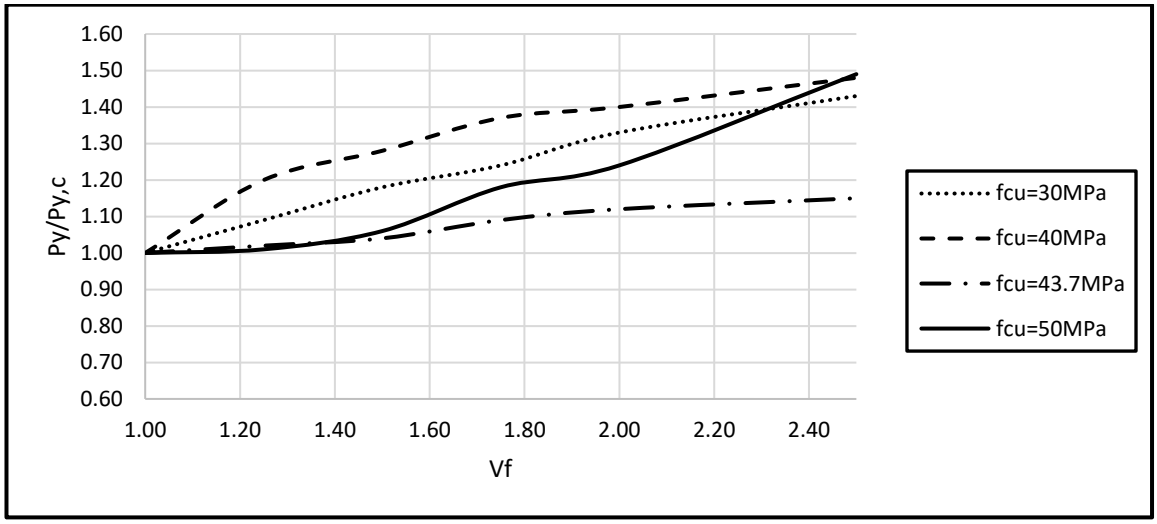

Figure 7.36: Graph of V_f against $P_y/P_{y,c}$ with varying f_{cu} for Edge Panel

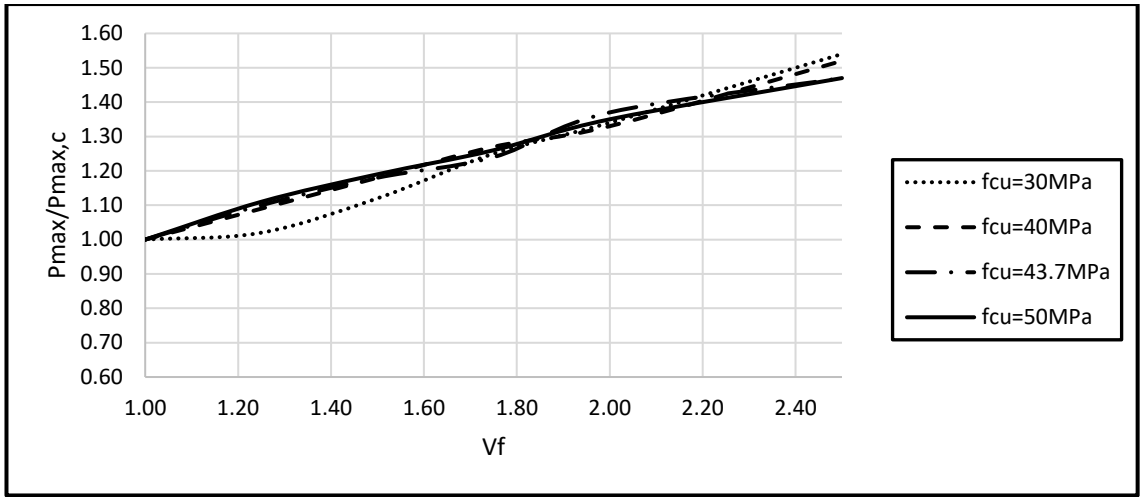

Figure 7.37: Graph of V_f against $P_{max}/P_{max,c}$ with varying f_{cu} for Edge Panel

Figure 7.36 shows the graph of $P_y/P_{y,c}$ against V_f while Figure 7.37 display the graph of $P_{max}/P_{max,c}$ against V_f. A rising trend is seen in the graphs of $P_y/P_{y,c}$ and $P_{max}/P_{max,c}$ as the V_f increases. The $P_y/P_{y,c}$ is high as the value of f_{cu} decreases while $P_{max}/P_{max,c}$ which is high when f_{cu}, is high as V_f increases.

In a bid to create a simple equation for maximum loading carrying capacity for the edge panel, more analyses with the span/depth ratio taken as 33.3 were undertaken with different f_{cu}, and V_f [all other parameters remain the same]. This is intended at generating an equation with variables covering most of the essential parameters used in the analyses in the determination of the maximum load carrying capacity of the slab. The summary of these analyses is in Table 7.15. The mode of failure of the slabs with span/depth ratio of 33.3 and 30 are the same, they all failed in bending.

Table 7.15: Strength Ratios for various V_f for Edge Panel

V_f [%]	f_{cu}, [MPa]	P_y [kN]	δ_y [mm]	P_{max} [kN]	δ_{max} *[mm]*
1.00	30.0	144.7	14.5	178.4	74.8
1.25		148.9	15.5	188.1	74.9
1.50		157.0	14.5	198.6	74.9
1.75		173.0	19.6	208.2	61.8
2.00		183.6	20.9	219.8	63.7
2.50		199.4	22.5	242.2	65.9
1.00	40.0	164.0	12.1	205.2	76.6
1.25		174.3	13.6	218.8	75.5
1.50		184.6	15.6	230.0	77.8
1.75		194.5	17.0	243.2	82.3
2.00		205.5	18.6	253.7	65.0
2.50		228.0	30.0	259.2	72.3
1.00	50.0	185.5	10.8	234.1	82.8
1.25		201.6	13.8	249.8	73.0
1.50		207.3	13.7	269.9	79.0
1.75		218.8	14.7	280.0	72.1
2.00		233.9	17.3	292.4	73.6
2.50		260.3	21.0	328.3	89.2

7.6.5 Proposed Equation for Maximum Load Carrying Capacity for Edge Panel

An equation is suggested based on regression analysis, for estimating the maximum load carrying capacity of the edge panel in a 9-panel SFRC suspended floor. The equation has the characteristic strength [f_{cu}], fibre volume ratio [V_f], span depth ratio [L/d] on one side and central displacement [δ] on the other side as dependent variables.

Using the regression analysis of the MS-Excel [with input and results shown in Appendix B5], the yield load and maximum load carrying capacity [P_{max}] of the panel are:

$$P_y = 4.64f_{cu} + 64.3V_f - 51.68\,{}^{L}/_{d} + 1751.76 \quad \text{- Eqn. 7.5}$$

$$P_y = 6.85\delta y + 45.55 \quad \text{- Eqn. 7.6}$$

$$P_{max} = 3.75f_{cu} + 75.8V_f - 0.26\,{}^{L}/_{d} \quad \text{- Eqn. 7.7}$$

$$P_{max} = -1.45\delta max + 368.2 \quad \text{- Eqn. 7.8}$$

Where L – Span of the panel

d – Overall depth of the panel

δ – central displacement

7.7 Part III: Corner Panel

As deployed in the middle and edge panels, a loading rig of 200mm square was set-up at the centre of the corner panel and was used to test for destruction. In the quarter-size model [Figure 7.38], the loading-rig remains 200mm square for the FEA. There is no need to multiply the result with any factor as the full panel was in the model. In the experimental work, the loading rig was unloaded twice being the last test on the slab. The maximum load carrying capacity happens before the first unloading.

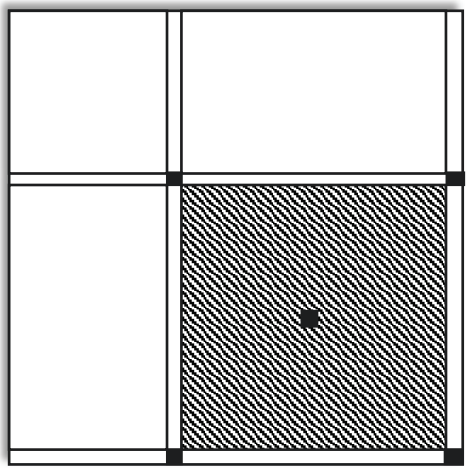

Figure 7.38: Loading Pattern at ULS [Quarter-Size] for Corner Panel

The two continuous adjacent sides are fixed in their plane [XSYMM and ZSYMM]. The fixation allows the software to recognise the continuity of the slab in x and z directions respectively. As stated earlier, the concept of a fraction model shows the versatility of the FEM in reducing both time and resources.

7.7.1 Load-Displacement Curves

Figure 7.39 shows the load-displacement curve for the validation of the experimental results using NLFEA of ABAQUS CDP and Lok & Xiao's constitutive model. Comparing the two results, the NLFEA appears stiffer than the experimental work. These data are about

3.10% greater than the experiment. The summary of the results is presented in Table 7.16.

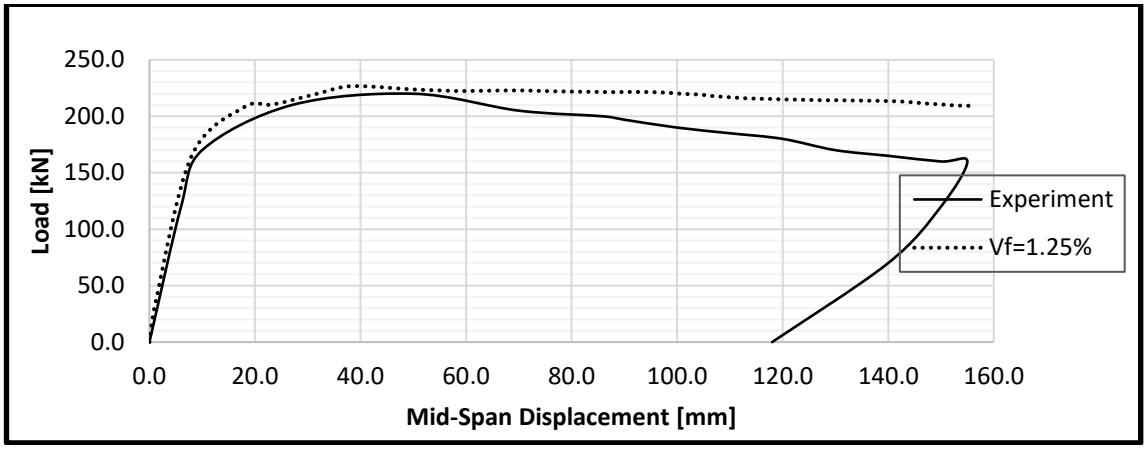

Figure 7.39: Load-Displacement Curve for Validation work for Corner Panel

Table 7.16: Comparison of Experimental and FEA Validation Results for Corner Panel

	Corner Panel		% Variance
	Experiment	FEA	
Load at First Crack [kN]	120.0	121.0	0.8
Displacement at First Crack [mm]	6.0	6.0	0.0
Maximum Load [kN]	220.0	226.8	3.1
Displacement at Maximum Load [mm]	50.0	50.7	1.4

A good look into the crack pattern of the model of NLFEA both at the initial and the failure [final] stages agree with the experiment crack patterns. The compatibility of the curves in Figure 7.39 and crack patterns in Figure 7.40 further demonstrate NLFEA capacity in simulating the behaviour of the effect of steel-fibres on the concrete strength [yield and maximum loads] and ductility [ratio of displacement at yield and ultimate load] correctly. The corner panel has a smaller load carrying capacity when compared to the middle and edge panels.

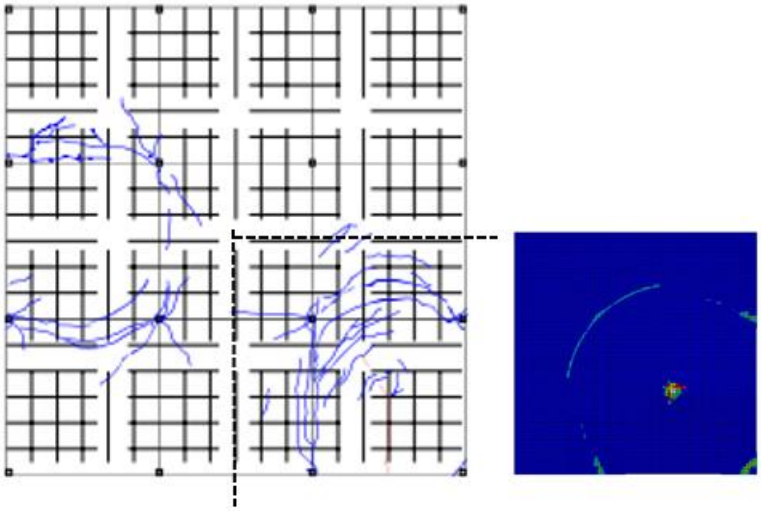

Figure 7.40: Comparison between Crack Patterns in Experiment and FEA for Corner Panel

Table 7.17 displays a summary of the critical structural parameters in respect to the yield, and the maximum [P_y, and P_{max}] with corresponding displacements [δ_y, and δ_{max}] respectively. Further simulations for the complete parametric studies use the same NLFEA parameters that produced the validated result.

7.7.2 The Strength

The preceding Table 7.17 and Figure 7.41 show the results of parametric studies on the edge panel with varying values of V_f. The increment in the fibre volume ratio leads to increases in the load carrying capacity of the SFRC suspended slab specifying that stiffness increases as V_f increases. 10 – 35% increment in the load carrying capacity of the slab is noticeable as V_f increases are leading to greater strength. The yield strength also increases as the V_f increase thus proving a higher load before the propagation of the first crack. The propagation of the cracks continue as the loading exceeds the yield load. The flexural strength of the SFRC matrix come into play by preventing the sudden collapse of the slab. These cracks are bridged by the steel-fibres thus preventing sudden collapse.

Table 7.17: Strength Ratios for Corner Panel

V_f [%]	P_y [kN]	δ_y [mm]	P_{max} [kN]	δ_{max} [mm]
1.00	187.9	10.0	221.8	46.0
1.25	194.9	11.0	226.8	50.7
1.50	201.2	11.8	242.7	55.4
1.75	205.0	12.0	253.8	91.5
2.00	212.9	12.9	278.9	84.8
2.50	246.3	19.8	309.2	88.7

Just as observed in previous analyses, the increase in the fibre volume ratio considerably enhanced the values of P_y and P_{max}. The FEA results of the yield load show an increase as V_f increases. The maximum load has a steady increase as more steel-fibres were added. An increase of 28.73% is seen in P_{max} as V_f gets to 2.50%. The load at failure in the FEA is 30.88% higher than that of the experiment. This can be attributed to the unloading done in the experimental work. The displacement at failure in FEA is 0.77% higher than that of the experiment. Stiffness is enhanced as V_f are increasing. The different between the experimental result graph and that of the FEA was due to the unloading done during the experimental work.

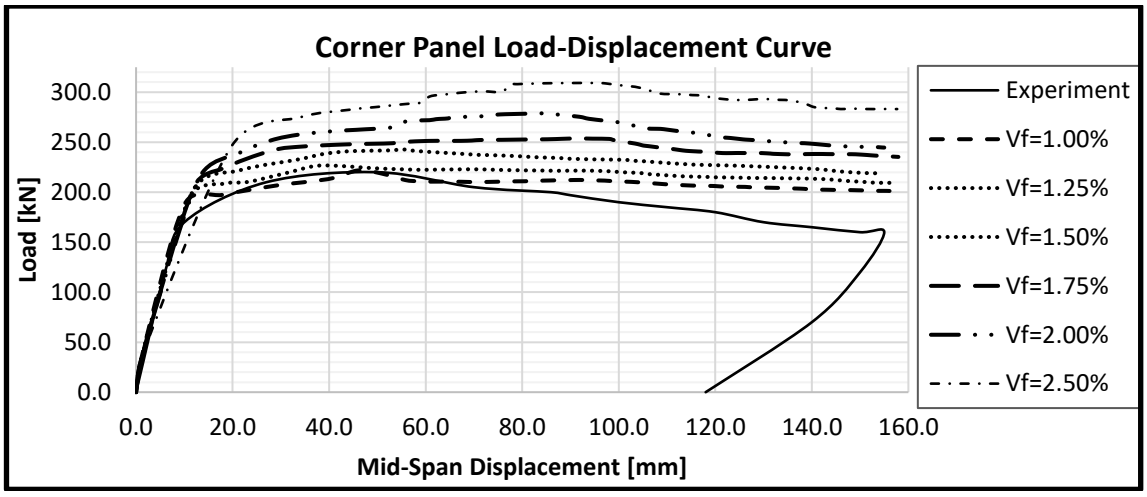

Figure 7.41: Load-Displacement Curves for various fibre volume ratio V_f for Corner Panel

7.7.2.1 Crack Patterns [Principal Strain Contours]

Figures 7.42 [a-f] is the representation of the principal strain contours revealed by the analyses carried out on the quarter-size corner-panel. The minimum and maximum principal strains contours at yield point are taken as -0.0035 and 0.02 corresponding to the ultimate compressive and tensile strains of SFRC. Cracks formation at the top surface of the panel was in radial form with the point of load application as a centre, and it is across the supports.

At the top surface, the grey area signifying the principal stain occurs at the point of the load application. The radial crack propagation at a radius R highlighted in light blue, signifies that it has not reached the maximum principal strain value. The grey area is surrounded by a light blue area, which indicates micro-cracks that emerged but the strain at the light blue area not yet reached the principal stain value, It also reveals that the steel-fibres adequately covers the micro-cracks. The pattern also shows cracking on the surface at which the support had contact with the slab [punching was averted].

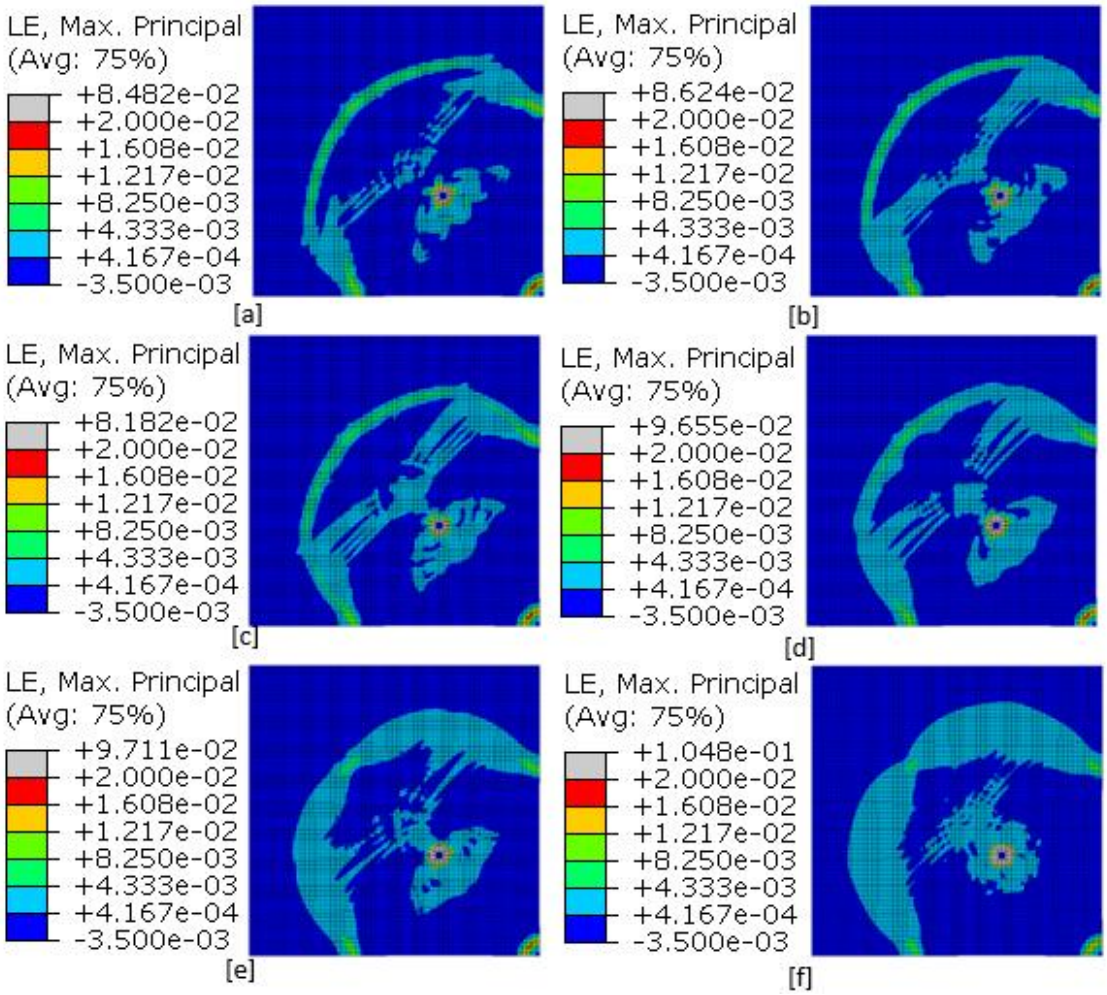

Figure 7.42: Principal Strain Contours for Corner Panel with V_f [a]= 1.00%, [b]= 1.25%, [c]= 1.50%, [d]= 1.75%, [e]= 2.00% and [f]= 2.5%

The failure pattern is similar in all the analyses done on the quarter-size slabs. The micro-cracks spreads across the supports. These cracks reduce as the fibre dosage increases. The point at the centre of the panel is where the maximum displacement took place, and it appears in grey, showing that the principal tensile strain of 0.02 was exceeded.

7.7.2.2 Crack Patterns [Principal Strain Vectors] for Corner Panel

To further appreciate the cracks pattern at failure, the strain vectors are used to understand the pattern [Figure 7.43]. The principal vectors in all the axes were viewed in the transparent mode to observe the top and soffit cracks at the same time. From interpretations of the contour shapes, crack propagation occurs in three areas at the top: [i] area under the load application [ii] area above the four [4] columns that around the corner panel and [iii] a radial crack.

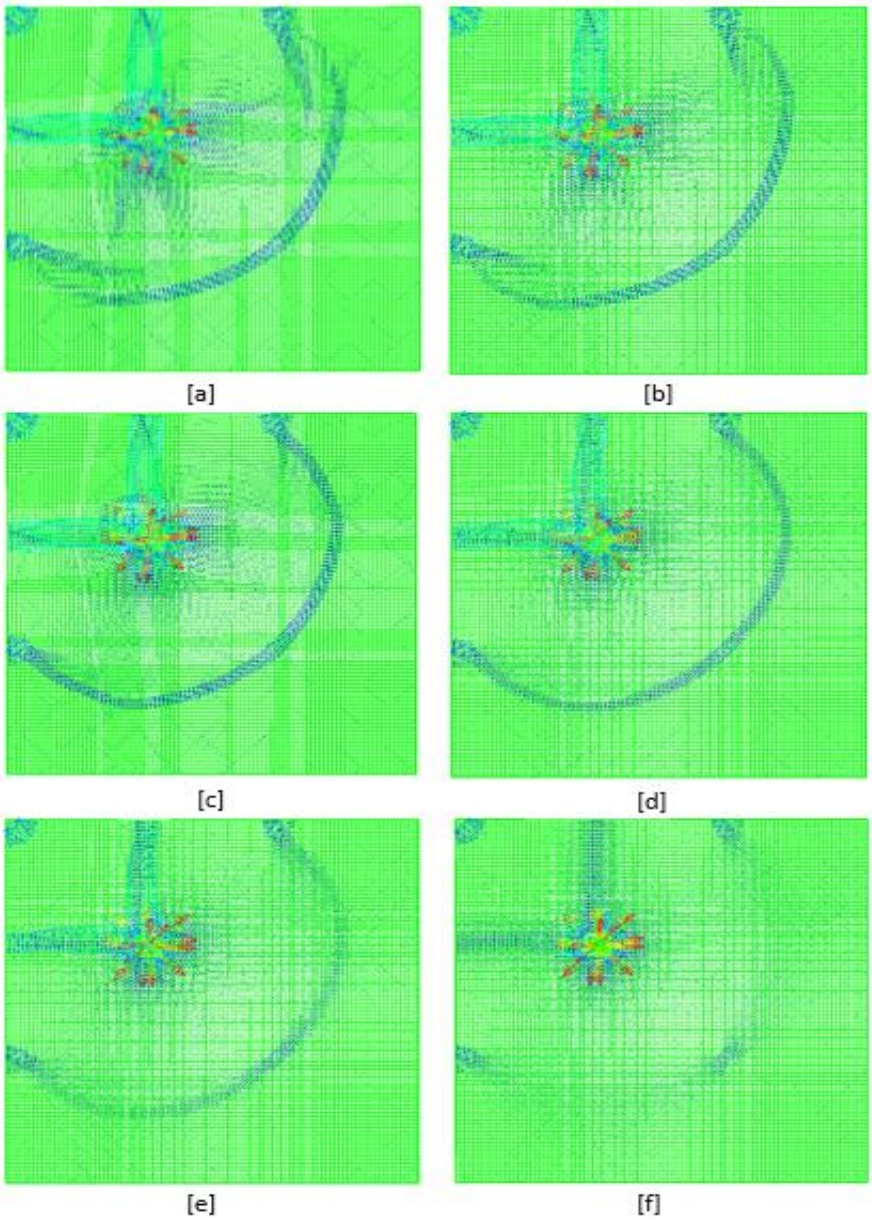

Figure 7.43: Principal Strain Vectors for Corner Panel with V_f [a]= 1.00%, [b]= 1.25%, [c]= 1.50%, [d]= 1.75%, [e]= 2.00% and [f]= 2.5%

The cracks occur in two areas at the soffit of the panel which are the areas under load application and two legs of cracks from the centre to the middle of two supports on the edges. These cracks formation is similar to the pattern obtained in the experimental works. The slab with V_f=1.00% has the vector spreads from the one edge support to another passing through the internal support, and this continues to reduce both in length and width as the fibre volume increase. The mode of failure in the slabs is bending at the mid-span of the corner panel.

7.7.2.3 Crack Patterns [Deflected Shapes] for Corner Panel

The deflected shapes of the deformed slab are presented in Figures 7.43 [a-f]. The slabs deflect at the mid-span [the point of load-application]. These sags indicate bending failure. The displacement at the maximum load continues to decrease steadily as V_f increases. This shows that the more the steel-fibres, the greater the stiffness of the slabs. The load resisting capacity of the slabs increases as the V_f increases.

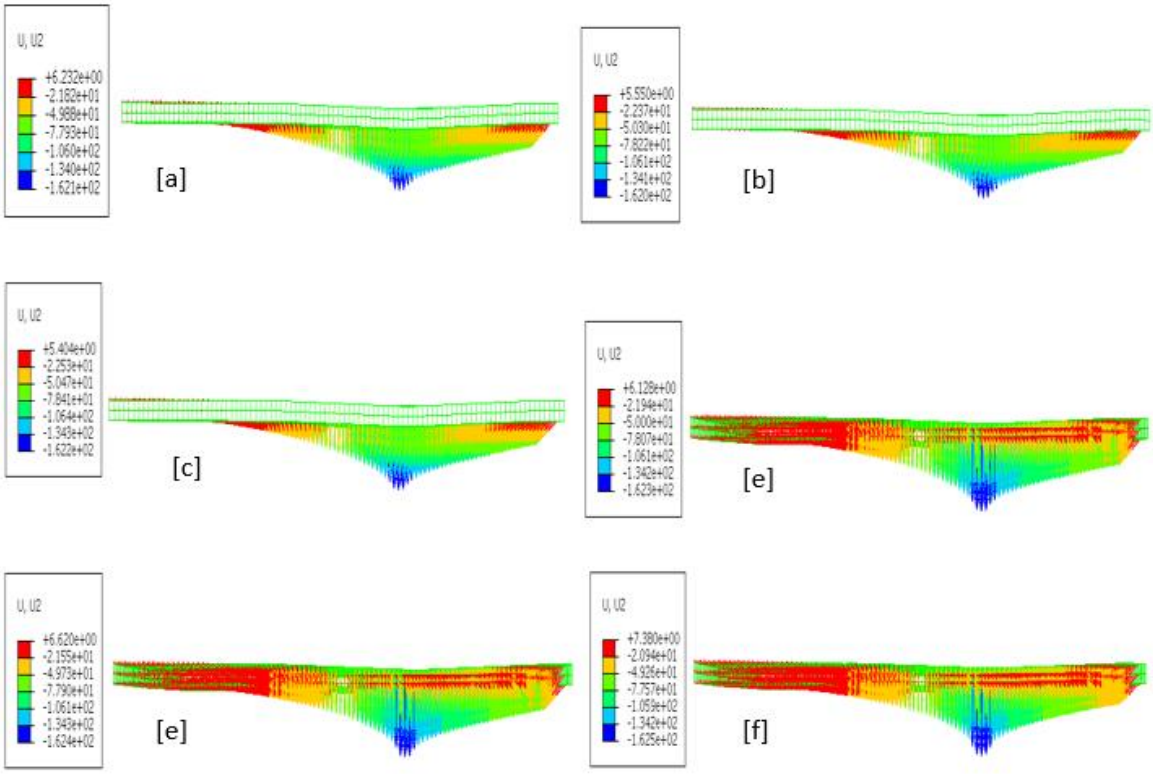

Figure 7.44: Deflected Shapes for Corner Panel with V_f [a]= 1.00%, [b]= 1.25%, [c]= 1.50%, [d]= 1.75%, [e]= 2.00% and [f]= 2.5%

7.7.2.4 Crack Patterns [Tensile Damaged Shapes]

The crack patterns were further understudied using the damaged tensile shapes [Figure 7.44]. The crack formation is at the top and soffit of the slabs with direct correlation to the point of load application. The influence of the loading at the mid-span of the slab from the top surface is like that of principal strain contours. It also shows the crack formation. The cracks propagate at the point where the load was applied and then a radial crack with a radius equivalent to the distance of the loading point to the support. As the V_f increases, the crack lines reduce gradually until V_f=2.50%, where the crack has diminished significantly, leaving it only on the slab contact area with the supports.

Likewise, at the point of load application, the grey areas continue to reduce as more fibres are added.

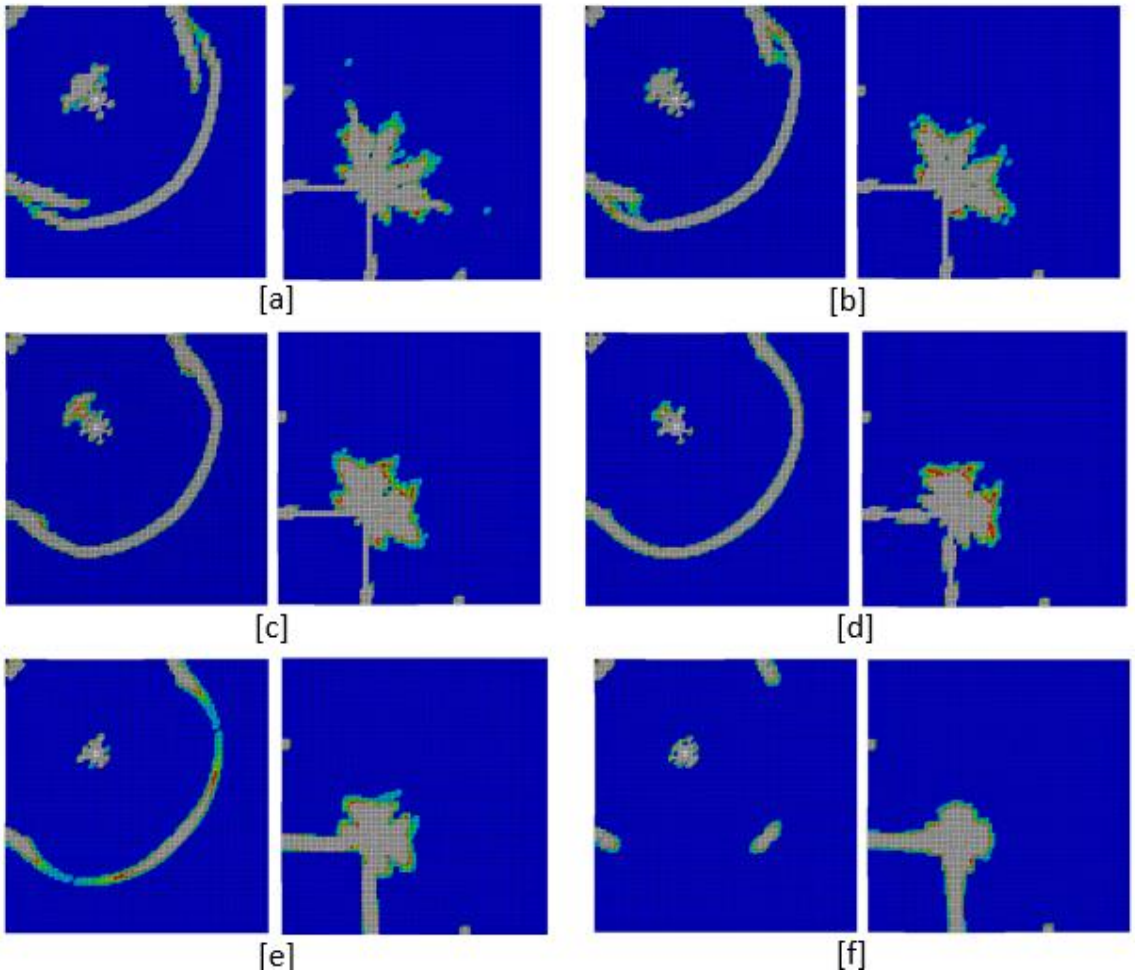

Figure 7.45: Tensile Damaged Shapes [Top and Soffit] for Corner Panel with V_f [a]= 1.00%, [b]= 1.25%, [c]= 1.50%, [d]= 1.75%, [e]= 2.00% and [f]= 2.5%

The cracks at the soffit of the panel occur directly under the point of load application with two legs at a right angle to each other and from the point of load application passing between two adjacent supports of the discontinued sides. When the V_f=1.0% in the first slab, the cracks at the centre of the panel spread widely over an area with two tiny legs. As the V_f increases, the cracks at the centre reduces tremendously and concentrate at the point of load application. The patterns in these damaged tensile figures affirm that the slabs failed in bending. This shows the effectiveness of the steel-fibres in bridging the crack opening, thus enhancing both the yield and maximum load of the slabs.

7.7.3 Comparative Study with Experimental Specimen using Non-Dimensional Ratios

This section presents a comparison between the control specimen [experimental result] and the FEA results of the slabs with various V_f utilizing non-dimensional ratios. The outcomes of ductility and strength were normalised by dividing them by the control specimen.

7.7.3.1 Strength Ratio for Corner Panel

The strength ratios, $P_y/P_{y,c}$ and $P_{max}/P_{max,c}$ [$P_{y,c}$ and $P_{max,c}$ are from the control slab], are plotted against V_f and are presented in Table 7.18, Figures 7.45 and 7.46. The results show a rise in strength.

Table 7.18: Strength Ratios for Corner Panel

V_f [%]	P_y [kN]	$\frac{P_y}{P_{y,c}}$	P_{max} [kN]	$\frac{P_{max}}{P_{max,c}}$
Control	187.9		221.8	
1.00	187.9	1.00	221.8	1.00
1.25	194.9	1.04	226.8	1.02
1.50	201.2	1.07	242.7	1.09
1.75	205.0	1.09	253.8	1.14
2.00	212.9	1.13	278.9	1.26
2.50	246.3	1.31	309.2	1.39

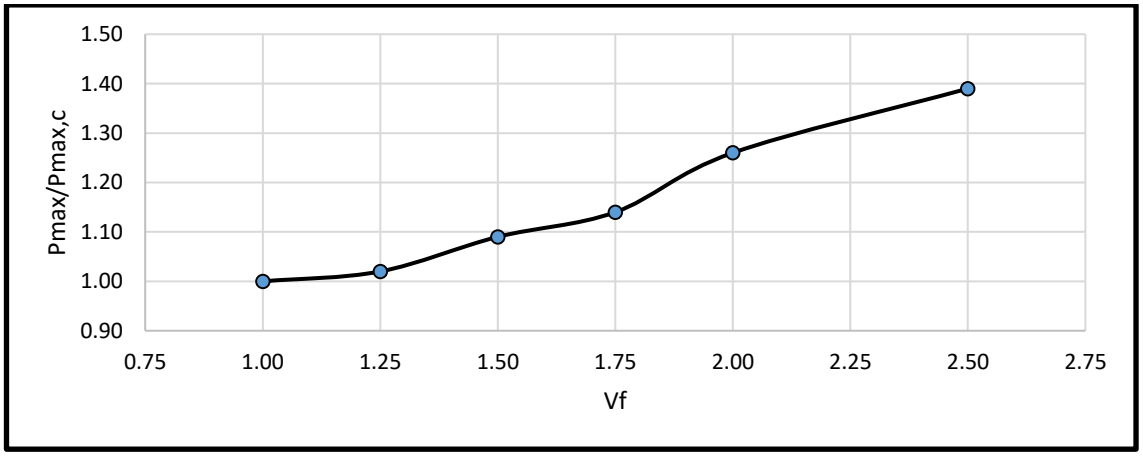

Figure 7.46: Graph of V_f against $P_{max}/P_{max,c}$ for Corner Panel

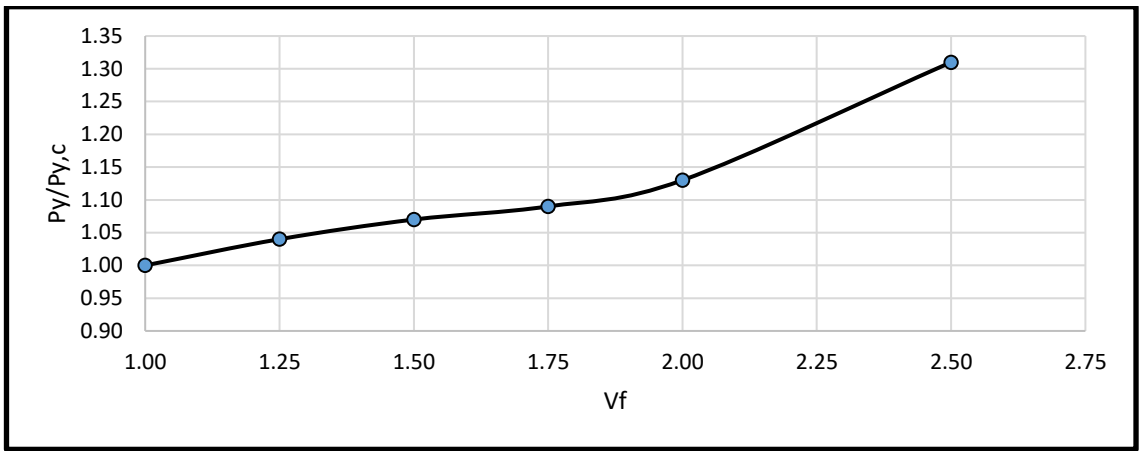

Figure 7.47: Graph of V_f against $P_y/P_{y,c}$ for Corner Panel

The responses in the strength of the corner panel centrally loaded steadily rise as V_f increases. There is a sizeable increase of 102.0% and 40.0% in the strength ratio $P_y/P_{y,c}$ and $P_{max}/P_{max,c}$ as the V_f increases.

7.7.4 Further Analysis with Different f_{cu} for Corner Panel

To appreciate the responses of the slab, different characteristic strength f_{cu} [30MPa, 40MPa and 50MPa] and varying fibre dosage V_f [1.00%, 1.25%, 1.50%, 1.75%, 2.00% and 2.50%] are used for further analyses and their results presented in Table 7.19 and Figures 7.47 - 7.49.

7.7.4.1 The Influence of the f_{cu} for Corner Panel

Additional parametric analyses carried out with different f_{cu} and V_f are reported with their effects on the yield load [P_y and δ_y], maximum load carrying capacity [P_{max} and δ_{max}] and the ultimate load [P_u and δ_u] below. All other parameters [concrete and damaged plasticity] remain unchanged.

Table 7.19: Strength Ratios for various V_f for Corner Panel

V_f [mm]	f_{cu} [MPa]	P_y [kN]	$\frac{P_y}{P_{y,c}}$	P_{max} [kN]	$\frac{P_{max}}{P_{max,c}}$
Control	30.0	146.9		180.7	
1.00		146.9	1.00	180.7	1.00
1.25		154.5	1.05	195.5	1.08
1.50		161.5	1.10	210.2	1.16
1.75		171.9	1.17	222.8	1.23
2.00		174.0	1.18	234.3	1.30
2.50		192.2	1.31	266.9	1.47
Control	40.0	176.9		205.0	
1.00		176.9	1.00	205.0	1.00
1.25		179.7	1.02	220.2	1.07
1.50		187.9	1.06	229.4	1.12
1.75		199.4	1.13	249.2	1.22
2.00		213.0	1.20	266.7	1.30
2.50		218.9	1.24	287.8	1.40
Control	43.7	187.9		221.8	
1.00		187.9	1.00	221.8	1.00
1.25		194.9	1.04	226.8	1.02
1.50		201.2	1.07	242.7	1.09
1.75		205.0	1.09	253.8	1.14
2.00		212.9	1.13	278.9	1.26
2.50		246.3	1.31	309.2	1.39
Control	50.0	211.0		229.8	
1.00		211.0	1.00	229.8	1.00
1.25		215.7	1.02	239.6	1.04
1.50		219.9	1.04	254.6	1.11
1.75		234.9	1.11	270.6	1.18
2.00		239.7	1.14	286.7	1.25
2.50		262.1	1.24	320.2	1.39

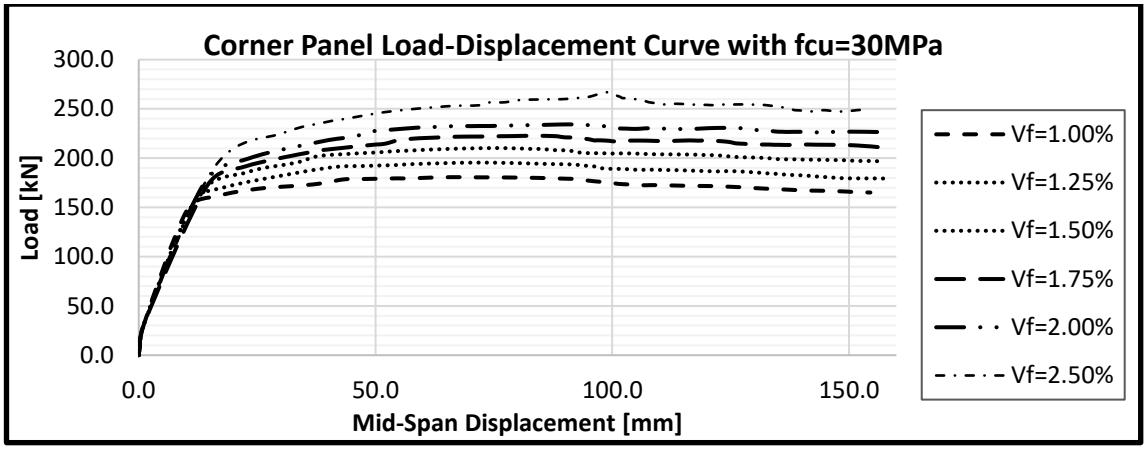

Figure 7.48: Load-Displacement Curves for various V_f with f_{cu}=30MPa for Corner Panel

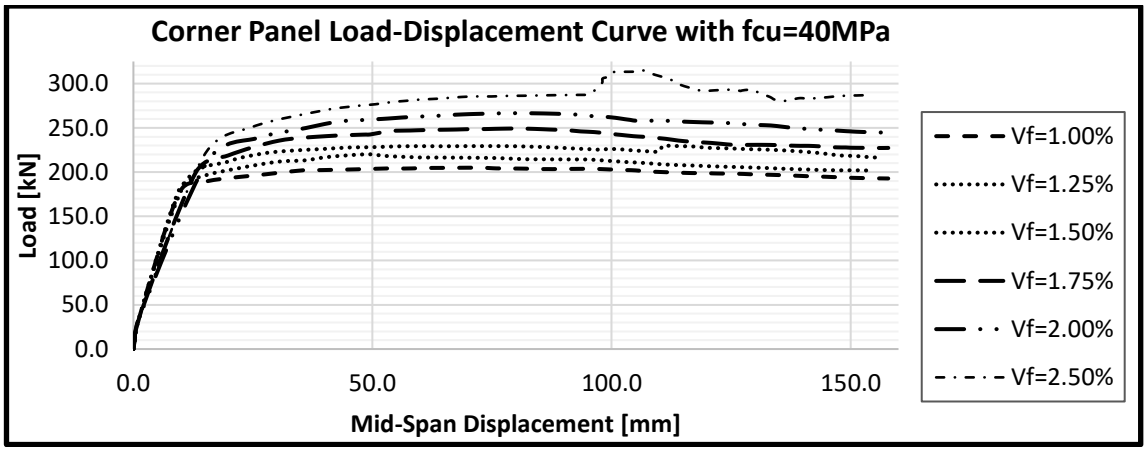

Figure 7.49: Load-Displacement Curves for various V_f with f_{cu}=40MPa for Corner Panel

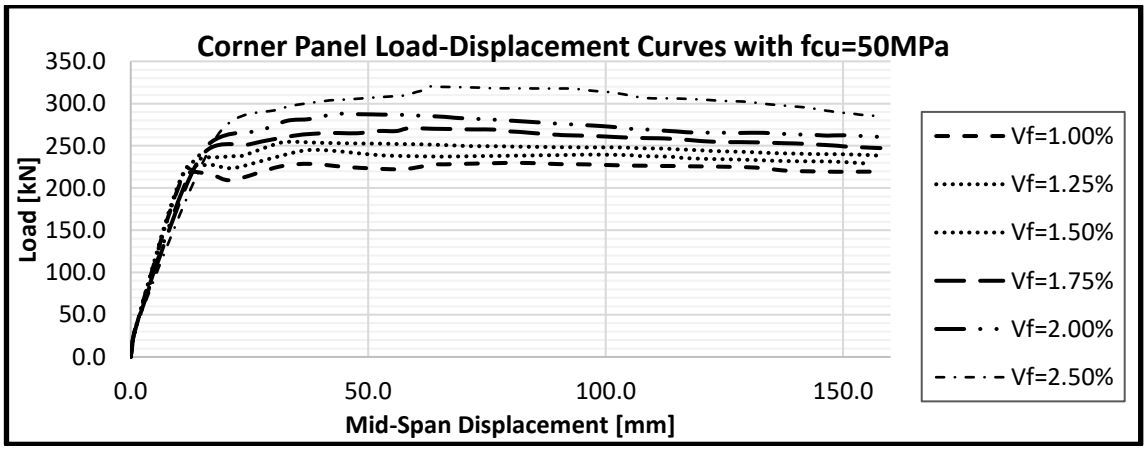

Figure 7.50: Load-Displacement Curves for various V_f with f_{cu}=50MPa for Corner Panel

The effect of a change in characteristic strength f_{cu}, and fibre dosage V_f of a centrally loaded Corner panel on a 9-panel SFRC suspended slab are presented as load-displacement curves in Figures 7.47-7.49. The figures show the load carrying capacity

from the start of loading to failure and the corresponding central displacement. The overall response of the slabs a failure in bending. The load carrying capacity of the corner panel in the slab was enhanced by over 41.0% as V_f gets to 2.50%. The cracking shapes are the same in all the slabs.

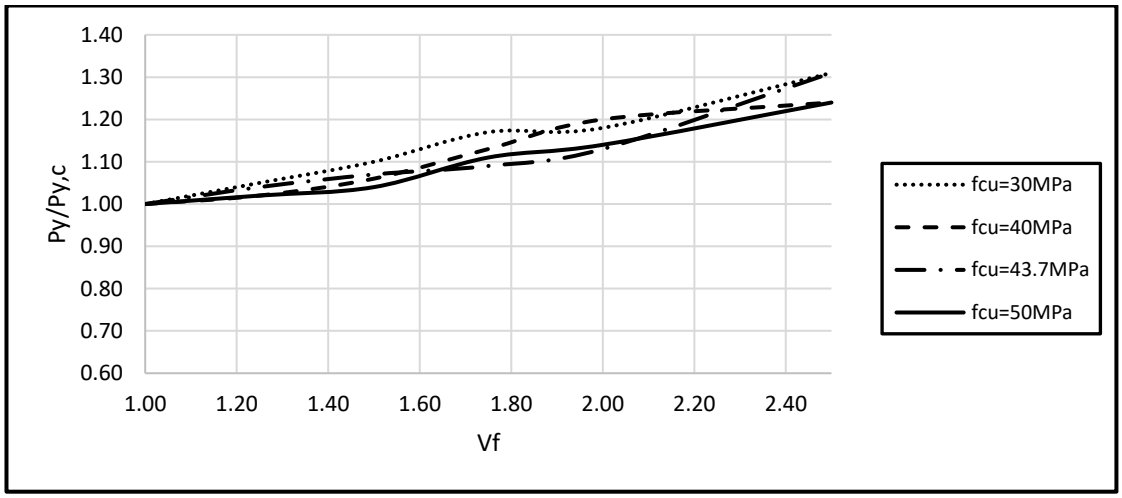

Figure 7.51: Graph of V_f against $P_y/P_{y,c}$ with varying f_{cu} for Corner Panel

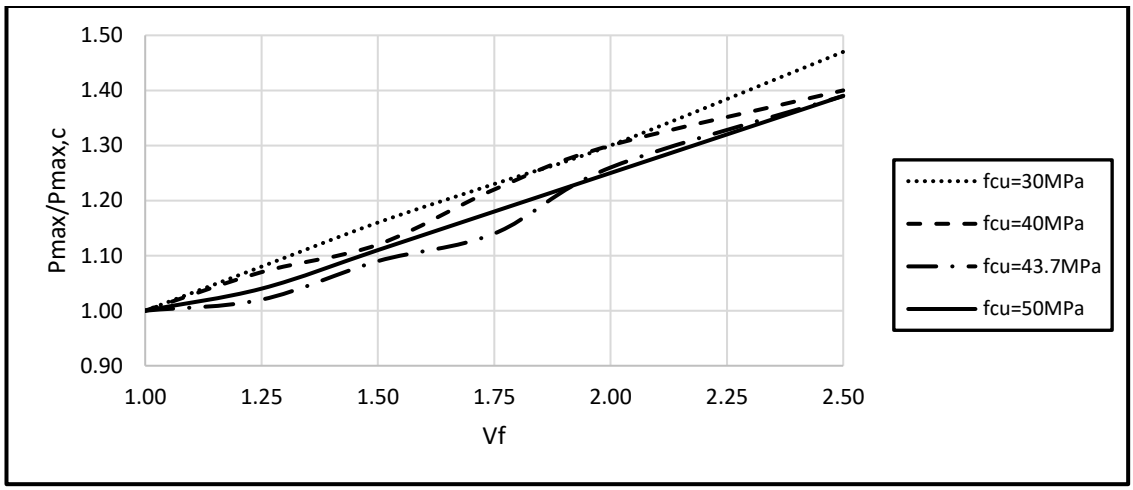

Figure 7.52: Graph of V_f against $P_{max}/P_{max,c}$ with varying f_{cu} for Corner Panel

The graphs of $P_y/P_{y,c}$ and $P_{max}/P_{max,c}$ against V_f are presented in Figures 7.51 and 7.52. An upward trend is seen in the graphs of $P_y/P_{y,c}$ and $P_{max}/P_{max,c}$ as the V_f increases. Additional analyses with span/depth ratio of 33.3 with different characteristic strengths f_{cu} and fibre volume dosage V_f while sustaining other parameters of SFRC and concrete damaged plasticity. The additional analyses will help in creating a design equation for

maximum load carrying capacity and the corresponding displacement. The intended equation will have f_{cu}, V_f, and L/d as variables. Table 7.20 contains the summary of these analyses. The slabs with span/depth ratio of 33.3 failed in bending like the slabs with span/depth ratio of 30.

Table 7.20: Strength and Ductility Ratios for various V_f for Corner Panel

V_f [%]	f_{cu} [MPa]	P_y [kN]	δ_y [mm]	P_{max} [kN]	δ_{max} *[mm]*
1.00	30.0	116.1	10.1	146.6	48.4
1.25		121.3	11.1	158.6	75.2
1.50		127.6	12.6	166.5	87.5
1.75		138.8	15.7	180.0	105.6
2.00		149.6	18.6	190.1	114.0
2.50		146.3	14.9	212.2	131.3
1.00	40.0	141.4	10.4	164.4	75.6
1.25		149.3	11.9	174.8	58.7
1.50		152.2	12.0	185.3	74.7
1.75		162.2	14.7	201.3	75.9
2.00		173.0	17.6	212.2	101.9
2.50		195.7	23.8	237.0	64.2
1.00	50.0	167.6	11.1	192.0	100.4
1.25		170.2	11.2	196.5	95.2
1.50		179.7	13.1	205.7	48.7
1.75		182.8	13.1	217.0	52.0
2.00		193.3	15.7	226.6	70.5
2.50		201.0	15.8	259.3	80.6

7.7.5 Proposed Equation for Yield Load and Maximum Load Carrying Capacity for Corner Panel

Equations are proposed for estimating the yield load, and maximum load carrying capacity of the corner panel in a 9-panel SFRC suspended floor using regression analysis. The equation has the characteristic strength [f_{cu}], fibre volume ratio [V_f], span depth ratio [L/d] in the first equation and displacement [δ] in the second equation as dependent variables.

The yield load [P_y] and maximum load carrying capacity [P_{max}] and the corresponding central displacement of the corner panel using the regression analysis of the MS-Excel is:

$$P_y = 3.58f_{cu} + 36.98V_f - 0.79\,{}^{L}/_{d} \quad \text{- Eqn. 7.9}$$

$$P_y = 13.14\delta y \quad \text{- Eqn. 7.10}$$

$$P_{max} = 3.25f_{cu} + 61.4V_f - 0.34\,{}^{L}/_{d} \quad \text{- Eqn. 7.11}$$

$$P_{max} = 6.85\delta max + 45.55 \quad \text{- Eqn. 7.12}$$

Where L – Span of the panel

d – Overall depth of the panel

δ – central displacement

Appendix B6 contains the input data and the summary of the regression analysis result

7.8 Comparison with Existing Guidelines and Codes using Middle Panel

Table 7.21 shows the results of FEA and existing design guidelines and codes using the middle panel. Using a fibre dosage of 1.25% to determine the response of the slab when loaded at the middle panel, the results show that the equation derived for the estimation of maximum carrying load through FEA is in agreement with the experimental result for the slab and falls within the acceptable variation of 15% of the experimental value. The slab depth is 200mm.

Table 7.21: Comparison with Existing Guidelines

Design Guideline	Formula for Moment	Load [kN]	Remarks
Experiment [Yield Load]		80.00	
Experiment [Max Load]		472.00	
TR 34	$Q_t \frac{L_e}{4} + q_u \frac{L_e^2}{8}$	556.49	Over estimated by 17.9% of Max Load
Swedish	$\frac{f_{fld}.h^2}{6}$	31.26	Under estimated by 60.9% of Yield Load
fib MC 2010	$\frac{f_{Ftu} b h_{sp}^2}{2}$	562.68	Over estimated by 19.2% of Max Load
TR 63	$08 f_{cd} f_{td} bh^2 \left[0.5 + \frac{0.1 f_{td}}{0.8 f_{cd} + f_{td}}\right] / [0.8 f_{cd} + f_{td}]$	543.21	Over estimated by 15.0% of Max Load
Dutch Code NEN 6720	$\alpha n l^2$	142.56	Over estimated by 78.2% of Yield Load
RILEM TC 162	$\frac{F_2}{2}\frac{L}{2}$	84.40	Over estimated by 5.5% of Yield Load
Proposed FEA Equation [Yield Load]	$P_y = 4.09 f_{cu} + 61.09 V_f - 20.37\, {}^{L}/_{d} + 636.89$	79.65	Under estimated by 0.44% of Yield Load
Proposed FEA Equation	$P_{max} = 5.98 f_{cu} + 75.45 V_f - 45.26\, {}^{L}/_{d} + 1473.01$	470.85	Under estimated by 0.2% of Max Load

The comparison of the Experiential work, the FEA and existing guidelines as shown in Table 7.21 revealed that some guidelines [RILEM TC 162, Dutch Code NEN 6720 and Swedish] are close to yield load while the others [TR 34, fib MC 2010 and TR 63] are close to the maximum carrying load capacity of the experimental result. The results of the comparison show that the FEA has the closest value to the experimental value. It also shows the reliability of the equation derived from regression analysis.

7.9 Conclusions

This chapter contains the results of the parametric studies on a 9-panel steel-fibre reinforced concrete suspended slabs with loads at the ultimate limit state considered at the middle, edge and corner panels [Figure 7.5]. The parametric studies include a change in V_f [1.00% to 2.50%], f_{ck} [30MPa, 40MPa, 43.7MPa and 50MPa] and the depth of the slab [180mm, 200mm and 220mm for the middle panel]. All other material and plasticity parameters were kept the same. The slabs were reinforced with steel-fibres [without any rebar]. For each of the panels, calibration was done using the experimental data to determine the accuracy of the FEA results. The full parametric study was then carried out after establishing a good agreement between the FEA and the experimental results. From the results obtained from the FEA analyses,

- There is a consistent rise in the strength of the slabs as the fibre dosage increases.
- It can be observed that steel-fibres minimise crack width opening by controlling the cracking.
- For the middle panel, the cracks developed in two legs at approximately angle 45^0 to each other at the soffit of the panel, and this continues to reduce as the fibre volume increases. There is an increase in strength as the fibre dosage increases. This is not so for ductility, which experiences a decline as fibre dosage increases up to 2.50% and then rise at V_f=2.50%.
- In the edge panel, the cracks develop in a radial arc at a radius R to the point of load application. The radial cracks propagate from external support to the

internal one. Likewise, there are cracks at the point of load application which reduces in size as the fibre dosage increases. The width of the cracks reduces as the fibre dosage increases. The ductility was the same for fibre dosage ≤ 1.75% and fall in its value as the fibre dosage approach 2.50%.

- Also, in the corner panel, the cracks propagate in radial form around three supports surrounding the loading point. The is also cracks under the point at which the load was applied. As the fibre dosage increases, the areas covered by the cracks reduces, confirming that the steel-fibres bridge the cracks as the form. The ductility ratio reduces as the fibre dosage increases, but there is a steady increase in strength of the slabs.

Comparing the FEA with existing design guidelines show that the guidelines are either over conservative or overestimated when compared with the experimental result.

Chapter 8: Conclusions and Recommendations

8.1 Summary of Research Work

8.1 Highlights of Research Work

There are some advantages in the design of elevated SFRC slabs. This research work aimed at investigating the post-cracking response of the analysis and design of elevated SFRC slabs. To appreciate the work done in the past on SFRC slabs, a wide-ranging review of the literature was undertaken. Based on the review, some deductions were made as follows:

- Fibres are made of different materials and come in different shapes of which the steel-fibres with hook-end or crimped body are the most deployed in the industry and researches. Because of their irregular shapes, they possess high pull-out resistance. The anchorage mechanism and pull-out resistance provided during crack propagation are the vital factors in the performance of SFRC. Early researches have shown that steel-fibres have an insignificant impact on the compressive behaviour of RC, so they are assumed to be the same as that of plain concrete.
- The post-cracking tensile behaviour of concrete is enhanced by the introduction of steel fibres which prevents the sharp drop witnessed in plain concrete. The SFRC material constitutive models were used to study the post-cracking behaviour. The ABAQUS CDP and Lok and Xiao (1999) model for SFRC were selected for this research work.
- The characteristic and flexural properties of SFRC elements are determined by the uni-axial tension [split] test, the beam [3-point and 4-point] bending tests and the plate test respectively. Some researchers concluded that beam test could not be used to interpret statically indeterminate panel hence the plate test. However, the plate test cannot be used to derive material properties
- Slabs considered are single-panel slabs, elevated slab and pile-supported slab. The existing designs methods of the pile-supported slabs are by the elastic and yield-line methods. Various design guidelines examined are found to be based on the yield-line method and the elastic method. The YLM is often used for both the design of pile-supported and elevated slabs.

- There are shortcomings in the design methods in use for SFRC slabs. The YLM considered most efficient for pile-supported slabs is deficient in the choice of design bending moment. Additional steel-fibres in the matrix will not increase the peak load in the elastic method.
- Case study 1 consists of three [3] experimental works on single-panels with different support conditions [isolated, continuous and semi-continuous]. Case study 2 is the 4-panel pile-supported SFRC slab with and without rebar. Finally, case study 3 is the 9-panel elevated slab. All the slabs were placed under concentrated loading at the middle. Three cases were considered in the 9-panel slab.
- Calibration works were carried out on the FE models to determine the most appropriate methods to us. The parametric results are presented in load-displacement and strength ratios graphs. From these, the loads [yield and peak] with their corresponding central displacements and material [f_{cu}] and physical [span (L) and depth (d)] properties of slab are used to develop equations using regression analysis in MS Excel.

8.2 Summary of Conclusions

Observations on each case are presented in their respective sections in this report. However, the summary of the significant findings are presented herewith:

- In this research work, The ABAQUS CDP and the constitutive model developed by Lok and Xiao (1999) has proved very valuable in determining the responses [yield and ultimate load capacity, central displacement, stress distributions, deflected shapes and crack patterns] of the whole test specimen [beams and slabs]. The predictions from the two models were in good agreement with the experimental values [up to 99.9% in agreement with the yield and peak loads]. The two models were adopted for the entire case studies.
- Findings from Case Study 1 indicate that the load-carrying capacity of the single-plate improved as the volume of steel fibres increases by 73% from fibre dosage of 1.00% to 2.50%. Likewise, the strength, stiffness and reduction in crack formation were much improved, thus achieving a ductile failure mode. It was

noted that the crack opening was controlled by the fibres bridging the opening as the fibre dosage increases, thus making the panels to become stiffer with less displacement.

- In Case Study 1, as the fibres dosage increases, ductility was improved. Interestingly, the different characteristic strengths produce an increase in ductility and strength, which shows that the higher the characteristic strength of the SFRC matrix, the higher the ductility and strength. On the other hand, there was an increase in the strength as the fibre volume increases. Categorically, it has been established that the addition of steel fibres enhances the load-carrying capacity of the single plates and a more ductile response. This also leads to a rise in ductility and strength enhancement.
- The results of the studies on the statically indeterminate pile-supported SFRC 4-panel slab without rebar under concentrated load show that the strength of the slabs increases with the increase in fibre dosage. Further observations revealed that the addition of fibres up to an optimum fibre dosage leads to an enhancement in stiffness and ductility of the SFRC slabs. The ductility is observed to remain the same after an optimum fibre dosage. Similarly, as the f_{cu} increases the strength ratio also increases. Effective crack control is achieved as the fibre dosage increases.
- The provisions of three-6mm rebar over the piles in addition to the SFRC matrix produce a strain hardening post-cracking behaviour. Strength and stiffness get higher as the fibre dosage increases. Ductility, on the other hand, reduces after an optimum value of fibre dosage. The addition of the rebar enhances the load carrying capacity of the slab. Moreover, the rebar also guides against the progressive collapse of the slab. It is also observed that the increase in f_{ck} leads to increases in the strength of the slabs.
- Conclusively, it can be established that steel fibres improve the strength, stiffness and ductility of the pile-supported 4-panel slabs [with or without rebar] under concentrated loading condition. Thus, the post-cracking behaviour of the SFRC slabs [with or without rebar] is enhanced and crack propagation mitigated.

- The parametric studies [V_f (1.00% to 2.50%), f_{ck} (30MPa, 40MPa, 43.7MPa, and 50MPa) and the depth of the slab (180mm, 200mm and 220mm)]on a 9-panel SFRC suspended slabs with loadings at the ULS considered at the middle, edge and corner panels have the following results from the FEA analyses:

    - The FEA agrees with the experimental results considering the load-displacement curve in the validation work.
    - As the fibre dosage increases, a consistent rise in the strength of the slabs is also noticed.
    - It can also be seen that steel-fibres controlling the cracking minimise that crack width opening. Crack development in all the three cases shows a considerable reduction as the fibre dosage increases.
    - There is an increase in strength as the fibre dosage increases in all the three panels considered. As the fibre dosage increases, the cracks areas reduces, confirming that the steel-fibres bridge the cracks as they appear. There is a steady increase in strength of the slabs.

Comparing the FEA and existing design guidelines with the experimental result, some of the guidelines provisions are in agreement with the yield load and others with maximum load carrying capacity of the experimental works, and this is so because of the methods [YLM and elastic limit] upon which they were formulated. The equations proposed through the FEA produces results which are within 10% of the experimental results.

In the preliminary works on studying relevant literature and the cases considered in this thesis, the objectives of the research work have been satisfactorily met which has led to the

- Critical examination of current design guidelines and numerical models
- Production of load-displacement curves
- Comparing the FEA predictions with the experimental and design guidelines results.

8.3 Recommendations and Future Work

This research work has contributed to the present knowledge on SFRC suspended floors and opened up new areas for further research works. Some areas are yet to be considered particularly in the actual conducting physical experiment, and these are but not limited to the following:

- Experimental work to determine the significance of the distribution of the steel-fibres in the post-cracking behaviour of elevated slabs
- The entire work on elevated slabs can be considered under cyclic loading to cater for seismic effect on structural elements
- Further works involving different types of fibre geometry, notably the 4D and 5D of hook-end steel fibre should be explored.
- Exploring other natural materials, particularly those found in Nigeria for their suitability in the design of suspended slab.
- Extending the present research to include other depths and spans of the slabs in other to propose a design consideration that will be extensive in coverage.

References

Author (2009)*: ABAQUS Analysis user's manual*.

Abbas, A., Syed Mohsin, S. and Cotsovos, D. (2014a) 'Seismic response of steel fibre reinforced concrete beam-column joints', *Engineering Structure,* 59, pp. 261-283.

Abbas, A. A., Pavlović, M. and Kotsovos, M. D. (2004) 'Permissible-stress design of ground-floor slabs', *Proceedings of the ICE-Structures and Buildings,* 157(6), pp. 369-384.

Abbas, A. A., Syed Mohsin, S. M., Cotsovos, D. M. and Ruiz-Teran, A. M. (2014b) 'Shear behaviour of steel-fibre-reinforced concrete simply supported beams', *Proceedings of the ICE - Structures and Buildings,* 167(9), pp. 544-558.

ADINA (2012) *ADINA Theory and Modeling Guide* Watertown, MA: ADINA.

Ahmed, A. (2014) 'Modeling of a reinforced concrete beam subjected to impact vibration using ABAQUS', *International Journal Of Civil And Structural Engineering,* 4(3), pp. 227-236.

Álvarez, A. B. (2013) *Characterization and Modelling of SFRC Element.* PhD, Universitat Politècnica de Catalunya, Barcelona.

America Concrete Institute (1999) *Measurement of Properties of Fibre Reinforced Concrete. Manual Of Concrete Practice* Naples FL: American Concrete Institute.

Author (2002)*: State-of-the-Art Report on Fibre Reinforced Concrete*: American Concrete Institute.

ArcelorMittal (2010) *ArcelorMittal Steel-Fibre Reinforced Concrete Technical Details.* Sheffield: ArcelorMittal.

ArcelorMittal (2011) *Steel Fibre Reinforced Concrete (SFRC) For Industrial Floors Especially Slabs without Joints and Slabs on Piles*: ArcelorMittal.

Banthia, N. and Sappakittipakorn, M. (2007) 'Toughness enhancement in steel fiber reinforced concrete through fiber hybridization', *Cement and Concrete Research,* 37(9), pp. 1366-1372.

Barros, J. and Antunes, J. 'Experimental Characterizationof the Flexural Behaviour of SFRC According to RILEM TC 162-TDF Reccommendations', *Test and Design Methods for Steel Fibre Reinforced Concrete*, Bochum, Germany, 2003: RILEM TC 162-TDF Workshop, 77-90.

Barros, J., Pereira, E. and Santos, S. (2007) 'Lightweight panels of steel fiber-reinforced self-compacting concrete', *Journal of Materials in Civil Engineering,* 19(4), pp. 295-304.

Barros, J. A., Cunha, V. M., Ribeiro, A. F. and Antunes, J. (2005) 'Post-cracking behaviour of steel fibre reinforced concrete', *Materials and Structures,* 38(1), pp. 47-56.

Barros, J. A. O. (2004) 'Post-cracking behaviour of steel fibre reinforced concrete', *Materials and Structures,* 38(275), pp. 47-56.

Barros, J. A. O. 'Technology, Design And Applications Of SFRCSCC', *Fibre Concrete*, Prague, 8th – 9th September 2011, 1-43.

Barros, J. A. O. and Cruz, J. S. 'Energy Absorption Capacity of SFRC', *IRF'99 : Integrity, Reliability and Failure*, Porto, Portugal: ISISE - Comunicações a Conferências Internacionais.

Barros, J. A. O. and Cruz, J. S. (2001) 'Fracture Energy of SFRC', *Journal of Mechanics of Composite Materials and Structures,* 8(1), pp. 29-45.

Barros, J. A. O. and Figueiras, J. A. (1999) 'Flexural Behavior of Sfrc: Testing and Modeling', *Journal of Materials in Civil Engineering©ASCE,* 11(4), pp. 0331-0339.

Barros, J. A. O. and Figueiras, J. A. (2001) 'Model for the analysis of steel fibre RC slabs on Grade', *Computer and Structures,* 79, pp. 97-106.

Barros, J. A. O., Lourenco, L. A. P., Soltanzadeh, F. and Taheri, M. (2013a) 'Steel fibre reinforced concrete for elements failing in bending and in shear', *Advances in concrete construction,* 1(1), pp. 1-27.

Barros, J. A. O., Lourenço, L. A. P., Soltanzadeh, F. and Taheri, M. (2013b) 'Steel fibre reinforced concrete for elements failing in bending and in shear', *European Journal of Environmental and Civil Engineering*, pp. 1-73.
Barros, J. A. O., Salehian, H., Pires, N. M. M. A. and Gonçalves, D. M. F. (2012) 'Design And Testing Elevated Steel Fibre Reinforced Self-Compacting Concrete Slabs', *BEFIB*.
Barros, J. A. O., Teixeira, M. D. E., Cunha, V. M. C. F., Morais Neto, B. N. and Ventura-Gouveia, A. 'Numerical Modelling Of The Punching Behaviour Of Steel Fibre Reinforced Self Compacting Concrete Flat Slabs', *FIBRE CONCRETE 2013*, Prague, Czech Republic, September 12–13, 2013, 1-15.
Bažant, Z. P. and Cao, Z. (1987) 'Size effect in punching shear failure of slabs', *ACI Structural Journal,* 84(1), pp. 44-53.
Beckett, D. (2004) 'The performance of concrete slabs', *Concrete*, pp. 30-33.
Beddar, M. (2004) 'Fibre-Reinforced Concrete: Past, Present and Future', *Concrete*, pp. 47-49.
Bekaert (2012) *Dramix Brochure.* Belgium: NV Bekaert SA.
Berard, A. 1874a. Improvement in artificial stone. Google Patents.
Berard, A. (1874b) *Improvement in artificial stone*. [Online]. Available at: https://www.google.com/patents/US157903.
Bernard, E. S. (2000) 'Behaviour of round steel fibre reinforced concrete panels under point loads', *Materials and Structures,* 33, pp. 181-188.
Bernardi, P., Cerioni, R. and Michelini, E. (2013) 'Analysis of post-cracking stage in SFRC elements through a non-linear numerical approach', *Engineering Fracture Mechanics,* 108(0), pp. 238-250.
Author (2004)*: Steel fibre reinforced concrete industrial floors on pile foundations - Design and construction*.
Blanco, A., Cavalaro, S., de la Fuente, A., Grünewald, S., Blom, C. and Walraven, J. (2014a) 'Application of FRC constitutive models to modelling of slabs', *Materials and Structures*, pp. 1-17.
Blanco, A., Cavalaro, S., De La Fuente, A., Grünewald, S., Blom, C. and Walraven, J. (2015) 'Application of FRC constitutive models to modelling of slabs', *Materials and Structures,* 48(9), pp. 2943-2959.
Blanco, A., Pujadas, P., Cavalaro, S., de la Fuente, A. and Aguado, A. (2014b) 'Constitutive model for fibre reinforced concrete based on the Barcelona test', *Cement and Concrete Composites,* 53, pp. 327-340.
Blanco, A., Pujadas, P., de la Fuente, A., Cavalaro, S. and Aguado, A. (2013) 'Application of constitutive models in European codes to RC–FRC', *Construction and Building Materials,* 40, pp. 246-259.
Bresler, B. and Scordelis, A. C. 'Shear strength of reinforced concrete beams'. *Journal Proceedings*, 51-74.
British Standard Institute 1994. Eurocode 4: Design of composite steel and concrete structures. Part.
British Standard Institute (1997) 'structural use of concrete Part 1, Code of practice for design and construction', *London: British Standards Institution*.
British Standard Institute (2004) *BS EN 1992, Eurocode 2, Design of concrete structures, Part 1-1: General rules and rules for buildings.* London: British Standard Institute.
Author (2005)*: BS EN 14651-Test method for metallic fibered concrete – Measuring the flexural tensile strength (limit of proportionality (LOP), residual)*. London: British Standard Institute.
British Standard Institute (2006) *BS EN 14889-1-2006 - Fibres for concrete - Steel fibres.* London: British Standard Institution, p. 1.
Cameron, G. (2002) 'Steel-fibre-reinforced pile-supported car park in Belfast', *Concrete*.
Cameron, G. (2003) 'Providing a Floor Slab fit for Rolls-Royce', *Concrete,* (no. 7), pp. 36-37.

Campione, G. (2002) 'The effects of fibers on the confinement models for concrete columns', *Canadian Journal of Civil Engineering,* 29(5), pp. 742-750.
Caratelli, A., Imperatore, S., Meda, A. and Rinaldi, Z. (2016) 'Punching shear behavior of lightweight fiber reinforced concrete slabs', *Composites Part B: Engineering,* 99, pp. 257-265.
Carr, K. (2000) 'Polypropylene and steel fibre combinations', *Concrete*, pp. 60-61.
Cerioni, B. B. R., Meda, A. and Plizzari, G. A. 'Experimental And Numerical Analyses Of Frc Slabs On Grade'. *FraMCoS*, usa.
CHANH, N. V. (1990) 'Steel Fibre-Reinforced-Concrete', *Advances in concrete technology,* 3(Japan Society of Civil Engineers), pp. 108-115.
Chen, S. (2005) 'Strength of steel fibre RC GFS', *Proceedings of the Institution of Civil Engineers Structures & Buildings,* 157.
Choi, K.-K., Kim, S.-D., Truong, G. T. and Choi, I.-R. (2015) 'Punching shear behaviour of shear reinforced concrete slabs', *Proceedings of the ICE - Structures and Buildings,* 168(6), pp. 402-420.
Concrete-Society (2007) *TR63 - Guidance for the design of Steel Fibre Reinforced Concrete* [Design Guidelines], UK: The Concrete Society (ISBN 1-904482-32-5.
Concrete Centre (2006) *The Concrete Centre special issue*: ACIFC. Available at: www.acifc.org (Accessed: March 10, 2016.
Crowther, D. (2009) 'Fibre-Reinforced Concrete - Origin Of The Species', *Concrete*, pp. 22-23.
de Montaignac, R., Massicotte, B., Charron, J.-P. and Nour, A. (2011) 'Design of SFRC structural elements: post-cracking tensile strength measurement', *Materials and Structures,* 45(4), pp. 609-622.
Desayi, P. and Seshadri, H. K. (1996) 'Punching shear strength of flat slab corner column connections. Part 2. Fibre-reinforced concrete connections', *Proc. Instn Civ. Engrs Structs & Bldgs,* 122, pp. 6.
Destree, X. 'Structural application of steel fibre as only reinforcing in free suspended elevated slabs: conditions-design-examples'. *6th International RILEM Symposium on Fibre Reinforced Concretes*: RILEM Publications SARL, 1073-1082.
Destrée, X. (2001) 'Steel fibre reinforcement for suspended slabs', *Concrete*, pp. 58-59.
Destrée, X. 'Concrete Free Suspended Elevated Slabs Reinforced with Only Steel Fibers: Full Scale Testing Results and Conclusions-Design Examples'. *International RILEM Workshop on High Performance Fiber Reinforced Cementitious Composites in Structural Applications*: RILEM Publications SARL, 287-294.
Destrée, X. (2007a) 'Steel-Fibre-Reinforced Pile-Supported Slabs', *Concrete*, pp. 26-27.
Destrée, X. (2007b) 'Structural Steel-Fibre-Reinforced Concrete Construction', *Concrete*, pp. 23-24.
Destrée, X. and Jürgen, M. (2008) 'Steel fibre only reinforced concrete in free suspended elevated slabs: Case studies, design assisted by testing route, comparison to the latest SFRC standard documents', *Tailor Made Concrete Structures*, pp. 437-445.
Destrée, X., Oscarsson, H. and Pettersson, M. 'The suspended foundation slab of the Swedbank arena in Stockholm (Sweden): 16,000 m3 (21,000 cu yd) of steel fiber reinforced concrete'. *American Concrete Institute, ACI Special Publication*, 130-140.
Destrée, X. and Silfwerbrand, J. 'Steel fibre reinforced concrete in free suspended slabs: Case study of the Swedbank Arena in stockholm'. *fib Symposium 2012: Concrete Structures for Sustainable Community - Proceedings*, 97-100.
di Prisco, M., Colombo, M. and Dozio, D. (2013) 'Fibre-reinforced concrete in fib Model Code 2010: principles, models and test validation', *Structural Concrete,* 14(4), pp. 342-361.
Dinh, H. H., Parra-Montesinos, G. J. and Wight, J. K. (2010) 'Shear Behavior of SFRC Beams without Stirrup Reinforcement', *ACI Structural Journal,* 107(5), pp. 597-606.

Døssland, Å. L. (2008) *Fibre Reinforcement in Load Carrying Concrete Structures.* PhD, Norwegian University of Science and Technology, Norway.
Dupont, D. (2003) *Modelling and Experimental Validation of The Constitutive Law (σ−ε) and Cracking Behaviour Of Steel Fibre Reinforced Concrete.* PhD Thesis, KATHOLIEKE UNIVERSITEIT LEUVEN.
Eddy, D. (2003) 'New guide for suspended concrete Ground Floor Slab', *Concrete*, pp. 26-27.
Eddy, D. (2008) 'Fibre-Only Suspended Ground-Floor Slabs - Do They Work', *Concrete*, pp. 14-15.
Edgington, J. (1973a) *Steel Fibre Reinforced Concrete Volume B.* PhD, University of Surrey, UK.
Edgington, J. (1973b) *Steel Fibre Reinforced Concrete Volume B.* University of Surrey.
Engström, B. 2011. Design and analysis of slabs and flat slabs. Division of Structural Engineering, Concrete Structures, Chalmers University of Technology, Göteborg, Sweden.
Fall, D. (2014) *Steel Fibres in Reinforced Concrete Structures of Complex Shapes.* PhD, CHALMERS UNIVERSITY OF TECHNOLOGY, Gothenburg, Sweden.
Fathima, A. and Varghese, S. (2014) 'Behavioral Study Of Steel Fiber And Poly Propylene Fiber Reinforced Concrete', *IMPACT: International Journal of Research in Engineering & Technology,* 2(10), pp. 17-24.
Ferrara, L., Bamonte, P., Caverzan, A., Musa, A. and Sanal, I. 'Testing the Fresh and Hardened SFRSCC'. *BEFIB2012 – Fibre reinforced concrete*, UM, Guimarães, 1-12.
Garcia, J. A. I. and Borrell, C. M. I. (2010) 'Study Of The Viability Of Using Steel Fibre Reinforced Concrete At Pavements', *Concrete Society*.
Ghaffar, A., Chavhan, A. S. and Tatwawadi, R. (2014) 'Steel Fibre Reinforced Concrete', *International Journal of Engineering Trends and Technology (IJETT),* 9(15), pp. 791-797.
Ghosh, S., Bhattacharjya, S. and Chakraborty, S. (2007) 'Compressive behaviour of short-fibre-reinforced concrete', *Magazine of Concrete Research,* 59(8), pp. 567-574.
Goltermann, P. (2013) *Reinforced Concrete Slabs – Analysis and Design*.
Goodchild, C. (2004) 'Design Guidance on Large Area Pours for Suspended Slabs', *Concrete*, pp. 19-20.
Hadi, M. N. S. 'Behaviour of FRC slabs', *Structural Engineering and Construction Conference*, London: Francis Taylor, 407-412.
Hassan, M. K. (2016) *Behaviour of hybrid stainless-carbon steel composite beam-column joints.* Western Sydney University (Australia).
Hedebratt, J. (2012a) *Industrial Fibre Concrete Floors-Experiences and Test on Pile-Supported Slab.* PhD, Royal Institute of Technology (KTH), Stockholm.
Hedebratt, J. (2012b) *Thesis-Industrial FRC Floors-Experiences and Tests on Pile-Supported Slab.* KTH, Stockholm.
Hedebratt, J. and Silfwerbrand, J. 'An Innovative Approach to Design of Pile Supported SFRC Slabs'. *6th RILEM Symposium on Fibre-Reinforced Concretes*, Italy, September 2004: RILEM, 945-954.
Hedebratt, J. and Silfwerbrand, J. (2008) 'Full-scale test on a pile supported floor slab – steel fibre concrete only or in a combination with steel', *Tailor Made Concrete Structures*, pp. 1015-1018.
Hedebratt, J. and Silfwerbrand, J. (2014) 'Full-scale test of a pile supported steel fibre concrete slab', *Materials and structures,* 47(4), pp. 647-666.
Higashiyama, H., Ota, A. and Mizukoshi, M. (2011) 'Design Equation for Punching Shear Capacity of SFRC Slabs', *International Journal of Concrete Structures and Materials,* 5(1), pp. 35-42.
Hillerborg, A., Modéer, M. and Petersson, P.-E. (1976) 'Analysis of crack formation and crack growth in concrete by means of fracture mechanics and finite elements', *Cement and concrete research,* 6(6), pp. 773-781.

Hughes, G. and Speirs, D. (1982) *An investigation of the beam impact problem.*
Hulett, T. and Sketchley, C. (2009) 'Design of Pile-Supported Concrete Industrial Floors', *Concrete*, pp. 45-46.
Author (2007)*: Guide for the Design and Construction of Fiber-Reinforced Concrete Structures*. Rome: Italian National Research Council.
Author (2011)*: Building Code Requirement for Structural Concrete (ACI 318-11) and Commentary*. Farmington Hills, Michigan: America Concrete Institute [Standard].
Author (2007)*: BS EN 14651-2005+A1-2007-Test method for metallic fibre concrete — Measuring the flexural tensile strength (limit of proportionality (LOP), residual)*. UK: British Standard Institute.
Author (1999)*: Interim Guidance On The Design Of Reinforced Concrete Structures Using Fibre Composite Reinforcement*. London: The Institution of Structural Engineers.
Jansson, A. (2008) *Fibres in Reinforced Concrete Structures - Analysis, Experiment and Design.* DEGREE OF LICENTIATE, Chalmers University Of Technology, Göteborg, Sweden.
Jansson, A. (2011) *Effects of Steel Fibres on Cracking in Reinforced Concrete.* PhD, CHALMERS UNIVERSITY OF TECHNOLOGY, Gothenburg, Sweden.
Author (1984)*: JCI-SF4-Method of test for flexural strength and flexural toughmess of fiber reinforced concrete*. Tokyo: Japanese Concrete Institute.
Jensen, S. M. F. (2013) *Numerical Investigation of a Post-tensioned Flat Slab with Steel Fibre Reinforcement.* MSc, Norwegian University of Science and Technology.
Johansen, K. (1972) 'Yield-Line Formulae for Slabs, Cement and Concrete Association', *London, UK*.
Johansson, L. 2003. Lardomar Fran 30 Ars Golvutredningar (Lessons Learned from 30 Years of Concrete Floor Investigation). Stockholm, Sweden: Swedish Cement and Concrete Research Institute.
Kennedy, G. and Goodchild, C. (2003) *Practical Yield Line Design.* Reinforced Concrete Council.
Kennedy, G. and Goodchild, C. H. (2004) *Practical Yield Line Design.* UK: The Concrete Centre.
Khan, Y., Ansari, M. A., Saroj, M., Haider, S. and Kulkarni, S. (2016) 'A Critical Review On Experimental Studies Of Strength And Durability Properties Of Fibre Reinforced Concrete Composite', *International Journal of Research in Engineering and Technology,* 05(03), pp. 20-26.
Kooiman, A. G. (2000) *Modelling steel fibre reinforced concrete for structural design.* TU Delft, Delft University of Technology.
Kooiman, A. G., Veen, C. v. d. and Walraven, J. C. (2000) 'Modelling the post-cracking behaviour of steel fibre reinforced concrete for structural design purposes', *HERON,* 45(4), pp. 275-307.
Kotsovos, M. and Spiliopoulos, K. (1998) 'Modelling of crack closure for finite-element analysis of structural concrete', *Computers & structures,* 69(3), pp. 383-398.
Kotsovos, M. D. (1995) *Structural concrete: finite-element analysis for limit-state design.* Thomas Telford.
Labib, W. and Eden, N. (2004) 'An Investigation Into The Use Of Fibres In Concrete Industrial Ground-Floor Slabs', *SAETAEQUINA*.
Labib, W. A. (2008) *An Experimental Study And Finite Analysis Of Punching Shear Failure In Steel Fibre-Reinforced Concrete Ground-Suspended Floor Slabs.* PhD, Liverpool John Moores University.
Lee, J.-H., Cho, B. and Choi, E. (2017) 'Flexural capacity of fiber reinforced concrete with a consideration of concrete strength and fiber content', *Construction and Building Materials,* 138, pp. 222-231.
Lim, T., Paramasivam, P. and Lee, S. (1987) 'Analytical model for tensile behavior of steel-fiber concrete', *ACI Materials Journal,* 84(4).

Löfgren, I. (2005) *Fibre-reinforced Concrete for Industrial Construction--a fracture mechanics approach to material testing and structural analysis.* Chalmers University of Technology.
Lok, T.-S. and Pei, J.-S. (1998) 'Flexural Behavior of Steel Fibre Reinforced Concrete', *Journal of Materials in civil engineering ASCE,* 10(2), pp. 0086-0097.
Lok, T. S. and Xiao, J. R. (1998) 'Tensile behaviour and moment–curvature relationship of Steel Fibre Reinforced Concrete', *Magazine of Concrete Research,* 50(4), pp. 359-368.
Lok, T. S. and Xiao, J. R. (1999) 'Flexural Strength Assessment of Steel Fiber Reinforced Concrete', *Journal of Materials in Civil Engineering©ASCE,* 11(3), pp. 0188-0196.
Loks, T. S. and Xiao, J. R. (1999) 'Steel-Fibre-Reinforced Concrete Panels Exposed To Air Blast Loading', *Proc. Instn Civ. Engrs Structs & Bldgs,* 134, pp. 319-331.
Lubliner, J., Oliver, J., Oller, S. and Oñate, E. (1989) 'A plastic-damage model for concrete', *International Journal of Solids and Structures,* 25(3), pp. 299-326.
Marčiukaitis, G. and Šalna, R. (2017) 'Calculation of Punching Shear Strength of Steel Fiber Reinforced Concrete Flat Slabs', *Procedia Engineering,* 172, pp. 1110-1114.
Maya, L. F., Fernández Ruiz, M., Muttoni, A. and Foster, S. J. (2012) 'Punching shear strength of steel fibre reinforced concrete slabs', *Engineering Structures,* 40, pp. 83-94.
McCraven, S. 2002. fibers-for-tomorrow. *Concrete Construction.*
Meda, A. (2005) 'Shear behaviour of steel fibre reinforced concrete beams', *Materials and Structures,* 38(277), pp. 343-351.
Metwally, I. M. (2013) 'Prediction of punching shear capacities of two-way concrete slabs reinforced with FRP bars', *HBRC Journal,* 9(2), pp. 125-133.
Mobasher, B. and Destrée, X. 'Design and construction aspects of steel fiber-reinforced concrete elevated slabs'. *American Concrete Institute, ACI Special Publication*, 95-107.
Mobasher, B. and Destrée, X. 'Design and construction aspects of steel fiber-reinforced concrete elevated slabs'. *ACI Fall 2009 Convention*.
Mohsin, S. M. B. S. (2012a) *Behaviour Of Fibre-Reinforced Concrete Structures Under Seismic Loading.* PhD, Imperial College, London.
Mohsin, S. M. B. S. (2012b) *Behaviour Of Fibre-Reinforced Concrete Structures Under Seismic Loading.* PhD, Imperial College, London.
N., B. 2009. Fibre-Reinforced Concrete.
Naaman, A. and Reinhardt, H. 'Setting the stage: toward performance-based classification of FRC composites'. *High Performance Fiber Reinforced Cement Composites*, 1-4.
Naaman, A. E. and Gopalaratnam, V. (1983) 'Impact properties of steel fibre reinforced concrete in bending', *International journal of cement composites and lightweight concrete,* 5(4), pp. 225-233.
Najim, K. B., Saeb, A. and Al-Azzawi, Z. (2018) 'Structural behaviour and fracture energy of recycled steel fibre self-compacting reinforced concrete beams', *Journal of Building Engineering,* 17, pp. 174-182.
Nakov, D. 'Design Charts for SFRC Elevated Slab', *BEFIB2012 – Fibre reinforced concrete*, UM, Guimarães, 1-12.
Narayan, N. T. 2014. Steel Fibre Reinforced Concrete (SFRC)-Area of Application. *The Masterbuilder.*
Neal, F. (2000) 'Design of Steel Fibre Floors - Problems and Pitfalls', *The Structural Engineer,* 78(11), pp. 14-16.
Neto, B. N. M., Barros, J. A. O. and Melo, G. S. (2012) 'The Predictive Performance Of Design Models For The Punching Resistance Of Sfrc Slabs In Inner Column Loading Conditions', *BEFIB*, pp. 1-12.

Nguyen-Minh, L., Rovňák, M., Tran-Quoc, T. and Nguyenkim, K. (2011) 'Punching shear resistance of steel fiber reinforced concrete flat slabs', *Procedia Engineering,* 14, pp. 1830-1837.

Nguyen, T. N., Nguyen, T. T. and Pansuk, W. (2017) 'Experimental study of the punching shear behavior of high performance steel fiber reinforced concrete slabs considering casting directions', *Engineering Structures,* 131, pp. 564-573.

Author (2007)*: Guide for the Design and Construction of Fiber-Reinforced Concrete Structures*. Italy: Italian NRC.

Author (2006)*: NZS 3101: Part 1: The Design of Concrete Structures*. New Zealand: New Zealand Standard Council.

Oikonomou-Mpegetis, S. (2013) *Behaviour and Design of Steel-Fibre Reinforced Concrete Slab.* PhD, Imperial College, London.

Oliveira, F. L. d. (2010) *Design Oriented Constitutive model for Steel Fibre Reinforced Concrete.* PhD, Universitat Politècnica de Catalunya, Barcelona.

Olivito, R. and Zuccarello, F. (2010) 'An experimental study on the tensile strength of steel fiber reinforced concrete', *Composites Part B: Engineering,* 41(3), pp. 246-255.

Ombres, L. (2015) 'Structural performances of reinforced concrete beams strengthened in shear with a cement based fiber composite material', *Composite Structures,* 122, pp. 316-329.

Oslejs, J. (2008) 'New Frontiers for Steel Fibre Reinforced Concrete', *Concrete International*.

Ragi, S. (2015) 'A Comparative And Experimental Study On The Mechanical Properties Of Various Steel And Glass Fiber Reinforced High Strength Concrete', *International Research Journal of Engineering and Technology (IRJET),* 2(4), pp. 5.

Rai, A. and Joshi, D. Y. P. (2014) 'Applications and Properties of Fibre Reinforced Concrete', *Int. Journal of Engineering Research and Applications,* 4(5), pp. 123-131.

Rana, A. (2013) 'Some Studies on Steel Fiber Reinforced Concrete', *International Journal of Emerging Technology and Advanced Engineering,* 3(1), pp. 120-127.

Regan, P. E. (1989) *Behaviour of Reinforced Concrete Flat Slabs*, London: CIRIA.

Richardson, A. (2008) 'Post Crack Flexural Toughness In Steel Fabric And Fibres Reinforced Concrete', *Northumbria Working Paper Series: Interdisciplinary Studies in the Built and Virtual Environment*.

RILEM, T. (2000) 'RILEM TC 162-TDF - Test and design methods for SFRC - design method', *Materials and Structures,* 33, pp. 75-81.

RILEM, T. (2001) 'RILEM TC 162-TDF - Test and design methods for SFRC - Uni-axial tension test', *Materials and Structures,* 34, pp. 3-6.

RILEM, T. (2002a) 'RILEM TC 162-TDF - Test and design methods for SFRC - principles and applications', *Materials and Structures,* 35, pp. 262-278.

RILEM, T. (2002b) 'RILEM TC 162-TDF - Test and design methods for Steel Fibre Reinforced Concrete - Bending test - final Recommendation', *Materials and Structures,* 35, pp. 579-528.

RILEM, T. (2003) 'RILEM TC 162-TDF - Test and design methods for SFRC - design method - finaL Recommendation', *Materials and Structures,* 36, pp. 560-567.

Roesler, J. R. and Gaedicke, M. C. (2004) 'Technical Note 3 - Fiber Reinforced Concrete', *Center of Excellence for Airport Technology*, pp. 1-11.

Rossi, P. (1999) 'A model for cracking in fibre-reinforced concrete structures', *Materials and Structures,* 32, pp. 125-130.

Salehian, H. and Barros, J. A. (2017) 'Prediction of the load carrying capacity of elevated steel fibre reinforced concrete slabs', *Composite Structures,* 170, pp. 169-191.

Salehian, H. and Barros, J. A. O. (2015) 'Assessment of the performance of steel fibre reinforced self-compacting concrete in elevated slabs', *Cement and Concrete Composites,* 55, pp. 268-280.

Sarzalejo, A. G., Rossi, B., Perri, G., Winterberg, R. and Aristeguieta, R. E. P. (2008) *Fibers as structural element for the reinforcement of concrete -Technical Manual*.
Shaaban, A. and Gesund, H. (1994) 'Punching shear strength of steel fiber reinforced concrete flat plates', *ACI Structural Journal,* 91(4).
Silfwerbrand, J. (2008) 'Codes for SFRC structures –A Swedish proposal', *Tailor Made Concrete Structures*.
Simpson, D. (2003) 'Design of suspended slabs on ground', *Concrete Advice*.
Singh, H. (2015) 'Steel Fibers as the Only Reinforcement in Concrete Slabs: Flexural Response and Design Chart', *Structural Engineering International,* 25(4), pp. 432-441.
Singh, H. (2017) 'Analysis and Design of SFRC Slabs', *Steel Fiber Reinforced Concrete*: Springer, pp. 123-158.
Soranakom, C. and Mobasher, B. 'Flexural modeling of strain softening and strain hardening fiber reinforced concrete'. *Proceeding of the Fifth International RILEM Workshop, High Performance Fiber Reinforced Cement Composites (HPFRCC5)*, 155-164.
Soranakom, C. and Mobasher, B. (2009) 'Flexural design of fiber-reinforced concrete', *ACI Materials Journal,* 106(5), pp. 461.
Soranakom, C., Mobasher, B. and Destrée, X. (2007) 'Numerical simulation of FRC round panel tests and full-scale elevated slabs', *Deflection and Stiffness Issues in FRC and Thin Structural Elements*, pp. 31-40.
Sukontasukkul, P. 'Flexural Behaviour of Circular Steel Fibre Reinforced Concrete Plates'. *Proceedings of the International Symposium dedicated to Professor Surendra Shah, Northwestern University, USA*, 193-200.
Swamy, R. N. 'The Technology Of Steel Fibre Reinforced Concrete For Practical Applications'. *Proc. Instn Civ. Engrs*, 143-159.
Swamy, R. N. and Lankard, D. R. (1974) 'Some practical applications of steel fibre reinforced concrete', *Proceedings,* 56, pp. 143-159.
Teixeira, M. D. E., Barros, J. A. O., Cunha, V. M. C. F., Moraes-Neto, B. N. and Ventura-Gouveia, A. (2015) 'Numerical simulation of the punching shear behaviour of self-compacting fibre reinforced flat slabs', *Construction and Building Materials,* 74, pp. 25-36.
TGB NEN 6720 (1995) *Regulations for concrete–Structural requirements and calculation methods*: Tech. Rep. NEN 6720, Nederlands Normalisatieinstituut.
Author (2003)*: TR34 Concrete IGF - third edition - 2003*. UK: The Concrete Society.
Author (2009) *64: TR64 - Guide to the design and construction of RC flat slabs*: The Concrete Society [Book].
Author (2014)*: TR 34 - Concrete Industrial Ground Floors*. Surrey: The Concrete Society.
Author (2007) *63: TR63 - Guidance for the design of Steel Fibre Reinforced Concrete*. UK: The Concrete Society [Design Guidelines].
Author (2007) *64: TR64-Guide to the design and construction of RC flat slabs*. Surrey: The Concrete Society.
Thomas, N. (1985) *The Holy Bible. New King James Version, Compact Reference Edition*: Thomas, N.
Thooft, H. 'Design of Steel Fibre Reinforced Floors on Foundation Piles'. *Specialist Techniques and Materials for Concrete Construction: Proceedings of the International Conference Held at the University of Dundee, Scotland, UK on 8-10 September 1999*: Thomas Telford, 343.
Thooft, H. (2000) 'Structural behaviour of Steel Fibre Reinforced pile-supported concrete floors', *Concrete*.
Tlemat, H., Pilakoutas, K. and Neocleous, K. (2006a) 'Modelling of SFRC using inverse finite element analysis', *Materials and Structures,* 39(2), pp. 221-233.
Tlemat, H., Pilakoutas, K. and Neocleous, K. (2006b) 'Stress-strain characteristic of SFRC using recycled fibres', *Materials and Structures,* 39, pp. 365-377.

Van Chanh, N. 'Steel fiber reinforced concrete'. *Faculty of Civil Engineering Ho chi minh City university of Technology. Seminar Material*, 108-116.

Vandewalle, L., Rossi, P. and Chanvillard, G. 'Design method for steel fiber reinforced concrete proposed by RILEM TC 162-TDF'. *Fifth International RILEM Symposium on Fibre-Reinforced Concrete (FRC)*: RILEM Publications SARL, 51-64.

Viney, T. (2007) 'Piled floor design - the Dutch method', *Concrete*, pp. 2.

Vollum, R. (2007) 'Design of steel-fibre-reinforced pile-supported slabs', *Concrete*, pp. 12-14.

Wahalathantri, B. L., Thambiratnam, D. P., Chan, T. H. T. and Fawzia, S. 'A Material Model For Flexural Crack Simulation In Rc Elements Using Abaqus'. *Infrastructure, Transport and Urban Development - eddBE2011 Proceedings*: Queensland University of Technology, Queensland University of Technology, Brisbane, Qld, 260-264.

Wang, N., Mindess, S. and Ko, K. (1996) 'Fibre reinforced concrete beams under impact loading', *Cement and Concrete Research,* 26(3), pp. 363-376.

Xie, J. H., Guo, Y. C., Liu, L. S. and Xie, Z. H. (2015) 'Compressive and flexural behaviours of a new steel-fibre-reinforced recycled aggregate concrete with crumb rubber', *Construction and Building Materials,* 79, pp. 263-272.

Zollo, R. F. (1997) 'Fiber-reinforced concrete: an overview after 30 years of development', *Cement and Concrete Composites,* 19(2), pp. 107-122.

Appendix

Appendix 1

Step by Step for RC Modelling with ADINA

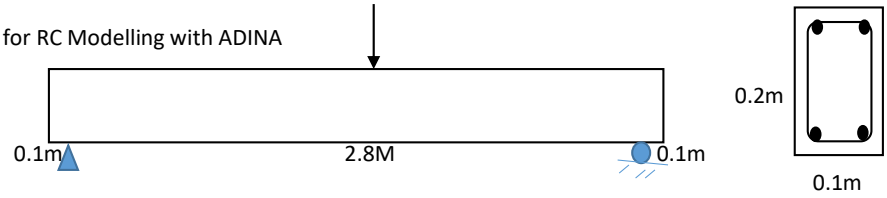

Invoke ADINA AUI and Click on Define Points

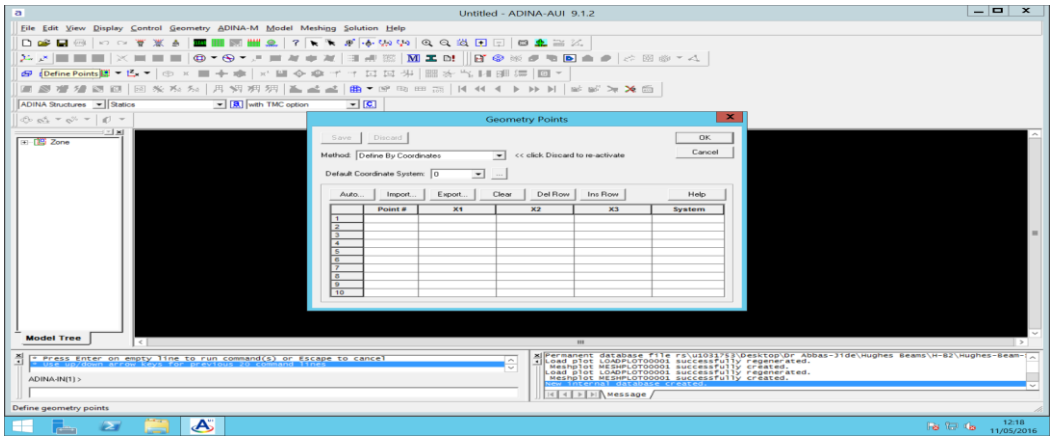

Enter the coordinates of the points and press ok

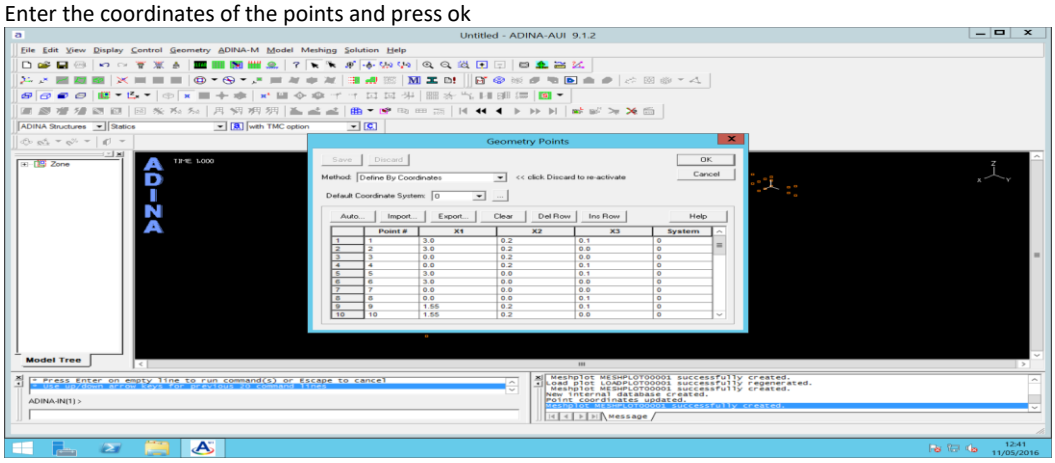

Click on define volumes, to express the beam and supports volumes

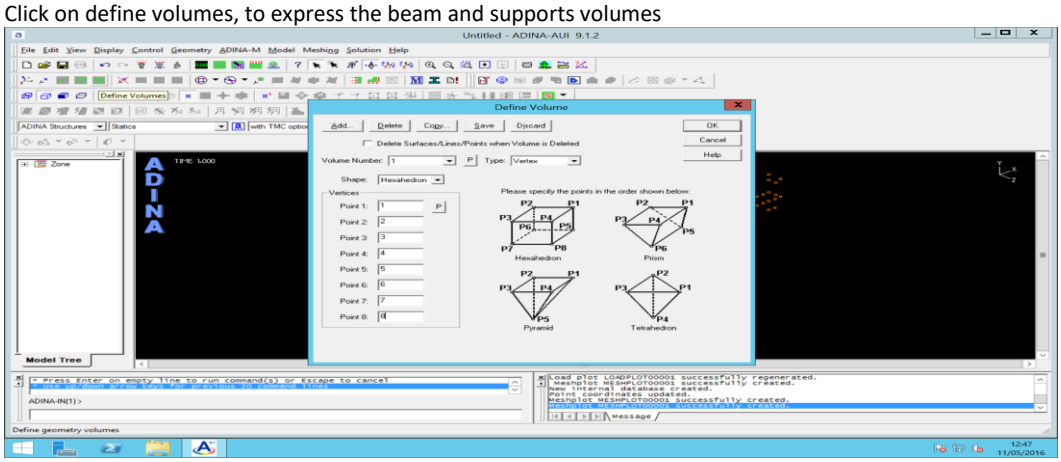

Click on define surface to define the Load-Plate and click add on the pop-up window, enter the coordinate of the plate 9, 10, 11, 12

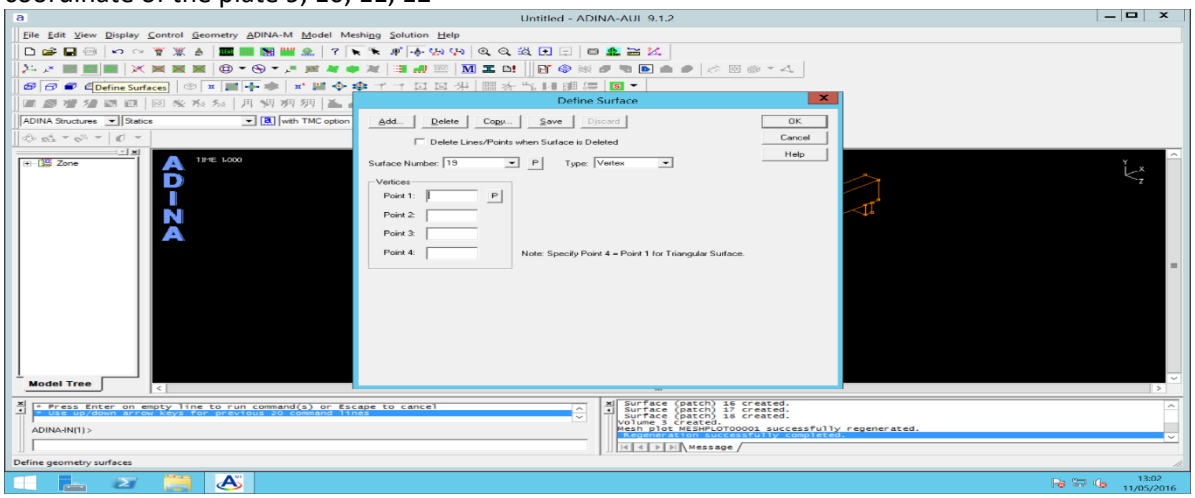

Click on define lines to define the rebar as lines 41 Pts[29,30], 42 Pts[31,32], 43 Pts[33,34] and 44 Pts[35,36]

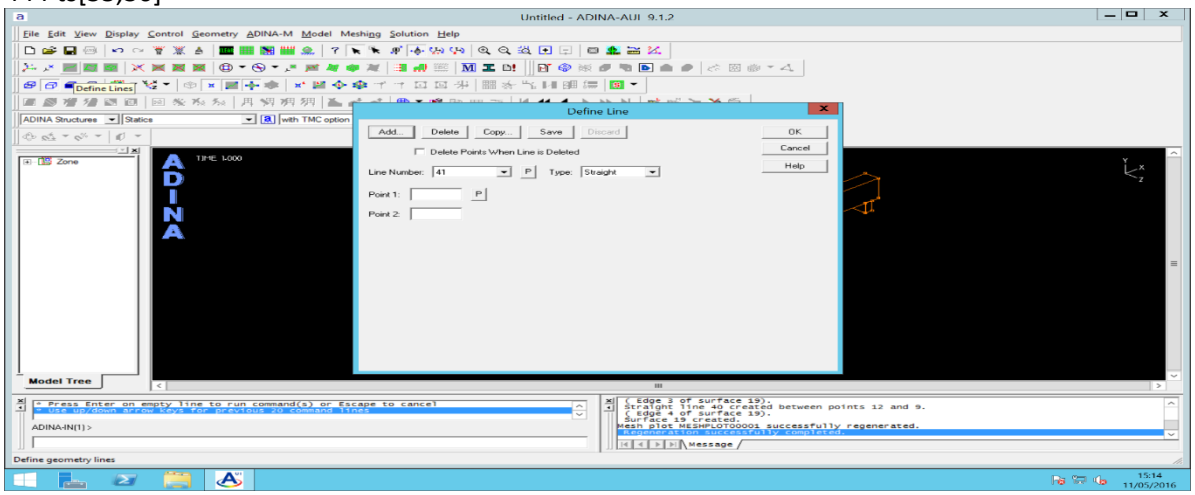

Click add on define lines to define the stirrups [links]. First use lines to join the nodes together. Lines 45 Pts[29,31], 46 Pts[31,35], 47 Pts[35,33], and 48 Pts[33,29]. Click add again for line number 49 and change type to Combined. Then enter 45, 46, 47, 48 and save

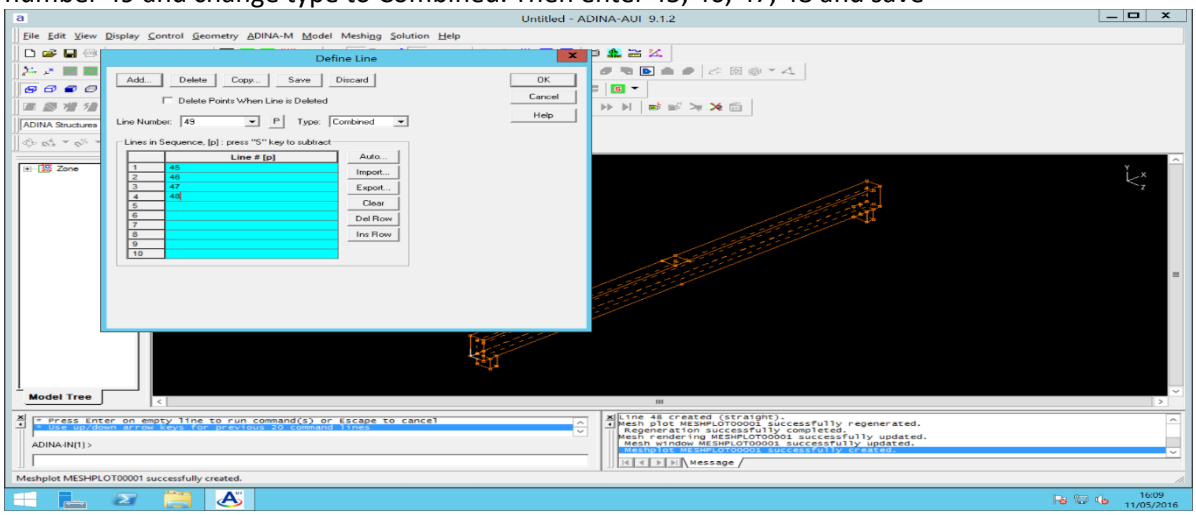

To transform the links into the entire beam, click add again on define lines, then change type to transformed. The parent line is 49 [line number of the first link]. Input the number of links to be provided in Number of Copies and click the button in front of transformation label to have define Transformation window popping out. Input the links spacing in X. Click add. Click the button in front of the Coordinate System and click add in the pop up window. Specify the start of the link as the origin and in this case, X=0.025, Y=0.025 and Z=0.025

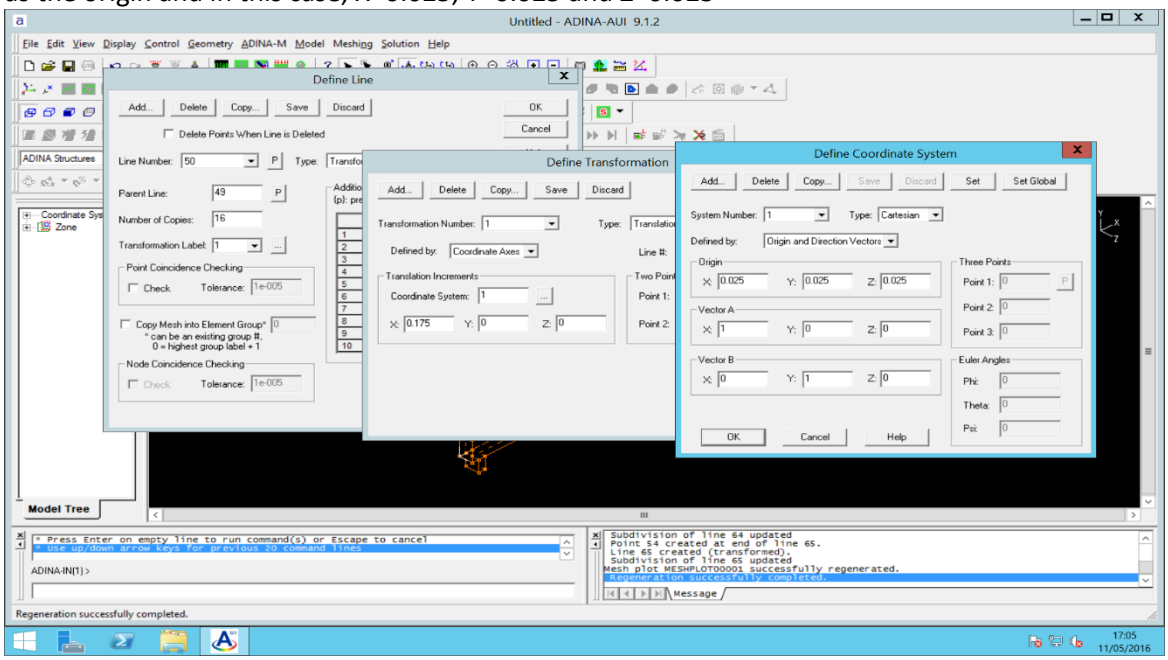

Then specify boundary conditions

The base of the support will be fixed [Surfaces 12 & 18] and the contact surfaces [7, 13 & 19] between the support, load plate and beam would be allowed freedom in Y. Click on apply fixity and change apply to, to face/surface

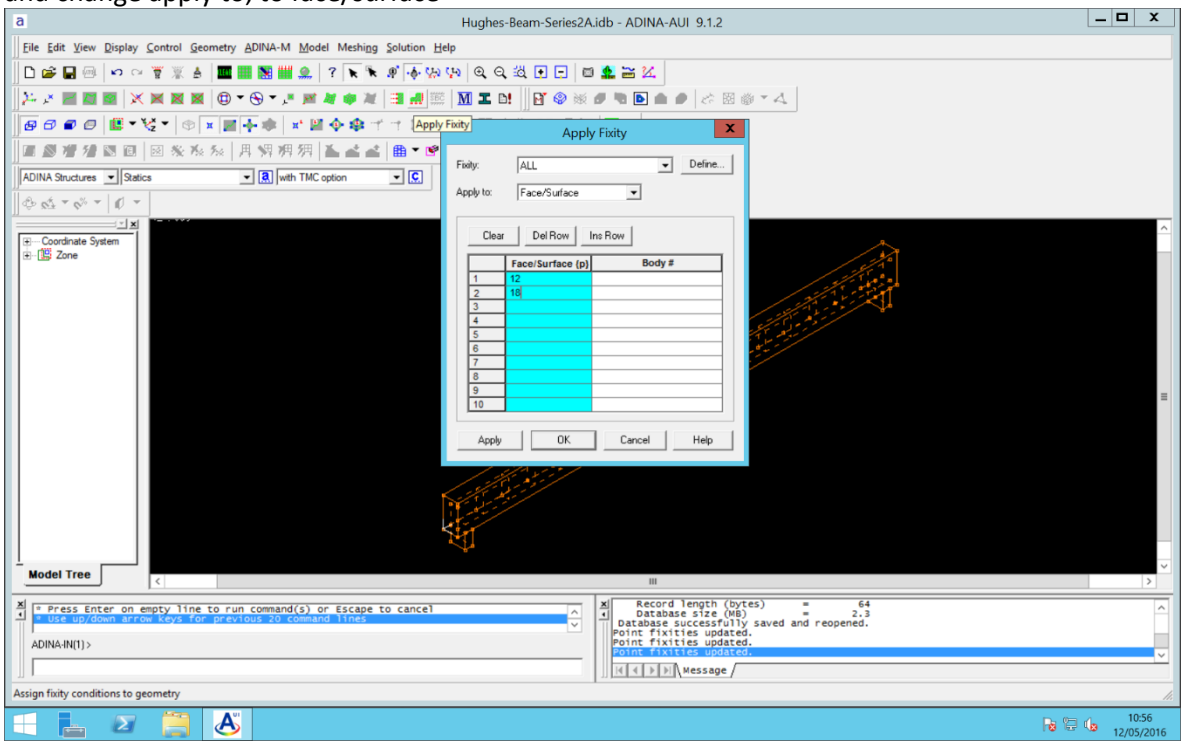

Next are the material properties
Click on Manage Material

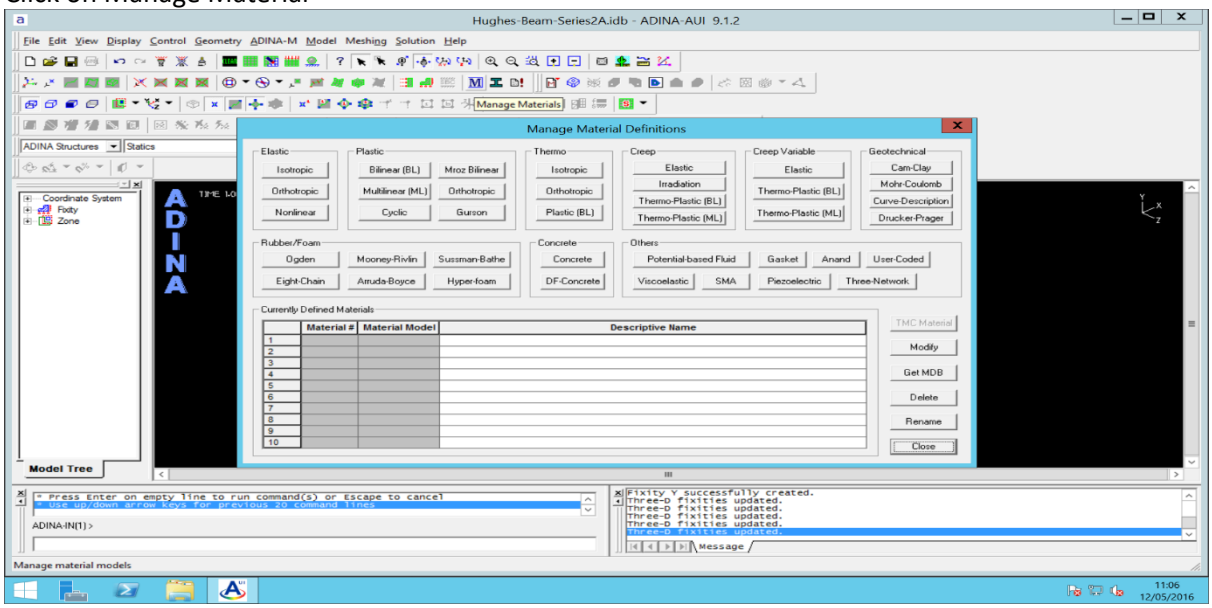

For steel plate and support
Click Elastic Isotropic, and click Add

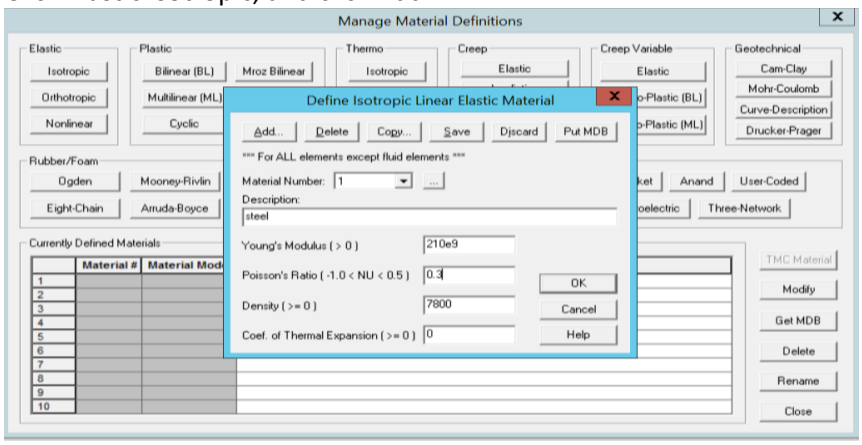

For Rebar, click Plastic Bilinear and click Add

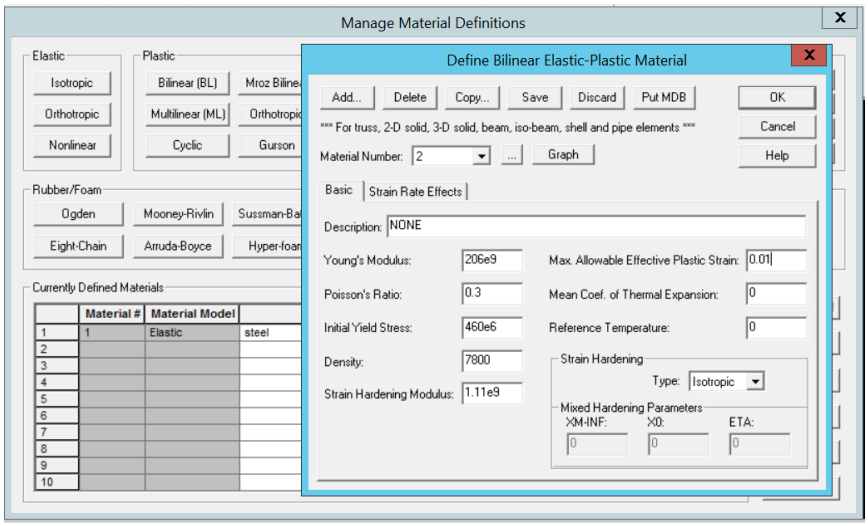

For Concrete properties, click on concrete and click Add

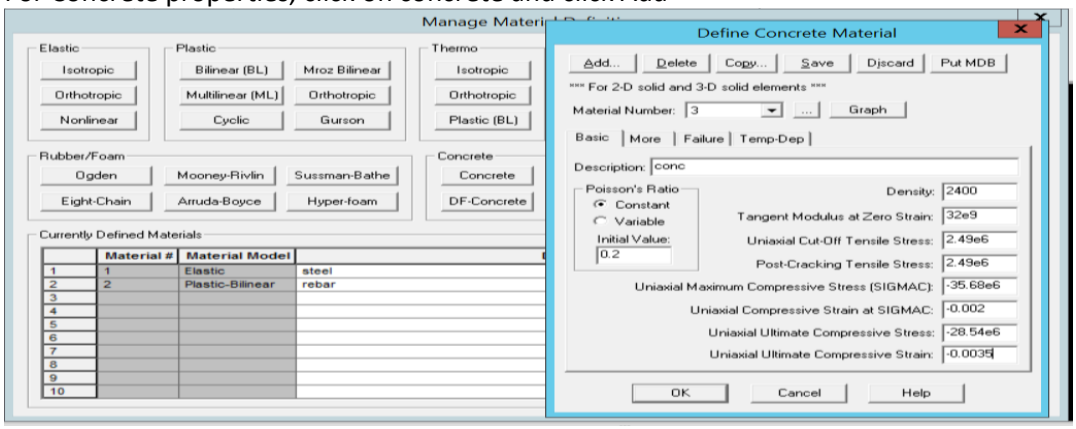

Close the Manage Material Definitions

Define the Element Group

For supports, click Add and pick a 3D Solid and specify thickness

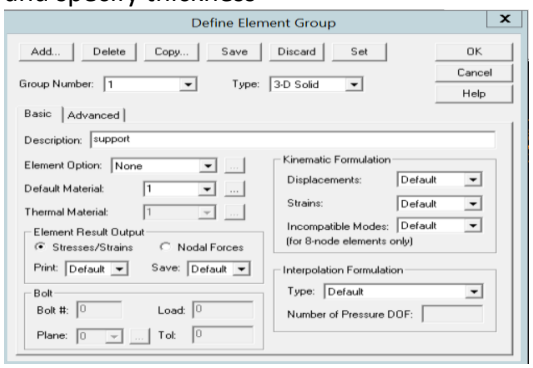

Click Add and choose a Shell for Load Plate

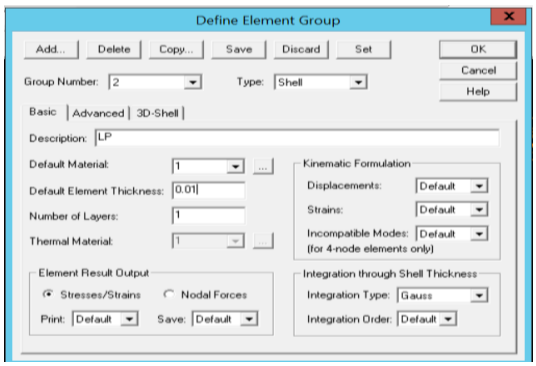

Click Add and choose Truss for Rebar

Change the Material to 2 and provide the area of the rebar

Click Advanced Tap and change Element Option to Use as Rebar. Specify the line number that represent rebar

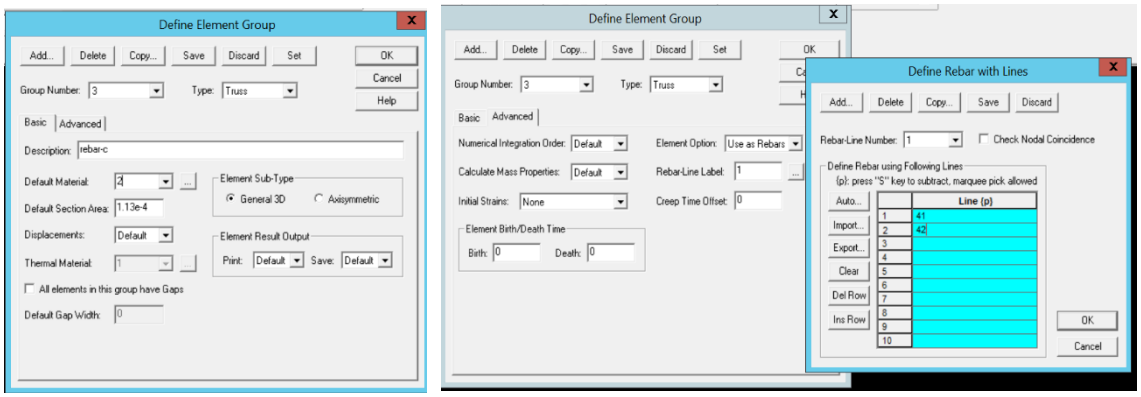

Do same for other Rebar and also for the Beam use 3-D Solid

Next is to define the Analysis Controls

Click on Control, from the drop down, click ‘Analysis Assumptions’ and pick ‘Kinematics’. From the pop-up window, click ok

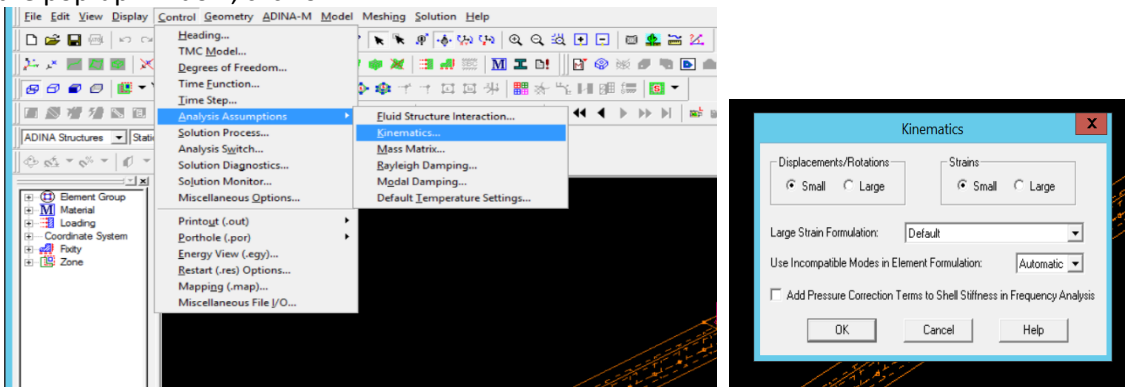

Click control again and from the drop-down menu, click Solution Process. Click Iteration Method and set the ‘Use of Line Searches to Yes and click ok. Click also on ‘Iteration Tolerance’, change the ‘Convergence Criteria’ to Displacement, and then click ok. And click ok on Solution Process

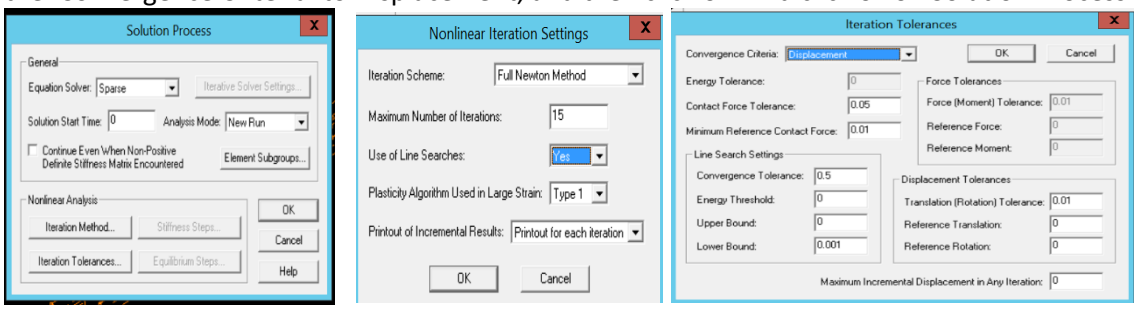

Next click control again and set the Time Function and Time Step

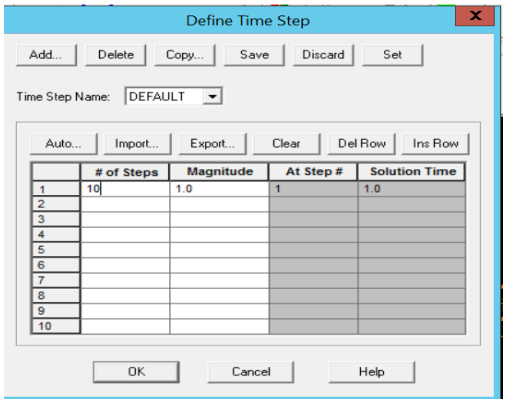

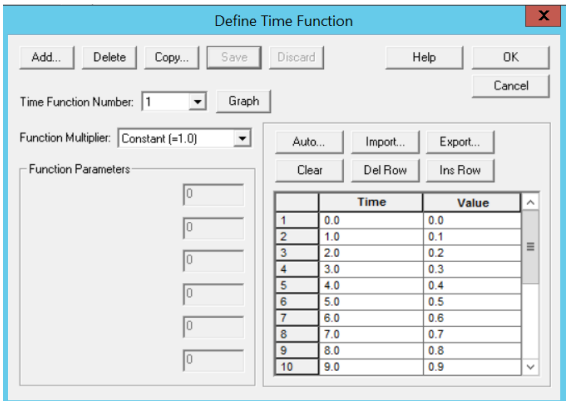

Meshing the Model

Click on Meshing, Mesh Density and complete Model. Subdivision Mode: Use End-Point Sizes

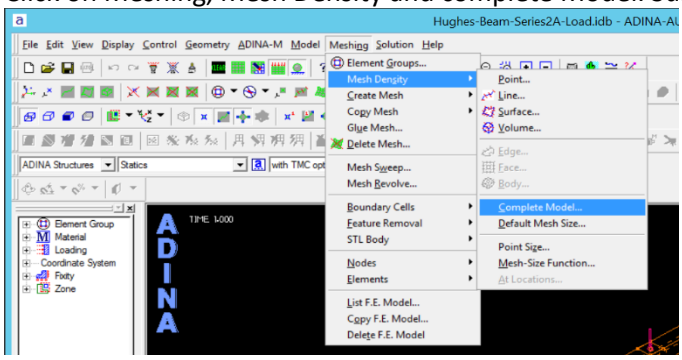

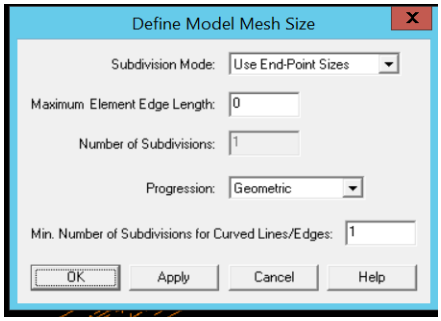

Click on Meshing again, Mesh Density and Point size. Pick ‘All Geometry Points’ from ‘Points Defined from’ and specify the mesh size in Maximum. Click Apply and then OK

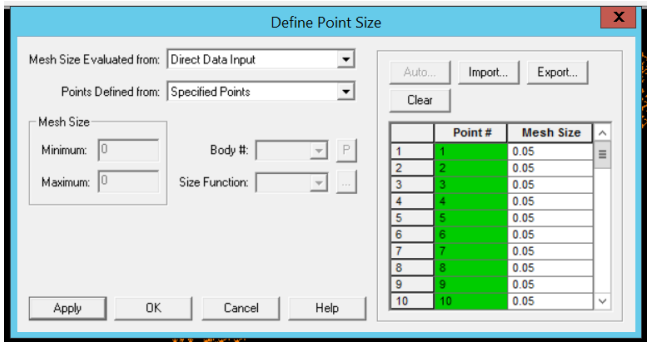

Click on Mesh Volume and select the Element Group and the Volume number

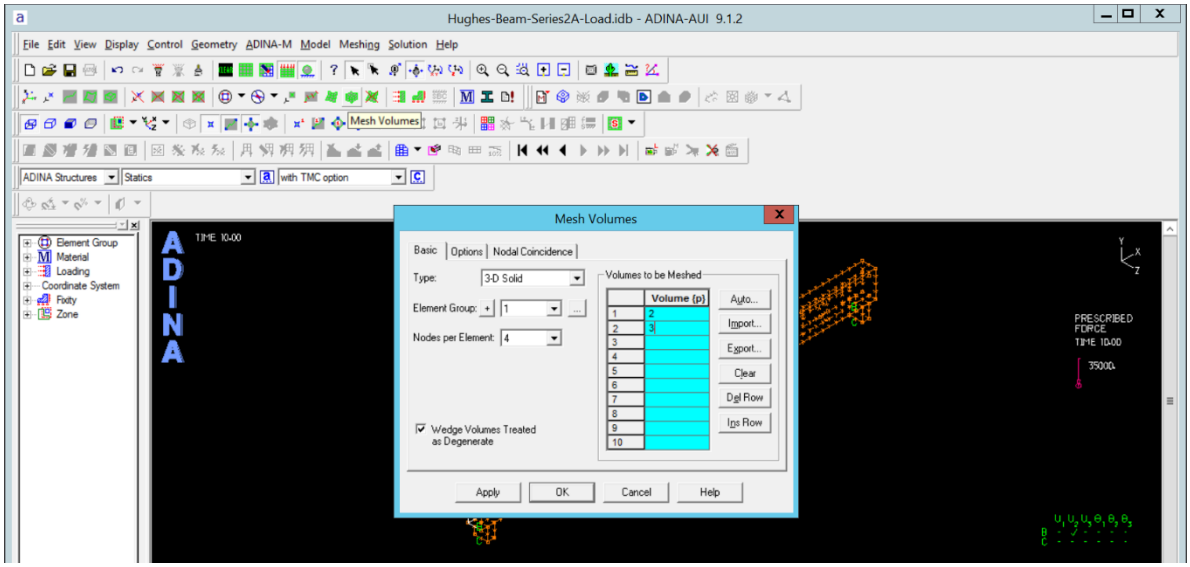

Click on Mesh Surface and select the Element Group and the Surface number

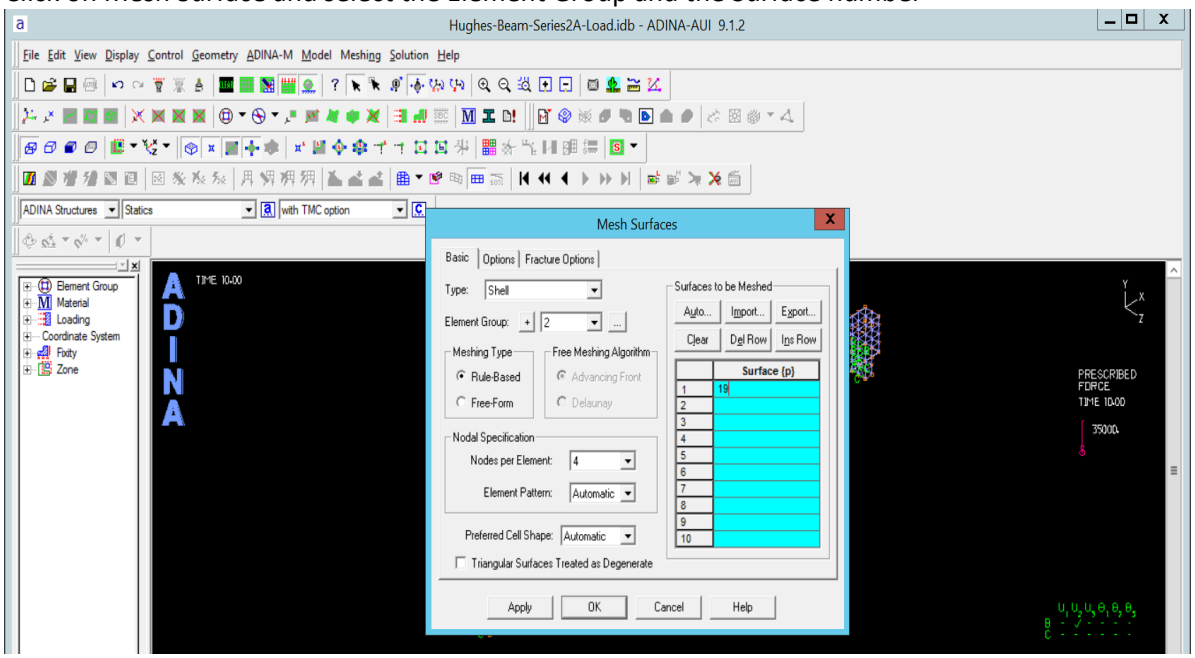

Click on Save and Data File/Solution

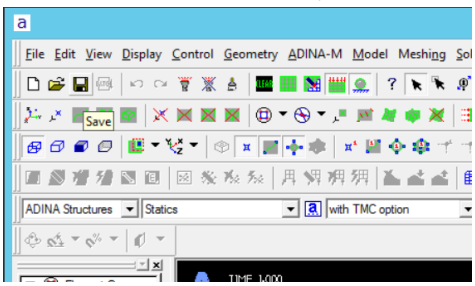

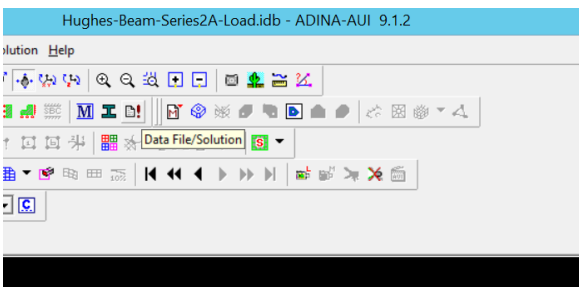

Provide a file name and save for ADINA to analyse

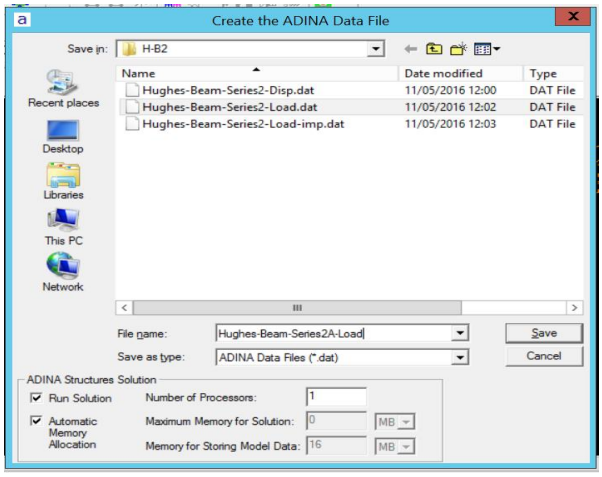

To get the Load-Deflection Graph, I followed Example 26 in ADINA Primer

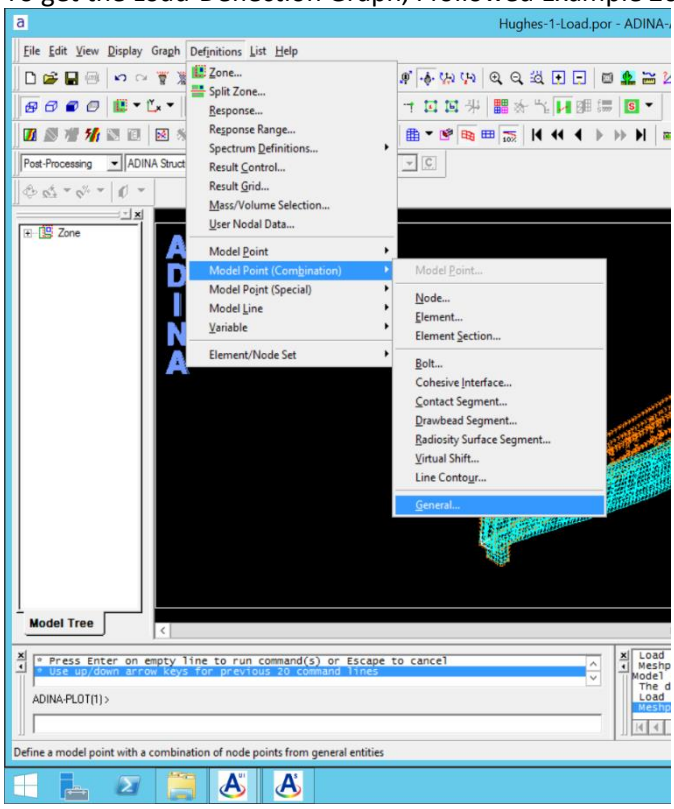

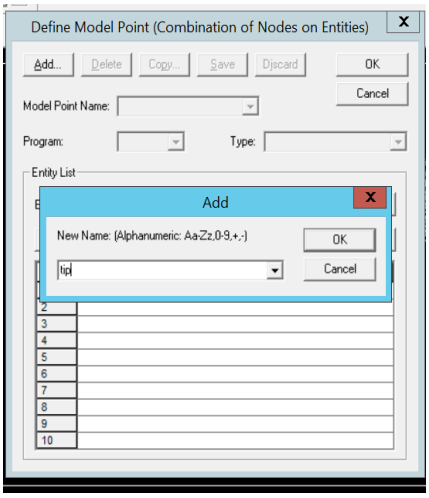

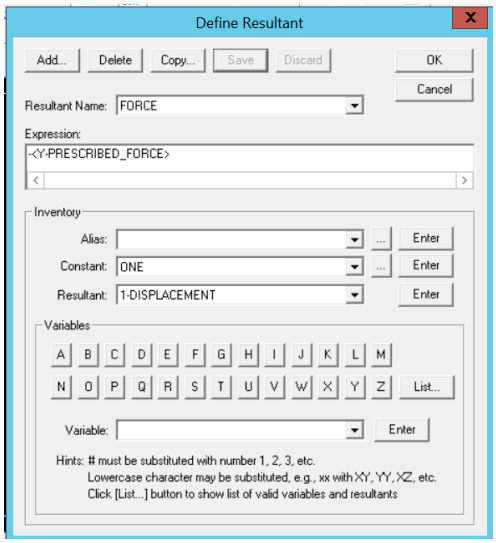

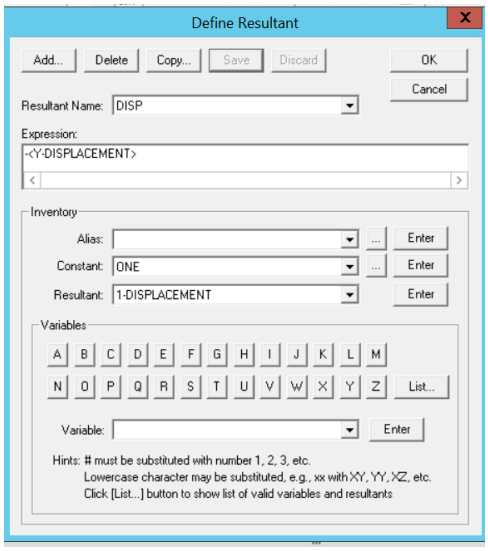

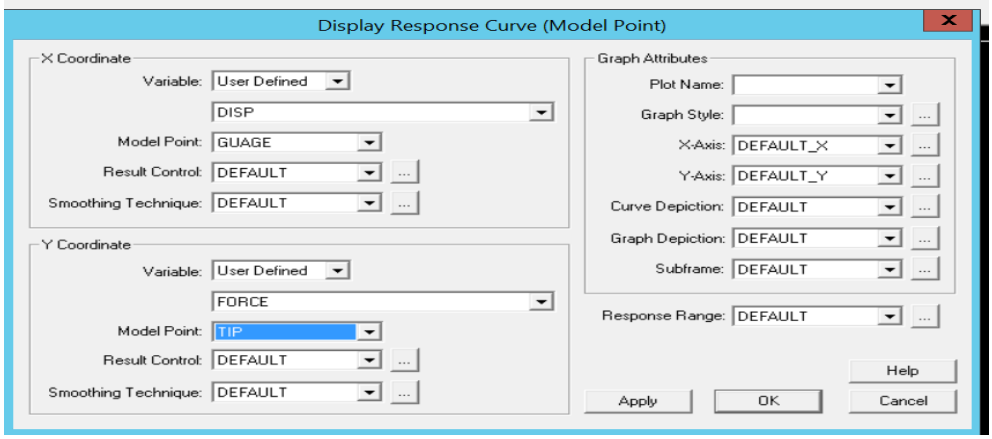

The result I got is far from the experimental results as shown in the graph below

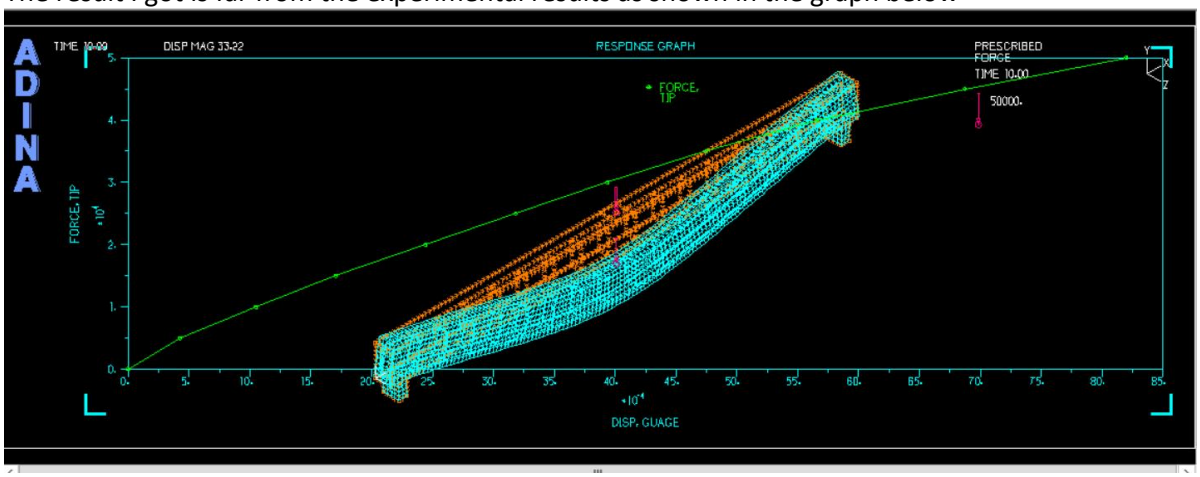

Apply displacement also, and the results are in the table and graph below

Experimental		ADINA-Conc-LOAD		ADINA-Conc-Load-None	ADINA-Conc-Imp-Disp-0.0035			
Deflection	Load	Deflection	Load		Deflection	R1	R2	Load
0.000	0	0	0	0.000	0.000	0	0	0.00
0.001	3.5	4.09E-04	5	0.000	0.004	1.74E+01	17.32	17.35
0.003	7	8.96E-04	10	0.001	0.007	3.24E+01	32.14	32.25
0.005	10.5	1.46E-03	15	0.002	0.011	43.18	42.92	43.05
0.008	14	2.01E-03	20	0.002	0.014	49.59	49.17	49.38
0.009	17.5	2.64E-03	25	0.003	0.018	45.68	45.16	45.42
0.012	21	3.29E-03	30	0.004	0.021	49.08	48.72	48.90
0.015	24.5	3.97E-03	35	0.005	0.025	51.38	50.94	51.16
0.018	28	4.77E-03	40	0.006	0.028	54.8	54.2	54.50
0.023	31.5	5.75E-03	45	0.007	0.032	56.38	56.02	56.20
0.040	35	7.06E-03	50	0.008	0.035	56.4	52.87	54.64

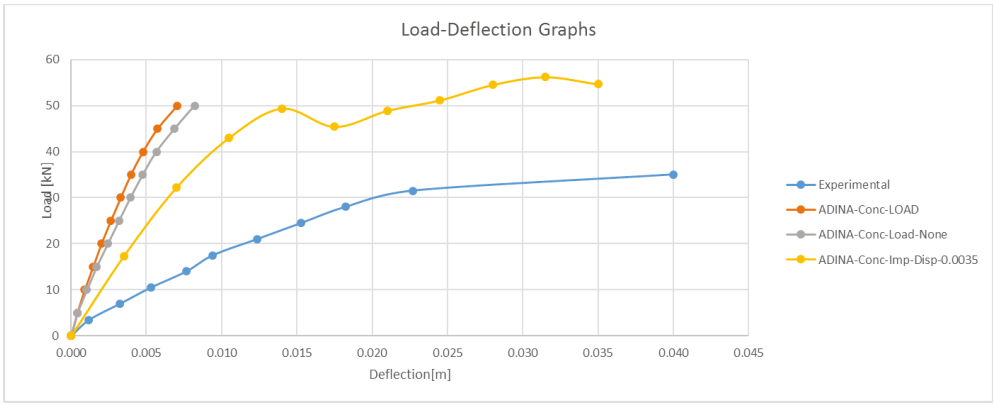

Appendix B1					
Py	dy	fck	vf	L/d	
65.22	2.84	30.0	0.50	14.29	
73.21	2.86	30.0	1.00	14.29	
78.00	3.08	30.0	1.25	14.29	
83.36	3.38	30.0	1.50	14.29	
92.35	4.12	30.0	1.75	14.29	
96.65	4.28	30.0	2.00	14.29	
103.20	7.62	30.0	2.50	14.29	
76.58	2.07	40.0	0.50	14.29	
82.54	2.61	40.0	1.00	14.29	
88.50	3.00	40.0	1.25	14.29	
96.25	3.00	40.0	1.50	14.29	
104.55	3.62	40.0	1.75	14.29	
110.84	4.35	40.0	2.00	14.29	
120.07	6.16	40.0	2.50	14.29	
79.00	2.98	45.0	0.50	14.29	
59.00	3.80	45.0	1.00	14.29	
101.70	1.76	45.0	1.25	14.29	
102.30	1.78	45.0	1.50	14.29	
110.70	2.24	45.0	1.75	14.29	
114.40	3.15	45.0	2.00	14.29	
125.80	3.00	45.0	2.50	14.29	
87.00	2.16	50.0	0.50	14.29	
96.90	2.30	50.0	1.00	14.29	
109.00	2.30	50.0	1.25	14.29	
118.00	2.72	50.0	1.50	14.29	
134.00	3.11	50.0	1.75	14.29	
141.07	3.80	50.0	2.00	14.29	
160.41	4.14	50.0	2.50	14.29	
78.26	3.06	30.0	0.50	12.5	
87.85	3.08	30.0	1.00	12.5	
93.60	3.30	30.0	1.25	12.5	
100.03	3.60	30.0	1.50	12.5	
110.82	4.32	30.0	1.75	12.5	
115.98	5.18	30.0	2.00	12.5	
123.84	7.85	30.0	2.50	12.5	
88.83	2.25	40.0	0.50	12.5	
95.75	2.79	40.0	1.00	12.5	
102.66	3.00	40.0	1.25	12.5	
111.65	3.19	40.0	1.50	12.5	
121.28	3.81	40.0	1.75	12.5	
134.84	4.54	40.0	2.00	12.5	
139.28	6.38	40.0	2.50	12.5	
108.75	2.16	50.0	0.50	12.5	
121.13	2.30	50.0	1.00	12.5	
136.25	2.30	50.0	1.25	12.5	
147.50	2.72	50.0	1.50	12.5	
167.50	3.11	50.0	1.75	12.5	
176.33	3.80	50.0	2.00	12.5	
200.51	4.14	50.0	2.50	12.5	

SUMMARY OUTPUT

Regression Statistics	
Multiple R	0.937451
R Square	0.878814
Adjusted F	0.870735
Standard E	10.32776
Observatio	49

ANOVA

	df	*SS*	*MS*	*F*	*ignificance F*
Regressior	3	34807.28	11602.43	108.7769	1.22E-20
Residual	45	4799.818	106.6626		
Total	48	39607.09			

	Coefficients	*tandard Err*	*t Stat*	*P-value*	*Lower 95%*	*Upper 95%*	*ower 95.0%*	*pper 95.0%*
Intercept	163.8814	23.6245	6.936927	1.26E-08	116.2992	211.4636	116.2992	211.4636
fck	2.037032	0.190757	10.67869	6.39E-14	1.652828	2.421236	1.652828	2.421236
vf	30.43306	2.409309	12.63145	2.13E-16	25.58046	35.28566	25.58046	35.28566
L/d	-13.5185	1.670887	-8.09064	2.55E-10	-16.8839	-10.1532	-16.8839	-10.1532

RESIDUAL OUTPUT

Observatior	*redicted P*	*Residuals*
1	47.0289	18.1911
2	62.24543	10.96457
3	69.8537	8.146304
4	77.46196	5.898038
5	85.07023	7.279773
6	92.67849	3.971508
7	107.895	-4.69502
8	67.39922	9.18078
9	82.61575	-0.07575
10	90.22402	-1.72402
11	97.83228	-1.58228
12	105.4405	-0.89055
13	113.0488	-2.20881
14	128.2653	-8.19534
15	77.58438	1.41562
16	92.80091	-33.8009
17	100.4092	1.290824
18	108.0174	-5.71744
19	115.6257	-4.92571
20	123.234	-8.83397
21	138.4505	-12.6505
22	87.76954	-0.76954
23	102.9861	-6.08607
24	110.5943	-1.59434
25	118.2026	-0.2026
26	125.8109	8.189133
27	133.4191	7.650868
28	148.6357	11.77434
29	71.2271	7.032905
30	86.44363	1.406374
31	94.05189	-0.45189
32	101.6602	-1.63016
33	109.2684	1.551578
34	116.8767	-0.89669
35	132.0932	-8.25322
36	91.59741	-2.76741
37	106.8139	-11.0639
38	114.4222	-11.7622
39	122.0305	-10.3805
40	129.6387	-8.35874
41	137.247	-2.40701
42	152.4635	-13.1835
43	111.9677	-3.21773

SUMMARY OUTPUT

Regression Statistics	
Multiple R	0.251341
R Square	0.063172
Adjusted F	0.04324
Standard E	28.09748
Observatio	49

ANOVA

	df	*SS*	*MS*	*F*	*ignificance F*
Regressior	1	2502.078	2502.078	3.169319	0.081499
Residual	47	37105.02	789.4684		
Total	48	39607.09			

	Coefficients	*tandard Err*	*t Stat*	*P-value*	*Lower 95%*	*Upper 95%*	*ower 95.0%*	*pper 95.0%*
Intercept	90.92625	11.26153	8.074058	1.98E-10	68.27097	113.5815	68.27097	113.5815
dy	5.427554	3.048745	1.780258	0.081499	-0.70573	11.56084	-0.70573	11.56084

RESIDUAL OUTPUT

Observatior	*redicted P*	*Residuals*
1	106.3405	-41.1205
2	106.4491	-33.2391
3	107.6431	-29.6431
4	109.2714	-25.9114
5	113.2878	-20.9378
6	114.1562	-17.5062
7	132.2842	-29.0842
8	102.1613	-25.5813
9	105.0922	-22.5522
10	107.2089	-18.7089
11	107.2089	-10.9589
12	110.574	-6.024
13	114.5361	-3.69611
14	124.36	-4.28998
15	107.1004	-28.1004
16	111.551	-52.551
17	100.4787	1.221253
18	100.5873	1.712702
19	103.084	7.616027
20	108.023	6.376953
21	107.2089	18.59109
22	102.6498	-15.6498
23	103.4096	-6.50963
24	103.4096	5.590374
25	105.6892	12.3108
26	107.8059	26.19406
27	111.551	29.51904
28	113.3963	47.01367
29	107.5346	-29.2746
30	107.6431	-19.7931
31	108.8372	-15.2372
32	110.4654	-10.4354
33	114.3733	-3.55329
34	119.041	-3.06098
35	133.5326	-9.69255
36	103.1382	-14.3082
37	106.0691	-10.3191
38	107.2089	-4.54891
39	108.2401	3.409851
40	111.6052	9.674767
41	115.5673	19.27265
42	125.554	13.72595
43	102.6498	6.100232

Pmax	dmax	fck	vf	L/d
69.65	4.70	30.0	0.50	14.29
75.59	7.45	30.0	1.00	14.29
79.35	7.67	30.0	1.25	14.29
84.90	13.26	30.0	1.50	14.29
93.09	13.28	30.0	1.75	14.29
97.52	13.61	30.0	2.00	14.29
103.84	19.46	30.0	2.50	14.29
77.79	11.79	40.0	0.50	14.29
83.99	10.97	40.0	1.00	14.29
90.11	7.08	40.0	1.25	14.29
99.52	7.52	40.0	1.50	14.29
105.28	8.48	40.0	1.75	14.29
111.61	4.35	40.0	2.00	14.29
123.70	12.14	40.0	2.50	14.29
81.50	8.85	45.0	0.50	14.29
88.00	3.80	45.0	1.00	14.29
96.30	3.10	45.0	1.25	14.29
104.80	5.80	45.0	1.50	14.29
110.70	7.14	45.0	1.75	14.29
114.50	9.92	45.0	2.00	14.29
127.10	12.61	45.0	2.50	14.29
89.84	11.84	50.0	0.50	14.29
98.00	10.51	50.0	1.00	14.29
113.91	8.44	50.0	1.25	14.29
120.64	11.08	50.0	1.50	14.29
135.57	8.09	50.0	1.75	14.29
147.07	10.21	50.0	2.00	14.29
163.41	10.21	50.0	2.50	14.29
83.58	4.92	30.0	0.50	12.5
90.71	7.67	30.0	1.00	12.5
95.23	7.89	30.0	1.25	12.5
101.88	13.56	30.0	1.50	12.5
111.70	13.53	30.0	1.75	12.5
117.02	13.81	30.0	2.00	12.5
124.60	19.69	30.0	2.50	12.5
90.24	12.16	40.0	0.50	12.5
97.42	11.15	40.0	1.00	12.5
104.52	7.08	40.0	1.25	12.5
115.44	7.27	40.0	1.50	12.5
122.12	8.67	40.0	1.75	12.5
134.84	4.54	40.0	2.00	12.5
143.49	12.36	40.0	2.50	12.5
110.99	6.73	50.0	0.50	12.5
122.25	9.57	50.0	1.00	12.5
142.38	8.44	50.0	1.25	12.5
150.80	11.08	50.0	1.50	12.5
169.46	8.09	50.0	1.75	12.5
183.83	10.21	50.0	2.00	12.5
204.26	10.21	50.0	2.50	12.5

SUMMARY OUTPUT

Regression Statistics	
Multiple R	0.943065
R Square	0.889372
Adjusted R	0.881997
Standard E	9.824336
Observatio	49

ANOVA

	df	*SS*	*MS*	*F*	*ignificance F*
Regressior	3	34917.08	11639.03	120.5897	1.58E-21
Residual	45	4343.291	96.51758		
Total	48	39260.37			

	Coefficients	*tandard Err*	*t Stat*	*P-value*	*Lower 95%*	*Upper 95%*	*ower 95.0%*	*Upper 95.0%*
Intercept	163.7089	22.47293	7.284715	3.86E-09	118.4461	208.9717	118.4461	208.9717
fck	2.129774	0.181458	11.73699	2.73E-15	1.764298	2.49525	1.764298	2.49525
vf	29.58122	2.291868	12.90704	9.91E-17	24.96517	34.19728	24.96517	34.19728
L/d	-13.4931	1.58944	-8.48923	6.76E-11	-16.6944	-10.2918	-16.6944	-10.2918

RESIDUAL OUTPUT

Observatio	*edicted Pm*	*Residuals*
1	49.57596	20.07404
2	64.36657	11.22343
3	71.76188	7.588121
4	79.15719	5.742814
5	86.55249	6.537508
6	93.9478	3.572202
7	108.7384	-4.89841
8	70.8737	6.916299
9	85.66431	-1.67431
10	93.05962	-2.94962
11	100.4549	-0.93493
12	107.8502	-2.57023
13	115.2455	-3.63554
14	130.0361	-6.33615
15	81.52257	-0.02257
16	96.31318	-8.31318
17	103.7085	-7.40849
18	111.1038	-6.3038
19	118.4991	-7.7991
20	125.8944	-11.3944
21	140.685	-13.585
22	92.17144	-2.33144
23	106.9621	-8.96205
24	114.3574	-0.44736
25	121.7527	-1.11267
26	129.148	6.422029
27	136.5433	10.52672
28	151.3339	12.07611
29	73.72865	9.851345
30	88.51927	2.190733
31	95.91457	-0.68457
32	103.3099	-1.42988
33	110.7052	0.994815
34	118.1005	-1.08049
35	132.8911	-8.2911
36	95.02639	-4.78639
37	109.817	-12.397
38	117.2123	-12.6923
39	124.6076	-9.16762

SUMMARY OUTPUT

Regression Statistics	
Multiple R	0.123729
R Square	0.015309
Adjusted F	-0.00564
Standard E	28.67994
Observatio	49

ANOVA

	df	*SS*	*MS*	*F*	*ignificance F*
Regressior	1	601.0324	601.0324	0.730704	0.396992
Residual	47	38659.33	822.539		
Total	48	39260.37			

	Coefficients	*tandard Err*	*t Stat*	*P-value*	*Lower 95%*	*Upper 95%*	*ower 95.0%*	*pper 95.0%*
Intercept	102.6258	12.0662	8.505229	4.54E-11	78.35175	126.8999	78.35175	126.8999
dmax	1.007171	1.178237	0.854812	0.396992	-1.36314	3.377478	-1.36314	3.377478

RESIDUAL OUTPUT

Observatio	*edicted Pm*	*Residuals*
1	107.3595	-37.7095
2	110.1292	-34.5392
3	110.3508	-31.0008
4	115.9809	-31.0809
5	116.0011	-22.9111
6	116.3334	-18.8134
7	122.2254	-18.3854
8	114.5004	-36.7104
9	113.6745	-29.6845
10	109.7566	-19.6466
11	110.1997	-10.6797
12	111.1666	-5.88663
13	107.007	4.602983
14	114.8529	8.84712
15	111.5393	-30.0393
16	106.4531	-18.4531
17	105.7481	-9.44805
18	108.4674	-3.66742
19	109.817	0.882976
20	112.617	1.88304
21	115.3263	11.77375
22	114.5507	-24.7107
23	113.2112	-15.2112
24	111.1263	2.783653
25	113.7853	6.854721
26	110.7738	24.79616
27	112.909	34.16096
28	112.909	50.50096
29	107.5811	-24.0011
30	110.3508	-19.6408
31	110.5724	-15.3424
32	116.2831	-14.4031
33	116.2528	-4.55285
34	116.5349	0.485144
35	122.457	2.142978
36	114.873	-24.633
37	113.8558	-16.4358
38	109.7566	-5.23659
39	109.948	5.492043
40	111.358	10.762
41	107.1984	27.64162
42	115.0745	28.41554

377

Appendix B2					
Py	dy	Vf	fck	L/d	
71.4	5.7	0.50	30.0	14.29	
80.6	3.7	1.00	30.0	14.29	
104.9	4.2	1.25	30.0	14.29	
119.2	4.6	1.50	30.0	14.29	
136.0	5.5	1.75	30.0	14.29	
147.7	6.1	2.00	30.0	14.29	
185.7	9.2	2.50	30.0	14.29	
79.2	4.5	0.50	40.0	14.29	
82.3	3.6	1.00	40.0	14.29	
106.0	4.0	1.25	40.0	14.29	
121.3	4.1	1.50	40.0	14.29	
143.6	4.6	1.75	40.0	14.29	
158.5	5.7	2.00	40.0	14.29	
198.2	8.0	2.50	40.0	14.29	
81.2	4.2	0.50	45.0	14.29	
112.7	3.6	1.00	45.0	14.29	
131.2	3.7	1.25	45.0	14.29	
151.0	4.0	1.50	45.0	14.29	
163.9	4.3	1.75	45.0	14.29	
178.2	4.9	2.00	45.0	14.29	
203.7	7.3	2.50	45.0	14.29	
83.5	3.2	0.50	50.0	14.29	
120.2	3.6	1.00	50.0	14.29	
140.0	3.7	1.25	50.0	14.29	
161.1	4.0	1.50	50.0	14.29	
174.9	4.3	1.75	50.0	14.29	
190.1	4.9	2.00	50.0	14.29	
216.9	7.3	2.50	50.0	14.29	
84.1	2.9	0.50	30.0	12.5	
103.0	3.6	1.00	30.0	12.5	
129.7	4.5	1.25	30.0	12.5	
142.3	4.1	1.50	30.0	12.5	
166.3	5.6	1.75	30.0	12.5	
187.5	7.9	2.00	30.0	12.5	
205.7	9.0	2.50	30.0	12.5	
94.6	1.8	0.50	40.0	12.5	
129.1	3.3	1.00	40.0	12.5	
131.6	3.5	1.25	40.0	12.5	
132.8	4.0	1.50	40.0	12.5	
135.8	4.4	1.75	40.0	12.5	
145.6	4.7	2.00	40.0	12.5	
160.2	4.8	2.50	40.0	12.5	
99.9	2.2	0.50	50.0	12.5	
114.2	2.9	1.00	50.0	12.5	
138.3	3.3	1.25	50.0	12.5	
162.5	3.7	1.50	50.0	12.5	
181.1	4.3	1.75	50.0	12.5	
207.7	4.5	2.00	50.0	12.5	
251.0	5.6	2.50	50.0	12.5	
136.6	2.3	0.50	50.0	12.5	
201.3	2.9	1.00	40.0	10.0	
239.0	3.4	1.25	40.0	10.0	
250.3	3.5	1.50	40.0	10.0	
286.8	4.5	1.75	40.0	10.0	
323.4	4.7	2.00	40.0	10.0	
358.9	7.3	2.50	40.0	10.0	

SUMMARY OUTPUT

Regression Statistics	
Multiple R	0.914588
R Square	0.836471
Adjusted F	0.827037
Standard E	25.0035
Observatio	56

ANOVA

	df	*SS*	*MS*	*F*	*ignificance F*
Regressior	3	166288.1	55429.36	88.66214	1.92E-20
Residual	52	32509.1	625.1751		
Total	55	198797.2			

	Coefficients	*tandard Err*	*t Stat*	*P-value*	*Lower 95%*	*Upper 95%*	*ower 95.0%*	*pper 95.0%*
Intercept	324.7393	37.69681	8.614504	1.38E-11	249.0951	400.3835	249.0951	400.3835
Vf	65.10194	5.467583	11.9069	1.79E-16	54.13043	76.07345	54.13043	76.07345
fck	1.559664	0.454718	3.429954	0.00119	0.647204	2.472123	0.647204	2.472123
L/d	-25.1324	2.445597	-10.2766	4.02E-14	-30.0398	-20.2249	-30.0398	-20.2249

RESIDUAL OUTPUT

Observatior	*redicted P*	*Residuals*
1	44.93886	26.46114
2	77.48983	3.110171
3	93.76531	11.13469
4	110.0408	9.159201
5	126.3163	9.683715
6	142.5918	5.10823
7	175.1427	10.55726
8	60.53549	18.66451
9	93.08647	-10.7865
10	109.362	-3.36195
11	125.6374	-4.33744
12	141.9129	1.687079
13	158.1884	0.311594
14	190.7394	7.460623
15	68.33381	12.86619
16	100.8848	11.81522
17	117.1603	14.03973
18	133.4358	17.56425
19	149.7112	14.18876
20	165.9867	12.21328
21	198.5377	5.162305
22	76.13213	7.367869
23	108.6831	11.5169
24	124.9586	15.04141
25	141.2341	19.86593
26	157.5096	17.39044
27	173.785	16.31496
28	206.336	10.56399
29	89.92577	-5.82577
30	122.4767	-19.4767
31	138.7522	-9.05222
32	155.0277	-12.7277
33	171.3032	-5.00319
34	187.5787	-0.07868
35	220.1296	-14.4296
36	105.5224	-10.9224
37	138.0734	-8.97337
38	154.3489	-22.7489
39	170.6243	-37.8243
40	186.8998	-51.0998
41	203.1753	-57.5753
42	235.7263	-75.5263
43	121.119	-21.219
44	153.67	-39.47
45	169.9455	-31.6455
46	186.221	-23.721

SUMMARY OUTPUT

Regression Statistics	
Multiple R	0.440395
R Square	0.193948
Adjusted R	0.179021
Standard E	54.47406
Observatio	56

ANOVA

	df	*SS*	*MS*	*F*	*ignificance F*
Regressior	1	38556.3	38556.3	12.99319	0.000682
Residual	54	160240.9	2967.424		
Total	55	198797.2			

	Coefficients	*tandard Err*	*t Stat*	*P-value*	*Lower 95%*	*Upper 95%*	*ower 95.0%*	*pper 95.0%*
Intercept	80.09776	22.31019	3.590188	0.000713	35.36854	124.827	35.36854	124.827
dy	16.64851	4.618677	3.604607	0.000682	7.388625	25.9084	7.388625	25.9084

RESIDUAL OUTPUT

Observatior	*redicted P*	*Residuals*
1	174.9943	-103.594
2	141.6973	-61.0973
3	150.0215	-45.1215
4	156.6809	-37.4809
5	171.6646	-35.6646
6	181.6537	-33.9537
7	233.2641	-47.5641
8	155.0161	-75.8161
9	140.0324	-57.7324
10	146.6918	-40.6918
11	148.3567	-27.0567
12	156.6809	-13.0809
13	174.9943	-16.4943
14	213.2859	-15.0859
15	150.0215	-68.8215
16	140.0324	-27.3324
17	141.6973	-10.4973
18	146.6918	4.308177
19	151.6864	12.21362
20	161.6755	16.52451
21	201.6319	2.068079
22	133.373	-49.873
23	140.0324	-19.8324
24	141.6973	-1.69727
25	146.6918	14.40818
26	151.6864	23.21362
27	161.6755	28.42451
28	201.6319	15.26808
29	128.3785	-44.2785
30	140.0324	-37.0324
31	155.0161	-25.3161
32	148.3567	-6.05667
33	173.3294	-7.02945
34	211.621	-24.121
35	229.9344	-24.2344
36	110.0651	-15.4651
37	135.0379	-5.93786
38	138.3676	-6.76757
39	146.6918	-13.8918
40	153.3512	-17.5512
41	158.3458	-12.7458
42	160.0106	0.189365
43	116.7245	-16.8245
44	128.3785	-14.1785
45	135.0379	3.262137
46	141.6973	20.80273

Pmax	dmax	Vf	fck	L/d	
102.6	45.7	0.50	30.0	14.29	
145.1	44.6	1.00	30.0	14.29	
159.2	44.8	1.25	30.0	14.29	
175.3	44.7	1.50	30.0	14.29	
193.3	44.6	1.75	30.0	14.29	
209.4	44.6	2.00	30.0	14.29	
244.0	43.8	2.50	30.0	14.29	
126.1	45	0.50	40.0	14.29	
155.8	44	1.00	40.0	14.29	
170.3	44.7	1.25	40.0	14.29	
185.5	45.4	1.50	40.0	14.29	
203.1	44.8	1.75	40.0	14.29	
221.8	43.9	2.00	40.0	14.29	
254.1	43.2	2.50	40.0	14.29	
133.2	44.1	0.50	45.0	14.29	
174.0	44.6	1.00	45.0	14.29	
190.8	44.7	1.25	45.0	14.29	
207.0	44.5	1.50	45.0	14.29	
221.1	44.7	1.75	45.0	14.29	
240.7	45.2	2.00	45.0	14.29	
263.7	44.5	2.50	45.0	14.29	
142.2	44.1	0.50	50.0	14.29	
185.7	44.6	1.00	50.0	14.29	
203.6	44.7	1.25	50.0	14.29	
220.8	44.5	1.50	50.0	14.29	
235.9	44.7	1.75	50.0	14.29	
256.8	45.4	2.00	50.0	14.29	
281.3	44.5	2.50	50.0	14.29	
142.8	45.1	0.50	30.0	12.5	
191.1	42.8	1.00	30.0	12.5	
212.7	44.5	1.25	30.0	12.5	
234.1	45.0	1.50	30.0	12.5	
261.2	44.2	1.75	30.0	12.5	
282.7	44.5	2.00	30.0	12.5	
354.8	44.3	2.50	30.0	12.5	
144.7	45.4	0.50	40.0	12.5	
202.7	43.3	1.00	40.0	12.5	
227.7	42.8	1.25	40.0	12.5	
248.2	42.8	1.50	40.0	12.5	
269.7	43.6	1.75	40.0	12.5	
293.2	42.9	2.00	40.0	12.5	
310.2	43.1	2.50	40.0	12.5	
157.1	43.0	0.50	50.0	12.5	
214.3	44.5	1.00	50.0	12.5	
239.2	43.7	1.25	50.0	12.5	
259.9	43.6	1.50	50.0	12.5	
283.9	44.5	1.75	50.0	12.5	
305.0	44.5	2.00	50.0	12.5	
351.2	42.9	2.50	50.0	12.5	
227.3	43.9	0.50	50.0	12.5	
340.5	44.2	1.00	40.0	10.0	
382.4	44.4	1.25	40.0	10.0	
420.3	43.2	1.50	40.0	10.0	
464.0	41.7	1.75	40.0	10.0	
504.7	42.8	2.00	40.0	10.0	
584.2	43.3	2.50	40.0	10.0	

SUMMARY OUTPUT

Regression Statistics	
Multiple R	0.954841
R Square	0.911721
Adjusted R	0.906628
Standard E	28.63528
Observatio	56

ANOVA

	df	*SS*	*MS*	*F*	*ignificance F*
Regressior	3	440363.6	146787.9	179.0141	2.18E-27
Residual	52	42638.93	819.9793		
Total	55	483002.5			

	Coefficients	*tandard Err*	*t Stat*	*P-value*	*Lower 95%*	*Upper 95%*	*ower 95.0%*	*Upper 95.0%*
Intercept	700.8689	43.1723	16.23423	5.24E-22	614.2374	787.5005	614.2374	787.5005
Vf	85.66183	6.261754	13.68017	7.31E-19	73.09671	98.22696	73.09671	98.22696
fck	1.76252	0.520767	3.384471	0.001363	0.717525	2.807515	0.717525	2.807515
L/d	-50.1407	2.800822	-17.9021	6.93E-24	-55.7609	-44.5204	-55.7609	-44.5204

RESIDUAL OUTPUT

Observatior	*edicted Pm*	*Residuals*
1	80.06522	22.53478
2	122.8961	22.20387
3	144.3116	14.88841
4	165.727	9.572951
5	187.1425	6.157492
6	208.558	0.842033
7	251.3889	-7.38888
8	97.69042	28.40958
9	140.5213	15.27867
10	161.9368	8.363209
11	183.3522	2.14775
12	204.7677	-1.66771
13	226.1832	-4.38317
14	269.0141	-14.9141
15	106.503	26.69698
16	149.3339	24.66607
17	170.7494	20.05061
18	192.1648	14.83515
19	213.5803	7.519692
20	234.9958	5.704233
21	277.8267	-14.1267
22	115.3156	26.88438
23	158.1465	27.55347
24	179.562	24.03801
25	200.9774	19.82255
26	222.3929	13.50709
27	243.8084	12.99163
28	286.6393	-5.33928
29	169.817	-27.017
30	212.6479	-21.5479
31	234.0634	-21.3634
32	255.4789	-21.3789
33	276.8943	-15.6943
34	298.3098	-15.6098
35	341.1407	13.65931
36	187.4422	-42.7422
37	230.2731	-27.5731
38	251.6886	-23.9886
39	273.1041	-24.9041
40	294.5195	-24.8195
41	315.935	-22.735
42	358.7659	-48.5659
43	205.0674	-47.9674
44	247.8983	-33.5983
45	269.3138	-30.1138
46	290.7293	-30.8293
47	312.1447	-28.2447
48	333.5602	-28.5602
49	376.3911	-25.1911
50	205.0674	22.23258
51	355.6248	-15.1248
52	377.0403	5.359722

SUMMARY OUTPUT

Regression Statistics	
Multiple R	0.528339
R Square	0.279142
Adjusted F	0.265793
Standard E	80.29763
Observatio	56

ANOVA

	df	*SS*	*MS*	*F*	*ignificance F*
Regressior	1	134826.3	134826.3	20.91073	2.85E-05
Residual	54	348176.3	6447.709		
Total	55	483002.5			

	Coefficients	*tandard Err*	*t Stat*	*P-value*	*Lower 95%*	*Upper 95%*	*ower 95.0%*	*pper 95.0%*
Intercept	2854.088	571.0855	4.997654	6.46E-06	1709.131	3999.046	1709.131	3999.046
dmax	-59.1229	12.92918	-4.57282	2.85E-05	-85.0443	-33.2014	-85.0443	-33.2014

RESIDUAL OUTPUT

Observatio	*edicted Pm*	*Residuals*
1	152.1736	-49.5736
2	217.2088	-72.1088
3	205.3842	-46.1842
4	211.2965	-35.9965
5	217.2088	-23.9088
6	217.2088	-7.80875
7	264.507	-20.507
8	193.5596	-67.4596
9	252.6825	-96.8825
10	211.2965	-40.9965
11	169.9105	15.58954
12	205.3842	-2.28418
13	258.5947	-36.7947
14	299.9807	-45.8807
15	246.7702	-113.57
16	217.2088	-43.2088
17	211.2965	-20.4965
18	223.121	-16.121
19	211.2965	9.803536
20	181.735	58.96496
21	223.121	40.57896
22	246.7702	-104.57
23	217.2088	-31.5088
24	211.2965	-7.69646
25	223.121	-2.32104
26	211.2965	24.60354
27	169.9105	86.88954
28	223.121	58.17896
29	187.6473	-44.8473
30	323.6299	-132.53
31	223.121	-10.421
32	193.5596	40.54039
33	240.8579	20.34211
34	223.121	59.57896
35	234.9456	119.8544
36	169.9105	-25.2105
37	294.0685	-91.3685
38	323.6299	-95.9299
39	323.6299	-75.4299
40	276.3316	-6.63161
41	317.7176	-24.5176
42	305.893	4.306964
43	311.8053	-154.705
44	223.121	-8.82104
45	270.4193	-31.2193
46	276.3316	-16.4316
47	223.121	60.77896
48	223.121	81.87896
49	317.7176	33.48239
50	258.5947	-31.2947
51	240.8579	99.64211

Appendix B4

Pmax	μ	fcu	vf	L/d
384.00	39.20	30.00	1.00	30.00
448.00	47.50	40.00	1.00	30.00
472.90	57.79	43.70	1.00	30.00
522.40	68.96	50.00	1.00	30.00
400.90	47.60	30.00	1.25	30.00
463.50	44.50	40.00	1.25	30.00
475.30	46.92	43.70	1.25	30.00
521.90	64.94	50.00	1.25	30.00
409.00	45.60	30.00	1.50	30.00
489.90	50.10	40.00	1.50	30.00
482.10	44.54	43.70	1.50	30.00
534.60	59.86	50.00	1.50	30.00
422.60	61.30	30.00	1.75	30.00
492.80	50.40	40.00	1.75	30.00
512.30	70.20	43.70	1.75	30.00
543.30	60.70	50.00	1.75	30.00
462.00	70.30	30.00	2.00	30.00
561.00	57.62	40.00	2.00	30.00
513.10	54.02	43.70	2.00	30.00
541.60	61.64	50.00	2.00	30.00
489.40	54.80	30.00	2.50	30.00
579.30	61.40	40.00	2.50	30.00
590.70	69.07	43.70	2.50	30.00
647.20	66.56	50.00	2.50	30.00
263.20	54.10	30.00	1.00	33.30
292.90	54.20	40.00	1.00	33.30
330.20	54.00	50.00	1.00	33.30
272.20	50.40	30.00	1.25	33.30
301.10	54.00	40.00	1.25	33.30
346.40	54.00	50.00	1.25	33.30
282.50	52.40	30.00	1.50	33.30
312.00	52.50	40.00	1.50	33.30
351.00	54.30	50.00	1.50	33.30
296.00	51.00	30.00	1.75	33.30
321.30	53.60	40.00	1.75	33.30
357.20	54.30	50.00	1.75	33.30
310.20	52.00	30.00	2.00	33.30
336.20	54.20	40.00	2.00	33.30
366.10	54.40	50.00	2.00	33.30
336.40	52.60	30.00	2.50	33.30
360.20	53.80	40.00	2.50	33.30
387.60	54.20	50.00	2.50	33.30
390.40	54.50	30.00	1.00	27.27
538.20	55.90	40.00	1.00	27.27
631.50	47.00	50.00	1.00	27.27
496.90	45.50	30.00	1.25	27.27
573.90	51.40	40.00	1.25	27.27
642.70	56.50	50.00	1.25	27.27
494.10	44.60	30.00	1.50	27.27
579.80	51.10	40.00	1.50	27.27
664.30	43.70	50.00	1.50	27.27
505.10	41.60	30.00	1.75	27.27
602.60	46.90	40.00	1.75	27.27
665.80	53.00	50.00	1.75	27.27
552.10	51.80	30.00	2.00	27.27
613.90	47.60	40.00	2.00	27.27
689.80	52.90	50.00	2.00	27.27

SUMMARY OUTPUT

Regression Statistics	
Multiple R	0.975141
R Square	0.9509
Adjusted R	0.94827
Standard E	28.63348
Observatio	60

ANOVA

	df	*SS*	*MS*	*F*	*ignificance F*
Regressior	3	889186.3	296395.4	361.5124	1.32E-36
Residual	56	45913.07	819.8762		
Total	59	935099.4			

	Coefficients	*tandard Err*	*t Stat*	*P-value*	*Lower 95%*	*Upper 95%*	*ower 95.0%*	*Upper 95.0%*
Intercept	1473.014	53.03136	27.77628	1.96E-34	1366.779	1579.248	1366.779	1579.248
fcu	5.98186	0.472402	12.66265	4.5E-18	5.035525	6.928194	5.035525	6.928194
vf	75.45029	7.498005	10.06271	3.64E-14	60.42998	90.47059	60.42998	90.47059
L/d	-45.2565	1.580023	-28.6429	3.92E-35	-48.4217	-42.0913	-48.4217	-42.0913

Appendix B5

Py	μ	fck	vf	L/d	
384.0	39.2	30.00	1.00	30.00	
448.0	47.5	40.00	1.00	30.00	
472.9	57.8	43.70	1.00	30.00	
522.4	69.0	50.00	1.00	30.00	
400.9	47.6	30.00	1.25	30.00	
463.5	44.5	40.00	1.25	30.00	
475.3	46.9	43.70	1.25	30.00	
521.9	64.9	50.00	1.25	30.00	
409.0	45.6	30.00	1.50	30.00	
489.9	50.1	40.00	1.50	30.00	
482.1	44.5	43.70	1.50	30.00	
534.6	59.9	50.00	1.50	30.00	
422.6	61.3	30.00	1.75	30.00	
492.8	50.4	40.00	1.75	30.00	
512.3	70.2	43.70	1.75	30.00	
543.3	60.7	50.00	1.75	30.00	
462.0	70.3	30.00	2.00	30.00	
561.0	57.6	40.00	2.00	30.00	
513.1	54.0	43.70	2.00	30.00	
541.6	61.6	50.00	2.00	30.00	
489.4	54.8	30.00	2.50	30.00	
579.3	61.4	40.00	2.50	30.00	
590.7	69.1	43.70	2.50	30.00	
647.2	66.6	50.00	2.50	30.00	
263.20	54.10	30.00	1.00	33.30	
292.90	54.20	40.00	1.00	33.30	
330.20	54.00	50.00	1.00	33.30	
272.20	50.40	30.00	1.25	33.30	
301.10	54.00	40.00	1.25	33.30	
346.40	54.00	50.00	1.25	33.30	
282.50	52.40	30.00	1.50	33.30	
312.00	52.50	40.00	1.50	33.30	
351.00	54.30	50.00	1.50	33.30	
296.00	51.00	30.00	1.75	33.30	
321.30	53.60	40.00	1.75	33.30	
357.20	54.30	50.00	1.75	33.30	
310.20	52.00	30.00	2.00	33.30	
336.20	54.20	40.00	2.00	33.30	
366.10	54.40	50.00	2.00	33.30	
336.40	52.60	30.00	2.50	33.30	
360.20	53.80	40.00	2.50	33.30	
387.60	54.20	50.00	2.50	33.30	

SUMMARY OUTPUT								
Regression Statistics								
Multiple R	0.980754							
R Square	0.961878							
Adjusted F	0.958869							
Standard E	20.66911							
Observatio	42							
ANOVA								
	df	*SS*	*MS*	*F*	*ignificance F*			
Regressior	3	409616	136538.7	319.6039	5.43E-27			
Residual	38	16234.06	427.2122					
Total	41	425850.1						
	Coefficients	*tandard Err*	*t Stat*	*P-value*	*Lower 95%*	*Upper 95%*	*ower 95.0%*	*Upper 95.0%*
Intercept	1751.757	65.67111	26.67469	3.27E-26	1618.813	1884.701	1618.813	1884.701
fck	4.639195	0.416594	11.13602	1.58E-13	3.795845	5.482545	3.795845	5.482545
vf	64.30041	6.469108	9.939609	4.04E-12	51.20438	77.39643	51.20438	77.39643
L/d	-51.6819	1.956436	-26.4164	4.65E-26	-55.6425	-47.7213	-55.6425	-47.7213

SUMMARY OUTPUT								
Regression Statistics								
Multiple R	0.485919							
R Square	0.236118							
Adjusted F	0.217021							
Standard E	90.18028							
Observatio	42							
ANOVA								
	df	*SS*	*MS*	*F*	*ignificance F*			
Regressior	1	100550.8	100550.8	12.36409	0.001105			
Residual	40	325299.3	8132.483					
Total	41	425850.1						
	Coefficients	*tandard Err*	*t Stat*	*P-value*	*Lower 95%*	*Upper 95%*	*ower 95.0%*	*Upper 95.0%*
Intercept	45.54884	108.3534	0.420373	0.676463	-173.442	264.5393	-173.442	264.5393
μ	6.853514	1.949092	3.516261	0.001105	2.914253	10.79277	2.914253	10.79277

Appendix B6				
Py	dy	fck	vf	L/d
146.90	10.20	30.00	1.00	30.00
154.50	11.50	30.00	1.25	30.00
161.50	12.50	30.00	1.50	30.00
171.90	14.40	30.00	1.75	30.00
174.00	13.76	30.00	2.00	30.00
192.20	16.20	30.00	2.50	30.00
176.90	9.60	40.00	1.00	30.00
179.70	9.60	40.00	1.25	30.00
187.90	10.80	40.00	1.50	30.00
199.40	13.00	40.00	1.75	30.00
213.00	15.60	40.00	2.00	30.00
218.90	14.80	40.00	2.50	30.00
187.90	10.00	43.70	1.00	30.00
194.90	8.00	43.70	1.25	30.00
201.20	11.80	43.70	1.50	30.00
205.00	12.00	43.70	1.75	30.00
212.90	12.91	43.70	2.00	30.00
246.30	19.80	43.70	2.50	30.00
211.00	10.80	50.00	1.00	30.00
215.70	11.00	50.00	1.25	30.00
219.90	11.30	50.00	1.50	30.00
234.90	14.50	50.00	1.75	30.00
239.70	14.51	50.00	2.00	30.00
262.10	18.20	50.00	2.50	30.00
116.10	10.10	30.00	1.00	33.30
121.30	11.10	30.00	1.25	33.30
127.60	12.60	30.00	1.50	33.30
138.80	15.70	30.00	1.75	33.30
149.60	18.60	30.00	2.00	33.30
146.30	14.90	30.00	2.50	33.30
141.40	10.40	40.00	1.00	33.30
149.30	11.90	40.00	1.25	33.30
152.20	12.00	40.00	1.50	33.30
162.20	14.70	40.00	1.75	33.30
173.00	17.60	40.00	2.00	33.30
195.70	23.80	40.00	2.50	33.30
167.60	11.10	50.00	1.00	33.30
170.20	11.20	50.00	1.25	33.30
179.70	13.10	50.00	1.50	33.30
182.80	13.10	50.00	1.75	33.30
193.30	15.70	50.00	2.00	33.30
201.00	15.80	50.00	2.50	33.30

SUMMARY OUTPUT

Regression Statistics	
Multiple R	0.98714
R Square	0.974445
Adjusted R	0.972428
Standard E	5.668159
Observatio	42

ANOVA

	df	*SS*	*MS*	*F*	*gnificance F*
Regressior	3	46553.94	15517.98	483.0044	2.73E-30
Residual	38	1220.865	32.12803		
Total	41	47774.81			

	Coefficients	*tandard Err*	*t Stat*	*P-value*	*Lower 95%*	*Upper 95%*	*ower 95.0%*	*pper 95.0%*
Intercept	382.681	18.00921	21.24919	1.09E-22	346.2233	419.1388	346.2233	419.1388
fck	2.82038	0.114244	24.68737	5.3E-25	2.589106	3.051655	2.589106	3.051655
vf	30.78857	1.774045	17.35501	1.18E-19	27.19721	34.37994	27.19721	34.37994
L/d	-11.6358	0.53652	-21.6875	5.3E-23	-12.7219	-10.5497	-12.7219	-10.5497

SUMMARY OUTPUT

Regression Statistics	
Multiple R	0.303988
R Square	0.092409
Adjusted R	0.069719
Standard E	32.92415
Observatio	42

ANOVA

	df	*SS*	*MS*	*F*	*gnificance F*
Regressior	1	4414.818	4414.818	4.072712	0.050323
Residual	40	43359.99	1084		
Total	41	47774.81			

	Coefficients	*tandard Err*	*t Stat*	*P-value*	*Lower 95%*	*Upper 95%*	*ower 95.0%*	*pper 95.0%*
Intercept	138.918	22.31606	6.225026	2.28E-07	93.81559	184.0205	93.81559	184.0205
dy	3.287949	1.629233	2.018096	0.050323	-0.00485	6.580752	-0.00485	6.580752